# Effets de spin et de charge dans les états liés d'Andreev

Cyril Metzger

université
PARIS-SACLAY

# Spin & charge effects in Andreev Bound States

*Effets de spin et de charge dans les états liés d'Andreev*

**Thèse de doctorat de l'université Paris-Saclay**

École doctorale n° 564, Physique en Île-de-France (EDPIF)
Spécialité de doctorat : Physique
Graduate School : Physique. Référent : Faculté des sciences d'Orsay

Thèse préparée au **Service de Physique de l'Etat Condensé (Université Paris-Saclay, CEA, CNRS)**,
sous la direction de **Marcelo GOFFMAN**, directeur de recherche,
et la co-direction de **Hugues POTHIER**, directeur de recherche

**Thèse soutenue à Paris-Saclay, le 10 mars 2022, par**

**Cyril METZGER**

## Composition du jury

| | |
|---|---|
| **Anne ANTHORE**<br>Professeure des universités, C2N, Université Paris-Saclay | Présidente |
| **Ioan POP**<br>Docteur, HDR, Karlsruher Institut für Technologie | Rapporteur & Examinateur |
| **Christian SCHÖNENBERGER**<br>Professeur, Universität Basel | Rapporteur & Examinateur |
| **Juan Carlos CUEVAS**<br>Professeur, Universidad Autónoma de Madrid | Examinateur |
| **Valla FATEMI**<br>Professeur assistant, Cornell University | Examinateur |
| **Julia MEYER**<br>Professeure des universités, CEA, Université Grenoble-Alpes | Examinatrice |
| **Marcelo GOFFMAN**<br>Directeur de recherche, CEA, Université Paris-Saclay | Directeur de thèse |

THESE DE DOCTORAT
NNT : 2022UPASP032

*Spin & charge effects in Andreev Bound States*


This document was typeset with KOMA-Script and LaTeX using the kaobook class available at:
https://github.com/fmarotta/kaobook

*À Miss Sarriette, mon épice la plus précieuse*

*"C'est l'inconnu qui m'attire. Quand je vois un écheveau bien enchevêtré, je me dis qu'il serait bien de trouver un fil conducteur."*

– Pierre-Gilles de Gennes, Le Monde, 1991

# Remerciements

Au terme de ces trois années et demie de thèse, je me sens un besoin fort d'exprimer mes remerciements et ma gratitude la plus sincère pour toutes les personnes, collègues et amis qui ont contribué à cette thèse et son aboutissement, et qui m'ont accueilli, côtoyé, soutenu, supporté pendant ces quelques années qui me resteront gravées comme parmi les plus belles de ma vie parisienne. Je prends le temps aujourd'hui pour le faire, d'une façon qui pourra peut-être sembler maladroite par l'impression qu'elle donne — un recueil longuet d'anecdotes personnelles et de blagues d'initiés davantage qu'une liste succincte de remerciements formels — mais peut-être aussi ce choix de format rendra-t-il davantage compte du message premier que j'aimerais donner à ces quelques pages, dont il est devenu l'usage d'orner le préambule d'une thèse tant elles décrivent l'aspect essentiel que l'histoire souvent oublie quand elle ne se souvient que des seules publications et de la production scientifique : l'importance de garder trace de l'aventure humaine, de l'esprit et du souffle qui ont animé un groupe et qui l'ont fait vivre.

Ces années dans le groupe Quantronique ont été pour moi d'une grande richesse intellectuelle et l'occasion d'un travail sur soi qui m'a beaucoup épanoui et donné en maturité. Des années pleines d'émotions, de défis, de curiosités et de découvertes, chacune tout autant scientifiques qu'humaines.

Avant tout, je me sens un besoin irrépressible et tout particulier d'exprimer mes remerciements les plus chaleureux à mes deux directeurs de thèse favoris, Marcelo Goffman et Hugues Pothier. Travailler à vos côtés est pour moi une source d'enrichissement continuel et de dépassement. Quelles joie et satisfaction, alors que je signe l'écriture de ce manuscrit, de contempler du haut de ces trois années et demie tout le chemin parcouru. Même s'il faut être prudent — toujours ! — dans l'usage du superlatif, je le dis sans hésiter : je n'aurais pu espérer meilleure formation à la recherche que celle que j'ai vécue à vos côtés. Je me sens dans l'âme une gratitude éternelle à votre égard pour tout ce que vous m'avez enseigné, transmis, inspiré et suscité en moi. Grâce à vous, j'ai pu préparer ma thèse dans les meilleures conditions, bénéficier d'un encadrement exceptionnel par sa qualité, son engagement et sa rigueur que beaucoup envieraient, mais aussi découvrir la vraie réalité de la physique expérimentale et du monde de la recherche, celle qui avance quand on ose mettre les mains dans le cambouis et s'y donner entièrement. Merci aussi pour toute l'application que vous avez mise à la relecture attentive de ce manuscrit, pour vos encouragements et votre soutien inconditionnel pendant les petits coups de mou de la rédaction et la dernière ligne droite.

Hugues, les mots me manquent pour t'exprimer toute ma reconnaissance et mon amitié. Tu as été un encadrant de thèse fabuleux, un mentor, et bien plus. Je suis fasciné par ta vivacité d'esprit, ton efficacité et ta rigueur incroyable dans tout ce que tu fais, tes blagues, ton humour si génialement décalé qui imprègne chaque discussion, et ton sens si unique de l'autodérision. Fasciné aussi par ta curiosité incessante et ton côté joueur qui m'évoque une grande sensibilité et un émerveillement pour la physique et tout ce qui t'entoure, que je trouve formidablement motivant et inspirant. Merci pour ta générosité incroyable, ta disponibilité en toute circonstance et pour la grande confiance que tu m'as toujours accordée. Je garde un souvenir nostalgique de tous les moments échangés au labo et en dehors ; de nos nombreux dîners rue Alphonse Daudet, des soirées jeux autour du *Havre* et d'*Agricola*, de nos parties interminables de Lomo (« *Ah, là il y a deux groupes !* »), de nos apéros pistaches/Bénédictine pour nous mettre en route (Louange éternelle à Ourdia pour nous avoir initié aux délices de Fécamp !) et de la traditionnelle tisane à la verveine en fin de soirée pour ne pas piquer du nez avant la barre des 200 points. Merci aussi de m'avoir fait tant profiter de votre ludothèque exceptionnelle (dédicace spéciale pour *Ricochet robots*, *Azul*, *le 6-qui-prend* et les parties de *Mito* avec Max) et à chaque fois que j'étais convié chez toi et Katrin, de vous être « *chargé de mon bonheur pendant tout le temps que j'étais sous votre toit* » (la formule est de Brillat-Savarin).

Merci Katrin pour tous tes conseils et astuces en matière de cuisine, pour m'avoir partagé tes recettes, fait découvrir l'incroyable épicerie *Izraël*, initié à la gastronomie d'Ottolenghi, et pour tous tes bons plats qui vont beaucoup me manquer (souvenir éternel des figues à la mélasse de grenade, des asperges vertes aux amandes grillées et du plateau de fromage toujours incroyablement garni).

Souvenir ému aussi de notre atelier pâtisserie pour la confection des Stollen, du week-end de Novembre à Bayeux, de la visite guidée de la cathédrale et ses coulisses par les deux experts mondiaux de la Normandie médiévale, du concert privé d'orgue, du verre de pommeau chez François Neveux, et de notre échange absurdement drôle sur la Sprachmagie et le « Dingen des Dinges » dans la pensée de Heidegger.

Marcelo, merci d'avoir été un directeur de thèse exceptionnel, pour ton écoute toujours attentive, tes encouragements et ton soutien inconditionnel (*'Vamos Cyril !!'*), et ta disponibilité à toute épreuve : il n'était à vrai dire jamais très difficile de te trouver, puisqu'il suffisait de tendre un peu l'oreille et d'être attentif aux lâchers stochastiques de *'Qué boludo !'* affectueux et aux airs de tango déclamés dans les couloirs (je t'ai d'ailleurs plus d'une fois fait sursauter violemment en déboulant brusquement dans ton bureau ou dans la salle de manip où tu pensais travailler sans être dérangé !). Merci pour ton enthousiasme et la chaleur que tu as toujours mise dans chacun de nos échanges ; tu apportes une énergie incroyable à tout le groupe par ta joie de vivre et ta personnalité si unique. Qui d'autre que toi au labo saurait esquisser quelques pas de tango passionnés au beau milieu d'une conversation, ou encore rythmer sur les airs de *Madame Ivonne* de Julio Sosa la lecture des croix d'alignements pendant les lithos électroniques ? Marcelo, c'est aussi un grand cœur qui t'accueille le matin avec une part du meilleur halva à la pistache de tout Paris ; et qui te garde bien au chaud les derniers alfajores alors que tous les gourmands du labo n'ont qu'une idée, se précipiter dessus. Un grand merci aussi pour la passion que tu m'as transmise de l'Argentine et de sa culture, notamment le goût pour la Yerba maté qui m'a accompagné pendant toute la thèse, et sauvé plus d'une fois la mise pendant les soirées interminables de rédaction. J'ai souvenir aussi de tes envolées lyriques à l'hélium, de notre compétition amicale à la cantine pour la dernière crème brûlée ou le dernier ramequin de fromage blanc, de nos fous rires en imitant John Malkovich dans *Burn After Reading* et la scène d'anthologie du comptage des vis par Ricardo Darín dans *Il Chino* (*¿ Cómo sé que son cien gramos, pedazo de pelotudo ? ¡ Porque siempre le pongo de más ! ¿ Cómo sé que sos un pelotudo ? Porque tenés cara de pelotudo*). Souvenir aussi de la soirée pizza avec la Ferrari G3 et des parties inoubliables de ping pong à Aussois avec la bande des Andreeviens et la randonnée mythique au barrage.

Un autre Argentin à qui je dois tant, c'est Leandro, qui m'a appris tous les fils, tous les rouages du métier : de la micro-soudure et des tricks de nanofab à la théorie des bogoliubons et des spineurs de Nambu. J'espère un jour être pour un autre thésard un aussi bon postdoc que celui que tu as été pour moi. J'ai adoré la complicité qu'on a développée tous les deux. Travailler à tes côtés a été une vraie aventure humaine, riche en émotions et il faut le dire : en sensations fortes ! car Leandro, c'est tout un personnage. . . une passion débordante et une ténacité parfois têtue qu'on ne retrouve que chez les Argentins (*'El ego es ese pequeño argentino que todos llevamos dentro'*), mais qui n'a d'égal que son grand cœur et son amitié si précieuse. Je ne compte plus nos fous rires et déconnades quotidiennes, nos blagues, nos jeux de mots, nos citernes de maté partagées chaque jour, nos soirées innombrables passées coudes à coudes à faire fonctionner la manip, nos trajets quotidiens à vélo et la montée mythique du plateau de Saclay à Vauhallan où nos chemins finissaient toujours pas se croiser. Tu m'as toujours impressionné par ton dynamisme et ta motivation, par ton engouement en toute chose que l'on retrouve si bien par exemple dans ton amour pour la culture et la chanson française ; maniper en chantant Brel, Brassens et Barbara était devenu presque naturel ! Pendant cette thèse, je n'aurais pas réussi hélas l'exploit d'apprendre jusqu'au bout l'espagnol, mais je repars tout de même avec quelques classiques. Merci de m'avoir initié à la Cumbia et au tango argentin. Gilda, Mercedes Sosa, Atahualpa Yupanqui et Goyeneche font maintenant partie de mon répertoire et avec eux, je découvre toujours un peu plus de cette si belle Argentine dont tu m'as fait tant découvrir toi aussi et que je rêve toujours plus de visiter ! Peut-être un jour, la Patagonie. . . *'el que pisa nuestro suelo, no se va si toma un mate'*. Je me souviens des soirées lomo où tout était permis, de nos fous rires sur Maïté et la cuisine de l'ortolan, de ta collection de couvercles de boîtes d'allumettes qui aura traversé les âges. Je me rappelle aussi toutes nos péripéties en Île-de-France, la virée le long du canal de l'Ourcq où la chaîne de mon vélo n'arrêtait pas de casser (et où j'ai bien cru te faire perdre patience !), nos randonnées à Fontainebleau (le massif des Trois Pignons et notre triathlon vélo/rando/vélo des 25 bosses avec toi et Nadim), notre voyage à Barcelone, la randonnée avec Martha dans le massif du Montseny, nos soirées Tapas à Madrid et tant d'autres moments chaleureux qui me laisseront toujours un petit air de nostalgie. Tu vas beaucoup me manquer.

Cristian, merci pour ta sagesse, ta bienveillance, ton incroyable finesse d'esprit et tes remarques toujours extrêmement justes et mesurées. J'ai beaucoup appris avec toi, pas simplement en physique, mais sur la vie ; en méditant par exemple tes proverbes argentins (*'Mas sabe el diablo por viejo que por diablo'*) ou encore *La fábula del gramático y el pescadero* de Gonzalo Celorio qui, plus qu'une fable de la concision pour la rédaction d'articles, est devenue un art de vie et de questionnement au quotidien. Tu m'as toujours frappé par ton incroyable modestie et ton fair-play aussi, qui ont souvent été une belle leçon d'humilité. Merci enfin de m'avoir fait redécouvrir les œuvres de St Exupéry, notamment *Terre des Hommes* qui m'a incroyablement ému (*'Il est inexplicable que nous soyons vivants. . . '*), nos discussions sur Richard Dawkins et le *Gène Egoïste* qui m'ont beaucoup inspiré, et toutes les autres lectures que tu m'as suscitées.

Mes pensées vont aussi à Manas et à Maria qui prennent la relève et que j'aurais aimé connaître davantage. Votre arrivée tardive dans le groupe à cause de la crise sanitaire m'aura empêché de maniper avec vous quand j'en avais encore le temps, avant d'être plongé corps et âme dans la rédaction de ce manuscrit. *Manas, Maria, it was a great pleasure to meet both of you and I wish you all the best for your future carriers! Manas, I will remember with laughter when you came and asked me out of the blue if I could play the postman for Himadri during my visit in Pittsburgh and deliver his mysterious parcel to Amrita, I had the impression I was smuggling something sensitive through the airport, that was a funny one! Maria, I keep great memories from our week at Les Houches and the nice hikes we enjoyed together to the Aiguillette des Houches and the trip to Aiguille du Midi, we were all impressed with your energy, fitness and enthusiasm in all activities. Keep your breezy and cheerful mood and best of luck!*

J'aimerais aussi remercier chaleureusement nos théoriciens préférés, Alfredo et Sunghun, pour leur contribution inestimable à cette thèse et pour tous les bons moments partagés ensemble. Je repense avec sourire à nos premières interactions par téléphone interposé, aux longues heures passées derrière le combiné à disséquer chaque phrase, décortiquer chaque mot du PRX que l'on écrivait alors ; puis la Covid-19 qui aura balayé ces pratiques archaïques pour laisser place à nos réunions Zoom du mercredi après-midi, un peu plus dans l'air du temps, mais tout aussi interminables qu'avant ! *Alfredo, he disfrutado mucho trabajando con vos durante estos cuatro años. Cuando miro hacia atrás y recuerdo los primeros espectros de nanohilos que medimos, nunca habría pensado en aquel momento que llegaríamos a tal nivel de comprensión teórica de este hermoso lío de líneas dispersas. Me siento muy feliz y agradecido por haber contribuido a esta hermosa colaboración. Gracias de corazón y espero que continuemos discutiendo sobre física apasionante todavía durante mucho tiempo. También tengo muy buenos recuerdos de nuestra visita a Madrid con Leandro. Por cierto, me acuerdo de la botellita de excellente 'Vermut de la casa' de Taberna la Concha que no pude llevar al aeropuerto de Madrid y que te dejé como depósito ¡ asegúrate de tenerla fresca para nuestra próxima visita ! Sunghun, it was a great pleasure meeting you and working together on this beautiful topic. I owe you a great deal for the model you developed and that I used many times throughout this thesis, and for all the theory results we asked you to compute. We gave you quite a lot of homework, I have to say ; thank you so much for all the energy you put into it. I wish you all the best and hope you find a great position in Korea.*

Enfin, un merci tout particulier pour Francisco (et Julia), qui à peine arrivé nous a tous épaté par son implication et son apport inestimable au projet. *FJ, tengo maravillosos recuerdos del March Meeting en Chicago, donde jugamos al juego de los pequeños turistas europeos descubriendo América. Fue una semana memorable, llena de emociones y anécdotas: la habitación de hotel sobrecalentada ( ¡ donde la única solución para mantener una temperatura razonable era encender la calefacción y el aire acondicionado al mismo tiempo ! ), la tarjeta del hotel que se desmagnetizaba todos los días, los donuts de colores químicos en el desayuno, la cena con los chicos de Delft en el restaurante de Chinatown donde todos los platos estaban cubiertos de una extraña gelatina y habíamos pedido el doble de comida de la que necesitábamos, el Chicken & Waffles en Harold's, el pollo 'jerk' a la jamaicana que nos hizo hacer novillos durante una tarde, nuestra memorable velada en Giordano's y la enorme 'deep-dish' pizza ( ¡ que se nos habrá resistido hasta el cierre ! ), y finalmente nuestra comida de borrachera en Il Culaccino el último día. Me encantó mucho descubrir Chicago contigo. No me cabe la menor duda de que tendrás una tesis muy brillante y una gran carrera de física ¡ mucha suerte !*

Un immense merci également au groupe Quantronique dans son ensemble. A chacune de mes visites à l'international, j'ai toujours été frappé par la réputation exceptionnelle dont il jouit et l'enthousiasme avec lequel tout le monde m'en parle. C'est qu'il y a bien quelque chose de tout à fait

extraordinaire dans ce groupe. Pour moi, c'est bien sûr la qualité impressionnante de la recherche qui y est menée — une recherche intègre, humble, sincère et surtout incroyablement passionnée — mais aussi l'organisation du groupe et son modèle de recherche qui se distingue par l'implication exceptionnelle de ses permanents, leur encadrement et leur investissement dans toutes les aspects techniques, scientifiques et logistiques de la vie du laboratoire, qui permet de faire perdurer l'expertise au sein du groupe et de transmettre les valeurs et l'esprit si unique et typique de la Quantro des premiers jours. Cet esprit un peu vieille école, mais tellement jeune et débordant, où le plaisir de faire de la physique (et de partager ce plaisir) reste moteur de toute chose. Et cela, on le doit à beaucoup de personnes qui donnent tant à tout le groupe :

Daniel Estève, merci pour ton soutien affectueux et attentionné, ta disponibilité, et pour ta curiosité et ton implication toujours soucieuse dans la vie des doctorants du groupe. J'ai beaucoup apprécié échanger avec toi, pas seulement de physique d'ailleurs : merci pour tes nombreuses recommandations de lectures et en matière de théâtre et événements culturels. J'aime ton sens pratique et des priorités, et ton pragmatisme en toute circonstance, par exemple pour l'aménagement des salles de manip (j'ai souvenir de notre virée mémorable à Conforama où sur un soudain coup de tête nous avions acheté un lot d'étagères pour faire avancer l'aménagement de la nouvelle manip Andreev !). L'achat du vélo de groupe aussi, qui aura dépanné plus d'une fois pour les trajets sur le plateau.

Denis Vion, merci pour ta grande sympathie, ta disponibilité en toute circonstance, les nombreux coups de pouce en Python et Sonnet, et pour ton aide inestimable pour développer l'interfaçage et le pilotage de nos nouveaux instruments. Tu incarnes l'expertise technique du groupe et tu m'as toujours impressionné par ton implication totale dans tous les aspects de la vie du labo, par ta clairvoyance aussi, ta finesse d'esprit et ta logique d'une grande profondeur. Merci enfin pour tous tes encouragements pendant ma période de rédaction et nos longues soirées passées au labo alors que je planchais sur une figure ou la fin d'un chapitre et toi sur la gestion du projet de nouvelle salle blanche dans lequel on t'aura vu t'investir corps et âme avec une détermination extraordinaire. Nos taquineries mutuelles sur qui allait craquer en premier et partir avant l'autre du labo m'auront été, figure-toi, d'un grand soutien moral !

Merci aussi à Hélène le Sueur pour nos nombreuses causeries amicales, les après-midis à écouter Brassens quand nos manips cohabitaient en Pièce 102, et les fous rires à la cantine concernant mes habitudes alimentaires un peu spéciales. Merci aussi pour les nombreux coups de main en matière de cryogénie, ton aide pour les problèmes réseau et de connexion à distance (le nombre de fois où tu m'as sauvé la mise avec Sonnet et les licences fantôme !), l'installation de la bulle Windows et la configuration des serveurs NAS dans les salles de manip, et le développement pendant le confinement d'un système de messagerie interne pour le groupe, via Riot, qui a complètement révolutionné les échanges au sein du groupe.

Philippe Joyez et Pief Orfila, merci pour nos nombreuses discussions vélo et pour les coups de pouce en matière de mécanique et réparation vélo. Avec Marcelo et vous, c'était devenu notre petit rituel de discuter les actus vélos chaque midi, nos coups de gueule sur la route, les pannes et les accidents, et les derniers déboires dans l'aménagement des infrastructures cyclables sur le Plateau et dans Paris. Pief, un remerciement tout particulier pour ton aide et tes conseils précieux pour la nanofabrication. Avec Sébastien Delprat, vous représentez véritablement l'ADN de l'A.d.N.

Merci Emmanuel Flurin pour ton intérêt dans la manip Andreev, tes nombreux conseils avisés et recommandations pour améliorer notre setup, et nos discussions qui ont suggéré la nouvelle géométrie pour notre échantillon. Merci aussi pour le TWPA que tu nous as prêté, sans lequel les mesures temporelles de cette thèse auraient été bien pauvres, et pour nous avoir branché avec *Quantum Machines*.

Merci Patrice Bertet pour m'avoir initié à la Coulée Verte et fait découvrir le fameux chemin du Picotois à Igny comme alternative bucolique à la montée de Vauhallan. C'est en suivant ton excellent cours sur les circuits quantiques au master ICFP que j'ai découvert mon enthousiasme pour ce sujet de recherche et persévéré dans ce domaine !

Je souhaiterais enfin remercier tout particulièrement Pascal Sénat pour la conception d'une grande partie de la mécanique basse température de notre nouvelle manip BlueFors et pour son investissement dans son installation en Pièce 8, ce qui a demandé un travail conséquent. Merci aussi pour ta sympathie au quotidien et nos brefs échanges toujours très agréables.

La force d'un groupe, c'est aussi tous ses thésards et ses postdocs. Ma première pensée va à Marianne Le Dantec, ma camarade de master et sœur jumelle de thèse. Je garde un beau souvenir de nos écoles d'été la première année à Innsbruck et à Bad Honnef, de nos randonnées en montagne et de la fois où on a tous eu quelques frayeurs lors de la traversée du névé, qui aura laissé quelques vilaines égratignures (je m'en suis toujours voulu !). Tu as toujours eu, aussi, une longueur d'avance sur moi pour les questions administratives, et tu m'en as toujours fait gentiment profiter en partageant ton expérience par exemple sur la rédaction et la préparation de la soutenance, ce qui m'a fait gagner un temps précieux et évité bien des déboires avec l'ED. Bon vent à Brest !

Merci aussi à mes aînés : Bartolo Albanese et Emmanuele Albertinale pour l'esprit mafia italienne, les plaisanteries à table et les nombreux délices de Sicile dont vous nous avez fait profiter ; et Nicolas Bourlet pour tes tartes au maroilles et la passation de la gestion de la salle café (mission qui m'aura fait rencontrer bien du monde dans tout le service !). Une pensée aussi pour tous les doctorants du groupe : merci Eric Billaud, pour le bilan carbone du labo et nos taquineries sur l'impact écologique d'un steak de boeuf ; Léo Balembois, notre champion du vélo, pour nos nombreuses discussions cyclisme et notre débat nostalgique sur les roues libres ; merci aussi à Zhiren Wang, qui nous a bluffé par sa maîtrise du québécois, et Louis Pallegoix qui connaît l'histoire de France comme sa poche ; je vous souhaite à tous beaucoup de réussite pour votre thèse !

Un grand merci enfin aux postdocs du groupe pour leur coaching et toutes les connaissances précieuses qu'ils nous transmettent : Daniel Flanigan, pour les innombrables coups de pouce en Python, pour nous avoir mis à la page en nous initiant aux arcanes de PyCharm et GitHub et pour le temps incroyable que tu as consacré pour l'upgrade de Quantrolab en Python 3. Merci aussi à Anil Murani pour ta sympathie et nos discussions toujours intéressées sur la physique d'Andreev ; Miloš Rančić pour tes blagues sur le pays des kangourous, nos brins de causette à vélo toujours plein d'anecdotes et l'humour pince-sans-rire qui te caractérise si bien, et pour ton côté bricoleur et touche-à-tout qui m'aura toujours impressionné (une batterie 1kW sur un vélo, il faut quand même l'oser !). Merci aussi à Vishal Ranjan, Boris Yavkin et Yutian Wen.

Puisse l'esprit de la Quantro perdurer par-delà les âges.

J'aimerais remercier également tous les membres du SPEC que j'ai côtoyés et qui ont contribué par petites touches au bon déroulement de cette thèse. Merci infiniment à Dominique Duet et Vincent Padilla pour la fabrication des pièces mécaniques pour notre manip, et pour les quelques coups de pouce à l'atelier. Plus généralement, j'ai beaucoup aimé nos petites discussions toujours pleines d'humour, surtout quand il s'agissait de collecter les sous pour les consommations café ! Vincent, je me souviens de nos discussions cinéma et de nos fous rires sur les films des Charlots ; merci aussi pour l'exemplaire du *Retour aux Sources*, BD la plus incongrue de toute ma collection. Merci aussi à Carles Altimiras et François Parmentier, mes parrain et tuteur au SPEC pour le suivi attentif de ma thèse et pour leurs encouragements ; Paul Foulquier, qui m'a épaulé efficacement pour la comptabilité et la gestion des commandes pour la salle café ; François Ladieu, pour avoir suivi avec tant de ferveur et de passion les quelques 50 doctorants du SPEC (une tâche que j'imagine bien difficile et infiniment pénible !). Nos entretiens annuels ont été brefs mais toujours incroyablement motivants : merci pour ta vision très inspirante de la recherche et de l'apprentissage, et ton initiation à la philosophie du « désir mimétique » de René Girard, qui nous aura bien fait rigoler. A la cryogénie, merci Philippe Forget (client café le plus fidèle !), Mathieu de Combarieu (pour le coup de pouce avec les MMR3), Patrick Pari, allias « *P.P. la diluette* » pour ses anecdotes nostalgiques et souvenirs de Cryo, et Aurélia Charrier pour tes salutations toujours très chaleureuses à mon arrivée au labo au petit matin. Merci aussi à Nathalie Royer au secrétariat pour ton efficacité administrative hors du commun, ton aide pour l'organisation de mon voyage aux USA et avec la paperasse parfois lourde du CEA, et pour les intercalaires saumon de ta papeterie personnelle qui se baladent maintenant dans les versions papier de ma thèse. Un grand merci enfin à Nadine le Bail, à l'entretien, pour nos bavardages quotidiens dans les couloirs et à la salle café, pour ton sourire, ta bienveillance et ton immense gentillesse en toute circonstance (alors que j'ai laissé plus d'une fois déborder la récup' de café ou encore crotté le sol avec mes chaussures pleines de boue séchée au sortir de la forêt de Gif !).

La réussite de ma thèse, je la dois aussi à Mélissa, Antonietta et Nathalie au restaurant des Algorithmes qui m'ont nourri, alimenté, materné, gâté, chouchouté de tout leur cœur pendant trois ans et demi et avec toute la générosité que les mères seules savent offrir. Vous allez me manquer. La mousse au chocolat du mardi et la crème brûlée du jeudi ont été les véritables jalons psychologiques qui m'ont permis de tenir bond de semaine en semaine et de maintenir le cap au milieu des épreuves. Sans la soupelette journalière et la ration de fromage blanc, sans la piqûre hebdomadaire de coco, sans les tropéziennes et les gâteaux basques, le cœur n'aurait pas été à l'ouvrage. Un grand merci aussi à Didier, à sa bonne humeur contagieuse, sa tchatche amicale et son professionnalisme. Je crois ne pas exagérer en affirmant que les Algorithmes ont été le véritable moteur de cette thèse. Sans eux, la chaudière aurait tourné à vide et le cœur n'y aurait pas été.

J'aimerais remercier aussi nos collègues et amis du Collège de France, Çağlar Girit, Joël Griesmar et Léo Peyruchat, pour nos nombreuses discussions sur la physique d'Andreev, pour le partage du logiciel 3D-MLSI et votre aide pour les simulations magnétostatiques qui ont servi à cette thèse.

Un grand merci aussi à Benjamin Huard et Audrey Bienfait de l'ENS Lyon pour m'avoir invité si chaleureusement et ouvert les portes de votre labo, qui m'a laissé de bien belles impressions. J'aurais beaucoup aimé travailler avec vous et j'espère avoir d'autres occasions de collaborer ensemble à l'avenir. Merci aussi à Réouven Assouly, Alexis Jouan, Arne Bahr, Antoine Essig et Antoine Marquet pour une semaine mémorable aux Houches.

J'aimerais aussi remercier chaleureusement Ramon Szmuk et Yoav Romach de *Quantum Machines* pour leur énorme soutien technique, leur aide précieuse et leur grande implication dans la résolution des bugs liés à l'OPX. Merci aussi pour leur intérêt dans nos expériences et les nombreuses améliorations de notre setup et système de mesure que nos discussions auront suscitées.

Merci enfin à Sergey Frolov, Michael Hartridge, Valla Fatemi et Konrad Lehnert pour leur accueil chaleureux lors de ma tournée aux USA, pour m'avoir fait visiter leur groupe et pour tous les bons moments passés avec eux et leurs étudiants. Je garde un souvenir ému de ce premier voyage aux USA, et de ces 10 jours plein de péripéties qui ont été d'un grand dépaysement. J'aimerais remercier plus particulièrement Valla Fatemi pour sa relecture très attentive de mon manuscrit et les nombreux commentaires et conseils pour l'améliorer. *Thanks a lot Valla for your participation in my PhD committee. I feel very grateful and indebted for your detailed feedback on this manuscript. Thanks also for the very warm welcome you gave me in Cornell and for all the good times spent in Ithaca. I enjoyed very much getting to know you and all our discussions, too. I hope we will have many more such opportunities in the future.*

Il me tient également tout particulièrement à cœur de remercier Cheryl Feuillet-Palma, qui m'a aiguillé vers la Quantro quand j'étais en master et sans qui je n'aurais pas vécu ces si belles années à Saclay. J'ai une pensée aussi pour mes professeurs à l'ESPCI qui m'ont insufflé leur passion pour la physique du solide : Nicolas Bergeal pour son initiation à la mécanique quantique et Dimitri Roditchev qui m'a appris les bases de la supraconductivité (trois heures de BCS à raison de trois ans de Ginzburg-Landau, pas étonnant que cela ait éveillé une curiosité !). J'ai eu la chance aussi, pendant mon année de master à l'ICFP, de suivre des cours de physique particulièrement inspirants ; merci à Benoît Douçot pour ses homélies passionnées sur la Théorie de la matière condensée, à Philippe Lecheminant pour son cours d'une incroyable clarté sur la seconde quantification et les modes de Majorana, à Jean-Noël Fuchs pour son introduction très pédagogique et pleine d'humour à la théorie quantique des champs, à Alberto Rosso pour le meilleur tutorat au monde sur la transformée de Joukovsky, et à Marc Gabay et Marcello Civelli, le duo de choc du LPS à l'humour si génialement décalé.

Si le SPEC est un peu devenu ma nouvelle maison pendant ces quelques années de thèse, je n'oublie pas tous les bons moments passés en dehors du laboratoire. Un grand merci à la Cité Universitaire et à la Maison de l'Île-de-France qui m'ont accueilli et hébergé pendant presque quatre année. J'y ai trouvé l'endroit idéal pour m'épanouir, préparer ma thèse dans les meilleures conditions, mais aussi m'en évader et me changer les idées dès que j'en ressentais le besoin. Les moments passés à la Cité Universitaire ont été autant de bouffées d'air frais, de convivialité, d'invitation au voyage, à l'ouverture et au partage, sans lesquelles mon expérience de doctorat n'aurait pas été la même. Pendant la pandémie de Covid-19 et la période de confinement que nous avons tous traversée, j'ai pu trouver à la MIDF la solidarité et la camaraderie qui m'ont permis de garder la motivation et de maintenir le cap.

Alors que mes travaux de thèse se sont trouvés soudainement gelés par la situation, avec la fermeture du laboratoire et l'impossibilité d'expérimenter, j'ai pu aller de l'avant et rester productif sur d'autres fronts. Je ne l'aurais peut-être pas été sans la Cité universitaire, si j'étais rentré au domicile familial ou si je m'étais retrouvé, comme beaucoup, contraint et cloisonné sur mon petit balcon parisien au milieu d'une capitale en souffrance. C'est une chance incroyable que nous avions — humbles privilégiés en cette période si tragiquement exceptionnelle — de pouvoir profiter de tous les espaces verts du campus (alors fermés aux Parisiens !), de n'avoir rien que pour nous le magnifique parc de la Cité Universitaire : ses cerisiers du japon, les allées de ginkgo, sa glycine et ses roseraies et quelques puissants hectares en fleur d'une belle nature à grignoter ! ce parc qui m'a permis de m'évader chaque jour, de refaire le plein de soleil et de m'aérer dès que le télétravail prolongé commençait à exhaler une odeur de renfermé. C'est tout cet endroit si singulier et si unique, ce sentiment déferlant de vie et de liberté qui anime le campus, nos nombreuses soirées et nos fêtes innombrables, tout cela qui va tant me manquer et que j'aimerais aujourd'hui embrasser sur le papier.

J'ai une pensée forte pour tous mes amis de la Cité Universitaire, pour toutes les rencontres que j'ai pu y faire sans lesquelles ces années de doctorat n'auraient pas eu la même saveur. Une attention toute particulière d'abord pour Keipi et Shreeshti, mes deux âmes sœur, avec qui j'ai partagé mon quotidien pendant la période Covid. Nous avons vécu et échangé tellement de choses ensemble qu'il faudrait un chapitre entier de cette thèse pour étaler le récit de nos péripéties nombreuses et exprimer ce lien, cette amitié, cet attachement si fort que nous avons développé tous les trois. C'est d'abord un retour à l'essentiel, à l'émerveillement devant les petites choses et les petits plaisirs de la vie que nous avons partagé et redécouvert ensemble. Par nos sorties quotidiennes dans le parc, notamment : avec la venue presque providentielle du printemps qui coïncidait avec le décret du premier confinement, nous nous amusions à recenser chaque jour les nouvelles fleurs apparues dans le parc, à suivre pas à pas le déroulement devant nos yeux du printemps 2020, la profusion des couleurs et des parfums ; un printemps aux mille trésors dont le rythme de la vie citadine et étudiante nous avait distrait et dont nous avions avec le temps presque oublié la grâce. Le souvenir aussi de nos sessions yoga au milieu de cette nature en fleur et des 108 salutations au soleil, au réveil, pour échauffer le corps et l'esprit.

Nos journées de confinement à la Cité Universitaire ont été rythmées aussi par nos ateliers quasi-quotidiens de cuisine et de pâtisserie ! ces deux mois ont été bien plus qu'une initiation aux cuisines vietnamienne et népalaise, c'est un véritable voyage en Asie du Sud-Est que vous m'avez fait vivre (comme si j'y avais été physiquement !), une découverte de sa gastronomie (aux saveurs si riches et exotiques pour un Européen !), et l'expérience de sa culture et de ses traditions ancestrales, comme la fête de la mi-automne (à l'occasion de laquelle nous avions confectionné une quantité déraisonnable de mooncakes !) et les festivités du Nouvel An lunaire Vietnamien, le Têt, qui nous aura demandé plusieurs semaines pour préparer tous les pickles! C'est aussi plein de mets et de saveurs que vous m'avez fait découvrir : la douceur du Nepali Chiya — le thé au lait épicé népalais dont la préparation était devenue comme un rituel chaque aprèm, et le café aux œufs vietnamien. Merci Shreesh de m'avoir initié au *Dark side of the momo* et Keipi pour les *Bánh bao*, leur homologue vietnamien si moelleux. Merci aussi Keipi de m'avoir révélé ta recette secrète pour la sauce aigre-douce, pour m'avoir préparé tant de plats (dont le délicieux *Chè chuôi* au gingembre), montré comment cuisiner les *Bánh mi* et les crêpes vietnamiennes *Bánh cuôn* et *Bánh xèo*, et initié à l'art subtil du *Phô*. Souvenir aussi de nos pérégrinations interminables dans Paris à la recherche des élusives feuilles de pandan, des courgettes amères, *Momordica charantia* que je n'aurais jamais appris à cuisiner sans vous deux, et de *Momordica cochinchinensis* pour la préparation du traditionnel *xôi gâc*. Shreeshti, j'ai un souvenir ému de notre défi 'biryani' dans lequel j'ai adoré m'investir : quels efforts pour rassembler tous les ingrédients et la trentaine d'épices nécessaires, et puis l'excitation après 4h de préparation et de cuisson quand on a ouvert la marmite et respiré les mille effluves (*'Despite the staggering number of spices, a Kolkata mutton biryani is not spicy'*). Je repense aussi à nos retrouvailles chaque week-end au Viahe caphe à Bastille, qui était devenu un peu comme l'extension de notre quartier général de la cuisine du 4$^{è}$ étage à la MIDF, et à notre ballade sur le Viaduc des Arts une après-midi d'été.

Je repense enfin à toutes mes belles rencontres à la Cité Universitaire. A Sofia, qui m'a ouvert son cœur. Je te dois ma passion dévorante pour la cuisine et la culture indienne, cette journée à Rennes où tu as passé la matinée aux fourneaux à me préparer un thâli me restera à jamais en mémoire, et quelle nostalgie quand je repense à ton fish curry et aux aloo paratha.

A Cecilia aussi, à tous nos moments passés ensemble, nos petits déjeuners pancake/dulce de leche au soleil sur la pelouse de la Cité U à écouter les Velvet Underground, nos ateliers empanadas, nos gros fous rires pendant les films de Gastón Duprat ('La ballena de la pampa'), notre randonnée à Giverny et le long de la Loire (cet après-midi irréelle à Chinon, ivres de fouasses et de vin, et notre promenade à Provins sous les remparts).

Je ne peux bien sûr pas oublier le cartel péruvo-colombien sans qui l'ambiance à la MIDF n'aurait pas été la même : Laura, infatigable sur le dance floor et ton don inégalé pour mettre l'ambiance aux soirées (*Arriba, abajo, al centro y pa dentro !*), tu nous as donné l'amour de la Colombie et de sa cuisine : on se souviendra tous de ta bandeja paisa monumentale (et le coup du chicharrón au bicarbonate !), des arepas et patacónes, et de la soirée tamales ; Omar et sa bonne humeur permanente, cuisinier hors pair (ton lomo saltado, une tuerie !) et toujours prêt à toute heure du jour et de la nuit pour te préparer un pisco sour, à danser la salsa et tout simplement faire la fête ; Dominique et Sari, charmantes en toute situation, vous allez me manquer ; Rodrigo pour le déjeuner clandestin impromptu à La Escondida et pour la découverte de la chicha morada et la mazamorra morena ; et Ernesto, le grand Sage de la bande, toujours partant pour une discussion philosophique. Merci aussi à Murat, pour son grand cœur et sa façon si unique de cuisiner les chicken wings ; à Yelda pour sa sensibilité, sa joie de vivre et son inspiration infinie en matière musicale ; à Eduardo, pour nos after hours à la cuisine du 4è, nos nombreuses discussions passionnées sur la médecine et la santé numérique, et cette soirée mémorable où tu nous as préparé ta recette basque de confit de cœurs de canard glacé au vinaigre de framboise ! Pensée aussi pour Solenne qui m'a appris à cuisiner sans coriandre et sans piment (je te souhaite le meilleur pour ton voyage linguistique en Corée), à Gog pour les gros fous-rires ; à Annalisa pour nos discussions sur les mystères dantesques et l'art de la pâte carbo' véritable ; à Thomas Jouannès docteur ès histoire/économie/géographie/culture sud-asiatique pour ta tchatche contagieuse et nos nombreux fous rires ; à Sami pour l'initiation à la coupe égyptienne et aux 50 nuances de poulet ; à Brennan pour les soirées couscous-harissa et la nostalgie irlandaise ; à Camilo pour ses arpèges à la guitare sur des airs de Yupanqui et nos discussions sur le nucléaire ; à Amina et Côme mes voisins de palier préférés, à Flaminia, Bastien, Julie, Yang, et tant d'autres.

Une belle pensée aussi pour Evrard, mon infatigable compagnon d'aventure, toujours au rendez-vous pour une nouvelle sortie (et la binouz' pour la clôturer), à nos innombrables pérégrinations en banlieue francilienne (le fin fond de l'Essonne et la Seine-et-Marne n'ont plus de secret pour nous !) et à nos virées mythiques au Falstaff. La dégustation du « Oh my God » du haut de ses 6 étages de barbaque restera dans l'histoire. Pensée émue au souvenir de nos errances à Mennecy et à Meaux, les pieds dans la gadoue à Meudon, l'Isle-Adam et nos déboires cartographiques à Corbeil-Essonne, le bar belge d'Alfortville et ses 300 bières au menu, la cueillette des muguets en forêt de Rambouillet, le kit de survie banane/choco au retour de Carrières-sur-Seine, notre escapade à l'ISG, à St Cloud, en Malmaison et au bois de St Cucufa. Merci aussi à Cécile et Tristan pour l'initiation aux joies cataphiles et la découverte souterraine du gruyère parisien.

Merci à Lukas Splitthoff, Matthias, André et Murad, mes compagnons cyclistes et physiciens pour notre randonnée inoubliable le long du Danube. *Special thanks to Lukas, my German physicist friend, for all the good times spent together around Europe, and for the lifelong memories of our biketour to Belgrade. I hope we'll keep on sharing our passion for cycling and physics and to ride together for many more adventures to come!* Merci Murad pour ta gentillesse, pour tes nombreuses invitations aux concerts de musique azérie, et pour toutes nos virées cyclistes en Île-de-France. Merci à mes copains de l'ESPCI : Boule, Quille, Mons', Not', Pôl, Gourme, Mousse et JC, pour nos ripailles mémorables et toutes nos sorties et soirées qu'il serait vain ici d'essayer de dénombrer.

Pour finir, je tiens à remercier toute ma famille qui m'a toujours soutenu et encouragé dans tout ce que j'entreprenais. Merci à mes parents, Daniel et Isabelle, pour m'avoir fait comme je suis, pour votre amour et soutien inconditionnel, et pour avoir pu vous rendre disponible le jour J pour assister à ma soutenance. Merci à mes frères, Arnaud et Alexis, à qui je dois tant, et à mes grands-parents pour tous les magnifiques souvenirs que vous nous laissez, et les valeurs incroyablement précieuses transmises pendant toutes ces années.

Merci enfin à Sarah, Miss Sarriette, qui illumine mes jours.

A Paris, le 9 mai 2022.

**Le groupe Quantronique, mai 2018**.
*De gauche à droite, 1er rang :* Jessica Fernanda Da Silva Barbosa, Lukas Splitthoff, Cyril Metzger, Vishal Ranjan, Riya Sett, Emmanuele Albertinale, Denis Vion, Hugues Pothier.*2è rang :* Ambroise Peugeot, Daniel Estève, Leandro Tosi, Marcelo Goffman, Cristian Urbina, Milos Rancic, Marianne Le Dantec, Philippe Joyez, Moonju Lee, Hélène le Sueur. *3è rang :* Daniel Flanigan, Igor Mekhov, Bartolo Albanese, Nicolas Bourlet, Patrice Bertet, Anil Murani, Pascal Sénat.

# Abstract

We probe experimentally the properties of Andreev states in superconducting weak links based on Indium Arsenide (InAs) nanowires. Andreev states are localized fermionic states that appear at the junction (or weak link) between two superconducting electrodes. They are at the core of the microscopic description of the Josephson effect. InAs nanowires implement finite-length weak links characterized by spin-orbit coupling and electrostatically-tunable conduction properties.

By coupling the weak link to a high quality factor microwave resonator, following the circuit quantum electrodynamics (cQED) approach, the Andreev states can be efficiently isolated from external noise, and the resonator frequency readout gives access to their microscopic occupancies. We model this coupling to achieve optimal sensitivity and to understand in detail the response of the resonator coupled to the weak link.

We have performed the microwave spectroscopy of Andreev states, and measured their dependence on the superconducting phase difference. The spectra reveal two effects. The first one is the lifting of the states' spin degeneracy due to spin-orbit coupling. This results in spectroscopic lines characterizing the change of the spin state of a single quasiparticle in the weak link. The second one is the influence of Coulomb interactions between quasiparticles, reminiscent of the splitting in singlet and triplet states of two interacting spin-1/2 electrons. Theoretical modeling of finite-length weak links allows to account for these effects.

We also characterize the Andreev states by time-resolved measurements. Quantum bits (qubits) are obtained using either the even-parity ground state and a state where a pair of quasiparticles is excited; or two odd-parity states with a quasiparticle trapped in different Andreev states. We have measured the lifetimes and coherence times of these two types of "Andreev qubits".

# Résumé

Nous présentons les résultats d'expériences sondant les propriétés des états d'Andreev dans des liens faibles supraconducteurs à base de nanofils d'Arséniure d'Indium (InAs). Les états d'Andreev sont des états fermioniques localisés qui apparaissent à la jonction (ou lien faible) entre deux électrodes supraconductrices. Ils sont au coeur de la description microscopique de l'effet Josephson. Les nanofils d'InAs permettent d'obtenir des liens faibles de longueur finie, caractérisés par un couplage spin-orbite et des propriétés de conduction ajustables électrostatiquement.

Par la technique d'électrodynamique quantique en circuit (cQED), qui consiste à coupler le lien faible à un résonateur micro-onde de fort facteur de qualité, les états d'Andreev peuvent être isolés efficacement du bruit extérieur, et la lecture de la fréquence du résonateur donne accès à leur occupation microscopique. Nous modélisons ce couplage pour atteindre une sensibilité optimale et comprendre en détail la réponse du résonateur couplé au lien faible.

Nous avons mesuré les spectres des états d'Andreev, et leur dépendance en différence de phase supraconductrice. Ces spectres mettent en évidence deux effets. Le premier est la levée de la dégénérescence de spin des états du fait du couplage spin-orbite. Cela se traduit par des lignes spectroscopiques caractérisant le changement de l'état de spin d'une quasi-particule unique dans le lien faible. Le second est l'influence des interactions coulombiennes entre quasi-particules, réminiscentes de la séparation entre états singulet et triplet de deux spins 1/2 en interaction. La modélisation théorique des liens faibles de longueur finie permet de rendre compte de ces effets.

Nous caractérisons également les états d'Andreev par des mesures temporelles. Des bits quantiques (qubits) sont obtenus soit en utilisant l'état fondamental pair et celui où une paire de quasi-particules est excitée ; soit deux états impairs avec une quasi-particule piégée dans des états d'Andreev différents. Nous avons mesuré les temps de vie et de cohérence de ces deux types de « qubits d'Andreev ».

# Synthèse

Cette thèse de physique s'inscrit dans le domaine des **circuits quantiques**. La motivation initiale de ce champ de recherche, dans les années 1980, était d'explorer la possibilité d'une variable macroscopique obéissant aux lois de la mécanique quantique. En particulier, il s'agissait de savoir si cette dernière, alors jusque-là restreinte à l'explication des phénomènes fondamentaux à l'œuvre à l'échelle atomique et subatomique, pouvait également se manifester par des effets visibles à notre échelle, notamment dans des circuits électriques. L'idée alors était de recourir aux matériaux dits *supraconducteurs* : ils sont caractérisés par un gap d'énergie dans leur densité d'états, ce qui confère une protection naturelle contre les fluctuations thermiques et les excitations de basse énergie de type quasi-particule.

Un des éléments de base des circuits supraconducteurs est la jonction tunnel Josephson, qui consiste en une fine couche d'un matériau isolant pris en sandwich entre deux électrodes supraconductrices. A tension nulle, une telle nanostructure a la particularité de pouvoir supporter un courant non-dissipatif déterminé par un paramètre macroscopique : la différence de phase supraconductrice à travers la jonction. En 1985, Martinis, Devoret et Clarke ont démontré que cette dernière suivait les lois de la mécanique quantique de sorte qu'un circuit construit autour d'une jonction Josephson pouvait présenter des niveaux d'énergie quantifiés [1]. Cette découverte a ouvert la voie à un vaste domaine de recherche exploitant la non-linéarité du supercourant dans les jonctions Josephson pour concevoir des "atomes artificiels" aux propriétés accordables. Les jonctions Josephson sont aujourd'hui au cœur de nombreuses technologies visant à utiliser les modes électromagnétiques d'un circuit supraconducteur pour implémenter des "bits quantiques" (qubits) et y stocker de l'information [2, 3].

## 1 Etats d'Andreev : le degré de liberté interne d'une jonction Josephson

Du point de vue fondamental, l'effet Josephson est en fait bien plus riche, et pas une simple spécificité des jonctions tunnel. Le supercourant qui circule à travers un lien faible entre deux matériaux supraconducteurs est une conséquence directe et générique de la cohérence de l'état supraconducteur. Le lien faible peut être une fine couche isolante ou métallique, une constriction ou tout autre type de conducteur cohérent : indépendamment de la nature spécifique du lien, le supercourant est donné par une fonction périodique de la différence de phase supraconductrice entre les deux électrodes [4]. Une description microscopique de cet effet a été donnée en terme d'états électroniques localisés qui se forment dans chaque canal de conduction du lien faible : les **états liés d'Andreev (ABS)** [5, 6, 7, 8, 9]. Ces derniers peuvent être perçus comme les modes électroniques d'un guide d'onde aux parois supraconductrices : ils résultent des réflexions cohérentes que subissent les électrons du lien faible à chacune de ses deux interfaces et que l'on connaît sous le nom de réflexions d'Andreev [10, 11, 12]. Bien que cette formulation remonte à près de soixante ans, ce n'est qu'il y a une dizaine d'années que des preuves directes des états d'Andreev ont été obtenues expérimentalement. Ils ont depuis été révélés grâce à des techniques variées et dans divers systèmes, allant des nanotubes de carbone [13] et des contacts atomiques [14, 15, 16] aux nanofils semi-conducteurs [17, 18, 19].

Dans une jonction tunnel, la non-linéarité du supercourant est une manifestation des propriétés de l'état fondamental de millions d'états d'Andreev agissant collectivement. Alors que la grande majorité des électrons de conduction participent à la réponse collective bosonique du condensat supraconducteur, chaque état d'Andreev constitue *individuellement* un degré de liberté fermionique, capable d'être peuplé par des excitations électroniques connues sous le nom de quasi-particules de Bogoliubov. Si la jonction tunnel à la base des qubits supraconducteurs actuels contient une densité d'états bien trop importante pour que ces derniers puissent être manipulés individuellement, d'autres types de nanostructures, conçues de telle sorte à ce que le lien faible ne conduise qu'à travers quelques canaux bien transmis, n'accommodent en fait qu'un petit nombre d'états d'Andreev. Comme illustré en Figure 1, ces derniers sont alors suffisamment bien séparés en énergie pour devenir adressables à l'aide d'excitations micro-ondes.

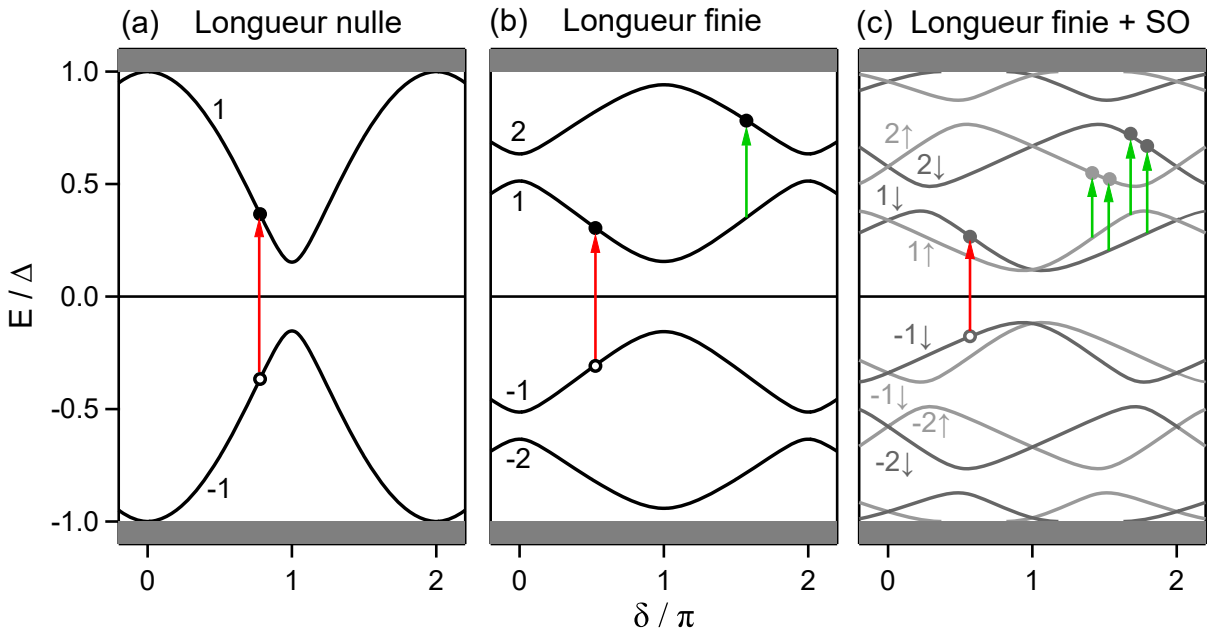


**Figure 1:** Spectre en énergie des états d'Andreev en fonction de la différence de phase $\delta$, pour un lien faible (a) de longueur nulle, (b) de longueur finie, et (c) de longueur finie en présence d'un couplage spin-orbite (SO). Dans (a,b), toutes les lignes sont dégénérées en spin. Dans (c), les lignes en gris foncé et gris clair correspondent aux états d'Andreev avec différents pseudo-spins $\uparrow, \downarrow$. Dans l'état fondamental, tous les niveaux d'énergie négative sont occupés, à la fois les niveaux discrets d'énergie $-\Delta < E \leq 0$ associés aux états d'Andreev, ainsi que le continuum d'états aux énergies $E < -\Delta$. Deux types de transitions peuvent se produire : les transitions de paire (PT), représentées par des flèches rouges et qui créent deux excitations supplémentaires (électron + trou), et les transitions à une seule quasi-particule (SQPT), en vert, qui consistent à exciter une quasi-particule piégée dans un niveau vers un état de plus haute énergie.

L'intérêt de ces systèmes est que l'occupation microscopique des états d'Andreev détermine une quantité macroscopique mesurable : le flot du supercourant à travers le lien faible. Ainsi, en couplant un "atome d'Andreev" à un résonateur micro-onde, il est possible de détecter son état quantique, car l'occupation microscopique des états modifie la fréquence de résonance du système couplé, qui peut être sondée par réflectométrie micro-onde. Le rôle du résonateur est double : il permet non seulement de mesurer l'état du système mais également de l'isoler efficacement du bruit externe. En appliquant un deuxième signal micro-onde pour exciter des transitions entre états d'Andreev, on peut en balayant sa fréquence remonter au spectre d'excitations du lien faible. En effet, dès que le signal est résonant, il modifie l'occupation des états, ce qui se traduit par un décalage mesurable de la fréquence du résonateur. Cette idée est à la base des expériences dites d'**électrodynamique quantique en circuit (cQED)** [20]. Elle a été mise en œuvre précédemment dans le groupe Quantronique pour sonder la réponse micro-onde des états d'Andreev dans la configuration la plus minimale possible : un contact ponctuel à un atome entre deux électrodes supraconductrices.

Dans un contact atomique, une seule paire d'états d'Andreev se forme dans le gap supraconducteur, à une énergie $-\Delta \leq E \leq +\Delta$ (cf. Figure 1(a)). En irradiant le lien faible avec des photons micro-ondes résonants, on peut promouvoir une quasi-particule d'un niveau à l'autre (flèche rouge dans la Figure 1(a)), via une **transition de paire** (PT), dénommée ainsi car elle revient à créer deux excitations microscopiques : une de type "trou" dans le niveau du bas et une seconde de type "électron" dans celui du haut. La détection et manipulation de ces paires d'excitations a été démontrée pour la première fois dans le groupe Quantronique dans l'expérience sur les contacts atomiques, donnant lieu à des applications concrètes telles que le "qubit d'Andreev", dont les propriétés de cohérence ont fait l'objet d'une précédente étude [21]. Dans un lien faible de longueur finie, plusieurs paires d'états d'Andreev existent et un deuxième type de transition micro-onde peut avoir lieu : une quasi-particule piégée dans un état peut absorber un photon et être excitée vers un autre état d'énergie supérieure. Ce processus, auquel on se réfère sous le nom de **transition à une quasi-particule** (SQPT), est illustré par une flèche verte dans la Figure 1(b). Comme les états d'Andreev sont en général dégénérés en spin, l'utilisation de ces transitions pour la manipulation du spin des quasi-particules est jusque-là restée hors de portée.

# 2 Observation de la *structure fine* des états d'Andreev et manipulation d'un spin unique

Le rôle du spin dans les excitations fermioniques est un sujet de recherche très en vogue dans le domaine des circuits supraconducteurs hybrides [22, 23, 24] et de la supraconductivité topologique [25, 26, 27, 28]. En 2003, il a été proposé que le spin d'une quasi-particule confinée dans un lien faible possédant un fort couplage spin-orbite pouvait être utilisé pour implémenter un qubit [29, 30, 31, 32]. En effet, pour des liens faibles de longueur finie, la combinaison d'une différence de phase supraconductrice, qui brise la symétrie de renversement du temps, et d'un couplage spin-orbite, qui brise l'invariance par rotation du spin, est suffisante pour lever la dégénérescence de spin des états d'Andreev, donnant lieu à un supercourant Josephson dépendant du spin, et ce en l'absence d'un champ magnétique externe [33, 34]. Comme illustré dans la Figure 1(c), on s'attend alors à avoir quatre transitions à une quasi-particule possibles entre deux doublets d'Andreev résolus en spin. Deux d'entre elles conservent le spin de la quasi-particule, tandis que les deux autres le renversent. Réaliser de telles transitions reviendrait donc à manipuler le spin d'une quasi-particule unique piégée dans le lien faible.

Dans ce contexte, le but de cette thèse était d'adresser le degré de liberté de spin des états d'Andreev et d'étudier sa physique. Pour ce faire, nous avons conçu une expérience d'électrodynamique quantique basée sur des liens faibles Josephson définis dans des **nanofils d'arséniure d'indium (InAs)**, connus pour être le siège d'une forte interaction spin-orbite de type Rashba [35, 36]. Les nanofils utilisés dans cette thèse ont été fabriqués par croissance épitaxiale à l'Université de Copenhague au sein du Center for Quantum Devices. A l'issue de leur croissance, ils sont recouverts sous ultravide d'une gaine nanométrique d'aluminium.

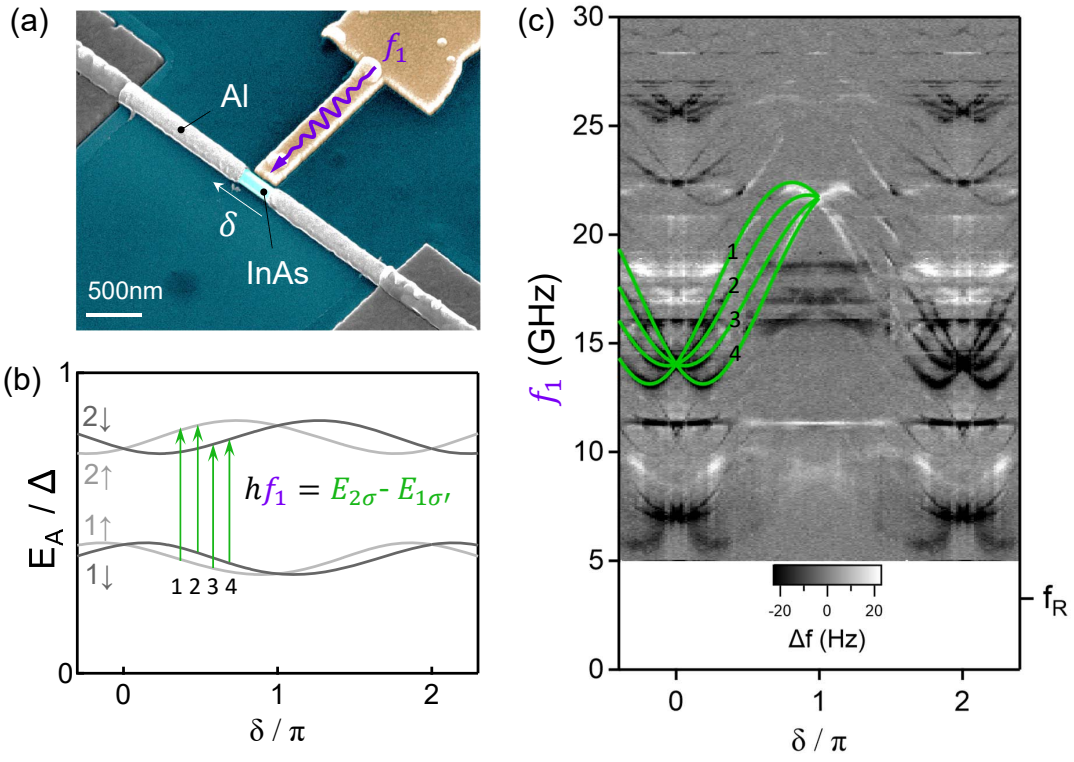


**Figure 2:** (a) Lien faible Josephson défini dans un nanofil d'InAs/Al en gravant chimiquement la gaine d'aluminium (gris) couvrant le crystal d'InAs (vert) sur une longueur $L \approx 370$ nm. La différence de phase $\delta$ est obtenue en intégrant le lien faible dans une boucle supraconductrice et en balayant l'intensité d'un faible champ magnétique externe à travers celle-ci. Une tension DC est appliquée sur la grille électrostatiques (doré) pour contrôler les propriétés de conduction du nanofil. Cette grille est également utilisée comme antenne pour envoyer des impulsions micro-ondes à la fréquence $f_1$ et exciter des transitions entre états d'Andreev. (b) Dispersion en énergie des états d'Andreev dans un lien faible de longueur finie avec couplage spin-orbite, d'après le modèle analytique de A. Levy Yeyati et de Sunghun Park. (c) Spectre d'absorption micro-onde mesuré sur le dispositif en (a) montrant une série de quatre lignes spectroscopiques associées aux transitions à une quasi-particule (vert) entre les deux doublets d'états d'Andreev montrés en (b).

Lorsque le matériau est refroidi à température cryogénique (< 1.2 K), l'aluminium devient supraconducteur et induit la supraconductivité dans le nanofil par effet de proximité. La particularité de ces nanofils repose sur l'existence d'un contact épitaxié entre le semi-conducteur et la couche d'aluminium, qui renforce l'effet de proximité et garantit une bonne supraconductivité induite [37, 38]. Cela fait de ces nanofils une plateforme idéale pour la réalisation de liens faibles Josephson : en gravant la couche d'aluminium sur une région donnée, on peut ainsi définir localement une jonction Josephson au sein du nanofil, comme illustré en Figure 2(a). Par ailleurs, ces nanofils étant semi-conducteurs, les propriétés d'une telle jonction peuvent être ajustées à l'aide d'une grille électrostatique déposée à proximité du nanofil. Celle-ci permet, par effet de champ, de contrôler le potentiel chimique du semiconducteur et d'atteindre un régime où la conduction dans le lien faible se produit à travers seulement quelques canaux de forte transparence [39] ; une condition nécessaire pour sonder la physique d'états d'Andreev individuels.

Cette thèse présente deux résultats majeurs, qui introduisent une physique nouvelle par rapport aux contacts atomiques étudiés précédemment dans le groupe [40, 21]. Premièrement, l'observation à champ magnétique nul de la "structure fine" des états d'Andreev, qui résulte de la présence d'un couplage spin-orbite dans le semi-conducteur. Deuxièmement, la mise en évidence d'interactions Coulombiennes entre quasi-particules piégées dans différents états d'Andreev, indiquant l'importance d'effets de charge dans l'électrodynamique d'un lien faible Josephson. Nous démontrons également la manipulation cohérente des états d'Andreev par des mesures résolues en temps, en recourant à diverses transitions observées dans leurs spectres micro-ondes. Des qubits sont obtenus en utilisant, soit l'état fondamental et un état où une paire de quasi-particules est excitée ; soit deux états avec une quasi-particule dans des états d'Andreev différents. Nous avons mesuré les temps de vie et de cohérence de ces deux types de "qubits d'Andreev".

Pour mettre en évidence la structure fine des états d'Andreev, nous avons réalisé la spectroscopie micro-onde de nos liens faibles à nanofil d'InAs. Dans la Figure 2(c), nous présentons un spectre micro-onde typique mesuré sur ce système. Ce spectre présente une série caractéristique de quatre lignes distinctes qui se croisent lorsque la différence de phase supraconductrice $\delta$ à travers le lien faible est nulle ou égale à $\pi$, et que nous interprétons comme des transitions à une quasi-particule entre états d'Andreev résolus en spin en l'absence de champ Zeeman (cf. figure Figure 2(b)). Un modèle analytique simple, supposant un couplage spin-orbite de type Rashba dans un nanofil à plusieurs bandes de conduction, a été développé par Alfredo Levy Yeyati et Sunghun Park de l'Université autonome de Madrid. Nous avons montré qu'il permet de rendre compte de ces lignes et de leur évolution avec un champ magnétique externe, ce qui supporte leur identification à des transitions à une quasi-particule et confirme le caractère de spin de ces excitations. Nous avons également développé une théorie générale du couplage d'un résonateur à un système quantique multi-niveaux, en incorporant les contributions adiabatiques et dispersives au couplage pour rendre compte de l'intensité des lignes spectroscopiques mesurées. Ces résultats offrent la première démonstration expérimentale que le degré de liberté de spin d'une jonction Josephson peut être adressé et constituent une première étape vers sa manipulation cohérente.

Parallèlement à nos travaux, le groupe de Michel Devoret à l'Université de Yale a réalisé des expériences très similaires sur le même genre de système en recourant à un type de résonateur micro-onde et à un schéma d'excitation différents. Alors que la plupart de nos résultats repose sur la spectroscopie micro-onde des transitions possibles entre états d'Andreev, l'équipe de Yale s'est davantage concentrée sur leur manipulation temporelle [19, 41, 42]. En se basant sur notre compréhension des transitions à une quasi-particule, Hays *et al.* ont réalisé le contrôle cohérent du spin d'une quasi-particule unique piégée dans un état d'Andreev [41, 42]. Dans ce manuscrit, nous démontrons indépendamment la manipulation d'un spin unique, bien que nous n'ayons pas pu réaliser une lecture *single-shot* du spin comme cela a été fait à Yale.

## 3 Interactions Coulombiennes dans les liens faibles à nanofils

Enfin, nous montrons en combinant une approche expérimentale et théorique que certaines caractéristiques du spectre d'un nanofil ne peuvent être expliquées qu'en supposant l'existence d'une énergie de charge au sein du lien faible. En particulier, notre analyse montre que du fait du temps de vol non nul des électrons dans le nanofil, deux quasi-particules dans des états d'Andreev différents peuvent interagir et que leur

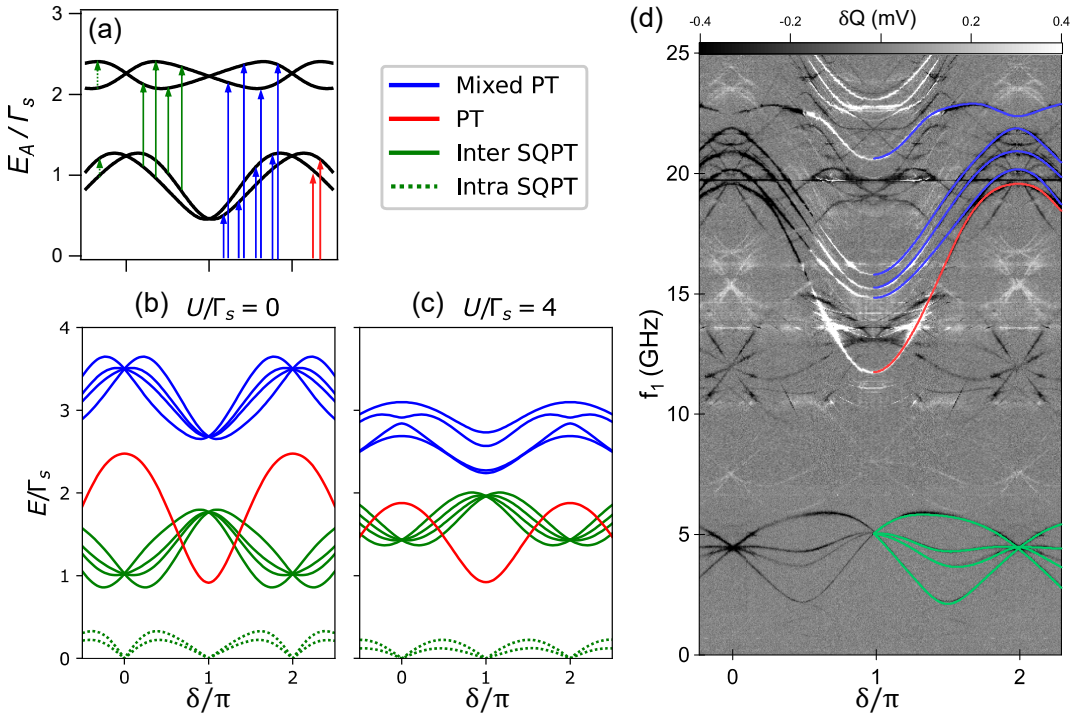


**Figure 3:** (a) Spectre en excitations des états d'Andreev dans un lien faible de longueur finie avec interaction spin-orbite. Les énergies sont normalisées par une amplitude effective $\Gamma_s$, traduisant l'intensité des corrélations supraconductrices. Les flèches colorées illustrent les différentes transitions micro-ondes possibles, dont la dépendance en phase est représentée dans les cas sans (b) ou avec (c) interactions Coulombiennes (paramétrées par l'énergie de charge $U$). Les lignes de transition sont classées en transitions de paires (rouge), de paires mixtes (bleu) et en transitions à une quasi-particule inter- (vert plein) ou intra-niveaux (vert pointillé). On observe que l'effet des interactions est de splitter les quatre transitions de paires mixtes. (d) Spectre micro-onde typique ; les lignes d'absorption principales sont surlignées avec le même code couleur qu'en (b,c).

interaction Coulombienne conduit à un splitting des énergies des quatre états possibles de la paire, rappelant la séparation singulet-triplet de deux spins 1/2 en interaction dans un système à faible couplage spin-orbite. Cet effet est illustré dans la Figure 3(b,c) où nous représentons en bleu la dépendance en phase des transitions de paires dites "mixtes", c'est-à-dire impliquant une excitation dans deux doublets d'Andreev différents, et ce en présence ou non d'une énergie de charge Coulombienne. Un exemple de spectre expérimental décrivant cette physique est donné en Figure 3(d). Les transitions de paires mixtes, surlignées en bleu, sont regroupées en un triplet non dégénéré et un singulet à plus haute fréquence. A noter que leur splitting, aisément mis en évidence par spectroscopie micro-onde, reste un effet faible (~ 2 $\mu$eV) et serait par conséquent difficile à résoudre au moyen des mesures classiques de transport électrique (DC/audiofréquence), qui offrent une résolution en énergie plus basse de presque deux ordres de grandeur.

En conclusion, les expériences rapportées dans cette thèse ont permis de mettre en évidence plusieurs phénomènes nouveaux dans le domaine de la supraconductivité mésoscopique ; une physique traduisant une compétition complexe entre les degrés de liberté orbital, de spin et de charge d'un électron dans un lien faible semi-conducteur. Le domaine des circuits quantiques cherche actuellement à exploiter cette riche physique des semi-conducteurs pour développer des dispositifs hybrides et susciter de nouvelles applications basées sur leurs propriétés de cohérence quantique. Les liens faibles à nanofils semi-conducteurs se sont maintenant largement imposés comme nouvelle ressource de base de ces circuits, avec l'idée de tirer profit de leur degré de liberté fermionique accordable. Dans cette thèse, nous avons montré comment la spectroscopie micro-onde permettait de sonder les rouages de ces "atomes artificiels", de la même manière que la spectroscopie UV-visible a permis de comprendre la physique des atomes et des molécules. Nous envisageons deux expériences futures comme perspectives immédiates à ces travaux. Premièrement, la spectroscopie des liens faibles à nanofil d'InAs sous fort champ Zeeman, pour sonder la transition vers une potentielle phase topologique prédite par la théorie [43, 44, 45]. Deuxièmement, la spectroscopie de jonctions multi-terminales, un système censé simuler la physique des semi-métaux de Weyl [46, 47, 48].

# Contents

# List of Figures

# Introduction 1

## 1.1 The Josephson effect in terms of Andreev bound states

The Josephson supercurrent that flows through a weak link between two superconductors is a direct and generic manifestation of the coherence of the many-body superconducting state. The link can be a thin insulating barrier, a small piece of normal metal, a constriction or any other type of coherent conductor. Regardless of the link specific nature, the supercurrent is a periodic function of the superconducting phase difference between the two electrodes [4]. A unifying microscopic description of this effect has been achieved in terms of the spectrum of discrete quasiparticle states that form in each conduction channel of the weak link: the **Andreev bound states (ABS)** [5, 6, 7, 8, 9].

ABS are formed from the phase-coherent reflections that quasiparticles undergo at both ends of a weak link, known as Andreev reflections. They can be viewed as the electronic modes of a box with superconducting walls. Their existence therefore results from the general properties of an NS interface and the topology of the weak link, rather than from the geometric and material properties of the region where they are confined, which explains the universality of the Josephson effect. While the connection between ABS and the Josephson effect was predicted long ago, it was not until rather recently that direct evidence of these current-carrying states was obtained. ABS have now been revealed with various spectroscopy techniques and in various systems, ranging from carbon nanotubes [13] and atomic contacts [14, 15, 16] to semiconducting nanowires [17, 18, 19]. A few examples are shown in Figure 1.1.

## 1.2 Quantum information within a single Josephson junction

Josephson circuits have wide applications in the field of quantum information processing [2]. They are currently at the core of most superconducting qubit technologies being developed, where information is encoded in bosonic collective electromagnetic modes of the circuits [3]. Comparatively, little attention was paid so far to the internal degrees of freedom of a Josephson junction arising from the microscopic ABS that it hosts, although such fermionic states could actually be used to store quantum information *within the junction itself*. The key point here is that the many-body occupancy of the ABS determines a macroscopic and measurable quantity, the supercurrent flowing through the weak link, and therefore the electrodynamics of the circuit in which the junction is embedded. This make these microscopic degrees of freedom addressable.



[4]: Golubov et al. (2004), 'The current-phase relation in Josephson junctions'
[5]: Andreev (1966), 'Electron Spectrum of the Intermediate State of Superconductors'
[6]: Kulik (1970), 'Macroscopic quantization and proximity effect in S-N-S junctions'
[7]: Beenakker and Houten (1991), 'Josephson current through a superconducting quantum point contact shorter than the coherence length'
[8]: Furusaki and Tsukada (1991), 'Dc Josephson effect and Andreev reflection'
[9]: Bagwell (1992), 'Suppression of the Josephson current through a narrow, mesoscopic, semiconductor channel by a single impurity'
[13]: Pillet et al. (2010), 'Andreev bound states in supercurrent-carrying carbon nanotubes revealed'
[14]: Bretheau et al. (2013), 'Exciting Andreev pairs in a superconducting atomic contact'
[15]: Bretheau et al. (2013), 'Supercurrent Spectroscopy of Andreev States'
[16]: Janvier et al. (2015), 'Coherent manipulation of Andreev states in superconducting atomic contacts'
[17]: Woerkom et al. (2017), 'Microwave spectroscopy of spinful Andreev bound states in ballistic semiconductor Josephson junctions'
[18]: Lee et al. (2013), 'Spin-resolved Andreev levels and parity crossings in hybrid superconductor-semiconductor nanostructures'
[19]: Hays et al. (2018), 'Direct Microwave Measurement of Andreev-Bound-State Dynamics in a Semiconductor-Nanowire Josephson Junction'
[2]: Devoret and Schoelkopf (2013), 'Superconducting Circuits for Quantum Information'
[3]: Krantz et al. (2019), 'A quantum engineer's guide to superconducting qubits'

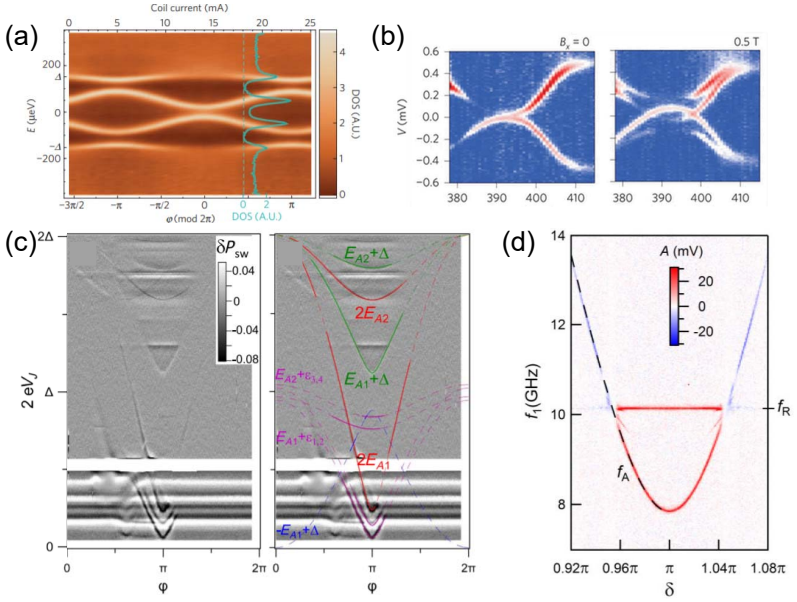


**Figure 1.1:** Spectroscopy of ABS: (a) in a carbon nanotube (tunnel spectroscopy, from Ref. [13]); (b) on a InAs/InP core/shell nanowire connected to a superconducting Vanadium electrode (tunnel spectroscopy as a function of plunger gate voltage and magnetic field, from Ref. [18]), and on atomic contacts: (c) supercurrent spectroscopy (from Ref. [15]); (d) microwave spectroscopy (from Ref. [16]).

### 1.2.1 Tunnel junctions vs few-channels weak links

Most existing superconducting qubits rely on tunnel junctions which, as a collection of many low-transmitted conduction channels, typically host millions of ABS. The fact that these ABS hardly detach from the superconducting gap and show only little phase dispersion precludes their manipulation in such systems. On the contrary, Josephson weak links tailored in few-channels conductors are characterized by only a few ABS, which offers a chance to isolate and manipulate them individually. Since they may disperse deeply in the superconducting gap when they arise from well-transmitted channels, they may carry substantially more supercurrent and are therefore easier to couple to a readout probe. For the same reason, at least part of the associated excitation spectrum falls in the SHF (3-30 GHz) frequency range, easily explored using well-established microwaves techniques, in particular those of circuit-quantum electrodynamics (cQED) [20]. For quantum information applications, nanowire weak links made out of semiconducting materials appear particularly appealing due to their gate tunability, which allows to reach conditions where conduction occurs through only a few high-transmitted channels [39].

In the present thesis, we investigate the effect of spin and charge on the physics of Andreev bound states. Our results are based on cQED experiments which were performed on Josephson weak links tailored in epitaxially grown InAs/Al core/shell nanowires. In these hybrid nanostructures, grown in the Center for Quantum Devices, Copenhagen, by the groups of P. Krogstrup and J. Nygård, the high quality interface between the InAs core of the nanowire and its aluminium shell (see Figure 1.2(b,c)) induces a "hard" superconducting gap in the semiconductor by proximity effect [38].

[20]: Blais et al. (2004), 'Cavity quantum electrodynamics for superconducting electrical circuits'

[39]: Goffman et al. (2017), 'Conduction channels of an InAs-Al nanowire Josephson weak link'

[38]: Chang et al. (2015), 'Hard gap in epitaxial semiconductor-superconductor nanowires'

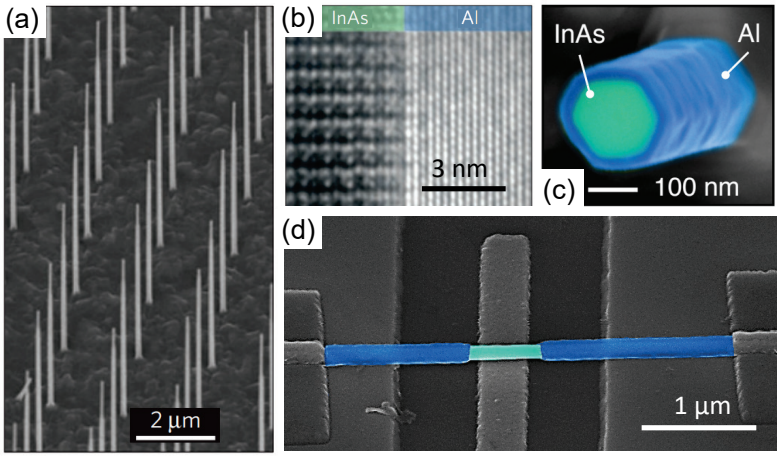


**Figure 1.2:** Josephson weak links tailored in InAs/Al core/shell nanowires. (a) Tilt-view scanning electron micrograph of an array of epitaxial InAs/Al NWs grown in the $[0001]_{WZ}$ direction on an InAs (111)B substrate (adapted from Ref. [37]). (b) High-resolution TEM image from [37] showing that the Al shell forms a perfectly sharp and uniform interface to the InAs core. (c) Colorized electron micrograph from Ref. [49], showing the ~ 25 nm full-shell epitaxial Al (blue) grown on the hexagonal InAs core (green) with diameter ~ 140 nm. (d) Josephson weak link obtained from such a full-shell nanowire by etching away the Al over a length 550 nm (sample named S2 in the thesis).

[37]: Krogstrup et al. (2015), 'Epitaxy of semiconductor-superconductor nanowires'

[49]: Vaitiekėnas et al. (2018), 'Effective $g$ Factor of Subgap States in Hybrid Nanowires'

This makes these nanowires a suitable platform to implement a Josephson weak link: by simply etching away the aluminium shell over a small section of the nanowire, one naturally defines a SNS junction, as illustrated in Figure 1.2(d).

In parallel to our work, the group of Michel Devoret at Yale University also performed experiments on InAs nanowire weak links using a cQED setup. While we were investigating full-shell nanowires, theirs had aluminium only on 2 facets of the InAs crystals[1] . They also used another type of microwave resonator and another excitation scheme. Whereas most of our results rely on the two-one spectroscopy of weak links, they focused more on time-domain measurements [19, 41, 42] and detailed analysis of single-tone spectra [50]. Because of the strong proximity between their work and ours, we will often refer to their experiments.

[19]: Hays et al. (2018), 'Direct Microwave Measurement of Andreev-Bound-State Dynamics in a Semiconductor-Nanowire Josephson Junction'

[41]: Hays et al. (2020), 'Continuous monitoring of a trapped superconducting spin'

[42]: Hays et al. (2021), 'Coherent manipulation of an Andreev spin qubit'

[50]: Fatemi et al. (2021), 'Microwave susceptibility observation of interacting many-body Andreev states'

1: Contrary to our nanowires which have their six facets covered ("full-shell" nanowires, see Figure 1.2(c)), two-facets nanowires allow for additional tuning since the chemical potential in the leads and their coupling to the weak link may be tuned by means of supplementary gates, while in a full-shell nanowire the superconducting shell screens any external electrical field.

We present two main findings. First, the observation at zero magnetic field of the "fine structure" of the Andreev states, arising from the presence of spin-orbit coupling in the semiconductor. Second, spectroscopic signatures of electron-electron interactions between quasiparticles trapped in different ABS. We also demonstrate time-domain manipulation of ABS, using various transitions observed in the spectra.

## 1.3 Observation of the ABS fine structure

The role of spin in fermionic excitations like ABS is a topical issue in the rapidly growing fields of hybrid superconducting devices [22, 23, 24] and of topological superconductivity [25, 26, 27, 28]. It has been predicted that for finite-length weak links the combination of a superconducting phase difference, which breaks time-reversal symmetry, and of spin-orbit coupling, which breaks spin-rotation symmetry, is enough to lift the spin degeneracy, giving rise to spin-dependent Josephson supercurrents even

[22]: Michelsen et al. (2008), 'Manipulation with Andreev states in spin active mesoscopic Josephson junctions'

[23]: De Franceschi et al. (2010), 'Hybrid superconductor-quantum dot devices'

[24]: Linder and Robinson (2015), 'Superconducting spintronics'

[25]: Prada et al. (2017), 'Measuring Majorana nonlocality and spin structure with a quantum dot'

[26]: Zazunov et al. (2017), 'Josephson effect in multiterminal topological junctions'

[27]: Deng et al. (2018), 'Nonlocality of Majorana modes in hybrid nanowires'

[28]: Hart et al. (2017), 'Controlled finite momentum pairing and spatially varying order parameter in proximitized HgTe quantum wells'

in the absence of an external magnetic field [29, 33, 30, 31, 34]. We report here the first observation of microwave transitions between zero-field spin-split ABS.

[29]: Chtchelkatchev and Nazarov (2003), 'Andreev Quantum Dots for Spin Manipulation'
[33]: Béri et al. (2008), 'Splitting of Andreev levels in a Josephson junction by spin-orbit coupling'
[30]: Padurariu and Nazarov (2010), 'Theoretical proposal for superconducting spin qubits'
[31]: Reynoso et al. (2012), 'Spin-orbit-induced chirality of Andreev states in Josephson junctions'
[34]: Cayao et al. (2015), 'SNS junctions in nanowires with spin-orbit coupling'

### 1.3.1 ABS in a multi-channel Rashba nanowire

The phase dependence of ABS levels arising in a weak link with a single occupied channel is illustrated in Figure 1.3 in the semiconductor picture[2] for three cases of increasing complexity:

(a) For a zero-length junction, there is only one pair of subgap, spin-degenerate ABS levels $i = \pm 1$ detaching from the gap edge $\Delta$. As the superconducting phase difference $\delta$ across the weak link is increased, the two levels fall deeper in the gap until $\delta = \pi$, value for which superconductivity is maximally frustrated. Their energy difference reaches there its minimum value $2\Delta\sqrt{1-\tau}$, with $0 \leq \tau \leq 1$ the channel transparency. This picture describes well weak links with length $L \ll \xi$, where $\xi$ is the superconducting coherence length. For ballistic conduction channels, $\xi = \hbar v_F/\Delta$, where $v_F$ is the Fermi velocity at the weak link.

(b) For finite-length weak links, without spin-orbit coupling, more spin-degenerate ABS levels arise in the gap. The parameter $\lambda = L/\xi$ determines the number of such ABS pairs: depending on $\delta$ and channel transmission $\tau$, it is $1+\lfloor 2\lambda/\pi \rfloor$ or $2+\lfloor 2\lambda/\pi \rfloor$ ($\lfloor x \rfloor$ is the integer part of $x$). For the parameters of Figure 1.3b ($\lambda = 1.7, \tau = 0.97$), the levels are labelled $i = \pm 1, \pm 2$.

(c) When spin-orbit interaction is present in the weak link, the spin-degeneracy of the ABS levels can be lifted when $\delta \neq 0, \pi$, as the result of a spin-dependent Fermi velocity which leads to different values of $\lambda$ for the two spin textures [32]. This is depicted in Figure 1.3(c) where the pseudospin of each ABS is encoded in grayscale. This regime describes well InAs nanowire weak links that are investigated in this thesis.

2: Different representations are generally used in the literature to describe the energy spectrum of superconductors: the single-particle picture, the excitation picture and the semiconductor picture. Depending on the context and the type of experiment being discussed, one representation may be more convenient than the another. For a detailed comparison of these representations, see Ref. [40].

[40]: Bretheau (2013), 'Localized Excitations in Superconducting Atomic Contacts', pp. 16-21
[32]: Park and Levy Yeyati (2017), 'Andreev spin qubits in multichannel Rashba nanowires'

#### Pair *vs.* single-quasiparticle transitions

In the many-body ground state, the negative-energy levels are occupied in the *single-particle* picture. This includes the negative-energy ABS levels as well as the continuum of states at energies $E < -\Delta$. Each level can be occupied by 0 or 1 quasiparticle. By irradiating the weak link with photons at the right energy, one can promote a quasiparticle from the lower (-1) to the upper (+1) level (red arrows in Figure 1.3), which in the *excitation* picture amounts to creating both a hole-like and an electron-like excitation. This process is therefore referred to as a **pair transition** (PT). The ground and excited states involved in such transitions were first observed in atomic contacts : they give rise to the *Andreev level qubit*, which was investigated previously in the Quantronics group [21].

[21]: Janvier (2016), 'Coherent manipulation of Andreev Bound States in an atomic contact'

In finite-length weak links, a second type of parity-conserving transitions arises: a quasiparticle trapped in one ABS can absorb a photon and be excited to another one. We refer to this process illustrated by green arrows

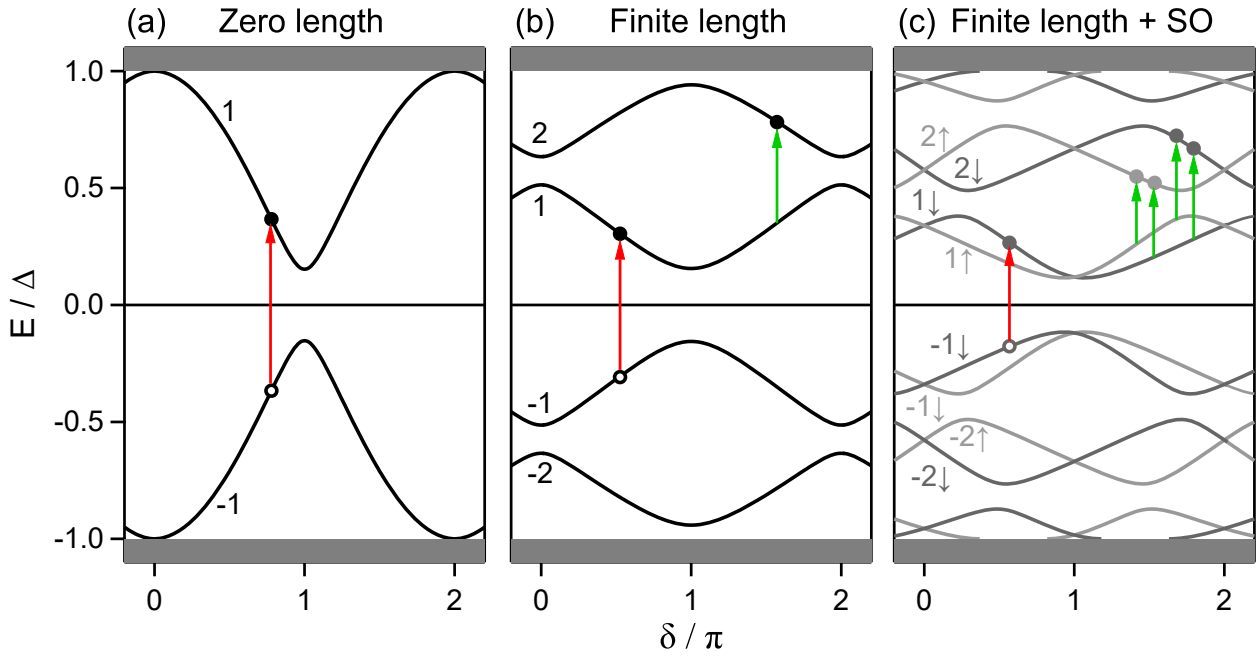


**Figure 1.3:** Energy spectrum of the Andreev states in the semiconductor picture as a function of the phase difference $\delta$ between the two superconducting electrodes, as obtained by solving the BdG equations, for (a) a zero-length weak link, (b) a finite-length weak link, and (c) a finite-length weak link in presence of spin-orbit coupling. In (a,b), all lines are spin-degenerate. In (c), dark and light gray lines correspond to Andreev levels with different pseudospins. In the ground state, all levels with negative energy are occupied. Two types of transitions can occur: pair transitions (PT), leading to two additional excitations, are represented with red arrows crossing the Fermi energy. Single-quasiparticle transitions (SQPT) are possible when quasiparticles are present in the system. They correspond to atomic-like transitions between two levels both at either positive or negative energies (green arrows).

in Figure 1.3 as a **single-quasiparticle transition** (SQPT). When the ABS are spin-split as a result of the spin-orbit interaction, the spin character of such excitations becomes relevant. As illustrated in Figure 1.3(c), there can now be four transitions of this type between a given pair of spin-split ABS doublets. Two of them conserve the pseudospin of the quasiparticle, while the two others flip it. Performing such single-quasiparticle transitions therefore amounts to manipulating a single fermionic spin trapped at the weak link, which could be used to implement an *Andreev spin qubit*.

Probing these spin effects requires to engineer weak links in a few-channel conductor where spin-orbit interaction is at play. In addition to a good proximity effect, the InAs nanowires mentioned above are known to host sizeable spin-orbit interactions [35, 36], which makes them good candidates to implement spin-active junctions. In the present work, we performed the microwave spectroscopy of such InAs nanowire weak links by coupling them to microwave resonators in a cQED setup. The role of the microwave resonator is two-fold: it allows to efficiently isolate the weak link from external noise and to read out its microscopic state. Due to the coupling with the weak link, the resonator frequency is shifted by an amount that depends on the many-body occupancy of the ABS states. Probing its frequency with microwaves then gives direct access to the weak link state. In particular, the excitation spectrum of the latter can be obtained by applying an additional microwave tone to drive transitions between ABS. When resonant, this drive changes the occupancies of the ABS, which reflects in a shift of the resonator frequency.

[35]: Roulleau et al. (2010), 'Suppression of weak antilocalization in InAs nanowires'
[36]: Scherübl et al. (2016), 'Electrical tuning of Rashba spin-orbit interaction in multigated InAs nanowires'

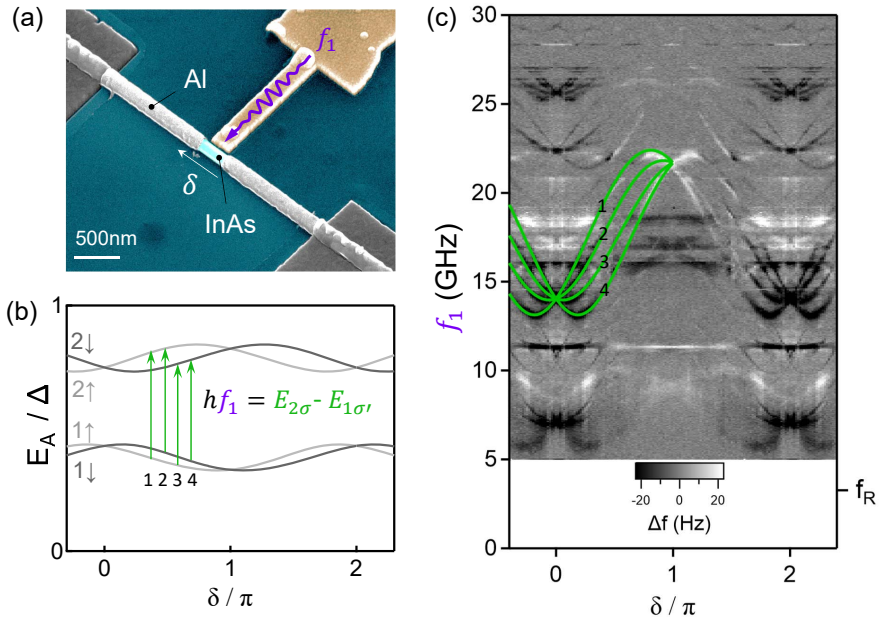


**Figure 1.4:** (a) Josephson weak link tailored in an InAs/Al core/shell nanowire by etching away part of the aluminium shell (grey) covering the InAs core (green) over a length $L \approx 370$ nm. A superconducting phase difference $\delta$ may be applied across the weak link by embedding the nanowire in a superconducting loop and threading it by a small magnetic field. A DC voltage applied on a side gate (gold) near the nanowire allows to tune its conduction properties. The gate is also used as a local antenna on which a microwave tone at frequency $f_1$ is applied to drive transitions between the ABS hosted by the weak link. (b) Typical spectrum of spin-split Andreev states and their $\delta$-dependence drawn in the excitation picture. This spectrum can be understood by considering a finite-length weak link with Rashba-type spin-orbit interaction in a nanowire containing several transverse subbands. (c) Microwave spectrum of an InAs nanowire weak link showing a bundle of four lines corresponding to single-quasiparticle transitions (green) between the spin-split ABS shown in (b). The two outer transitions 1,4 conserve the quasiparticle pseudo-spin $\sigma \in \{\uparrow, \downarrow\}$, while the two inner transitions 2,3 flip it.

This is illustrated in Figure 1.4(c), where we present a typical excitation spectrum of an InAs nanowire weak link. The superconducting phase difference $\delta$ across the weak link is varied by embedding the weak link in a loop and sweeping an external magnetic field through it. The spectrum shows generic features with bundles of four lines crossing when the superconducting phase difference across the weak link is 0 or $\pi$. Hence, we interpret these distinctive features as SQPT transitions between zero-field spin-split Andreev states, as shown in Figure 1.4(b). A simple analytical model, which takes into account the Rashba spin-orbit interaction in a nanowire containing several transverse subbands, explains these features and their evolution with magnetic field. Our results show that the spin degree of freedom is addressable in Josephson junctions. They are a first step towards its coherent manipulation.

### 1.3.2 Trapping a single spin in a superconducting box

Using a similar cQED setup but a different resonator design, the group of Michel Devoret at Yale University was independently working on demonstrating such manipulation of an Andreev spin. Following our understanding of the single-quasiparticle transitions in nanowire spectra, Hays *et al.* achieved the coherent manipulation of a single quasiparticle trapped in the lowest ABS manifold [41, 42].

[41]: Hays et al. (2020), 'Continuous monitoring of a trapped superconducting spin'
[42]: Hays et al. (2021), 'Coherent manipulation of an Andreev spin qubit'

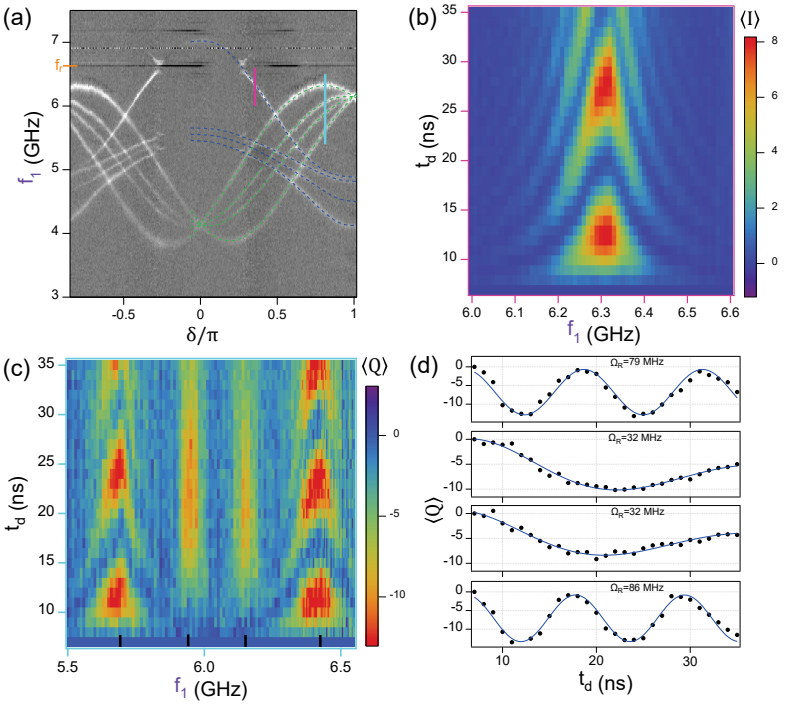


**Figure 1.5:** (a) Microwave spectrum of an InAs nanowire weak link showing of bundle of SQPTs (dashed green lines) and a series of PTs (dashed blue). $f_r \approx 6.6$ GHz denotes the resonator frequency. (b,c) Rabi flopping of the SQPTs (c) and of one of the PTs (b) obtained by varying the duration $t_d$ of a square microwave driving pulse of frequency $f_1$. Measurements were performed at the phase values indicated in (a) by magenta and cyan bars. (d) Linecuts of (c) at the frequencies of the four SQPT (highlighted with black ticks on the frequency axis) evidencing different Rabi frequencies between spin-conserving and spin-flipping SQPTs.

Here, we independently demonstrate such a manipulation of a single spin, although we could not achieve single-shot readout of the spin as was done in [41]. Figure 1.5 illustrates typical time-resolved measurements that we performed, evidencing coherent oscillations in the mean value of a demodulated readout pulse obtained by varying the duration of a driving pulse resonant with a PT (b) or with each of the four lines of a SQPT bundle (c). Remarkably, when driving at the same power, the Rabi frequency associated to spin-flipping SQPTs is shown to be ~ 2.5 times smaller than for spin-conserving transitions, consistent with the existence of approximate selection rules for the spin*.

* In principle, a microwave drive is not expected to induce spin-flipping transitions. This is because the magnetic field of the drive is too weak to couple to the spin of an electron; as for the electric field, it only couples to the motional degree of freedom of the electron and so cannot flip the spin when it is a good quantum number. In the present case, spin-orbit coupling in the nanowire partly solves this issue since it hybridizes the spin and spatial character of the electron wavefunction into a so-called *pseudospin*. However, it can be shown that a selection rule still forbids spin-flipping transitions : while the spin-orbit breaks the rotational symmetry along the nanowire axis, there still remains a transverse mirror symmetry, such that one spin state of each Andreev doublet would be mirror-symmetric and the other anti-symmetric (see Ref. [42]). Therefore, if the electric field of the microwave drive points along the nanowire and respects this mirror symmetry, it cannot flip the spin. Still, in practice, this symmetry may be broken by the presence of a side gate, and by any non-ideality in the device, which makes this selection rule only approximate. All inter-doublet spin transitions can therefore be induced, although the spin-flipping ones remain a bit harder to drive, as evidenced here.

### 1.3.3 General theory for the cQED of phase-biased weak links

While focusing on the understanding of spectroscopy, we evidenced additional peculiarities in nanowire spectra. First, transitions were observed at frequencies far detuned from that of the resonator. Second, the response of the resonator appeared to depend on the curvature of the transition lines. These facts are at odds with the dispersive theory, which describes the coupling in terms of exchange of photons with the resonator. To solve this issue, we developed in collaboration with the group of Alfredo Levy Yeyati, from the Condensed Matter Physics Center in Madrid, a general theory for the response of a resonator to changes in the occupancies of a multi-level quantum system coupled to it, as is the case for ABS systems. We also acknowledge a collaboration with Leandro Tosi and Andres Reyonoso from Instituo Balseiro in Bariloche, who contributed to the tight-binding calculations presented in this thesis. The main result of the collaboration with Madrid is the expression of the resonator shift due to a single occupied level:

$$h\delta f_r^{(i)} \propto E_i'' + \sum_{j\neq i} \mathscr{M}_{i,j}^2 \left( \frac{2}{E_j - E_i} - \frac{1}{E_j - E_i - hf_r} - \frac{1}{E_j - E_i + hf_r} \right). \tag{1.1}$$

This equation describes the adiabatic and dispersive contributions to the coupling between an oscillator with resonant frequency $f_r$ and a quantum system with discrete energy spectrum $\{E_i\}$. When the two systems are strongly detuned, $hf_r \ll |E_j - E_i| \ \forall i, j$ , the quantum system mainly shifts the resonator frequency through an effective stiffness, viewed as the second derivative of its energy levels $E_i'' = \partial^2 E_i / \partial q^2$ with respect to the coupling parameter $q$ (usually a phase difference or an offset charge). At small detuning, when $\exists i, j \mid hf_r \sim |E_j - E_i|$, the shift is dominated by the exchange of virtual photons between the two systems, which depends on the matrix elements of the coupling operator $\mathscr{M}_{i\sigma,j\sigma'} = |\langle \Phi_i | \partial H / \partial q | \Phi_j \rangle|$, with $H$ the Hamiltonian of the quantum system.

## 1.4 Evidence of Coulomb interactions in nanowire weak links

While most of the features of nanowire weak link spectra can be explained by means of a non-interacting theory, we show using a combined experimental and theoretical approach that they contain additional features that reveal the effect of electron-electron interactions. In particular we demonstrate that, when a Cooper pair is broken into two quasiparticles residing on different Andreev levels, their interaction leads to a splitting of the energies of the four possible many-body states, reminiscent of singlet-triplet splitting in systems with weak spin-orbit coupling. This is illustrated in Figure 1.6(b,c) where we show with blue lines "mixed" pair transitions involving two ABS manifolds with and without interactions, as computed from a minimal four-sites model which will be introduced in Chapter 8. One of the many spectra showing such mixed pair transitions is presented in Figure 1.7. Mixed pair transitions, highlighted in blue, are grouped into a non-degenerate triplet and a singlet at higher energy.

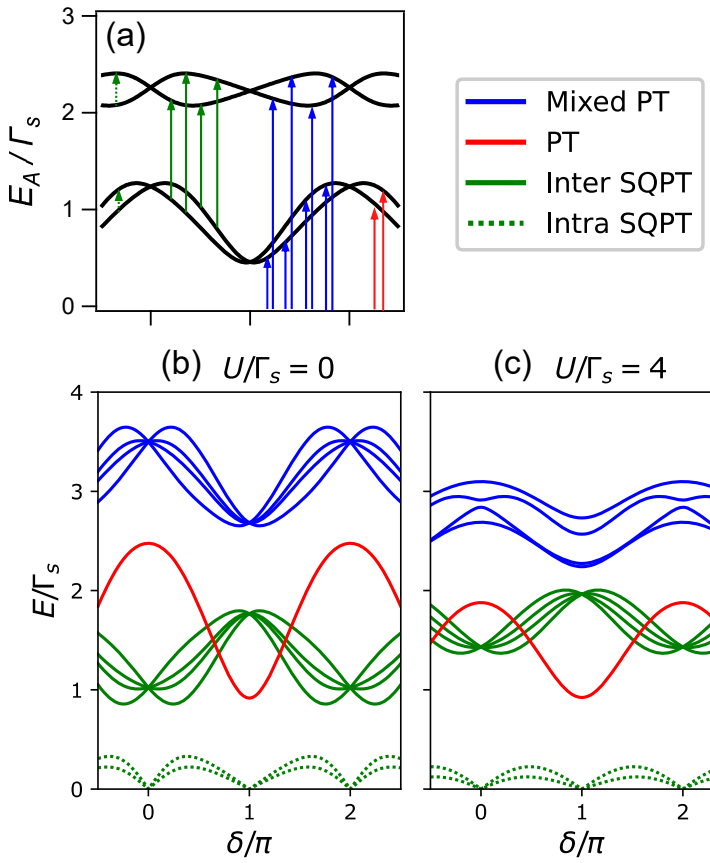


**Figure 1.6:** (a) Andreev spectrum of a typical finite-length weak link with spin orbit interaction drawn in the excitation picture. Energies are normalized by an effective singlet pairing intensity $\Gamma_s$. Colored arrows highlight the possible microwave absorption lines, the phase dependence of which is depicted in (b,c) without and with the effect of Coulomb interactions, parametrized by an interaction strength $U$. Transition lines are classified into pair (red) and mixed pair (blue) transitions and inter- (solid green) and intra-manifold (dashed green) single particle transitions. Interactions are observed to split the four mixed pair transitions.

Even if the interactions are strongly screened in these weak links, microwave spectroscopy is sensitive enough to reveal their effects, which would otherwise be difficult to identify by means of conventional transport measurements. This illustrates how solid-state devices like Josephson weak links allow to probe many-body physics at the microscopic scale.

**The manuscript is organized as follows.** In Chapter 2, starting from the concept of Andreev reflection and quasiparticles in a superconductor, we discuss the origin of ABS and review how their energy spectrum depends on the weak link length and on the presence of back-scattering. We further investigate in Chapter 3 the effect of spin-orbit interaction, how it arises in crystalline solids and how it allows for a zero-field spin splitting of the ABS by giving rise to a spin-dependent Fermi velocity. Using a scattering approach, we derive the energy spectrum of a finite-length weak link in presence of spin-orbit interaction when only the lowest band of the nanowire is occupied.

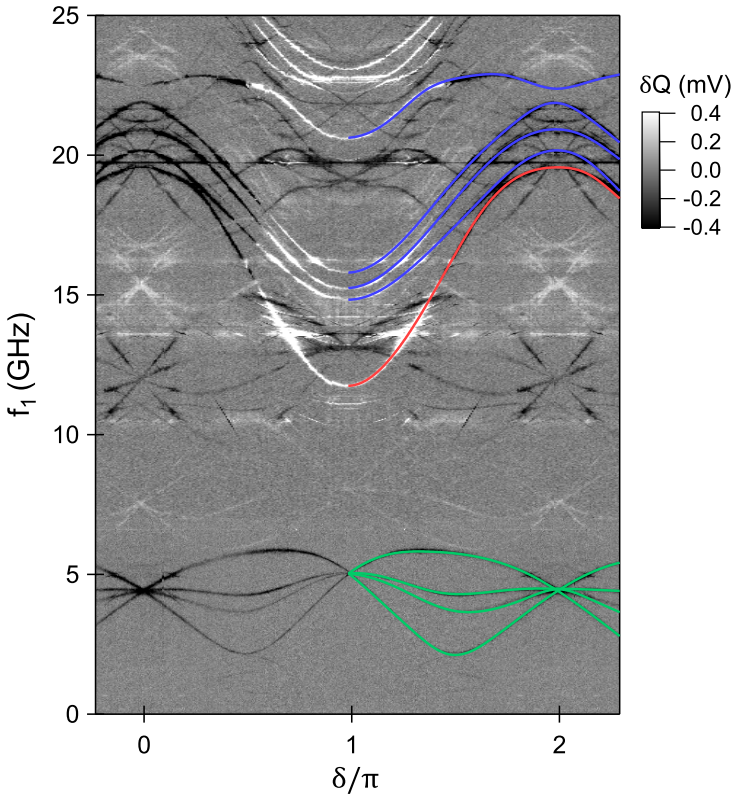


**Figure 1.7:** Spectrum measured on sample S2, with splines to highlight pair transitions (red), single particle transitions (green) and mixed pair transitions (blue).

The second part, encompassing Chapters 4 and 5, is devoted to the detection of ABS with the technique of cQED. In Chapter 4, starting from a general model of the coupling between a resonator and a phase-biased weak link, we discuss two ways of calculating the resonator shift in terms of the microscopic occupancies of a multilevel Andreev system. The derived result is shown to capture well the generic crossover between adiabatic and dispersive readout of a quantum circuit. First, we relate the resonator shift to the imaginary part of the weak link's complex admittance, which can be expressed in terms of the ABS occupancies using the Kubo formalism from linear response theory. The second approach is based on a Hamiltonian description of the coupling. Both show that the resonator shift scales like the square amplitude of the zero-point phase fluctuations on the weak link, which we seek to optimize for a good coupling to the detection resonator. Guided by this result, we describe in Chapter 5, the design of microwave resonators, in particular quarter-wave coplanar waveguide (CPW) and coplanar stripline (CPS) resonators.

In a third part, comprising Chapters 6-8, we present our experimental results on the microwave spectroscopy of nanowire weak links. First, we demonstrate how the fine structure of ABS is revealed by the observation of single-quasiparticle transition lines and their magnetic field dependence, and how the frequency of the transitions can be explained with the scattering model derived in Chapter 3. We then apply the formalism developed in Chapter 4 to describe other features of the measured spectra, in particular the transition lines intensity and the existence of selection rules associated to the spin, which affect the visibility of some transitions depending on the type of driving. In addition to the SQPTs, we identify

in Chapter 7 additional recurring features in our spectra, which evidence a multichannel situation as well as the presence of Coulomb interactions in the weak link. In Chapter 8 we introduce a model to incorporate the effect of such interactions and compare it to the measured spectra.

The fourth part, comprising Chapters 9-11, presents our results on the coherent dynamics of ABS in nanowire weak links. We start in Chapter 9 by discussing the readout of the weak link many-body state using time-resolved measurements. In Chapters 10 and 11 respectively, we demonstrate the manipulation of an Andreev pair qubit and present preliminary results on the manipulation of an Andreev spin qubit.

The final part, Chapters 12-15, reviews the experimental techniques used in this thesis, from sample fabrication to low-temperature and microwave measurements, as well as our setup for data acquisition. Details on the theoretical models are presented in an Appendix, along with supplemental microwave data and a discussion on the origin of spin-orbit in InAs nanowires and a classical derivation of the dispersive shift of two oscillators.

Some of the results presented in this manuscript are reported in the following articles:

- [51] *Spin-Orbit splitting of Andreev states revealed by microwave spectroscopy*, L. Tosi, C. Metzger, M. F. Goffman, C. Urbina, H. Pothier, Sunghun Park, A. Levy Yeyati, J. Nygård, P. Krogstrup, Phys. Rev. X **9**, 011010 (2019), arXiv:1810.0259

- [52] *From adiabatic to dispersive readout of quantum circuits*, Sunghun Park, C. Metzger, L. Tosi, M. F. Goffman, C. Urbina, H. Pothier, and A. Levy Yeyati, Phys. Rev. Lett. **125**, 077701 (2020), arXiv:2007.05030

- [53] *Circuit-QED with phase-biased Josephson weak links*, C. Metzger, Sunghun Park, L. Tosi, C. Janvier, A. A. Reynoso, M. F. Goffman, C. Urbina, A. Levy Yeyati, H. Pothier, Phys. Rev. Research **3**, 013036 (2021), arXiv:2010.00430

- [54] *Signatures of interactions in the Andreev spectrum of nanowire Josephson junctions*, F. J. Matute Cañadas, C. Metzger, Sunghun Park, L. Tosi, P. Krogstrup, J. Nygård, M. F. Goffman, C. Urbina, H. Pothier, A. Levy Yeyati, arXiv:2112.05625

# Spin-resolved Andreev Bound States

# Mesoscopic description of the Josephson effect

# 2

In the following sections, we introduce in a nutshell the concept of *Andreev bound states* (ABS), while focusing on the physical picture and keeping the math input as low as necessary. For a detailed mathematical derivation of ABS using the scattering formalism, we kindly refer the reader to Part I of Ref. [40]. Starting from the mode conversion process called *Andreev reflection* (AR) taking place at the interface between a normal metal and *one* superconductor, we extend it to the case of a short weak link between *two* superconductors and show how it gives rise to the ABS subgap states. We then introduce gradually different ingredients to enrich their physics: the finite length of the weak link, the effect of spin and finally the effect of spin-orbit coupling in the normal region.



[40]: Bretheau (2013), 'Localized Excitations in Superconducting Atomic Contacts', pp. 15-30

## 2.1 Andreev reflection

### 2.1.1 Electron-to-hole conversion

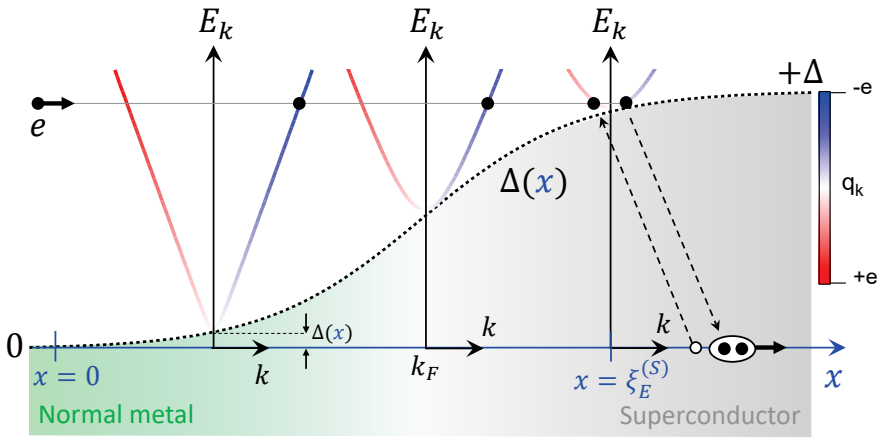


**Figure 2.1:** The normal metal-superconductor interface is characterized by a spatial variation of the superconducting order parameter $\Delta(x)$ from $\Delta$ deep in the superconducting region, $x \to +\infty$ (grey region), to 0 deep in the normal region, $x \to -\infty$ (green). As a normal electron (black dot) moves towards positive $x$, it converts into a quasiparticle of the superconductor, with energy $E_k$ and charge $q_k$ encoded in blue-white-red color-scale.

Let us analyze what happens at the interface between a normal metal and a superconductor and how a current carried by normal electrons is converted into a supercurrent of Cooper pairs. For simplicity, we will describe this problem considering a 1D geometry. The following argument is inspired by the textbook discussion from Ref. [55] and will only require knowledge of the expression for the energy of quasiparticles in a superconductor. The normal metal-to-superconductor transition is characterized by an order parameter corresponding to the energy gap $\Delta(x)$ of the superconductor, which has its maximum $\Delta(x \to +\infty) = \Delta$ deep inside the superconducting region (depicted in grey in Figure 2.1)

[55]: Schmidt et al. (1997), *The Physics of Superconductors*, pp. 167-174

and is zero deep inside the normal region depicted in green, $\Delta(x \to -\infty) = 0$. This transition region where the order parameter varies from 0 to $\Delta$ constitutes the NS interface so to speak.

We want to examine what happens to an electron in the normal region when it encounters such NS interface. We can write the kinetic energy of the incoming electron as $\epsilon_k = \hbar^2 k^2/(2m) - \mu$, with $k$ its momentum in the $x$-direction, $m$ its effective mass and $\mu = \hbar^2 k_F^2/(2m)$ the chemical potential. Importantly, let us assume that its energy $\epsilon_k$ is smaller than $\Delta$, so that no state is available with such an energy in the bulk superconductor. As illustrated in Figure 2.1, at some point when approaching the superconducting domain, this normal electron reaches a place where superconducting correlations already exist but to a small amount, $\Delta(x) \ll \Delta$. At this moment, it converts into an electron-like quasiparticle of the superconductor, filling the appropriate $k$-state in momentum space (positive/right branch of the spectrum), corresponding to its energy $E_k = \sqrt{\epsilon_k^2 + \Delta(x)^2}$. Its charge gets also dressed by the superconducting correlations, evolving from $-e$ to $q_k = (-e)\epsilon_k/E_k$.

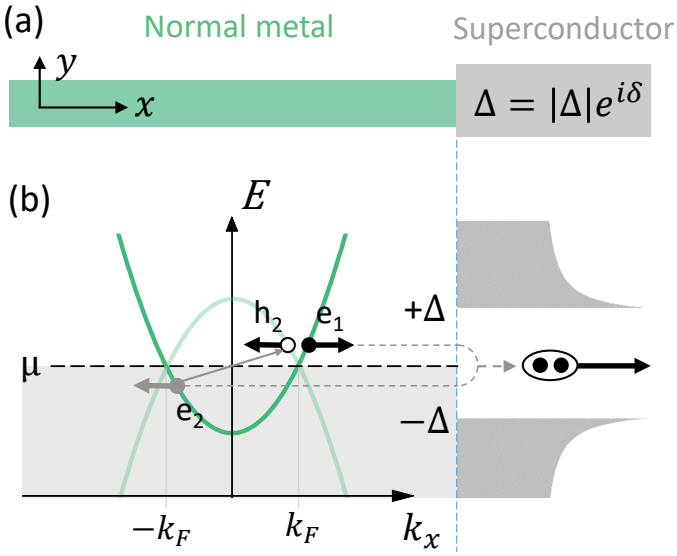


**Figure 2.2:** (a) Andreev reflection viewed as a scattering problem at the interface between a normal metal (green) and a superconductor (grey), characterized by an order parameter $\Delta$. (b) Energy dispersion $E(k_x)$ of a normal electron in a 1D metal (thick green curve). Density of states in the superconductor is sketched in grey on the right. A normal electron $e_1$ with excitation energy $\epsilon < \Delta$ above the chemical potential $\mu$ is propagating with momentum $k_1 = k_F + \delta k$ in the $x$-direction towards the superconductor. To form a Cooper pair, it pairs with another electron $e_2$ with energy $-\epsilon$ and momentum $k_2 = -k_F + \delta k$, leaving a hole $h_2$ behind, whose energy dispersion is shown in thin green lines. It is drawn at the negative momentum and energy of the missing electron $e_2$. For simplicity, spin indices are omitted for now.

Then, as the quasiparticle moves closer to the superconductor, it reaches another point with a larger value of the gap and consequently evolves in momentum space to another $k$-state closer to $k_F$, which results in an increase of the quasiparticle charge $q_k$. Finally, when approaching further, its momentum is decreased exactly to $k_F$ and the quasiparticle excitation is left with zero group velocity and zero charge. This happens when it reaches $x = \xi_E^{(S)}$, where its energy is equal to the local value of the gap (we shall derive heuristically the value of $\xi_E^{(S)}$ in the next section). At this

point, the quasiparticle is reflected back from the interface, moving to the left branch of the energy spectrum corresponding to *holes*. In this branch, the group velocity is negative and the charge $q_{k<k_F}$ positive. But a positive charge propagating to the left is equivalent to a negative charge propagating to the right. Therefore, this whole process of conversion from electron-like excitation to hole-like excitation gives effectively rise to a charge transfer from the normal metal to the superconductor.

Actually, as it approaches the superconductor, the quasiparticle charge decreases by being gradually transferred to the superconducting condensate. This means physically that the quasi-electron finds itself a partner to pair up with and enter the condensate as a Cooper pair, while the resulting hole goes backwards to the normal metal. This mode conversion process from electron to hole is known in the literature as **Andreev reflection** (contrasting with the conventional specular reflection) and was independently discovered by Andreev in 1964 [10] and by de Gennes and Saint-James in 1963-64 [11, 12]. It is further illustrated in Figure 2.2.

[10]: Andreev (1964), 'The Thermal Conductivity of the Intermediate State in Superconductors'

[11]: Gennes and Saint-James (1963), 'Elementary excitations in the vicinity of a normal metal-superconducting metal contact'

[12]: Saint-James (1964), 'Excitations élémentaires au voisinage de la surface de séparation d'un métal normal et d'un métal supraconducteur'

**Now with some math...**

If $\Delta \ll \mu$, one can approximate linearly the electronic dispersion around $\mu$, $E(k) \approx \mu + \hbar v_F(k - k_F)$, with $k_F$ the Fermi momentum and $v_F = \hbar k_F/m$ the Fermi velocity, which allows to rewrite the electron excitation energy as $\epsilon = \hbar v_F(k - k_F)$.

We can now formalize Andreev reflection as following, keeping with the notations from Figure 2.2: a Landau quasiparticle $e_1$ from the normal metal, with momentum $k_1 = k_F + \delta k_1$, spin $\uparrow$ and excitation energy $\epsilon_1 = \hbar v_F \delta k_1$, pairs up with another quasiparticle $e_2$ with momentum $k_2 = -k_F + \delta k_2$, spin $\downarrow$ and excitation energy $\epsilon_2 = -\hbar v_F \delta k_2$. It does so in order to build a Cooper pair and as such, it leaves a hole behind. To enter the condensate at the pair chemical potential $2\mu$, it requires $\epsilon_1 = -\epsilon_2 = \epsilon$, which imposes $\delta k_2 = \delta k_1 = \delta k = \epsilon/(\hbar v_F)$. In the excitation picture, this missing quasi-electron in the spin-$\downarrow$ band can equivalently be seen as a hole-like excitation $h_2$ with energy $-\epsilon_2 = +\epsilon_1$ propagating backwards with momentum $-k_2 = k_F - \delta k$, group velocity $v_2 = -v_F$, and spin $\uparrow$ (a missing spin $\downarrow$). This is illustrated in Figure 2.2, where the energy dispersion of the hole $h_2$ is depicted by the thin green line.

Andreev reflection therefore appears as the scattering of an electron-like excitation with charge $-e$, momentum $k_F + \delta k$ and velocity $v_F$ into a hole-like excitation with charge $+e$, momentum $k_F - \delta k$ and velocity $-v_F$. This electron-to-hole conversion process hence conserves energy and spin but not charge, and momentum is only approximately conserved $-k_2 \approx k_1 \approx k_F$. The charge excess $-2e$ and the momentum $Q = 2\delta k$ are actually transferred to the superconducting condensate [1] : the two quasi-electrons with opposite spins enter the superconductor to create a Cooper pair with non-zero pair momentum $Q$, which joins the condensate. The electron-hole pair of excitations gives rise to a current density $-ev_F + e(-v_F) = -2ev_F$, *i.e.* twice the current of the incoming electron, which corresponds to the supercurrent carried by the transmitted Cooper pair with charge $-2e$.

1: Provided that a Fermi momentum mismatch exists at the interface, which is the case when the normal region may be doped, part of the momentum $Q$ is thereby transferred to the interface and the other part to the condensate resulting into a supercurrent consistent with total charge conservation.

### 2.1.2 A phase-coherent process

During the reflection, the phases of the incoming electron and the reflected hole remain correlated, meaning that Andreev reflection is actually a phase-coherent process. We just showed that during the conversion, the electron and hole amplitudes penetrate into the superconductor over a length scale $\xi_\epsilon^{(S)}$, which depends on the energy $\epsilon_k$ of the incoming electron. This propagation is therefore associated with an energy-dependent dynamical phase $\varphi(\epsilon)$, associated to the Andreev reflection. We will need this phase in the next section to understand how Andreev states arise. Without going into much math, we can retrieve simply the expression of $\varphi(\epsilon)$ with the following reasoning, based on expressing the energy-dependent momentum of a quasi-electron ($k_e$) and quasi-hole ($k_h$) excitation. Starting from $\epsilon_k = \frac{\hbar^2(k^2-k_F^2)}{2m} = \mu(\frac{k^2}{k_F^2} - 1)$ and using that $E_k = \sqrt{\epsilon_k^2 + \Delta^2}$, we can rewrite the quasiparticle momentum as a function of its energy $E$ :

$$k_{e,h}(E) = k_F\left(1 + \eta_{e,h}\,\mathrm{sgn}(E)\frac{E^2-\Delta^2}{\mu}\right)^{1/2}, \tag{2.1}$$

where $\eta_{e,h} = \pm 1$ stands for the choice of electron (+1) or hole (-1). This shows that as long as $|E| > \Delta$, $k_{e,h} \in \mathbb{R}$ and we are dealing only with propagating states. If $|E| < \Delta$, $k_{e,h} \in \mathbb{C}$ and we have $\sqrt{E^2-\Delta^2} = i\mathrm{sgn}(E)\sqrt{\Delta^2-E^2}$. When $\Delta \ll \mu$, we can Taylor expand Eq. (2.1) to first order (*Andreev approximation*), and obtain:

$$\boxed{k_{e,h}(E) = k_F + i\eta_{e,h}\kappa(E) \quad \text{with } \kappa(E) = k_F\frac{\sqrt{\Delta^2-E^2}}{2\mu} \ll k_F.} \tag{2.2}$$

Therefore, the wave vector $k_{e,h}$ is complex, which means that the associated wavefunction is evanescent in the superconductor over a length scale $\kappa(E)^{-1} \gg k_F^{-1}$, which corresponds precisely to the quantity $\xi_E^{(S)}$ introduced before:

$$\boxed{\xi_E^{(S)} = \frac{\hbar v_F}{\sqrt{\Delta^2-E^2}}.} \tag{2.3}$$

From this we can deduce the time needed for the Cooper pair to enter the condensate, $\tau_E^{(S)} = \xi_E^{(S)}/v_F$. This time also determines the delay between the maximum of the incoming electron wave packet and the maximum of the reflected hole wave packet. By treating asymptotically the conversion from electron to hole as a scattering problem and using the method of stationary phase, one can express it as $\tau_E^{(S)} = \hbar\partial_E\varphi(\epsilon)$. Using Eq. (2.3) for $\xi_E^{(S)}$ and the useful trigonometric identity $\arccos'(x) = -1/\sqrt{1-x^2}$, we finally deduce the expression for the energy-dependent phase acquired over an Andreev reflection*:

$$\boxed{\varphi(E) = -\arccos(E/|\Delta|).} \tag{2.4}$$

* Another way to guess the expression for $\tau_E^{(S)}$ is to invoke the energy-time formulation of the Heisenberg principle, $\tau \sim \hbar/\Delta E$, which can be interpreted (amongst other) as the time frame $\tau$ needed for two particles in interaction to exchange an energy quantity $\Delta E$. As the electron is converted into a hole, its energy is changed by an amount $\Delta E \sim |\epsilon| = \sqrt{\Delta^2-E^2}$ for subgap states $|E| < \Delta$, from which we recover Eq. (2.3).

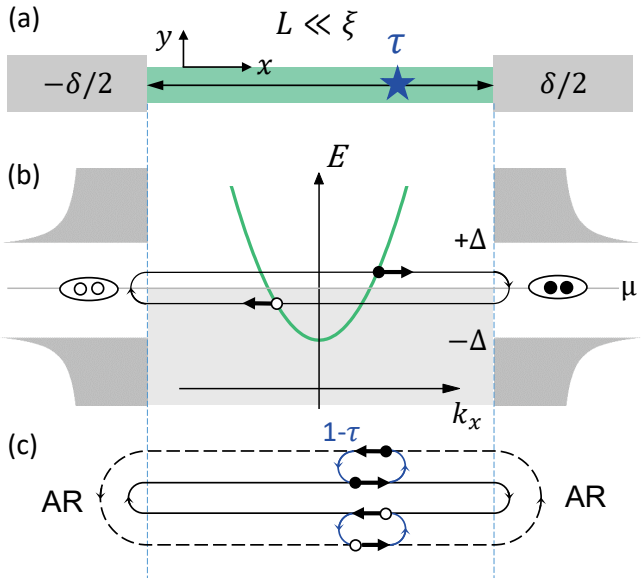


**Figure 2.3:** Andreev bound states (ABS) in a short weak link between two superconductors. (a) A Josephson weak link is formed by sandwiching a piece of normal coherent conductor (green) between two superconducting electrodes (grey). A difference $\delta$ of superconducting phases is applied between the two electrodes. The normal region is assumed to be *short*, *i.e.* to have a length $L \ll \xi$, with $\xi$ the superconducting coherence length of the electrodes. Local impurities, depicted as a blue star, may limit the junction transparency to a finite value $0 \leq \tau \leq 1$. (b) Energy dispersion $E(k_x)$ of a 1D electron (black disk) moving in the $x$-direction and retro-reflected as a hole (black circle) when undergoing an Andreev reflection (AR) on the right interface. The Fermi sea in the normal region is denoted in light grey. Density of states in the superconductors is sketched in darker shades of grey on the left and right hand sides, evidencing the existence of an energy gap $2\Delta$. (c) ABS emerge as closed orbits of right-moving (full line) and left-moving (dashed line) electrons confined in the normal region by Andreev reflection (AR). Back-scattering happening with a probability $1-\tau$ connect right and left movers.

The superconducting order parameter is not only characterized by an amplitude $|\Delta|$, but also by a macroscopic phase $\chi$, such that $\Delta = |\Delta|e^{i\chi}$. This phase is also picked by the quasi-electron as it penetrates the superconductor. Therefore, the phase difference between an incoming electron and a reflected hole can be written $\varphi(E) - \chi$. Conversely, it is $\varphi(E) + \chi$ between an incoming hole and a reflected electron. We have now everything at hand to understand the emergence of ABS.

## 2.2 How do ABS arise ?

Figure 2.1 illustrates how the spatial variations of the order parameter $\Delta(x)$ act as a barrier of potential for an incoming electron. By putting two such barriers on either side of a piece of normal coherent conductor, one can expect to confine the electronic fluid and give rise to bound states, similarly to a particle-in-box problem. Let us now discuss this more formally. We consider the geometry described in Figure 2.3(a), where a piece of normal conductor (green) is connected on either sides to two superconducting electrodes (grey), thus forming a *Josephson weak link*. We assume that both left ($L$) and right ($R$) electrodes have a different superconducting phase $-\delta/2$ and $+\delta/2$ [2] . As discussed in Section 2.1.2, this means that the phase difference between an incoming electron and the reflected hole at the right interface will be $\varphi_R = -\arccos(E/\Delta) - \delta/2$, with $E < \Delta$ the excitation energy of the right-moving electron.

2: Such a superconducting phase difference can be applied in practice by embedding the junction in a superconducting loop and threading it with a magnetic flux, see Chapter 4.

To begin with, let us assume for simplicity that the length $L$ of the normal region is small enough for the dynamic phase developed by the electron during its propagation on the length $L$ to be negligible (as we shall see, this amounts to assuming that $L \ll \xi$, with $\xi = \hbar v_F/L$ and $v_F$ the Fermi velocity in the weak link). As illustrated in Figure 2.3(b), the reflected hole will then undergo a second Andreev reflection on the left interface and be converted back into a right-moving electron, which corresponds to removing one Cooper pair from the left electrode[3] . The phase difference acquired over this second reflection is $\varphi_L = -\arccos(E/\Delta) - \delta/2 = \varphi_R$. Similarly, if considering initially a left-moving electron, the two phases acquired after each reflection would be $\varphi_L = \varphi_R = -\arccos(E/\Delta) + \delta/2$. Now, if this total phase $\varphi_L + \varphi_R$ acquired over a round-trip in the normal metal (see Figure 2.3(c)) is a multiple of $2\pi$, a stationary mode similar to Fabry-Pérot resonances in an optical cavity can develop, giving rise to electronic bound states in the weak link. The energy of such state is given by the resonant condition:

$$\boxed{\pm\delta - 2\arccos(E_A/\Delta) \equiv 0\,[2\pi] \quad \Rightarrow\ \epsilon = \frac{E_A}{\Delta} = \pm\cos(\delta/2) < \Delta,} \tag{2.5}$$

where the + sign (resp. − sign) corresponds to right-moving (resp. left-moving) electrons. These states, which are characterized by a subgap energy $\epsilon < 1$, are known in the literature as **Andreev bound states** (ABS). They correspond to a coherent superposition of electron- and hole-like excitations, which are spatially confined at the junction between the two superconductors and can be interpreted as a localized Cooper pair trapped at the junction. Figure 2.3(b) illustrates that over a round-trip of the incoming electron in the weak link, one Cooper pair has been effectively transmitted from the left superconducting electrode to the right one, therefore contributing to a positive superconducting current[†]. Therefore, although being localized at the junction, Andreev states actually mediate the supercurrent flow and can be viewed as the microscopic mechanism of the Josephson effect [6, 7, 8, 9].

In a real device, the weak link transparency is necessarily limited, either due to the presence of impurities in the normal region which are responsible for some back-scattering, or from a likely Fermi momentum mismatch between the normal and superconducting region acting as an effective barrier at each interface [56]. Equation (2.5) can be generalized to the case of transmission $\tau$ smaller than 1 as follows:

$$\boxed{\epsilon = \pm\sqrt{1 - \tau\sin^2(\delta/2)},} \tag{2.6}$$

with $\epsilon = E_A/\Delta$ the reduced ABS energy. The effect of back-scattering is to couple the right (thin full line) and the left (thin dashed line) branches of the spectrum, which opens a gap around $\delta = \pi$, as illustrated in Figure 2.4. At $\delta = \pi$, which corresponds to the phase value where superconductivity is maximally frustrated, the ABS energy is minimal and equals $\Delta\sqrt{1-\tau}$. Because of the symmetry of the spectrum around zero energy, we will represent from now on only its positive part (excitation picture).

[†] At equilibrium, and in the absence of a macroscopic supercurrent, this left-to-right current is exactly canceled by the inverse process where a Cooper pair enters the normal metal through the right electrode and converts a right-moving hole into a left-moving electron.

3: Notice that we simplified a bit the picture compared to Figure 2.2. For the purpose of easier notations we represented the reflected hole in Figure 2.3(b) as the missing left-moving electron ; this shortcut of notation may be confusing since it gives a wrong picture where the hole has opposite energy and momentum compared to the incoming electron, while it has indeed same spin, energy and (almost) same momentum as we argued in Section 2.1.1.

[6]: Kulik (1970), 'Macroscopic quantization and proximity effect in S-N-S junctions'
[7]: Beenakker and Houten (1991), 'Josephson current through a superconducting quantum point contact shorter than the coherence length'
[8]: Furusaki and Tsukada (1991), 'Dc Josephson effect and Andreev reflection'
[9]: Bagwell (1992), 'Suppression of the Josephson current through a narrow, mesoscopic, semiconductor channel by a single impurity'
[56]: Prada et al. (2020), 'From Andreev to Majorana bound states in hybrid superconductor-semiconductor nanowires'

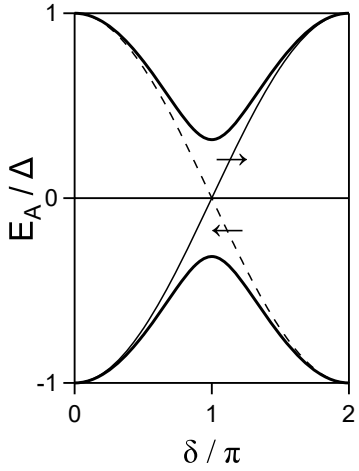


**Figure 2.4:** Energy spectrum $E_A(\delta)$ of Andreev states in a *short* Josephson weak link as a function of the superconducting phase difference $\delta$ in the single-particle picture. Thin lines correspond to a junction transparency $\tau = 1$ (full line is for right-moving electrons, dashed line for left-moving electrons). Thick lines describe the case $\tau = 0.9$.

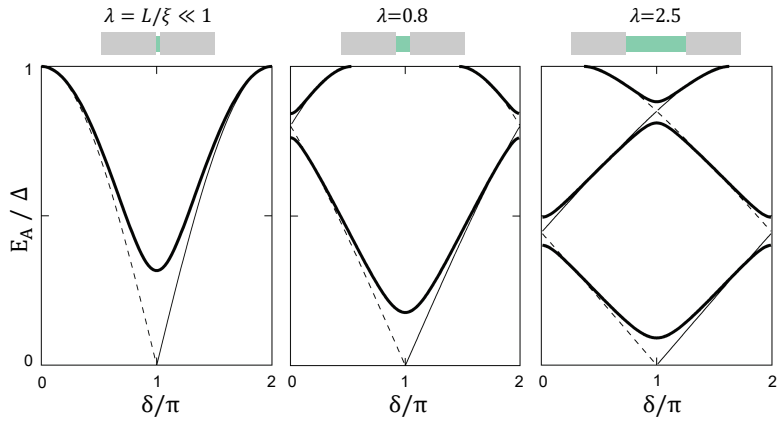


**Figure 2.5:** Effect of the finite length $L$ of the normal region on the ABS spectrum. The positive spectrum (excitation picture) is shown for three different values, $\lambda = 0$ (left), $\lambda = 0.8$ (middle) and $\lambda = 2.5$ (right). Thin lines give the energy dispersion of the right-moving (full) and left-moving (dashed) electrons for the $\tau = 1$ limit of perfect junction transparency. Thick lines correspond to $\tau = 0.9$.

## 2.3 From short to long junctions

Let us now investigate how the finite length $L$ of the normal region affects the previous picture. In Section 2.1.1, we wrote the wave-vector of the right-moving electron as $k_1 = k_F + E/(\hbar v_F)$, and of the missing left-moving electron as $k_2 = -k_F + E/(\hbar v_F)$. The dynamical phase acquired by these two charge carriers over a round-trip in the normal region can then be expressed as $k_1 L + k_2 L = 2EL/(\hbar v_F) = 2\lambda\epsilon$, with $\epsilon = E/\Delta$ the reduced energy and $\lambda = L/(\hbar v_F/\Delta)$. The parameter $\lambda$ can be rewritten as $L/\xi$, where $\xi = \hbar v_F/\Delta$ has the form of a (ballistic) superconducting coherence for a material with Fermi velocity $v_F$ and gap $\Delta$, but here, $v_F$ is the Fermi velocity in the weak link and $\Delta$ is the gap in the superconducting electrodes. The resonant condition from Eq. (2.5) therefore generalizes to

$$\boxed{\pm\delta - 2\arccos(\epsilon) + 2\lambda\epsilon \equiv 0\,[2\pi].} \tag{2.7}$$

There is no analytical solution to Eq. (2.7), however we may get approximate solutions in the limit $\epsilon \ll 1$ or $\lambda \ll 1$. Restricting to $\delta \in [0, 2\pi]$, Eq. (2.7) may be rewritten:

$$\begin{aligned}\epsilon = \pm\cos\left(\lambda\epsilon \pm \frac{\delta}{2}\right) &= \pm\cos(\lambda\epsilon)\cos\left(\frac{\delta}{2}\right) \mp \sin(\lambda\epsilon)\sin\left(\frac{\delta}{2}\right) \\ &\overset{\lambda\ll 1}{\approx} \pm\cos\left(\frac{\delta}{2}\right) \mp \lambda\epsilon\sin\left(\frac{\delta}{2}\right),\end{aligned} \tag{2.8}$$

from which we deduce

$$\boxed{\epsilon \overset{\lambda\ll 1}{\approx} \pm\frac{\cos(\delta/2)}{1+\lambda\sin(\delta/2)} \quad \text{with}\,\lambda = \frac{L}{\xi} = \frac{L\Delta}{\hbar v_F}} \tag{2.9}$$

In the $\lambda \to 0$ limit, we recover the result Eq. (2.5) for a short weak link in absence of backscattering: $\epsilon = \pm\cos(\delta/2)$. To get the exact solution for a finite length weak link, we can solve numerically Eq. (2.7). The associated solutions are plotted in thin lines in Figure 2.5 for three illustrative values of $\lambda$ (solid lines are for right-moving electrons, dashed lines for left-moving ones).

It shows how, as the length $L$ of the normal region is increased, more and more ABS levels are fit in the superconducting gap $\Delta$. By analyzing Eq. 2.7, on finds that the number of ABS at positive energy is $1 + \lfloor 2\lambda/\pi \rfloor$ or $2 + \lfloor 2\lambda/\pi \rfloor$ ($\lfloor x \rfloor$ is the integer part of $x$), depending on $\delta$. In addition, we can investigate the effect of backscattering in the finite-length weak link [9]. We observe that it opens additional gaps at $\delta = 0$, $\pi$ and $2\pi$, where the left and right branches of the spectrum mix, depending on the value of $\lambda$.

[9]: Bagwell (1992), 'Suppression of the Josephson current through a narrow, mesoscopic, semiconductor channel by a single impurity'

So far in the analysis we neglected the effect of spin. Since the energy dispersion of spin $\uparrow$ and spin $\downarrow$ electrons illustrated in Figure 2.5 is degenerate, both species have the same Fermi velocity $v_F$ and follow the same resonant condition given in Eq. (2.7). Consequently, we expect the ABS spectrum shown in Figure 2.5 to be also spin-degenerate. In Appendix A, we put forward a connection existing between Andreev reflection and quantum information, suggesting that Josephson weak links could be seen as confining structures for spin information, and therefore a suitable platform to implement a spin quantum dot. This leads to the following question: *is there a way to lift the inherent spin degeneracy of ABSs and build a spin-active weak link where the spin degree of freedom of the electronic states would matter ?* This question, which has already been extensively investigated in the literature [29, 33, 30], will be the focus of the next chapter.

[29]: Chtchelkatchev and Nazarov (2003), 'Andreev Quantum Dots for Spin Manipulation'
[33]: Béri et al. (2008), 'Splitting of Andreev levels in a Josephson junction by spin-orbit coupling'
[30]: Padurariu and Nazarov (2010), 'Theoretical proposal for superconducting spin qubits'

# Breaking ABS spin degeneracy 3



As we have shown in the previous chapter, ABSs are formed from the coherent Andreev reflections that quasiparticles undergo at both ends of the weak link. Quasiparticles acquire a phase at each of these Andreev reflections an also while propagating along the weak link. To lift the inherent spin degeneracy of ABSs, it is necessary that spin $\uparrow$ and spin $\downarrow$ quasiparticles acquire different phases over a round trip in the weak link, which means that they must have a spin-dependent Fermi velocity. This may be achieved by means of a possible *spin-orbit interaction* (SOI) in the weak link, the effect of which on the Josephson current has been a long subject of investigation [57, 58, 59, 60]. Similarly to the case of atomic spectra where the fine structure arises from interaction between the spin and orbital degrees of freedom of electrons, we show here how the ABS spectrum is modified in the presence of SOI in the weak link.

[57]: Bezuglyi et al. (2002), 'Combined effect of Zeeman splitting and spin-orbit interaction on the Josephson current in a superconductor–two-dimensional electron gas–superconductor structure'
[58]: Krive et al. (2004), 'Charge and spin effects in mesoscopic Josephson junctions (Review)'
[59]: Dimitrova and Feigel'man (2006), 'Two-dimensional S-N-S junction with Rashba spin-orbit coupling'
[60]: Dell'Anna et al. (2007), 'Josephson current through a quantum dot with spin-orbit coupling'

## 3.1 Foreword on spin-orbit interaction

### 3.1.1 Spin-orbit in vacuum

When a charged particle moves in an electric field $\vec{E}$, it experiences an effective magnetic field that couples to its spin through the Zeeman effect. The corresponding Hamiltonian is usually written as:

$$\boxed{H_{SO} = \vec{\alpha} \cdot (\vec{\sigma} \times \vec{k}),} \tag{3.1}$$

where $\vec{k}$ is the electron wavevector, $\vec{\sigma}$ the vector of Pauli matrices in spin space and $\vec{\alpha}$ the spin-orbit coupling, which determines the strength of the interaction between the spin and the momentum of the electron. This expression can be easily recovered from the following argument, writing the effective magnetic field* in SI units as $\vec{B} = -(\vec{v} \times \vec{E})/c^2$ with $\vec{v}$ the electron velocity and $c$ the speed of light. The Zeeman Hamiltonian describing the coupling of the electron spin with the magnetic field then writes $H = -\vec{\mu} \cdot \vec{B}$, where $\vec{\mu} = -g\mu_B\vec{\sigma}/2$ is the magnetic moment of the electron with $\mu_B$ the Bohr magneton, $g$ the electron gyromagnetic ratio, and $\vec{\sigma}$ the Pauli matrix vector. Rewriting the electron velocity $\vec{v}$ in terms of its momentum $\vec{k} = m\vec{v}/\hbar$, we recover Eq. (3.1) from the Zeeman Hamiltonian with $\vec{\alpha} = -g\mu_B\hbar\vec{E}/(2mc^2)$. Although this rough derivation gives the correct analytical form for the spin-orbit Hamiltonian, it predicts a wrong prefactor by many orders of magnitude. In solids, instead of scaling like the Dirac gap $mc^2$, which is of the order of MeV,

* True in the non-relativistic limit $v \ll c$. This result comes from the Joules-Bernoulli equations describing the transformation of E and B fields between two inertial frames. The magnetic field $\vec{B}'$ in a frame moving at the velocity $\vec{v}$ can be expressed in terms of the $\vec{E}, \vec{B}$ fields in the rest frame as $\vec{B}' = \gamma\left(\vec{B} - \frac{\vec{v}\times\vec{E}}{c^2}\right) - (\gamma - 1)(\vec{B} \cdot \hat{v})\hat{v}$ with $\hat{v} = \vec{v}/||\vec{v}||$ and $\gamma = 1/\sqrt{1 - v^2/c^2}$ the Lorentz factor from special relativity.

the denominator of $\vec{\alpha}$ contains a combination of splittings in the energy bands of the crystal, which are rather in the eV range.

### 3.1.2 Spin-orbit in solid-state devices

There are generally two ways in which an electric field can arise in a nanostructure. On the one hand, the crystal itself can develop an intrinsic electric field when its unit cell lacks an inversion center. This is generally known as *bulk* inversion asymmetry, which gives rise to a *Dresselhaus* kind of spin-orbit coupling. On the other hand, an electric field may arise when the lack of inversion symmetry is due to an external potential, which can be due to crystal surfaces, spatial inhomogeneities, or voltages from external metallic gates. This case is generally referred to as a *structural* inversion asymmetry and corresponds to the *Rashba* spin-orbit interaction.

In the most general case, the spin-orbit Hamiltonian assumes the form $H_{SO} = \vec{\Omega}(\vec{k}) \cdot \vec{\sigma}$, with $\vec{\Omega}(\vec{k})$ the spin-orbit field. Since time-reversal reverts both spin and momentum, time-reversal symmetry requires that $\vec{\Omega}(\vec{k}) = -\vec{\Omega}(-\vec{k})$, which imposes the spin-orbit field to be an odd function of momentum $\vec{k}$ [61]. This is indeed the case in the Hamiltonian of Eq. (3.1), which contains only linear terms in $\vec{k}$. Time-reversal symmetry actually imposes stringent constraints on the energy spectrum of a spin 1/2 system, which we are now going to briefly review before investigating quantitatively the effect of linear SOI on the ABS spectrum.

[61]: Dresselhaus (1955), 'Spin-Orbit Coupling Effects in Zinc Blende Structures'

## 3.2 ABS in presence of spin-orbit

In Appendix B, we show with symmetry arguments that SOI can split the Andreev levels, but that the Andreev spectrum must be mirror-symmetric around the two time-reversal invariant phases $\delta = 0, \pi$, where the doublets of $\uparrow, \downarrow$ states must cross.

We consider a normal wire infinitely long in the $\hat{x}$ direction. Assuming that the electric field due to the bulk or structural asymmetry is in the $\hat{z}$ direction, the Hamiltonian of the normal region can be written:

$$H = H_0 + H_{SO} = \frac{\hbar^2 \vec{k}^2}{2m^*} + U(y) - \alpha \hat{z} \cdot (\vec{k} \times \vec{\sigma}), \tag{3.2}$$

with $m^*$ the effective mass of the electron in the solid and $U(y)$ the confining potential in the transverse direction.

### 3.2.1 1D wire

In a first step we consider a purely one-dimensional wire, and are left with:

$$H_{1D} = \frac{\hbar^2 k_x^2}{2m^*} - \alpha k_x \sigma_y = \frac{\hbar^2 (k_x - k_\alpha \sigma_y)^2}{2m^*} - \frac{m^* \alpha^2}{2\hbar^2} \quad \text{with } k_\alpha = \frac{m^* \alpha}{\hbar^2}, \tag{3.3}$$

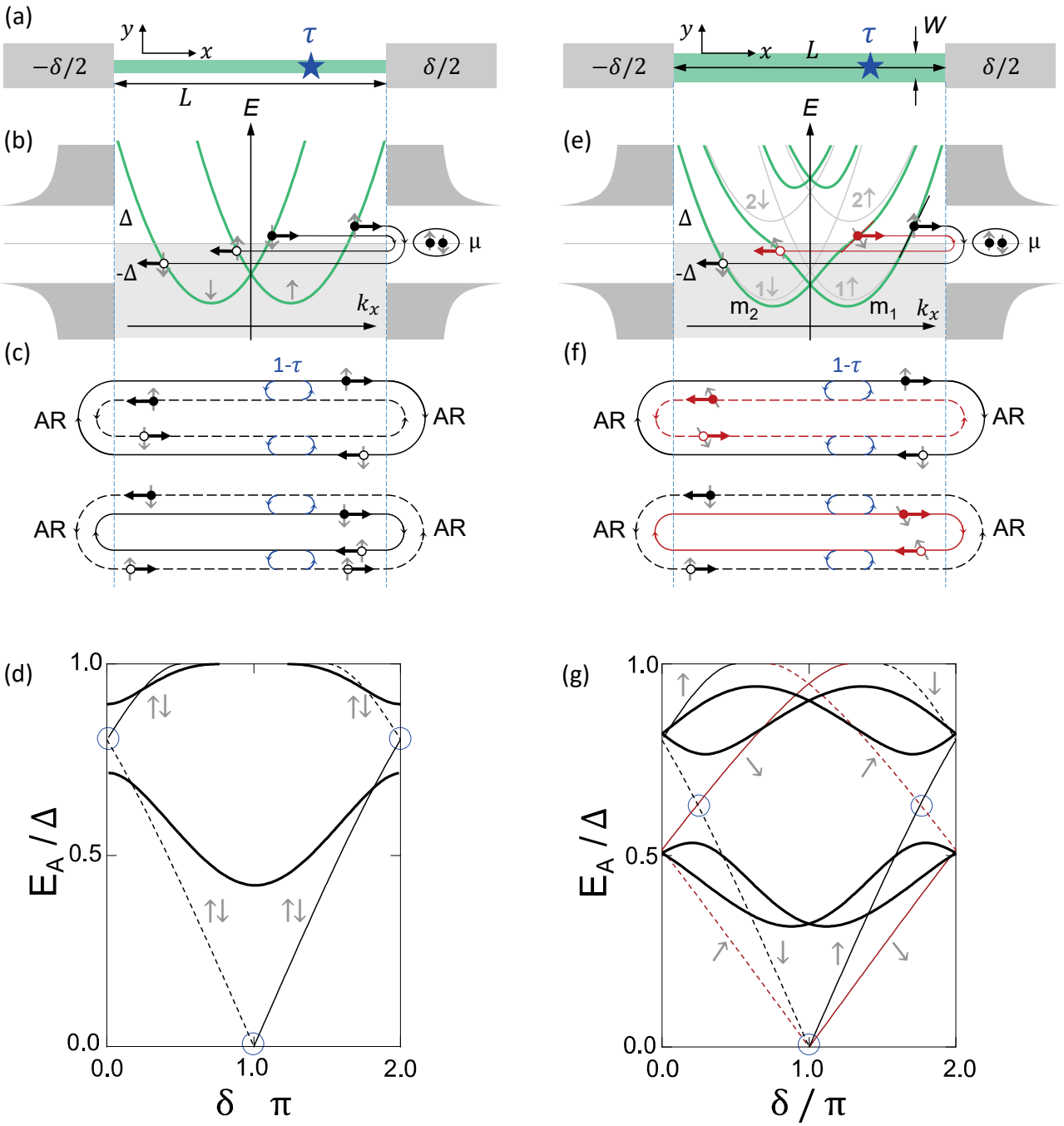


**Figure 3.1:** Same as in Figure 2.3 but including SOI in the normal region. (a) Schematic of a weak link of length $L$, with a single scatterer (blue star) with transmission $\tau$. (b) Dispersion relation for a purely one-dimensional weak link in the presence of SOI (green solid lines, labels $\uparrow\downarrow$ indicate spin in y-direction). Density of states of superconducting electrodes is sketched at both ends of the wire. (c) Andreev reflections (AR) at the superconductors couples electrons (full circles) with holes (open circles) of opposite spins and velocities, leading to the formation of ABS. Blue arrows indicate reflections due to a scatterer. (d) Energy of ABS (excitation picture). Thin lines in (d) and (g): $\tau = 1$, ABS formed from right-moving electrons and left-moving holes (solid) or the opposite (dashed). Backscattering ($\tau \neq 1$) leads to opening of gaps at the crossings highlighted with blue circles in (d). Resulting spin-degenerate Andreev levels are shown with thick solid lines. (e-g) Effect of SOI in the presence of two transverse subbands, only the lowest one being occupied. (e) Grey solid lines labelled $1\uparrow\downarrow$ and $2\uparrow\downarrow$ are dispersion relations for uncoupled subbands. SOI couples states of different subbands and opposite spins, leading to hybridized bands (green solid lines) with energy-dependent spin textures. Fermi level $\mu$ is such that only the lowest energy bands $m_1$ and $m_2$ are occupied. AR couples for example a fast electron from $m_2$ to a fast hole (in black), and a slow electron from $m_1$ to a slow hole (in red). (f) Construction of ABS: black and red loops are characterized by different absolute velocities. Spins pointing in different directions symbolize spin textures of the bands. Thin red and black lines, solid and dashed in (f,g): ABS at $\tau = 1$, associated with different spin textures. Thick black lines in (g): ABS when crossings highlighted with blue circles are avoided due to backscattering (parameters used in the figure: $\lambda_1 = 0.8$, $\lambda_2 = 2.0$, $\tau = 0.8$ and $x_r = 0$).

which describes two energy parabolas shifted around $k_x = 0$ by an amount $k_\alpha$ linear in the spin-orbit strength $\alpha$. Since the effective magnetic field causing the SOI is directed along $\hat{y}$, spin polarization occurs along this direction. For spin $\uparrow$ electrons, $\sigma_y = +1$, corresponding to the right-shifted parabola. The left-shifted one corresponds to spin $\downarrow$ electrons with $\sigma_y = -1$. Therefore, as shown by the green lines in Figure 3.1(b), SOI splits the parabolic dispersion relation according to the electron spin direction [62]. We recover the result from Figure B.1(b) that we had intuited qualitatively reasoning in terms of the system's symmetries.

[62]: Bychkov and Rashba (1984), 'Oscillatory effects and the magnetic susceptibility of carriers in inversion layers'

Now, as shown in Figure 3.1(c), Andreev reflections (AR) at the superconductors couples electrons (full circles) with holes (open circles) of opposite spins and velocities. When the transmission probability across the wire is perfect ($\tau = 1$), ABS arise when the total accumulated phase along closed paths that involve two AR and the propagation of an electron and a hole in opposite directions is a multiple of $2\pi$ [5, 6]. Figure 3.1(d) shows, in the excitation representation, the energy of the resulting ABS as a function of $\delta$ for a finite length $\lambda = 0.8$. ABS built with right- (left-) moving electrons are shown with thin solid (dashed) lines in Figure 3.1(d). Backscattering in the weak link ($\tau \neq 1$), due either to impurities or to the spatial variation of the electrostatic potential along the wire, couples electrons (as well as holes) of the same spin travelling in opposite directions, leading to avoided crossings at the points indicated by the open blue circles in Figure 3.1(d). Given that both spin species still have the same Fermi velocity, they acquire the same phase over a round-trip in the weak link, $k_{1\uparrow} + k_{2\downarrow} = k_{1\downarrow} + k_{2\uparrow}$. Consequently, the resonant condition to form bound states is the same for both, and is still described by Eq. (2.7): one obtains, for this value of $\lambda$, one or two distinct ABS (thick solid lines) that remain spin-degenerate, as illustrated in Figure 3.1(d).

[5]: Andreev (1966), 'Electron Spectrum of the Intermediate State of Superconductors'
[6]: Kulik (1970), 'Macroscopic quantization and proximity effect in S-N-S junctions'

### 3.2.2 Quasi-1D wire

If we now consider that the nanowire has a finite size $W$ in the transverse directions $\hat{y}$ and $\hat{z}$, new terms appear in the normal region Hamiltonian:

$$H_{2D} = \frac{\hbar^2}{2m^*}(k_x^2 + k_y^2 + k_z^2) + U(y,z) - \alpha(k_x\sigma_y - k_y\sigma_x). \tag{3.4}$$

Assuming a harmonic confinement $U(y,z) = m\omega_0^2(y^2 + z^2)$ in the transverse section, $k_y$ and $k_z$ become quantized. We recognize in $\hbar^2(k_y^2 + k_z^2)/(2m^*) + U(y,z)$ a 2D harmonic oscillator which can be solved exactly as $\hbar\omega_0 n$ with $n \in \mathbb{N}^*$ and $\omega_0 = \hbar/(m^*(W/2)^2)$ involving the effective nanowire diameter $W$. We are then left with:

$$H_{2D} = \frac{\hbar^2(k_x - k_\alpha\sigma_y)^2}{2m^*} + \alpha k_y\sigma_x + n\hbar\omega_0 - \frac{m^*\alpha^2}{2\hbar^2}, \tag{3.5}$$

the last two terms being only energy offsets. As illustrated in gray curves in Figure 3.1(e), the energy dispersion now consists in a series of transverse bands shifted in energy by $E_n^\perp = n\hbar\omega_0$ with $n \in \mathbb{N}^*$, while each band is itself spin-split in two $k_x$-shifted subbands. As for the remaining spin-orbit term $\alpha k_y\sigma_x$, it couples different transverse sub-bands with different spin, which has the effect to lift the degeneracies at their crossing points. As a result, the sub-bands become non-parabolic, as shown in green curves in Figure 3.1(e). Because of this subband mixing, spin is no longer

a conserved quantity and an energy-dependent spin texture arises along each subband. However, it is still possible to assign a *pseudospin* index $\sigma \in \{\downarrow, \uparrow\}$ for each subband.

We focus on a situation in which only the two lowest subbands (labelled *m1* and *m2* in Figure 3.1(e)) are occupied. One can derive the following expression for their energy dispersion [32]:

[32]: Park and Levy Yeyati (2017), 'Andreev spin qubits in multichannel Rashba nanowires'

$$E_s(k_x) = \frac{\hbar^2 k_x^2}{2m^*} + \frac{E_1^\perp + E_2^\perp}{2} - \sqrt{\left(\frac{E_1^\perp - E_2^\perp}{2} - s\alpha k_x\right)^2 + \eta^2}, \tag{3.6}$$

where $s = -1$ corresponds to $m_1$ (pseudospin $\sigma = \uparrow$) and $s = +1$ to $m_2$ (pseudospin $\sigma = \downarrow$), and where $\eta = \sqrt{2}\alpha/W$ is the strength of the subband mixing due to the SOI. Linearizing around the chemical potential $\mu$, we obtain the Fermi velocity associated to both modes $j = 1, 2$:

$$v_{Fj} = \frac{\hbar k_{Fj}}{m^*} + (-1)^j \frac{\alpha\left(E_1^\perp/2 - (-1)^j \alpha k_{Fj}\right)}{\hbar\sqrt{\left(E_1^\perp/2 - (-1)^j \alpha k_{Fj}\right)^2 + \eta^2}}, \tag{3.7}$$

where $k_{Fj}$ are the Fermi wave vectors satisfying $E_s(k_{Fj}) = \mu$. If there is no subband mixing, i.e. $\eta = 0$, (gray parabolas in Figure 3.1(e)), Eqs. (3.6) and (3.7) show that $k_{F1} - k_{F2} = 2m^*\alpha/\hbar^2 = 2k_\alpha$ and $v_1 - v_2 = (k_{F1} - k_{F2})\hbar/m^* - 2\alpha/\hbar = 0$, indicating that the Fermi velocities are the same. Importantly, when $\eta \neq 0$, Eq. (3.7) shows that we have now two modes which are characterized by different Fermi velocities. In the absence of particle backscattering, the phase accumulated in the Andreev reflection processes at $x = -L/2$ and $x = L/2$, as illustrated in Figure 3.1(f), leads to the following transcendental equation for the energy $\epsilon = E_A/\Delta$ as a function of $\delta$ [32]:

[32]: Park and Levy Yeyati (2017), 'Andreev spin qubits in multichannel Rashba nanowires'

$$\boxed{\sin\left(\epsilon\lambda_1 - s\delta/2 - \arccos\epsilon\right)\sin\left(\epsilon\lambda_2 + s\delta/2 - \arccos\epsilon\right) = 0,} \tag{3.8}$$

where $\lambda_{j=1,2} = L/\xi_j$ with $\xi_j = \hbar v_{Fj}/\Delta$, the (ballistic) superconducting coherence length associated to both modes with Fermi $v_{Fj}$. It can be viewed as a two-mode generalization of Eq. (2.7). The two zeros of this equation are given by:

$$\pm s\delta - 2\arccos\epsilon + 2\epsilon\lambda_1 = 0 \mod 2\pi \tag{3.9}$$

These two families of ballistic ABSs, built from states with different spin textures, are represented by red and black thin lines in Figure 3.1(f,g). Approximate solutions are

$$\epsilon_j(\delta) = \frac{\pm\cos\delta/2}{1 + \lambda_j \sin\delta/2} \tag{3.10}$$

for $\lambda\epsilon_j \ll 1$, and

$$\epsilon_j(\delta) = \frac{(2k+1)\pi \pm s\delta}{2(1+\lambda_j)}, \tag{3.11}$$

with $k \in \mathbb{Z}$, for $\epsilon \ll 1$. This last expression accounts well for the quasi linear dispersion of the Andreev energy (except close to the gap energy) when $\lambda$ departs from 0.

### 3.2.3 Effect of backscattering

To model backscattering in the normal region, we add a point-like impurity at the position $x_0$ with $-L/2 \leq x_0 \leq L/2$, described in the Hamiltonian by a potential barrier $U_0\delta(x - x_0)$. Accounting for this extra boundary condition, one can derive the following transcendental equation for the ABSs energy [32, 51] :

[32]: Park and Levy Yeyati (2017), 'Andreev spin qubits in multichannel Rashba nanowires'
[51]: Tosi et al. (2019), 'Spin-Orbit Splitting of Andreev States Revealed by Microwave Spectroscopy'

**ABS energies in a finite-length weak link with SOI**

$$\tau \cos\Big[(\lambda_1 - \lambda_2)\epsilon \mp \delta\Big] + (1-\tau)\cos\Big[(\lambda_1 + \lambda_2)\epsilon x_r\Big] = \cos\Big[2\arccos(\epsilon) - (\lambda_1 + \lambda_2)\epsilon\Big], \quad (3.12)$$

where $x_r = 2x_0/L \in [-1, 1]$ indexes the impurity position and $0 \leq \tau \leq 1$ is the transmission probability at the impurity. The detailed derivation of this equation is provided in Appendix E. As before, introducing a finite backscattering probability $1 - \tau > 0$ couples left and right-movers,[1] leading to avoided crossings at the points indicated by the open blue circles in Figure 3.1(e). The resulting ABSs group in manifolds of spin-split states, represented in thick black lines. Remarkably, this splitting takes place in the absence of any Zeeman field. A finite magnetic field would however be needed to lift the residual *Kramers* degeneracies at $\delta = 0$ and $\pi$, which hold as long as time-reversal symmetry is preserved (see Appendix B). When $\lambda_1 = \lambda_2 = \lambda$, Eq. (3.12) can be expanded up to second order in $\epsilon$:

$$(2 - \tau + \tau\cos\delta) - \Big[2 + 4\lambda + 2\lambda^2 + 2x_r^2\lambda^2(1-\tau)\Big]\epsilon^2 = 0, \quad (3.13)$$

from which we obtain an approximate expression of $E_A$, valid near $\delta = \pi$, and for not-too-small transmissions:

$$E_A(\delta) \approx \Delta_{\text{eff}}\sqrt{1 - \tau\sin^2(\delta/2)} \quad (3.14)$$

$$\text{with } \Delta_{\text{eff}} = \frac{\Delta}{\sqrt{(1+\lambda)^2 + (x_r\lambda\sqrt{1-\tau})^2}} \overset{1-\tau\ll 1}{\approx} \frac{\Delta}{1+\lambda}. \quad (3.15)$$

It turns out that this expression also accounts correctly for the dependence near $\delta = \pi$ of the average of the two solutions $E_{A1}$ and $E_{A2}$ of Eq. (3.12) when $\lambda_1 \neq \lambda_2$. One then takes $\lambda = (\lambda_1 + \lambda_2)/2$. Equation (3.14) shows that at low energy and close to $\delta = \pi$, the energy of the lowest-in-energy pair transition behaves like that of a zero-length weak link with a reduced superconducting gap $\Delta_{\text{eff}}$. This approximate result is used at many instances in the following.

Another model was investigated assuming a more physical situation where backscattering takes place at the left ($x = -L/2$) and right ($x = L/2$) edges of the wire. It results in another transcendental equation for the ABS energies, with a slightly more cumbersome expression (see Eq. (A.13) in Ref. [51] or Eq. (E.49) in Appendix E), but with the same number of parameters: two transparencies $\tau_L$, $\tau_R$ associated to the left and right barriers, instead of one transparency $\tau$ and the position $x_r$ for the single-

1: Actually, because spin is no longer a good quantum number in presence of SOI, forward scattering should in principle also be allowed, although it is not treated here for simplicity. Including other scattering terms would certainly cause additional repulsion between levels, but it is not expected to modify the overall picture.

[51]: Tosi et al. (2019), 'Spin-Orbit Splitting of Andreev States Revealed by Microwave Spectroscopy'

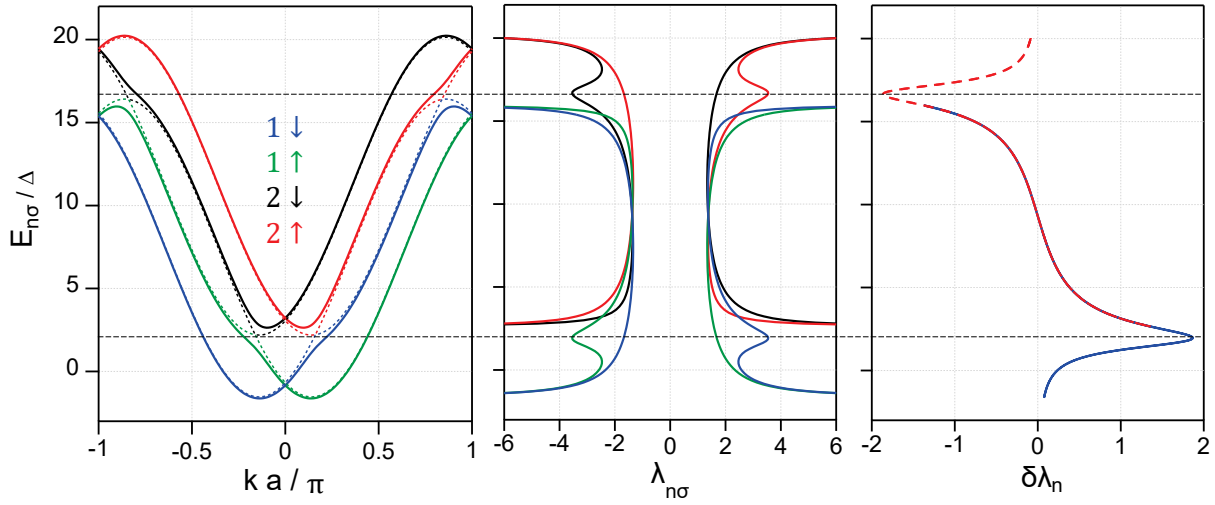


**Figure 3.2:** Spin-dependent Fermi velocities for the two lowest transverse modes, as obtained from a discrete tight-binding description of the normal region. Left plot: Energy dispersion $E_{n\sigma}/\Delta$ as a function of the electron momentum $k$ (normalized by the unit cell size $a$), when 2D-spin orbit ($\alpha_x \neq 0, \alpha_y \neq 0$) is taken into account. The curves were computed from Eq. (C.2), see Appendix C for the parameters. The bands for ($\alpha_x \neq 0, \alpha_y = 0$) are shown in dotted lines to highlight the hybridization points. Middle plot: Inverse Fermi velocities (horizontal axis) $\lambda_{n\sigma} = L/\xi_{n\sigma} = L\Delta/\hbar v_{n\sigma} \propto 1/v_{n\sigma}$ for each subband $n\sigma$ as a function of the band energy $E_{n\sigma}/\Delta$ (vertical axis). Right plot: difference of normalized inverse Fermi velocities $\delta\lambda_n = \lambda_{n,\downarrow} - \lambda_{n,\uparrow}$ as a function of energy $E_{n\sigma}/\Delta$, showing a maximum at the bands hybridization points.

barrier model presented above. Both models predict similar dispersions for the spin-split ABSs and can fit the data equally well, as we will show in Chapter 6.

### 3.2.4 Spin-dependent Fermi velocities

In the following, we generalize to the situation where the second transverse band may also be occupied. For this purpose, we relabel the model parameters with the subscripts $n\sigma$, where $n = 1, 2$ is the band number and $\sigma \in \{\downarrow, \uparrow\}$ is the pseudospin index associated to each subband. We have just shown that when it comes to ABSs, the figure of merit is not the Fermi velocity $v_{n\sigma}$ of the subband $n$ with pseudospin $\sigma$, but the dimensionless ratio $\lambda_{ns} = \frac{L}{\xi_{n\sigma}}$ with $\xi_{n\sigma} = \hbar v_{n\sigma}/\Delta$, which gives the number of ABS in the window $[-\Delta, \Delta]$ around $\mu$. More precisely, the number of ABS in the gap equals $1 + \lfloor 2\lambda/\pi \rfloor$ or $2 + \lfloor 2\lambda/\pi \rfloor$, depending on $\delta$ and $\tau$. Also, the quantity $\delta\lambda_n = \lambda_{n\downarrow} - \lambda_{n,\uparrow}$ directly determines the spin splitting of the Andreev states.

In Figure 3.2, we plot as a function of the band energy $E_{n\sigma}$ both $\lambda_{n\sigma}$, for each of the four subbands $n\sigma$, and $\delta\lambda_n$ for the two transverse bands in the presence of SOI. These quantities were obtained using a two-channel tight-binding (TB) description of the normal region, as further detailed in Appendix C. We will make use later of this TB description in Chapter 7, which provides a simple way to extend the previous theory to the case of a multimode weak link (not tractable analytically!) and to add extra ingredients in the normal region like scattering barriers, on-site Coulomb repulsion, etc. Note that in this discrete model, the bands in absence of SOI are given by shifted cosine arches. In the continuum limit, we would recover the parabolic bands described in the previous section. As evidenced with horizontal dashed lines in Figure 3.2, $\delta\lambda_n$

exhibits a maximum close to the band bottom, at the hybridization points where the band mixing from SOI is the largest. Therefore, to get sizeable spin splitting for the ABSs, one should operate in a situation where the chemical potential $\mu$ lies close to the bottom of a transverse band, where $\delta\lambda_n$ gets a finite appreciable value. As $\mu$ increases, the subband hybridization drops and $\delta\lambda \to 0$. [2]

2: Until $\mu$ gets close to the top of a subband where $\delta\lambda$ departs again from 0. However, the latter is shown for illustrative purposes only, because in practice the chemical potential never reaches the ionization energy associated to the top of the bands.

## 3.3 Implementation with semiconducting nanowires

In the previous sections, we have shown how a linear SOI is able to lift the ABS spin degeneracy except at a few phase values $\delta = 0, \pi$, which are protected by time reversal symmetry. Now, *can such a linear SOI take place in solids and is the Hamiltonian in Eq. (3.1) a good approximation for it ?*

As discussed in Section 3.1, the spin-orbit field in crystals $\vec{\Omega}(\vec{k})$ can be shown to generically contain both linear and cubic powers of $\vec{k}$, which can contribute to different extent depending on the crystalline structure of the solid. Nanostructures made from III-V semiconductor materials appear as interesting systems to explore spin physics as they benefit for free from a Dresselhaus SOI due to the inherent inversion asymmetry of their crystal unit cell. Growing semiconducting nanowires out of these materials offers even further appeal as the quantum confinement generated by their typical small transverse dimensions may allow for an extra Rashba contribution to the overall SOI, which can be further tuned by applying external electric field using close-by metallic gates. By controlling their growth conditions, these materials can typically crystallize in the zincblende (ZB) or wurtzite (WZ) phases. In ZB nanowires, bulk effects are expected to be negligible since they are only cubic in momentum [63]. On the other hand, WZ crystals are known to exhibit linear SOI already in the bulk, which is well described by a Hamiltonian of the from from Eq. (3.1).

[63]: Campos et al. (2018), 'Spin-orbit coupling effects in zinc-blende InSb and wurtzite InAs nanowires'

As a major breakthrough in material science, Krogstrup *et al.* demonstrated in 2015 the growth by molecular beam epitaxy of semiconducting nanowires made from an InAs core in the WZ phase covered by a thin aluminium shell [37]. The uniform and perfectly sharp interface of aluminium to the InAs core was shown to induce a "hard" superconducting gap in the semiconductor by proximity effect [38], making such nanowires attractive systems to implement Josephson weak links. The presence of linear SOI was confirmed in such InAs nanowires by measuring the weak antilocalization effect [36]. These two reasons make InAs nanowires good candidates to explore the spin physics of Andreev states.

[37]: Krogstrup et al. (2015), 'Epitaxy of semiconductor-superconductor nano-wires'

[38]: Chang et al. (2015), 'Hard gap in epitaxial semiconductor-superconductor nanowires'

[36]: Scherübl et al. (2016), 'Electrical tuning of Rashba spin-orbit interaction in multigated InAs nanowires'

Quite remarkably, although many experimental results are consistent with the presence of significant SOI in these nanowires, its exact origin still appears (partially) unclear. Indeed, the intrinsic SOI due to bulk effects is known to depend strongly on the crystal directions and interestingly in the usual nanowires grown along the [0001] direction, it vanishes by symmetry for each individual transverse mode in the wires, as discussed in Appendix D. Therefore, this would point towards an extrinsic structural inversion asymmetry as being the main source of the linear Rashba SOI measured experimentally.

# Probing Andreev levels with cQED

In the previous part, we described how ABS generally arise in weak links between two superconductors and discussed how the spin degeneracy of ABS can be lifted in weak links where spin-orbit coupling is present. In this second part, we review how the Andreev spectrum of such systems is measured using the techniques of circuit quantum electrodynamics (cQED). This detection technique consists in coupling the phase-biased weak link to a microwave resonator. The coupling arises through current fluctuations in the resonator, which induce phase fluctuations across the weak link. In Chapter 4, we develop a general theory to describe the resonator-weak link coupling and derive an expression for the resonator frequency shift as a function of the microscopic occupancies of the ABS levels. These results guide the design of microwave resonators, which is the object of Chapter 5.

# Modeling the coupling between a resonator and a phase-biased weak link

# 4



In cQED, the coupling of a weak link to a microwave resonator shifts the frequency of the latter. If the coupling is small enough, then the presence of the weak link does not affect the structure of the resonator mode and can be treated as a perturbation. In the following I will discuss two ways of calculating this shift in terms of the microscopic occupancies of ABS. The first one follows the treatment done by Kurilovich *et al.* [64]. The weak link is considered as a circuit element characterized by a complex admittance. We will see that the resonator shift due to the weak link will be directly proportional to the imaginary part of the weak link admittance. By using linear response theory, the admittance of the weak link, hence the frequency shift of the resonator, are expressed in terms of the occupancies of ABS. The second approach is a Hamiltonian-based description of the resonator coupled to the weak link, which we developed in Refs. [52, 53].

[64]: Kurilovich et al. (2021), 'Microwave response of an Andreev bound state'

[52]: Park et al. (2020), 'From Adiabatic to Dispersive Readout of Quantum Circuits'
[53]: Metzger et al. (2021), 'Circuit-QED with phase-biased Josephson weak links'

## 4.1 Resonator shift from an electrical engineer point of view

### 4.1.1 Resonator admittance

Following the treatment of Ref. [64], let us treat the weak link as a two-port black box coupled in parallel to a microwave resonator described by its admittance matrix $Y_{ij}^{\text{res}}[\omega]$, where $i, j \in L, R$ label the two ports of the weak link (see Figure 4.1). The admittance matrix relates the currents flowing in the resonator to the voltages at nodes L and R,

$$I_i(\omega) = \sum_{j=L,R} Y_{ij}^{res}[\omega] V_j(w). \tag{4.1}$$

For simplicity, let us assume that the resonator is lossless and reciprocal* (the latter is always true for R,L,C circuits). In this case, $Y^{\text{res}}$ is a purely imaginary matrix [65]. The condition for a parallel resonance that the imaginary part of the circuit admittance goes to zero, then translates into the more general condition of zero admittance. In other words, the bare frequency of a lossless resonator, *i.e.* in the absence of the weak link, can be determined by the frequency at which the equivalent admittance of the resonator goes to zero. The latter, which we denote $Y^*$, is defined as the admittance seen from one port when the other is open. To compute $Y^*$ in terms of the admittance matrix's components $Y_{ij}$, consider the circuit

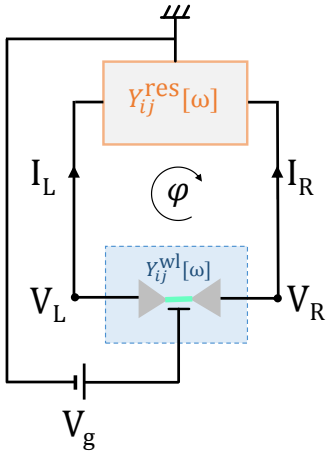


**Figure 4.1:** Weak link galvanically connected in parallel to a resonator with admittance $Y_{ij}^{\text{res}}$. A magnetic flux $\phi$ sets the average phase difference $\varphi$ across the weak link, and a gate voltage $V_g$ tunes the charge density profile in the junction region.

[64]: Kurilovich et al. (2021), 'Microwave response of an Andreev bound state'

[65]: M.Pozar (2011), *Microwave Engineering, 4rd Ed*

* If a network is lossless, the net real power delivered to it must be zero: $P = \text{Re}(V^T I^*) = \frac{1}{2}(V^T I^* + V^{*T} I) = \frac{1}{2}(V^{*T} I + I^{*T} V) = V^{*T}\left(\frac{Y+Y^{*T}}{2}\right) V = 0$. Since $V$ is external to the network and can therefore be chosen arbitrarily, $Y + Y^{*T}$ must be zero for a lossless network, *i.e.* $Y$ is anti-Hermitian: $Y = -Y^\dagger$. If moreover the network is reciprocal ($Y = Y^T$), then $Y = -Y^*$ *i.e.* $\text{Re}(Y) = 0$.

depicted in Figure 4.2. Applying Eq. (4.1) gives

$$\begin{cases} I_1 = Y_{11}V_1 + Y_{12}R_2I_2 \\ I_2 = Y_{21}V_1 + Y_{22}R_2I_2 \end{cases} \Rightarrow I_2 = \frac{Y_{21}}{1 - Y_{22}R_2}V_1,$$

from which we get, by definition of $Y^*$:

$$\begin{aligned} Y^* \equiv \left.\frac{I_1}{V_1}\right|_{R_2\to\infty} &= Y_{11} + Y_{12}R_2\left.\frac{I_2}{V_1}\right|_{R_2\to\infty} \\ &= Y_{11} + \left.\frac{R_2Y_{21}}{1 - Y_{22}R_2}\right|_{R_2\to\infty} Y_{12} \\ &= Y_{11} - \frac{Y_{12}Y_{21}}{Y_{22}}. \end{aligned}$$

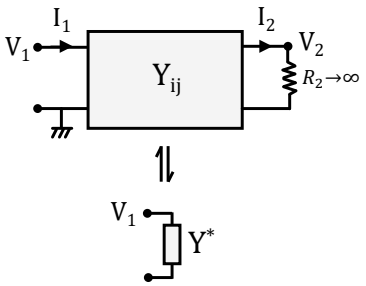


**Figure 4.2:** From two-ports admittance matrix $Y_{ij}$ to equivalent admittance $Y^*$. Note that we have defined $Y^*$ as the admittance seen from one port when no current flows at the other.
⚠ $Y^*_{11} = \left.\frac{I_1}{V_1}\right|_{I_2\to 0} \neq \left.\frac{I_1}{V_1}\right|_{V_2\to 0} = Y_{11}$

The condition $Y^* = 0$ then amounts to $Y_{11}Y_{22} - Y_{12}Y_{21} = 0$ *i.e.* $\det Y = 0$. Therefore, the bare frequency $\omega_0$ of the resonator can be found as the solution of the characteristic equation:

$$\boxed{\det Y^{\text{res}}_{ij}[\omega_0] = 0.} \tag{4.2}$$

This implies that the admittance matrix $Y^{\text{res}}$ has zero as an eigenvalue, that is to say there exists a non-trivial voltage mode $V_{\text{res}}$, such that $Y^{\text{res}}V_{\text{res}} = 0$, *i.e.* $I^{\text{res}}_i[\omega_0] = \sum_{j=L,R} Y^{\text{res}}_{ij}[\omega_0]V_{\text{res},j} = 0$ from Eq. (4.1), and we are indeed looking at a *current* (parallel) type of resonance[1] .

1: In the general case, for a parallel (=current) type of resonance, the resonator impedance equals its resistance $Z = R$ and the total current is minimal. Here because we assumed initially that $R = 0$ (no photon loss in the resonator), this means that we have $I = 0$ at resonance, therefore $\det Y = 0$.

### 4.1.2 Resonator shift

Let us now investigate the resonance frequency $\omega_0'$ of the coupled system. Since the weak link and resonator are connected in parallel (see Figure 4.1), the total admittance of the coupled system is given by the sum of their two contributions $Y^{\text{tot}} = Y^{\text{res}} + Y^{\text{wl}}$. The resonance condition obtained from Eq. (4.2) therefore changes to $\det(Y^{\text{res}}_{ij}[\omega_0'] + Y^{\text{wl}}_{ij}[\omega_0']) = 0$. For a weakly coupled system, we expect the resonator frequency to be shifted by only a small amount $|\delta\omega| \ll \omega_0$, such that $\omega_0' = \omega_0 + \delta\omega$. The structure of the mode $V_{\text{res},j}$ is then given by

$$\sum_{i,j=L,R} V^T_{\text{res},i}\left(Y^{\text{res}}_{ij}[\omega_0 + \delta\omega] + Y^{\text{wl}}_{ij}[\omega_0 + \delta\omega]\right)V_{\text{res},j} = 0.$$

Expanding this equation to first order in $\delta\omega$ and using that $V^T_{\text{res}}Y^{\text{res}}[\omega_0]V_{\text{res}} = 0$ by definition of $\omega_0$, one is left with:

$$\sum_{i,j=L,R}\left(V^T_{\text{res},i}\delta\omega(Y^{\text{res}}_{ij})'[\omega_0]V_{\text{res},j} + V^T_{\text{res},i}Y^{\text{wl}}_{ij}[\omega_0]V_{\text{res},j}\right) = 0.$$

from which we deduce:

**Resonator frequency shift due to the weak link**

$$\delta\omega = -\frac{\sum_{i,j=L,R} V^T_{\mathrm{res},i} Y^{\mathrm{wl}}_{ij}[\omega_0] V_{\mathrm{res},j}}{\sum_{j=L,R} V^T_{\mathrm{res},i} (Y^{\mathrm{res}}_{ij})'[\omega_0] V_{\mathrm{res},j}}. \tag{4.3}$$

Note that because the resonator is assumed lossless, its admittance matrix is anti-Hermitian, which implies that $\mathrm{Re}(V^T_{\mathrm{res}} Y^{\mathrm{res}} V_{\mathrm{res}}) = 0$ [2] and therefore also $\mathrm{Re}(V^T_{\mathrm{res}} (Y^{\mathrm{res}})' V_{\mathrm{res}}) = 0$. Consequently, $\mathrm{Im}(Y^{\mathrm{wl}})$ has to be non-zero to give a real frequency shift $\delta\omega$. We obtain here a general result: the resonator shift is proportional to the imaginary part of the weak link admittance, and the magnitude of the shift scales like $\left(\sum V^T_{\mathrm{res}} (Y^{\mathrm{res}})'[\omega_0] V_{\mathrm{res}}\right)^{-1}$, which depends on the resonator geometry, encoded in its admittance matrix, and on the voltage structure $V_{\mathrm{res}}$ of the resonator mode used to probe the weak link.

2: For an anti-Hermitian operator A: $x^\dagger A x = -x^\dagger A^\dagger x = -(Ax)^\dagger x = -\overline{x^\dagger (Ax)}$ $\Rightarrow \mathrm{Re}(x^\dagger A x) = 0$.

### 4.1.3 Admittance from susceptibility

One can compute the admittance of the weak link $Y^{\mathrm{wl}}_{ij}$ using linear response theory. The weak link is sensitive to two external parameters: the applied magnetic flux $\phi$ which tunes the phase difference $\varphi$ across the weak link and the gate voltage $V_g$ which affects the charge in the junction region. The response of the weak link to weak external drives $\delta V_g(t)$ and $\delta\phi(t) = \varphi_0 \delta\varphi(t)$ (where $\varphi_0 = \hbar/2e$ is the reduced flux quantum) is captured by its response function to the external biases $\chi$, which has the form of a *susceptibility*. Given the finite length of a nanowire weak link, a non-zero charge can develop in the junction region. Consequently, to capture properly the electrodynamic response of the weak link, its response function must have the structure of a 2x2 matrix, *i.e.* both the *current* $I$ through the weak link and the *charge* $Q$ on it have to be considered, because both quantities respond to the phase and gate biases. The relation between the external parameters $\{\phi, V_g\}$ and the internal variables $\{I, Q\}$ is given by the response function $\chi_{AB}$ through:

$$\begin{pmatrix} \delta Q(\omega) \\ \delta I(\omega) \end{pmatrix} = \chi[\omega] \begin{pmatrix} \delta V_g(\omega) \\ \delta\phi(\omega) \end{pmatrix}, \quad \chi = \begin{pmatrix} \chi_{QQ} & \chi_{QI} \\ \chi_{IQ} & \chi_{II} \end{pmatrix}, \tag{4.4}$$

where $\delta Q$ and $\delta I$ describe the deviations of the mean charge and current from their stationary values.

To relate the admittance of the weak link $Y^{\mathrm{wl}}_{ij}$ (with $i, j \in L, R$) to its response function to the external biases $\chi_{AB}$ (where $A, B \in I, Q$)[3], one needs to express $\{\delta\phi, \delta V_g\}$ and $\{\delta Q, \delta I\}$ in terms of $\{V_L, V_R\}$ and $\{I_L, I_R\}$, respectively the potentials of the left/right resonator leads and the current flowing through them. According to the conventions used in Figure 4.1, one has:

$$\begin{cases} \partial_t \hat{Q} = -(\hat{I}_R + \hat{I}_L) \\ \hat{I} = \dfrac{\hat{I}_R - \hat{I}_L}{2} \end{cases} \Rightarrow \begin{pmatrix} \delta Q(\omega) \\ \delta I(\omega) \end{pmatrix} = \begin{pmatrix} -(I_R(\omega) + I_L(\omega))/i\omega \\ (I_R(\omega) - I_L(\omega))/2 \end{pmatrix}.$$

3: $I$ and $Q$ refer here to the current flowing through the weak link region and to its charge, not to the in-phase and in-quadrature components of a modulated signal.

Now, to relate the external biases to the lead voltages, one has to make some assumptions on the setup. Let us suppose here that the capacitance $C_g$ between the weak link and the gate is much larger than the capacitances $C_L, C_R$ coupling the weak link to the superconducting leads. This assumption can be motivated if the gate is located close enough to the weak link and if the weak link is in the dot regime, meaning weakly coupled to the superconducting leads[4] . If neglecting also the weak link capacitance to ground (reasonable because the grounded parts of the circuit are far from the weak link), then the voltage $V_g(t)$ supplied to the gate simply translates into a voltage $-V_g(t)$ applied simultaneously on both leads $L$ and $R$, so that:

4: Note that this is likely *not* to be the case in our experiment. However, this assumption remains a convenient limit as it simplifies greatly the general form of the results. So let us first go ahead with it and then, once the results are derived, mention how they are affected when a finite capacitance to the leads is taken into account.

$$\begin{cases} \delta\phi(\omega) = \dfrac{V_L - V_R}{i\omega} \\ \delta V_g(\omega) = -\dfrac{V_L(\omega) + V_R(\omega)}{2}. \end{cases}$$

Substituting into Eq. (4.4), one obtains:

$$\begin{pmatrix} -(I_R(\omega) + I_L(\omega))/i\omega \\ (I_R(\omega) - I_L(\omega))/2 \end{pmatrix} = \begin{pmatrix} \chi_{QQ} & \chi_{QI} \\ \chi_{IQ} & \chi_{II} \end{pmatrix} \begin{pmatrix} -(V_L(\omega) + V_R(\omega))/2 \\ (V_L(\omega) - V_R(\omega))/i\omega \end{pmatrix}.$$

Then, solving for $\{I_L, I_R\}$ as a function of $\{V_L, V_R\}$, one obtains after identification with Eq. (4.1) the following set of equations relating the admittance matrix of the weak link to its response function[5] :

5: These equations are valid only for $C_g \gg C_L, C_R$. The more general case of arbitrary ratio between the capacitances to the gate/leads has been described by Kurilovich *et al.* [64].

$$\begin{cases} \Upsilon^{\mathrm{wl}}_{LL} = -\dfrac{\chi_{II}}{i\omega} + \dfrac{i\omega}{4}\chi_{QQ} + \dfrac{1}{2}(\chi_{IQ} - \chi_{QI}) \\ \Upsilon^{\mathrm{wl}}_{LR} = +\dfrac{\chi_{II}}{i\omega} + \dfrac{i\omega}{4}\chi_{QQ} + \dfrac{1}{2}(\chi_{IQ} + \chi_{QI}) \\ \Upsilon^{\mathrm{wl}}_{RL} = +\dfrac{\chi_{II}}{i\omega} + \dfrac{i\omega}{4}\chi_{QQ} - \dfrac{1}{2}(\chi_{IQ} + \chi_{QI}) \\ \Upsilon^{\mathrm{wl}}_{RR} = -\dfrac{\chi_{II}}{i\omega} + \dfrac{i\omega}{4}\chi_{QQ} - \dfrac{1}{2}(\chi_{IQ} - \chi_{QI}). \end{cases} \tag{4.5}$$

Because each component of the admittance matrix is a linear combination of the diagonal and non-diagonal elements of the response function, it shows that in general the resonator frequency shift reflects both the current *and* charge response of the weak link.

Now, because the numerator of Eq. (4.3) depends on the structure of the mode (*i.e.* on the voltage on both leads), an important consequence of these equations appears: by choosing an adequate geometry/symmetry for the resonator, it is possible to probe particular components of the response function of the weak link. In particular, if the resonator shows a left/right symmetry with respect to ground and $V_{\mathrm{res},L} = V_{\mathrm{res},R} = V_0$, then:

$$\frac{V^T_{\mathrm{res}} \Upsilon^{\mathrm{wl}}[\omega_0] V_{\mathrm{res}}}{V_0^2} = i\omega_0 \chi_{QQ}[\omega_0] \propto \chi_{QQ}. \tag{4.6}$$

On the other hand, if the resonator has a left/right *anti*symmetry and $V_{\mathrm{res},L} = -V_{\mathrm{res},R} = V_0$, then:

$$\frac{V^T_{\mathrm{res}} \Upsilon^{\mathrm{wl}}[\omega_0] V_{\mathrm{res}}}{V_0^2} = \frac{4i\chi_{II}[\omega_0]}{\omega_0} \propto \chi_{II}. \tag{4.7}$$

Importantly, this means that by probing the weak link either through a *common* mode of the resonator or through a *differential* mode, one can measure either the charge or the current response of the weak link. In the more general case where the capacitances $C_L$ and $C_R$ between the weak link and the superconducting leads are taken into account [64], which better describes the system studied in this thesis, one can show that for a common mode of the resonator:

[64]: Kurilovich et al. (2021), 'Microwave response of an Andreev bound state'

$$\frac{V_{\text{res}}^T Y^{\text{wl}} V_{\text{res}}}{V_0^2} = \left(\frac{C_g}{C_g + C_L + C_R}\right)^2 i\omega_0 \chi_{QQ},$$

which is still proportional to the charge response $\chi_{QQ}$. However, when probing the weak link through a differential mode of the resonator, one is no longer measuring purely the current response:

$$\frac{V_{\text{res}}^T Y^{\text{wl}} V_{\text{res}}}{V_0^2} = \frac{4i}{\omega_0}\chi_{II} - 2\frac{C_L - C_R}{C_g + C_L + C_R}(\chi_{IQ} - \chi_{QI}) + \left(\frac{C_L - C_R}{C_g + C_L + C_R}\right)^2 i\omega_0 \chi_{QQ}$$

except if $C_L - C_R \ll C_g + C_L + C_R$ in which case one recovers approximately Eq. (4.7). This will be the case for any left/right asymmetry in the coupling between the probe (resonator) and the weak link.

### 4.1.4 Kubo expression for the current-current susceptibility $\chi_{II}$

Trif *et al.* [66] used the Kubo formula from linear response theory to derive a general expression for the finite frequency current response (susceptibility) of a nanowire junction[6] $\chi(\phi, \omega) = i\omega Y(\phi, \omega)$, where $Y(\phi, \omega)$ is the junction admittance (see also Refs. [67] and [68] for the use of this approach on mesoscopic rings). By describing the junction in the Bogoliubov-de Gennes framework (see 4.20), the response function[7] can be decomposed into three parts, the Josephson ($\chi_J$), the diagonal ($\chi_D$) and the non-diagonal ($\chi_{ND}$ or Kubo) contributions :

[66]: Trif et al. (2018), 'Dynamic current susceptibility as a probe of Majorana bound states in nanowire-based Josephson junctions'

6: In this section, we omit the subscript $II$ and note $\chi = \chi_{II}$.

7: See Eqs. (29-32) in the suppl. material of Ref. [66]

$$\chi(\phi, \omega) = \underbrace{\frac{\partial I_J}{\partial \phi}}_{\chi_J} + \underbrace{\sum_n \frac{\omega}{\omega + i\gamma_{nn}} \left(\frac{\partial \epsilon_n}{\partial \phi}\right)^2 \frac{\partial f_n}{\partial \epsilon_n}}_{\chi_D} - \underbrace{\hbar\omega \sum_{n \neq m} \frac{|\langle m|\hat{I}|n\rangle|^2}{\epsilon_n - \epsilon_m} \frac{f_n - f_m}{\epsilon_n - \epsilon_m - \hbar\omega - i\hbar\gamma_{nm}}}_{\chi_{ND}}, \tag{4.8}$$

with $I_J(\phi) = -\sum_n f_n \frac{\partial \epsilon_n}{\partial \phi}$ being the supercurrent flowing for the static flux $\phi$, the coefficient $f_n$ being the occupancy number of the single-particle state $\epsilon_n$, $\hat{I} = -\partial \hat{H}_{wl}/\partial\phi$ the current operator and $\gamma_{nm}$, the $nm$ component of the relaxation tensor†. From this expression, one can rewrite $\chi(\phi, \omega) = \sum_n \chi^{(n)}(\phi, \omega)$ to identify the contribution from one Andreev level $n$:

[67]: Trivedi and Browne (1988), 'Mesoscopic ring in a magnetic field'

[68]: Dassonneville (2014), 'Dynamics of Andeev states in a normal metal-superconductor ring'

$$\chi^{(n)} = \chi_J^{(n)} + \chi_D^{(n)} + \sum_{m \neq n} \chi_{ND}^{(nm)}, \tag{4.9}$$

where $\chi_J^{(n)} = -f_n \frac{\partial^2 \epsilon_n}{\partial \phi^2}$, $\chi_D^{(n)} = \frac{\omega}{\omega + i\gamma_D} \left(\frac{\partial \epsilon_n}{\partial \phi}\right)^2 \frac{\partial f_n}{\partial \epsilon_n}$.

† Its diagonal elements $\gamma_{nn}$ describe the relaxation of the populations $f_n$ due to inelastic scattering arising from electron-phonon or electron-electron collisions. Non-diagonal elements $\gamma_{nm}$ capture the relaxation of the coherences due to transitions between levels.

Neglecting the inter-level relaxation rates $\gamma_{nm} \to 0$ and writing $f_{nm} = f_n - f_m$ and $\epsilon_{nm} = \epsilon_n - \epsilon_m$ for ease of reading, the non-diagonal part, which accounts for transitions between Andreev levels, reads:

$$\begin{aligned}
\chi_{ND}^{(n)} &= -\hbar\omega \sum_{m\neq n} \frac{|\langle m|\hat{I}|n\rangle|^2}{\epsilon_{nm}} \frac{f_{nm}}{\epsilon_{nm}-\hbar\omega} - \hbar\omega \sum_{n\neq m} \frac{|\langle n|\hat{I}|m\rangle|^2}{\epsilon_{mn}} \frac{f_{mn}}{\epsilon_{mn}-\hbar\omega} \\
&= \sum_{m\neq n} \left[ \frac{|\langle m|\hat{I}|n\rangle|^2}{\epsilon_{nm}} \frac{-\hbar\omega f_{nm}}{\epsilon_{nm}-\hbar\omega} + \frac{|\langle m|\hat{I}|n\rangle|^2}{\epsilon_{nm}} \frac{\hbar\omega f_{nm}}{\epsilon_{nm}+\hbar\omega} \right] \\
&= \sum_{m\neq n} |\langle m|\hat{I}|n\rangle|^2 f_{nm} \left[ \frac{(\cancel{\epsilon_{nm}} - \hbar\omega) - \cancel{\epsilon_{nm}}}{\epsilon_{nm}(\epsilon_{nm}-\hbar\omega)} + \frac{(\cancel{\epsilon_{nm}} + \hbar\omega) - \cancel{\epsilon_{nm}}}{\epsilon_{nm}(\epsilon_{nm}+\hbar\omega)} \right] \\
&= \sum_{m\neq n} |\langle m|\hat{I}|n\rangle|^2 f_{nm} \left( \frac{2}{\epsilon_{nm}} - \frac{1}{\epsilon_{nm}-\hbar\omega} - \frac{1}{\epsilon_{nm}+\hbar\omega} \right).
\end{aligned}$$

Isolating the contribution where level $n$ is occupied and the others are not, *i.e.* $f_n = 1, f_m = 0$, one has $\chi_D^{(n)} = 0$. Using that $\partial_\phi = \varphi_0 \partial_\delta$, $\hat{I} = -\frac{1}{\varphi_0}\frac{\partial \hat{H}_{wl}}{\partial \delta}$, we are left with the following expression for the current susceptibility, to which the resonator shift due to level $n$ being occupied is proportional:

$$\boxed{\chi_n(\omega) = -\frac{1}{\varphi_0^2}\frac{\partial^2 \epsilon_n}{\partial \delta^2} + \sum_{m\neq n} \frac{|\langle m|\hat{H}'_{wl}|n\rangle|^2}{\varphi_0^2} \left( \frac{2}{\epsilon_{nm}} - \frac{1}{\epsilon_{nm}-\hbar\omega} - \frac{1}{\epsilon_{nm}+\hbar\omega} \right).} \tag{4.10}$$

### 4.1.5 Application to practical geometries

The easiest way to implement those considerations is to resort to a circuit design with two coupled microstrip lines for the resonator, like the one used by Hays *et al.* [69]. Indeed, for a configuration with two conductors and ground, any signal can be decomposed into a *differential* (odd) and a *common* (even) mode component. Both modes can be addressed independently because they have in general different boundary conditions, and also different characteristic impedances and mode velocities and as a result will resonate at different frequencies. A detailed description of this coplanar stripline implementation will be given later in Section 5.3.

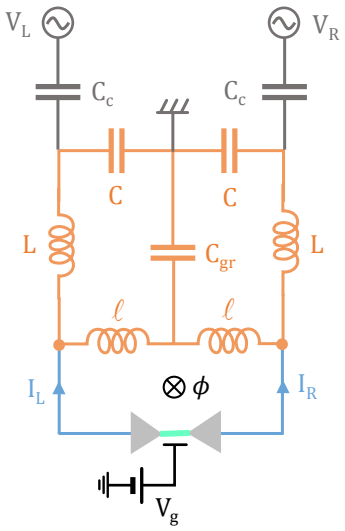


**Figure 4.3:** Lumped element model for the coupled microstrips design, showing the resonator circuit (orange), the probe lines (dark grey), the weak link loop (light blue) as well as the two external parameters (black): the flux $\phi$ and the gate voltage $V_g$.

#### Coupled microstrips design

To estimate the resonator shift for such a design, let us consider a simple lumped element analogue of the coupled microstrips, as depicted in Figure 4.3. The admittance matrix of the resonator can be computed easily knowing the admittance-to-ground of the left/right nodes $y_L, y_R$ and the equivalent admittance connecting them $y_{LR}$. Those can be identified from an equivalent circuit after a $T - \Pi$ transformation (see Figure 4.4):

$$Y^{\text{res}} = \begin{pmatrix} y_L + y_{LR} & -y_{LR} \\ -y_{LR} & y_R + y_{LR} \end{pmatrix}, \quad \begin{cases} y_L = y_R = \dfrac{1}{iL\omega + \frac{1}{iC\omega}} + \dfrac{1}{i\ell\omega + \frac{2}{i\omega C_{gr}}} \\ y_{LR} = \dfrac{1}{2\ell i\omega - \ell^2 C_{gr} i\omega^3}. \end{cases}$$

Solving the characteristic equation (4.2), one obtains the following fre-

quencies for the *odd* and *even* resonator modes:

$$\omega_{\text{odd}} = \frac{1}{\sqrt{C(L+\ell)}}, \quad \omega_{\text{even}} = \sqrt{\frac{C_{gr}+2C}{C_{gr}C(L+\ell)}}. \tag{4.11}$$

Indeed, when probing the resonator with a differential drive, *i.e.*$V_{\text{res},L} = -V_{\text{res},R} = V_0$, the voltage across the ground capacitor $C_{gr}$ is zero and we are left with the frequency of two parallel $(L+\ell)//C$ resonators, *i.e.* of a $(L+\ell)/2$ // $2C$ resonator, therefore resonating at the frequency $\omega_{\text{odd}}$. Let us now apply Eq. (4.3) to compute the resonator shift of such a circuit. After some math, one obtains:

$$\frac{V_{\text{res}}^T (Y^{\text{res}})'[\omega_{\text{odd}}] V_{\text{res}}}{V_0^2} = \frac{4iC(L+\ell)^2}{\ell^2}.$$

Then, using Eq. (4.7):

**Odd mode shift**

$$\frac{\delta\omega}{\omega_{\text{odd}}} = \frac{\ell^2}{L+\ell}\chi_{II} \overset{L\gg\ell}{\approx} \frac{\ell^2}{L}\chi_{II}. \tag{4.12}$$

As expected, the relative shift is proportional to the coupling factor $\ell/L$ (which is the ratio of the shared inductance between resonator/weak link to the total resonator inductance) and to the current-current response $\chi_{II}$ of the weak link (because of the differential probe).

Similarly, for the even mode:

$$\frac{V_{\text{res}}^T (Y^{\text{res}})'[\omega_{\text{even}}] V_{\text{res}}}{V_0^2} = \frac{4iC_{gr}C(C_{gr}+2C)(L+\ell)^2}{(C_{gr}\ell - 2CL)^2}.$$

**Even mode shift**

$$\frac{\delta\omega}{\omega_{\text{even}}} = \frac{(C_{gr}\ell - 2CL)^2}{4CC_{gr}(C_{gr}+2C)(L+\ell)^2}\chi_{QQ} \overset{\substack{C_{gr}\gg C \\ L\gg\ell}}{\approx} \frac{1}{4C}\left(\frac{\ell}{L}\right)^2 \chi_{QQ}. \tag{4.13}$$

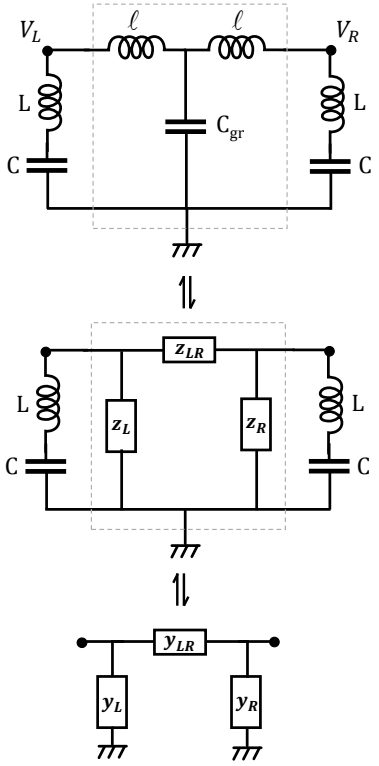


**Figure 4.4:** $T - \Pi$ transformation for admittance matrix extraction.

### Shunted CPW design

In this thesis, we used quarter-wave coplanar waveguide (CPW) resonators. They consist in a short-circuited transmission line of length $\lambda/4$, which can be modeled at resonance by a parallel LC circuit (see Figure 4.5). In a galvanic coupling scheme[8] , the nanowire weak link can be simply put across the gap of the CPW, acting as a shunt-inductance to ground for the CPW mode.

Now, because the weak link is grounded on one side, it is no longer excited purely in charge or in current, as described by Eqs. (4.6)-(4.7), and its response is a linear combination of *both* the diagonal $\chi_{II}, \chi_{QQ}$ *and* non-diagonal $\chi_{IQ}, \chi_{QI}$ response functions. By construction, $V_{\text{res}} = \begin{pmatrix} V_0 \\ 0 \end{pmatrix}$

8: The nanowire weak link can also be *inductively* coupled to the resonator, in which case the same description applies by just replacing the shared inductance $\ell$ by the mutual inductance $M$ between the resonator short-circuit and the loop in which the weak link is embedded for the phase bias. This equivalence will be detailed later in Figure 5.4.

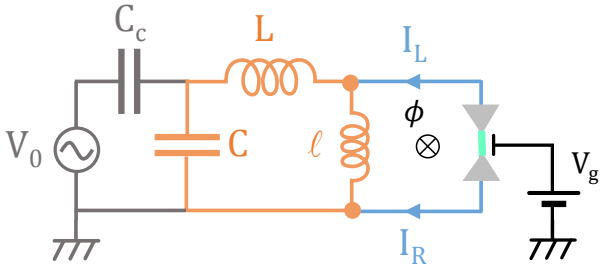


**Figure 4.5:** Lumped element model for the shunted CPW design, showing the resonator circuit (orange), the probe lines (dark grey),the weak link loop (light blue) as well as the two external biases (black): the flux $\phi$ and the gate voltage $V_g$.

and so:

$$\frac{V_{\text{res}}^T Y^{\text{wl}}[\omega_0] V_{\text{res}}}{V_0^2} = -\frac{\chi_{II}}{i\omega} + \frac{i\omega}{4}\chi_{QQ} + \frac{1}{2}(\chi_{IQ} - \chi_{Qi}) = Y_{LL}. \tag{4.14}$$

Again, by identifying the admittance-to-ground $y_L, y_R$ of the left/right nodes and the admittance $y_{LR}$ coupling them (see equivalent circuit Figure 4.6), one can easily write the admittance matrix of the resonator:

$$Y^{\text{res}} = \begin{pmatrix} y_L + y_{LR} & -y_{LR} \\ -y_{LR} & y_R + y_{LR} \end{pmatrix}, \quad \begin{cases} y_L = \dfrac{1}{iL\omega + \frac{1}{iC\omega}}, \quad y_R = \dfrac{1}{i\epsilon\omega} \\ y_{LR} = \dfrac{1}{i\ell\omega}. \end{cases}$$

Solving the characteristic equation $\det(Y^{\text{res}}) = 0$, one obtains the following expression for the resonance frequency, as expected for a LC circuit:

$$\omega_0 = \frac{1}{\sqrt{C(L + \ell + \epsilon)}} \underset{L \gg \ell}{\overset{\epsilon \to 0}{\to}} \frac{1}{\sqrt{LC}}. \tag{4.15}$$

The inverse coupling factor is then:

$$\begin{aligned} \frac{V_{\text{res}}^T (Y^{\text{res}})'[\omega_0] V_{\text{res}}}{V_0^2} &= \frac{iC(L + \ell + \epsilon)(2\ell(L + \ell) + 3\ell\epsilon + \epsilon^2)}{\ell(\ell + \epsilon)^2} \\ &\overset{\epsilon \to 0}{\to} 2iC\frac{(L + \ell)^2}{\ell^2} \overset{L \gg \ell}{\to} 2iC\left(\frac{L}{\ell}\right)^2, \end{aligned} \tag{4.16}$$

and the resonator shift using Eqs. (4.3) and (4.14):

$$\begin{aligned} \frac{\delta\omega}{\omega_0} &= \frac{1}{2iC\omega_0}\left(\frac{\ell}{L + \ell}\right)^2 \left(-\frac{\chi_{II}}{i\omega_0} + \frac{i\omega_0}{4}\chi_{QQ} + i\text{Im}(\chi_{IQ})\right) \\ &= \frac{\ell^2}{2(L + \ell)}\left(\chi_{II} + \frac{\omega_0^2}{4}\chi_{QQ} + \omega_0 \text{Im}(\chi_{IQ})\right) \\ &\overset{L \gg \ell}{\to} \frac{\ell^2}{2L}\chi_{II} + \frac{\ell^2}{8CL^2}\chi_{QQ} + \frac{\ell^2}{2\sqrt{C}L^{3/2}}\text{Im}(\chi_{IQ}). \end{aligned} \tag{4.17}$$

For a mirror-symmetric weak link, it is known [64] that for any $\varphi$ and $V_g$, $\text{Im}(\chi_{IQ}) = 0$ and we are left with a linear combination of the diagonal responses only:

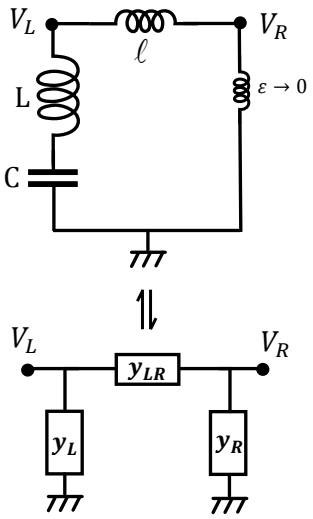


**Figure 4.6:** $T - \Pi$ model of the resonator for the shunted CPW design. The right node is normally grounded. To compute the shift without any divergence in the admittances, a small inductance $\epsilon$ is added and the limit $\epsilon \to 0$ is taken at the end.

[64]: Kurilovich et al. (2021), 'Microwave response of an Andreev bound state'

**Resonator shift (Shunted CPW design)**

$$\frac{\delta\omega}{\omega_0} \overset{L\gg\ell}{=} \frac{1}{2}\left(\frac{\ell^2}{L}\chi_{II} + \frac{1}{4C}\left(\frac{\ell}{L}\right)^2 \chi_{QQ}\right) = \frac{1}{2}\left(\frac{\delta\omega}{\omega_{\text{odd}}} + \frac{\delta\omega}{\omega_{\text{even}}}\right). \tag{4.18}$$

- The factor $1/2$ in the result comes from the fact that in this geometry the shared and total inductances are $\ell$, $L$ while they were effectively $2\ell$ and $2L$ in the coupled microstrip design (Figure 4.3): $\frac{1}{2}\frac{(2\ell)^2}{2L} = \frac{\ell^2}{L}$.
- Using Eq. (4.5), the relative shift can be rewritten in a more general form:
$$\frac{\delta\omega}{\omega_0} = \frac{\ell^2}{2L}\omega_0 \,\text{Im}(Y_{LL}^{\text{wl}}[\omega_0]). \tag{4.19}$$
- $\text{Im}(Y_{LL}^{\text{wl}}[\omega_0])$ can be seen as the effective inductance of the weak link at the resonator frequency: $Y_{LL}^{\text{wl}} = \frac{1}{jL_{\text{wl}}\omega_0}$, which allows to recover the expected classical result: $\frac{\delta\omega}{\omega_0} = -\frac{1}{2}\frac{\delta L}{L}$ with $\delta L = -\frac{\ell^2}{L_{\text{wl}}}$. $\delta L$ is the change of resonator inductance when $L_{\text{wl}}$ is connected in parallel to a fraction $\ell/L$ of the total resonator inductance: $L \longrightarrow L - \ell + (\ell // L_{\text{wl}}) = L + \delta L$.
- The assumption of a mirror-symmetric weak link can be no longer valid for non-fullshell nanowire weak links, for which the nanowire is only covered on 2 or 3 facets by superconducting aluminium. Lateral back gates can then be used to tune the chemical potential in the superconducting leads and this may also affect the height of the barriers at the left/right interfaces and so modify the coupling to the leads $\Gamma_L \neq \Gamma_R$. This can break the mirror symmetry and eventually allow for $\text{Im}(\chi_{IQ}) \neq 0$.

## 4.2 Hamiltonian description of the resonator shift

In the previous section, we reviewed how, using an electrical engineer approach, the resonator frequency shift can be related to the imaginary part of the weak link admittance, and how this admittance can be calculated. Here, we follow an alternative approach: we introduce a quantum description of both the weak link and the resonator as well as of their coupling. Starting from the microscopic Bogoliubov–de Gennes (BdG) equations for a weak link of arbitrary length, we derive the expression for the resonator shift as a function of the microscopic occupancy of individual Andreev levels. This second derivation, which yields the same final expression for the resonator shift, highlights how the latter scales with the strength of the phase fluctuations of the resonator and has the benefit of being more compact and straightforward. It also provides a general framework that can be applied to compute the frequency shift of a resonator weakly coupled to any generic quantum circuit, not necessarily to an ABS system and also whatever the coupling scheme.

### 4.2.1 Model for resonator – weak link coupling

Assuming that the microwave resonator is characterized by a single mode of frequency $\omega_r$, it can be described by the Hamiltonian $\hat{H}_r = \hbar\omega_r a^\dagger a$, where we have introduced the photon annihilation (creation) operators $a$ ($a^\dagger$). Let us denote by $\hat{H}_{wl}(\delta)$ the Hamiltonian of the weak link. For simplicity, we do not address the $\mu-$dependence of $\hat{H}_{wl}$. As for the weak link, its Hamiltonian can be written in the form

$$\hat{H}_{wl}(\delta) = \frac{1}{2}\int dx\ \hat{\Psi}^\dagger(x)\mathscr{H}_{wl}(\delta)\hat{\Psi}(x), \tag{4.20}$$

where $\hat{\Psi}(x) = \left(\psi_\uparrow(x), \psi_\downarrow(x), \psi_\downarrow^\dagger(x), -\psi_\uparrow^\dagger(x)\right)^T$ is the Nambu bispinor field operator and $x$ is the position along the weak link. We denote by $|\phi_{i\sigma}\rangle$ the eigenstates of the Bogoliubov-de Gennes (BdG) equation $\mathscr{H}_{wl}(\delta)|\phi_{i\sigma}\rangle = E_{i\sigma}|\phi_{i\sigma}\rangle$, which correspond to Andreev states when $|E_{i\sigma}| < \Delta$, where $\Delta$ is the superconducting gap in the leads. In this notation the subscript $i\sigma$ refers to the level $i$ with spin $\sigma$ and levels labeled with positive $i$ are above the Fermi level.[9]

The coupling between resonator and weak link occurs through current fluctuations in the resonator (assumed to be in its ground state), which induce phase fluctuations across the weak link, so that $\delta \longrightarrow \delta_0 + \hat{\delta}_r$, where $\hat{\delta}_r = \delta_{zp}(a + a^\dagger)$ with $\delta_{zp}$ the amplitude of zero-point phase fluctuations. The zero-point energy of a LC resonator is given by [70]:

$$\frac{\hbar\omega_r}{2} = \frac{\langle\hat{q}^2\rangle}{2C} + \frac{\langle\hat{\phi}^2\rangle}{2L} = \frac{\langle\hat{\phi}^2\rangle}{L},$$

where the brackets $\langle.\rangle$ denotes the average over the resonator ground state. The second equality follows from equipartition of energy between quadratic degrees of freedom[10] . From this, one can express the zero-point phase fluctuations of the resonator from the RMS fluctuations of its flux:

$$\delta_{zp}^{res} = \frac{\phi_{zp}}{\varphi_0} = \frac{\sqrt{\langle\hat{\phi}^2\rangle}}{\varphi_0} = \frac{2e}{\hbar}\sqrt{\frac{\hbar L\omega_r}{2}} = \sqrt{\frac{2e^2 Z_r}{\hbar}} = \sqrt{\frac{\pi Z_r}{R_Q}}, \tag{4.21}$$

where we introduced the resistance quantum $R_Q = h/4e^2 \approx 6453\ \Omega$ and the resonator impedance $Z_r = \sqrt{L/C}$. These phase fluctuations occur over the inductance $L$ of the resonator. Because only a part $\ell/L$ of the total inductance is shared with the weak link loop[11] , one has to multiply Eq. (4.21) by the geometric participation ratio $p = \ell/L$ to get the zero-point phase fluctuations across the weak link:

**Zero-point phase fluctuation across the weak link**

$$\delta_{zp} = p\,\delta_{zp}^{res} = \frac{\ell}{L}\sqrt{\frac{\pi Z_r}{R_Q}}. \tag{4.22}$$

In accordance with experiments where $\ell/L$ is kept small, we assume $\delta_{zp} \ll 1$, which allows us to expand the weak link Hamiltonian up to second order[12] in $\delta_{zp}$ and identify the coupling Hamiltonian:

9: Due to the electron-hole symmetry implicit in the BdG formalism, each state $i\sigma$ is associated to a state with opposite spin at opposite energy $-i\bar{\sigma}$. Notice that when spin-orbit interaction is at play, as can be the case in a nanowire weak link, spin is no longer a good quantum number and $\sigma$ has to be understood as a pseudospin index. Keeping this in mind, we will continue to denote spin textures as $\sigma = \uparrow, \downarrow$.

[70]: Vool and Devoret (2017), 'Introduction to quantum electromagnetic circuits'

10: The average energy in the inductor is $\frac{\langle\phi^2\rangle}{2L} = \frac{L\langle I^2\rangle}{2} = \frac{L}{2}\langle d_t Q^2\rangle$. Since the system's energy oscillates between L and C at a period $\omega_r = 1/\sqrt{LC}$, $\langle d_t Q^2\rangle \sim \omega_r^2 Q^2 = Q^2/LC$, from which we deduce $\langle\phi^2\rangle/2L = \langle Q^2\rangle/2C$.

11: For an inductive coupling scheme, replace $\ell$ by $M$, the mutual inductance between the resonator short-circuit and the weak link loop.

12: As will be explained in Chapter 6, expanding up to second order was necessary to be able to understand the measured signal in our spectroscopy data, namely the change of sign in the line intensities of single particle transitions far from the resonator.

$$\hat{H}_{wl}(\delta) = \hat{H}_{wl}(\delta_0) + \hat{\delta}_r \hat{H}'_{wl}(\delta_0) + \frac{\hat{\delta}_r^2}{2}\hat{H}''_{wl}(\delta_0) + o(\delta_{\mathrm{zp}}^2),$$

where we have adopted the notations $\hat{H}'_{wl} = d\hat{H}_{wl}/d\delta$ and $\hat{H}''_{wl} = d^2\hat{H}_{wl}/d\delta^2$. The total Hamiltonian describing the resonator, the weak link and their coupling is therefore:

$$\hat{H} \approx \underbrace{\hbar\omega_r a^\dagger a}_{\text{resonator}} + \underbrace{\hat{H}_{wl}(\delta_0)}_{\text{weak link}} + \underbrace{\delta_{\mathrm{zp}}\hat{H}'_{wl}(\delta_0)(a+a^\dagger) + \frac{\delta_{\mathrm{zp}}^2}{2}\hat{H}''_{wl}(\delta_0)(a+a^\dagger)^2}_{\text{coupling}}. \tag{4.23}$$

If the weak link was described as a two-level system and the term involving $\hat{H}''_{wl}$ was neglected, this model would correspond to the Jaynes-Cummings Hamiltonian [52].

[52]: Park et al. (2020), 'From Adiabatic to Dispersive Readout of Quantum Circuits'

To compute the second order correction of the energy levels of this Hamiltonian we introduce a basis set $\{|\Phi_i n\rangle \equiv |\Phi_i\rangle \otimes |n\rangle\}$, where $|\Phi_i\rangle$ corresponds to the eigenstates of $\hat{H}_{wl}$ with eigenvalue $E_i$ and $|n\rangle$ to a state with $n$ photons in the resonator. Assuming that the $|\Phi_i\rangle$ states are non-degenerate‡, the lowest order correction to the combined system energy levels can be written as $\delta E_{i,n} = \delta E_{i,n}^{(1)} + \delta E_{i,n}^{(2)}$ where

$$\begin{aligned}
\delta E_{i,n}^{(1)} &= \frac{\delta_{\mathrm{zp}}^2}{2}\langle\Phi_i n|\hat{H}''_{wl}\left(2a^\dagger a + 1\right)|\Phi_i n\rangle = \delta_{\mathrm{zp}}^2\langle\Phi_i|\hat{H}''_{wl}|\Phi_i\rangle\left(n+\frac{1}{2}\right) \\
\delta E_{i,n}^{(2)} &= -\delta_{\mathrm{zp}}^2\sum_{j\neq i,n'}\frac{|\langle\Phi_j n'|\hat{H}'_{wl}\left(a+a^\dagger\right)|\Phi_i n\rangle|^2}{E_j + \hbar\omega_r(n'-n) - E_i} \\
&= -\delta_{\mathrm{zp}}^2\sum_{j\neq i}|\langle\Phi_j|\hat{H}'_{wl}|\Phi_i\rangle|^2\left(\frac{n+1}{E_j+\hbar\omega_r-E_i} + \frac{n}{E_j-\hbar\omega_r-E_i}\right).
\end{aligned} \tag{4.27}$$

A more compact expression for the energy levels shifts can be obtained by relating the mean value $\langle\Phi_i|\hat{H}''_{wl}|\Phi_i\rangle$ to $E''_i = d^2E_i/d\delta^2$. The Hellmann–Feynman theorem establishes that

$$E'_i = \langle\Phi_i|\hat{H}'_{wl}|\Phi_i\rangle.$$

‡ In the presence of degeneracy, the derivatives $\hat{H}'_{wl}$ and $\hat{H}''_{wl}$, may, or may not, break the degeneracy. When a degeneracy is preserved (for example the spin of Andreev levels in a weak link), this perturbation result remains valid. This can be seen by expressing the current matrix element in an alternative way as,

$$\langle\Phi_i|\hat{H}'_{wl}|\Phi_j\rangle = E'_j\,\delta_{ij} + (E_j - E_i)\langle\Phi_i|\Phi'_j\rangle, \tag{4.24}$$

leading to

$$\langle\Phi_i|\hat{H}''_{wl}|\Phi_i\rangle = E''_i + 2\sum_{j\neq i}\frac{|\langle\Phi_i|\hat{H}'_{wl}|\Phi_j\rangle|^2}{E_j - E_i} = E''_i + 2\sum_{j\neq i}(E_j - E_i)|\langle\Phi_i|\Phi'_j\rangle|^2, \tag{4.25}$$

which exhibits no singular behavior in the degenerate case. If there exists a $g$-fold degeneracy (for example, orbital degeneracy) at energy $E = E_i$ with degenerate states, $\{|\Phi_{ia}\rangle\}$ with $a = 1, 2, \ldots, g$, and if the states $|\Phi_{ia}\rangle$ do not diagonalize $\hat{H}'_{wl}$ and $\hat{H}''_{wl}$, we need to solve the following secular equation to obtain $\delta E_{i,n}^{(1)}$ in Eq. (S1),

$$\mathrm{Det}\left|\frac{\lambda^2}{2}\hat{M}_i(2n+1) - \delta E_{i,n}^{(1)}\right| = 0, \tag{4.26}$$

where $\hat{M}_i$ is the $g \times g$ matrix whose elements are given by $(\hat{M}_i)_{a,b} = \langle\Phi_{ia}|\hat{H}''_{wl}|\Phi_{ib}\rangle$.

Taking the derivative on both sides gives

$$E_i'' = \langle\Phi_i'|\hat{H}_{wl}'|\Phi_i\rangle + \langle\Phi_i|\hat{H}_{wl}''|\Phi_i\rangle + \langle\Phi_i|\hat{H}_{wl}'|\Phi_i'\rangle. \tag{4.28}$$

From $\hat{H}_{wl}|\Phi_i\rangle = E_i|\Phi_i\rangle$, one can express $|\Phi_i'\rangle = d|\Phi_i\rangle/d\delta$ as $|\Phi_i'\rangle = -G_i(G_i^{-1})'|\Phi_i\rangle$ where $G_i = (E_i - \hat{H}_{wl})^{-1}$. Substituting this into Eq. (4.28) and using the closure relation $\sum_i |\Phi_i\rangle\langle\Phi_i| = 1$, one obtains a relation between the diagonal matrix element of $\hat{H}_{wl}''$ and the curvature $E_i''$ of the energy level $i$, which allows to simplify the expressions for the shifts:

$$\langle\Phi_i|\hat{H}_{wl}''|\Phi_i\rangle = E_i'' + 2\sum_{j\neq i}\frac{\mathscr{M}_{ij}^2}{E_j - E_i}, \tag{4.29}$$

where we have introduced the notation $\mathscr{M}_{ij} = |\langle\Phi_j|\hat{H}_{wl}'|\Phi_i\rangle|$ for the modulus of the matrix element of the current operator.

A similar sum rule was used to derive the expression given in Section 4.1.4 for the susceptibility of a junction based on linear response theory. Substituting in Eq. (4.27), we get finally the expression for the shift $\delta E_{i,n}$ of the energy of the coupled system when the circuit is in state $|\Phi_i\rangle$ and the resonator contains $n$ photons:

$$\delta E_{i,n} = \delta_{\mathrm{zp}}^2\left\{E_i''\left(n+\frac{1}{2}\right) - \sum_{j\neq i}\mathscr{M}_{ij}^2\left(\frac{n+1}{E_j - E_i + \hbar\omega_r} + \frac{n}{E_j - E_i - \hbar\omega_r} - \frac{2n+1}{E_j - E_i}\right)\right\}, \tag{4.30}$$

or, equivalently as

$$\delta E_{i,n} = \hbar\delta\omega_{r,i}\left(n+\frac{1}{2}\right) - \frac{\delta_{\mathrm{zp}}^2}{2}\sum_{j\neq i}\mathscr{M}_{ij}^2\left(\frac{1}{E_j - E_i + \hbar\omega_r} - \frac{1}{E_j - E_i - \hbar\omega_r}\right), \tag{4.31}$$

from which we finally identify the resonator frequency shift:

**Resonator frequency shift for weak link in state $|\Phi_i\rangle$**

$$\frac{\hbar\delta\omega_{r,i}}{\delta_{\mathrm{zp}}^2} = E_i'' + \sum_{j\neq i}\mathscr{M}_{ij}^2\left(\frac{2}{E_j - E_i} - \frac{1}{E_j - E_i + \hbar\omega_r} - \frac{1}{E_j - E_i - \hbar\omega_r}\right)$$
$$\text{where} \quad \mathscr{M}_{ij} = |\langle\Phi_j|\hat{H}_{wl}'|\Phi_i\rangle|. \tag{4.32}$$

- The $\omega_r$-independent terms on the right-hand side of Eq. (4.32) are the contributions involving $\hat{H}_{wl}''$ that arise from Eq. (4.29), while the $\omega_r$-dependent terms correspond to those obtained from a multi-level Jaynes-Cummings Hamiltonian.
- It can be seen from Eq. (4.32) that all transitions which couple a given state $i$ with other states $j$ via $\hat{H}_{wl}'$ are relevant to calculate the shift $\delta\omega_{r,i}$ of the resonance frequency. The equation includes the contribution from both, virtual transitions that do not depend on the resonator and other mediated by the absorption and emission of photons. Note that Eq. (4.32) only holds far from resonances, *i.e.* when all transitions between Andreev states have energies that differ from $\omega_r$ by much more than the coupling energy.

- In the so-called **adiabatic** limit where $\hbar\omega_r \ll |E_j - E_i|$ for all transitions, Eq. (4.32) simplifies to $\delta\omega_{r,i} \approx \delta\omega_{r,i}^{\text{curv}} = \delta_{\text{zp}}^2 E_i''/\hbar$ corresponding to a frequency shift proportional to the phase curvature of the Andreev level $i$. Noting that $\varphi^2 \left(\partial^2 E_i/\partial\delta^2\right)^{-1}$ is the effective inductance $L_{\text{wl},i}$ due to level $i$, this limit finds a simple interpretation: the resonator inductance obtains a contribution from that of the weak link, which is given by the phase curvature of all populated levels. Using $\delta_{\text{zp}}^2 = \varphi_0^{-2}\frac{\hbar\omega_r}{2}\frac{\ell^2}{L}$ from Eqs. (4.21) and (4.22), we can rewrite $\delta\omega_{r,i}^{\text{curv}} = \frac{\ell^2}{2L} \times \frac{1}{L_{\text{wl},i}}$ and recover the same expression for the resonator shift as the one derived classically in the previous section (see Eq. (4.18)). In addition, we also interpret the weak link inductance as directly arising from the phase curvature of the Andreev levels.
- Another interesting regime can be identified: the so-called **dispersive** regime when $\hbar\omega_r \sim |E_j - E_i|$ for a set of $i, j$. In this case, the terms involving the exchange of virtual photons dominate and one recovers the result that can be derived from the generalized Jaynes-Cummings Hamiltonian [71, 72].
- Although Eq. (4.32) derives from a quantum description of the resonator, the result is the same as the one deduced from the susceptibility in Trif *et al.* (Eq. (4.10)), where the resonator is treated classically.

[71]: Zueco et al. (2009), 'Qubit-oscillator dynamics in the dispersive regime'
[72]: Kohler (2018), 'Dispersive readout'

### 4.2.2 Many-body configurations

In the previous paragraph, we had written $|\Phi_{i\sigma}\rangle$ the eigenstates of the Bogoliubov-de Gennes (BdG) equation $\hat{H}_{wl}(\delta)|\Phi_{i\sigma}\rangle = E_{i\sigma}|\Phi_{i\sigma}\rangle$, which correspond to Andreev states when their energy satisfies $|E_{i\sigma}| < \Delta$, where $\Delta$ is the superconducting gap in the leads. In Figure 4.7(a) and (b), we now show a typical spectrum of Andreev states for two cases of interest: zero- and finite-length weak links. Due to the electron-hole symmetry implicit in the BdG formalism, each state $i\sigma$ is associated to a state with opposite spin at opposite energy $-i\bar{\sigma}$. Note that we have chosen here to represent the states in the *semiconductor picture*, which makes the intrinsic particle-hole symmetry explicit. This representation is better suited for the computations of the resonator frequency shift and also better illustrates the nature of the two possible families of transitions between ABS that we had distinguished in the introduction[13] : **pair transitions** (PT) *vs.* **single-quasiparticle transitions** (SQPT).

13: As was illustrated in Figure 1.3, PT are viewed as transitions crossing the Fermi energy, *i.e.* from negative energy states to positive energy ones, while SQPT correspond to atomic-like transitions between positive energy levels.

Writing explicitly the spin indices $\sigma, \sigma'$, Eq. (4.32) for the resonator frequency shift reads:

$$\begin{aligned}\frac{h\delta f_r^{(i\sigma)}}{\delta_{\text{zp}}^2} &= E_{i\sigma}'' + \sum_{j\sigma'\neq i\sigma} \mathscr{M}_{i\sigma,j\sigma'}^2 \left(\frac{2}{E_{i\sigma,j\sigma'}} - \frac{1}{E_{i\sigma,j\sigma'} - hf_r} - \frac{1}{E_{i\sigma,j\sigma'} + hf_r}\right) \\ &= E_{i\sigma}'' + \sum_{j\sigma'\neq i\sigma} \mathscr{V}_{i\sigma,j\sigma'}, \end{aligned} \tag{4.33}$$

where we introduced the transition energies $E_{i\sigma,j\sigma'} = E_{j\sigma'} - E_{i\sigma}$. The coupling strength $g_{i\sigma,j\sigma'}$ is related to $\mathscr{M}_{i\sigma,j\sigma'}$ by $\hbar g_{i\sigma,j\sigma'} = \delta_{\text{zp}}\mathscr{M}_{i\sigma,j\sigma'}$, and we have noted $\mathscr{V}_{i\sigma,j\sigma'}$, the term associated to virtual transitions from $i\sigma$ to $j\sigma'$.

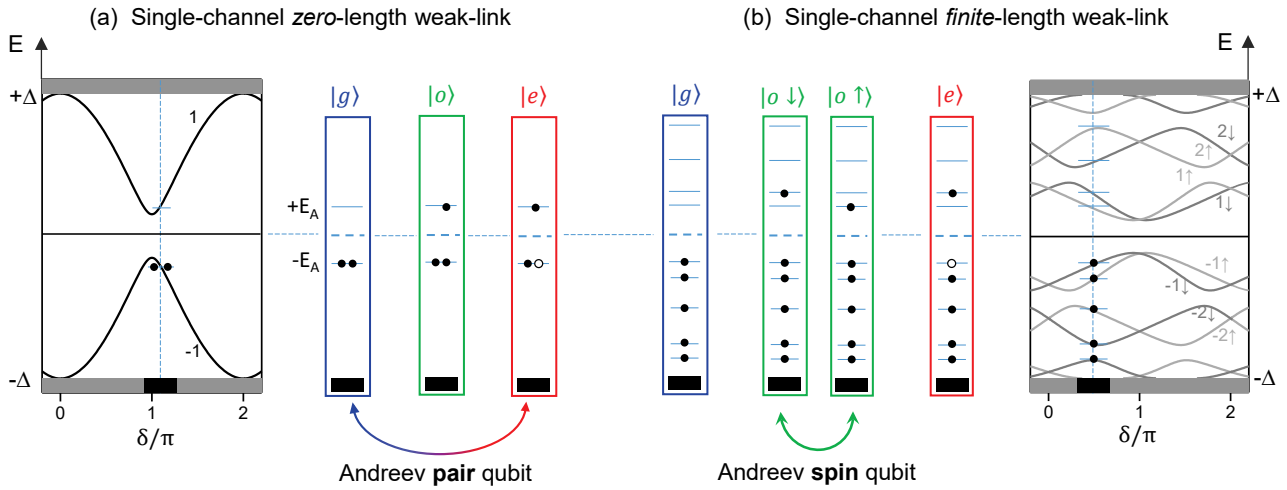


**Figure 4.7:** Low-lying many-body states for (a) zero-length weak links and (b) finite-length weak links with spin-orbit coupling. A typical spectrum of ABS levels is shown for both cases in the semiconductor picture. The ground state $|g\rangle$ at a given phase difference $\delta$ is obtained by filling all levels of negative energy with quasiparticles, represented as black dots. We depict the level occupancies associated to the three lowest-lying many-body states above the ground state, which are obtained by adding one quasiparticle of either spin in the lowest non-occupied ABS (states labeled $|o\uparrow\rangle$ and $|o\downarrow\rangle$) or by adding two of them to form a doubly-excited state (labeled $|e\rangle$). As shown in the red boxes, one can alternatively view the latter as being obtained from promoting the quasiparticle filling the highest occupied state to the lowest unoccupied one. For single-channel zero-length weak links, these four many-body states are actually the only possible ones, as the Andreev spectrum comprises only one pair of states, labeled ±1 in the leftmost plot. As they are spin-degenerate, $|o\uparrow\rangle$ and $|o\downarrow\rangle$ actually coincide. The space spanned by the two states of even parity, $|g\rangle$ and $|e\rangle$, allows to implement what is known as an *Andreev pair qubit*. Alternatively, finite length weak links with spin-split levels should in principle give rise to an *Andreev spin qubit*, using the two lowest energy states of odd parity $|o\uparrow\rangle$ and $|o\downarrow\rangle$.

The resonator frequency shift, however, is determined not by a single but by all Andreev levels which are populated in a given many-body state of the weak link. Let us first consider the ground state $|g\rangle$, which is obtained by filling up all negative energy levels. The frequency shift associated to $|g\rangle$ is then given by

$$\delta f_r^{|g\rangle} = \frac{1}{2}\sum_{i<0,\sigma} \delta f_r^{(i\sigma)}\,, \tag{4.34}$$

where the factor 1/2 compensates for the redundancy of the BdG description. Note how we differentiate in the notation the shift $\delta f_r^{(i\sigma)}$ (with parentheses) associated to the occupancy of a single level $i\sigma$ and the shift $\delta f_r^{|\Psi\rangle}$ (with a ket) associated to a many-body state $|\Psi\rangle$.

When combining Eq. (4.33) and Eq. (4.34), and taking into account that $\mathscr{V}_{i\sigma,j\sigma'} = -\mathscr{V}_{j\sigma',i\sigma}$, only virtual transitions to positive energy levels contribute:

$$\frac{h\delta f_r^{|g\rangle}}{\delta_{\mathrm{zp}}^2} = E''_{|g\rangle} + \frac{1}{2}\sum_{\substack{i<0,\sigma\\ j>0,\sigma'}} \mathscr{V}_{i\sigma,j\sigma'}, \tag{4.35}$$

where $E_{|g\rangle} = (1/2)\sum_{i<0,\sigma} E_{i\sigma}$ is the energy of the ground state. Further simplification occurs in the absence of a magnetic field and in the presence of a mirror symmetry, where the operator $\mathscr{H}_0'$ does not mix opposite pseudospins ($\sigma$ and $\bar{\sigma}$) [32], so that $\mathscr{V}_{i\sigma,j\bar{\sigma}} = 0$.

[32]: Park and Levy Yeyati (2017), 'Andreev spin qubits in multichannel Rashba nanowires'

Once $\delta f_r^{|g\rangle}$ is known, one can compute the shift associated to any many-body state $|\Psi\rangle$, as the latter can be built by creating appropriate electron-like $\gamma_{i\sigma}^\dagger|g\rangle$ ($i>0$) or hole-like $\gamma_{i_\sigma}|g\rangle$ ($i<0$) excitations from the ground state. Here $\gamma_{i\sigma}^\dagger$ ($\gamma_{i\sigma}$) stands for the Bogoliubov quasiparticle creation (annihilation) operator. Notice also that $\gamma_{-i\bar{\sigma}}^\dagger = -s\gamma_{i\sigma}$ due to double counting in the semiconductor picture that we are using, where $s=1(-1)$ for $\sigma=\uparrow(\downarrow)$. The frequency shift in $|\Psi\rangle$ is then given by

$$\delta f_r^{|\Psi\rangle} = \delta f_r^{|g\rangle} + \sum_{i>0,\sigma}\left[n_{i\sigma}\delta f_r^{(i\sigma)} - (1-n_{-i\sigma})\,\delta f_r^{(-i\sigma)}\right], \tag{4.36}$$

where $n_{i\sigma}=0,1$ is the occupancy of the state $i\sigma$. More generally, $n_{i\sigma}$ has to be understood as the average occupancy of the state $i\sigma$. The number of fermionic quasiparticle excitations in the weak link given by $N_{|\Psi\rangle}=\sum_{i>0,\sigma}[n_{i\sigma}+1-n_{-i\sigma}]$ can be even or odd, but states with different parity are not coupled by photons.

In Appendix H, we use these results to revisit data taken in the group prior to this thesis on atomic contacts, which implement zero-length weak links. The case of finite length weak links is the object of the next paragraph.

### 4.2.3 Resonator shift for finite-length junctions

#### Importance of the continuum

As compared to the simple situation of zero-length junctions (Figure 4.7(a) and Appendix H), the case of finite-length junctions is richer due to their multilevel structure (Figure 4.7(b)) and the role played by the continuum of states. In particular, the weak link inductance has contributions of the continuum, in addition to that of the ABS. This is because any state with energy $\epsilon$ smaller than the Thouless energy $\epsilon \lesssim E_{\mathrm{Th}} = \hbar v_F/L$ may exhibit sensitivity to the superconducting phase difference $\delta$ and therefore carry some phase curvature[§]. In the long junction limit $L \gg \xi$, the Thouless energy is small compared to the superconducting gap, $E_{\mathrm{Th}} = \Delta\xi/L \ll \Delta$, therefore all the current-carrying states are at subgap energy $\epsilon \lesssim E_{\mathrm{Th}} \ll \Delta$, *i.e.* only ABS carry the Josephson current. For zero-length junctions, it is also established analytically that the entire current is still given by the ABS, as an artefact from the limit $E_{\mathrm{Th}} \to \infty$ [73]. However for the intermediate situation corresponding to finite-length junctions, as is the case for our nanowire weak links, the situation is more complicated because $E_{\mathrm{Th}} > \Delta$. Consequently, one expects that the extended states in the range $\Delta < \epsilon < E_{\mathrm{Th}}$ also have some phase dependence and thus contribute to both the Josephson current and inductance. Furthermore, when the coupling between the weak link and the superconducting leads is strong – as is the case in our nanowire weak link due to the high quality epitaxial contact between the aluminium shell and the InAs nanowire – the effect of the extended states from the continuum can become comparable to that of the ABS, as shown in Ref. [64] .

[73]: Levchenko et al. (2006), 'Singular length dependence of critical current in superconductor/normal-metal/superconductor bridges'

[64]: Kurilovich et al. (2021), 'Microwave response of an Andreev bound state'

[§] This expression for the Thouless energy is valid for a ballistic junction for which $\xi = \hbar v_F/\Delta$ and $L < l_e$, where $l_e$ stands for the elastic mean free path. For a weak link made out of a diffusive conductor, *i.e.* when $L > l_e$, the Thouless energy would read $E_{\mathrm{Th}} = \Delta(\xi/L)^2 = \hbar D/L^2$, with $D$ the quasiparticles diffusion coefficient.

This effect can make the quantitative fitting of single-tone resonator spectroscopy quite challenging, as the curvature of the continuum and of all other subgap levels (which may be numerous when $L/\xi \gtrsim 1$) will contribute to adding a smooth phase-dependent background to the total resonator shift. This means that depending on the phase range where the data is to be fit, it may no longer be enough to merely add a small constant offset to the overall shift, as done to account for the contributions of unknown low-transmitted channels in the case of atomic contacts in Appendix H. Although it is well established that two-tone measurements can reveal the phase dispersion of pair transitions involving low lying ABS, from which one can deduce their associated curvature, this technique is in our case limited to the 0-40 GHz range and therefore does not allow to access the phase curvature of higher ABS. Consequently, a quantitative fit of the resonator shift, as we did in Figure H.3 and H.5 for the atomic contact single-tone spectroscopy data, may in general not be within reach for finite-length weak links, since it would require the knowledge of the phase curvature of all subgap levels and of the continuum, which is not experimentally accessible. A recent work by Fatemi *et al.* [50] shows that in the adiabatic regime achieved with a low resonator frequency and the specific limit of small $L/\xi$ such that essentially a single ABS level exists in the gap, the adiabatic contribution from the continuum assumes a simple form and it is still possible to describe quantitatively the state-dependent resonator shift.

[50]: Fatemi et al. (2021), 'Microwave susceptibility observation of interacting many-body Andreev states'

Note also that for differential measurements like two-tone spectroscopy, the measured signal reflects differences of resonator shifts due to the drive, and not absolute shifts. Therefore, it does not involve the unknown curvature from all other states, although the latter may still have a dispersive contribution through virtual transitions (see Eq. (4.33)). This contribution can even become sizeable when some transition frequencies between ABS are close to the resonator frequency. This is even more likely as $L/\xi$ is large and many ABS are present. In general, this would prevent any fitting of the line intensity of nanowire two-tone data, as it would require knowledge of the phase-dispersion of possible higher ABS levels that are out of the experimentally accessible frequency range. However, two limiting situations may still allow for quantitative local comparisons within restricted frequency windows. First, when the resonator frequency is low enough compared to all possible transition frequencies, so that the state-dependent shift is merely given by the adiabatic curvature of the states. Second, when the line intensity that we seek to fit is associated to a transition anticrossing the resonator line or coming very close to it, such that the dispersive shift associated to this single transition dominates all other contributions. Those two cases will be detailed in the next paragraph and illustrated with experimental results in Section 6.5.

**Spin-resolved levels**

Let us now review in detail the case of finite-length junctions with spin-orbit coupling. As already mentioned, the situation becomes richer when there are several Andreev levels within the gap as in Figure 4.7(b). Furthermore, in the presence of spin-orbit the subgap states are spin split, which gives rise to a larger number of possible transitions between all spin-split levels. The term $\mathcal{V}_{-i\sigma,j\sigma}$ in Eq. (4.35) depends on the matrix

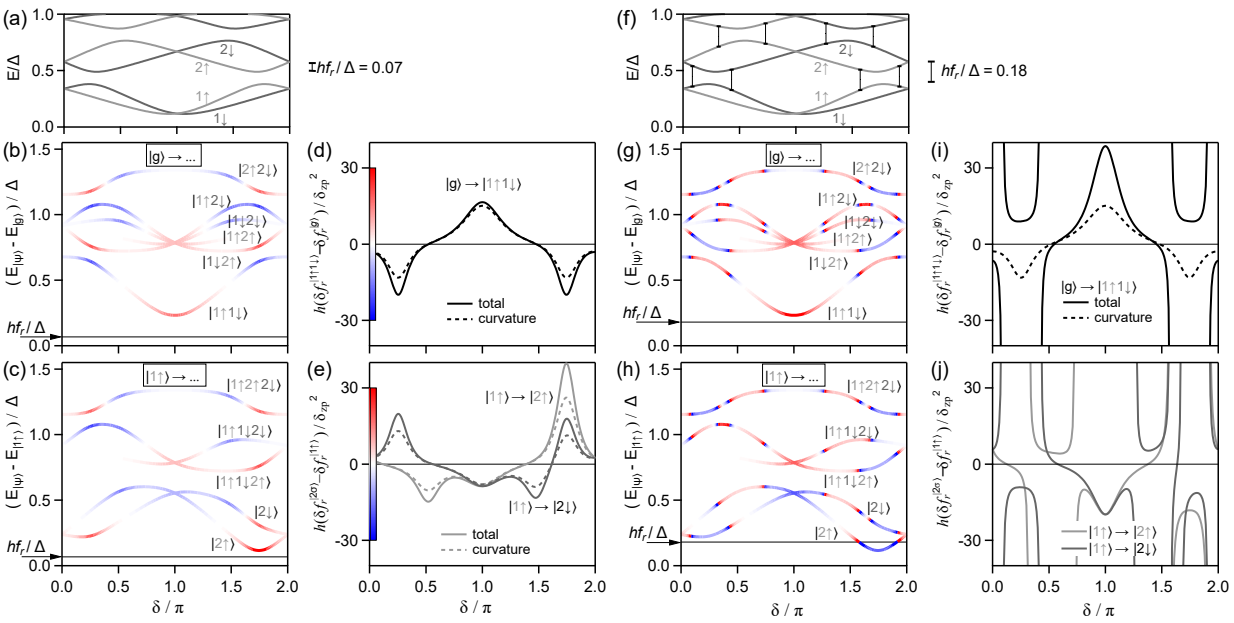


**Figure 4.8:** Resonator frequency shift for finite-length junction with spin-orbit coupling (same parameters as in Figure 4.7(b)). (a-e) Resonator at $f_r = 0.07\Delta/h$; (f-j) $f_r = 0.18\Delta/h$. (a,f) Spectrum of Andreev states at positive energies, with vertical bars in (f) indicating places where energy difference between levels of same spin is equal to $hf_r$. (b,g) Energy of transitions from state $|g\rangle$; (c,h) *idem* from state $|1\uparrow\rangle$. The color of the lines encodes the resonator frequency difference between initial and final state (colorscale on y-axis of (d) and (e)). (d,e) Resonator frequency shift difference between $|g\rangle$ and $|1\uparrow 1\downarrow\rangle$ (pair transition), and contribution of the states' curvature (dashed line). (e,j) *Idem* for the transitions from $|1\uparrow\rangle$ to $|2\uparrow\rangle$ or $|2\downarrow\rangle$ (single-quasiparticle transitions). The resonator shifts are calculated from matrix elements obtained with a tight-binding model.

elements of $\hat{H}'_{wl}$ which do not have analytic forms in this case. However, they can be obtained by solving numerically the BdG equation, for which we use two complementary approaches: the scattering model of Ref. [51], discussed in Section 3.2, and a discretized tight-binding model of the nanowire (see Appendix C). As these methods rely on different approximations one cannot expect a one-to-one correspondence of their results. For instance, the scattering method is based on a linearization of the electrons and holes dispersion relations around the Fermi level (Andreev approximation) which is not assumed in the tight-binding model. On the other hand the tight-binding model used here includes only two sites to describe the nanowire cross-section. We have checked, however, that the methods yield qualitatively similar results for the limits where their approximations are both valid.

[51]: Tosi et al. (2019), 'Spin-Orbit Splitting of Andreev States Revealed by Microwave Spectroscopy'

In Figure 4.8, we show the predictions for the frequency shifts in the typical case of a weak link with three spin-split manifolds of Andreev levels (same parameters as for Figure 4.7(b)), at zero Zeeman field. Two values of the bare resonator frequency are considered: $f_r = 0.07\Delta/h$ (panels (a–e)) and $f_r = 0.18\Delta/h$ (panels (f–j)). The frequency shift in the ground state $|g\rangle$ is first evaluated using Eq. (4.35). All matrix elements are computed with the tight-binding model. We assume that scattering takes place only in the longitudinal direction, and hence does not mix the subbands. Thus, in absence of a magnetic field, the matrix elements of $\hat{H}'_{wl}$ are zero for all pseudospin-non-conserving transitions [32]. Frequency shifts in the other states are found from Eq. (4.36). Transitions from $|g\rangle$ create pairs of excitations (pair transitions), leading for example to the state $\gamma^\dagger_{1\downarrow}\gamma_{-1\downarrow}|g\rangle = -\gamma^\dagger_{1\downarrow}\gamma^\dagger_{1\uparrow}|g\rangle = -|1\uparrow 1\downarrow\rangle$. Because of the redundancy between negative- and positive-energy states, we use here only labels corresponding to positive energies (Figure 4.8(a,f)).

The states accessible from $|g\rangle$ and involving only the two lowest subgap levels are therefore those shown in Figure 4.8(b,g). We also consider the closest-in-energy states that can be reached from the single-particle state $|1\uparrow\rangle$ (Figure 4.8(c,h)). On the one hand, states with a single quasiparticle are accessible through single-quasiparticle transitions, like $|2\uparrow\rangle = \gamma^\dagger_{2\uparrow}\gamma_{1\uparrow}|1\uparrow\rangle$, or $|2\downarrow\rangle$. On the other hand, the same fermion parity is also maintained with pair transitions that lead to states with three quasiparticles: $|1\uparrow 1\downarrow 2\uparrow\rangle = -\gamma^\dagger_{1\downarrow}\gamma_{-2\downarrow}|1\uparrow\rangle$, $|1\uparrow 1\downarrow 2\downarrow\rangle$, and $|1\uparrow 2\uparrow 2\downarrow\rangle$. For all these possible states, frequency shifts are given by Eq. (4.36), which simplifies to

$$\delta f_r^{|\Psi\rangle} = \delta f_r^{|g\rangle} + \sum_{i>0,\sigma} n_{i\sigma}\delta f_r^{(i\sigma)} \,. \tag{4.37}$$

Figure 4.8(b,c,g,h) shows the transition energies from $|g\rangle$ and $|1\uparrow\rangle$, with line colors encoding the resonator frequency shift for each transition (color scale in (d) or (e)). The phase asymmetry of the transition energies shown in panels (c) and (h) comes from the fact that we consider an initial state with a given pseudospin ($|u\rangle$). The mirrored spectra about $\delta = \pi$ would be obtained when considering transitions from $|1\downarrow\rangle$. The situation is the simplest when the resonator photons energy $hf_r$ is smaller than the energy of all the virtual transitions entering in the calculation of $\delta f_r^{(i\sigma)}$. All $\delta f_r^{(i\sigma)}$ are then dominated by the curvature term, and the resonator frequency shift for each transition is essentially related to the curvature of the transition energy. This is seen in Figure 4.8(b,c) with the red color ($\delta f_r^{|\Psi\rangle} - \delta f_r^{|g\rangle/|1\uparrow\rangle} > 0$) of the transition lines when they have positive curvature, blue for negative curvature. Detailed comparisons of the total shift with the curvature contribution are shown in Figure 4.8(d) for the pair transition $|g\rangle \to |1\uparrow 1\downarrow\rangle$ and in Figure 4.8(e) for the single-quasiparticle transitions $|1\uparrow\rangle \to |2\uparrow\rangle$ and $|1\uparrow\rangle \to |2\downarrow\rangle$.

The results look more complicated in Figure 4.8(g,h), with many sign inversions of the frequency shift when sweeping $\delta$. Sign inversions occur when the energy of one of the virtual transitions entering in the calculation of the frequency shift in the initial or the final state coincides with $hf_r$. These coincidences are marked in panel (f) with small vertical bars linking levels of same spin and distant by $hf_r$. For example, there is one of them at $\delta/\pi \approx 1.92$, where $E_{2\uparrow} - E_{1\uparrow} = hf_r$. Correspondingly, $\delta f_r^{(1\uparrow)}$ and $\delta f_r^{(2\uparrow)}$ present abrupt changes of sign at this phase, which is seen in all the lines involving $1\uparrow$ or $2\uparrow$ in Figure 4.8(g,h). Similarly, there is another such coincidence at $\delta/\pi \approx 1.27$, where $E_{3d} - E_{2\downarrow} = hf_r$, leading to color changes in the transition lines $|g\rangle \to |...2\downarrow\rangle$. Detailed plots of the frequency shift for pair and single particle transitions are shown in Figure 4.8(i,j), with divergences when energy differences match $hf_r$.

# Designing microwave resonators

# 5



In the preceding chapter, we showed that the shift of resonator frequency when coupled to a weak link is proportional to a dimensionless parameter, the square amplitude of the zero point phase fluctuations on the weak link $\delta_{zp}^2 = \left(\frac{\ell}{L}\right)^2 \frac{\pi Z_r}{R_Q}$ (see Eqs. (4.21),(4.33),(4.37)). In order to be sensitive to the many-body states of the weak link, the phase fluctuations must be sufficiently large, thus there must be a current anti-node at the coupling region. Here, we discuss two types of distributed quarter-wave transmission lines: shunted coplanar waveguide (CPW) as we have used, and coplanar striplines (CPS) resonators, as have been used by our colleagues at Yale [19, 41, 42, 50].

[19]: Hays et al. (2018), 'Direct Microwave Measurement of Andreev-Bound-State Dynamics in a Semiconductor-Nanowire Josephson Junction'
[41]: Hays et al. (2020), 'Continuous monitoring of a trapped superconducting spin'
[42]: Hays et al. (2021), 'Coherent manipulation of an Andreev spin qubit'
[50]: Fatemi et al. (2021), 'Microwave susceptibility observation of interacting many-body Andreev states'

## 5.1 Quarter-wave resonators

### 5.1.1 Short-circuited $\lambda/4$ line

One can show that a short-circuited transmission line hosts a current type of resonance when it is excited by a signal which wavelength matches 4 times the length of the line. At frequencies near resonance, the line can be modeled by a parallel RLC lumped-element equivalent circuit. This allows to model with a simple circuit the coupling with the weak link and estimate the expected frequency shift associated to the given geometry. The following derivation of this property is largely based on the textbook description from Pozar [65].

[65]: M.Pozar (2011), *Microwave Engineering, 4rd Ed*, pp. 281-282

Consider a length of lossy transmission line, short-circuited at one end, as depicted in Figure 5.1(a). The line has a characteristic impedance $Z_0$, a propagation constant $\beta$ and an attenuation constant $\alpha$. Let us define $\omega = \omega_0$, the frequency at which the length of the line is $\ell = \lambda/4$, where $\lambda = 2\pi/\beta$. The input impedance of a line loaded at its end by an impedance $Z_L$ is:

$$Z_{\text{in}} = Z_0 \left[ \frac{Z_L + Z_0 \tanh((\alpha + j\beta)\ell)}{Z_0 + Z_L \tanh((\alpha + j\beta)\ell)} \right]. \tag{5.1}$$

In our case, the line is short-circuited, so $Z_L = 0$ and we are left with:

$$\begin{aligned} Z_{\text{in}} &= Z_0 \tanh((\alpha + j\beta)\ell) \\ &= Z_0 \frac{\tanh(\alpha\ell) + j\tan(\beta\ell)}{1 + j\tan(\beta\ell)\tanh(\alpha\ell)} \\ &= Z_0 \frac{1 - j\tanh(\alpha\ell)\cot(\beta\ell)}{\tanh(\alpha\ell) - j\cot(\beta\ell)}. \end{aligned} \tag{5.2}$$

When $\beta\ell = \pi/2$, *i.e.* $\cot(\beta\ell) = 0$, this input impedance is maximal and a parallel type of resonance occurs. This condition defines the frequency

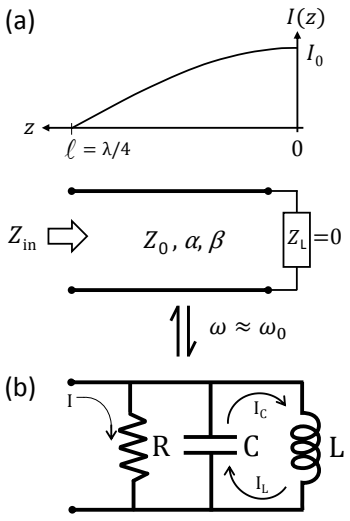


**Figure 5.1:** (a) Short-circuited transmission line and current distribution for the $\lambda/4$ mode. (b) Lumped element equivalent circuit at resonance.

of the $\lambda/4$ mode:

$$\beta\ell = \frac{2\pi}{\lambda_0}\ell = \frac{\pi}{2} \Rightarrow \frac{\omega_0\ell}{v} = \frac{\pi}{2} \quad i.e. \quad \omega_0 = \frac{\pi v}{2\ell}, \tag{5.3}$$

where $v$ is the phase velocity of the transmission line, assuming a TEM mode.

### 5.1.2 RLC equivalent circuit near resonance

Lets us now expand $Z_{\text{in}}$ close to the resonance frequency $\omega = \omega_0 + \delta\omega$ with $\delta\omega \ll \omega_0$:

$$\beta\ell = (\omega_0 + \delta\omega)\frac{\ell}{v} = \frac{\pi}{2} + \frac{\pi}{2}\frac{\delta\omega}{\omega_0},$$

which allows to rewrite

$$\cot(\beta\ell) = \cot(\frac{\pi}{2} + \frac{\pi}{2}\frac{\delta\omega}{\omega_0}) = -\tan(\frac{\pi}{2}\frac{\delta\omega}{\omega_0}) \overset{\delta\omega\ll\omega_0}{\approx} -\frac{\pi}{2}\frac{\delta\omega}{\omega_0}.$$

Assuming also small loss coefficient $\alpha$, we have $\tanh(\alpha\ell) \approx \alpha\ell$, from which we get the input impedance of the line close to resonance:

$$Z_{\text{in}} = Z_0\frac{1 + j\alpha\ell\pi\delta\omega/2\omega_0}{\alpha\ell + j\pi\delta\omega/2\omega_0} \approx \frac{Z_0}{\alpha\ell + j\pi\delta\omega/2\omega_0}. \tag{5.4}$$

It has the same form as the impedance of a parallel RLC circuit near resonance (see Figure 5.1(b)):

$$\begin{aligned} Z_{\text{RLC}} &= \left(\frac{1}{R} + \frac{1}{j\omega L} + j\omega C\right)^{-1} \\ &\approx \left(\frac{1}{R} + \frac{1 - \delta\omega/\omega_0}{j\omega_0 L} + j(\omega_0 + \delta\omega)C\right)^{-1} \quad \text{using } (1+x)^{-1} \overset{x\ll1}{\approx} 1 - x \\ &= \left(\frac{1}{R} + j\frac{\delta\omega}{\omega_0^2 L} + j\delta\omega C\right)^{-1} \quad \text{since } \omega_0^2 = 1/LC \\ &= \left(\frac{1}{R} + 2j\delta\omega C\right)^{-1} = \frac{R}{1 + 2j\delta\omega RC}. \end{aligned} \tag{5.5}$$

Identifying Eq. (5.4) with Eq. (5.5), we obtain the parameters of the equivalent RLC circuit for the quarter-wave line near resonance:

$$\boxed{R = \frac{Z_0}{\alpha\ell} \quad L = \frac{4Z_0}{\pi\omega_0} \quad C = \frac{\pi}{4Z_0\omega_0}.} \tag{5.6}$$

This allows to express the total impedance $Z_r$ of the quarter-wave line:

$$Z_r = \sqrt{\frac{L}{C}} = \frac{1}{\omega_0 C} = \frac{4}{\pi}Z_0 \approx 1.27 \times Z_0, \tag{5.7}$$

where $Z_0$ is the characteristic impedance of the line. Note that $Z_r \neq Z_0$. This is because the line is not matched: as it is short-circuited ($Z_L = 0$), magnetic energy is stored at the line's end due to the return currents flowing in the ground, so that the line effectively gains more inductance, hence $Z_r \gtrapprox Z_0$[1].

1: Similarly, for an open-circuited $\lambda/2$ line, one would have $Z_r = \frac{2}{\pi}Z_0 \lessapprox Z_0$ because of the extra capacitive contribution due to the open end.

### 5.1.3 Practical implementations

The transmission-line topologies generally used for microwave applications include the microstrip (MS), coplanar waveguide (CPW) and coplanar stripline (CPS) geometries. All three have in common to belong to the family of *coplanar* transmission lines for which all conductors lie on the same plane, namely, on the top surface of a dielectric substrate.

The CPW geometry is advantageous in many respects. First, it allows for a wide range of line impedance, simply by tuning the spacing between the central microstrip and the lateral ground planes. When this spacing is only a few microns tight, one can reach as low as a few tens of Ω impedance; as it is increased, so does the impedance: the lateral grounds have less and less effect and when the spacing is high enough, the central conductor of the CPW starts resembling electrically to a microstrip circuit. Due to their strong ground structure, CPWs are also capable of lower-loss performance at higher frequencies than microstrip circuits. This is because for microstrips, the EM fields are contained mainly within the dielectric material between the strip and the bottom ground plane below the substrate, while for CPWs the circuit's effective dielectric constant is reduced, as part of the EM field resides in the vacuum above the circuit rather than in the substrate's dielectric material. Finally, as they are a planar version of coaxial cables, CPWs also allow gradual transitions towards the Printed circuit board (PCB) connectors.

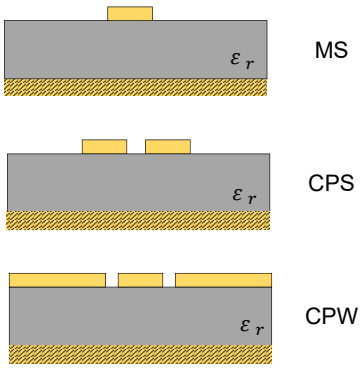


**Figure 5.2:** Transmission line topologies: microstripline (MS); coplanar stripline (CPS) and coplanar waveguide (CPW). Yellow: conductor. Grey: dielectric substrate. Cross-hatched yellow: ground plane.

The fundamental difference between the CPW and CPS topologies is that the CPS is a *balanced* line, meaning that it consists of two conductors, each having the same impedance to the surrounding ground planes. Therefore, a CPS allows to carry microwaves in two possible modes: an *odd* mode, where both conductors oscillate in opposite phase, and an *even* mode, where the two conductors oscillate together in phase with respect to the ground potential. Since these two modes resonate at different frequencies, this topology has the advantage that one can independently explore (see Section 4.1.5) the current-current susceptibility $\chi_{II}$ (encoded in changes in the odd frequency mode) and the charge-charge susceptiblity $\chi_{QQ}$ (even mode). The CPW on the other hand is an *unbalanced* line consisting in a single planar conductor surrounded on both sides by ground planes, which act as return lines. It is the 2D version of a coaxial cable and as such, it is also the easiest to implement since it can be directly routed to external coaxial cables delivering microwaves to the PCB. However, connecting in series one end of an unbalanced line to the weak link does not allow to probe it differentially: the measured response will be sensitive to a combination of both $\chi_{II}$ and $\chi_{QQ}$.

If targeting a differential drive, one needs in this case to implement a *balun* to convert the unbalanced readout signal into a balanced one. This can be done either using discrete microwave components like a 180° hybrid coupler, or by directly integrating such a device on-chip [74, 75, 76]. Still, there may be other designs in which unbalanced lines may actually do the trick, like for example by placing the weak link in the middle of a half-wave CPW line, but ultimately this may just be seen as an unfolded version of a quarter-wave balanced line connected at its end to the weak link.

[74]: Baek et al. (2009), '94-GHz Log-Periodic Antenna on GaAs Substrate Using Air-Bridge Structure'
[75]: Dehollain et al. (2012), 'Nanoscale broadband transmission lines for spin qubit control'
[76]: Vasylchenko et al. (2008), 'A very compact CPW-to-CPS balun for UWB antenna feeding'

## 5.2 Shunted CPW design

During this thesis, two generations of CPW resonators have been used — the main difference lying in the coupling scheme with the nanowire weak link. In the first generation, represented by sample S1 (Section 6.3), the coupling was achieved through a mutual inductance between the weak link loop and the strip shorting the CPW at its current antinode. We gained about two orders of magnitude in the coupling by later implementing a galvanic coupling scheme (section 5.2.2), in which the shorting inductance was physically shared by the resonator and the weak link loop. Sample S2, on which all the data except these of Section 6.3 were obtained, belongs to this generation. Recently, we further adapted this geometry towards a gradiometric design suitable for microwave spectroscopy under magnetic field (see Appendix J). The recipes for the fabrication of samples S1 and S2 are given in Chapter 12. Let us review here the different steps that guided the design of these three generations of resonators.

### 5.2.1 Inductive coupling

The first experiment on InAs nanowires that we designed was similar in principle to the latest one realized on atomic contacts in the group, namely: a CPW resonator inductively coupled to the phase-biased loop containing the weak link (see Figure 5.3(a)). In the experiments with atomic contacts, with a resonator impedance[2] $Z_r = 90\ \Omega$, a resonance frequency $f_r = 10$ GHz and a mutual inductance $M = 27$ pH between the loop and the resonator, the inductive coupling scheme provided zero-point fluctuations of about $\delta_{zp} = 2\pi f_r M\sqrt{\pi/Z_r R_Q} \approx 0.004$ (see Eq. (4.21)), which for an Andreev pair transition energy frequency $f_A = 8$ GHz at $\delta = \pi$, gave a typical coupling factor of $g = \delta_{zp}\frac{\Delta}{2}\left(1-(f_A/2\Delta)^2\right) \approx 100$ MHz [21]. With such a high coupling, the typical dispersive shift experienced by the resonator, $\chi = g^2/(f_r - f_A) \approx 5$ MHz, was high enough to resolve well the states of the Andreev pair qubit.

2: The resonator was made out of a $\lambda/4$ CPW line with characteristic impedance $Z_0 = 70\ \Omega$ on a kapton substrate ($\epsilon_r \sim 3.2$). Using Eq. (5.7), this gives a resonator impedance $Z_r = 4Z_0/\pi \approx 90\ \Omega$.

[21]: Janvier (2016), 'Coherent manipulation of Andreev Bound States in an atomic contact', p. 61

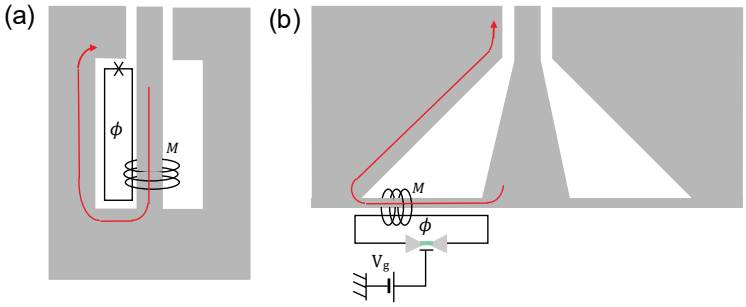


**Figure 5.3:** (a) Resonator design for the atomic contact experiment [21]. The phase-biased loop containing the atomic contact is located in the gap of the CPW resonator and the coupling between the two occurs through a mutual inductance $M$. Superconducting film is shown in grey and current as a red arrow. (b) For the nanowire experiment [51], a DC gate has to be brought close enough to the weak link, the loop is therefore placed outside the CPW gap of the resonator and a trumpet-like shape is needed for the resonator end to achieve similar coupling with the loop.

If the same design had been used to probe Andreev states in nanowires, similar considerations would have held but the coupling factor $g$ would have been weaker, as the effective superconducting gap $\Delta^*$ is lower due to the finite length of the weak links (see Eq. 3.14). Also, compared to the atomic contact experiment, it would have been necessary to adapt the design of the resonator end so as to bring a DC gate close to the nanowire. To avoid the complexity of having the gate bridging the ground plane, we

initially chose to put the superconducting loop containing the nanowire outside the gap of the CPW resonator (see Figure 5.3(b)). This lowers the mutual inductance $M$ as the return current through the ground plane no longer contributes to the coupling. In order to compensate this effect and keep the mutual inductance as high as possible, the end of the CPW was given the shape of a trumpet, which maximizes the length of the current path that couples to the loop (see Figure 5.3(b)). To affect as little as possible the resonator mode, this termination was designed such that the aspect ratio of the CPW remains constant at the same time as the gap is gradually increased. Reducing the spacing $s$ between the loop and the resonator short-circuit also increases the coupling, but because of fabrication constraints this spacing can not be arbitrarily small and we chose $s \approx 2\ \mu$m. Another difference with the atomic contact experiment was the target frequency $f_r$ for the resonator. For the nanowires, the initial goal of the experiment was to make evident intra-manifold spin-flip transitions, the frequency of which would go as the energy splitting of the ABS. As this splitting was expected to be weak [32], we targeted a low frequency resonator around $f_r \approx 3$ GHz. This also decreased the overall resonator-nanowire coupling, because $\delta_{\text{zp}} \propto f_r$.

[32]: Park and Levy Yeyati (2017), 'Andreev spin qubits in multichannel Rashba nanowires'

**Estimation of the mutual inductance**

The coupling between the weak link and the resonator mode depends on the mutual inductance $M$ between the resonator and the loop containing the weak link. To compute M, the following trick is used. We use Sonnet to estimate with the finite-element method the loop inductance $L_{\text{loop}}$ as well as the resonator's inductance to which the loop is coupled, which we write $\ell$ when there is no loop and $\ell'$ when the loop is coupled. Then, the following formula yields the mutual:

$$M = \sqrt{L_{\text{loop}}(\ell - \ell')}. \tag{5.8}$$

Indeed, using the convention from Figure 5.4, we can compute the input impedance $Z_{\text{in}}$ seen by the resonator:

$$\begin{aligned} Z_{\text{in}} &= j\omega(\ell + M) + j\omega(-M) \;//\; (\ell + M \;+\; L_{\text{loop}} - \ell) \\ &= j\omega(\ell + M) - j\omega \frac{M}{L_{\text{loop}}}(L_{\text{loop}} + M) \\ &= j\omega\ell' \quad \text{with } \ell' = \ell - \frac{M^2}{L_{\text{loop}}}, \end{aligned} \tag{5.9}$$

from which we deduce Eq. (5.8). For this inductive coupling design, the resonator's short-circuit to which the loop is coupled was designed to be 100-µm-long, similar to the experiment on atomic contact for which this design value had proved to provide a high-enough coupling [21]. The loop itself was designed *a posteriori*, because the rudimentary nanowire deposition technique that we were using at the time was not precise enough to deposit a unique nanowire at a given location (see Section 12.2.2). The shape of the loop had to be adapted so that it would connect to the nanowire. Therefore, its exact shape was not known before the nanowire deposition, and so a Sonnet simulation was run *a posteriori* with the exact shape of the loop to determine the loop-resonator coupling (see Figure 5.5(b)).

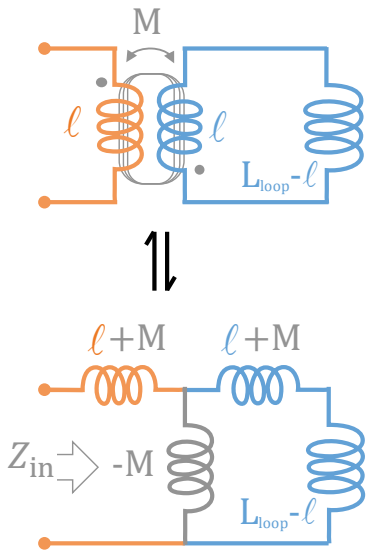


**Figure 5.4:** A loop of inductance $L_{\text{loop}}$ is inductively coupled to a wire of inductance $\ell$ through a mutual inductance $M$. Equivalent circuit useful to compute the input impedance $Z_{\text{in}}$ viewed from the left.

[21]: Janvier (2016), 'Coherent manipulation of Andreev Bound States in an atomic contact', pp.61-63

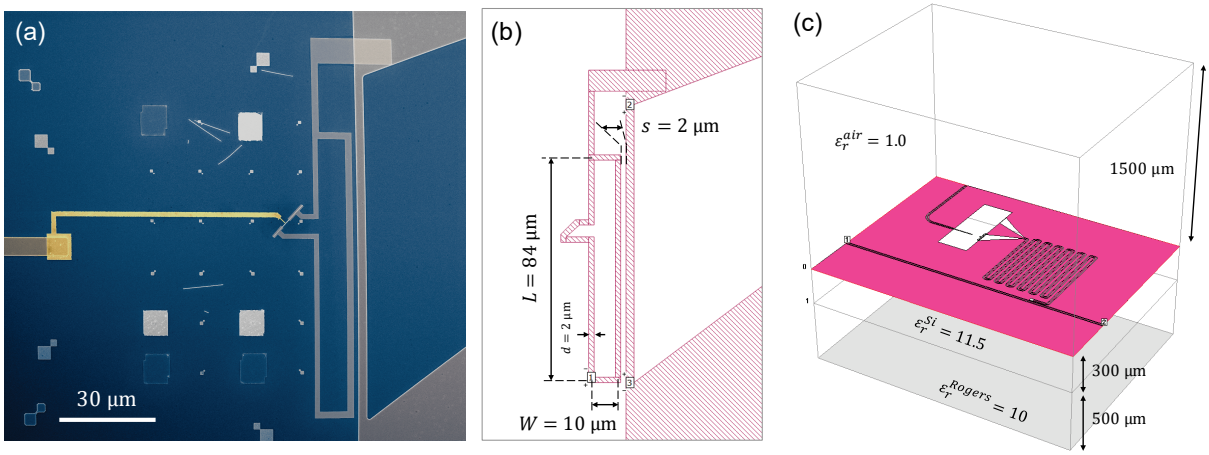


**Figure 5.5:** (a) False-color scanning-electron-microscope image of the experimental device with inductive coupling (sample S1), showing on the right hand side the 100-µm-long inductive wire shorting the resonator's end to which the nanowire loop is coupled. (b) Simplified geometry of the loop used for the Sonnet simulation. (c) Full simulation geometry comprising the CPW resonator (meander) coupled to a 2-port transmission line. Measuring the transmission coefficient $S_{21}(f)$ along this lines allows to extract the resonator's frequency $f_0$ and its quality factor.

Using Sonnet , the following values were obtained: $L_{\text{loop}} = 113.4$ pH, $\ell = 539.9$ pH and $\ell' = 536.3$ pH. From this, Eq. (5.8) gives a mutual inductance $M = 20.9$ pH, not far from the 27 pH which were achieved in the experiment on atomic contacts with a slightly different loop geometry [21]. This value is consistent with the simple estimate from the analytical result for the mutual inductance of a rectangular loop of size $L \times W$ coupled to an infinitely thin straight wire at a distance $s$:

$$M^{\text{th}} = \frac{\mu_0}{2\pi} L \ln\left(\frac{s+W}{s}\right).$$

The loop fabricated for the experiment was almost rectangular, made from a $d = 2$ $\mu$m-wide strip with a length $L = 84$ $\mu$m and a width $W = 10$ $\mu$m (see Figure 5.5(a)). Using the nominal spacing $s = 2$ $\mu$m, we get $M^{\text{th}} = 30$ pH. However, this simple model assuming infinitely thin wires and given that the strips were 2 $\mu$m wide, we should rather use $s = 4$ $\mu$m for the distance between the inner part of the loop and the center of the straight wire, which gives $M^{\text{th}} = 21$ pH, quite close to the value simulated with Sonnet.

### Resonator frequency shift

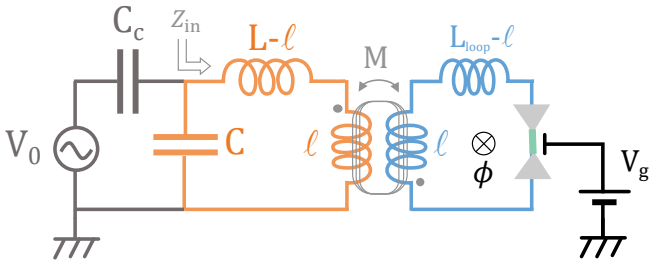


**Figure 5.6:** LC resonator coupled through a mutual inductance $M$ to the weak link loop modelled by the inductance $L_{\text{loop}}$. We call $Z_{\text{in}}$, the input impedance seen from the coupling capacitance $C_c$.

The resonator frequency shift due to the coupling with the loop inductance $L_{\text{loop}}$ through the mutual $M$ can be computed by expressing the

total resonator impedance $Z_{\text{in}}$ seen from the coupling capacitance $C_c$ (see Figure 5.6):

$$Z_{\text{in}} = \left[jC\omega + \left(j\omega(L+M) - j\omega\frac{M}{L_{\text{loop}}}(L_{\text{loop}}+M)\right)^{-1}\right]^{-1}$$
$$= \left[jC\omega + \frac{1}{j\omega(L-\frac{M^2}{L_{\text{loop}}})}\right]^{-1} = \frac{j\omega(L-\frac{M^2}{L_{\text{loop}}})}{1-C\omega^2(L-\frac{M^2}{L_{\text{loop}}})}.$$

The circuit exhibits a parallel type of resonance when $Z_{\text{in}}(\omega_r) \longrightarrow \infty$, from which we identify:

$$\omega_r = \frac{\omega_0}{\sqrt{1-\frac{M^2}{L_{\text{loop}}L}}} \overset{M/L\ll 1}{\approx} \omega_0(1+\frac{1}{2}\frac{M^2}{L_{\text{loop}}L}) \quad \text{, with } \omega_0 = 1/\sqrt{LC}. \quad (5.10)$$

Using the frequency $f_0 = \omega_0/2\pi$ and impedance $Z_r = \sqrt{L/C}$ of the bare resonator, its frequency shift due to the coupling with the weak link loop can be re-expressed as

$$\boxed{\Delta f_r = \frac{\Delta\omega_r}{2\pi} = \pi\frac{M^2 f_0^2}{Z_r L_{\text{loop}}}.} \quad (5.11)$$

The only unknown here is the resonator impedance $Z_r$. Using Sonnet , we simulate the input impedance near resonance of the bare CPW resonator and model it with Eq. (5.5) for a parallel RLC circuit. The simulation geometry which we use is the one of sample S1 presented in Figure 6.3(c) and Figure 5.7(b). Fitting of the resonance yields $f_0 = 3.213322$ GHz, $C = 767$ fF and $R > 20\,\text{M}\Omega$ (the metal layer in the simulation was assumed lossless and no dielectric losses were included for simplicity, so we expect R to be unbounded). From this, we deduce the equivalent inductance of the resonator, $L = 1/(C\omega_0^2) = 3.19$ nH, and its equivalent impedance $Z_r = 1/(C\omega_0) = 64.6\ \Omega$. Assuming a perfect quarter-wave line for the CPW resonator, we can independently estimate $Z_r$ from the characteristic impedance $Z_0$ of the CPW with Eq. (5.7). Using the transmission-line calculator TXLine from Cadence™ Inc. [77], we estimate $Z_0 = 47.6\ \Omega$ for a "CPW-Ground" topology with silicon as a dielectric ($\epsilon_r = 11.9$, no dielectric loss for simplicity), a width $S = 12\ \mu$m for the central conductor, a gap $W = 6\ \mu$m and a substrate thickness-to-ground $h = 700\ \mu$m. From Eq. (5.7), this gives $Z_r = \frac{4Z_0}{\pi} = 60.6\ \Omega$, not far from the above value, obtained independently by fitting the resonator input impedance with a RLC model.

We have now everything at hand to estimate the expected zero-point phase fluctuations $\delta_{zp}$ for this design. Note that for the participation ratio in Eq. (4.22), we should use $M/2$ instead of $M$. Indeed, in the design shown in Figure 5.3(b), the current $I_{\text{tot}}$ flowing through the CPW is effectively split in two at the short-circuit, so that only ~half of the current contributes to phase-fluctuations in the loop[3] . The flux induced in the loop would then read $\Phi_{\text{loop}} \approx M\frac{I_{\text{tot}}}{2} = \frac{M}{2L}\Phi_{\text{tot}}$, so that the participation ratio would be $\frac{\Phi_{\text{loop}}}{\Phi_{\text{tot}}} \approx \frac{M^*}{L}$ with $M^* = M/2$. From this, we get both the phase fluctuations $\delta_{\text{zp}}$ and the frequency shift due to the coupling with

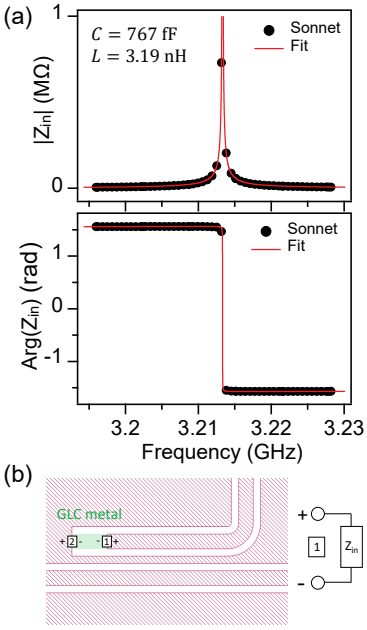


**Figure 5.7:** (a) Amplitude and phase of the resonator input impedance $Z_{\text{in}}$ for the inductive design, simulated using Sonnet. Fit with Eq. (5.5), shown in red line, gives $C = 767$ fF and $f_0 = 3.213322$ GHz, from which we deduce the equivalent inductance $L = 3.19$ nH. (b) $Z_{\text{in}}$ was simulated using a pair of two co-calibrated internal ports: port 1 being connected to the CPW central conductor and port 2 to the ground plane in front. To ensure that the impedance seen from port 1 indeed corresponds to $Z_{\text{in}}$, we define both ports as "floating" calibrated ports, which means that during the EM analysis, Sonnet will add extra metal to connect both ports (shown in green), which will act as a local ground for both. This metal is then removed during the de-embedding process.

3: Since $M^2/L_{\text{loop}} \ll \ell$, with $\ell$ the bare inductance of the short-circuit in Eq. (5.9), $\ell' \approx \ell$ and the CPW current splits almost equally in both $\ell$ and $\ell'$ to which the loop is coupled (we showed that the two inductances vary by only 3.6 pH). Exactly, the current flowing in the short-circuit where the loop is coupled would be $I_{\ell'} = \frac{\ell}{\ell+\ell'}I_{\text{tot}} = \frac{1}{2-M^2/(\ell L_{\text{loop}})} \approx 0.50 \times I_{\text{tot}}$.

the weak link loop inductance:

$$\delta_{zp} = \frac{M^*}{L}\sqrt{\frac{\pi Z_r}{R_Q}} = 2\pi f_0 M^* \sqrt{\frac{\pi}{Z_r R_Q}} = 5.6 \times 10^{-4}, \tag{5.12}$$

$$\Delta f_r = \pi \frac{M^{*2} f_0^2}{Z_r L_{\text{loop}}} = 450 \text{ kHz}. \tag{5.13}$$

Using again Sonnet , we can independently estimate this shift by simulating the resonance frequency of the bare resonator and of the one to which the actual loop (sample S1, see Figure 6.3(b)) is coupled. By fitting the simulated amplitude and phase of the transmission coefficient $S_{21}(f)$, we obtain $f_0 = 3.203433$ GHz for the bare resonator (with an external quality factor $Q_{\text{ext}} = 176 \times 10^3$) and a shift $\Delta f_r = 545 \pm 0.5$ kHz when adding the loop, which is about $\sim 16\%$ away from (5.13). This small discrepancy is likely traced back to our estimation of the mutual inductance: had we chosen $M^* = 11.1$ pH, slightly different from the 10.1 pH value, Eq. (5.11) would have given $\Delta f_r \approx 540$ kHz. Finally, to confirm that the simulated mode indeed corresponds to a current resonance, we verified the associated current distribution, which does show the structure of a $\lambda/4$ mode (see Figure 5.8).

As we will review in Chapter 9, the zero-point fluctuations associated to this inductive design provided too weak a coupling to the nanowire to allow single-shot readout of the weak link many-body states. Although this design was ill-suited for any time-domain applications, we could still well detect the ABS, due to the high total quality factor $Q_{\text{tot}} \approx 170 \times 10^3$, which allowed for the resolution of very small frequency shifts. Provided long integration times ($\sim$ 10-100 ms), we could evidence single-particle transitions between ABS by performing two-tone spectroscopy with this sample. This will be the focus of Chapter 6.

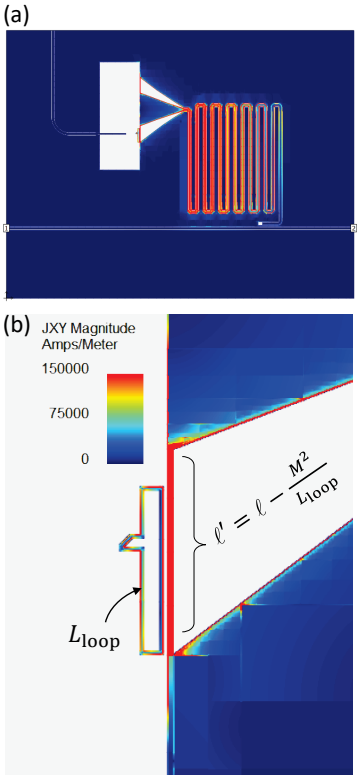


**Figure 5.8:** (a) Current distribution simulated with Sonnet for the geometry shown in Figure 6.3. It shows the structure of the $\lambda/4$ mode at frequency $f_0 = 3.203433$ GHz with an antinode at the shorted end of the CPW, where the weak link loop is coupled. (b) Enlargement on the short-circuit region showing the induced current in the loop. $\ell$ refers to the partial bare inductance of the short-circuit wire and $\ell'$ to its inductance when the loop is added. M denotes the mutual inductance between the wire and the loop and $L_{\text{loop}}$, the loop inductance of the latter.

## 5.2.2 Galvanic coupling

Moving to a galvanic coupling scheme was the natural extension to achieve higher coupling between the resonator and the weak link. The easiest way to implement it was to build on the existing resonator geometry by simply depositing and contacting the nanowire weak link across the gap of the CPW, thus acting as a shunt-inductance to ground for the CPW (see Figure 5.9). This design, which was suggested to us by Emmanuel Flurin from the Quantronics group, has the advantage that the central conductor of the CPW and its return path-to-ground naturally define a DC loop in the gap area, which can be used to phase bias the nanowire weak link.

### Transmission line model

The sCPW geometry can be described as a series association of two pieces of transmission line, with a given characteristic impedance each (see Figure 5.9(a)). The terminating piece of line located after the nanowire behaves like a *stub*, as it is shorted to ground to make the resonator quarter-wave. Let us denote by $Z_s$ the characteristic impedance of the stub and by $Z_0$ the one of the main transmission line forming the resonator.

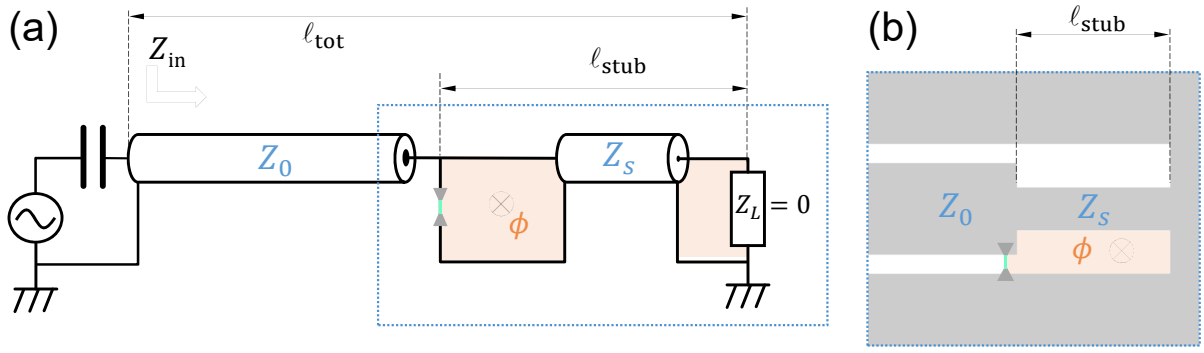


**Figure 5.9:** Shunted CPW resonator. (a) Transmission line model of the sCPW. (b) Scheme of the physical implementation corresponding to the end part of the resonator, highlighted by the dashed box in (a). The grey area depicts the superconducting thin film deposited on the substrate. The nanowire weak link is shunting the central conductor of the CPW to the ground, naturally defining a loop used to control the superconducting phase difference across it.

Using the impedance transformation rule from Eq. (5.1), one can see that for a lossless piece of line ($\alpha = 0$) with characteristic impedance $Z_s$ and terminated by a short $Z_L = 0$, the input impedance reads simply $Z_{stub} = jZ_s \tan(\beta \ell_{stub})$, with $\ell_{stub}$ the length of the stub.

Resonance is achieved when $\lambda_0 = 4\ell_{tot}$, where $\ell_{tot}$ stands for the total length of the resonator. This allows to rewrite Eq. (5.3): $\beta\ell_{stub} = \frac{\pi}{2}\frac{\ell_{stub}}{\ell_{tot}}\frac{\lambda_0}{\lambda} = \frac{\pi}{2}\frac{\ell_{stub}}{\ell_{tot}}\frac{\omega}{\omega_0}$, so that close to resonance ($\omega \approx \omega_0$), the tangent can be approximated by its argument when the stub is small compared to the total length of the resonator line ($\ell_{stub} \ll \ell_{tot}$). We are then left with $Z_{stub} \approx j\omega L_{stub}$, where $L_{stub} = Z_s \frac{\pi}{2\omega_0}\frac{\ell_{stub}}{\ell_{tot}} \ll 1$ stands for the stub inductance. In short, if the stub stays short compared to the resonator length, it essentially behaves near resonance like a pure inductor $L_{stub}$. Therefore by adding a stub with $Z_s > Z_0$, one expects to increase the total inductance of the resonator and as a result, to decrease its frequency. This can be modeled using a transmission line description of the resonator. Introducing the length ratio $\epsilon = \ell_{stub}/\ell_{tot} \ll 1$, one can express the input impedance of the sCPW resonator:

$$\begin{aligned} Z_{in} &= \frac{Z_{stub} + jZ_0 \tan(\beta(1-\epsilon)\ell_{tot})}{1 + j\frac{Z_{stub}}{Z_0}\tan(\beta(1-\epsilon)\ell_{tot})} \\ &= jZ_0 \frac{\frac{Z_s}{Z_0}\tan(\beta\epsilon\ell_{tot}) + \tan(\beta(1-\epsilon)\ell_{tot})}{1 - \frac{Z_s}{Z_0}\tan(\beta\epsilon\ell_{tot})\tan(\beta(1-\epsilon)\ell_{tot})} \\ &\equiv jZ_0 \frac{\tan(\beta\ell_{tot}C) + \tan(\beta(1-\epsilon)\ell_{tot})}{1 - \tan(\beta\ell_{tot}C)\tan(\beta(1-\epsilon)\ell_{tot})} \\ &= jZ_0 \tan(\beta\ell_{tot}(1-\epsilon+C)). \end{aligned} \tag{5.14}$$

To get the above simplification, we needed to enforce the following expression:

$$\frac{Z_s}{Z_0}\tan(\beta\epsilon\ell_{tot}) = \tan(\beta\ell_{tot}C).$$

When $\epsilon = \ell_{stub}/\ell_{tot} \ll 1$, this is true to first order in $\epsilon$ if we set $C = \epsilon\frac{Z_s}{Z_0}$. From this expression, we deduce that a parallel type of resonance is achieved when $\beta\ell_{tot}(1-\epsilon+C) = (2n+1)\pi/2$ with $n \in \mathbb{N}$, which defines the resonance frequencies of the sCPW:

**sCPW resonance frequencies**

$$f = f_r \frac{1}{1-\epsilon(1-\frac{Z_s}{Z_0})} \underset{\epsilon\to 0}{\approx} f_r\left[1-\epsilon\left(\frac{Z_s}{Z_0}-1\right)\right] \quad \text{with } f_r = \frac{(2n+1)v}{4\ell_{\text{tot}}}. \tag{5.15}$$

As a check we see that either by removing physically the stub $\epsilon \to 0$ or by equating $Z_s = Z_0$, we recover $f = f_r$, the bare resonance frequencies of the quarter-wave line. Also, when $Z_s > Z_0$, the renormalized resonator frequency is smaller than its bare value $f_r$ and as expected, increasing the stub length further decreases the resonator frequency.

In section 5.1.2, we showed that near resonance a lossless quarter-wave resonator can be modelled by an equivalent LC circuit. By comparing the impedance and frequency of an ideal LC circuit with the ones of the quarter-wave line (Eqs. (5.3,5.7)), one can express the equivalent discrete elements $L_{\text{sCPW}}, C_{\text{sCPW}}$ in terms of the line parameters: the inductance and capacitance per unit length, respectively $\mathcal{L}_r$ and $\mathcal{C}_r$:

$$\begin{cases} Z_r = \frac{4}{\pi} Z_0 = \frac{4}{\pi}\sqrt{\frac{\mathcal{L}_r}{\mathcal{C}_r}} \equiv \sqrt{\frac{L_{\text{sCPW}}}{C_{\text{sCPW}}}} \\ f_{r,0} = \frac{v}{4\ell_{\text{tot}}} = \frac{1}{4\ell_{\text{tot}}\sqrt{\mathcal{L}_r\mathcal{C}_r}} \equiv \frac{1}{2\pi\sqrt{L_{\text{sCPW}}C_{\text{sCPW}}}}. \end{cases}$$

Solving this set of equations for $\{L_{\text{sCPW}}, C_{\text{sCPW}}\}$, one deduces the equivalent discrete model for the $\lambda/4$ resonance of the shunted CPW resonator:

$$\begin{cases} L_{\text{sCPW}} = \frac{8\ell_{\text{tot}}}{\pi^2}\mathcal{L}_r \\ C_{\text{sCPW}} = \frac{\ell_{\text{tot}}}{2}\mathcal{C}_r. \end{cases} \tag{5.16}$$

From this, one can now estimate the coupling between the resonator and the nanowire weak link using Eq. (4.22). First let us express the participation ratio, *i.e.* the ratio of the inductance shared between the resonator and the weak link loop (=the stub inductance here) to the total resonator inductance:

$$\begin{cases} L_{\text{stub}} = Z_s \frac{\pi}{2\omega_0}\frac{\ell_{\text{stub}}}{\ell_{\text{tot}}} \\ L_{\text{sCPW}} = \frac{Z_r}{2\pi f_{r,0}} \overset{5.7}{=} \frac{4}{\pi}\frac{Z_0}{\omega_0} \end{cases} \Rightarrow \frac{L_{\text{stub}}}{L_{\text{sCPW}}} = \frac{\pi^2}{8}\frac{Z_s}{Z_0}\frac{\ell_{\text{stub}}}{\ell_{\text{tot}}}, \tag{5.17}$$

from which we deduce the phase fluctuations induced in the weak link loop:

$$\boxed{\delta_{\text{zp}}^{\text{sCPW}} = \frac{L_{\text{stub}}}{L_{\text{sCPW}}}\sqrt{\frac{\pi Z_r}{R_Q}} = \frac{\pi^2}{4}\frac{\ell_{\text{stub}}}{\ell_{\text{tot}}}\sqrt{\frac{Z_s^2}{Z_0 R_Q}}.} \tag{5.18}$$

- The coupling to the resonator of a pair transition arising from a single finite-length ($L/\xi \gtrapprox 1$) channel of transmission $\tau$ would be given at phase $\delta = \pi$ by

$$g(\pi) = \frac{\delta_{\text{zp}}^{\text{sCPW}}}{\hbar}\frac{\Delta}{1+L/\xi}\frac{\tau}{2} \propto \delta_{\text{zp}}^{\text{sCPW}}. \tag{5.19}$$

Therefore, in this shunted CPW geometry, the coupling increases linearly with the length ratio of the stub to the resonator's total length. This provides a simple means to tune the coupling by adjusting the length of the stub, remembering that it still needs to be small compared to $\ell_{\text{tot}}$ so that our perturbative approach remains valid and $\delta_{\text{zp}} \ll 1$. Increasing the stub length $\ell_{\text{stub}}$ provides a better coupling, but on the other hand, one also has to keep its inductance low compared to the weak link's inductance, so that the relation between the phase drop $\delta$ across the weak link and the applied flux $\phi$ through the loop does not become hysteretic (see discussion on the loop inductance in Section H.2). This means the stub length should be chosen as a trade-off between a good coupling and a proper phase biasing.

- To maximize the coupling, we see from Eq. (5.18) that the characteristic impedance of the stub $Z_s$ should be as large as possible as compared to the *geometric mean* of the resonator's characteristic impedance $Z_0$ and of the resistance quantum $R_Q$.

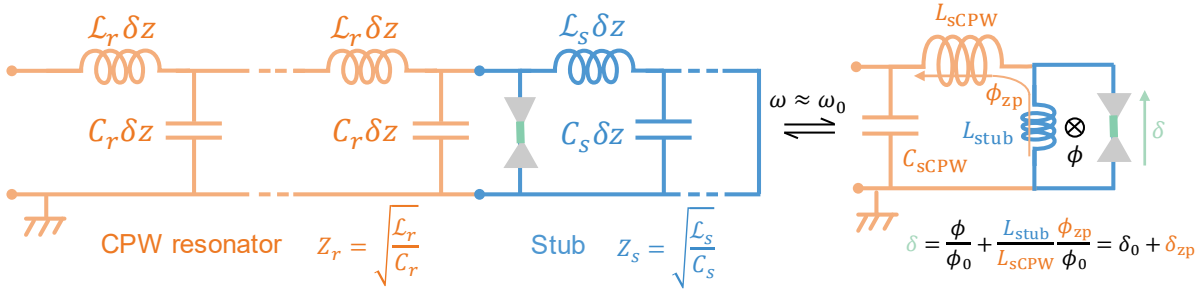


**Figure 5.10:** Equivalent LC circuit of the shunted CPW line near resonance.

### Resonator shift

Using the equivalent LC model of the resonator that we just found we can easily recover the expression for the classical resonator shift, in accordance with the general derivation done in section 4.1.5. Following the notations of Figure 5.10, we can express the total equivalent inductance $L_{\text{eq}}$ of the circuit and deduce the change of resonator inductance $\delta L$ when the weak link is coupled to it:

$$L_{\text{eq}} = (L_{\text{sCPW}} - L_{\text{stub}}) + (L_{\text{stub}} // L_{\text{wl}}) = L_{\text{sCPW}} - \frac{L_{\text{stub}}^2}{L_{\text{wl}} + L_{\text{stub}}} \Rightarrow \delta L \approx -\frac{L_{\text{stub}}^2}{L_{\text{wl}}}.$$

The resonator shift $\delta\omega$ due to the coupling with the weak link inductance $L_{\text{wl}}$ is then given by:

$$\frac{\delta\omega}{\omega_0} = -\frac{1}{2}\frac{\delta L}{L_{\text{sCPW}}} \approx \frac{L_{\text{stub}}^2}{2L_{\text{sCPW}}} \times \frac{1}{L_{\text{wl}}}. \tag{5.20}$$

Finally, combining Eqs. (5.17) and (5.20), one can express the resonator shift due to the inductive response of the weak link as a function only of

the geometric parameters of the sCPW:

$$\delta f = \frac{\delta\omega}{2\pi} = \frac{\varphi_0^2}{h}\delta_{zp}^2 L_{wl}^{-1} = \left(\frac{\pi}{8}\frac{\ell_{stub}}{\ell_{tot}}\right)^2 \frac{Z_s^2}{Z_0 L_{wl}}. \tag{5.21}$$

### Design parameters

In experiments on atomic contacts [21], the loop in which the weak link was embedded was chosen to be $90 \times 20\ \mu m^2$, which proved to provide a good phase bias of the weak link. We set the stub length to $\ell_{stub} = 100\ \mu m$ so as to get in a similar loop size for our nanowire experiment. As for the lengths of the resonators, they were chosen between $\ell_{tot} = 3.9 - 4.2$ mm for the resonances to fall in the $6 - 7$ GHz range below the dispersive feature of our TWPA amplifier used for detection. Within this frequency range, the TWPA typically gives ~20 dB amplification.

The characteristic impedances of the two CPW parts (resonator and stub) were chosen to maximize the coupling. According to Eq. (5.21), this means having a low impedance resonator $Z_0$ and a high stub impedance $Z_s$ so as to maximize the phase fluctuations over the loop region. The CPW topology is well suited for that, as it allows to easily tune the line impedance in a wide range by simply adjusting the gap width. Reducing the gap width decreases consequently the impedance. But it is limited by the spatial resolution of optical lithography system used to pattern the resonators in superconducting thin films, which lies typically around 1 µm. Optical lithography allows to reach minimal structure size as low as half a µm. However, to keep the recipe reliable on the whole resonator area, we prefered to set the CPW gap to $W = 2\ \mu m$.

In Figure 5.11 we show the evolution of the CPW line impedance $Z_0$ with the gap $W$ (a) and the width $S$ (b) of its central conductor, as estimated from a two-port Sonnet simulation of a piece of line. The simulated results show good agreement with the simple theory for a CPW of negligible thickness on top of an infinitely thick substrate ($h \to \infty$) obtained by conformal mapping techniques [78]:

$$Z_0^{CPW} = \frac{30\pi}{\sqrt{\frac{\epsilon_r+1}{2}}}\frac{K'(k)}{K(k)} \quad \text{with } k = \frac{S}{S+2W}, \tag{5.22}$$

where K is the complete elliptic integral of the first kind and $K'(k) = K(\sqrt{1-k^2})$.

Taking $S = 30\ \mu m$ gives a characteristic impedance $Z_0 = 27.9\ \Omega$. Using the transmission-line calculator TXLine from Cadence™ Inc. [77], we recover the same value within $\pm 0.1\ \Omega$ for this "CPW-Ground" geometry (lossless metal on a 700 $\mu$m thick silicon substrate with $\epsilon_r = 11.9$, assuming no loss for simplicity). For the stub region, we set a width $S_s = 14\ \mu m$, resulting in a gap of $W_s = 10\ \mu m$ to keep the same total distance between the ground planes. From a Sonnet simulation, we expect this second piece of CPW to have a nominal characteristic impedance of $Z_s = 52.7\ \Omega$, again in agreement with the prediction from TXLine.

With this geometry, we checked the validity of Eq. (5.21) giving the resonator shift due to the coupling with the weak-link inductance. To

[21]: Janvier (2016), 'Coherent manipulation of Andreev Bound States in an atomic contact'

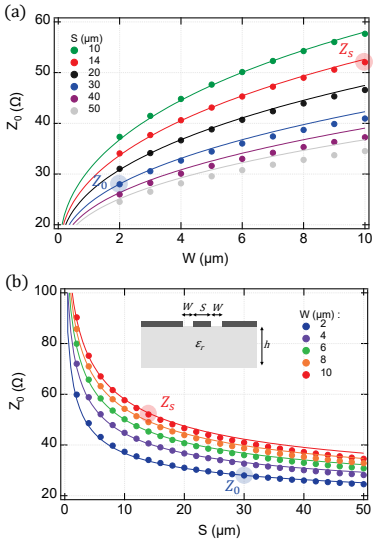


**Figure 5.11:** CPW characteristic impedance $Z_0$ as a function of the gap W (a) and the width S (b) of the CPW central conductor. The values highlighted by black and red disks correspond to the design values for the CPW resonator and its stub termination used in the experiment. Simulation points shown in disks and theory from Eq. (5.22) in continuous lines.

[78]: Gupta et al. (1979), *Microstrip Lines and Slotlines*, pp.261-262

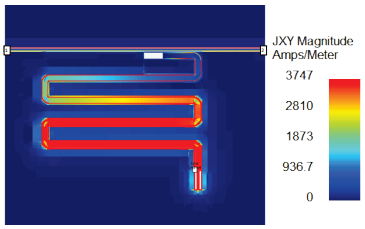


**Figure 5.12:** Current distribution of a sCPW resonator simulated in Sonnet showing the structure of the $\lambda/4$ mode with an antinode at its shorted end where the weak link is coupled.

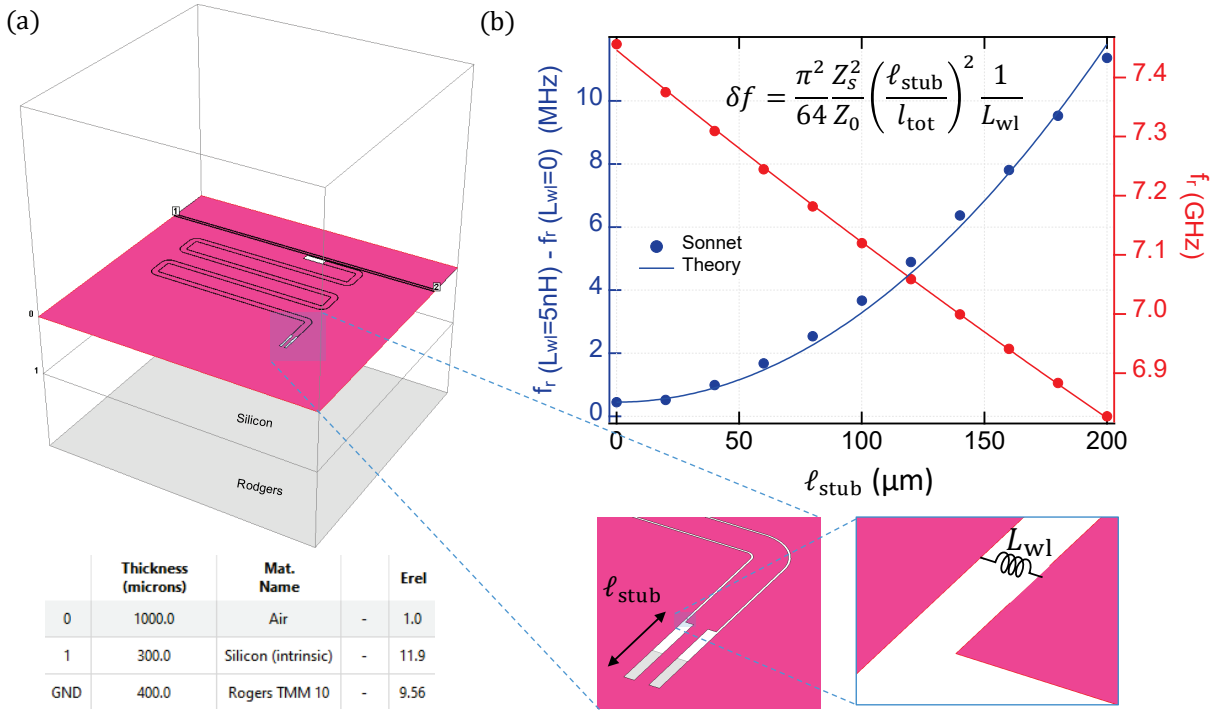


| | Thickness (microns) | Mat. Name | | Erel |
|---|---|---|---|---|
| 0 | 1000.0 | Air | - | 1.0 |
| 1 | 300.0 | Silicon (intrinsic) | - | 11.9 |
| GND | 400.0 | Rogers TMM 10 | - | 9.56 |

**Figure 5.13:** Frequency shift of a sCPW resonator as a function of the stub length. (a) Model used for the Sonnet simulation, comprising a sCPW resonator connected in a notch geometry to a two-port transmission line. The weak link is modelled by an ideal inductor $L_{\rm wl} = 5$ nH shunting the CPW gap before the stub region terminating the $\lambda/4$ resonator. The CPW gap was set to $s = 2$ $\mu$m and the central width to $W = 30$ $\mu$m. For the stub region, the gap is increased to $s = 10$ $\mu$m, leaving a width of $W_s = 14$ $\mu$m for the central conductor. The parameters for the substrate layers (material, thickness, dielectric constant) are given in the table above. (b) Resonance frequency $f_r$ and its shift when the shunt inductance $L_{\rm wl}$ is added, as extracted from a Sonnet simulation of the $S_{21}(f)$ along the transmission line. Simulation points shown in solid circles and best fit with Eqs. (5.21,5.15) in solid lines.

do so, we ran a parameter sweep varying the stub length and, for each simulation, extracted from the $S_{21}(f)$ data the resonance frequency with and without the weak link, which was modelled by a $L_{wl} = 5$ nH to get an idea (this corresponds to the expected inductance for a perfectly transmitted channel and with $\Delta_{\rm Al} = 45$ GHz [40]). Looking at the simulated distribution of current, shown in Figure 5.12, we confirm the $\lambda/4$ nature of the investigated resonator mode, showing a node of the current at its open end coupled to the transmission line and an antinode at its shorted end. Figure 5.13 shows both the expected linear decrease of the resonance frequency and the quadratic behaviour of the frequency shift as a function of the stub length. The simulation data was fitted with Eq. (5.21), while fixing the parameters $L_{\rm wl} = 5$ nH and $\ell_{\rm tot} = 3966$ $\mu$m.

[40]: Bretheau (2013), 'Localized Excitations in Superconducting Atomic Contacts', pp. 4 & 40

Note that the shift is not identically zero when the stub length is reduced to $\ell_{\rm stub} = 0$. This is because the inductor modelling the weak link was not put exactly at the discontinuity delimiting the beginning of the stub, but a few microns away to mimic the actual geometry of sample S2. A global offset of 0.45 MHz was therefore added to account for this residual shift. The best fit of both the resonance frequency and its shift yields the following values for the resonator and stub characteristic impedances: $Z_0^{\rm fit} = 18.4$ Ω and $Z_s^{\rm fit} = 51.5$ Ω. Those values fall a few ohms away from the nominal values given above, which are expected for infinite lines. Note that a perfect agreement with the model is not to be expected, because the latter considers two ideal pieces of transmission

lines connected in series and does not account for spurious effects like the extra capacitance-to-ground arising from the step discontinuity in the width of the CPW's central conductor at the stub transition. The microwave engineering literature provides semi-analytical formulas to estimate such a capacitance [79], but the fine modeling of these extra non-ideal effects was not the purpose of the present work.

[79]: Sinclair and Nightingale (1992), 'An equivalent circuit model for the coplanar waveguide step discontinuity'

From Eq. (5.18) and using those values of $Z_0^{\text{fit}} = 18.4\ \Omega$, $Z_s^{\text{fit}} = 51.5\ \Omega$ along with $\ell_{\text{tot}} = 3966\ \mu$m and $\ell_{\text{stub}} = 100\ \mu$m, we estimate the zero-point phase fluctuations associated to this coupling design to be:

$$\delta_{\text{zp}}^{\text{sCPW}} = \frac{\pi^2}{4}\frac{\ell_{\text{stub}}}{\ell_{\text{tot}}}\sqrt{\frac{Z_s^2}{Z_0 R_Q}} \approx 9.3\times10^{-3}. \tag{5.23}$$

Fitting of a single-tone spectroscopy measurement of a resonator with this design (sample S2) gives a result quite close to this nominal value $\delta_{\text{zp}} = 1.2\times10^{-2}$ (see Section 6.5.2). Note that compared to the inductive design from sample S1 (Section 5.2.1), we gained a factor ×16.6 in $\delta_{\text{zp}}$ (see Eq. (5.12)), which means a factor ∼ 275 for the nanowire-resonator coupling. Compared to the mutual coupling design used for the atomic contact experiment [16], a factor ×3 in $\delta_{\text{zp}}$ was also achieved. Given that for finite-length junctions, the coupling factor $g$ is further reduced by a factor $1/(1 + L/\xi)$ (see Eq. (5.19)), this new design is expected to offer a globally similar coupling for pair transitions in $L/\xi \approx 2$ weak-links compared to what was achieved with atomic contacts implementing $L \to 0$ weak links.

From Figure 5.13, we see that a stub length of $\ell_{\text{stub}} = 100\ \mu$m yields a sizeable resonator shift of almost 4 MHz when $L_{\text{wl}} = 5$ nH. Using again Eq. (5.21), one can now compute by how much the resonance frequency would change when the shunt inductance modeling the weak link is varied from $L_{\text{wl}}$ to $L_{\text{wl}} + \delta L_{\text{wl}}$ (see Figure 5.14). This is precisely the quantity that we want to optimize: in the spectroscopy measurements that we seek to perform, the microwave drive induces transitions between Andreev states which result in a change of inductance of the weak link and therefore shift the resonance frequency. Following our illustrating case where $L_{\text{wl}} = 5$ nH, we see that a change of weak link inductance of ±1 nH typically shifts the resonator in the range ±700 kHz. To optimize the detection one requires this shift to be comparable to the resonator linewidth $\Delta f_r$. For a resonance at $f_r = 7$ GHz, this means a total quality factor of typically $Q = f_r/\Delta f_r \approx 10000$. Then, assuming low internal loss $Q_{\text{int}} \gg Q_{\text{ext}}$, we need to design the external coupling of our resonators to the feedline so as to target $Q_{\text{ext}} \approx 10\times10^3$.

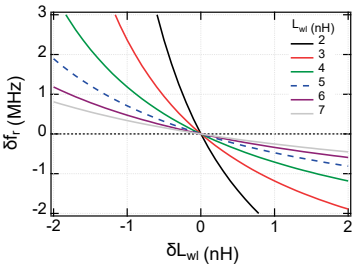


**Figure 5.14:** Change of resonance frequency $\delta f_r$ of a sCPW resonator when the shunt inductance modelling the weak link is varied by an amount $\delta L_{\text{wl}}$.

### 5.2.3 Coupling resonators to a readout transmission line

Contrary to the experiments on atomic contacts [21], where the resonator was probed in reflection, we read out the resonators using a notch-type coupling to a common transmission line (TL). This allows to implement relatively weak resonator-feedline coupling without perturbing significantly the off-resonant modes propagating in the feedline. Because of this property, notch-port couplers enable frequency multiplexing schemes, where many CPW resonators of different frequencies can be coupled

[21]: Janvier (2016), 'Coherent manipulation of Andreev Bound States in an atomic contact'

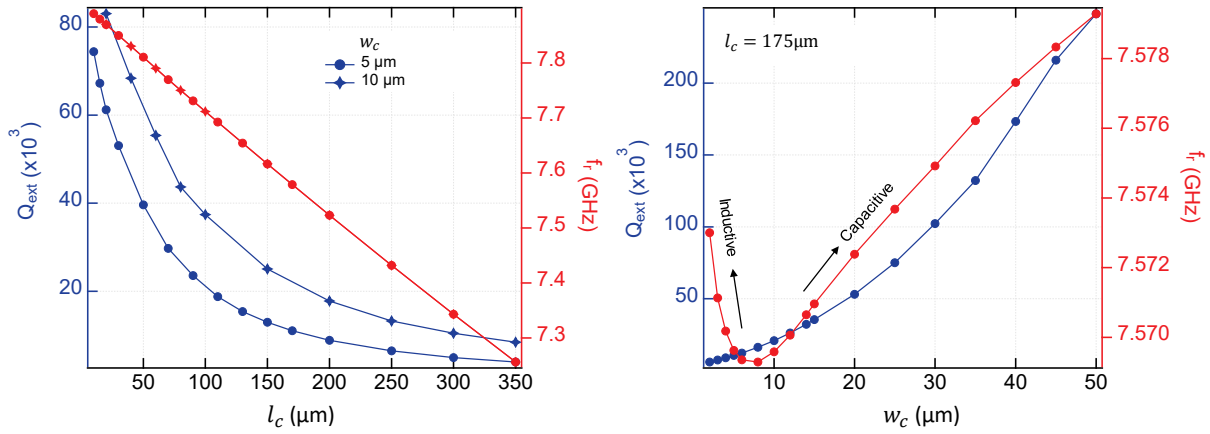


**Figure 5.15:** Dependence of the sCPW frequency and external quality factor on the length of the coupler region and distance to the transmission line, obtained from a 2-port Sonnet simulation. Same simulation geometry as for Figure 5.13.

to a single feedline in a so-called *hanger* geometry. This offered us a convenient possibility to fabricate and probe multiple resonators on a single chip to maximize the fabrication success rate and end up after the fab process with a least one working nanowire resonator (see Section 12.2 for details about the weak link fabrication). Finally, using our currently available 6-ports PCBs, we could fit up to four resonators on a single chip: two ports for the transmission line and one port to address the gate of each resonator (see Figure 12.1 and 12.2).

Using a transmission line coupling scheme also allows to measure easily the internal losses of a resonator, simply by connecting the TL to a vector network analyzer (VNA) and measuring the scattering parameter $S_{21}$ as a function of the probe frequency $f$. For a two port network, the complex scattering parameter can be written in the form [80, 81]:

$$S_{21}(f) = ae^{2\pi i f \tau_{el}}\left[1 - \frac{e^{i\phi}Q/Q_{ext}}{1 + 2iQ(f/f_r - 1)}\right], \tag{5.24}$$

with $f_r$ the resonance frequency and Q, the loaded quality factor of the resonator. The additional parameters $a, \tau_{el}, \phi$ are introduced to model the transmission through the cables and other components of the measurement system[4] .

For high quality resonances, losses are perturbatively small and the total loss rate can be decomposed as a sum of partial loss rates over the different loss channels. For a TL-coupled resonator, the external losses related to the emission of radiation into the TL can be separated from the dissipative losses occuring inside the resonator (in particular dielectric losses): $Q^{-1} = Q_{int}^{-1} + Q_{ext}^{-1}$. For most applications, one wishes for the internal quality factor $Q_{int}$ to be as high as possible and for the external quality factor $Q_{ext}$ to fall close to the design value.

To tune the coupling of the resonators to the transmission line, described by $Q_{ext}$, one can play with two geometrical parameters (see Figure 5.16(a)): the length $l_c$ of the notch coupler parallel to the transmission line and its distance $w_c$ to the line. To check how they affect the coupling, we ran two-parameter sweeps in Sonnet. For each simulation, we fitted with Eq. (5.24) the amplitude and phase of the transmission coefficient $S_{21}(f)$

[80]: Khalil et al. (2012), 'An analysis method for asymmetric resonator transmission applied to superconducting devices'
[81]: Deng et al. (2013), 'An analysis method for transmission measurements of superconducting resonators with applications to quantum-regime dielectric-loss measurements'

4: Note that in realistic circuits, the resonance line shape may be asymmetric due to impedance mismatches at the TL ports. This phenomenon is well described and modelled in Refs. [80, 81].

as a function of frequency to extract the resonance frequency $f_r$ and the external quality factor $Q_{\text{ext}}$ (see Figure 5.15).

Using conformal mapping techniques, Besedin *et al.* [82] have derived analytical expressions for the external quality factor $Q_{\text{ext}}$ and frequency shift $\Delta f_r$ of a TL-coupled CPW resonator. In the general case, when the input and output ports of the TL are not matched, the quality factor depends crucially on the position of the resonator along the line. This is because standing waves arise in the feedline due to impedance mismatch, thus making the coupling position-dependent. For matched ports, the quality factor has no leading-order dependence on the position of the coupler section and its expression assumes a simple form. Let us note $l_c$ the length of the coupling region and $l_r$ the total length of the resonator. Assuming that the resonator is coupled to the TL at its open end and that it is shorted at the other end, we then have:

$$\begin{cases} \Delta f_r = -\dfrac{3\kappa^2}{2\pi} f_r \sin\left(\pi \dfrac{l_c}{l_r}\right) \\ Q_{\text{ext}} = \dfrac{\pi}{2\kappa^2 \sin^2\left(\frac{\pi}{2}\frac{l_c}{l_r}\right)}. \end{cases} \tag{5.25}$$

These expressions result from a perturbative expansion in the coupling strength $\kappa$ and describe only the leading order terms for the quality factor and frequency shift. Although they reproduce the trend of the data simulated with Sonnet (Figure 5.16), they yield a systematically higher estimate of the quality factor. This discrepancy can be attributed to the spurious couplings between the resonator and the feedline, mainly arising from the conductor arcs attached to the notch coupler (see simulation geometry in Figure 5.13), which lead to a larger effective coupler length. Note also that the small dimensionless parameter $\kappa$ characterizing the strength of the coupling does not have any analytical expression, in particular its dependence on the TL-resonator separation $w_c$ is not explicit and therefore such theory cannot be used for synthesis, only for analysis. Fitting jointly with Eq. (5.25) the $f_r$ and $Q_{\text{ext}}$ data obtained from Sonnet simulation, one obtains a coupling coefficient $\kappa = 0.18$. Note that compared to Eq. (5.25) a global offset of +340 MHz was added to $f_r$ to fit the data. This agrees with the qualitative remark above that the model underestimates the coupling and therefore also overestimates the resonance frequency. Therefore it cannot be used to predict quantitatively the coupling and to assist the design. For completeness, it would be interesting to improve the agreement with theory, but this lies beyond the scope of this work; for our purpose it was enough to run microwave simulations to get a quantitative estimate of the external coupling and tune the design accordingly.

Finally, note that for this method to work, the simulated transmission $S_{21}(f)$ data needs to be fine enough in frequency, so that the resonance curve is well-sampled to be fitted and to extract reliably $Q_{\text{ext}}$. In practice this often means to run iteratively several simulations over successively smaller frequency ranges. Designing microwave resonators in this manner can be time consuming since it requires many simulation runs. Note that there exists a smart alternative method allowing to retrieve accurately and much faster $f_r$ and $Q_{\text{ext}}$ from a single simulation with a wide frequency sweep [83]. It consists in adding an internal (virtual) port in the Sonnet

[82]: Besedin and Menushenkov (2018), 'Quality factor of a transmission line coupled coplanar waveguide resonator'

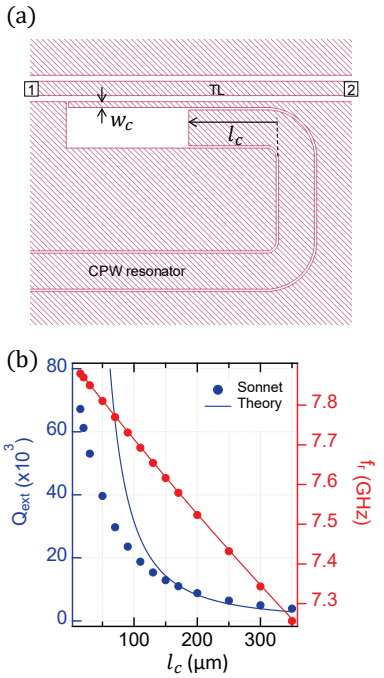


**Figure 5.16:** (a) Sonnet geometry used to tune the coupling of the resonator to the TL. The two parameters are the length $l_c$ of the notch coupler and the width $w_c$ of the electrode separating it from the TL. A small gap of 2 $\mu m$ was put between this electrode and the close-by ground plane in order to avoid a second closed DC loop that could perturb the phase bias of the weak link. (b) External quality factor $Q_{\text{ext}}$ and resonance frequency $f_r$ of a TL-coupled CPW resonator vs the length $l_c$ of the notch coupler. Data points from Sonnet simulations are compared to analytical predictions obtained by conformal mapping techniques [82].

[83]: Wisbey et al. (2014), 'New Method for Determining the Quality Factor and Resonance Frequency of Superconducting Micro-Resonators from Sonnet Simulations'

model and examining the input impedance viewed from this added port. The latter should be placed near a current maximum so as to represent the impedance near resonance of a an equivalent series RLC circuit. By looking at the slope and zero-crossing of $\mathrm{Im}(Z_{\mathrm{in}})$, one can directly extract $f_r$ and $Q_{\mathrm{ext}}$.

From Figure 5.15, we deduce the length of the coupler and its distance to the TL to choose, so as to implement the $Q_{\mathrm{ext}} = 10 \times 10^3$ value that we had targetted. In practice, to maximize SNR for states discrimination, we require the resonator shift to be comparable to the resonator linewidth, which is directly determined by $Q_{\mathrm{ext}}$ when $Q_{\mathrm{ext}} \ll Q_{\mathrm{int}}$. This condition cannot be unconditionally implemented, because the resonator shift is not a design parameter but depends on the weak link's microscopic inductance, which may be tuned by the external flux $\phi$ and the gate voltage $V_g$. More importantly, pair transitions between Andreev states may couple differently to the resonator that single-quasiparticle transitions. Indeed, current matrix elements between odd states were estimated to be a hundred times smaller than for states of even parity, therefore making their observation in microwave experiments challenging [32] as they would shift the resonator by a much smaller amount than states of even parity.

Therefore, to check *a posteriori* which coupling was best, we fabricated resonators with various coupler lengths to cover a wide range of external coupling to the feedline, with four target values for the quality factor: $Q_{\mathrm{ext}} = 10^3, 4 \times 10^3, 10 \times 10^3$ and $40 \times 10^3$ (see Figure 12.2). Ideally, designing the resonators to have an in-situ tunable coupling to the TL would allow to optimize the SNR and state discrimination depending on their parity. Some tunable coupling schemes have been proposed using either SQUIDs and an external magnetic field as the tuning knob [84] or relying on the intrinsic non-linearity of superconducting thin films due to their kinetic inductance and using a DC current to tune it [85]. For our first experiment on nanowires, implementing such a tunable coupling scheme would have added complexity to the design and so we decided not to go ahead with this option.

[32]: Park and Levy Yeyati (2017), 'Andreev spin qubits in multichannel Rashba nanowires'

[84]: Wulschner et al. (2016), 'Tunable coupling of transmission-line microwave resonators mediated by an rf SQUID'

[85]: Bockstiegel et al. (2016), 'A tunable coupler for superconducting microwave resonators using a nonlinear kinetic inductance transmission line'

## 5.3 Coplanar stripline design

In the course of this thesis, another resonator design was investigated, following the works of Hays *et al.*. It consists in a differential pair of two coupled microstrip lines (see Figure 5.17(a)), known also as *coplanar stripline* (CPS). This appears as the simplest design to implement a differential excitation of the weak link, using the odd mode of the two coupled lines. As reviewed in section 4.1.5, measuring the weak link through the differential mode of the resonator allows to probe only the diagonal current component of the weak link susceptibility matrix, which in principle should make easier the resolution of the spin states. This strategy was chosen by Hays *et al.* and allowed them to demonstrate the manipulation of a nanowire-based Andreev spin qubit [41, 42]. We came to understand rather late the relevance of such a design compared to a simple CPW implementation, and why the intrinsic left/right symmetry of the resonator mattered at all.

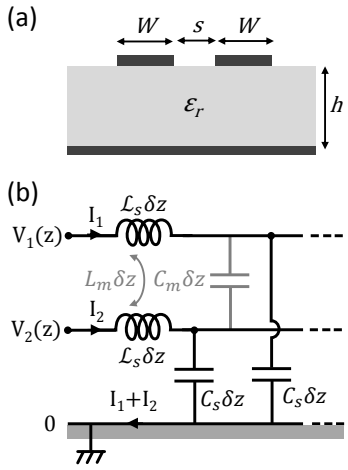


**Figure 5.17:** (a) Two coupled coplanar microstrip lines over a dielectric substrate of thickness $h$ and relative permittivity $\epsilon_r$. (b) Distributed-element model of the coupled lines. Coupling elements are shown in grey.

To test this idea of a differential pair to probe the weak link, we designed similar resonators at the end of this thesis. The motivation was twofold: (1) trying to reproduce the published results from Hays *et al.* on a slightly different platform, using fullshell nanowires instead of partially-covered ones (2) performing not an *indirect* (Raman) manipulation of the spin states as in [42], but a *direct* manipulation through the intramanifold SQPT that we had identified in [53]. At the time of writing this manuscript, the sample was cooled down. Let us review in this section the basics of differential pairs in PCB transmission lines and how to design them.

[53]: Metzger et al. (2021), 'Circuit-QED with phase-biased Josephson weak links'

### 5.3.1 Even & odd modes

All the properties that we derived in the previous section 5.2 for the sCPW resonator design depend on the characteristic impedance $Z_0$ of the single-ended transmission line from which the resonator is made. This impedance relates the voltage and current at any point $z$ on the line through the relation $V(z) = Z_0 I(z)$. For an almost lossless line, this impedance reads $Z_0 = \sqrt{\mathcal{L}/\mathcal{C}}$, where $\mathcal{L}$ and $\mathcal{C}$ are respectively the inductance and capacitance per unit length of the line.

However, for a differential pair, the relation between current and voltage can no longer be described by a single characteristic impedance. This is because the two lines of the pair may be coupled electromagnetically if close enough to each other. Therefore, a current flowing in line 1 may also induce a voltage in line 2 of the pair through a coupling or *mutual* impedance. In this situation, the relation between voltage and current for the coupled system is now described by a 2x2 impedance matrix:

$$\begin{pmatrix} V_1 \\ V_2 \end{pmatrix} = \begin{pmatrix} Z_{11} & Z_{12} \\ Z_{21} & Z_{22} \end{pmatrix} \Rightarrow \begin{cases} V_1 = Z_{se} I_1 + Z_m I_2 \\ V_2 = Z_{se} I_2 + Z_m I_1, \end{cases} \tag{5.26}$$

where we have labeled $Z_{se} = Z_{11} = Z_{22}$ the characteristic impedance of a single-ended line, and $Z_m = Z_{12} = Z_{21}$ the mutual impedance between lines 1 and 2. We assume here that both lines of the pair are identical and uniform, with a fixed separation along the whole length of the lines.

The mutual impedance $Z_m$ arises due to coupling between the two lines, which can be modeled in the general case by a coupling capacitance $\mathcal{C}_m$ and a mutual inductance $\mathcal{L}_m$ per unit length (see Figure 5.17(b)). Relating the voltage $V(z)$ to the current $I(z)$ on an infinitesimally small length of line $\delta z$ allows to write the set of coupled equations describing the propagation of time-varying signals along the line:

| *Maxwellian* form | *Physical* form |
|---|---|
| $-\frac{\partial V_1}{\partial z} = \mathcal{L}_{11}\frac{\partial I_1}{\partial t} + \mathcal{L}_{12}\frac{\partial I_2}{\partial t}$ | $-\frac{\partial V_1}{\partial z} = \mathcal{L}_s\frac{\partial I_1}{\partial t} + \mathcal{L}_m\frac{\partial I_2}{\partial t}$ |
| $-\frac{\partial V_2}{\partial z} = \mathcal{L}_{21}\frac{\partial I_1}{\partial t} + \mathcal{L}_{22}\frac{\partial I_2}{\partial t}$ | $-\frac{\partial V_2}{\partial z} = \mathcal{L}_m\frac{\partial I_1}{\partial t} + \mathcal{L}_s\frac{\partial I_2}{\partial t}$ |
| $-\frac{\partial I_1}{\partial z} = \mathcal{C}_{11}\frac{\partial V_1}{\partial t} + \mathcal{C}_{12}\frac{\partial V_2}{\partial t}$ | $-\frac{\partial I_1}{\partial z} = (\mathcal{C}_s + \mathcal{C}_m)\frac{\partial V_1}{\partial t} - \mathcal{C}_m\frac{\partial V_2}{\partial t}$ |
| $-\frac{\partial I_2}{\partial z} = \mathcal{C}_{21}\frac{\partial V_1}{\partial t} + \mathcal{C}_{22}\frac{\partial V_2}{\partial t}$ | $-\frac{\partial I_2}{\partial z} = -\mathcal{C}_m\frac{\partial V_1}{\partial t} + (\mathcal{C}_m + \mathcal{C}_s)\frac{\partial V_2}{\partial t}.$ |

Voltages and currents on both lines of the pair are related through 2x2 inductance and capacitance matrices $L_{ij}$ and $C_{ij}$ with $i, j \in \{1, 2\}$. To make contact with the circuit model in Figure 5.17(b), one can rewrite the set of equations in terms of their physical parameters $\{L_s, C_s\}$ and $\{L_m, C_m\}$ (Table 5.1), describing respectively the properties of the isolated lines (subscript $s$, for *self*) and of their coupling (subscript $m$, for *mutual*).

**Table 5.1:** Correspondence between *physical* & *Maxwellian* parameters

| |
|---|
| $\mathcal{L}_{11} = \mathcal{L}_{22} = \mathcal{L}_s$ |
| $\mathcal{L}_{12} = \mathcal{L}_{21} = \mathcal{L}_m$ |
| $\mathcal{C}_{11} = \mathcal{C}_{22} = \mathcal{C}_s + \mathcal{C}_m$ |
| $\mathcal{C}_{12} = \mathcal{C}_{21} = -\mathcal{C}_m$ |

Although it is enough to solve numerically this set of differential equations to get the time-evolution of a propagating signal at each point of the two lines, one can get further physical insight by introducing the concepts of *even* and *odd* modes. Indeed, any two arbitrary signals $V_1$ and $V_2$ can always be expressed in terms of their average value and of their difference:

$$\begin{cases} V_1 = V_{\text{com}} + \dfrac{V_{\text{diff}}}{2} \equiv V_e + V_o \\ V_2 = V_{\text{com}} - \dfrac{V_{\text{diff}}}{2} \equiv V_e - V_o, \end{cases}$$

where we have defined $V_{\text{com}} \equiv (V_1 + V_2)/2 = V_e$, the *common mode* or *even* signal, and $V_{\text{diff}} \equiv V_1 - V_2 = 2V_o$ the *differential* signal or *odd mode*. Those are actually the *normal modes* of the system, as they allow to diagonalize the inductance and capacitance matrices: even and odd mode currents can be seen as the eigenvectors of the symmetric impedance matrix. Likewise, even and odd mode voltages are the eigenvectors of the associated admittance matrix.

| **EVEN mode** | **ODD mode** |
|---|---|
| $-\frac{\partial V_e}{\partial z} = (\mathcal{L}_{11} + \mathcal{L}_{12})\frac{\partial I_e}{\partial t}$<br>$-\frac{\partial I_e}{\partial z} = (\mathcal{C}_{11} + \mathcal{C}_{12})\frac{\partial V_e}{\partial t}$ | $-\frac{\partial V_o}{\partial z} = (\mathcal{L}_{11} - \mathcal{L}_{12})\frac{\partial I_o}{\partial t}$<br>$-\frac{\partial I_o}{\partial z} = (\mathcal{C}_{11} - \mathcal{C}_{12})\frac{\partial V_o}{\partial t}$ |
| $V_e = \frac{1}{2}(V_1 + V_2) = V_{\text{com}}$<br>$I_e = \frac{1}{2}(I_1 + I_2) = I_{\text{com}}/2$ | $V_o = \frac{1}{2}(V_1 - V_2) = V_{\text{diff}}/2$<br>$I_o = \frac{1}{2}(I_1 - I_2) = I_{\text{diff}}$ |
| $Z_e \equiv \dfrac{V_e}{I_e} = \dfrac{2V_{\text{com}}}{I_{\text{com}}} = 2Z_{\text{com}}$<br>$= \sqrt{\dfrac{\mathcal{L}_{11} + \mathcal{L}_{12}}{\mathcal{C}_{11} + \mathcal{C}_{12}}}$<br>$= \sqrt{\dfrac{\mathcal{L}_s + \mathcal{L}_m}{\mathcal{C}_s}}$ | $Z_o \equiv \dfrac{V_o}{I_o} = \dfrac{V_{\text{diff}}}{2I_{\text{diff}}} = \dfrac{Z_{\text{diff}}}{2}$<br>$= \sqrt{\dfrac{\mathcal{L}_{11} - \mathcal{L}_{12}}{\mathcal{C}_{11} - \mathcal{C}_{12}}}$<br>$= \sqrt{\dfrac{\mathcal{L}_s - \mathcal{L}_m}{\mathcal{C}_s + 2\mathcal{C}_m}}$ |
| $v_e = \dfrac{1}{\sqrt{(\mathcal{L}_{11} + \mathcal{L}_{12})(\mathcal{C}_{11} + \mathcal{C}_{12})}}$<br>$= \dfrac{1}{\sqrt{(\mathcal{L}_s + \mathcal{L}_m)\mathcal{C}_s}}$ | $v_o = \dfrac{1}{\sqrt{(\mathcal{L}_{11} - \mathcal{L}_{12})(\mathcal{C}_{11} - \mathcal{C}_{12})}}$<br>$= \dfrac{1}{\sqrt{(\mathcal{L}_s - \mathcal{L}_m)(\mathcal{C}_s + 2\mathcal{C}_m)}}.$ |

Using the above notations, one can easily express the wave impedance of both modes $\{Z_e, Z_o\}$ and their propagation velocities $\{v_e, v_o\}$.

– Odd mode: $V_2 = -V_1$ and $I_2 = -I_1$
Therefore, no current flows in the return path $I_1 + I_2 = 0$. It is convenient to make the $1/2$ antisymmetry explicit and unfold both lines with respect to the symmetry axis of the pair, which coincides with a zero equipotential line (See Figure 5.18(a)). '$\mathcal{C}_m \delta z$' can then be split in two series capacitors of value $2\mathcal{C}_m \delta z$ each (because of the potential division between two equal capacitors). This equivalent drawing allows to identify the effective inductance and capacitance

(a) **Odd** mode

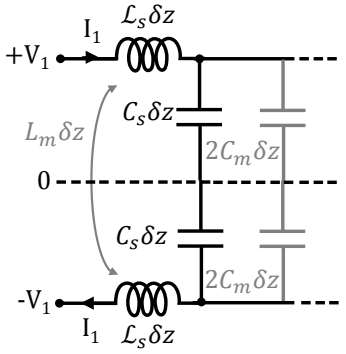


(b) **Even** mode

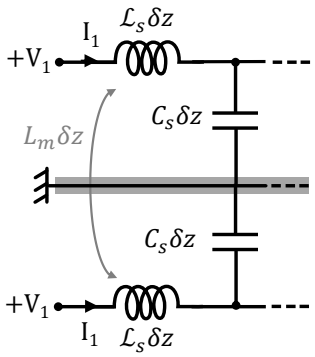


**Figure 5.18:** Equivalent circuits for the odd (a) and even (b) modes of two coupled transmission lines.

per unit length of each line in the odd mode. The inductive voltage in line 1 is due to current $I$ flowing through $\mathcal{L}_s\delta z$ and to current $I_2 = -I_1$ flowing through $\mathcal{L}_m\delta z$, which can be equivalently stated as due to I flowing through the inductor $(\mathcal{L}_s - \mathcal{L}_m)\delta z$. Therefore, $\mathcal{L}_o = \mathcal{L}_s - \mathcal{L}_m$. As to the effective capacitance per unit length between line 1 and the zero potential line, it reads $\mathcal{C}_o = \mathcal{C}_s + 2\mathcal{C}_m$, from which we deduce the wave impedance of the odd mode, $Z_o = \sqrt{\mathcal{L}_o/\mathcal{C}_o}$, and its propagation velocity $v_o = (\mathcal{L}_o\mathcal{C}_o)^{-1}$.

– Even mode: $V_2 = V_1$ and $I_2 = I_1$
Therefore, the two lines are identical and the coupling capacitance $\mathcal{C}_m\delta z$ is shunted, because the voltage on each side is the same $V_1 = V_2$ (See Figure 5.18(b)). It can therefore be ignored and we are left with $\mathcal{C}_e = \mathcal{C}_s$ for the effective capacitance per unit length of either line in the even mode. With the same reasoning as for the odd mode, one can identify the effective inductance of either line as $\mathcal{L}_e = \mathcal{L}_s + \mathcal{L}_m$ because $I_1 = I_2$.

### 5.3.2 Equivalent LC circuit

Knowing the impedance and velocity of the two modes, one can now build an equivalent lumped-element model for the *common-* and *differential*-mode resonances. At this point, it may be important to stress an important subtlety in the notations, namely the factor 2 in the definitions of odd/even vs differential/common modes [5] . Therefore, to compute the impedance $Z_{r,\text{diff}}$ of a resonator made from a differential pair, one has to use $Z_{\text{diff}}$ and note $Z_o$ as the characteristic impedance of the line. Indeed, $Z_o$ represents the wave impedance of a *single* transmission line, while $Z_{\text{diff}}$ refers to the impedance seen by a differential signal across the *pair* of lines. With this in mind, one can identify the equivalent LC circuit for both modes from the expression of their impedance and frequency (we note $\mathscr{L}$ the physical length of the resonator, *i.e.* of each of the coupled microstrips):

5: The odd (even) mode impedance is the impedance seen by a wave propagating through *one* of the transmission lines when the pair is excited with a differential (common) drive. On the other hand, the differential (common) impedance is defined as the impedance *between* the two lines when the pair is excited with a differential (common) drive.

– Differential mode

$$\begin{cases} Z_{r,\text{diff}} = \frac{4}{\pi}Z_{\text{diff}} = \frac{8}{\pi}Z_o = \frac{8}{\pi}\sqrt{\frac{\mathcal{L}_S-\mathcal{L}_m}{\mathcal{C}_s+2\mathcal{C}_m}} \equiv \sqrt{\frac{L_{\text{diff}}}{C_{\text{diff}}}} \\ f_o = \frac{v_o}{4\mathscr{L}} = \frac{1}{4\mathscr{L}\sqrt{(\mathcal{L}_s-\mathcal{L}_m)(\mathcal{C}_s+2\mathcal{C}_m)}} \equiv \frac{1}{2\pi\sqrt{L_{\text{diff}}C_{\text{diff}}}} \end{cases} \Rightarrow \begin{cases} \frac{\mathcal{L}_S-\mathcal{L}_m}{\mathcal{C}_s+2\mathcal{C}_m} = \frac{\pi^2}{64}\frac{L_{\text{diff}}}{C_{\text{diff}}} \\ (\mathcal{L}_S-\mathcal{L}_m)(\mathcal{C}_s+2\mathcal{C}_m) = \frac{\pi^2}{4\mathscr{L}^2}L_{\text{diff}}C_{\text{diff}} \end{cases} ;$$

– Common mode

$$\begin{cases} Z_{r,\text{com}} = \frac{4}{\pi}Z_{\text{com}} = \frac{2}{\pi}Z_e = \frac{2}{\pi}\sqrt{\frac{\mathcal{L}_S+\mathcal{L}_m}{\mathcal{C}_s}} \equiv \sqrt{\frac{L_{\text{com}}}{C_{\text{com}}}} \\ f_e = \frac{v_e}{4\mathscr{L}} = \frac{1}{4\mathscr{L}\sqrt{(\mathcal{L}_s+\mathcal{L}_m)\mathcal{C}_s}} \equiv \frac{1}{2\pi\sqrt{L_{\text{com}}C_{\text{com}}}} \end{cases} \Rightarrow \begin{cases} \frac{\mathcal{L}_S+\mathcal{L}_m}{\mathcal{C}_s} = \frac{\pi^2}{4}\frac{L_{\text{com}}}{C_{\text{com}}} \\ \mathcal{C}_s(\mathcal{L}_S-\mathcal{L}_m) = \frac{\pi^2}{4\mathscr{L}^2}L_{\text{com}}C_{\text{com}} \end{cases} .$$

Solving these equations for $\{L_{\text{diff}}, C_{\text{diff}}\}$ and $\{L_{\text{com}}, C_{\text{com}}\}$, we deduce the equivalent LC model for the two types of resonance:

| COMMON mode | DIFFERENTIAL mode |
|---|---|
| $L_{\text{com}} = \frac{4\mathscr{L}}{\pi^2}(\mathcal{L}_s + \mathcal{L}_m) = \frac{4\mathscr{L}}{\pi^2}(\mathcal{L}_{11} + \mathcal{L}_{12})$ | $L_{\text{diff}} = \frac{16\mathscr{L}}{\pi^2}(\mathcal{L}_s - \mathcal{L}_m) = \frac{16\mathscr{L}}{\pi^2}(\mathcal{L}_{11} - \mathcal{L}_{12})$ |
| $C_{\text{com}} = \mathscr{L}\mathcal{C}_s = \mathscr{L}(\mathcal{C}_{11} + \mathcal{C}_{12})$ | $C_{\text{diff}} = \frac{\mathscr{L}}{4}(\mathcal{C}_s + 2\mathcal{C}_m) = \frac{\mathscr{L}}{4}(\mathcal{C}_{11} - \mathcal{C}_{12}).$ |

Knowing the LC equivalent circuit, one can now easily express the zero-point phase fluctuations over the shared inductance $\ell$ using Eq. (4.22). We are interested in the case where the resonator is driven differentially, hence we should use $Z_0 = Z_{\text{diff}} = 2Z_o$, as the resonator is made from a differential pair:

$$\delta_{\text{zp}}^{\text{diff}} = \frac{\ell}{L_{\text{diff}}}\sqrt{\frac{\pi Z_{r,\text{diff}}}{R_Q}} = \frac{\pi^2}{8}\frac{\ell}{L_{\text{loop}}}\sqrt{\frac{4Z_{\text{diff}}}{R_Q}} = \frac{\pi^2}{4}\frac{\ell}{L_{\text{loop}}}\sqrt{\frac{Z_{\text{diff}}}{R_Q}}, \quad (5.27)$$

where we have introduced $L_{\text{loop}} \equiv 2\mathscr{L}(\mathcal{L}_s - \mathcal{L}_m) = \frac{\pi^2}{8}L_{\text{diff}} \approx 1.2 \times L_{\text{diff}}$, the geometrical loop inductance of the differential pair.

### 5.3.3 Design parameters

The target parameters are the frequency and the impedance of the resonator, the impedance determining the phase fluctuations and therefore the coupling with the weak link. For a given geometry $\{W, s, h, \epsilon_r\}$, it is possible to estimate the even/odd mode impedances of the coupled microstrip lines, using a closed-form expression obtained by the method of conformal transformation [78]:

[78]: Gupta et al. (1979), *Microstrip Lines and Slotlines*, pp. 322-323

$$Z_{o,e}^{\text{th}} = \frac{30\pi}{\sqrt{(\epsilon_r+1)/2}}\frac{K(k'_{o,e})}{k_{o,e}}, \quad \text{where} \quad \begin{cases} k_e = \tanh\frac{\pi}{4}\frac{W}{h}\tanh\frac{\pi}{4}\frac{W+s}{h}, & k_e'^2 = 1-k_e^2 \\ k_o = \tanh\frac{\pi}{4}\frac{W}{h}\coth\frac{\pi}{4}\frac{W+s}{h}, & k_o'^2 = 1-k_o^2, \end{cases} \quad (5.28)$$

with $K(k)$ and $K(k')$ the complete elliptic function of the first kind and its complement*. There exists simple expressions for the ratio $K/K'$, given by [78], which are accurate to within 3ppm:

[78]: Gupta et al. (1979), *Microstrip Lines and Slotlines*, p. 275

$$\frac{K(k)}{K(k')} \approx \begin{cases} \frac{1}{\pi}\ln\left[2\frac{1+\sqrt{k}}{1-\sqrt{k}}\right] & \text{for } \frac{1}{\sqrt{2}} \le k \le 1 \\ \frac{\pi}{\ln\left[2\frac{1+\sqrt{k'}}{1-\sqrt{k'}}\right]} & \text{for } 0 \le k \le \frac{1}{\sqrt{2}}. \end{cases}$$

These analytical expressions however are only approximations, valid for infinite lines and for geometries where the slab of vacuum above the microstrip is exactly as thick as the substrate layer. To compute better estimates of the even/odd mode impedances, one may resort to microwave finite-element simulations.

* Most of the programming languages (Python, Matlab, etc) use arithmetic–geometric sequences to compute efficiently elliptic functions. I noticed that for small $k < 10^{-8}$, due to convergence issues, the ratio K(k)/K(k') may be ill-estimated numerically with this method, giving rise to significant errors as much as a few tens of percent. One way to bypass this issue and estimate correctly the half-period ratio K'/K is to resort to the concept of *elliptic nome* $q = e^{-\pi\frac{K'}{K}}$, from the Jacobian elliptic function theory. For example in Matlab: use K/K'=`-pi/log(ellipticNome(k^2))` instead of `ellipke(k^2)/ellipke(1-k^2)`, which suffers from the convergence issue.

### Sonnet simulations

In Sonnet 17.54, there are several ways to extract the line impedance. The easiest possibility is to add a port on the box side and look at the result of the Sonnet port calibration. As a part of the EM analysis, the solver analyzes different calibration standards and plots as a side result the resulting line impedance and effective dielectric constant.

Sonnet is also well suited for the simulation of differential lines [86]. One can simulate a general case with 4 independent ports (labelled 1,2,3,4), or one can enforce specifically the differential or common mode by using multiple ports with the same number, with respectively opposite polarity (+1,-1 and +2,-2) or same polarity (+1,+1 and +2,+2).

[86]: Sonnet Software Inc. (2020), *Using Even and Odd Mode Parameters*

If the ports are labelled according to the differential or common mode convention, the value of line impedance computed by Sonnet during the port calibration will be the differential (common) impedance $Z_{\text{diff}}$ ($Z_{\text{com}}$), instead of the somewhat confusing $Z_{\text{odd}}$ ($Z_{\text{even}}$) definitions. This is because, for a microwave engineer point of view, the value that matters is $Z_{\text{diff}}$, since to have matched circuits one requires: port impedance = source impedance = load impedance = differential line impedance and not the odd mode impedance.

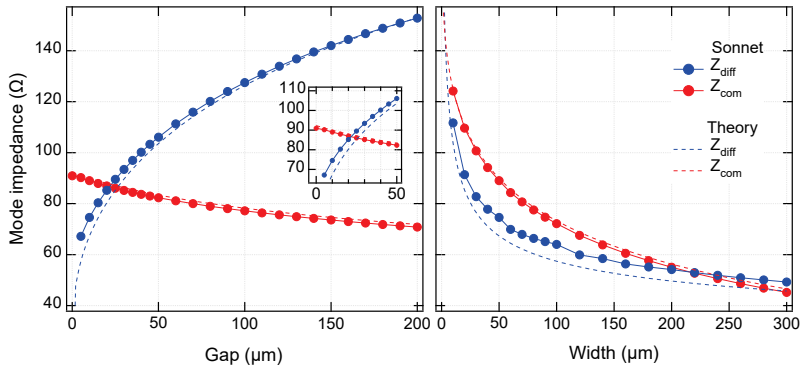


**Figure 5.19:** Dependence on the line geometry of the differential and common mode impedances of two coupled microstrip lines. (Left) Gap $s$ is varied for $W = 50$ $\mu$m. (Right) Width $W$ is varied for $s = 10$ $\mu$m. Theory (Eq. (5.28)) is shown in dashed lines.

In Figure 5.19, we show the differential and common mode impedance values extracted from a Sonnet simulation of a $\mathscr{L} = 3$ mm piece of coupled microstrips on top of a stack of 300 μm of sapphire substrate and 400 μm of Rodgers TMM 10 (see Figure 5.20(a)), as a function of the gap and width of the lines. The simulation results show reasonable agreement with the approximate theory (Eq. (5.28)). The comparison is quite good for the common mode, but for the differential mode, the theory shows a global negative offset of about 5 Ω compared to the simulation results. This error may come from the value of effective dielectric constant used to compute the theory curves[6] .

As an illustration, let us analyze a geometry similar to the differential pair of microstrip lines used by Hays *et al.* [69]. We fix $W = 50$ μm, $s = 10$ μm and $\mathscr{L} = 3$ mm. The distance from the microstrips to the bottom ground plane is $h = 300$ (sapphire) + 400 (Rodgers) = 700 μm. Sapphire is an anisotropic medium with $\epsilon_x = \epsilon_y = 9.3$ and $\epsilon_z = 11.5$. Here for simplicity, we treat it as a homogeneous substrate with an

6: As an approximation, it is estimated from the average value of the sapphire and air dielectric constants, therefore assuming that the field lines are equally spread in the substrate and in the slab of air above it (this would be true for a stripline geometry, where the line is buried in a homogeneous substrate with a top and bottom ground plane, but not exactly for a microstrip on top of a substrate). Second, sapphire does not have an isotropic $\epsilon_r$ and we took here an average of its $x$ and $z$ values. It is reasonable to assume that for the odd mode, the electric field lines are mainly directed in the $x$ direction, perpendicular to the microstrips and so $\epsilon_x = 9.3$ should be taken, instead of 10.4.

[69]: Hays (2020), 'Realizing an Andreev Spin Qubit', pp. 84-93

effective $\epsilon_r \approx (9.3 + 11.5)/2 = 10.4$. We assume a kinetic inductance microstrip thin films of $L_K = 0.6$ pH/□, which was the value used by Hays *et al.* in their design, and also close to what we measured for our Nb films.

For this geometry, the port calibration gives the following estimates for the even/odd mode impedances at 10 GHz: $Z_{\text{diff}} = 74.6\ \Omega$ and $Z_{\text{com}} = 89.0\ \Omega$ (Figure 5.20(b)). This means $Z_o = Z_{\text{diff}}/2 = 37.3\ \Omega$ and $Z_e = 2Z_{\text{com}} = 178\ \Omega$. The odd mode is quite insensitive to frequency: its impedance varies by less than 0.05 Ω over the 20 GHz range of the simulation. The even mode however varies a bit, by about 1.5 Ω.

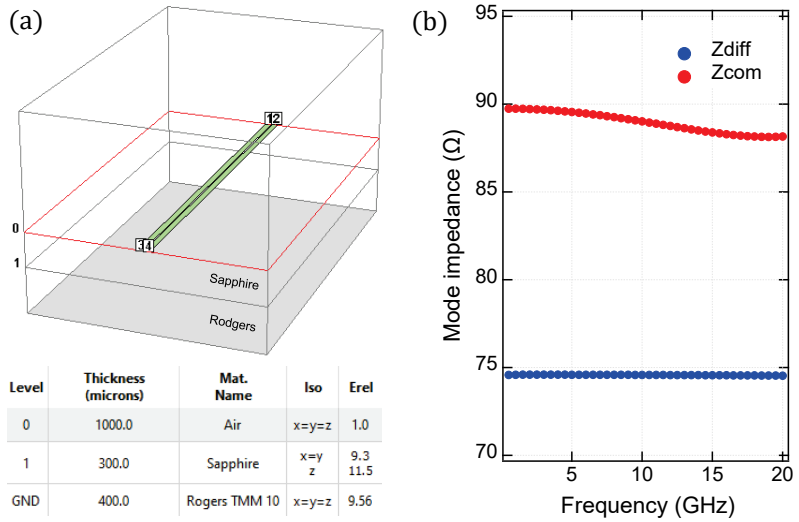


| Level | Thickness (microns) | Mat. Name | Iso | Erel |
|---|---|---|---|---|
| 0 | 1000.0 | Air | x=y=z | 1.0 |
| 1 | 300.0 | Sapphire | x=y<br>z | 9.3<br>11.5 |
| GND | 400.0 | Rogers TMM 10 | x=y=z | 9.56 |

**Figure 5.20:** (a) Sonnet simulation of two coupled microstrip lines. (b) Differential and common mode impedances extracted from Sonnet port calibration for a 3x3mm² simulation box.

These values compare reasonably well with the simple analytical estimates from Eqs. (5.28): $Z_o^{\text{th}} = 32.8\,\Omega$ and $Z_e^{\text{th}} = 175.1\,\Omega$. Actually, those formula do not take into account the possible kinetic inductance of the microstrips. Conducting again the simulation but with $L_K = 0$, we find this time, $Z_o = 35.1\,\Omega$ and $Z_e = 176.6\,\Omega$, which are in better agreement with $Z_{o,e}^{\text{th}}$.

Note that to simulate well the properties of a transmission line, the size of the simulation box has to be well chosen. Indeed, the box walls are grounded. This means that for small boxes, if the walls are too close, they can modify the capacitance per length of the line. One has to make sure then that the distance of the line to the lateral and top walls is way larger than the substrate thickness, so that the only contribution to the line capacitance is the one to the bottom ground where return current is supposed to flow. In Figure 5.21 we show how the extracted impedance of both modes is affected by the choice of the box size. When the box is taken too small, the capacitance to ground from the lateral walls can become sizeable. As the box increases, this parasitic capacitance becomes negligeable and the extracted impedance increases towards the nominal value for the line. As one may expect, the odd mode is quite insensitive to this effect because the em fields is mainly localized between the two strips. On the other hand, for the even mode, the field lines are directed mainly to the grounded box and so the parasitic capacitance to ground

affects significantly the line properties, which can give rise to an error in the estimation of the impedance as high as 50%. From this study, we see that by taking a box size of 3x3 mm², the extracted impedance no longer varies with the box size and corresponds well to the nominal mode impedance of the isolated line.

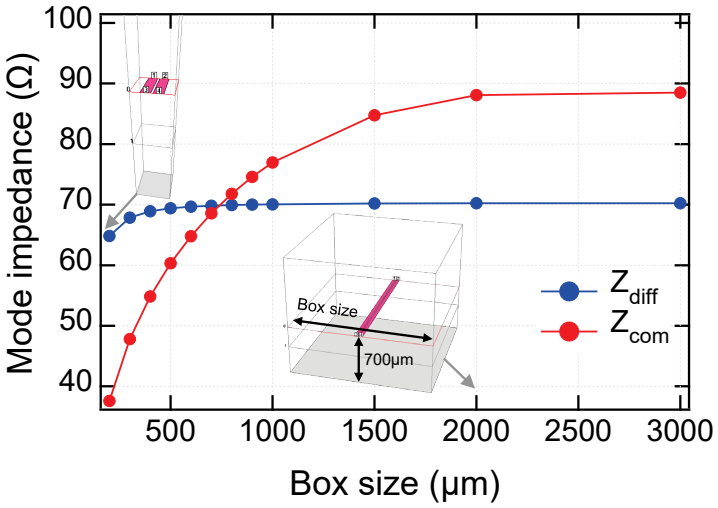


**Figure 5.21:** Differential and common mode impedances extracted from Sonnet port calibration as a function of the size of the square simulation box.

Another possibility to access the mode impedance is to use the *N-coupled Line Model* tool from Sonnet, which allows to extract the RLGC parameters from an EM simulation of a short section of transmission line. These parameters can then be used to model any length of line having the same cross-section. It also computes for free the impedance of the even/odd modes and the associated propagation constants. For the aforementioned geometry (with $L_K = 0.6$ pH/□), this method yields the following inductance and conductance matrices:

| | |
|---|---|
| $\mathcal{L}_{11} = \mathcal{L}_{22} = 886$ nH/m | $\mathcal{C}_{11} = \mathcal{C}_{22} = 136$ pF/m |
| $\mathcal{L}_{12} = \mathcal{L}_{21} = 571$ nH/m | $\mathcal{C}_{12} = \mathcal{C}_{21} = -90.3$ pF/m |

from which we deduce:

$$\begin{cases} Z_o = \sqrt{\dfrac{\mathcal{L}_{11} - \mathcal{L}_{12}}{\mathcal{C}_{11} - \mathcal{C}_{12}}} = 37.3\ \Omega \quad v_o = 1/\sqrt{(\mathcal{L}_{11} - \mathcal{L}_{12})(\mathcal{C}_{11} - \mathcal{C}_{12})} = 1.18 \times 10^8\ \text{m/s} \\ Z_e = \sqrt{\dfrac{\mathcal{L}_{11} + \mathcal{L}_{12}}{\mathcal{C}_{11} + \mathcal{C}_{12}}} = 179\ \Omega \quad v_e = 1/\sqrt{(\mathcal{L}_{11} + \mathcal{L}_{12})(\mathcal{C}_{11} + \mathcal{C}_{12})} = 1.23 \times 10^8\ \text{m/s}. \end{cases}$$

These values coincide with the ones extracted from the port calibration method. Using Eq. (5.3), we can now evaluate the resonance frequency of a line of length $\mathscr{L} = 3$ mm excited differentially or with a common mode:

$$\begin{cases} f_o = \dfrac{v_o}{4\mathscr{L}} = 9.88\ \text{GHz} \\ f_e = \dfrac{v_e}{4\mathscr{L}} = 10.2\ \text{GHz}. \end{cases}$$

These two resonances can be modelled with an equivalent LC circuit, using the notations from Sec. 5.3.2:

| | |
|---|---|
| $L_{\text{diff}} = 1.53$ nH | $L_{\text{com}} = 1.77$ nH |
| $C_{\text{diff}} = 0.170$ pF | $C_{\text{com}} = 0.137$ pF |
| $Z_{r,\text{diff}} = \sqrt{\frac{L_{\text{diff}}}{C_{\text{diff}}}} = \frac{4}{\pi} Z_{\text{diff}} = 95.0\ \Omega$ | $Z_{r,\text{com}} = \sqrt{\frac{L_{\text{com}}}{C_{\text{com}}}} = \frac{4}{\pi} Z_{\text{com}} = 114\ \Omega.$ |

Another important parameter for the design is the length of the inductive wire shared between the resonator and the weak link loop, as it directly determines the magnitude of the phase fluctuations over the weak link, and so the nanowire/resonator coupling.

There exists an analytical formula for the per-unit-length loop inductance $\mathcal{L}_{\text{ms}}$ of a microstrip line of width $W$ lying on top of a dielectric substrate of thickness $h$ and a ground plane below. Assuming zero thickness for the microstrip, it reads [87]:

[87]: Paul (2011), *Inductance: Loop and Partial*, p. 181

$$\mathcal{L}_{\text{ms}} = \begin{cases} \dfrac{60}{c} \ln\left(\dfrac{8h}{W} + \dfrac{W}{4h}\right) & \text{for } \dfrac{W}{h} \leq 1 \\ \dfrac{120\pi}{c}\left[\dfrac{W}{h} + 1.393 + 0.667 \ln\left(\dfrac{W}{h} + 1.444\right)\right]^{-1} & \text{for } \dfrac{W}{h} \geq 1 \end{cases} \text{H/m}, \tag{5.29}$$

where $c \approx 3 \times 10^8$ m/s is the speed of light in vacuum. This expression is a simplification of a more general formula for narrow strips derived by Wheeler using conformal transformations and the concept of effective dielectric constant [78]:

[78]: Gupta et al. (1979), *Microstrip Lines and Slotlines*, p. 11

$$\mathcal{L}_{\text{ms}} = \frac{60}{c}\left[\ln\left(\frac{8h}{W}\right) + \frac{1}{8}\left(\frac{W}{2h}\right)^2 - \frac{1}{2}\frac{\epsilon_r - 1}{\epsilon_r + 1}\left(\ln\frac{\pi}{2} + \frac{1}{\epsilon_r}\ln\frac{4}{\pi}\right)\right]. \tag{5.30}$$

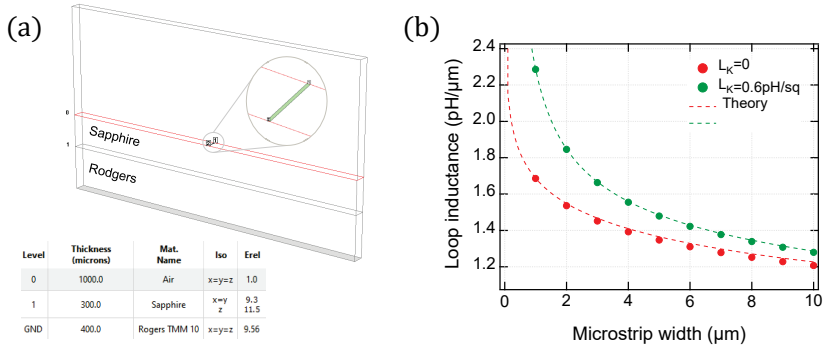


**Figure 5.22:** (a) Sonnet simulation of a piece of microstrip line. (b) Comparison between the loop inductance per unit length of a microstrip extracted by Sonnet (markers) with the approximate theory from conformal theory in Eq. (5.30) (dashed).

Using Sonnet, it is easy to simulate the properties of a piece of microstrip and extract its loop inductance by modeling the response with an equivalent series inductor in a two-port circuit. Figure 5.22 shows the evolution of this inductance with the width of the microstrip, revealing a good agreement with the theory from Eq. (5.30). For a $W = 5$-µm-wide microstrip, we find a loop inductance of about $\mathcal{L}_{\text{ms}} = 1.35$ pH/µm. If a kinetic inductance of $L_K = 0.6$ pH/□ is added, the loop inductance slightly increases to 1.48 pH/µm.

Putting all the pieces together, we can now estimate the phase fluctuations induced in the weak link loop for the above geometry with a 100-µm-long microstrip for the coupling inductance ($W = 50$ µm, $s = 10$ $\mu$m, $\mathscr{L} = 3$ mm, $\ell = 148$ pH):

$$\delta_{\mathrm{zp}}^{\mathrm{diff}} = \frac{\ell}{L_{\mathrm{diff}}}\sqrt{\frac{\pi Z_{r,\mathrm{diff}}}{R_Q}} = \frac{100\times 1.48}{1.53\times 10^3}\sqrt{\frac{3.14\times 95}{6453}} \approx 0.020 \ll 1. \quad (5.31)$$

This value is still small enough compared to 1, so that a perturbative treatment of the resonator/weak link coupling is valid (see Sec. 4.2.1), but high enough to be in the strong coupling regime with the weak link. As an example, with this geometry, the coupling to the resonator's differential mode of a pair transition arising from a single finite-length ($L/\xi \approx 1$) channel of transmission $\tau = 0.98$ would be at phase $\delta = \pi$:

$$g(\pi) = \frac{\delta_{\mathrm{zp}}^{\mathrm{diff}}}{\hbar}\frac{\Delta}{1+L/\xi}\frac{\tau}{2} = 0.02\times\frac{45}{2}\frac{0.98}{2} \approx 230\ \mathrm{MHz}.$$

The frequency of the pair transition at $\delta = \pi$ would be $f_A = 2\Delta^*\sqrt{1-\tau} \approx 6.4$ GHz with the effective pairing $\Delta^* = \Delta/(1+L/\xi) \approx 22$ GHz (see Eq. (3.14)), meaning $9.8 - 6.4 = 3.4$ GHz detuned from the resonator mode, which gives a dispersive shift of about $\chi = \frac{g^2}{f_{r,o}-f_A} \approx 15$ MHz.

# Microwave spectroscopy of nanowire weak links

# Observation of the fine structure of Andreev levels

# 6

*Most of the results presented in Section 6.3 were published in Ref. [51], and those of Section 6.4 and 6.5 in Ref. [53].*

In this chapter we report the experimental observation in InAs-Al nanowire weak links of single-quasiparticle transitions between zero-field spin-split ABS, which represents one of the main results of this thesis as it demonstrates that the spin degree of freedom can be addressed in Josephson junctions. First, building on the theory presented in Chapter 3, we review the parity-conserving transitions expected to show in the microwave absorption spectrum of multi-channel Rashba nanowire weak links. In section 6.2, we describe the device and microwave setup used to perform the microwave spectroscopy. Then we present in section 6.3 two typical microwave spectra measured on this device, which show distinctive features with bundles of four lines crossing when the superconducting phase difference across the weak link is 0 or $\pi$. We interpret these features as arising from zero-field spin-split Andreev states. In section 6.3.3, we show the evolution with magnetic field of such features and confirm the spin nature of the underlying single-particle transitions. Finally in section 6.3.2, we discuss the comparison with the analytical model of Chapter 3 and show that taking into account the Rashba SOI in a nanowire containing several transverse subbands is enough to explain these features and their evolution with magnetic field.



## 6.1 From ABS levels to absorption spectrum

In section 3.2, we showed that due to SOI and the presence of transverse subbands in the semiconductor, the ABS are expected to group in manifolds of spin-split states, which in the absence of a magnetic field, remain degenerate at $\delta = 0$ and $\pi$. In Figure 6.1(a), we show two such typical *Andreev doublets*, as predicted by the non-interacting theory developed in section 3.2. Note that for simplicity, we chose here an *excitation* representation, rather than the *semiconducting* picture, which, although redundant because it both shows the symmetric negative and positive energy states, still has the advantage to provide a better physical insight on the nature of the transitions. At a given phase difference $\delta \neq 0, \pi$ denoted by the dashed blue line, there are four possible states with distinct energies. In Figure 6.1(b), we classify all possible parity-conserving transitions between these four states that can be induced by absorption of a microwave photon. We distinguish two families of transitions, depending on the parity of the number of associated excitations. Red arrows correspond to **pair transitions** (PT) in which the system is initially in the ground state, and a pair of quasiparticles is created either in one manifold or in different ones. Green arrows correspond to **single-quasiparticle transitions** (SQPT) where a trapped quasiparticle – denoted by a black dot in the figure – already occupying an Andreev state is excited to another one, which can belong to the same or to another ABS doublet.

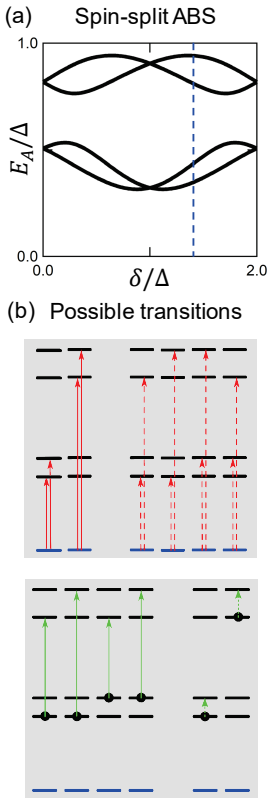


**Figure 6.1:** (a) Phase dependence of two typical spin-split Andreev doublets (excitation picture). (b) All possible parity-conserving transitions between the ABS shown in (a) at the phase denoted by the dashed blue line. They are grouped in two families: *Pair transitions* (PT) for which a pair of quasiparticles is created from the ground state, either both in the same manifold (solid) or not (dashed) ; *Single-quasiparticle transitions* (SQPT) for which a quasiparticle already present in one ABS (solid dot) is excited to another ABS, either in the same (dotted) or in another (solid) manifold.

The phase dependence of the transition energies in the absorption spectrum for both the pair and single-particle cases is shown in Figure 6.2(a). Pair transitions that create two quasiparticles in the same energy manifold do not carry information on the spin structure. On the contrary, pair and single-particle transitions involving different energy manifolds produce peculiar bundles of four distinct lines all crossing at $\delta = 0$ and $\pi$. We stress here that **they are a direct signature of the spin splitting of ABS**. Finally, single-particle transitions within a manifold give rise to bundles of two lines, shown with dotted green lines in Figure 6.2(a).

Figure 6.2(b) shows a two-tone microwave spectrum that we measured on an InAs nanowire weak link coupled between Al electrodes. The results corresponds to sample S1 (see Chapter 12 for fabrication details). The greyscale contrast shows at which frequencies $f_1$ microwave photons are absorbed, as a function of the phase difference $\delta$ across the weak link. The spectrum appears quite complex, with many transition lines amongst which we highlight with color lines two typical features on the right-hand side of the figure (not fits). The red line, with extrema at $\delta = 0$ and $\pi$, likely corresponds to a pair transition. Note that the frequency $f_1(\delta = 0) = 26.5$ GHz is much smaller than twice the gap of aluminum $2\Delta/h \approx 88$ GHz, which is indeed expected for a junction shorter than the coherence length. Second, we highlight in green a bundle of four lines showing clear crossings at $\delta = 0$ and $\delta = \pi$, which shows all the expected features of the single-particle transitions shown in Figure 6.2(a) that we expect to measure in InAs nanowire weak links. Their observation constitutes one of the main results of this thesis. Let us now review how the experiment was performed.

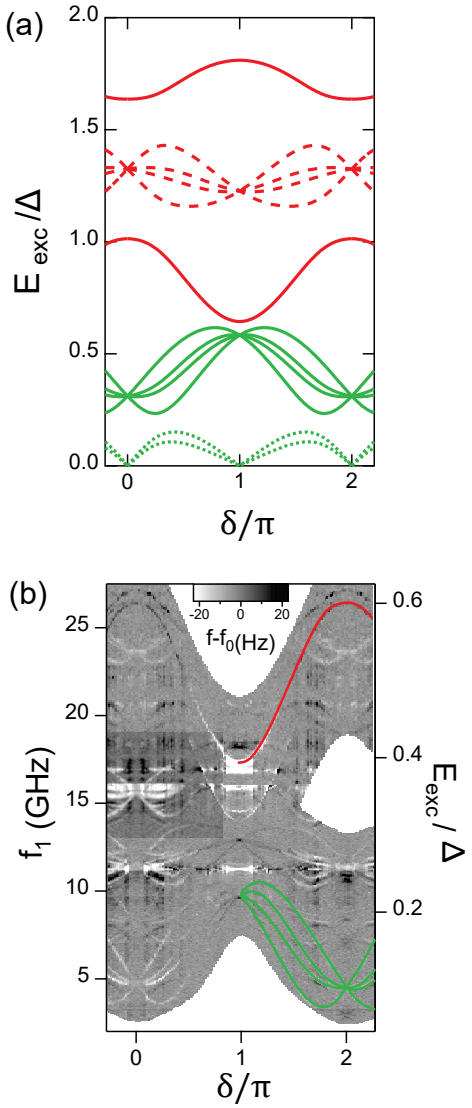


**Figure 6.2:** (a) Energies $E_{\text{exc}}$ of the possible transitions between the ABS shown in Figure 6.1 as a function of the phase difference $\delta$ across the weak link. (b) Microwave absorption spectrum measured on sample 1 at a gate voltage $V_g = -0.89$ V. The gray scale represents the frequency change $f - f_0$ of the resonator coupled to the weak link when a microwave excitation at frequency $f_1$ is applied as a function of the phase difference $\delta$ across the weak link. In the right half of the figure, some transition lines are highlighted. Red line corresponds to a pair transition; green lines are single-particle transitions.

## 6.2 Device & microwave setup

The measurements are obtained using sample S1 in the circuit QED setup shown in Figure 6.3(d), the design of which was presented in section 5.2.1. The experiment was performed at approximately 40 mK in a pulse-tube dilution refrigerator. Details on the sample holder and fridge wiring are provided in sections 13.1 and 13.2 of Chapter 13 whereas details on fabrication are presented in Chapter 12. The superconducting weak link of sample S1 is obtained by etching away, 370 nm-long section, the 25 nm-thick aluminum shell that fully covers a 140 nm-diameter InAs nanowire (see figures 6.3(a) and 6.3(b)). A side gate allows to tune the charge carrier density and the electrostatic potential in the nanowire, and therefore the Andreev spectra. The weak link is part of an aluminum loop of area $S \approx 10^3$ $\mu$m$^2$, which has a connection to ground to define a reference for the gate voltage (see Figure 6.3(c)). The phase difference $\delta$ across the weak link is imposed by a small magnetic field $B_z < 5$ $\mu$T perpendicular to the sample plane: $\delta = B_z S/\varphi_0$, with $\varphi_0 = \hbar/2e$ the reduced flux quantum. Two additional coils are used to apply a magnetic field in the $(x, y)$ plane of the sample. Their effect on the spectrum will be discussed in section 6.3.3.

The loop containing the nanowire weak link is inductively coupled to the shorted end of a $\lambda/4$ microwave resonator made out of Nb, with resonance frequency $f_0 \approx 3.26$ GHz and internal quality factor $Q_{\text{int}} \approx 3 \times 10^5$. A continuous signal at frequency $f_0$ is sent through the

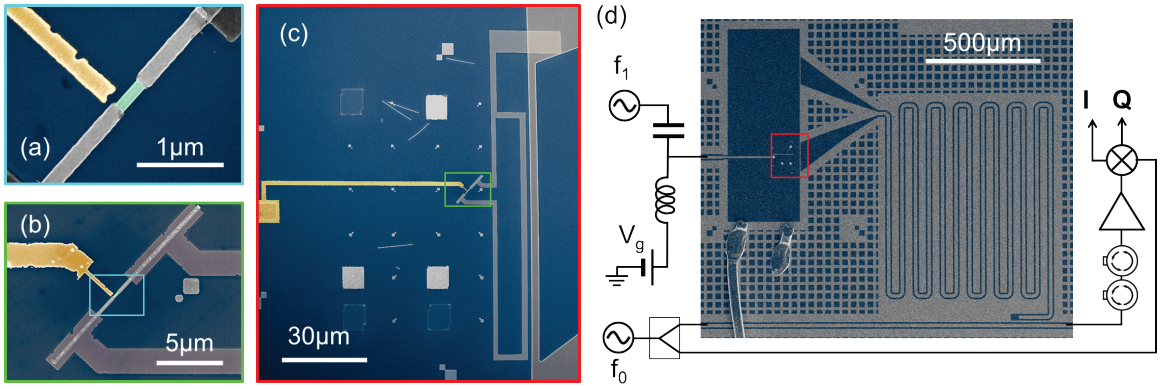


**Figure 6.3:** Experimental setup. (a) False-color scanning-electron-microscope image of the InAs-Al core-shell nanowire. The Al shell (gray) is removed over 370 nm to form the weak link between the superconducting electrodes. A close-by side electrode (Au, yellow) is used to gate the InAs exposed region (green). (b),(c) The nanowire is connected to Al leads that form a loop. This loop is located close to the shorted end of a coplanar wave-guide (CPW) resonator. (d) The CPW resonator is probed by sending through a bus line a continuous microwave tone at its resonant frequency $f_0 = 3.26$ GHz and demodulating the transmitted signal, yielding quadratures $I$ and $Q$. Microwaves inducing Andreev transitions are applied through the side gate (frequency $f_1$) using a bias tee, the dc port being used to apply a dc voltage Vg.

coplanar transmission line coupled to the resonator (coupling quality factor $Q_{\text{ext}} \approx 1.7{\times}10^5$), and the two quadratures $I$ and $Q$ of the transmitted signal are measured using homodyne detection (see Figure 6.3(d)). Andreev excitations in the weak link are induced by a microwave signal of frequency $f_1$ applied on the side gate, which is chopped by a square waveform at 3.3 kHz. The resulting modulation of the circuit response on the two quadratures $I$ and $Q$ is detected using two lock-in amplifiers, with an integration time of 0.1 s (see Chapter 14.2). We interpret these modulations as arising from shifts of the resonator frequency $f - f_0$. To calibrate this effect, we measure how the dc values of $I$ and $Q$ change for small variations of the measurement frequency $f_0$ around 3.26 GHz. With all of the measurement chain being taken into account, we find $\partial I/\partial f_0 = -40.3$ $\mu$V/Hz and $\partial Q/\partial f_0 = 34.4$ $\mu$V/Hz. This calibration allows us to express the response of the circuit encoded in $I$ and $Q$ in terms of the corresponding frequency shift $f - f_0$ in the resonator, which is plotted in gray scale in the two-tone spectra (see *e.g.* Figure 6.2).

## 6.3 Experimental evidence of zero-field ABS splitting

The fact that single-particle transitions are observed means that during part of the measurement time, the weak link indeed resides in an odd occupancy state with Andreev doublets being occupied by a single quasiparticle. This is in agreement with previous experiments on InAs nanowires in which the fluctuation rates for the occupancy of Andreev states by out-of-equilibrium quasiparticles were found to be in the $10 - 100$ ms$^{-1}$ range [88, 16, 19]. We are indeed integrating the response of our lock-in amplifiers over $\approx 100$ ms, *i.e.* on a duration longer than this typical parity-switching time.

[88]: Zgirski et al. (2011), 'Evidence for Long-Lived Quasiparticles Trapped in Superconducting Point Contacts'
[16]: Janvier et al. (2015), 'Coherent manipulation of Andreev states in superconducting atomic contacts'
[19]: Hays et al. (2018), 'Direct Microwave Measurement of Andreev-Bound-State Dynamics in a Semiconductor-Nanowire Josephson Junction'

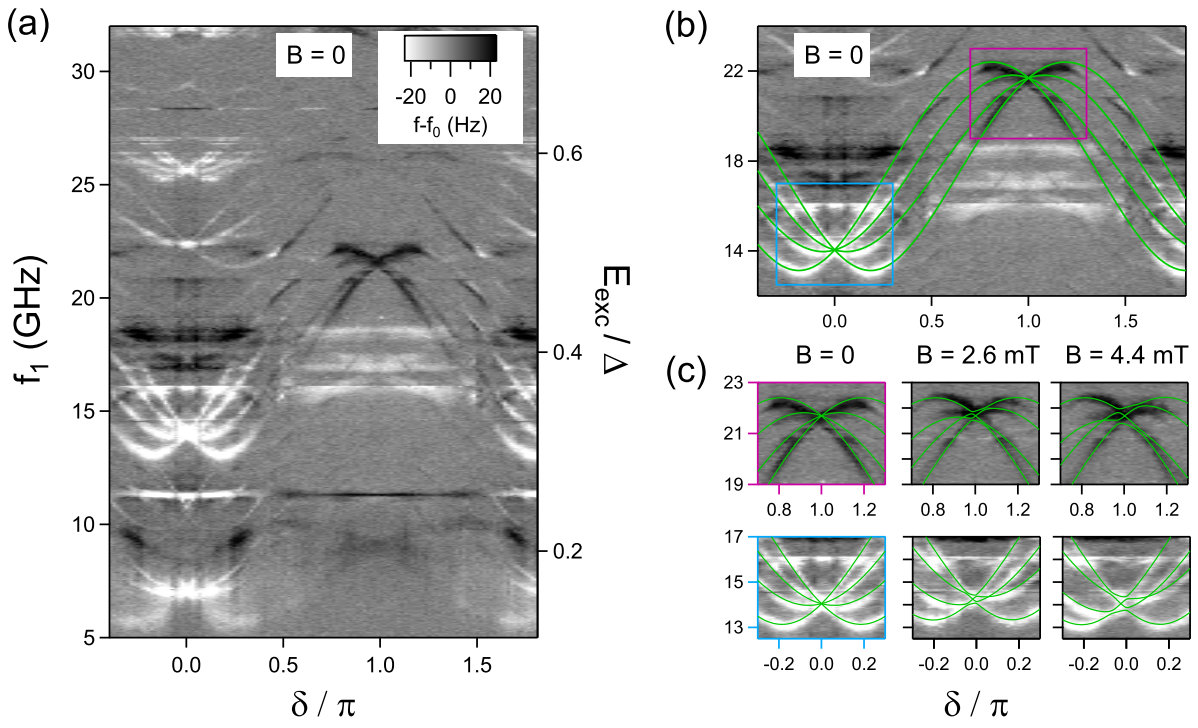


**Figure 6.4:** Two-tone spectrum measured on sample S1 at $V_g = 0.5$ V. (a) Large-scale spectrum at zero magnetic field. (b) Enlargement of the same data with fits of the main bundle of single-quasiparticle transitions. (c) Dependence of the spectrum near $\delta = 0$ and $\pi$ on the amplitude $B$ of an in-plane magnetic field applied at an angle of $-45°$ with respect to the nanowire axis. Green lines are fits using the parameters obtained for B=0, $g \parallel = 8$ and $g\perp = 12$ see section 6.3.3

### 6.3.1 Observation of single-particle transitions ($B = 0$)

Figure 6.4(a) presents another two-tone spectrum which was measured at at $V_g = 0.5$ V and zero magnetic field (apart from the tiny perpendicular field $B_z < 5$ $\mu$T required to phase bias the weak link). Contrary to the spectrum shown in Figure 6.1(b), pair transitions are hardly visible in Figure 6.4(a). A trained eye will notice however a very faint line around $f_1 \approx 22.7$ GHz at $\delta = 0$ and 21 GHz at $\delta = \pi$, with the typical shape for a pair transition, but showing surprisingly only very little phase dispersion. The associated current is therefore expected to be small, leading to a weak coupling to the resonator, hence a small dispersive shift resulting in a weak signature in the two-tone spectrum. On the other hand, one observes clearly at least 3 bundles of 4 lines, corresponding to single-particle transitions with crossings at 7.1, 14.0, and 22.4 GHz at $\delta = 0$ and 9, 21.5, and 26.0 GHz at $\delta = \pi$. Note also the presence in the spectrum of some spurious lines, corresponding to duplicates of transitions lines shifted by $f_0$ (see for example the bundle of lines near $f_1 = 11$ GHz around $\delta = 0$). Those replicas correspond to transitions between ABS involving the absorption of a photon from the resonator. We do observe them in our two-tone spectra because we probe continuously the resonator with a microwave tone at the frequency $f_0$. Because in this experiment the resonator frequency $f_r = 3.26$ GHz is particularly low compared to the range of excitation frequency $5 \leq f_r \leq 32$ GHz, numerous replicas of this type are visible and complicate the spectra.

Remarkably, the sign of the response appears correlated with the curvature of the transition lines. Indeed, in Figure 6.4(a), the resonator shift associated to the main bundle of 4 lines in the 13-23 GHz window varies continuously from negative to positive values. This suggests that the signal is mainly associated with a change in the effective inductance of the nanowire weak link. From the theory presented in Section 4.2, this is to be expected since the resonator frequency $f_r \approx 3.2$ GHz is far detuned from the transition lines between ABS that we are exciting: we are probing the resonator deep in the *adiabatic* regime and the frequency shift is therefore expected to be dominated by the phase curvature of the Andreev levels' energy (see Eq. (4.32)). This also explains why we measure frequency shifts of the resonator in such a broad frequency window. Transition lines which are strongly detuned from the resonator, like the bundle of 4 lines around $f_1 \approx 22 - 26$ GHz, would not show if the response was purely dispersive, as the resonator shift due to such transitions would decay like the inverse of their detuning to the resonator frequency $\Delta f_r \propto (g/2\pi)^2/(f_1 - f_r)$. This will be further detailed in Section 6.4 where we will revisit these data and provide a quantitative comparison with the expected theory for the resonator shift.

### 6.3.2 Fit with theory

To support the identification of the measured transition lines in Figure 6.4 with SQPT processes, we compared their phase dependence with the one expected from theory. We focus on the bundle of lines between 13 and 23 GHz, for which the effect of a magnetic field $B$ is also later explored (Section 6.3.3). The green lines in Figure 6.4(b) are fits of the data at $B = 0$. They were computed with the simple continuum model presented in Chapter 3.2, Eq. (3.12). The fit in Figure 6.4(b) corresponds to $\lambda_1 = 1.3$, $\lambda_2 = 2.3$, $\tau = 0.295$, $x_r = 0.525$ and we take $\Delta = 182\,\mu\text{eV} = h \times 44$ GHz for the gap of Al. These values can be related to microscopic parameters, in particular to the intensity $\alpha$ of the Rashba SOI entering in the Hamiltonian of the system as $H_R = -\alpha(k_x\sigma_y - k_y\sigma_x)$, with $\sigma_{x,y}$ the Pauli matrices acting in the spin [32]. Assuming a parabolic transverse confinement potential, an effective wire diameter of $W = 140$ nm and an effective junction length of $L = 370$ nm, the values of $\lambda_{1,2}$ are obtained for $\mu = 422$ $\mu$eV (measured from the bottom of the band) and $\alpha = 38$ meV.nm, a value consistent with previous estimations [89, 36].

[32]: Park and Levy Yeyati (2017), 'Andreev spin qubits in multichannel Rashba nanowires'

[89]: Fasth et al. (2007), 'Direct Measurement of the Spin-Orbit Interaction in a Two-Electron InAs Nanowire Quantum Dot'

[36]: Scherübl et al. (2016), 'Electrical tuning of Rashba spin-orbit interaction in multigated InAs nanowires'

However, we stress that this estimation is model dependent: very similar fits of the data from Figure 6.4(b) can be obtained using the *double-barrier model* presented in Chapter 3.2, which assumes scattering barriers located at the left $x = -L/2$ and right $x = L/2$ edges of the wire. Using this time the values $\lambda_1 = 1.1$ and $\lambda_2 = 1.9$, we obtain with the same reasoning the value $\alpha = 32$ meV.nm for the intensity of the Rashba SOI. Crucially, both models only give two Andreev doublets in the spectrum, and therefore account only for the four SQPT that were fit. Within this minimal model, they are the only transitions expected in this $5 - 32$ GHz window, as intra-doublet transitions would all fall below 3.5 GHz, due to the small spin splitting of each Andreev doublet. Therefore this model does not account for all the other observed bundles of transitions, which are likely attributed to other conduction channels. Indeed, although we considered so far only one occupied transverse subband, the same effect of spin-

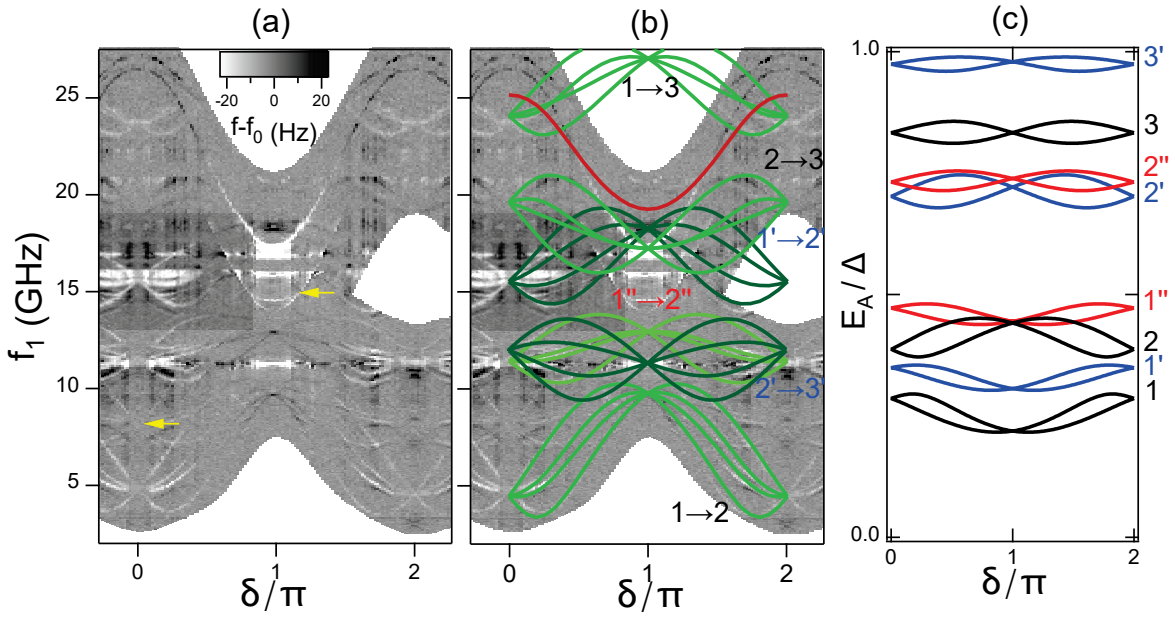


**Figure 6.5:** (a) Data from Figure 6.2 at $V_g = -0.89$ V, with yellow arrows pointing to transition lines that are replicas of lines appearing exactly $f_r = 3.26$ GHz above. (b) Same data superimposed with predictions of the single-barrier model using parameters corresponding to the spectrum of ABS shown in (c). To account for all visible SQPT lines, three sets of fitting parameters $\{\tau^{(i)}, \lambda_1^{(i)}, \lambda_2^{(i)}, x_r^{(i)}\}_{i\in\{1,2,3\}}$ had to be used, which can be understood as the contributions from three independent channels. They are summarized in Table 6.1. The ABS spectrum associated to each channel is plotted in the excitation picture in panel (c) with different colors. Green lines in (b) correspond to single-particle transitions between the two or three ABS manifolds arising for each channel. Note that all possible SQPT between the ABS shown in (c) that are supposed to fall in the frequency range probed in (b) are indeed observed in the experimental data. Red line in (b) is the pair transition leading to two quasiparticles in manifold 1 of the ABS depicted in black in (c).

dependent velocities is still found if several subbands are to cross the Fermi level. Eventually, a more elaborate model together with a realistic modeling of the nanowire bands is required to treat this situation and obtain a quantitative fit of the whole spectra. This will be the focus of Chapters 7 and 8, in which we will try to develop a better description of realistic multi-channel weak links based on tight-binding simulations.

Before moving on, let us pause for a moment and illustrate the success of the single-barrier model in rationalizing a complex spectrum like the one measured at $V_g = -0.89$ V, which was already presented in Figure 6.2. Indeed, it seems that most of the transition lines visible in this data can be accounted for by assuming three independent channels. This is illustrated in Figure 6.5, where we compare the experimental spectrum with the theory results from the single-barrier model using three sets of fitting parameters, summarized in Table 6.1. The Andreev levels associated to these 3 sets of parameters are shown in Figure 6.5(c) with a different color for each set. The spectrum comprises :

- three manifolds 1, 2 and 3 arising from the parameter set #1 encoded in black, which accounts for the lower bundle of 4 lines between 5 – 10 GHz (1 → 2 SQPT), the ones around 16 – 21 GHz (2 → 3) and 23 – 27 GHz (1 → 3) (all highlighted in green in Figure 6.5(b)), and for the PT in red between 23 – 26 GHz ;
- three manifolds labeled 1′, 2′ and 3′ arising from the parameter set #2 encoded in blue, which accounts for the observed bundles of 4 lines between 14 – 18 GHz and around 9 – 13 GHz, corresponding respectively to the 1′ → 2′ and 2′ → 3′ SQPT (highlighted in dark

**Table 6.1:** Fit parameters used in Figure 6.5

| # | $\tau$ | $\lambda_1$ | $\lambda_2$ | $x_r$ | Color |
|---|---|---|---|---|---|
| 1 | 0.25 | 2.81 | 4.7 | 0.17 | Black |
| 2 | 0.18 | 1.4 | 3.2 | 0.535 | Blue |
| 3 | 0.085 | 0.71 | 2.6 | 0.36 | Red |

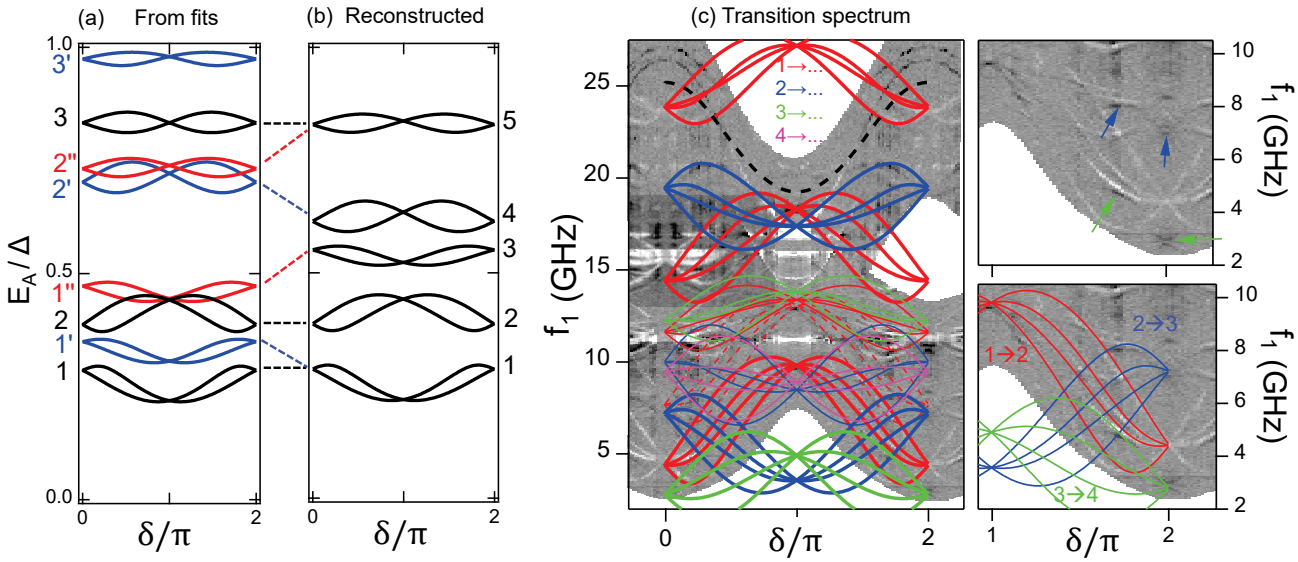


**Figure 6.6:** ABS spectrum inferred from the fit of SQPT lines in Figure 6.5. (a) Spectrum deduced by fitting the visible SQPT lines in Figure 6.5(a) with three sets of parameters given in Table 6.1 in the single barrier model. (b) Reconstructed ABS spectrum obtained from (a) by shifting some levels in energy to identify manifolds 2″ with 3 and manifolds 1 and 1′. All the possible SQPT transitions involving any two doublets of this spectrum are depicted in (c) and compared to the data. The color of the lines encodes the manifold from which the SQPT is initiated. Amongst them, we highlight in two enlargements the 2 → 3 (blue) and 3 → 4 (green) SQPT lines, which seem to correspond to faint features of the measured data indicated by small arrows. White areas correspond to regions where unfortunately no data was measured.

green in Figure 6.5(b)) ;

– two manifolds labeled 1″ and 2″ corresponding to the parameter set #3 encoded in red, which was used to fit the bundle of lines around 10 – 14 GHz, interpreted as the 1″ → 2″ SQPT (highlighted in light green in Figure 6.5(b)).

Altogether, these fitting parameters allow to capture well the main features of the measured spectrum. However on second thought, in view of Figure 6.5(c), the picture of three independent channels – the contributions of which merely adding linearly in the spectrum – does not seem very physical as it results in overlapping Andreev states (*e.g.* manifolds 2 and 1″ touching at $\delta = \pi$, or 2′ and 2″ almost superimposed) which are spaced in energy in a very irregular manner. As we will see in Chapter 7, tight binding simulations show that even in a multi-channel scenario when the chemical potential crosses several subbands, the spin-split doublets still repel each other and never cross. A second cause of worry is that one would naïvely expect to observe all possible SQPT lines between any two doublets of the spectrum, *i.e.* transitions like 1′ → 2 or 1′ → 1″, etc should also appear. This is not observed in the experimental data in Figure 6.5(b).

More striking about this ABS spectrum, which was inferred from the SQPT fits, is that doublets 2″ and 3 have almost the same shape ; same also for 1 and 1′ (see Figure 6.5(c)). Actually, in this picture of independent channels, nothing fixes the absolute energy of the states: only energy differences between manifolds define the SQPT frequencies. Therefore, manifold 2″ could be identified with 3, provided that manifold 1″ is pushed upwards to keep the same energy for the 1″ → 2″ process, which is visible in the spectrum. Similarly, it would be tempting to identify 1 with 1″, and manifold 2″ should then be pushed downwards to keep

the right relative energy spacing between 1′ and 2′. This transformation is illustrated in Figure 6.6, where we show in (a) the ABS spectrum obtained from the SQPT fit and interpreted as resulting from three independent channels, and in (b) the *reconstructed* ABS spectrum obtained after performing those 2 identifications between manifolds. The latter shows a significantly more regular structure, with no overlapping features. All possible SQPT transitions between any two manifolds of the spectrum in (b) are shown in Figure 6.6(c) and superimposed to the data.

Interestingly, this second picture seems to describe well and in a self-consistent way the experimental data, because if the manifolds are now relabeled from 1 to 5, then the expected $2 \rightarrow 3$ and $3 \rightarrow 4$ processes would predict lines at locations where very faint features of some SQPT can indeed be observed (see lower green and blue bundles of 4 lines in Figure 6.6(c)) and that were not predicted by the ABS level structure from Figure 6.6(a) deduced from the fit. The signal-to-noise ratio being $\sim 1$, this requires a trained eye to be observed. Also, the full dispersion of the bundles of 4 lines can unfortunately not be compared as there are missing data in this frequency region (depicted as white areas in the spectra). However, in Figure 6.6(c), we provide two enlargements pointing out to some features in the data, highlighted with arrows, that likely correspond to the $2 \rightarrow 3$ (blue) and $3 \rightarrow 4$ (green) SQPT processes expected from the reconstructed ABS level structure. In particular the crossings at $\delta = 2\pi$ of the four lines of each bundle seem to fall at the right frequency. One also observes faint features in black near the $1 \rightarrow 2$ SQPT that seem reminiscent of these SQPT lines. Finally, notice that because 1 and 1′ were identified despite their slightly different shape, the fit of the SQPT lines involving manifold 2′ (now labeled 4) is slightly worse than in Figure 6.5(b). To complete the analysis one should therefore fit again with this new shape for manifold 1′ and a better agreement with the data would probably be obtained.

### 6.3.3 Spin character of ABS ($B \neq 0$)

The splitting of the ABS in the absence of a Zeeman field and the resulting SQPT transitions reveal the difference of Fermi velocities associated to different spin textures, arising from the SOI in the nanowire. To confirm that the measured splitting is indeed a spin effect, we probed the ABS spectrum under a finite magnetic field and, in particular, its dependence on the field orientation with respect to the nanowire axis.

We consider a magnetic field lying in the $xy$-plane. The $y$-component $B_y$ (parallel to the spin states of the transverse subbands without SOI) Zeeman-shifts the energy of the subbands depending on the spin states and modifies the Fermi wave vectors as illustrated in Figure 6.7(c). On the other hand, the $x$-component $B_x$ mixes opposite-spin states and therefore contributes to opening a gap at the subbands crossings points, as illustrated in Figure 6.7(b). For both, $B \parallel x$ and $B \perp x$ cases, the resulting ABS and the corresponding transition lines are shown in the middle and bottom rows of each panel in Figure 6.7. Let us now compare this qualitative picture with the experimental results. Figure 6.4(c) shows the spectrum in the presence of an in-plane magnetic field with amplitudes $B = 0$, 2.6, and 4.4 mT applied at an angle of -45° with respect to the nanowire axis. We observe that the left/right symmetry of the SQPT lines

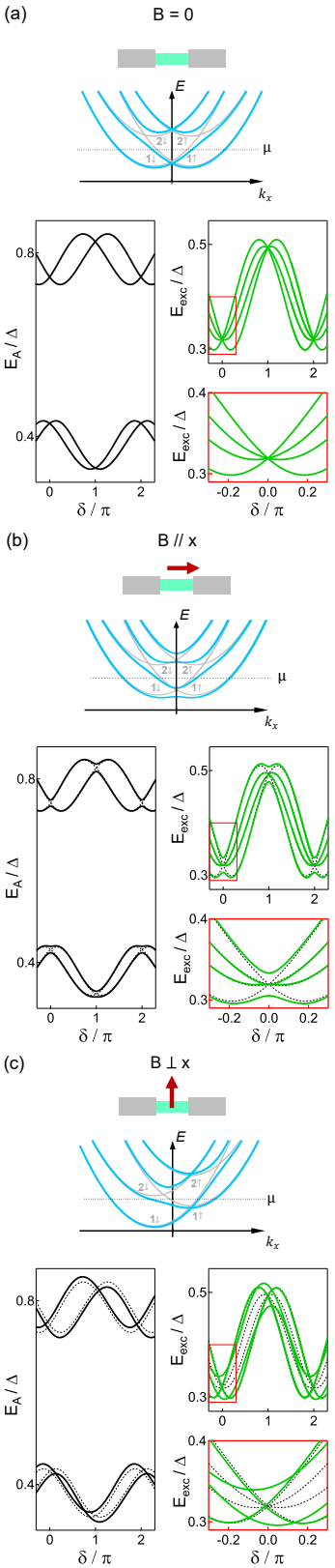


**Figure 6.7:** Effect of an in-plane parallel (b) or perpendicular to the wire (c) magnetic field on the band structure (top row), the Andreev levels (bottom row, left) and the excitation spectrum (bottom row, right) shown in (a) for no field. The field effect on the bands is exaggerated for clarity.

around $\delta = 0$ and $\delta = \pi$ is lost. Provided that an anisotropic $g$ factor is assumed (explained below), this effect can be quantitatively accounted for, using the extension of the single-barrier model at finite magnetic field, which is reviewed in Section E.3 of Appendix E (green lines).

The specific effects of an either parallel or perpendicular magnetic field on the ABS are now shown in Figure 6.8. When a field perpendicular to the nanowire is applied ($B \perp x$), we observe in Figure 6.8(b) and (d) that the ABS spectrum becomes asymmetric, as illustrated in Figure 6.7(c)). The stronger the field, the bigger this asymmetry. Indeed, the magnetic field is directly acting in the quantization direction of the spin-split transverse subbands from which the ABS are constructed, leading to Zeeman shifts of the energies. On the other hand, when the applied field is parallel to the nanowire axis ($B \parallel x$), and therefore perpendicular to the spin quantization direction, it mixes the spin textures and lifts partly the degeneracies at $\delta = 0$ and $\pi$. This modifies the ABS spectrum, although the latter remains this time symmetric around $\delta = 0$ and $\pi$ (see Figure 6.8(a) and (c)). As the parallel field is increased, we observe a gap opening more and more between the two outer lines of the SQPT bundle, as predicted by theory (see Figure 6.7(b)). This agreement with theory, both qualitative and quantitative, of the field orientation behaviour therefore confirm that the bundles of four lines observed in our spectra indeed correspond to SQPT transitions between ABS – eventually revealing their fine structure.

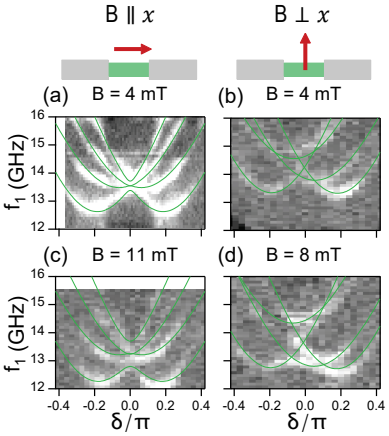


**Figure 6.8:** Effect of an in-plane magnetic field on the ABS excitation spectrum around $\delta$. This series of spectra were measured at $V_g = 0.5$, the same gate voltage as in Figure 6.4. Field is applied parallel [(a),(c)] or perpendicular [(b),(d)] to the nanowire axis. Green lines are the result from the theory using $g_\perp = 12$ and $g_\parallel = 8$.

In order to fit these data and reproduce accurately the lines' evolution with magnetic field, we realized that in addition to the parameters determined at zero field (see Figure 6.4(b)), an anisotropic $g$ factor had to be taken $g_\perp \neq g_\parallel$. Using the data taken with field in the parallel and perpendicular directions, we calculated for both series the correlation function between images of the measured spectra (taking the absolute value of the response $f - f_0$) and theory using various values of $g_\perp$ and $g_\parallel$. Figure 6.9 shows the dependence of the correlation functions with $g_\perp$ and $g_\parallel$. We observe that the best agreement is found for $g_\parallel = 8$ and $g_\perp = 12$, which are within the range of values reported in the literature [90, 91, 92, 49]. Green lines in Figure 6.8 show the theory result, using these two values for the $g$ factor and the fitting parameters at zero field estimated from the fit of Figure 6.4(b). Note that the determination of $g_\parallel$ is less accurate, and that overall, $g_\parallel = 4$ gives a similar correlation as $g_\parallel = 8$, but agreement is worse at the largest values of $B_\parallel$ where the effect is the strongest.

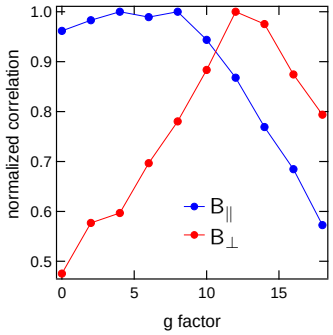


**Figure 6.9:** Correlation (normalized to maximum value) between finite magnetic field data and theory as a function of the $g$ factor, for field direction parallel (blue) or perpendicular (red) to the nanowire.

### 6.3.4 Absence of intra-doublet transitions

Initially, the experiment was designed with a low $f_r$ because we were targetting a dispersive readout of the intra-doublet transitions (depicted in dotted green lines in Figure 6.2) and this, without anticipating that single-quasiparticles transitions to higher ABS doublet could actually also fall in the accessible frequency range ! Eventually, those SQPT lines proved to be easier to evidence experimentally, as we saw in Figures 6.2 and 6.4, and turned out to provide equally well a signature of the underlying spin-splitting of the ABS. Despite many efforts, intra-doublet transitions could never be observed on this sample, probably due to a too low coupling between the resonator and the weak link. This process, corresponding

to the spin-flip of a single quasiparticle, was not only predicted to be strongly suppressed compared to the usual pair transition involving even parity states, but actually to also vanish in absence of parallel field [32]. In Section 6.4, we will discuss the existence of approximate spin selection rules and show that the intra-doublet transitions can actually be allowed at zero field, provided that the transverse spatial symmetry of the nanowire be broken. This can be achieved *a posteriori* by exciting the weak link through a lateral gate, but cannot happen if the microwave drive is sent through the resonator : in this case, the RF electric field is longitudinal and couples only to the phase difference across the weak link. Note that in a real device, the transverse symmetry may actually be broken *a priori*, for example by the superconducting shell itself (in other-than-fullshell nanowires) or by the presence of metallic gates and their applied voltages (see Supplemental of Ref. [42]).

[32]: Park and Levy Yeyati (2017), 'Andreev spin qubits in multichannel Rashba nanowires'

[42]: Hays et al. (2021), 'Coherent manipulation of an Andreev spin qubit'

Furthermore, as we noticed in Section 6.3, transition lines can be evidenced even when strongly detuned from the resonator frequency, *i.e.* far away from the dispersive regime. Indeed, if the zero-point phase fluctuations $\delta_{\mathrm{zp}}$ are high enough, thus providing a good resonator-weak link coupling, the phase curvature of the ABS can itself contribute to a still-small-but-measurable resonator shift, therefore allowing for their detection. With hindsight, this means eventually that the resonator frequency value does not matter that much, as long as it falls in the typical $2-30$ GHz range that we are probing. The constraint of a low $f_r$ to detect the intra-doublet transitions can therefore be lifted. Increasing the resonator frequency is actually helpful in two ways: fewer replicas are present in the same frequency range and the coupling with the weak link is also higher (see discussion in Section 5.2.1). This motivated the fabrication of a new sample with a higher resonator frequency (this time around $f_r \approx 6$ GHz) and a galvanic coupling with the phase-biased loop, which altogether allowed to detect intra-doublet spin flip transitions, as we will see in Section 6.5.2.

## 6.4 Modeling the resonator shift in spectroscopy measurements

Using the two-subband scattering model developed in Chapter 3.2 we have shown that both the position and shape of the PT and SQPT lines observed in our two-tone spectroscopies can be accounted for (see Figure 6.11(d')). However, understanding the lines' intensity appears more challenging. When transition lines are crossing the resonator frequency $f_r$, like the PT measured on atomic contact depicted in Figure 6.11(c'), the signal is characterized by a change of sign typical from a measurement in the *dispersive* regime where the resonator shift varies like $\Delta f_r \propto (g/2\pi)^2/(f_A - f_r)$, with $f_A$ the frequency of the pair transition. Surprisingly, when it comes to the nanowire weak link data, similar changes of sign can be seen along the bundle of SQPT lines (see Figure 6.11(d')), although they are far detuned from the resonance frequency, which lay around $f_r \approx 3.2$ GHz. This was attributed *qualitatively* to the resonator being probed in the *adiabatic* regime, where the frequency shift is expected to be dominated by the phase curvature of the ABS levels.

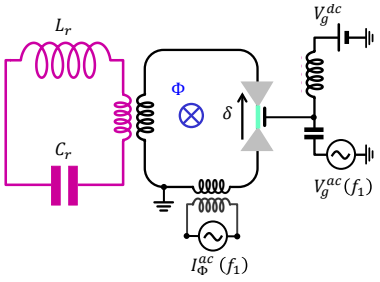


**Figure 6.10:** Schematics of a superconducting weak link (light green) placed in a superconducting loop and inductively coupled to a microwave resonator, represented as a lumped elements LC circuit. Transitions between Andreev states can be driven by an ac signal either through a gate ($V_g^{ac}$) or a flux line ($I_\Phi^{ac}$).

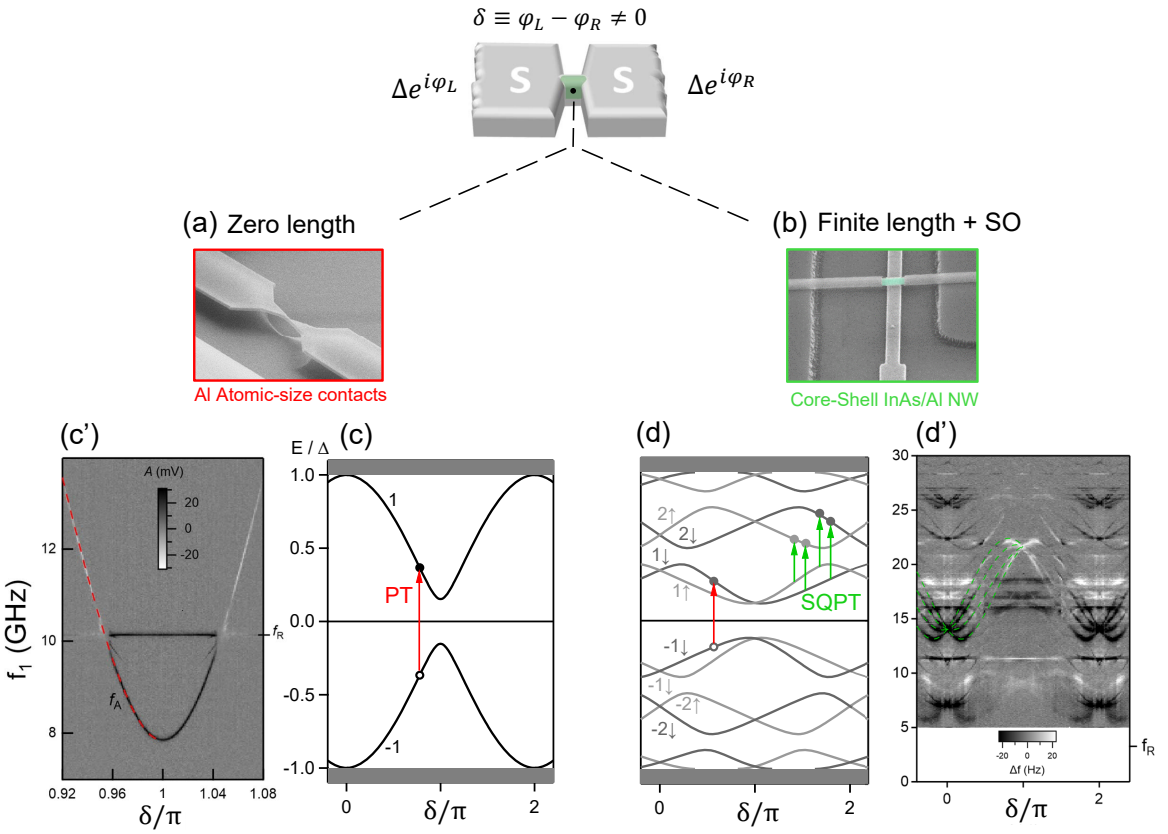


**Figure 6.11:** (a) Atomic contacts (AC) *vs.* nanowire (NW) weak links. Typical Andreev spectrum are shown both for AC (c) and NW (d) in the single-particle picture. In addition to *pair transitions* (PT), depicted in red, nanowire weak links allow, due to the multilevel structure of their ABS spectrum, for a new family of transitions, the so-called *single-quasiparticle transitions* (SQPT), shown in green. (c',d') Typical two-tone microwave spectrum for both cases, as a function of the superconducting phase difference $\delta$, evidencing a PT close to $\delta = \pi$ for the AC (data from [16]) and a bundle of SQPT for the NW weak link (data from [51], also shown in Figure 6.4). Fits are superimposed in dashed lines on the left half of the data. The bare resonator frequency $f_R$ is indicated for both experiments on the right axis of the spectra (c',d').

Still, to understand *quantitatively* the lines' intensity, one needs to use the theory for the crossover between dispersive and adiabatic regimes (Section 4.2.2), and to describe the response of the resonator to changes in the occupancies of the Andreev states induced by a drive. Here, we introduce a model to describe the driving through either an AC flux or an AC gate voltage [51] (see Figure 6.10). The AC flux can be applied either through an AC current in a conductor placed nearby the loop [19], or with an excitation applied directly through the resonator coupled to the superconducting loop [16, 41] (in this case, the excitation is filtered by the resonator and therefore this scheme only allows to drive the weak link in a restricted frequency window). We find under which conditions spin-non-conserving transitions can occur (Section 6.4.2), like the intra-doublet spin transition which was mentioned in Section 6.3.4. Finally, in Section 6.4.3 we derive the resonator frequency shifts in the presence of driving fields and compare in Section 6.5 the predictions from this theory to experimental data on superconducting atomic contacts and nanowire weak links.

[51]: Tosi et al. (2019), 'Spin-Orbit Splitting of Andreev States Revealed by Microwave Spectroscopy'

[19]: Hays et al. (2018), 'Direct Microwave Measurement of Andreev-Bound-State Dynamics in a Semiconductor-Nanowire Josephson Junction'

[16]: Janvier et al. (2015), 'Coherent manipulation of Andreev states in superconducting atomic contacts'

[41]: Hays et al. (2020), 'Continuous monitoring of a trapped superconducting spin'

### 6.4.1 Spin-conserving vs. spin-flipping transitions

In the model of two Andreev doublets, used to fit the data in Figure 6.4, the SQPT lines divide in two families: those between states with the same pseudo-spin (spin-conserving transitions), and those between states with opposite pseudo-spin (spin-flipping transitions). It turns out that driving through a flux modulation only allows for spin-conserving transitions between ABS levels. This observation is supported by a series of measurements performed on nanowire weak links by Hays *et al.* [41].

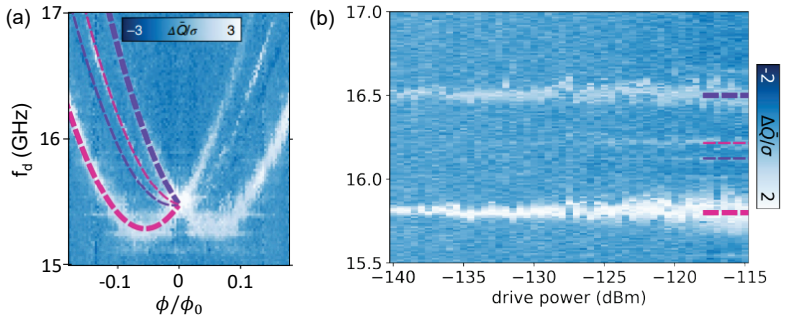


**Figure 6.12:** (adapted from Ref. [41]) (a) Two-tone spectroscopy of a nanowire weak link revealing four SQPT lines at high drive power. (b) Visibility of the bundle of SQPT at a given flux $\Phi$ as a function of the drive power sent through the resonator.

Using a similar c-QED setup, they were also able to evidence SQPT transitions, however only the two outer transition lines corresponding to spin-conserving processes were clearly visible at low drive power. This is illustrated in Figure 6.12(a), adapted from Ref. [41]. The two inner lines, associated to spin-flipping transitions, started to be faintly visible only when driving at much higher power (see Figure 6.12(b)) and still remained substantially dimmer at maximum power (-115 dBm) than the outer two spin-conserving transitions at the lowest power (-140 dBm). This tends to show that some spin selection rules are at play in the system *i.e.* that depending on the way it is driven, all transitions may not be allowed by their associated matrix elements. To understand this effect, one needs to model first the effect of the drive.

### 6.4.2 Gate vs flux drive: spin selection rules

To account for the driving at a frequency $\omega_d = 2\pi f_d$, the following term may be added to the system Hamiltonian given in Eq. (4.23)

$$\hat{A}(t) = \frac{1}{2} \sum_{i\sigma<j\sigma'} (A_{i\sigma,j\sigma'} \gamma^\dagger_{i\sigma} \gamma_{j\sigma'} e^{i\omega_d t} + \text{h.c.}), \tag{6.1}$$

In the case of a flux driving, which acts on the phase $\delta$, $A_{i\sigma,j\sigma'} \propto \langle \Phi_{i\sigma} | \hat{H}'_{wl} | \Phi_{j\sigma'} \rangle$. In the absence of magnetic field and for a ballistic model which preserves the transverse spatial symmetry [32], the current operator $\hat{H}_{wl}$ does not mix the transverse channels of the weak link and thus only pseudospin-conserving transitions are allowed. Notice, however, that whenever the driving field or the scattering breaks the transverse spatial symmetry, spin-flip transitions can take place [41].

In the case of a gate driving, the AC signal induces a displacement $\delta V(\vec{r})$ in the electrostatic potential experienced by the electrons in the junction region. The corresponding matrix elements in the driving Hamiltonian are thus $A_{i\sigma,j\sigma'} = \langle \Phi_{i\sigma} | \delta V(\vec{r}) \tau_z | \Phi_{j\sigma'} \rangle$, where $\tau_z$ is a Pauli matrix

in electron-hole space. As discussed in Section 3.2, the pseudospin of the Andreev states comes from nanowire's transverse modes with different spins hybridized by Rashba spin orbit coupling. A perturbation $\delta V(\vec{r}) = \delta V_0$ uniform in the transverse direction does not couple different transverse modes and therefore pseudospin flip transitions are not allowed, *i.e.* $A_{iu,jd} = 0$. Only a non-uniform perturbation couples transverse modes and allows pseudospin flip transitions. The fact that all possible transitions between two Andreev manifolds have been observed in the experiments (see Fig. 6.4 and 6.5(a)) indicates that the non-uniform component of the induced potential $\delta V$ by the gate electrode was significant. More insight into the possibility of engineering the selection rules using gate driving can be obtained by considering the model of Ref. [32] for the nanowire's transverse channels. Within this model, the nanowire confining potential is assumed to have cylindrical symmetry. Thus, the modes in the lowest subband have zero angular momentum along the nanowire axis ($l = 0$) and they have $l = 1$ on the first excited subband. A lateral gate would impose a perturbation $\delta V(\vec{r})$ which typically breaks the rotational symmetry and therefore would couple states on different subbands, naturally leading to both pseudospin flip transitions and pseudospin conserving transitions.

One could think, however, of a more general gate configuration like the one in Figure 6.13(a), where two lateral gates can be set such that $\delta V(y) = -\delta V(-y)$ (or $\delta V(y) = \delta V(-y)$) in an anti-symmetric (or symmetric) configuration as indicated in panel (b). In the anti-symmetric case, the $\delta V$ matrix elements vanish for states on the same subband, but are finite for states in different subbands. As a consequence we would have $A_{i\uparrow,j\uparrow} = A_{i\downarrow,j\downarrow} = 0$. The allowed transitions between spin-split ABS are indicated in Figure 6.13(c) with arrows of different colors for symmetric (blue), anti-symmetric (green) or an intermediate (magenta) configuration. We also plot in Figure 6.13(d) the phase-dependent matrix elements, which were calculated for each case with the scattering model of Section 3.2 and for the parameters that give the spectrum in (c). The latter corresponds to a fit of the data in Figure 6.4 evidencing SQPT lines, which were discussed in Section 6.3. Those matrix elements show that indeed the symmetric and anti-symmetric potentials lead to respectively pseudospin-conserving (dashed arrows in (c), dashed lines in (d)) and pseudospin-flipping (dashed-dotted and full arrows in (c), dashed-dotted and full lines in (d)) transitions, and that the mostly anti-symmetric potential results in both transitions with similar amplitudes. Note that for a transversally symmetric drive, which is also the case when driving in flux, the matrix elements squared are 3 orders of magnitude higher for spin-conserving transitions (Figure 6.13(d) top panel) than they are for spin-flipping transitions when the drive is purely anti-symmetric but of still similar magnitude (Figure 6.13(d) middle panel). This rationalizes the observation in Figure 6.12 that spin-flipping transitions corresponding to the inner two lines of SQPT bundles are strongly suppressed when the drive does not break the transverse symmetry of the nanowire. Note also that the matrix elements for the *intra-manifold* pseudospin-flipping transitions (solid lines) are also generally much lower than the one for *inter-manifold* transitions. In addition, the square matrix elements for intra-manifold transitions are ~ 15 times larger in the second manifold than in the first one, which at the scale of Figure 6.13(d) is barely visible.

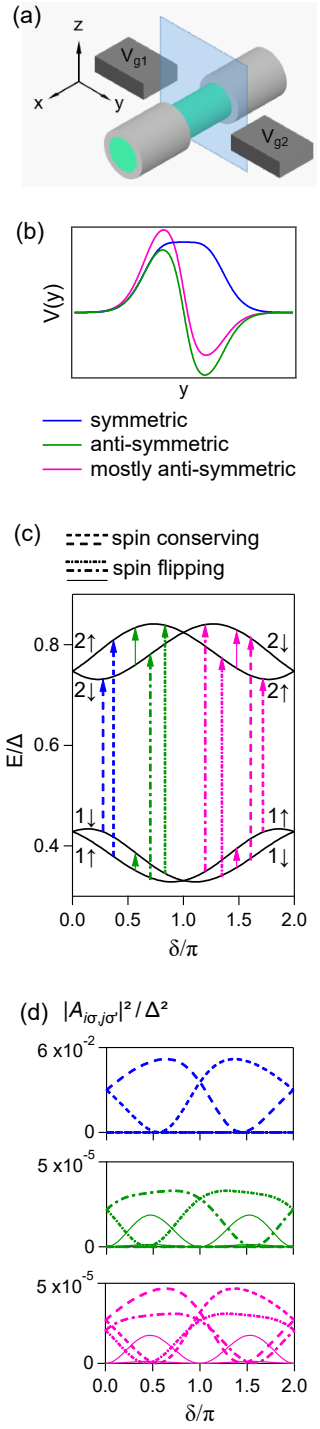


**Figure 6.13:** (a) Schematic of a nanowire weak link with local side gates. (b) Induced driving potential in the transverse ($y$) direction of the nanowire in various situations: symmetric (blue line), anti-symmetric (green line) or mostly anti-symmetric (magenta line) profiles can be obtained by controlling $V_{g1}$ and $V_{g2}$ applied to the gates. (c) Allowed transitions in the weak link with spin-split Andreev levels. Each color indicates the transitions induced by the driving potentials illustrated in (b). The associated matrix elements are shown in (d).

### 6.4.3 Weak driving of a multi-level system

In order to obtain the frequency shift for the resonator coupled to the *driven* weak link, we need a theory for the steady-state dynamics of a driven multi-level system. While the Bloch equations do well the work for the case of a driven two-level system [93], to our knowledge no generalization to the multi-level case seemed to be available. To keep it tractable, Sunghun Park and Alfredo Levy Yeyati developed such a theory by analysing the resonator spectral function $D^R(\omega) = -i\int_0^\infty dt e^{i\omega t}\langle[a(t), a^\dagger(0)]\rangle$ for the case of a weak drive. First, they make use of the interaction picture in which the time evolution of both the resonator and the weak link are provided by solving master equations including dissipation, and then treat the resonator-weak link coupling and the drive as small perturbations. The perturbation terms up to second order are calculated in both $\delta_{zp}$ and $A_{i\sigma,j\sigma'}$ (see Appendix A in Ref. [53] for details).

[93]: Palacios-Laloy (2010), 'Superconducting qubit in a resonator', p. 111

[53]: Metzger et al. (2021), 'Circuit-QED with phase-biased Josephson weak links'

The frequency shift for a single-quasiparticle transition from $|i_0\sigma_0\rangle$ is found to be given by

$$\delta f_r^{\mathrm{SQPT}} = 2\sum_{j\sigma>0}\frac{|A_{i_0\sigma_0,j\sigma}|^2}{|D_{i_0\sigma_0,j\sigma}|^2}\left(\delta f_r^{(j\sigma)} - \delta f_r^{(i_0\sigma_0)}\right), \tag{6.2}$$

where $D_{a,b} = \hbar\omega_d - |E_a - E_b| + i(\Gamma_a + \Gamma_b)\hbar/2$. $\omega_d$ is the driving field frequency and $\Gamma_{a(b)}$ are phenomenological parameters to account for the finite linewidths in the transition spectrum, which are associated to the states relaxation. The $\delta f_r^{(j\sigma)}$ terms still refer to the resonator shift due to single levels $(j\sigma)$, as given by Eq. (4.33).

For a pair transition from the ground state $|g\rangle$, one obtains

$$\delta f_r^{\mathrm{PT}} = 2\sum_{\{j\sigma,k\sigma'\}}\frac{|A_{-j\bar{\sigma},k\sigma'}|^2}{|D_{-j\bar{\sigma},k\sigma'}|^2}\left(\delta f_r^{(j\sigma)} + \delta f_r^{(k\sigma')}\right), \tag{6.3}$$

where $\{j\sigma, k\sigma'\}$ means a set of indices $j\sigma$ and $k\sigma'$ corresponding to positive energy levels ordered in energy, and does not contain a permutation of the indices. $j\sigma$ and $-j\bar{\sigma}$ are for a pair of particle-hole symmetric Andreev levels. With these two equations at hand, we can now attempt to model our two-tone spectroscopy data.

## 6.5 Understanding resonator shifts in nanowire weak links

*In this section, we reproduce figures from Ref. [53] where the x-axis of the spectra is the applied (reduced) flux phase $\varphi$. Neglecting the inductance of the loop in which the weak link is enclosed, the phase $\delta$ across the junction is equal to $\varphi$.*

### 6.5.1 Two-tone spectra of sample S1 (mutual coupling)

In Figure 6.2 and 6.4, we presented two microwave spectra measured on sample S1 at two different gate-voltages. We noticed that the measured signal could not be qualitatively explained by purely dispersive effects,

in particular that the intensity of SQPT lines was rather reflecting an adiabatic shift of the resonator frequency, which also explained why signal could be measured at frequencies much higher than the resonator one. Now that the equations are set, we can provide a quantitative comparison of those spectra with the theory for the resonator shift due to driving near a PT frequency (Eqs. (6.3)) or near a SQPT (Eq. (6.2)). In Figure 6.14 and 6.15, we compare the intensity of the main measured lines of Figure 6.2 and 6.4 with a full calculation of their associated shift, taking into account that the transitions were induced by microwaves applied on the gate. Both spectra correspond, like in Figure 4.8(a-e), to a situation in which the resonator frequency $f_r = 3.26$ GHz is very low as compared to most of the observed transition lines, meaning that the resonator shift is mainly given by adiabatic contributions.

A PT and several SQPT are clearly recognized in the spectrum of Fig. 6.14. From the analysis illustrated by Figure 4.8(a-e), one understands that the frequency shifts corresponding to transitions above the resonator bare frequency are essentially given by the curvature of the transition lines: with the color scale of Figure 6.14, lines are red when they have positive curvature, and blue when negative. For a more quantitative comparison with theory, we make use of the scattering model from Chapter 3.2 that we had used to fit the position of the bundle of SQPT appearing in the range 3-10 GHz (fitting parameters are those corresponding to #3 in Table 6.1). The calculated SQPT lines shown in the right half of Figure 6.14 reproduce well the observed SQPT energies, but the pair transition predicted from the same Andreev levels is observed to disperse less than in the experimental data. Using these parameters, we then calculate the matrix elements for $\hat{H}'_{wl'}$, which are needed to estimate the associated resonator shift.

Since the two-tone spectroscopy data was taken at very small power, the theory of weak-driving presented in Section 6.4.3 is fully applicable. We evaluate the matrix elements for the weak-driving through the gate and compute the resonator shift shown in the figure, using Eqs. (6.3, 6.2). Globally, the shifts calculated for the four SQPT reproduce quite well the observed ones. However, some details differ, notably for the highest single-quasiparticle transition, with shifts near $\varphi = 0$ larger in the data than in the calculation. Also, the shift for the PT is reproduced only at a qualitative level. Finally, note that the value of zero-point phase fluctuations deduced from this "fit", $\delta_{zp} = 1.2 \times 10^{-5}$, is about a factor 45 lower than the nominal one obtained from microwave simulations (see Eq. (5.12)). Indeed, the magnitude of the frequency shift depends strongly on the estimated matrix elements which are known to be model-dependent. It would not be surprising to obtain a different order of magnitude using a different model for the matrix elements.

A similar procedure was used to fit the data in Figure 6.15. The fitting parameters for the main SQPT were given in Section 6.3.2. In this case, the calculated PT lies outside the frequency range of the graph and only the bundle of four SQPT lines is clearly recognisable (transitions in the range 13-23 GHz). For this set of SPQT lines, theory captures most of the measured features. Note that in the experimental results reported in Figure 6.14 and 6.15, the resonator shift was remarkably low (tens of Hz) as compared to that observed for atomic contacts (tens of MHz) [16]. There are two reasons for this. On the one hand, the geometry of the

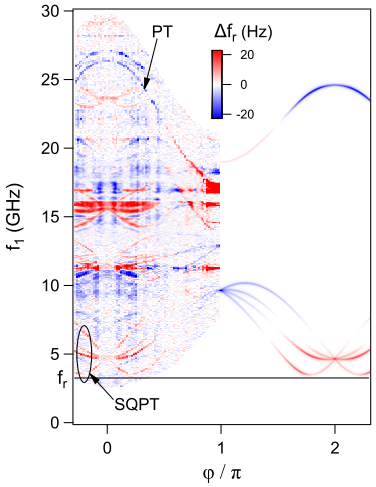


**Figure 6.14:** Fit of the nanowire two-tone spectroscopy shown in Figure 6.2. Left: experimental data obtained with sample S1. Colorscale represents the resonator frequency shift (sign corrected compared to Ref. [51]). A pair transition (PT) and a bundle of single particle transitions (SQPT) are pointed at. Right: calculation for a single occupied channel (see text). Colorscale is the difference in frequency shift between initial and final state. Solid line at 3.26 GHz indicates the resonator frequency. In the calculation, it was assumed that $\delta_{zp} = 1.2 \times 10^{-5}$ and the dissipation rate is $\Gamma_{1\sigma} + \Gamma_{2\sigma'} = 0.62$ GHz. The sign of the frequency shift in the experiment has been corrected compared to Ref. [51].

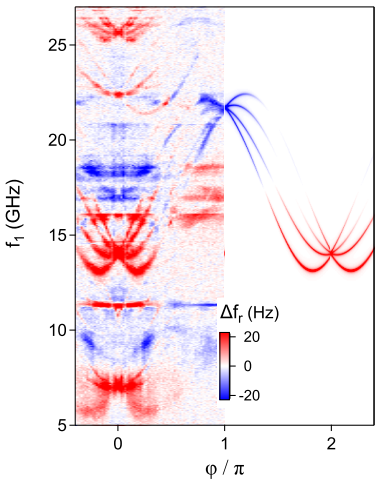


**Figure 6.15:** Fit of the nanowire two-tone spectroscopy shown in Figure 6.4. The measured transition lines are compared with a full calculation of the shift taking into account that the transitions were induced by microwaves applied on the gate. The parameters for the calculation are those that allowed fitting the spectrum and the matrix elements for the microwaves shown in magenta in Figure 6.13(c) are used. The same values of $\delta_{zp}$ and the dissipation rate are used as in Fig. 6.14.

circuit, which determines the phase fluctuations the resonator induces in the loop. It can be optimized with the circuit design. On the other hand, and more fundamental, the reduction of the matrix element of $\hat{H}'_{wl}$ in the long-junction limit [32]. As a rough approximation (see Eq. (3.14), the matrix element is that for a short junction with an effective gap $\Delta_{\text{eff}} = \frac{\Delta}{1+\lambda}$; this contributes to a $(1+\lambda)^2$ reduction in the coupling.

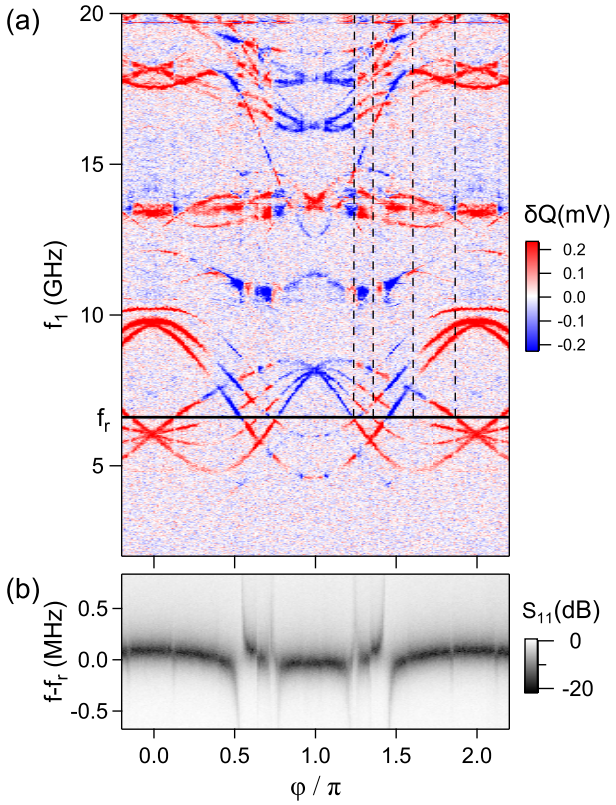


**Figure 6.16:** (a) Two-tone spectrum measured on sample S2 ($L \sim 550$ nm). The color-coded quadrature of the measured signal shows many sign changes along the transition lines, qualitatively in agreement with the behavior illustrated in Fig. 4.8(g,h): the sign changes are attributed to situations where the energy of some virtual transitions matches $hf_r$. (b) Associated single-tone spectrum.

### 6.5.2 Two-tone spectra of sample S2 (galvanic coupling)

We present now two-tone data obtained with sample S2, in which the nanowire is coupled to the resonator through a shared inductance (see Section 5.2.2). The resonator frequency was also increased from $f_r = 3.2$ GHz to 6.6 GHz and we diminished its impedance by about a factor 2, leading altogether to an enhanced coupling by about two orders of magnitude (a factor ×275 in $\delta^2_{\text{zp}}$, see Eq. (5.12) and Eq. (5.23)). An actual picture of the device is shown in Figure 10.1. Importantly, the coupling being much larger than in sample S1, the measured signal cannot be easily converted in a resonator shift, and we show in Figure 6.16 the change in one quadrature, $\delta Q$.

In the range between 5 and 10 GHz of the otherwise very busy spectrum of Figure 6.16, one recognizes three PTs and a bundle of SQPTs. The color-coded quadrature shows many abrupt sign changes along the transition lines, like the behavior illustrated in Figure 4.8(g,h): the sign changes

are attributed to situations where the energy of some virtual transition matches the resonator frequency (as indicated by the black dashed lines). This spectrum has other remarkable features, like the occurrence of sets of PTs very close in energy. Moreover, the shape of several other lines in the spectrum does not correspond to what our simplistic scattering model predicts. These features will be the focus of Chapter 8.

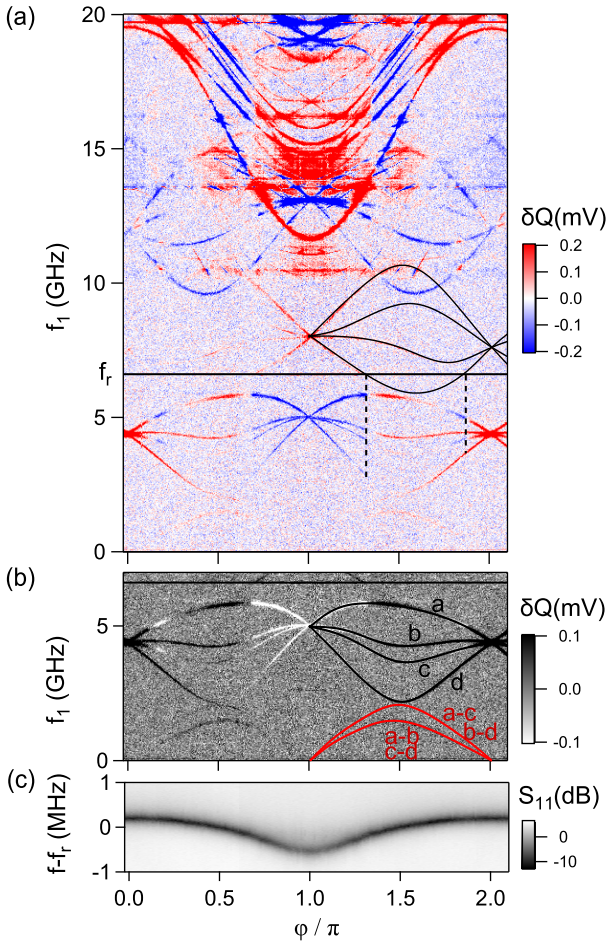


**Figure 6.17:** (a,b) Two-tone spectrum measured on sample S2 ($L \sim 550$ nm) for a different gate tuning compared to Fig. 6.16. The color-coded quadrature of the measured signal shows sign changes along the transition lines, qualitatively in agreement with the behavior illustrated in Fig. 4.8(g,h): the sign changes are attributed to situations where the energy of some virtual transitions match $hf_r$. For example when the lowest transition line of the second group of single particle transitions (underlined with black splines in (a)) crosses the resonator, the sign of frequency shift along the transition lines in the lowest group of SQPT changes. In (b), same data as (a) but stronger contrast and other colorscale, intra-manifold spin-flip transitions are visible. The red lines that superimpose on the data are obtained as differences between the inter-manifold transition energies underlined in black and labeled a,b,c,d. (c) Single-tone spectrum.

### Observation of direct spin-flip transitions

In Figure 6.17 we show data measured in a different cooldown. In this case, changes of sign of the displayed quadrature occur when the lowest transition of a SQPT bundle (drawn in black based on the signal of both quadratures) crosses the resonator line. The resonator shift measured in the CW single-tone spectroscopy (Figure 6.17(c)) shows a dominant contribution from the pair transition that lies at 12 GHz at $\delta = \pi$,

but the anti-crossings expected at the position of the dotted lines in Figure 6.16 (a) are not visible, indicating the very small occupancy of the initial state for the corresponding transition. This is in agreement with the difference in intensity between the transition lines in the two-tone spectroscopy. A remarkable feature in this spectrum is the presence of two very low-frequency lines (below 2 GHz), better seen in Figure 6.16(b). By analyzing their position in energy, they can be identified as spin-flip intra-manifold transitions, which were discussed in Section 6.3.4 on spin selection rules. The lines labelled a,b,c,d correspond to transitions between the first and the second manifold, at energies $E_{2\downarrow,1\downarrow}$, $E_{2\uparrow,1\downarrow}$, $E_{2\downarrow,1\uparrow}$, $E_{2\uparrow,1\uparrow}$. Their differences, labelled a-c, b-d, a-b and c-d, coincide two by two. They are shown with red lines and perfectly match the observed low-frequency transitions. The two first ones correspond to a transition energy $E_{1\uparrow,1\downarrow}$, the two last ones to $E_{2\downarrow,2\uparrow}$. The lines are dimmer at low frequency because the matrix elements go to zero at phases 0 and $\pi$ (see Figure 6.13(d)), and because the difference in occupancy of the two spin states diminishes when their energy difference is comparable to temperature: $k_B T/h \approx 0.8$ GHz. Note that such transitions have been recently driven indirectly through Raman processes [42, 94].

[42]: Hays et al. (2021), 'Coherent manipulation of an Andreev spin qubit'
[94]: Cerrillo et al. (2021), 'Spin coherent manipulation in Josephson weak links'

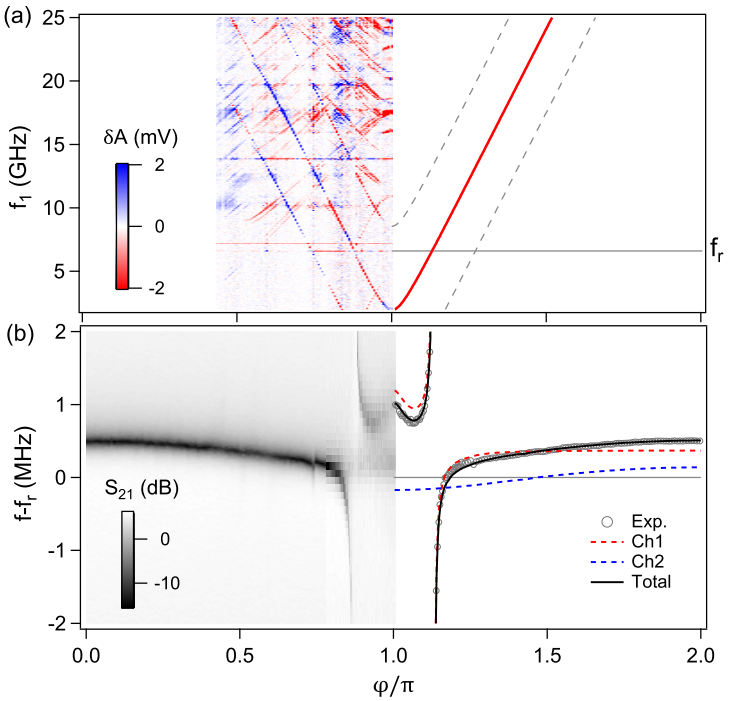


**Figure 6.18:** (a) Two-tone spectroscopy of sample S2, showing a pair transition $f_A$ anticrossing the resonator at $f_r = 6.60762$ GHz. Red line on the right-side is a fit of this transition (parameters given in Table 6.2) with its two replicas at $f_A \pm f_r$ shown in dashed gray. (b) Single-tone spectroscopy. (Left) Transmission coefficient amplitude $S_{21}$ measured with a VNA. (Right) Comparison with theory. For each phase value, the resonator frequency is extracted from the raw data ; the shift from its bare value is shown with gray disks and compared to the calculated shift due to a single channel (dashed red), whose pair transition towards the lowest Andreev manifold fits the transition line $f_A$ shown in (a). Blue dashed line: contribution of an effective second channel (parameters given in Table 6.2); because of its low transmission, the corresponding pair transition does not fall in the frequency range of (a)). Black line: total shift due to both channels.

A complete fit of the often complex spectra found in nanowire weak links is in general not possible with a simple modelling of the weak link. However, in the absence of a drive, the frequency shift of the resonator is often dominated by the contribution from a single channel, which allows for a simpler description. Before concluding this section dedicated to the modelling of the resonator shift in nanowire devices, let us flash a quick example of such situation where the resonator shift in the ground state is dominated by the contribution from one main PT transition.

In Figure 6.18(a) and (b), we show the two-tone spectroscopy and single-tone measurement of the same nanowire weak link as in Figure 6.17, again from another cooldown. Among the observed transition lines, there is a high-contrast PT that crosses the resonator at $\varphi = \pi(1 \pm 0.12)$. Within the scattering model of Section 3.2, it can be fitted as a PT towards the lowest of three Andreev manifolds arising from a high-transmission channel ($\tau = 0.996$). In Figure 6.18(a) we indicate this fit with a red line on the right hand side (parameters in Table 6.2), as well as two replicas shifted by $\pm f_r$, also visible in the data and associated to a strong measurement tone. The corresponding shift of the resonator, fitted with Eq. (4.33) and (4.34) with $\delta_{zp} = 0.012$ and using $f_r = 6.60762$ GHz (bare frequency measured when the nanowire is fully depleted), is shown in dashed red in the right hand side of Figure 6.18(b). This value of the zero-point phase fluctuations obtained from the fit falls close to the nominal value $\delta_{\mathrm{zp}}^{\mathrm{sCPW}} = 9.3 \times 10^{-3}$ expected for the shunted CPW design and estimated in Section 5.2.2 from Eq. (5.18). From this value of $\delta_{\mathrm{zp}}$ and the fit parameters given in Table 6.2, we can deduce using Eq. (5.19) the coupling factor at $\delta = \pi$ with the pair transition, $g(\pi) = 92$ MHz, which is close to the 100 MHz coupling that was achieved in the atomic contact experiment [21].

**Table 6.2:** Fit parameters used in Figure 6.18

| # | $\tau$ | $\lambda_1$ | $\lambda_2$ | $x_r$ | Color |
|---|---|---|---|---|---|
| Ch1 | 0.996 | 1.86 | 1.86 | 0 | Red |
| Ch2 | 0.26 | 0.95 | 0.95 | -1 | Blue |

[21]: Janvier (2016), 'Coherent manipulation of Andreev Bound States in an atomic contact', p. 61

Although the resonator shift contains contributions from both the continuum and the three Andreev manifolds, it is mainly dominated by the $\hat{H}'_{wl}$ contribution at energy $E_{-1,1}$ associated to the transition to the lowest manifold. Therefore it can be well approximated within a simplified Jaynes-Cummings description, taking Eq. (H.7) with a renormalized gap $\Delta_{\mathrm{eff}}/h = 15.4$ GHz and $f_A = 2E_{-1,1}$ (not shown in the figure for clarity, because it coincides almost exactly with the full theory for the channel shown in dashed red). Although it does not fit perfectly, it offers a simple analytical form that captures well the main features of the data around the anticrossing.

The small discrepancies with the experimental data are attributed to contributions from other possible channels. Many other transitions are indeed visible in the two-tone spectroscopy, which we model with an effective second channel (parameters in Table 6.2). Its contribution, shown with a dashed blue line in Figure 6.18(b), produces the smooth phase-dependent background that, added to the shift from the main transition, quantitatively accounts for the data at all phases (black line). Finally, let us stress once more that a rigorous fit of the resonator shift would require the knowledge of the continuum's curvature and of the phase dispersion of all subgap levels, which is not accessible given the restricted frequency range of our two-tone spectroscopies. By encompassing these other contributions into an effective second channel, we only seek to illustrate here that higher energy levels are indeed contributing to the total resonator shift by an extra phase-dependent offset, the detailed origins of which being inaccessible experimentally.

# Need for a multi-level description of the weak link

# 7



So far we have relied on a simple model of the Andreev spectrum consisting in only two spin-split doublets, as illustrated in Figure 6.1(a). As was shown in Chapter 6, such a minimal description is successful at explaining some features of the measured data, in particular the existence of single-quasiparticle transitions (SQPT) as a signature of the spin-splitting of Andreev levels in InAs weak links. However, as we shall now discuss, several features found regularly in nanowire spectra remain unexplained within such a minimal model. Using a galvanic coupling (sample S2, see Figure 10.1(a)), we improved significantly the quality and resolution of the spectra, allowing for better line identifications and an improved understanding. From these data, we could start drawing systematics in the phenomenologies of observed lines, which eventually allowed to rationalize the typical structure expected for a nanowire weak link transition spectrum in the $0-30$ GHz frequency window.

## 7.1 Unidentified spectroscopic lines in nanowire spectra

### 7.1.1 Long junction regime

A typical two-tone spectrum obtained with the galvanic coupling device is shown in Figure 7.1(a), where we highlighted the main transition lines : a PT (red), a set of four SQPT lines (green) and slightly above, a group of four unidentified lines (blue) sharing some similarity with PTs. At this stage, several remarks can already be made. First, the full phase dispersion of the pair transition is accessed at frequencies below 25 GHz, which is about half the measured value of the superconducting gap of aluminium. Contrary to atomic contacts where only a small part of the PT dispersion could be probed, this is made possible here because of the finite length of the weak link, which reduces the amplitude of the dispersion of the first ABS*.

We showed in Section 3.2.3 that at low energy and close to $\delta = \pi$, the lowest ABS manifold can be approximated by the expression for a zero-length junction with a reduced gap $\Delta_{\text{eff}} = \Delta/(1+\overline{\lambda})$, with $\overline{\lambda} = (\lambda_1+\lambda_2)/2$ (see Eq. (3.14)). The frequency of the lowest pair transition is then well captured close to $\delta = \pi$ by $f_A(\delta) = 2\Delta_{\text{eff}}\sqrt{1-\tau\sin^2(\delta/2)}$. This is illustrated in Figure 7.1(b) where we show in red solid line a fit of the lower pair transition close to $\pi$, which is obtained for $\tau = 0.934$ and $\Delta_{\text{eff}} = 11.9$ GHz. This indicates that we are indeed in a long junction regime with $\overline{\lambda} \approx L/\xi \sim 45/11.9 - 1 \sim 2.7$. As expected, this approximate dependence is less accurate away from $\delta = \pi$.

* A finite coupling to the superconducting leads, or a finite dwell-finite in the weak link region for any other cause, can also reduce the dispersion [64, 50].

[64]: Kurilovich et al. (2021), 'Microwave response of an Andreev bound state'
[50]: Fatemi et al. (2021), 'Microwave susceptibility observation of interacting many-body Andreev states'

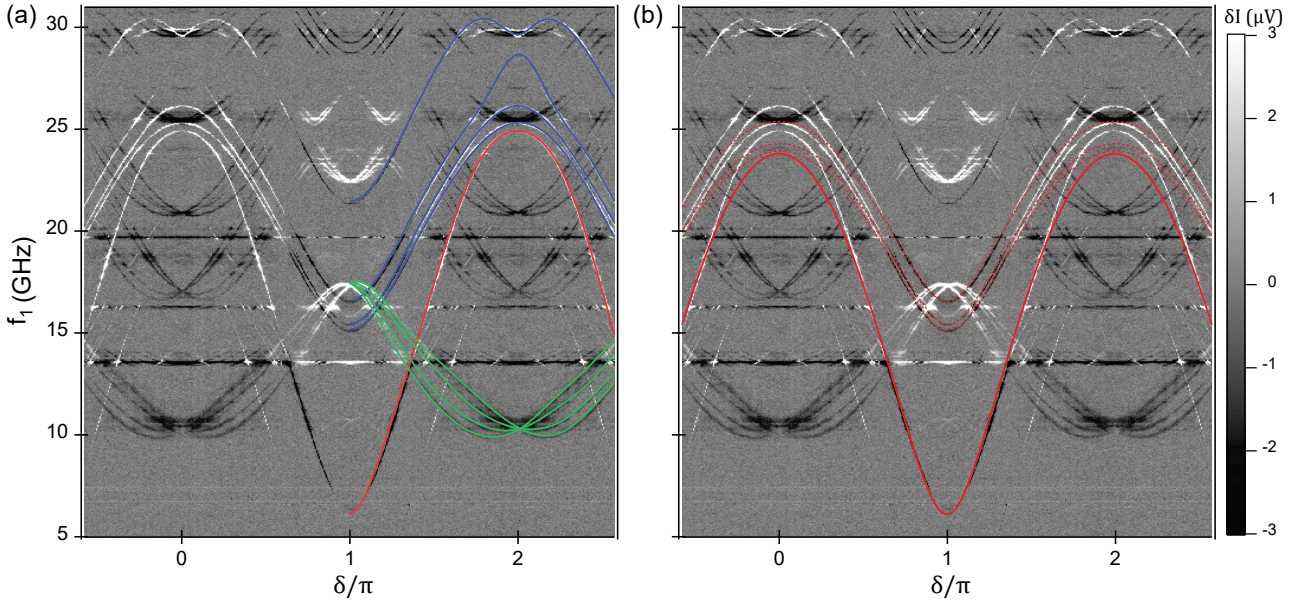


**Figure 7.1:** (a) Two-tone spectrum measured on sample S2. Main transition lines are highlighted by colored splines on half of the plot: a pair transition (red), a set of four single-particle transitions (green) and four lines (blue) sharing some similarity with pair transitions. Note that at least three other sets of SQPT are visible at higher frequencies (around 17.1, 20.9 and 25.4 GHz at $\delta = 0$). (b) Fit of the lower pair transition with the short junction formula $f_A(\delta) = 2\Delta_{\text{eff}}\sqrt{1 - \tau \sin^2(\delta/2)}$ (solid red line), yielding a transparency $\tau = 0.934$ and effective gap $\Delta_{\text{eff}} = 11.9$ GHz. The four transition lines highlighted in blue in panel (a) seem to be well fit around $\delta = \pi$ by $f_A(\delta)/2$ plus a constant offset (dashed red lines), indicating that these processes involve the creation of one quasiparticle in the lower ABS manifold and another quasiparticle in some level that disperses only little with $\delta$ around $\delta = \pi$.

### 7.1.2 Evidence for mixed pair transitions

With $L/\xi \sim 2.7$, one would expect that mixed pair transitions involving the creation of one quasiparticle in each of the two lowest Andreev doublets would be visible in the frequency range of Figure 7.1. They would display a set of four lines crossing at $\delta = 0, \pi$ similarly to SQPT lines and above the lowest PT. This is not observed. Instead, as a recurring feature in many measured two-tone spectra, we often observe a group of four transitions lines which show almost parallel phase dispersions close to $\delta \sim \pi$, like the ones highlighted in blue in Figure 7.1(a). It would be tempting to classify these lines as PTs, since their phase dispersion always features a local minimum at $\delta = \pi$. This interpretation can be discarded for at least two reasons: firstly, their behavior near $\delta = 0$ is more complex than PTs, with local kinks and avoided crossings. Secondly, on would need to invoke at least four extra channels with very similar transparencies, which is very unlikely. And if this was to happen for a certain value of the gate voltage, one would expect that the transparencies of these four channels would evolve differently with $V_g$ and the lines should move away from each other. Instead, the four lines evolve together, as illustrated in Figure 7.2. The fact that such sets of four lines, not more or not less, are routinely observed above the PT in various regimes of gate voltage indicates that they are generic features of low-energy spectra.

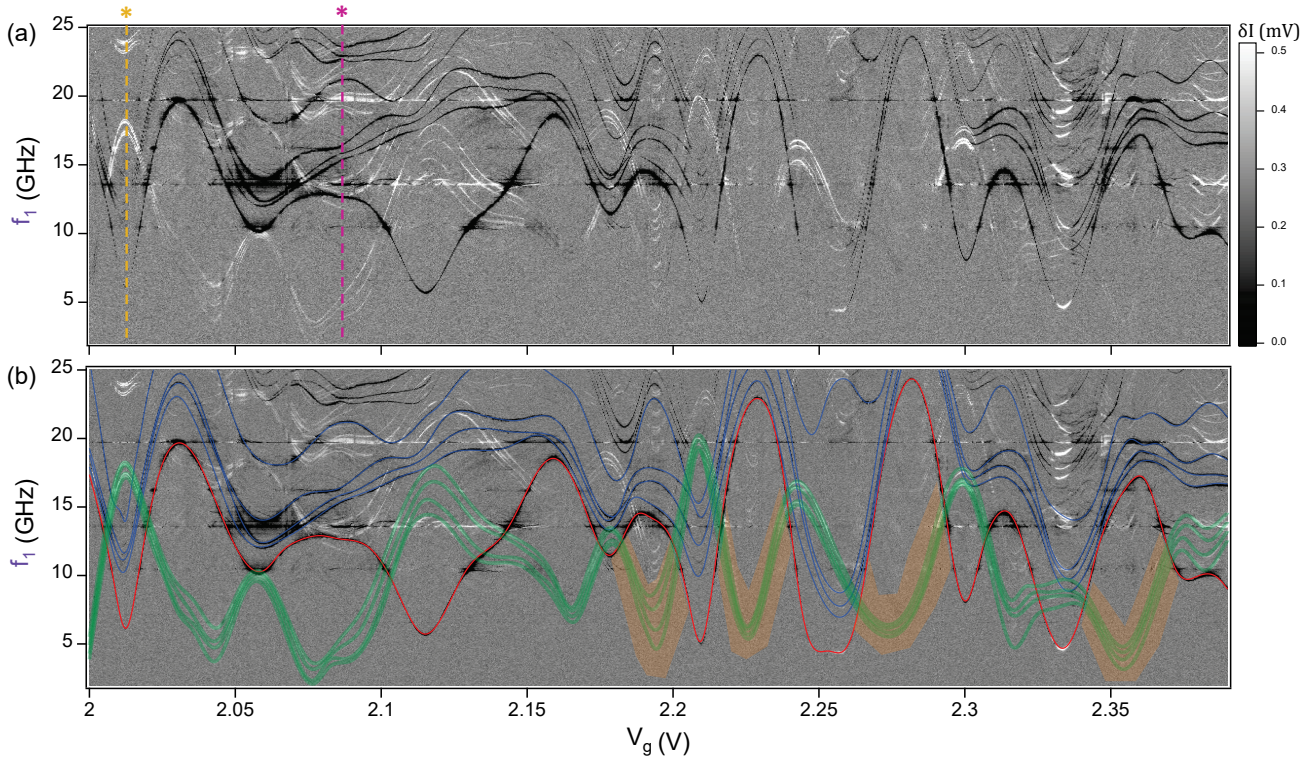


**Figure 7.2:** Evolution of the low-energy spectrum over a wide gate voltage region. (a) Two-tone spectrum showing in gray-scale one quadrature of the measurement field as a function of $V_g$ and taken at $\delta = 0.79\pi$ to reveal the splitting of the SQPT away from the $\pi$-degeneracies. (b) Same spectrum but with the main lines highlighted: the lower PT (red), the lowest set of SQPTs (green) and the four unidentified lines (blue), interpreted as mixed PTs between the two lowest ABS. As expected, PT and SQPTs evolve with $V_g$ in an out-of-phase manner: when the PT exhibits local maxima (minima) in $V_g$, then the bundle of SQPTs shows local minima (maxima). As they shift the resonator in opposite manners, SQPT lines therefore appear as white lines, while pair processes give rise to rather black lines. The four blue lines evolve more or less parallel with $V_g$ and follow the same global trend as the PT, which indicates that they may be associated to processes involving pairs of quasiparticles. In some gate voltage regions, indicated by light orange areas, the line contrast vanishes for SQPTs as they drop to low frequencies. This makes the line tracking unreliable and therefore the highlighted splines in these specific regions should be taken only as illustrative not quantitative, as some liberty was taken when drawing them. For this reason, they were also drawn with much thicker lines to stress the inherent uncertainty in their precise location. The two-tone spectrum shown in Figure 7.3 was taken at $V_g = 2.012$ V, highlighted by a dashed orange like and an asterisk. As for the spectrum from Figure 7.4, it was taken at $V_g = 2.087$ V which is highlighted by a magenta asterisk.

Strikingly, it is observed that close to $\delta = \pi$, these four lines are well approximated by $f_A(\delta)/2$ plus a constant energy offset, with $f_A$ the transition energy of the pair transition. This is illustrated in Figure 7.1(b), where the dashed red lines were obtained as $f_A/2$+offset. This is also observed for the blue lines in Figure 10.5. This tends to indicate that those lines may be associated to mixed processes involving the creation of one quasiparticle in the lowest ABS doublet and another quasiparticle in a level that disperses only little with $\delta$. As we shall demonstrate in the next chapter, these transition lines can be attributed to the expected mixed PTs involving the lowest two ABS doublets, with their degeneracies at $\delta = 0, \pi$ being lifted due to Coulomb interactions.

In Appendix K, we present a collection of two-tone spectra that have been measured on sample S2 in many different conditions. Most of them share the same common characteristics at low frequencies as Figure 7.1(a), including a PT, one or severals sets of SQPTs and four other lines similar to PTs that run more or less parallel as phase is varied and that are interpreted as mixed PTs involving the lowest two ABS manifolds.

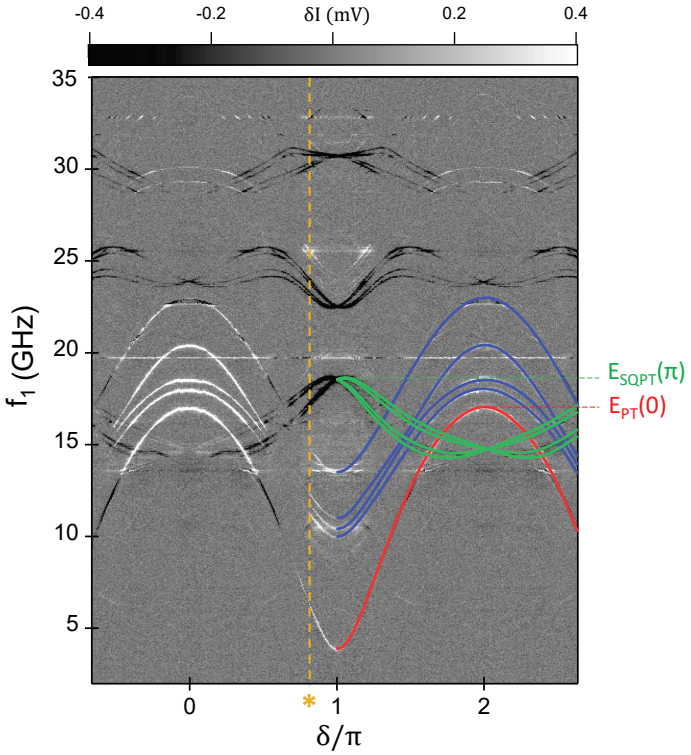


**Figure 7.3:** Spectrum measured at $V_g = 2.012$ V (orange asterisk in Figure 7.2(a); reciprocally, we highlight here with the same asterisk the phase value $\delta = 0.79\pi$ at which the gate map from Figure 7.2 was measured). Main transition lines are highlighted by colored splines on half of the plot: a PT (red), a set of four SQPTs (green) and four unidentified lines (blue) sharing some similarity with PTs transitions. Two other sets of SQPTs are visible at higher frequencies. The PT can be well fitted by the short junction formula with $\tau = 0.9486$ and $\Delta_{\text{eff}} = 8.6$ GHz. As a remarkable feature of this spectrum, the energy $E_{\text{SQPT}}$ at $\delta = \pi$ of the lowest bundle of SQPTs is higher than the energy $E_{\text{PT}}$ at $\delta = 0$ of the lowest PT.

## 7.2 Incorporating multi-channel effects

### 7.2.1 Hint of a second channel

In Figure 7.3 another two-tone spectrum measured on sample S2 is presented, measured at the gate voltage value indicated by an orange asterisk in Figure 7.2(a). This spectrum illustrates another instance of these four unidentified lines (blue) sitting above the low-lying PT (red). Here, the four blue rather show a more regular phase dispersion close to $\delta = 0$. However, sweeping $V_g$, we observe that at another close-by value of the gate voltage, indicated by a magenta asterisk in Figure 7.2(a), they show again a phase dispersion similar to the one from Figure 7.1(a), see Figure 7.4: the upper line is separated from the other three by a few GHz and presents a "camelback"-like dispersion around $\delta = 0$. This clear separation of the four transition lines into a triplet and singlet is observed in all three spectra from Figures (7.1, 7.3, 7.4) and is reminiscent of an exchange interaction effect, as will be further explained in Chapter 8.

As a remarkable feature of the spectrum from Figure 7.3, the energy $E_{\text{SQPT}}$ at $\delta = \pi$ of the lowest bundle of SQPTs is observed to be higher than the energy $E_{\text{PT}}$ at $\delta = 0$ of the lowest PT. Such an ordering is not compatible with the predictions of the minimal two-band model of Chapter 3.2, indicating that another effect is at play.

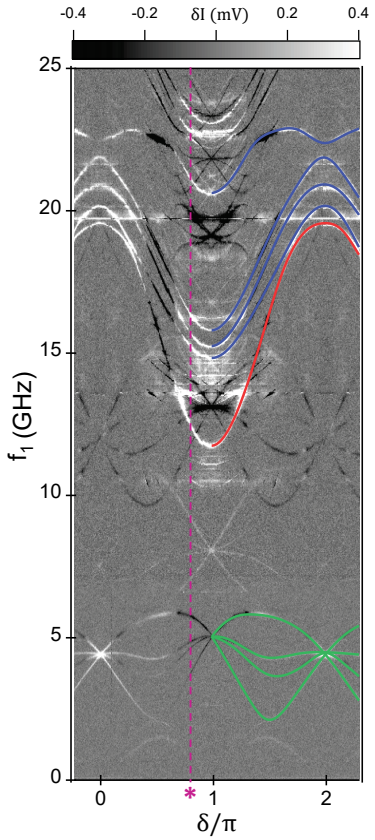


**Figure 7.4:** Two-tone spectrum measured at $V_g = 2.087$ V (magenta asterisk in Figure 7.2(a); Reciprocally, the same asterisk highlights in this plot the phase value $\delta = 0.79\pi$ at which the gate map from Figure 7.2 was measured). This spectrum is the same as in Figure 6.17 but extends to higher frequency. Full data is shown in Appendix K.

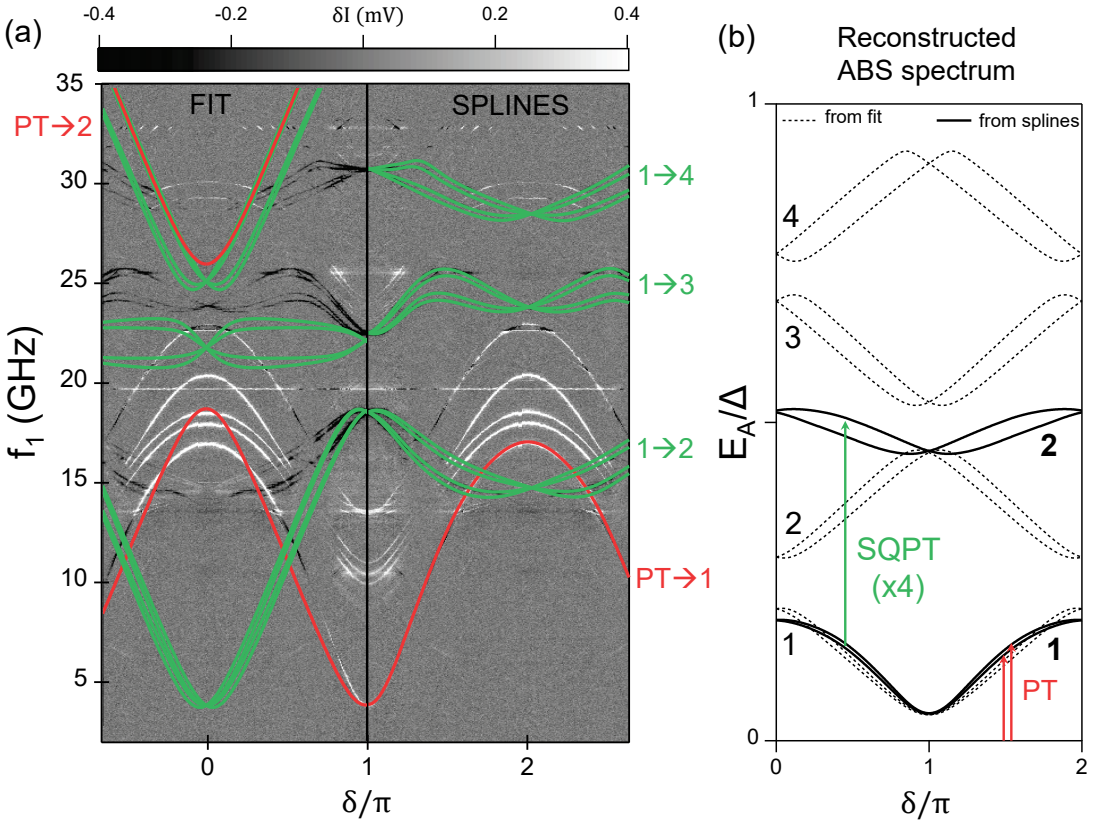


**Figure 7.5:** Hint of multichannel effects. (a) Same spectrum as in Figure 7.3 with the main features highlighted with splines on the right half of the plot : the lower PT (red) and three bundles of SQPTs (green) likely associated to transitions from the first to the second, third and fourth ABS manifolds. On the left half is overlaid the result of a tentative fit with the transcendental equation given by Eq. (3.12) with the following parameters adjusted to best reproduce the lower PT : $\lambda_1 = 5.0$, $\lambda_2 = 5.5$, $\tau = 0.93$ and $x_r = 1.0$. The topmost red line, showing the dispersion expected for the PT to the second ABS manifold, does not seem to correspond to any feature in the data. (b) Associated ABS spectrum in the excitation picture, obtained either from the PT fit with the transcendental equation (dashed lines) or reconstructed for the lowest two manifolds from the measured phase dispersion of the lowest PT and SQPT (solid lines).

Discrepancies with this model are made clearer when trying to fit the PT using the transcendental equation given by Eq. (3.12) (see left half of Figure 7.5(a)). Reproducing well the bottom of the phase dispersion at $\delta = \pi$ requires to set the transmission rather high, $\tau = 0.93$, but doing so we miss the rounded shape of the PT around $\delta = 0$ and the fit remains off by a few GHz even. The ABS spectrum that comes out of this fit comprises four manifolds with alternating curvatures, as illustrated in dashed lines in Figure 7.5(b) using the excitation picture. The two-tone spectrum features three bundles of SQPTs at around 18.5, 22.5 and 30.8 GHz at $\delta = \pi$. Although their respective shapes is not well reproduced, the tentative fit suggests that they likely correspond to SQPT transitions from the first to either the second, the third or the fourth ABS manifold, therefore supporting a long-junction scenario with at least 4 manifolds. The SQPTs between the lowest two manifolds that are expected from the fit fall at the right frequency at $\delta = \pi$, but are about 12 GHz too low at $\delta = 0$, showing a much bigger amplitude compared to what is observed in the data. To improve the match, one would need to reduce the energy of the first manifold around $\delta = 0$, but this would in turn reduce the phase dispersion of the PT and be incompatible with the data, or to increase the energy of the second manifold.

One can actually play the reverse game and reconstruct the lowest two manifolds from the measured dispersion of the lowest PT and SQPT, the mean energy of the first manifold being given by half the frequency dispersion of the measured PT, while differences between the inner and outer lines of the SQPT bundle provide the size of the ABS splitting. The deduced ABS spectrum is plotted in thick solid lines in Figure 7.5(b) and shows an unusual feature : both manifolds have a positive phase curvature around $\delta = \pi$, a feature not accountable by the continuum model which assumes that the chemical potential crosses only a single band. Precisely, this is because such feature actually suggests the presence of a second conduction channel being open in the weak link, meaning that at least two transverse bands are populated in the semiconductor. Unfortunately, none of the analytical models developed so far take explicitly into account such a second band. We may however gain valuable insight on what happens in such a regime by resorting to tight binding simulations, for which it is easy to incorporate finite-length and multi-channel effects.

### 7.2.2 Tight binding modeling

The continuum model presented in Chapter 3.2 focused on a single-band description of the weak link[†]. Extending this analytical model to a multi-band scenario presents some challenging difficulties. On the other hand, it is straight-forward to discretize it in a tight-binding model (TB), which can be adapted at will and solved numerically. In such a model, illustrated with Figure 7.6, the weak link region is described by a chain of longitudinal sites between which electrons can hop. Including many longitudinal sites therefore allows to easily model the case of a finite-length weak link. Similarly, one can add extra transverse chains of sites, which then directly accounts for the multi-channel nature of the weak link.

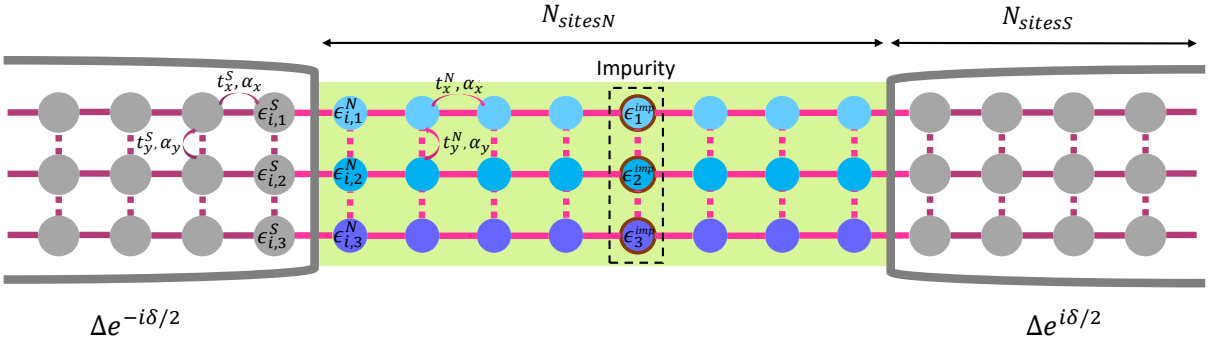


**Figure 7.6:** Sketch of the extended tight-binding models for a nanowire junction.

The TB Hamiltonian of this system can be written in full generality as

$$\begin{aligned} H_0 = & \sum_{i,\tau,\sigma} (\epsilon_{i,\tau} - \mu) c^\dagger_{i,\tau,\sigma} c_{i,\tau,\sigma} + t_x c^\dagger_{i,\tau,\sigma} c_{i+1,\tau,\sigma} \\ & + \sigma \alpha_x c^\dagger_{i,\tau,\sigma} c_{i+1,\tau,\bar{\sigma}} + \sum_{i,\tau} \Delta_i c_{i,\tau,\downarrow} c_{i,\tau,\uparrow} \\ & + \sum_{i,\tau,\sigma} t_y c^\dagger_{i,\tau,\sigma} c_{i,\tau+1,\sigma} + i\alpha_y c^\dagger_{i,\tau,\sigma} c_{i,\tau+1,\bar{\sigma}} + \text{h.c.}\,, \end{aligned} \tag{7.1}$$

[†] At least 2 transverse bands are required so that SOI gives rise to spin-dependent Fermi velocities and ABS spin splitting. However the deduced transcendental equation only describes the case where the chemical potential $\mu$ crosses a single band. It also enforces linearization around $\mu$, which may not be valid when $\mu$ lies at the bottom of a band.

where $c^{\dagger}_{i,\tau,\sigma}$ creates an electron with pseudospin $\sigma$ on the longitudinal site $i$ belonging to the transverse chain $\tau$ ; $\epsilon_{i,\tau}$ denotes the onsite potential, $\mu$ the chemical potential which is only changed in the normal region, $t_{x,y}$ and $\alpha_{x,y}$ are spin-conserving and spin-flip hopping amplitudes in the longitudinal and transverse direction respectively, and $\Delta_i$ is the pairing amplitude which we choose to be zero for the sites describing the wire and $\Delta e^{\pm i\delta/2}$ for the left and right superconducting electrodes, respectively. To incorporate the effect of scattering, we proceed as in the single-barrier model introduced in Chapter 3.2 by adding a local impurity at a given site $i$. This amounts to choosing at this specific site a different onsite energy $\epsilon^{\text{imp}}_{i,\tau}$ compared to the bulk one $\epsilon_{i,\tau}$. Note that such a *single-barrier* model gives qualitatively similar results to a more physical *two-barrier* model where scatterers are localized at the two interfaces with the superconducting leads, as was the case in the continuum model.

The parameters for the TB model are related to the ones from the continuous Hamiltonian through the following discretization:

$$t_x = \frac{t_0}{a^2}, t_y = \frac{t_0}{W^2};\ \alpha_x = \frac{\alpha}{a}, \alpha_y = \frac{\alpha}{W} \quad \text{with } t_0 = \frac{\hbar^2}{2m^*},$$

where $a$ is the lattice spacing in the $x$-direction, $W$ the width of the normal region and $\alpha \sim 10-30$ meV.nm is the spin-orbit coupling constant appropriate for InAs. In the following, we use $\alpha = 12$ meV.nm, $m^* = 0.023m_e$ and $\Delta = 190$ $\mu$eV. In Appendix C, we illustrate the dispersion of the two lowest energy bands associated to this TB Hamiltonian and detail how transverse spin-orbit coupling gives rise to an energy-dependent spin texture responsible for the splitting of ABSs.

### Chemical potential dependence of ABS

The continuum model from Chapter 3.2 describes well the case where a single band is crossed by the chemical potential $\mu$, when it lies far above the band bottom. This situation leads to analytical results after linearization of the bands around $\mu$. As a first generalization, we are interested in what happens both in low-density regime when $\mu$ approaches the band bottom, and conversely when $\mu$ increases and gets close to or crosses the second band. As this second band also hybridizes with the next one when $\alpha_y \neq 0$, we need to consider at least three chains of sites $\tau \in \{1, 2, 3\}$ to incorporate the third band and treat well the effect of the second one.

In Figure 7.7(a-c), we show a typical ABS energy spectrum for $\delta = 0, \pi/2$ and $\pi$ as a function of $\mu$, as obtained by numerical diagonalization of the TB Hamiltonian from Eq. (7.1) with three transverse chains made of 13 sites for the normal region of length $L = 560$ nm and width $W = 100$ nm, and 11 sites in each superconducting lead. The associated bulk bands of the normal region are depicted in panel (d) with the same x- (energy) axis. For simplicity, in order to illustrate the minimal physics at play, we choose the onsite energies to be uniform and constant for all three chains, except at a single site of the normal region where a repulsive impurity is introduced to incorporate the effect of scattering. This is done by setting there a higher onsite energy $\epsilon^{\text{imp}}$.

Starting from the insulating state where $\mu$ lies much lower than the first conduction band, we observe two ABS states detaching from the gap

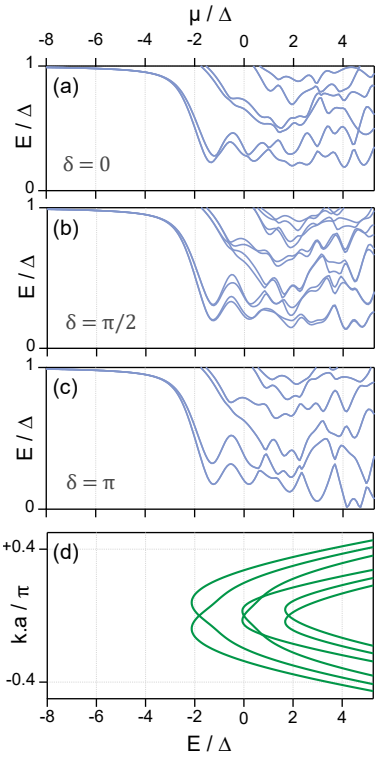


**Figure 7.7:** (a-c) Evolution with the chemical potential $\mu$ of the ABS energy spectrum of a three-channel weak link for $\delta = 0, \pi/2$ and $\pi$, as obtained by numerical diagonalization of the TB Hamiltonian (Eq. (7.1); parameters in Table 7.1). (d) Bulk bands of the normal region.

| | Figure 7.7 | Figure 7.8 | unit |
|---|---|---|---|
| $L =$ | 500 | 560 | nm |
| $W =$ | 90 | 100 | nm |
| $\epsilon_{i\in N,\tau} =$ | 1 | $(1.1, 1.1, 0.8)$ | $2t_0/a^2$ |
| $\epsilon_{7,\tau} =$ | 2 | $(0.8, 0.75, 0.9)$ | $2t_0/a^2$ |
| $\epsilon_{i\in S,\tau} =$ | 1 | 0.95 | $2t_0/a^2$ |
| $t_x^N =$ | $-1$ | $-0.9$ | $t_0/a^2$ |
| $t_x^S =$ | $-1$ | $-1.05$ | $t_0/a^2$ |
| $t_y^N =$ | $-1$ | $-1$ | $t_0/W^2$ |
| $t_y^S =$ | $-1$ | $-1.05$ | $t_0/W^2$ |
| $\alpha =$ | 12 | 12 | meV.nm |

**Table 7.1:** Parameters of the tight-binding calculations for Figure 7.7 and Figure 7.8. The number of transverse chains is 3. The superconducting leads are described with 11 sites each, the normal wire with 13 sites. The impurity is positioned at site 7 in the normal region.

edge $\Delta$ as $\mu$ approaches the bottom of the first band, $\mu \sim -2\Delta$. Although these states are initially spin-degenerate and carry low supercurrent, the amplitude of their phase dispersion increases as $\mu$ rises above the band bottom, as shown in Figure 7.7(a-c). When $\mu \sim -\Delta$, *i.e.* when the chemical potential lies deep in the first band and is higher than the band bottom by at least $\Delta$, the Andreev approximation is verified and we recover the typical situation described by the continuum model. The low-energy spectrum of the weak link then comprises two well-split ABS manifolds that are properly captured by the transcendental equation Eq. (3.12) ‡. As $\mu$ is further increased, a second pair of ABS manifolds detaches from the gap edge. Although those states dive deep in the gap, they initially feature a flat phase dispersion and therefore do not carry any supercurrent. However, for $\mu \sim 0$, when the chemical potential approaches the second band, the two manifolds of this second bundle start to split, disperse with phase and eventually contribute to the low-energy ABS spectrum. The same effect arises when $\mu \sim 2\Delta$, *i.e.* approaches the third band, which reflects the opening of a third conducting channel.

**Fabry-Pérot oscillations & resonant transmission**

Although these TB results illustrate well the gradual opening of the weak link as $\mu$ crosses the successive conduction bands of the normal region, Figure 7.7 also shows a complex non-monotonous dependence of the ABS energy spectrum with $\mu$, characterized by oscillations of the ABS energies with $\mu$. These oscillations of the weak link's effective transmission can be understood as Fabry-Pérot resonances in the normal region, which arise due to the Fermi momentum mismatch between the superconducting and normal regions. A minimal model describing this effect is the one of a perfect single mode SNS junction of finite length $L$ [56, 95], which predicts the following expression for the Andreev energies :

$$E_A(\delta) = \pm\Delta\sqrt{1 - \tau^{\text{eff}}(k_0)\sin^2(\delta/2)} \quad \text{with } \tau^{\text{eff}}(k_0) = \frac{1}{1 + \kappa\sin^2(k_0 L)}. \tag{7.2}$$

[56]: Prada et al. (2020), 'From Andreev to Majorana bound states in hybrid superconductor-semiconductor nanowires'

[95]: Cheng and Lutchyn (2012), 'Josephson current through a superconductor/semiconductor-nanowire/superconductor junction'

‡ Note that the transcendental equation would incorrectly predict a diverging number of ABS states as $\mu$ approaches the band bottom, since $\lambda = L/\xi \to \infty$ due to vanishing of the Fermi velocity $v_F$. However the model leading to the transcendental equation is valid only in the Andreev approximation, *i.e.* when $\mu$ lies far above the band bottom. TB calculations show that no such divergence occurs: the states continuously collapse to the gap edge as $\mu$ is lowered.

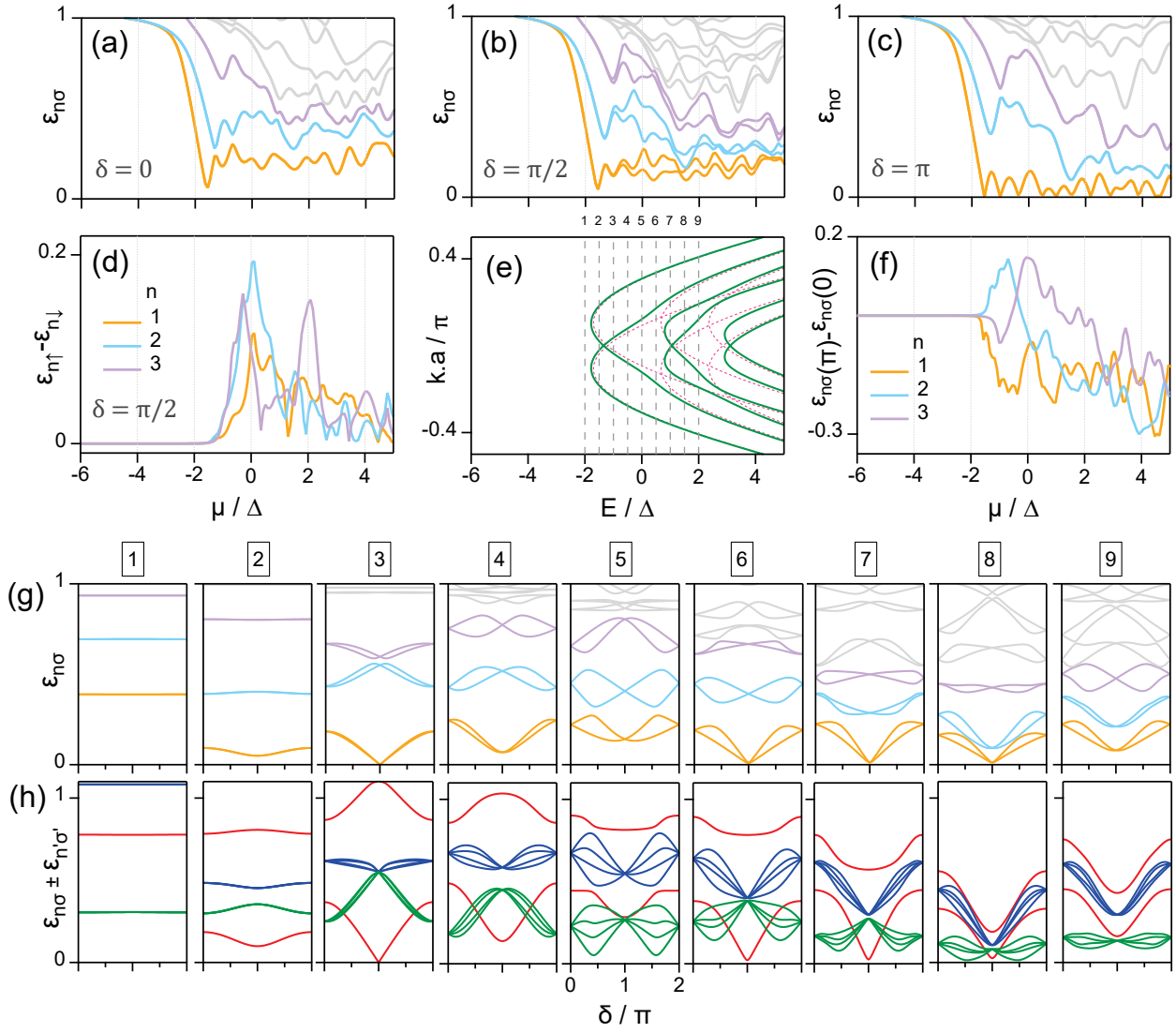


**Figure 7.8:** Evolution of the ABS energy spectrum and transitions with the chemical potential $\mu$, obtained by numerical diagonalization of the TB Hamiltonian from Eq. (7.1; parameters in Table 7.1). The reduced energies $\epsilon_{n\sigma} = E_{n\sigma}/\Delta$ of the ABS states are plotted in panels (a,b,c) as a function of $\mu$ for $\delta = 0, \pi/2$ and $\pi$. Throughout the series, the three lowest Andreev manifolds are highlighted in gold ($n = 1$), cyan ($n = 2$) and purple ($n = 3$). At $\delta \neq 0, \pi$, each state $n$ is spin-split in two sublevels $\sigma = \uparrow, \downarrow$, as exemplified in panel (b) for $\delta = \pi/2$. The intensity of this splitting $\epsilon_{n\uparrow} - \epsilon_{n\downarrow}$ is plotted for the lowest three manifolds $n = 1, 2, 3$ in panel (d) and shows maxima close to the energy where the hybridization of the lowest two bands is the highest. (e) Bulk bands of the normal region (dark green lines). Dashed red lines depict the bands when setting the transverse SO coupling $\alpha_y$ to 0 and illustrate that its effect is to hybridize the transverse subbands. Vertical dashed gray lines correspond to 9 different values of $\mu$ starting from below the first band until deep in the second band. For each of these 9 illustrative cases, the ABS energy spectrum is shown in the excitation picture in (g), with all possible transitions involving the lowest two Andreev manifolds in (h): SQPT transitions (green), PT transitions to the $n = 1$ and $n = 2$ manifolds (red), and the mixed transitions (blue). (f) Evolution with $\mu$ of $\epsilon_n(\delta = \pi) - \epsilon_n(\delta = 0)$, which reflects the sign of the phase curvature of ABS manifold $n$.

where $\kappa = [(k_F^S)^2 - k_0^2]/(2k_F^S k_0)$ models the effect of momentum mismatch between the normal and superconducting regions, the Fermi wavevectors of which being denoted respectively by $k_F^N$ and $k_F^S$, with $k_0 = \sqrt{(k_F^N)^2 + 4k_{SO}^2}$ and the SO momentum $k_{SO} = m^*\alpha/\hbar^2$. This minimal model shows that the $k_F$ mismatch acts as an effective barrier at each interface with transmission $\tau^{\text{eff}}(k_0) = \frac{1}{1+\kappa \sin^2 k_0 L} \leq 1$. Therefore, although no scattering takes place in the normal region, the weak link acquires a finite transmission which oscillates with $k_0$ and remains smaller than 1, except at resonant values where $k_0 L = n\pi$, $n \in \mathbb{Z}$. In the general case, scattering and spin-orbit in the normal region further mix this

simple picture, making the oscillations less regular and one can no longer distinguish in the ABS spectrum the contributions from each individual channel as bundles of state detaching from the gap edge when $\mu$ approaches the next band.

**Effect of a second transverse channel**

Using this TB model, let us now investigate the two-bands limit when the chemical potential lies close to the second transverse band, reflecting the opening of a second conduction channel in the weak link. This second situation is illustrated in Figure 7.8(g-h) where we show, for slightly different TB parameters than in Figure 7.7, the evolution of a typical ABS spectrum (g) and the associated transitions between ABS (h) for 9 values of $\mu$ crossing successively the first and second transverse conduction bands of the normal region.

Case 1 corresponds to the tunnel regime where the chemical potential $\mu$ lies below the first band: the ABS levels show almost flat phase dispersions. As $\mu$ crosses the bottom of the lowest band, they start acquiring a sizeable phase dispersion and carry supercurrent, as illustrated in Cases 2 and 3. For $\mu$ deep in the lowest band (Case 4), *i.e.* higher than the band bottom by at least $\Delta$, the Andreev approximation is verified and we recover the typical situation described by the transcendental equation from the continuum model (Eq. (3.12)). The corresponding transition spectrum in (h) shows opposite phase curvature for the PTs associated to the $n = 1$ and $n = 2$ manifolds (red), a bundle of well-split SQPT lines (green) crossing the lower PT and with a maximum at $\delta = \pi$, and a bundle of mixed PTs (blue) sandwiched between the two lowest PTs. This corresponds qualitatively to the typical picture described in Chapters 3.2 and 6. When $\mu \sim 0$, close to the energy where the hybridization between the lowest two bands is maximal (Case 5), the Fermi velocity difference between the two $n = 1$ spin subbands is maximal and the transition spectrum shows large splitting for both the SQPTs and the mixed PTs. Finally, as $\mu$ approaches the second band (Cases 6-9), the phase curvature of the PT to the $n = 2$ manifold gets inverted, which reflects the opening of a second channel in the weak link. This inversion is further illustrated in panel (f) where we plot as a function of $\mu$ the quantity $\epsilon_n(\delta = \pi) - \epsilon_n(\delta = 0)$ which describes the sign and magnitude of the phase curvature of a given ABS manifold $n$. While this curvature is always negative for the lowest manifold (gold), for the second one (cyan) it goes from positive to negative, canceling close to $\mu = 0$ (Case 5).

The cases 6-7, where $\mu$ lies close to the bottom of the second transverse band, seem to correspond qualitatively to the situations probed in the experimental spectra from Figs 7.1,7.3 and 7.4. Indeed, the transition spectrum in such a regime is characterized by mixed PTs at low energy lying close to the lower PT and by an almost flat phase dispersion for the $n = 2$ ABS manifold. As will be shown in the next chapter, this explains why the mixed pair transition disperse almost like half the lowest PT.

# ABS in presence of Coulomb interactions

# 8



*There is a large overlap between this chapter and our most recent article [54]. The theoretical developments that we reproduce here are essentially due to our colleagues in Madrid Francisco Matute, Sunghun Park and Alfredo Levy Yeyati.*

In the previous chapter, we presented microwave spectra showing features consistent with finite-length physics in the weak link and suggesting a multi-channel scenario. In addition, we evidenced as a recurring feature of our nanowire spectra a set of four transition lines lying above the lowest pair transition, which remain grouped together as $\delta$ or $V_g$ is changed, never cross each other, and feature a minimum at $\delta = \pi$ like pair transitions although they show more complex patterns close to $\delta = 0, 2\pi$. Besides, they often split spectrally into a low-lying triplet of lines and a singlet at higher frequency.

Surprisingly, we also noticed that the phase dispersion of those four lines appears to be generally well fit close to $\delta = \pi$ by half the dispersion of the lowest pair transition up to a frequency offset, thus indicating that they are likely related to processes involving the creation of one quasiparticle in the lowest ABS manifold and a second one into another spin-split level dispersing only little close to $\delta = \pi$. Because they appear above but still close to the lowest PT, this level is expected to be low-lying, and as it does disperse with phase, although little, there is no reason at first sight why it should be anything than an ABS, in the view of parsimony. On the other hand, we evidenced with a TB calculation in Section 7.2.2 that when a second channel is about to open, the second lowest ABS manifold may indeed show almost flat dispersion around $\delta = \pi$, up to its splitting, which makes it a possible candidate for this level.

Altogether, this gives hints that those four unidentified transition lines may correspond to mixed PTs involving the lowest two ABS manifolds, although they do not show degeneracies at $\delta = 0, \pi$ as one would first expect from non-interacting models. The recurring separation of those lines into a triplet and singlet further suggests that an exchange-interaction physics may be at play, and we shall now demonstrate that the weak Coulomb interactions expected in our nanowires actually result in a sizable splitting of the mixed PTs into a group of four lines, which disperse in phase similarly to the transition lines evidenced experimentally.

To discuss the effect of interactions we will resort in this chapter to different models ranging from *minimal* ones, which can be solved exactly, to an extended tight-binding model compared to the one from Chapter 7, where the effect of interactions is introduced in a perturbative fashion. As we will see, this extended model allows to predict spectra that have a close resemblance to those obtained in the measurements.

[54]: Cañadas et al. (2021), 'Signatures of interactions in the Andreev spectrum of nanowire Josephson junctions'

## 8.1 Modeling the effect of Coulomb interactions

### 8.1.1 Estimations on e-e interactions and their effect

Coulomb interactions in the nanowire weak link are expected to be strongly screened by the nearby metallic electrodes, by free charges in the nanowire and by the substrate. They can thus be approximated by a contact potential

$$\hat{V} = \frac{1}{2}\sum_{\sigma,\sigma'}\int_{\mathrm{WL}} d\mathbf{r}d\mathbf{r}'\Psi^{\dagger}_{\sigma}(\mathbf{r})\Psi^{\dagger}_{\sigma'}(\mathbf{r}')u(\mathbf{r}-\mathbf{r}')\Psi_{\sigma'}(\mathbf{r}')\Psi_{\sigma}(\mathbf{r}), \tag{8.1}$$

where $u(\mathbf{r}-\mathbf{r}') = u_0\delta(\mathbf{r}-\mathbf{r}')$ is non-zero only for $\mathbf{r}, \mathbf{r}'$ in the junction region and $\Psi_\sigma(\mathbf{r})$ are the field operators for electrons with pseudospin $\sigma$ in the wire. The typical junction dimensions (length $L \sim 500$ nm and diameter $W \sim 150$ nm) and the fact that a few conduction channels might be contributing to transport suggest that a 3D screening model should be appropriate. Within a Thomas-Fermi (TF) approximation we have $u(\vec{r}) \sim e^{-|\vec{r}|/\lambda_{\mathrm{TF}}}/|\vec{r}|$, where $\lambda_{\mathrm{TF}}$ is the screening length and thus

$$u_0^{3D} = \frac{e^2}{4\pi\epsilon_0\epsilon_r}4\pi\int_0^{\infty} dr r^2\frac{e^{-r/\lambda_{\mathrm{TF}}}}{r} = \frac{e^2}{4\pi\epsilon_0\epsilon_r}4\pi\lambda_{\mathrm{TF}}^2. \tag{8.2}$$

On the other hand, the TF screening length can be estimated as

$$\lambda_{\mathrm{TF}}^2 = \epsilon_0\epsilon_r/(e^2\rho_F) = \frac{a_B}{8}\frac{m_e}{m^*}\epsilon_r\lambda_F, \tag{8.3}$$

where $\rho_F = (2m^*/\hbar^2)^{3/2}\sqrt{E_F}/(2\pi^2)$ is the 3D density of states with $E_F$ the Fermi energy, $a_B = 4\pi\epsilon_0\hbar^2/(m_e e^2) \sim 0.05$ nm the Bohr radius, $\lambda_F$ the Fermi wavelength and $\epsilon_r \sim 15$ the dielectric constant of InAs. As the data presented in the previous chapter suggest, $\lambda_F$ should correspond to a situation where a second subband starts to be populated, i.e. $\lambda_F \sim W \sim 100$ nm, which gives $\lambda_{\mathrm{TF}} \sim 20$ nm using Eq. (8.3). Thus, as $\lambda_{\mathrm{TF}} \ll W$, a 3D model is indeed justified. In our TB calculations however, the wire was modeled as a planar quasi-1D geometry. This 2D $u_0$ can be deduced by $u_0 = u_0^{3D}/W$. From Eq. (8.2), we estimate the $u_0$ parameter relevant for our galvanic coupling device (see Figure 10.1(b)) to be of the order of $u_0 \sim 3$ eV.nm$^2$, a value similar to what was estimated in Ref. [96].

Some insight on the effect of interactions on the energy of Andreev excitations can be obtained by considering the random matrix theory analysis of Ref. [97] for an isolated mesoscopic grain. In that work it was shown that an interaction as in Eq. (8.1) leads to an effective exchange interaction $-J\vec{S}^2$, where with $\vec{S}$ is the total spin and $J \sim 2u_0/A$, $A$ being the area where the states are localized, which is of the order of 0.1 $\mu$m$^2$ in our experiments; leading to $J \sim 60$ $\mu$eV (*i.e.* ~10 GHz). As suggested in Ref. [98], such an interaction would lead to a splitting of the bundle of four mixed pair transitions at $\delta = 0$ into a degenerate triplet at lower energy and a singlet state lying roughly $2J$ above. This rough analysis is in agreement with the splitting into a triplet and a singlet seen in the spectra of Figs. (7.1,7.3,7.4), but it fails in explaining the breaking of the degeneracy of the triplet lines.

[96]: Manolescu et al. (2014), 'Coulomb interaction effects on the Majorana states in quantum wires'

[97]: Kurland et al. (2000), 'Mesoscopic magnetization fluctuations for metallic grains close to the Stoner instability'

[98]: Padurariu and Nazarov (2012), 'Spin blockade qubit in a superconducting junction'

### 8.1.2 Exactly solvable four-sites TB model

The TB Hamiltonian introduced in the previous chapter can be adapted to include the effect of interactions in the central normal region $N$ by adding in Eq. (7.1) a Hubbard-like term $H_{\text{int}} = \sum_{i\in N,\tau} U_i n_{i,\tau,\uparrow} n_{i,\tau,\downarrow}$, while assuming perfect screening in the superconducting regions. Here, $n_{i,\tau,\sigma} = c^\dagger_{i,\tau,\sigma} c_{i,\tau,\sigma}$ represents the number of electrons with pseudospin $\sigma$ on the site $(i,\tau)$. As was done in Section (7.2.2), discretizing the continuous model and setting a given value $a_{x,y}$ for the lattice spacings in the $x, y$ directions allows to get estimates for the model parameters appropriate for InAs wires coupled to Al leads. Similarly, the $U_i$ value, taken for simplicity as a constant $U$ in the normal region, can be related to the above $u_0$ estimate by $U \sim u_0/(a_x a_y)$. To make contact with the standard jargon commonly used to describe charging effect in nanostructures, one can also define here an *effective* charging energy of the normal region when disconnected from the leads $E_c^{\text{eff}}{=}u_0/A_N$, where $A_N$ denotes its area.

Unfortunately, this TB model cannot in general be solved exactly in the presence of interactions. In Refs. [64, 50], the nanowire weak link is described in terms of a quantum dot (QD) coupled to two superconducting leads, which amounts to taking a single site in the normal region, with adjustable couplings to the superconducting leads. Such a situation is generally analyzed in the literature by means of an Anderson model where a *single* level with Hubbard-like interaction is connected to the leads. Although this allows to account for some of the observed effects [50], it is not able to describe the experimental situation tackled in the present work, where at least two spin-split ABS manifolds are necessary to account for the experimental data. In addition, the coupling of transverse modes due to spin-orbit interactions is essential to explain the splitting of SQPTs, as already commented in the previous chapter. In order to incorporate both the finite-length and multi-channel ingredients, a minimal model includes 2 sites both in the longitudinal and transverse directions. We therefore restrict the normal region of our TB model to four sites only, two in the longitudinal direction and two in the transverse one.

[64]: Kurilovich et al. (2021), 'Microwave response of an Andreev bound state'
[50]: Fatemi et al. (2021), 'Microwave susceptibility observation of interacting many-body Andreev states'

[50]: Fatemi et al. (2021), 'Microwave susceptibility observation of interacting many-body Andreev states'

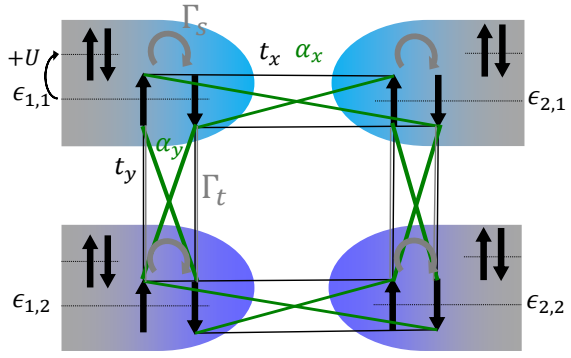


**Figure 8.1:** Sketch of the four-sites tight-binding model. The grey shading represents the effect of the superconducting leads projected into each site. This is achieved through the effective singlet and triplet pairings $\Gamma_s$ and $\Gamma_t$ (grey arrows and lines) between electrons (thick, black arrows), which have onsite energy $\epsilon_{i,\tau}$. Other lines depict the spin conserving (thin black) and spin flipping (thin green) hoppings. Finally, the interaction is represented with the gain in energy $+U$ when a site is occupied with two electrons.

To include the superconducting leads in a simplified manner, one can take the infinite gap limit* $\Delta_i \to \infty$, as suggested in several works on the superconducting Anderson model [99, 100]. By projecting the effect of the superconducting pairing in the leads into the central four sites (denoted by $\alpha = L, R$ (left,right) and $\tau = \pm$ (top, bottom)), the infinite system is mapped onto a simple "superconducting molecule" with a finite number of electronic configurations and can be diagonalized exactly†. One obtains the following effective pairing model :

$$H_{\text{pairing}} = \sum_{\alpha,\tau=\pm} \Gamma_{s,\alpha} c^\dagger_{\alpha,\tau,\uparrow} c^\dagger_{\alpha,\tau,\downarrow} + i \sum_{\alpha} \Gamma_{t,\alpha} \left( c^\dagger_{\alpha,+,\uparrow} c^\dagger_{\alpha,-,\uparrow} - c^\dagger_{\alpha,+,\downarrow} c^\dagger_{\alpha,-,\downarrow} \right) + \text{h.c.}, \tag{8.4}$$

where $\Gamma_{s,\alpha}$ and $\Gamma_{t,\alpha}$ are effective singlet and triplet pairing amplitudes for the $\alpha$=$L, R$ sites arising from the combination of s-wave pairing and spin-orbit interactions in the multi-channel leads. A sketch of such an effective model is provided in Figure 8.1.

While in the single-level model the infinite gap limit leads to an induced local singlet pairing in the dot, for the case of the multi-channel spin-orbit coupled lead one expects *both* local singlet *and* non-local triplet pairings to be induced on the central region, the amplitude of which being indicated here by $\Gamma_s$ and $\Gamma_t$. Obtaining their expressions in terms of the bare model parameters would require the calculation of the leads boundary Green functions [101] in the $\Delta_i \to \infty$ limit. While this calculation could be affordable using the techniques of Ref. [101], in the present work we just consider $\Gamma_{s,t}$ as tunable effective parameters.

### Splitting of the mixed pair transitions

For this minimal four-sites model, the scaling used to determine the parameters in Eq. (7.1) is not expected to hold. However, setting reasonable parameters (*e.g.* $\epsilon_{i,\tau}/2$=$\Gamma_s$=$-t_x$=$-t_y$ and $\Gamma_t$=$\alpha_x$=$\alpha_y$=$0.8\Gamma_s$), we get the typical results shown in Figure 8.2. As expected from the previous considerations, Coulomb interactions do lift the degeneracies of the mixed pair transitions at $\delta = 0$ and $\pi$. Moreover, in contrast to the simple argument based on the emergent exchange interaction, which splits the transition lines into triplet and singlet [98], we observe here a complete splitting of the four lines, as illustrated in Figure 8.2(b). This is due to the presence of a significant spin-orbit interaction which breaks spin symmetry.

[99]: Vecino et al. (2003), 'Josephson current through a correlated quantum level'
[100]: Meng et al. (2009), 'Self-consistent description of Andreev bound states in Josephson quantum dot devices'

[101]: Alvarado et al. (2020), 'Boundary Green's function approach for spinful single-channel and multichannel Majorana nanowires'

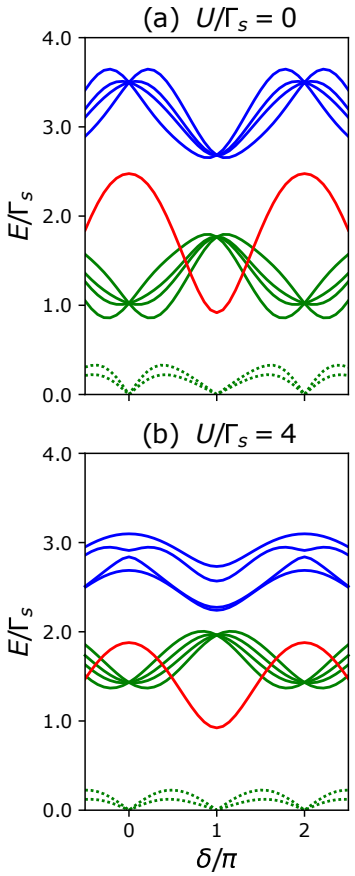


**Figure 8.2:** Transition lines within the four-site model without (a) and with (b) the effect of Coulomb interactions. Within this model effective singlet and triplet pairing, characterized by parameters $\Gamma_s$ and $\Gamma_t$, arise by assuming $\Delta \to \infty$ in the leads.

* For finite $\Delta$, the weak link region is coupled to both the Cooper pairs, which lie at the Fermi level and are responsible for the proximity effect, and to the quasiparticles in the leads, which give rise to conduction electrons excitations with energies higher than the gap. In the large $\Delta \to \infty$ limit, the quasiparticles are far in energy and their coupling to the weak link vanishes, which greatly simplifies the physics and makes an exact solution possible. However, as the weak link is still coupled to the Cooper pairs at the Fermi level, the proximity effect survives, manifesting as induced pairing terms in the central region of the weak link. When considering physics at energies $E \ll \Delta$, the effective Hamiltonian that is obtained gives a qualitatively good description of the behavior of the full model, as will be shown below.

† Although the full four-site model is not quadratic (Eq. (8.4) describes only the pairing terms, but the total Hamiltonian also contains the onsite Hubbard like terms, which are quartic in the fermionic operators), one can perform *numerically* an exact diagonalization.

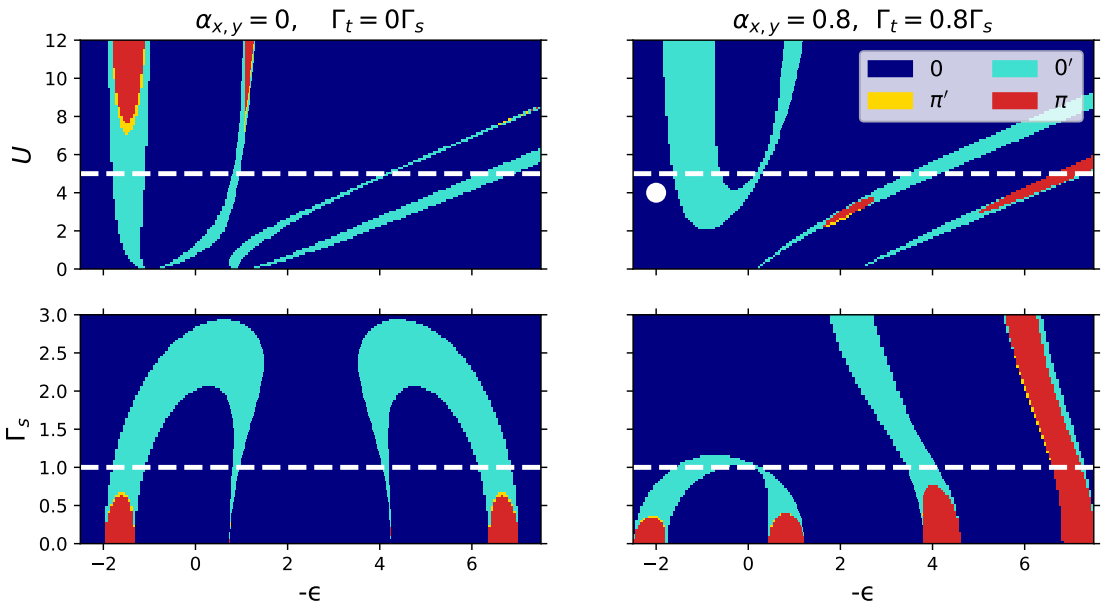


**Figure 8.3:** Phase diagrams of the four-sites model in the $U-\epsilon$ and $\Gamma_s-\epsilon$ planes, with and without SO respectively in the right and left columns. The white dashed lines in the upper (lower) row correspond to the values of $U$ ($\Gamma_s$) used in the lower (upper) row. The white point in the upper right figure corresponds to the parameters used for Fig. 3 in the main text (hopping parameters $t_{x,y}$ are fixed to $-1$).

On the other hand, the inter-manifold SQPT lines do not split at $\delta = 0, \pi$ but are rather shifted to higher energy. This is because these crossings are protected by time reversal symmetry (see Appendix B), which leads to a Kramers degeneracy for odd states even in the presence of interactions. As for the shift to higher energy, it can be understood as a consequence of level repulsion between the lower and upper Andreev manifold when coupled through Coulomb interaction. In contrast, no Kramers degeneracy is granted for even parity excitations, which explains the splitting of the mixed transitions. Finally, notice that the weak link effective charging energy in Figure 8.2(b) is $E_c^{\text{eff}} = U/4 = \Gamma_s$, *i.e.* of the order of the pair transition amplitude, therefore much lower than $\Delta$. Within this interaction range, the ground state parity is expected to remain even, meaning no $0-\pi$ transition.

### Phase diagrams of the four-sites model

To get an idea of the main properties of this model we show in Figure 8.3 phase diagrams for different parameter choices. If the normal region of the nanowire was to become more isolated from the leads, we would expect a QD-like behavior. The most typical feature that arises from the interplay of the superconducting pairing, the Coulomb interaction and the coupling with the leads, is the transition to a $\pi$-junction behaviour where the ground state (GS) changes parity. In Figure 8.3 the colors indicate the phases "0", where the GS is even for any $\delta$ and the absolute minimum is at $\delta$=0 (dark blue); "$\pi$", where the GS is odd for any $\delta$ and the absolute minimum is at $\delta$=$\pi$ (red); and "0'" and "$\pi$'" (bright blue and yellow), which are intermediate phases similar to the previous ones, but where the parity of the GS is not the same for all $\delta$.

The top row shows diagrams in the $U-\epsilon$ plane, where a "0" background develops vertical and diagonal regions with different phase at sufficiently

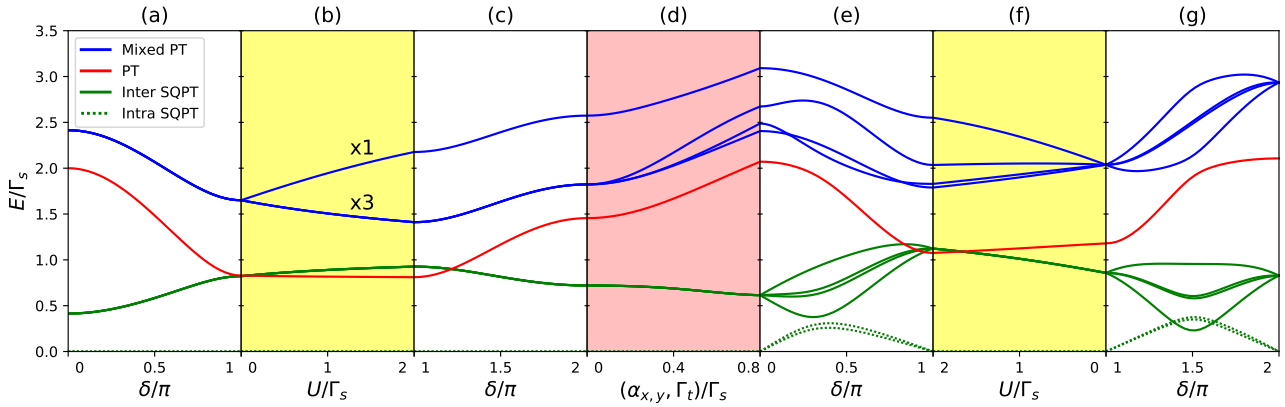


**Figure 8.4:** Evolution of the transitions in the four-sites model with phase difference (white background), SO (pink) and interaction (yellow). From left to right, it starts displaying the evolution in phase difference $\delta$ without SO nor interaction (a), then it includes interactions at $\delta=\pi$ (b), and evolves again in $\delta$ (c). In (d), it includes SO at $\delta=0$, then evolves in $\delta$ (e) and starts removing the interaction at $\delta=\pi$ (f). Finally, in (g) it shows the evolution in $\delta$ with SO but without interaction. Fixed parameters are $\epsilon_{i,\tau}=1.5\Gamma_s$, $t_x=2t_y=-\Gamma_s$. The higher PT to the second manifold is not shown because for these parameters it cannot be distinguished from other mixed PTs involving higher manifolds.

high value of $U$. Their structure is similar to the diagram associated to linear arrays of quantum dots between superconducting leads [102] when the number of dots is 4. As discussed in that reference, for a sufficiently large fixed interaction and weak coupling to the leads, the GS alternates parity as the dots filling increases (i.e. for increasing $-\epsilon$). The figures in the bottom row are diagrams in the $\Gamma_s-\epsilon$ plane, displaying 0′ regions with inverted "U" shapes that connect odd valleys. As can be observed in the right lower panel these regions become distorted when spin-orbit interactions is switched on.

[102]: Bergeret et al. (2007), 'Josephson effect through a quantum dot array'

### Interplay between Rashba spin-orbit & Coulomb interactions

The rich structure of the transition spectrum, characterized by the 4-fold degeneracies at phases $\delta=0$, $\pi$ of the odd transitions and the full splitting of the even ones, emerges from the presence of time reversal symmetry and the combination of spin-orbit coupling with Coulomb interaction. Let us describe progressively how these ingredients affect the ABS energy spectrum. Their consequences on the evolution of the transition lines is summarized in Figure 8.4.

In the situation without spin-orbit nor Coulomb interaction (Figure 8.4(a)), the four ABSs of lowest energy, which correspond to the odd states with 1 quasiparticle, consist of two manifolds, which are spin-degenerate for all $\delta$ (green line). In the even sector, there are 6 states made of 2 quasiparticles: 2 states where both quasiparticles are in the same manifold with opposite spin (they give rise to pair transitions from the ground state, the lowest one being shown in red), and 4 degenerate states where each quasiparticle is in one different manifold (these give rise to mixed pair transitions, shown in blue). When the interaction is introduced (Figure 8.4(b,c)), the odd states remain degenerate, while the mixed even states split into a singlet and a triplet. This behaviour stems from the spin rotational symmetry, encoded in $[H_0+H_{int}, S_i]=0$, since for any state with certain energy and spin, there is another state with the same energy but with rotated spin (same total spin, different spin projection) (Figure 8.4(b,c)).

In the non-interacting situation with spin-orbit (Figure 8.4(g)), relevant for long multi-channel weak links, spin is no longer a good quantum number. This allows for a splitting at almost all values of $\delta$. However, time reversal symmetry imposes some constraints. First, since $\delta$ is $2\pi$-periodic and ultimately originates from a magnetic flux, we have, respectively, $H(\delta+2\pi)=H(\delta)$ and $\mathscr{T}H(\delta)\mathscr{T}^{-1}=H(-\delta)$, so the spectrum over $\delta$ must be mirror-symmetric around $\delta=0,\pi$ (this constraint also applied for the previous situation without SO). Second, since in the odd states there is always at least one unpaired spin and $\mathscr{T}$ reverses it, there must be pairs of odd states with the same energy (Kramers degeneracy), as already discussed in Section B. Mixed even states inherit this degeneracy when no interactions are present, but in presence of interactions, nothing prevents the splitting (Figure 8.4(d-f)).

### 8.1.3 Perturbative resolution of the extended TB model

The four-site model is a minimal one that incorporates the multichannel character and the finite length of the junction while being amenable to exact diagonalization including the Hubbard terms. While it provides insight into the effect of interactions on the subgap states, it is based on the unphysical assumption of an infinite gap in the leads. The calculated energies not being referred to the gap energy, no quantitative comparison with experimental data can be reached. To counter this, we now introduce an extended TB model for which such a comparison becomes possible using realistic values for all the model parameters and that allows, in addition, to take higher energy levels into account.

To go beyond the four-site model, we use the eigenstates of the non-interacting Hamiltonian from Eq. (7.1) to write the interaction Hamiltonian $H_{\text{int}}$ in terms of the Bogoliubov operators $\gamma_n$. This is performed through the inverse Bogoliubov transformation $c_{i,\tau,\sigma} = \sum_{n\geq 1} u^n_{i,\tau,\sigma}\gamma_n + v^{n*}_{i,\tau,\sigma}\gamma^\dagger_n$, where $n\geq 1$ refers to states with positive energy and $(u/v)^n_{i,\tau,\sigma}$ are the (electron/hole)-like coefficients of the non-interacting wavefunctions. Assuming weak interactions, we may project $H_{\text{int}}$ to the subspace of states with zero ($|GS\rangle$), one ($\gamma^\dagger_n|GS\rangle$), and two ($\gamma^\dagger_n\gamma^\dagger_m|GS\rangle$) quasiparticles on the $N_{\text{pr}}$ lowest energy levels (*i.e.* $n, m \leq N_{\text{pr}}$). Due to parity conservation, we end up with effective Hamiltonians in the even and odd sectors that can be diagonalized exactly.

The eigenstates $\Phi_n$ of the non-interacting model are calculated by diagonalizing the corresponding Bogoliubov-de Gennes Hamiltonian

$$H_{BdG}\Phi_n=E_n\Phi_n, \quad H_0=\frac{1}{2}\hat{\Psi}^\dagger H_{BdG}\hat{\Psi}, \tag{8.5}$$

where $\hat{\Psi}=(\hat{c}_{1,1},\hat{c}_{1,2},\hat{c}_{2,1},\hat{c}_{2,2},...)^T$, $\hat{c}_{i,\tau}=(c_{i\tau\uparrow},c_{i\tau\downarrow},c^\dagger_{i\tau\downarrow},-c^\dagger_{i\tau\uparrow})^T$ and we parametrized the eigenstates as $(\Phi_n)_{i\tau}=(u^n_{i\tau\uparrow},u^n_{i\tau\downarrow},v^n_{i\tau\downarrow},-v^n_{i\tau\uparrow})^T$. The quasiparticle operators that diagonalize $H_0$ are related to the eigenvectors by $\gamma_n=\Phi^\dagger_n\hat{\Psi} \leftrightarrow \hat{\Psi}=\sum_n \Phi_n\gamma_n$, and the electron-hole symmetry implicit in the BdG formalism, that relates states with opposite energy ($\gamma^\dagger_n=\gamma_{-n}$, $E_{-n}=-E_n$), allows to write it in terms of the quasiparticle operators of

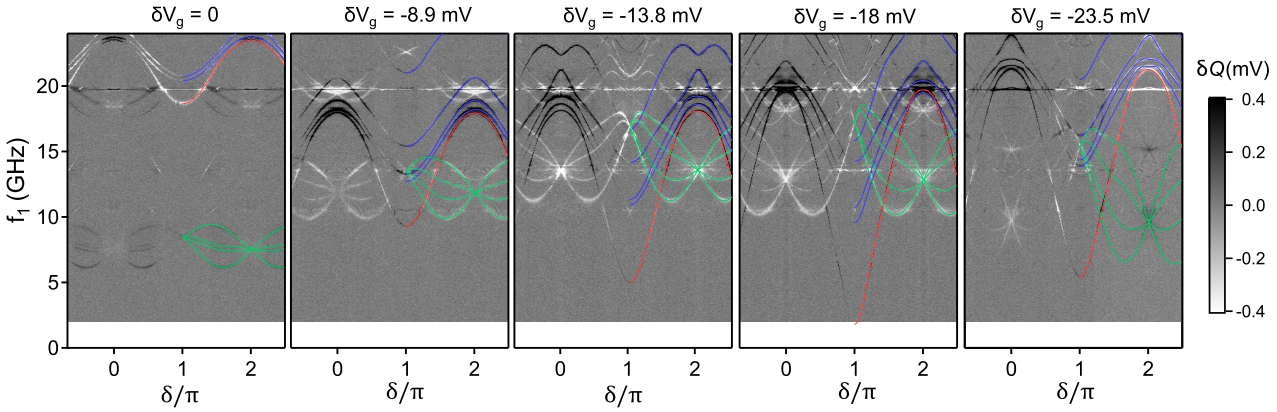


**Figure 8.5:** Experimental results showing microwave two-tone spectra as a function of phase difference ($\delta$) for a sequence of decreasing gate voltages $V_g = 5.563\,\text{V}+\delta V_g$. The gray scale represents the change of one quadrature of the measured signal when the drive signal at $f_1$ is applied. Both measurement and drive tones are applied simultaneously. Each pixel corresponds to averaging over 150 ms. The color lines on the right half of the spectra are guides to the eye indicating what we identify as single-quasiparticle (green), pair (red) and mixed pair (blue) transition lines. Note that a second group of SQPT is visible around 20 GHz; it likely corresponds to single-quasiparticle transitions from the first to the third Andreev doublet (not highlighted here).

states with positive energy:

$$H_0 = E_{GS} + \sum_{n\geq 1} E_n \gamma_n^\dagger \gamma_n, \tag{8.6}$$

where $E_{GS}=1/2\sum_{n\leq -1} E_n$ is the energy of the ground state (GS), in which all states with negative energy are occupied. Thus, quasiparticle excitations over the GS of *e.g.* 1 and 2 quasiparticles are represented by $\gamma_n^\dagger|GS\rangle$ and $\gamma_n^\dagger\gamma_m^\dagger|GS\rangle$ ($n, m\geq 1$), satisfying $\gamma_n|GS\rangle=0$.

Interactions are then introduced by projecting $H_{int}$ into the many-body states with zero (GS), one and two quasiparticles excitations of lowest energy ($n, m\leq N_{pr}$). This requires the calculation of cumbersome expectation values such as $\langle GS|\gamma_{i_2}\gamma_{i_1}\gamma_{n_1}^{(\dagger)}\gamma_{n_2}^{(\dagger)}\gamma_{n_3}^{(\dagger)}\gamma_{n_4}^{(\dagger)}\gamma_{j_1}^\dagger\gamma_{j_2}^\dagger|GS\rangle$, which can be efficiently computed using the `QuantumAlgebra.jl` package [103] written in Julia.

## 8.2 Comparison with experimental data

Let us now demonstrate how this extended TB model can be used to describe complex Andreev spectra measured on sample S2. We concentrate here on a series of microwave two-tone spectra taken successively in a narrow range of gate voltage $V_g$ (see Figure 8.5). Over the series, we recover the same generic features which were observed in the spectra from Figs. 7.1, 7.3, and 7.4‡. Namely, there are groups of four lines, such as the ones highlighted in green, which cross at phase 0 and $\pi$, and are identified as SQPTs. One also finds regular, almost sine-shaped lines, highlighted in red, attributed to PTs. Finally, there are groups of four lines highlighted in blue, behaving similarly to the four unidentified lines discussed in the previous chapter. We show in Figure 8.6 that, like Figure 7.1, the dispersion of the blue lines resembles, close to $\delta = \pi$, half that of the lowest pair transition, plus an offset. The "camel-back"

‡ This series of spectra was measured during a different cooldown of the galvanic coupling sample and therefore cannot be related to the gate evolution shown in Figure 7.2.

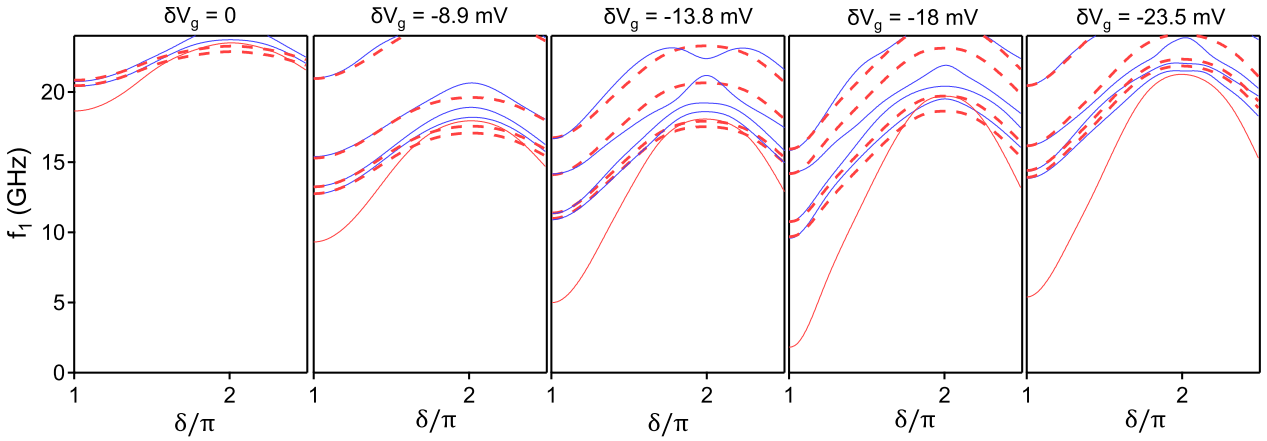


**Figure 8.6:** Evidencing the mixed PT character of the unidentified lines. Red and blue lines are the splines overlying the data in Figure 8.5. Dashed red lines are obtained by taking half the frequency of the red lines, and shifting vertically. This shows that, around $\delta = \pi$, the dispersion of the mixed pair transition has a curvature close to half that of the lowest pair transition.

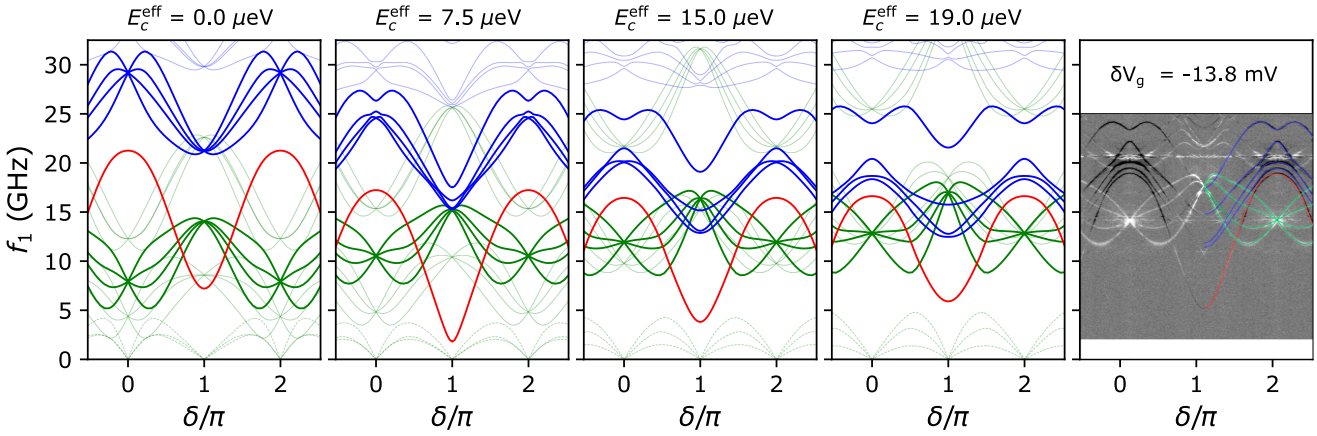


**Figure 8.7:** Evolution with the weak link effective charging energy $E_c^{\text{eff}}$ of the spectral lines as a function of phase difference $\delta$ as obtained from the extended TB model with 31 sites in the $x$-direction (11 in the normal region) and 3 transverse chains, describing a junction with length $\sim$ 550 nm and width $\sim$ 200 nm (TB parameters are given in the caption of Figure 8.8). Full lines correspond to the main inter-manifold SQPT (green), lowest PT (red) and mixed PTs (blue). The faint lines correspond to secondary transitions (*i.e.* from the first to the third or from the second to the third manifolds, intra-manifold and higher PTs). Excitations up to $N_{\text{pr}} = 12$ are included in the effective interacting Hamiltonians. Rightmost panel are the data of the central panel of Figure 8.5 shown for comparison.

phase dispersion near $\delta = 0, 2\pi$ seen in Figure 8.5 for the topmost blue line at $\delta V_g = -13.8$ mV is also very reminiscent of the one observed in the spectra of Figs. 7.4 and 7.1. The spectra measured at $\delta V_g = -8.9$ and $-23.5$ mV also show a clear separation of these lines into triplet and singlet, as was observed in Figs. 7.1, 7.4.

We searched for a set of parameters that best reproduce the central spectrum of Figure 8.5, in which the full dispersion of the mixed transitions in blue is visible. The result is shown next to the data in Figure 8.7. Most features of the spectrum, both for the relative frequencies of the transition lines and for their shape, are essentially reproduced. In particular, the camel-back dispersion of the upper mixed pair line around $\delta = 0$, absent in a non-interacting model, is well captured here. It should be mentioned, however, that these spectra are extremely sensitive to microscopic details in the potential profile, which are completely unknown for an actual experimental realization. Although an exact fit of experimental spectra with our extended TB model is not expected, many features of our com-

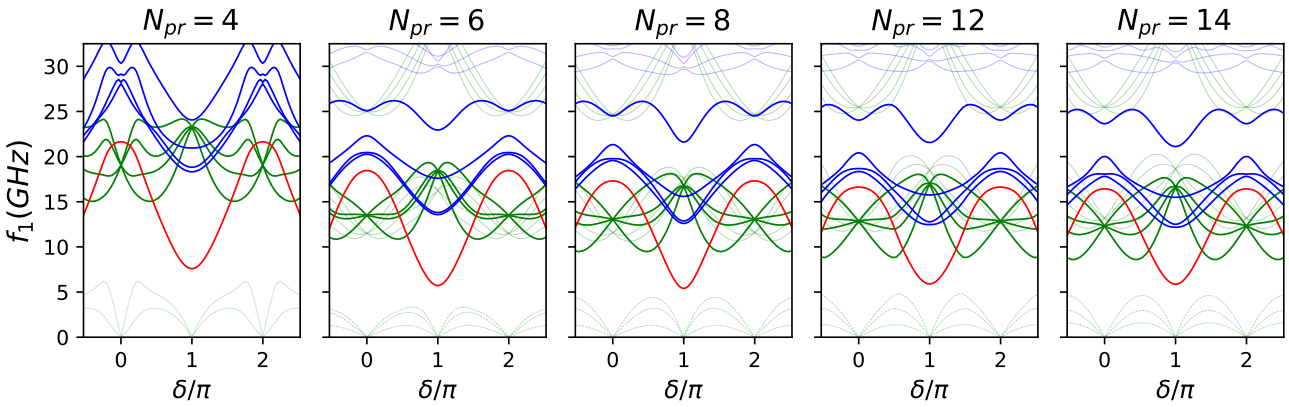


**Figure 8.8:** Transitions from the extended TB model for increasing values of $N_{pr}$ to include progressively higher states. Parameters are the same as in Figure 8.7 with $E_c^{\text{eff}} = 19.0$ $\mu$eV: $N_{\text{sitesN}} = 11$, $N_{\text{sitesS}} = 10$, $\mu$=0.14 meV (in the N region), $\Delta$=0.2 meV, $L$=550 nm, $a_x$=$L/N_{\text{sitesN}}$, $a_y$=100 nm, $\alpha/2$=11 meV.nm=$a_x\alpha_x$=$a_y\alpha_y$, $t_0$=$\hbar^2/2m^*$ ($m^*$=0.023$m_e$), ($\epsilon_{1N}, \epsilon_{2N}, \epsilon_{3N}$)=$(1.2, 1.1, 0.8)\cdot 2t_0/a_x^2$, $\epsilon_{1S}$=$\epsilon_{2S}$=$\epsilon_{3S}$=$2t_0/a_x^2-\Delta$, ($t_{xN}, t_{xS}$)=$(-0.85, -1)\cdot t_0/a_x^2$, $t_{yN}$=$t_{yS}$=$-t_0/a_y^2$. Impurity position: site 3 of N region, ($\epsilon_{\text{imp1}}, \epsilon_{\text{imp2}}, \epsilon_{\text{imp3}}$)=$(0.6, 0.75, 0.75)\cdot 2t_0/a^2$.

plex spectra are reproduced. In the other panels of Figure 8.7, we show how the spectrum evolves when changing only the Coulomb interaction strength, expressed in terms of an effective charging energy $E_c^{\text{eff}}$ for the weak link. As in the case of the four-site model from Section 8.1.2, the most remarkable effect of interactions is to lift the degeneracies of the mixed pair transition lines at $\delta = 0, \pi$. One also observes how the mixed pair transitions split into a triplet at lower energy and a singlet at higher energy, reminiscent of the triplet/singlet separation predicted in Ref. [98]. The inter-manifold SQPT lines are shifted to higher frequency without breaking their characteristic shape, which clarifies why they could already be identified and fit within the non-interacting theory previously described (see Chapter 6).

[98]: Padurariu and Nazarov (2012), 'Spin blockade qubit in a superconducting junction'

As a sanity check, we show in Figure 8.8 how the results using $E_c^{\text{eff}}$=19 $\mu$eV $\sim \Delta/10$ converge with the number of states $N_{pr}$ on which the interaction is projected. Little change is observed for $N_{pr} > 8$. For larger interaction strengths, a larger mixing with continuum states occurs and the convergence with $N_{pr}$ becomes slower.

As supplemental data, we show in Figure 8.9 the evolution in the excitation picture of the energy spectrum of quasiparticle states as a function of $E_c^{\text{eff}}$, as obtained from the extended TB model for the parameters of Figure 8.7. Green curves correspond to states with an odd number of excitations, while red ones are associated to states with an even number. In particular, we highlight in thick lines the states involving the lowest four ABS, out of which the SQPT, PT and mixed PT lines shown in Figure 8.7 arise. The green lines represent the evolution of the ABS spectrum as the interaction strength is increased. It shows that the degeneracies at $\delta = 0, \pi$ are indeed preserved and that the spin-split ABS manifolds slightly repel each other, resulting in an increase of the SQPT frequencies, as mentioned previously.

Above the first set of mixed states around $E\text{exc} = 0.6\Delta$ (involving excitations in both first and second ABS manifolds) the spectrum shows a very busy structure. In particular, the topmost thick red line around $E\text{exc} = 0.8\Delta$ corresponds to the state with two quasiparticles in the second ABS manifold. As interactions are introduced, it starts mixing

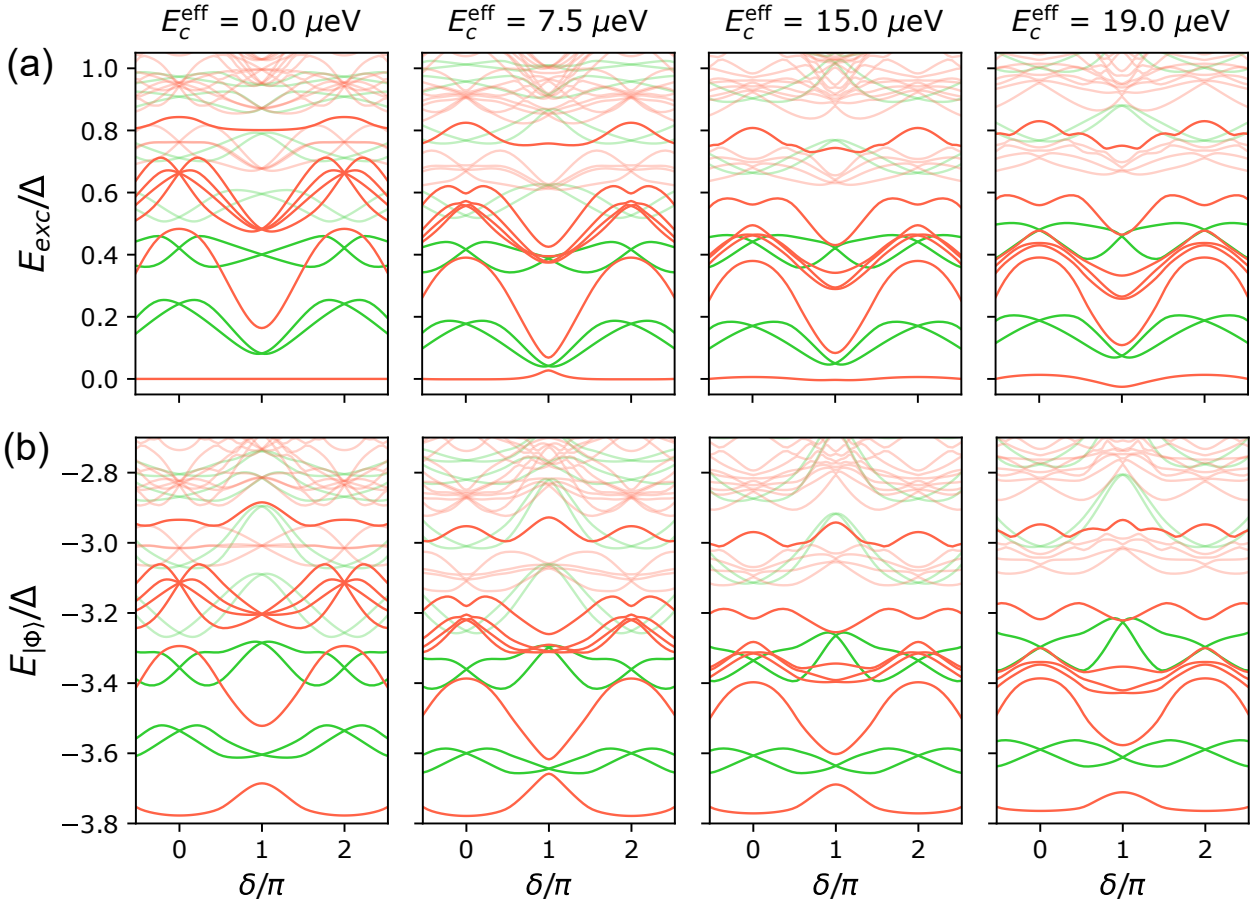


**Figure 8.9:** Energies of the quasiparticle states in the extended TB model as a function of the weak link effective charging energy $E_c^{\mathrm{eff}}$. Parameters are the same as in Figure 8.7. (a) States energies in the excitation picture, obtained by diagonalization of the extended TB Hamiltonian. Green (resp. red) lines correspond to states with an odd (resp. even) number of excitations. The set of green curves therefore represents the (one particle) ABS spectrum and how it evolves as the interaction strength is cranked up. We show all 12 ABS levels appearing for this set of TB parameters ; the states involving the lowest four ABS are highlighted with thick lines. Differences between these energies give the transition spectra shown in Figure 8.7. To keep the same energy axis and compare the spectra, the energy of the lowest state at $\delta = 0$ was substracted to the spectrum for each value of $E_c^{\mathrm{eff}}$. (b) Energies of all many-body states $|\Phi\rangle$ arising by creating excitations in the 12 possible ABS. The spectrum is the same as in (a) except that we added to each curve the energy of the non-interacting ground state $E_{\mathrm{GS}} = -1/2\Sigma_{n<=12}E_{\mathrm{exc},n}$ obtained by summing the energies of all 12 ABS (green lines in panel (a) for $E_c^{\mathrm{eff}} = 0$). The continuum is expected to add only an offset with a small phase dependence and is therefore not included in the sum.

with other even parity states, resulting in a complex line shape which makes its identification complicated. In particular, its phase dispersion is strongly modified compared to the regular one expected from a non-interacting model, as was shown in Figure 6.2. This illustrates why, even in microwave spectra associated to long weak links, where the pair transition to the second ABS manifold is expected to show in the measured frequency window, it is never identified as such. Only the lowest PT, SQPT and the first set of mixed PT are generally well visible and decoupled from the higher sets of transitions.

The energies of the many-body states involving excitations in the lowest two ABS manifolds are plotted in thick lines in Figure 8.9(b). They were obtained by adding to the states energies in the excitation picture from panel (a) the quantity $E_{\mathrm{GS}}$, corresponding to the sum of the energies of all 12 subgap states being occupied in the non-interacting ground state. As the continuum is expected to add only an offset with a small phase dependence, it is not included in $E_{\mathrm{GS}}$. Remarkably, we observe that for

this TB parameters, a $0-\pi$ transition is almost realized for $E_c^{\text{eff}} = 7.5\ \mu$eV: at this value, the energy at $\delta = \pi$ of the even-parity ground state (lowest thick red line) almost equals the one of the lowest energy state of odd parity (lowest thick green line). More work is needed to understand how such transitions would occur.

## 8.3 Thoughts on the model & link with atomic physics

Nanowire weak links offer a remarkable platform to observe in a tunable and controlled manner electronics many-body effects beyond what can be achieved with real atoms. Our microwave spectra reveal a rich interplay between spin-orbit physics and Coulomb interactions in the semiconducting region, which shares conceptual similarities with the spectra of real atoms. While the spectrum of hydrogen can be effectively modeled with a small number of parameters, we may wonder how many such parameters are minimally needed here to account for the generic features of our nanowire spectra.

As discussed above, the ingredients that matter are the finite length, at least two transverse channels, spin-orbit coupling and interactions. All these are required to account both for single-quasiparticle transitions and mixed pair transitions. Therefore, as argued before, a minimal model should include at least 2 longitudinal and 2 transverse normal sites between the two superconducting reservoirs, which is precisely the four-sites model introduced in Section 8.1.2. To incorporate the effect of disorder in the normal region, including one scatterer in a longer TB model is the least one can do. By adding more longitudinal sites and several scatterers, our extended TB model from Section 8.1.3 allows to reproduce correctly the measured spectra on the qualitative level, which comforts our understanding. This is at the price of non-analytical results, but has the credit of grasping the main effects that are relevant to account for our series of measurements. With additional parameters, one would probably be able to reach a quantitative fit of the spectra, but one would not gain more physical insight into the physical phenomena that are at play.

# Coherent dynamics of Andreev levels in a nanowire weak link

# State readout & time-resolved measurements

# 9



In Chapter 4 we developed a general framework to model the coupling of a phase-biased weak link with a microwave resonator. As a result of this coupling, the resonance frequency of the coupled system depends on the occupancy of the ABS levels in the weak link. In the limit of weak coupling, this manifests as a state-dependent shift of the resonator frequency around its bare value. By probing the resonator, one can therefore track the many-body state of the weak link, which is encoded in the resonator frequency shift.

So far, we focused on continuous probing of the resonator, where only the frequency of the readout microwave is varied. When associated to a second microwave tone to drive transitions between ABS, this allows to perform the microwave spectroscopy of the weak link and gain information on the level structure of the Andreev "atom". In Chapters 6, 7 and 8 we reported such spectroscopy on InAs nanowire weak links and used it to evidence the fine structure of the ABS levels and the role of Coulomb interactions. We described a general recipe to compute the resonator shift associated to any many-body state of the weak link and applied it to model the resonator shifts in two-tone spectra.

Let us now discuss *time-resolved* (=pulsed) measurements. As illustrated in Figure 4.7, the Andreev "atom" hosted by finite-length weak links is inherently a multi-qubit system, due to the presence of many ABS levels in the gap, which makes the system very rich. One generally seeks for simple situations, where the weak link hosts at best one or two high transparency channels such that the spectrum of excitations exhibits only a few well-isolated transition lines. Once a given transition has been identified among the many lines present in the spectrum, one can attempt to manipulate the states corresponding to the transition as a qubit using sequences of time-resolved microwave pulses. Those generically involve a sequence of drive pulses, used to prepare the qubit in a given state, followed by a readout pulse on the resonator to measure the resulting state of the qubit. As discussed in Figure 4.7, the four lowest-lying many-body states of an Andreev "atom", labelled $\{|g\rangle, |o\downarrow\rangle, |o\uparrow\rangle, |e\rangle\}$, allow to implement both an Andreev *pair* qubit ($|g\rangle \rightarrow |e\rangle$), and an Andreev *spin* qubit ($|o\downarrow\rangle \rightarrow |o\uparrow\rangle$). While the former involves a pair of excitations and therefore deals with the weak link's *charge*, the latter corresponds to manipulating the *spin* state of a single quasiparticle trapped in the lowest ABS level.

After a reminder on state detection and single-shot state readout, we present in Chapter 10 results on an Andreev pair qubit (APQ) and review in Chapter 11 preliminary results towards the spin manipulation of a single quasiparticle.

## 9.1 State readout from transmission measurements

Before delving into complicated math, let us start by sketching in a few words the idea behind state readout. As discussed previously, to track the many-body state of the weak link, one has to monitor the resonance frequency of the resonator to which it is coupled. Instead of measuring explicitly its resonance frequency, another possibility which is quicker to implement is to couple the resonator to a bus line in a notch-type geometry (see Figure 9.1(a)) and to measure the transmission $S_{21}(\omega)$ through this line of a microwave tone at a fixed angular frequency $\omega$, chosen close to the bare resonator frequency $\omega_0$. The transmitted signal will therefore depend on $\omega_0$ and whenever the state of the weak links changes, the associated shift $\delta\omega_0$ of the resonator frequency will modify the amplitude and phase of the transmitted signal, which we can then use as a marker of the weak link state. In the best scenario, amplitude and phase signatures will be enough to discriminate amongst the different many-body states of the weak link, so that a single-shot measurement will allow to unambiguously determine the actual weak link state.

As discussed in Section 5.2.3, Eq. (9.1), the complex scattering parameter for such a two-port network can be written:

$$S_{21}(\omega) = a e^{j\omega\tau_{\text{el}}}\left[1 - \frac{Q/Q_{\text{ext}}}{1 + 2jQ(\omega/\omega_0 - 1)}\right], \tag{9.1}$$

with $\omega_0$ the resonance frequency, $Q$ the loaded total quality factor of the resonator, $a > 0$ some real-valued amplitude capturing attenuation and gain factors in the measurement setup and $\tau_e l$ the electrical delay in the probe cables. As illustrated in Figure 9.1(b), the amplitude of the scattering coefficient shows a dip at $\omega_0$ and a jump in its phase. Introducing the parameter $\alpha = Q/Q_{\text{ext}} = \frac{Q_{\text{int}}}{Q_{\text{ext}}+Q_{\text{int}}}$, the reduced frequency $y = (\omega - \omega_0)/\omega_0$, one can rewrite Eq. (9.1) in a way that makes explicit the shape of this function in the complex plane:

$$\begin{aligned} S_{21}(y) &\propto 1 - \frac{\alpha}{1 + 2jQy} \\ &= 1 - \alpha\left[\frac{1 - 2jQy}{1 + 2jQy} + \frac{2jQy}{1 + 2jQy}\right] \\ &= 1 - \alpha\left[e^{i\theta} + \frac{2jQy}{1 + 2jQy}\right], \end{aligned} \tag{9.2}$$

where $\theta = -2\arctan(2Qy)$. Then, rewriting the second term in the bracket $\frac{2jQy}{1+2jQy} = 1 - 1/(1 + 2jQy) = 1 - (1 - S_{21})/\alpha$, we obtain:

$$\begin{aligned} S_{21} &= 1 - \alpha(1 + e^{i\theta}) + 1 - S_{21} \\ &\Rightarrow \boxed{S_{21} = 1 - \frac{\alpha}{2}(1 + e^{i\theta}).} \end{aligned} \tag{9.3}$$

One recognizes in Eq. (9.3) the parametric equation of a circle of radius $\alpha/2$ and center $1 - \alpha/2$ in the complex plane, which is also commonly called "$IQ$-plane" in reference to homodyne demodulation technique: the "In-phase" ("Quadrature") component is the real (imaginary) part of the complex amplitude of a demodulated signal. This is illustrated in Figure

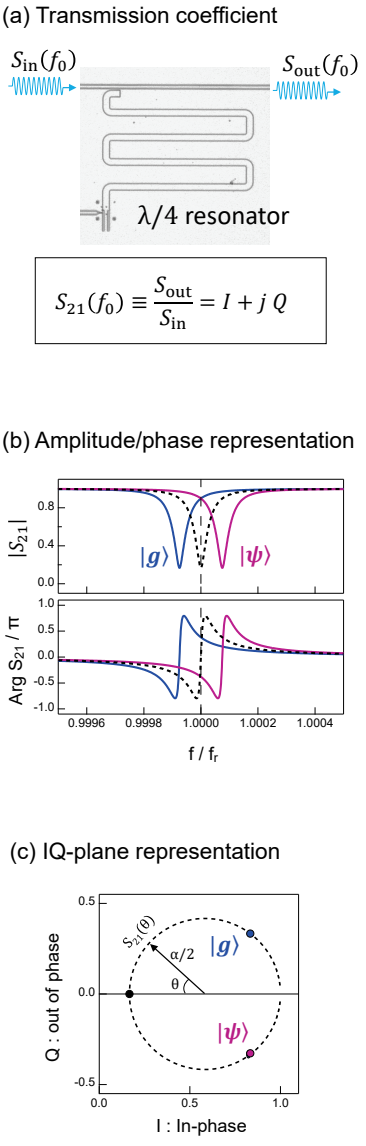


**Figure 9.1:** (a) The quarter-wave resonator is notched-coupled to a bus line. Its complex transmission coefficient $S_{21}$ depends on the resonator frequency which itself encodes the many-body state $|\Psi\rangle$ of the weak link coupled to it. (b) At resonance, the transmission coefficient shows a dip in amplitude and a jump in its phase. (c) $IQ$ representation of the tranmission coefficient. Each many-body state $|\Psi\rangle$ of the weak link is mapped to a point on the circle.

9.1(c), where we represent parametrically the $I$ and $Q$ quadratures of the transmission coefficient $S_{21}(\omega)$ given in Eq. (9.3). If we now measure the $I$ and $Q$ components of $S_{21}$ at the bare frequency of the resonator, any shift of its resonance frequency will be mapped to a point on this circle. The resonator and its coupling to the external lines should then be designed in such a way that the many-body states we want to resolve are maximally separated on the $IQ$ circle.

Since the circle radius is given by $\alpha$, to maximize its size, one should therefore choose $Q_{\text{ext}} \ll Q_{\text{int}}$. This condition is generally verified in practice when fabricating resonators out of superconducting materials: internal quality factors of several millions [104] have been achieved with aluminium resonators on low dielectric-losses substrates. The total loaded quality factor will therefore be limited by the external losses captured by $Q_{\text{ext}}$ and determined by the coupling of the resonator to the external bus line. This coupling should be chosen such that the resonator linewidth $\Delta\omega_0 \approx \omega_0/Q_{\text{ext}}$ is comparable to the expected resonator shifts $\delta\omega_0^{|\Psi\rangle}$ associated to the weak link's many-body states $|\Psi\rangle$ that we want to resolve. These constraints on the design were already discussed in Section 5.2.3.

Before moving on, let us note that for a reflection type of measurement, for which the scattering parameter being probed is this time $S_{11}$, one also obtains a circle in the $IQ$ plane but with a radius *twice larger* [21]:

[21]: Janvier (2016), 'Coherent manipulation of Andreev Bound States in an atomic contact', p. 38

$$\boxed{S_{11}(y) = 1 - \alpha(1 + e^{i\theta}).} \tag{9.4}$$

This factor 2 gain in the SNR can make reflection measurements more appealing than transmission ones. However, other difficulties may appear with reflection measurements, related in particular to the limited performances of available directional couplers, which are commonly used to route input/output signals in a reflectometry experiment. Due to their low directivity, part of the output signal is polluted by the small leakage through the coupler. This parasitic signal interferes with the one reflected from the resonator, and does not carry any information.

Physically, this factor 2 can be understood as follows: among the photons reflected off the resonator, only half of them are effectively routed through the output port, the other half being back-scattered towards the input port. In contrast, a reflection measurement only makes use of a single port, and all the reflected photons are recovered. One way to bypass both the factor 2 constraint on the SNR for a transmission measurement and the limitation in directionality for reflection measurements is to perform an *asymmetric* transmission measurements, whereby the input/output ports are asymmetrically coupled to the resonator [105] [106]. Making the output port very well coupled ensures to recover most of the reflected photons, while keeping the input port weakly coupled so as to minimize the perturbations from the environment.

[106]: Bienfait (2016), 'Magnetic resonance with quantum microwaves', p. 62

[105]: Heinsoo et al. (2018), 'Rapid High-fidelity Multiplexed Readout of Superconducting Qubits'

## 9.2 Time evolution of the resonator fields

To gain insight on the state readout through the resonator, an interesting situation to describe is the response of the resonator to a square pulse oscillating at an angular frequency $\omega \approx \omega_0$. For simplicity, we will first investigate the response to a step-like excitation, which corresponds to the limiting case of a square pulse of infinite duration.

### 9.2.1 Step-like excitation: resonator response

Let us model the readout pulse by a step-like excitation of real amplitude $A_0$ and angular frequency $\omega$:

$$V_{\text{in}}(t) = A_0\, e^{j\omega t} \cdot \Theta(t), \tag{9.5}$$

where $\Theta(t)$ denotes the unit-step Heaviside function and we use a complex amplitude notation to simplify the following math. So as to probe the resonator response, the angular frequency $\omega$ of this input pulse is chosen close to the frequency $\omega_0$ of the resonator, which we are now going to refer to as "the cavity", as its readout amounts to "load" it with photons. We introduce the detuning $\epsilon$, counted in number of linewidths away from the cavity resonance frequency $\omega_0$, so as to keep it a reduced parameter: $\omega = \omega_0\left(1 + \frac{\epsilon}{Q}\right)$. The time evolution of the outgoing pulse is readily obtained by Fourier transform:

$$\begin{aligned} V_{\text{out}}(t) &= \mathscr{F}^{-1}\{\mathscr{F}\{V_{\text{in}}(t)\} \cdot S_{21}(\omega)\} \\ &= (V_{\text{in}} * h)(t), \end{aligned} \tag{9.6}$$

where $h(t) = \mathscr{F}^{-1}\{S_{21}(\omega)\}$ is the impulse response of the two-port network and $*$ denotes the convolution operation. This impulse response is easily computed by inverse Fourier transform of Eq. (9.2):

$$\boxed{S_{21}(\omega) = 1 - \frac{\alpha}{1 + j\tau(\omega - \omega_0)} \quad \overset{\mathscr{F}^{-1}}{\Rightarrow} \quad h(t) = \delta(t) - \frac{\alpha}{\tau} e^{-\frac{t}{\tau}} e^{j\omega_0 t} \cdot \Theta(t),} \tag{9.7}$$

where we introduced the relaxation time of the cavity $\tau = \frac{2Q}{\omega} = \frac{2}{\kappa}$, with $\kappa$ the total loss rate of the cavity given by the full width at half maximum (FWHM) of the resonator line. In this terms, the angular frequency of the input pulse reads $\omega = \omega_0 + \kappa\epsilon$. From Eqs. (9.6, 9.7), we deduce the time evolution of the outgoing pulse:

$$\boxed{\begin{aligned} V_{\text{out}}(t) &= A_0 v(t) && \text{(9.8a)} \\ v(t) &= e^{j\omega t}\left[1 - \frac{\alpha}{1 + 2j\epsilon}\left(1 - e^{-\frac{\kappa t}{2}} e^{-j\kappa\epsilon t}\right)\right] \cdot \Theta(t). && \text{(9.8b)} \end{aligned}}$$

Writing $V_{\text{out}}(t) = (I_{\text{out}} - jQ_{\text{out}})A_0 e^{j\omega t} \cdot \Theta(t) = (I_{\text{out}} - jQ_{\text{out}})V_{\text{in}}(t)$, we can identify the time evolution* of the pulse coordinates $\{I_{\text{out}}, Q_{\text{out}}\}$ in the rotating frame at $\omega$, using that $\frac{1}{1+2j\epsilon} = \frac{1}{\sqrt{1+4\epsilon^2}} e^{-j \arctan(2\epsilon)}$:

* The minus sign in $V_{\text{out}}$ comes from the $+\omega$ convention in $e^{j\omega t}$. This way, $V_{\text{in}}(t) = \text{Re}[A_0 e^{i\omega t}] = A_0 \cos(\omega t)$ gives $V_{\text{out}}(t) = \text{Re}[(I - jQ)A_0 e^{i\omega t}] = A_0(I\cos(\omega t) + Q\sin(\omega t))$ and we recover the usual definition of the in-phase/in-quadrature components of a modulated signal.

$$\begin{cases} I_{\text{out}}(t) = 1 - \dfrac{\alpha}{1+4\epsilon^2} + \dfrac{\alpha e^{-\frac{\kappa t}{2}}}{1+4\epsilon^2}\left[\cos(\kappa\epsilon t) - 2\epsilon\sin(\kappa\epsilon t)\right] \\ Q_{\text{out}}(t) = -\dfrac{2\epsilon\alpha}{1+4\epsilon^2} + \dfrac{\alpha e^{-\frac{\kappa t}{2}}}{1+4\epsilon^2}\left[2\epsilon\cos(\kappa\epsilon t) + \sin(\kappa\epsilon t)\right]. \end{cases} \tag{9.9}$$

The complex amplitude $A_{\text{out}} = I_{\text{out}} - jQ_{\text{out}}$ can be seen to move at an angular frequency $\omega - \omega_0 = \kappa\epsilon$ on a circle of center $A^{\infty}_{\text{out}}$ and time-varying radius $R(t)$, given by $A_{\text{out}}(t) = A^{\infty}_{\text{out}} + R(t)e^{-j\kappa\epsilon t}$ with:

$$\begin{cases} A^{\infty}_{\text{out}} = 1 - \dfrac{\alpha}{1+2j\epsilon} = S_{21}(\omega) = 1 - \dfrac{\alpha}{\sqrt{1+4\epsilon^2}}e^{-j\arctan(2\epsilon)} \\ R(t) = \dfrac{\alpha e^{-\frac{\kappa t}{2}}}{\sqrt{1+4\epsilon^2}}e^{-j\arctan(2\epsilon)}. \end{cases} \tag{9.10}$$

After a time $t \sim \tau = 2/\kappa$, $R(t \to \infty) = 0$ and the complex amplitude has converged towards its stationary value:

$$A^{\infty}_{\text{out}} = 1 - \frac{\alpha}{\sqrt{1+4\epsilon^2}}e^{-j\arctan(2\epsilon)} = \left(1 - \frac{\alpha}{1+4\epsilon^2}\right) + j\frac{2\alpha\epsilon}{1+4\epsilon^2} = A_{\infty}e^{j\theta_{\infty}}, \tag{9.11}$$

with $$\begin{cases} A_{\infty} = \sqrt{1 + \dfrac{\alpha(\alpha-2)}{1+4\epsilon^2}} \underset{\epsilon\to 0}{\to} 1-\alpha \\ \theta_{\infty} = \arctan\left(\dfrac{2\alpha\epsilon}{1-\alpha+4\epsilon^2}\right) \underset{\epsilon\to 0}{\to} 0. \end{cases}$$

In absence of detuning $\epsilon = 0$, we recover the expected results:

$$V_{\text{out}}(t) = A_0 e^{j\omega t}\left[(1-\alpha) + \alpha e^{-\frac{\kappa t}{2}}\right]\cdot\Theta(t) \tag{9.12a}$$

$$|V_{\text{out}}| \underset{t\to\infty}{\to} A_0(1-\alpha) = A_0 \cdot |S_{21}(\omega_0)|, \tag{9.12b}$$

which consists in a linear superposition of the stationary response $S_{21}(\omega_0) \times V_{\text{in}}(t)$ and of a transient response $\alpha e^{-\frac{\kappa t}{2}} \times V_{\text{in}}(t)$ decaying over a time $\sim \tau$ given by the loss rate $\kappa = 2/\tau$ of the cavity.

When the input pulse has a finite detuning $\epsilon$ to the cavity frequency, then the output pulse $V_{\text{out}}(t)$ shows transient oscillations at the detuning frequency $\kappa\epsilon = \omega - \omega_0$ (period $Q/\epsilon$) as illustrated in Figure 9.2(b). The trajectory in the $IQ$-plane of the complex amplitude $A_{\text{out}}(t)$ presents a spiral-like behaviour around its stationary value $A^{\infty}_{\text{out}}$: its amplitude starts from 1 then decays exponentially at a rate $\kappa/2$ towards $A^{\infty}_{\text{out}}$ while its phase wraps at the angular frequency $\kappa\epsilon$ (see Figure 9.2(a)).

For zero detuning, the amplitude stays real and follows a straight line in the $IQ$ plane from amplitude 1 to amplitude $S_{21}(\omega_0) = 1 - \alpha$. As a finite detuning is introduced, this straight trajectory is deflected clockwise and swirls around its stationary value. If we were to describe the complex amplitude $A_{\text{out}}(t)$ as the position of a point moving in a 2D-plane seen from a frame rotating at $\omega$, this deviation from its straight trajectory would be understood as the action of a fictitious/inertial force, in a manner formally similar to the Coriolis force in Newton mechanics, which acts on objects in motion within a frame of reference that rotates with respect to an inertial frame.

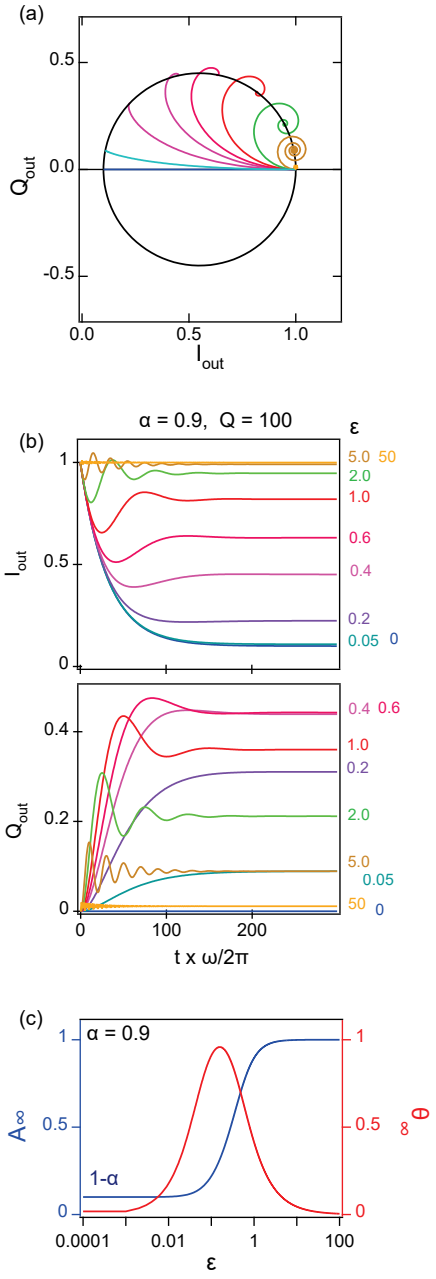


**Figure 9.2:** Time response of the two-port network to a unit-step excitation $V_{\text{in}}(t) = e^{j\omega t}\cdot\Theta(t)$ for $\alpha = 0.9$ and $Q = 100$. (a) Time evolution in the $IQ$-plane of the outgoing pulse $V_{\text{out}}(t) = (I_{\text{out}} - jQ_{\text{out}})e^{j\omega t}\cdot\Theta(t)$ for different detuning $\epsilon = (\omega - \omega_0)/\kappa$ to the cavity frequency $\omega_0$. The evolutions of both coordinates for each value of detuning are shown in (b). (c) Dependence on the detuning $\epsilon$ of the stationary amplitude $A_{\infty}$ and phase $\theta_{\infty}$ of the outgoing pulse $V_{\text{out}}$ as given by Eq. (9.11).

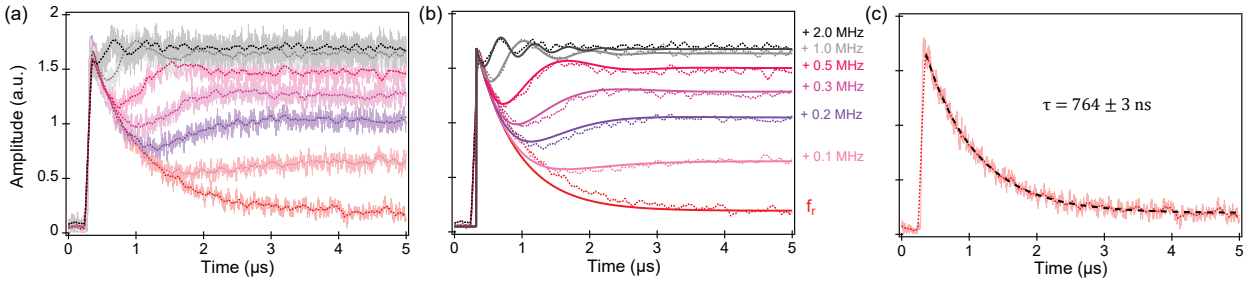


**Figure 9.3:** (a). Measured time evolution of the transmitted signal for an input square pulse of duration 5 μs for increasing detuning $\Delta f = \kappa\epsilon/(2\pi) = 0, 0.1, 0.2, 0.3, 0.5, 1.0, 2.0$ MHz to the resonator frequency $f_r = 6.60752$ GHz. The plotted signal corresponds to $\sqrt{(I_{\text{out}}^2 + Q\text{out}^2)}$, where $I_{\text{out}}$,$Q_{\text{out}}$ are obtained by numerical demodulation at $\omega_{IF}$ of the digitized down-converted signal. The curves in solid lines are the raw data after coherent averaging of 5000 pulses. The dotted lines are obtained by applying a moving average filter with a time window of 100 ns. (b) Comparison of the filtered experimental data (dotted) with theory (solid lines) from Eqs. (9.9). The plotted theory curves correspond to the best global fit of all curves with $\alpha = 0.91$ and $\kappa = 3.3 \times 10^{-3}$ rad.s$^{-1}$, *i.e.* a relaxation time $\tau = 2/\kappa = 604$ ns. (c) Single fit of the $\Delta f = 0$ data giving $\tau = 764 \pm 3$ ns.

In Figure 9.3, we show the measured time evolution of the transmitted signal for an input square pulse of duration 5 μs and frequency $f = f_r + \Delta f$, with various detuning $\Delta f = \frac{\kappa\epsilon}{2\pi} = 0$, 0.1, 0.2, 0.3, 0.5, 1.0 and 2.0 MHz around the resonator frequency $f_r = 6.60752$ GHz. The data were obtained on the sample with the shunted CPW resonator design with galvanic coupling (see Section 5.2.2). They were measured near $\delta = 0$, where we can probe the bare resonator response as it is expected to be only little affected by the weak link admittance. In Figure 9.3(a), we present the raw data obtained after averaging ~ 5000 pulses and overlay a filtered version to better evidence the oscillations of the transient response at the detuning frequency. The heterodyne modulation setup used to acquire this data is presented in Section 14. What appears as noise over the mean level of each curve is in fact a fast oscillation at twice the intermediate frequency $2\omega_{IF}$ (period 10 ns) arising from imperfections of the IQ mixer used for down-conversion. Indeed, because of the finite phase imbalance of the mixer, the circle in the $IQ$-plane is slightly distorted into an ellipse, which after numeric demodulation at $\omega_{IF}$ yields a spurious amplitude modulation at $2\omega_{IF}$. This could easily be corrected, either numerically after digitization of the pulses, or directly at the signal level by applying phase/amplitude corrections to the LO tone. This was not yet implemented at the time of these measurements.

In Figure 9.3(b), we compare the filtered data with the theory for $A_{\text{out}} = \sqrt{I_{\text{out}}^2 + Q_{\text{out}}^2}$ from Eq. (9.9), while leaving $\kappa$ and $\alpha$ as free parameters, as well as a global offset and scaling factor. The best fit yields $\alpha = 0.91$ and $\tau = 604$ ns. Note that although this value of $\tau$ gives the best comparison with theory when a global fit of all curves is performed, it remains ~ 100 ns smaller than the value extracted when fitting only the resonant response (see Figure 9.3(c)). Getting the right stationary values in panel (b) requires taking a smaller $\tau$ than the real relaxation time. If constraining $\tau$ to the value obtained in panel (c), then the stationary values for the time evolutions shown in (b) may be off by at most ~ 5%. Still, the values of $\alpha$ and $\tau$ obtained from the global fit of the transmitted signals compare well with the estimates obtained by a reciprocal method in the frequency domain, from single-tone measurements of $S_{21}(f)$ around the resonator frequency. As shown in Figure 9.4, a global fit of the amplitude and phase of the measured transmission coefficient $S_{21}(f)$ at $\delta = 0$ gives $Q_{\text{int}} \approx 93 \times 10^3$, $Q_{\text{ext}} \approx 17 \times 10^3$, from which we deduce the loaded

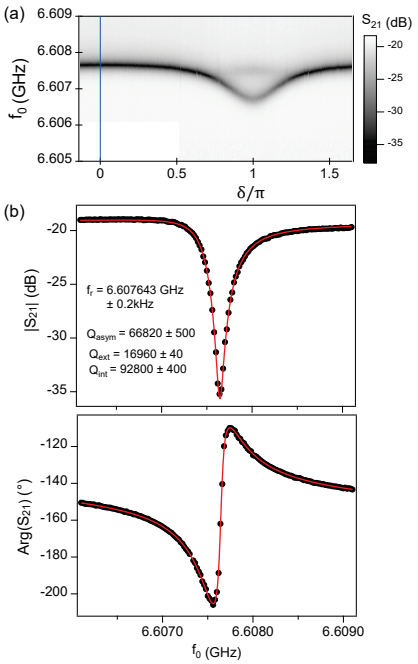


**Figure 9.4:** (a) Single-tone resonator spectroscopy measured on the device with the shunted CPW design and galvanic coupling. The magnitude of the transmission coefficient $S_{21}$ is plotted as a function of the probe frequency $f_0$. (b) Amplitude and phase of $S_{21}$ at $\delta = 0$ (blue line in panel (a)). The data is shown in black disks and a fit with Eq. (9.1) is overlaid in red. An extra fitting parameter $Q_{\text{asym}}$ is added to capture the small asymmetry in the resonance line that may arise due to finite impedance mismatches on both sides of the transmission line (see Eq. (23) in [81]). The fit yields $Q_{\text{int}} = 92800 \pm 400$, $Q_{\text{ext}} = 16960 \pm 40$ and $f_r = 6.607643$ GHz, from which we deduce the total loaded quality factor $Q \approx 14300$ and $\tau = 690$ ns.

quality factor $Q = \approx 14 \times 10^3$, $\alpha = Q/Q_{\text{ext}} = 0.84$ and $\tau = \frac{Q}{\pi f_r} = 690$ ns. This measured value of $Q$ falls close to the nominal $10 \times 10^3$ value that we had targeted for this design (see Section 5.2.3).

### 9.2.2 Time-resolved readout

The different states of the many-body system are characterized by different resonator frequencies, therefore different responses to the measurement pulse, *i.e.* different trajectories in the $IQ$ plane. In practice, one would send a readout pulse of duration $T_{\text{meas}}$ sufficiently long to separate the trajectories beyond the noise. As discussed in the preceding section, the maximum separation is achieved, with a square pulse, after a few $\tau$. Ultimately, states are better distinguished if they correspond to frequency shifts that differ by $\sim \kappa = 2/\tau$. When measuring spectra, one aims at observing several transitions, and one chooses $\kappa$ as a compromise between the frequency shifts of the different transitions. When aiming at manipulating states that cause small shifts [32], like different spin states, one would take a small $\kappa$, at the cost of needing a long time to separate the corresponding trajectories.

To circumvent the difficulty of the slow separation of the trajectories with square measurement pulses, one can resort to other types of pulses. For example, McClure *et al.* introduced so-called "CLEAR" pulses to demonstrate rapid load and reset of a resonator. Such pulses differ only slightly from standard square pulses by the addition of extra constant-amplitude segments designed to “kick” the resonator rapidly from one steady-state population to another [107]. It was shown that such simple shaped pulses could reduce the time scale for cavity ring-down by more than $2\tau$.

[107]: McClure et al. (2016), ‘Rapid Driven Reset of a Qubit Readout Resonator’,

Similarly, using a first constant segment of high amplitude and short[†] duration can allow to speed up the cavity ring-up. Such "fast-load" pulses can be described by the following functional form:

$$V_{\text{in, FL}}(t) = \Big[A_0 \cdot \Theta(t) - (A_0 - A_1) \cdot \Theta(t - t_0)\Big] e^{j\omega t}, \tag{9.13}$$

where $t_0$ denotes the duration of the fast-load pre-pulse and $A_0$ its amplitude. After this time $t_0$, the pulse amplitude does not decay to zero but maintains a constant sticky amplitude $A_1 < A_0$ during which the cavity readout is performed. When the frequency $\omega$ of the pulse is tuned to the cavity frequency $\omega_0$, the amplitude of the transmitted pulse decays exponentially at a rate $\kappa/2$, as illustrated in Figure 9.3(c). Therefore by choosing a duration $t_0$ such that $A_0 \exp(-t_0/\tau) = A_0 - A_1$, *i.e.*

$$\boxed{t_{\text{kick}} = \tau \ln\left(\frac{A_0}{A_0 - A_1}\right) \underset{\frac{A_1}{A_0} < 1 - \frac{1}{e}}{<} \tau,} \tag{9.14}$$

one ensures that at $t = t_0$, the transmitted pulse amplitude has reached its stationary value $A_1$.

This is illustrated in Figure 9.6, where we show the qualitative shape of the transmitted pulse for three illustrative values of $t_0$. When the pre-

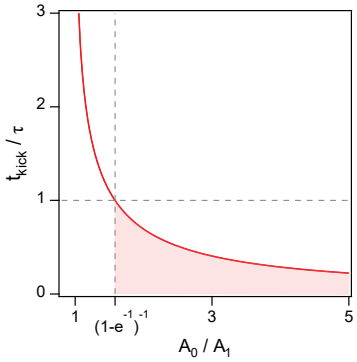


**Figure 9.5:** Dependence on the amplitude ratio $A_0/A_1$ of the optimal duration $t_0 = t_{\text{kick}}$ for the pre-pulse, as given by Eq. (9.14). The fast-load gives an advantage, $t_{\text{kick}} < \tau$, only in the region where $\frac{A_0}{A_1} > (1 - \frac{1}{e})^{-1} \approx 1.58$, denoted as red area.

[†] Short compared to the relaxation time $\tau = 2Q/\omega_0$ of the cavity

pulse (red solid line) is shorter than the value given by Eq. (9.14), there is only small improvement compared to a standard square pulse (dashed blue line): reaching the stationary value still takes a time $\sim \tau$. Similarly, when the pre-pulse is too long, there is an "overshoot" and the amplitude has to relax back, as shown in Figure 9.6(c). For a pre-pulse duration $t_0 = t_{\text{kick}}$, the transmitted pulse has exactly reached its stationary value at the end of the prepulse, *i.e.* over a time $t_{\text{kick}} < \tau$. This improvement over a square pulse provides a simple way to speed-up the readout, but note that the above considerations only hold for a resonant pulse. Finite detuning will necessarily introduce oscillations due to the transients, so that the overall pulse shape would still need to be optimized for the separation of a given pair of states.

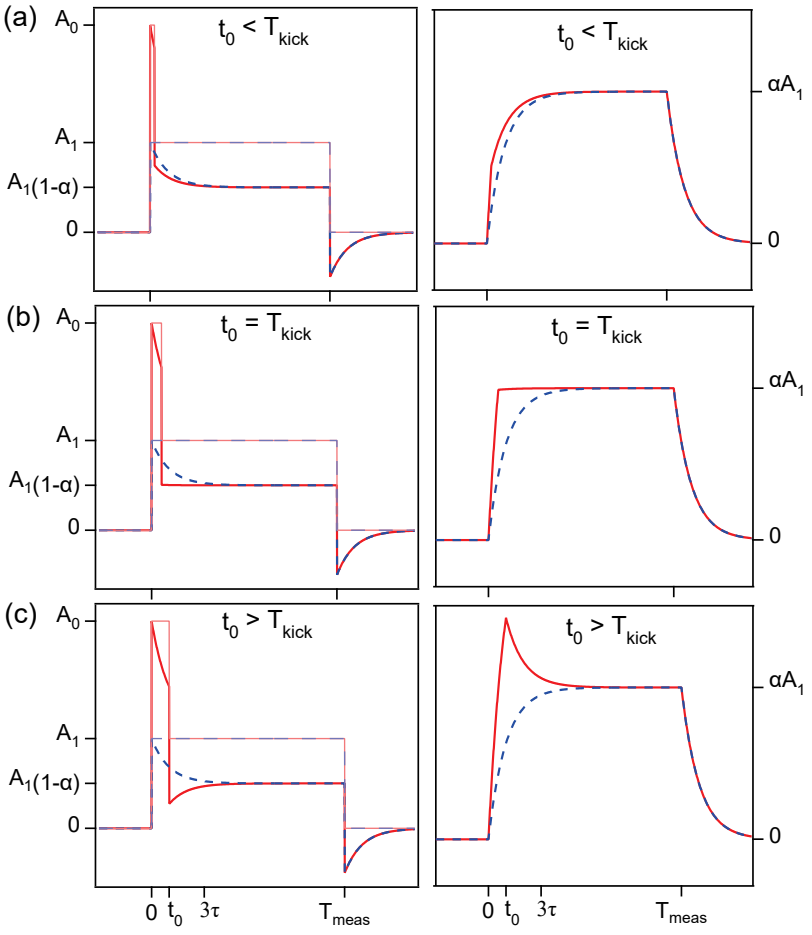


**Figure 9.6:** Adding a short pre-pulse of high amplitude before the readout square pulse can allow for faster readout. The transmitted pulse (left column) and the intra-cavity field (right column) are shown for the resonant case $\omega = \omega_0$ in three illustrative cases, both for a fast-load (solid red) or standard square (dashed blue) input pulse. The input fast-load/square pulses are depicted in the left column in thinner lines and paler color. (a) When the pre-pulse duration $t_0$ is smaller than $t_{\text{kick}}$ given by Eq. (9.14), then the transmitted pulse has not reached yet its stationary value at the end of the prepulse and a further relaxation over a time $\sim \tau$ still takes place. (b) When $t_0 = t_{\text{kick}}$, the stationary amplitude is exactly reached at the end of the pre-pulse: instead of waiting about $3\tau$, readout can be performed already at $t = t_0 < \tau$. The associated intra-cavity field shows an-almost square shape. (c) If the pre-pulse duration is chosen too long, $t_0 > t_{\text{kick}}$, then the transmitted pulse amplitude overshoots and has to relax back on a time $\sim \tau$, therefore removing any advantage of the fast-load.

To illustrate on real data the effect of a fast-load pulse, we show in Figure 9.7(a) measurements of one quadrature of the transmitted pulse for several durations of the high amplitude pre-pulse. The best performances are obtained for $t_0 = 200$ ns (green curve), which coincides well with the expected value of $t_{\text{kick}}$ for an amplitude ratio $A_0/A_1 = 4$ and $\tau = 764$ ns. In Figure 9.7(b), we compare the associated response to the one obtained without any pre-pulse, which shows that the stationary regime is reached about 4× earlier by using a fast-load sequence.

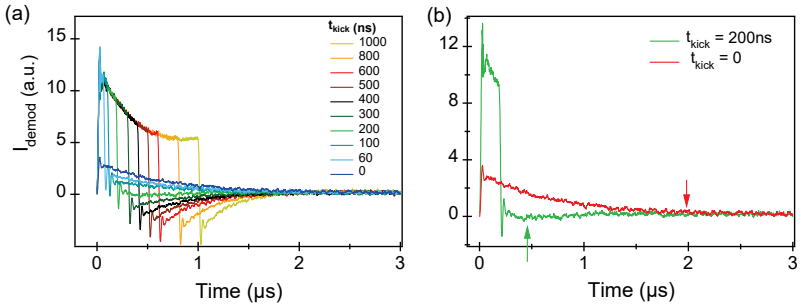


**Figure 9.7:** Tuning the pre-pulse duration. (a) One quadrature of the transmitted pulse is shown after demodulation for several values of $t_{\text{kick}}$, with $T_{\text{meas}} = 5$ µs, $A_0/A_1 = 4$ and $f = \omega/2\pi = 6.60725$ GHz. Each curve results from coherent averaging of 1000 pulses. When the duration is tuned to ~ 200 ns, the amplitude stays flat after the pre-pulse with no further evolution ; this value coincides well with the expected $t_{\text{kick}} \approx -760 \times \ln(1 - 1/4) = 220$ ns. (b) Comparison of the time responses for an initial pre-pulse of 200 ns (green curve) and without (red curve). With a standard square pulse, the stationary amplitude is reached after about $3\tau \approx 2.1$ µs (red arrow). With a fast-load however, it is reached as early as ~ 0.5 µs (green arrow).

Similarly as for the square pulse Eq. (9.5), we can derive an analytical expression for the time evolution of the outgoing pulse when a fast-load sequence is operated. With the input signal given by Eq. (9.13), we obtain using Eqs. (9.8, 9.7) the following generalization of Eq. (9.8):

$$\boxed{\begin{aligned} V_{\text{out, FL}}(t) &= A_0 v(t) + (A_1 - A_0) v(t - t_0) \\ v(t) &= e^{j\omega t}\left[1 - \frac{\alpha}{1 + 2j\epsilon}\left(1 - e^{-\frac{\kappa t}{2}} e^{-j\kappa\epsilon t}\right)\right] \cdot \Theta(t). \end{aligned}} \tag{9.15}$$

Writing this time $V_{\text{out, FL}}(t) = \left(I_{\text{out, FL}}(t) - jQ_{\text{out, FL}}(t)\right)e^{j\omega t}$, the coordinates in the $IQ$-plane after demodulation at $\omega$ are then easily deduced by linearity of the response:

$$\begin{cases} I_{\text{out, FL}}(t) = A_0\, I_{\text{out}}(t) \cdot \Theta(t) + (A_1 - A_0)\, I_{\text{out}}(t - t_0) \cdot \Theta(t - t_0) \\ Q_{\text{out, FL}}(t) = A_0\, Q_{\text{out}}(t) \cdot \Theta(t) + (A_1 - A_0)\, Q_{\text{out}}(t - t_0) \cdot \Theta(t - t_0), \end{cases} \tag{9.16}$$

where $I_{\text{out}}(t)$ and $Q_{\text{out}}(t)$ are the expressions for a square pulse excitation given by Eq. (9.9). In Figure 9.8, we compare the trajectories with a square and an optimized fast-load pulse (pre-pulse duration $t_0 = t_{\text{kick}}$), using $A_0 = 1$ and $A_1 = 0.3$.

In principle, one would use a large ratio $A_0/A_1$ to have the pre-pulse as short as possible. In practice, $A_0$ is limited by the maximum available voltage of the arbitrary-wave generator (generally ~ 1 V), and $A_1$ cannot be too small for a good performance of the mixer that combines the fast-load waveform with the microwave tone. We used typically $A_0/A_1 \sim 3 - 4$.

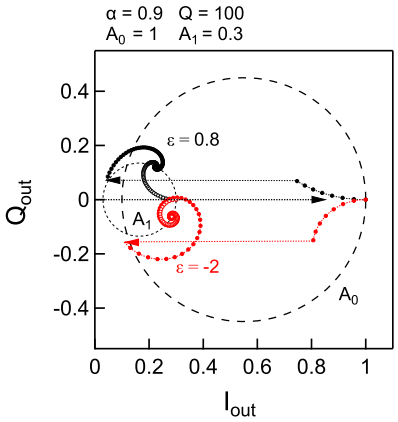


**Figure 9.8:** Trajectories in the $IQ$-plane during a fast-load pulse (solid dots) or a square pulse (open dots), for $\epsilon = 0.8$ (black) and $\epsilon = -2$ (red), using $A_0 = 1$ and $A_1 = 0.3$. With a square pulse, the trajectory develops from $(I, Q) = (A_1, 0)$ (open circles). During the pre-pulse, one starts from a large amplitude $(I, Q) = (A_0, 0)$, and reaches at $t_{\text{kick}}$ a larger amplitude in $Q_{\text{out}}$. When the pulse amplitude is reduced to $A_1$, the representative point jumps in $I_{\text{out}}$ by $A_1 - A_0$, then spirals towards the asymptotic value, which is on the circle corresponding to the amplitude $A_1$.

The actual measurement results from an average ‡ of $(I_{\text{out}}, Q_{\text{out}})$ during a time $T_{\text{meas}}$. This is illustrated in Figure 9.9, which shows how the pre-pulse allows to separate the states more efficiently. How this is done in practice is discussed in Section 14 and in Appendix I

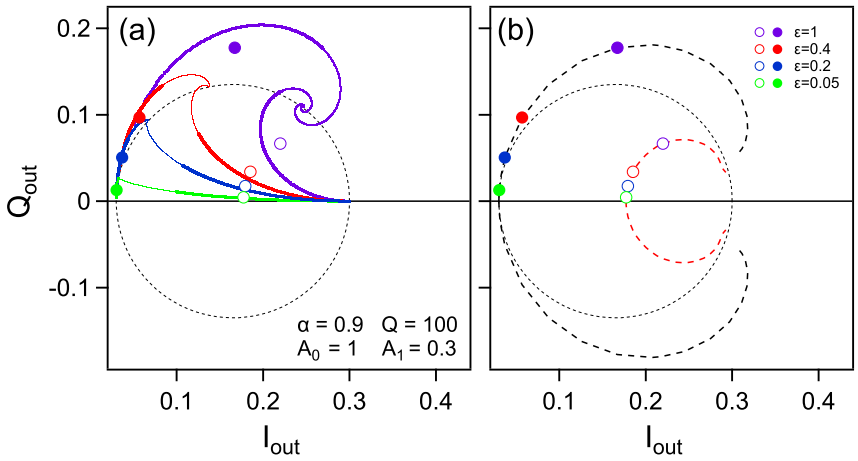


**Figure 9.9:** (a) Trajectories in the $IQ$-plane during time $T_{\text{meas}}$ (solid lines) and total trajectory (thin lines) after an optimized pre-pulse ($t_0 = t_{\text{kick}}$, trajectories starting on the left hand side) or with a standard square pulse (trajectories starting at $I_{\text{out}} = 0.3$), for 4 values of the detuning $\epsilon = 0.05, 0.2, 0.4, 1$. Without pre-pulse, we use $T_{\text{meas}} = t_{\text{kick}} + \tau$. With pre-pulse, $T_{\text{meas}} = \tau$. Solid and open dots show the average values of $(I, Q)$ on each trajectory. (b) Dotted lines show the position of the averages when $\epsilon$ is varied.

‡ More elaborate methods have been reported in the literature to distinguish two states of a simple qubit [108, 109, 110].

# Manipulation of an Andreev *pair* qubit

# 10



After this review on state readout, let us present experimental results on the coherent dynamics of Andreev levels in nanowire weak links and on the manipulation of a nanowire-based Andreev pair qubit. The device and experimental setup that were used for these measurements are depicted in Figure 10.1. The setup is essentially unchanged compared to the one used in Chapter 6 (see Figure 6.3), except that we moved to a heterodyne detection scheme to get rid of the slow drifts in the signal phase that were plaguing our measurements[1] . As the signal is now encoded in an amplitude modulation over the slowly-varying drifts, those are completely discarded after numerical demodulation at the intermediate frequency $\omega_{\text{IF}}$.

1: Those drifts in phase were mainly due to periodic changes of the room temperature due to the cycling of the air conditioning system used in the experiment room.

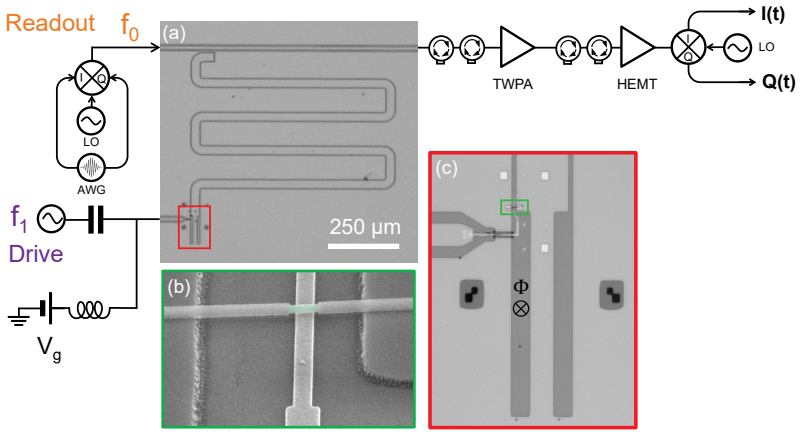


**Figure 10.1:** cQED setup used for time-domain measurements. (a) Optical image of the measured device (sample S2). Left port connected to the gate is devoted to tune the properties of the NW with a DC voltage $V_g$ and to drive microwave transitions between ABS with a tone at frequency $f_1$. (b) Close view (SEM image), showing the local back gate placed below the weak link. (c) (optical image) Shorted end of the resonator, with nanowire in green rectangle corresponding to the area shown in (b). A superconducting coil placed under the sample allows to control, through the flux $\Phi$, the superconducting phase difference across the weak link. The $\lambda/4$ CPW resonator is probed by a readout tone $f_0$ through a bus transmission line to which it is coupled in a hanger geometry. The readout tone $f_0$, generated by mixing a LO tone with $I$ and $Q$ pulses at $\omega_{\text{IF}}/2\pi = 50$ MHz, is sent to the bus line, then amplified (triangle) with a TWPA followed by a HEMT and a room-temperature amplifier (not represented); and finally down-converted with another IQ mixer in a process known as heterodyne detection. The $I$ and $Q$ outcomes are then digitized and numerically demodulated at $\omega_{\text{IF}}$ (not shown).

The experiments were performed with sample S2. An equivalent electrical circuit of the device is shown in Figure 10.2. As already mentioned, moving to a galvanic scheme increased the geometrical coupling to the nanowire by about two orders of magnitude (factor ×275 in $\delta_{\text{zp}}^2$), which allowed to better resolve the many-body states. In addition, the stronger coupling to the measurement port ($Q_{\text{ext}} \sim 17\times10^3$ instead of $\gtrsim 170\times10^3$ in sample S1) allows faster resonator readout.

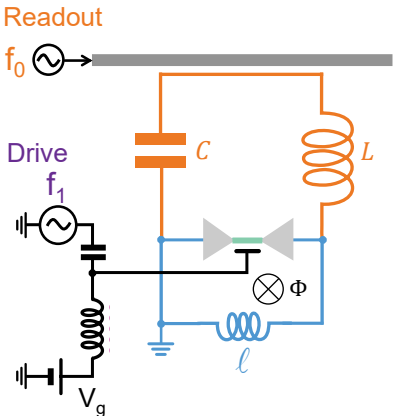


**Figure 10.2:** Equivalent electrical circuit of the cQED setup with galvanic coupling to the nanowire weak link. The readout resonator, probed by a microwave tone $f_0$, is modeled by a parallel LC circuit (orange). A part $\ell$ (light blue) of its total inductance $L$ is shunted by the nanowire weak link, symbolized by a green bar surrounded by two grey triangles for the superconducting electrodes. This naturally defines a DC loop through which a flux $\Phi$ is threaded to phase-bias the weak link. A bias tee is used to both gate the nanowire with a DC voltage $V_g$ and to apply an AC microwave drive $f_1$ to drive transitions between the ABS levels hosted by the weak link.

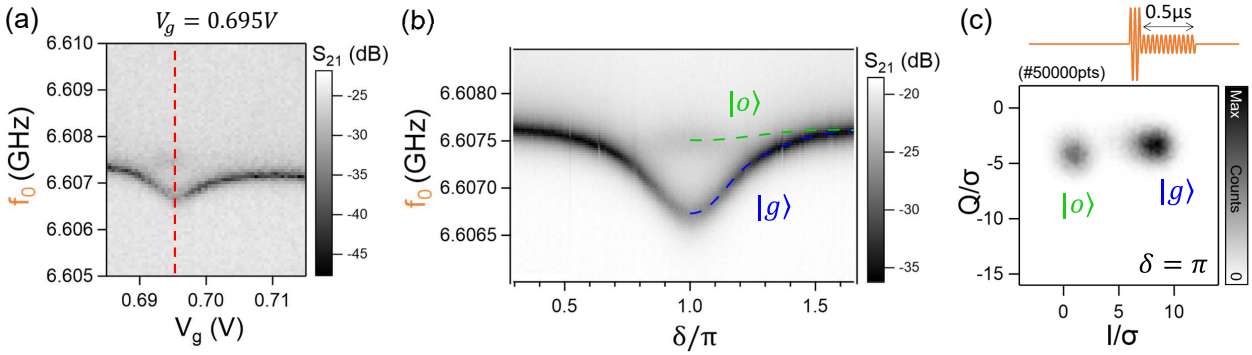


**Figure 10.3:** (a) Continuous-wave single-tone spectroscopy of the resonator showing the modulation of its frequency as a function of the applied gate voltage $V_g$, close to a sweet spot at $V_g = 0.695$ V. The color-scale encodes the magnitude of the transmission coefficient $S_{21}$ as a function of the frequency of the probe tone $f_0$. (b) Similar measurement performed at the sweet spot gate voltage showing the modulation of the resonator frequency as a function of the superconducting phase difference $\delta$, which is controlled by sweeping linearly the magnetic flux $\Phi$ in the weak link loop. Close to $\delta \sim \pi$, one observes two dips in the transmission coefficient, corresponding to the resonator frequency when the weak link resides either in the ground ($|g\rangle$) or in the odd state ($|o\rangle$). Same data as the one presented in Figure 9.4, which was used to characterize the resonator readout dynamics. (c) Histogram showing the outcome of 50000 measurements pulses taken at $\delta = \pi$ at the sweet spot in gate in absence of any driving. The pulse sequence shown in orange consists of a high amplitude fast-load pre-pulse of 220 ns duration followed by a 500 ns square pulse for readout. The results gather in two well-resolved clouds, which are identified as the ground ($|g\rangle$) and odd state ($|o\rangle$) of the weak link. The $I$ and $Q$ values are normalized by $\sigma$, which corresponds to the spread of the gaussian-fitted clouds.

## 10.1 Rates & population dynamics

### 10.1.1 Single-shot readout

We first performed a continuous-wave resonator spectroscopy to choose a working point in gate and flux. In Figure 10.3(a), we show how the resonator frequency is modulated with gate voltage around its bare frequency $f_r = 6.6076$ GHz, in the region of interest for the data presented in the following. At $V_g = 0.695$ V, the resonator frequency shows a local minimum in gate voltage: operating in such sweet spot is highly appreciated as it allows to be insensitive to first order noise in gate voltage.

Figure 10.3(b) shows the associated modulation in flux of the resonance around $\delta = \pi$ for the gate voltage value of the sweet spot. Note that this data is the same as the one presented before in Figure 9.4, which was used to characterize the resonator dynamics and from which we extracted the time constant $\tau \approx 700$ ns of the resonator and its bare frequency $f_r = 6.607643$ GHz. In this particular situation, one can observe that near $\delta = \pi$, the transmission coefficient features two dips in its magnitude, corresponding to the resonator frequency associated to the lowest two many-body states of the weak link. As this measure was performed in absence of any driving $f_1$, we expect the system to reside mainly in its ground state. Therefore, the lower dip around $f_0 = 6.6067$ GHz is associated to $|g\rangle$. As a now well-established characteristic of such nanowire weak link, we know that in some fraction of the time, the system is poisoned by some non-equilibrium quasiparticles and therefore resides in an odd-parity state, labelled $|o\rangle$ [19, 88]. Importantly, note that contrary to atomic contacts data, the resonator frequency still exhibits a small shift in the odd state of finite-length weak links. This was discussed in Section 4.2.3, where we attributed this effect to a contribution from the continuum.

To better evidence the two states, we show in Figure 10.3(c) a histogram of the outcome of 50000 measurement pulses taken at the sweet spot at $\delta = \pi$ without any driving. The measurement pulse, which was set at the frequency of the odd state $f_0 = 6.6075$ GHz, consists in a high amplitude pre-pulse of 220 ns to fast-load the resonator, followed by a 500 ns square pulse for readout. After down-conversion to the IF frequency ($\omega_{\rm IF} = 50$ MHz), the pulses were digitized and demodulated numerically, as described formally in Section 14.3 and in Appendix I. For each pulse record, averaging the demodulated samples over the time window corresponding to the readout part of the pulse yields one pair of $\{I, Q\}$ outcomes. As observed in Figure 10.3(c), the results cluster in two well-resolved clouds of points. As the system mainly resides in its ground state, the most intense cloud corresponds to $|g\rangle$. The other cloud, which is associated to $|o\rangle$, does not split when $\delta$ departs from $\pi$. The two spin substates $|o\uparrow\rangle$ and $|o\downarrow\rangle$ remain undistinguishable: this will be discussed in section 11.2. These measurements illustrate how in absence of any driving, the weak link resides in a steady mixed state, where the normalized number of points in each cloud of the $IQ$ histogram is a direct measurement of the states' population. Importantly, because the two clouds are separated enough, a single measurement pulse allows to discriminate between the two many-body states $|g\rangle$ and $|o\rangle$ of the weak link.

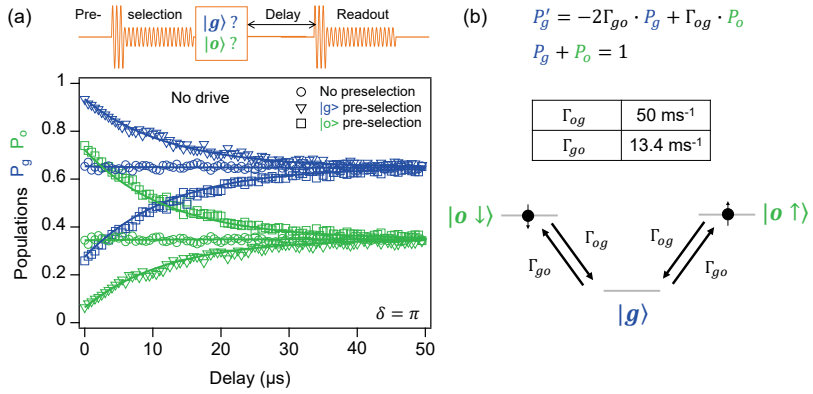


**Figure 10.4:** Parity switching rates. (a) Evolution of the ground (blue) and odd state (green) populations $P_g$ and $P_o$ as a function of the time delay between the state preparation by pre-selection and the readout, for three different cases: no state pre-selection (circle data), with $|g\rangle$ (triangle data) or $|o\rangle$ (square data) pre-selection. (b) Two-state master equation used to model the state population evolution. Best fit of the data obtained when pre-selecting $|g\rangle$, which gives $P_g(0) = 0.93$, $\Gamma_{og} = 50$ ms$^{-1}$ and $\Gamma_{go} = 13.4$ ms$^{-1}$, is overlaid on the data in (a), as well as the prediction for $P_g(0) = 0.275$ ($|o\rangle$ pre-selection) and $P_g(0) = 0.65$ (no pre-selection).

### 10.1.2 Parity-switching rates

We first explored the dynamics between $|g\rangle$ and $|o\rangle$ by measuring how the system relaxes to steady state after preselecting a starting point (see method in Section 14.4). In Figure 10.4(a), we show for three different cases the evolution of the ground and odd state populations $P_g(t)$ and $P_o(t)$ as a function of the time delay between the state preparation by pre-selection and the readout. The first case corresponds to no pre-selection. In such situation, the system resides in a mixed state with in average $P_{g,\infty} = 0.65$ and $P_{o,\infty} = 0.35$. The two other cases correspond to an initial pre-selection of either $|g\rangle$ (triangle data points) or $|o\rangle$ (square

data points). By preparing the state in $|g\rangle$, pre-selection allows to start with an initial population as high as $P_g = 0.93$. As the delay between state preparation and readout increases, $P_g$ relaxes back to $P_{g,\infty}$ at a rate $\Gamma_{go}$. Similarly, if $|o\rangle$ is pre-selected, we manage to start with an initial population $P_o = 0.74$, which relaxes back to $P_{o,\infty}$ at a rate $\Gamma_{og}$. We can model this 2-state dynamics using the following master equation for the populations $P_g$ and $P_o$, associated to a normalization condition:

$$\begin{cases} P'_g(t) = -2\Gamma_{go}P_g(t) + \Gamma_{og}P_o(t) \\ P_g(t) + P_o(t) = 1, \end{cases} \tag{10.1}$$

where the prime exponent denotes time derivative. Injecting the normalization condition in the first equation, we can rewrite it as a function of $P_g$ only:

$$P'_g(t) + (2\Gamma_{go} + \Gamma_{og})P_g(t) = \Gamma_{og}. \tag{10.2}$$

The solution of this first order equation is then easily found:

$$\boxed{P_g(t) = \Big(P_g(0) - P_{g,\infty}\Big)e^{-\Gamma_g t} + P_{g,\infty} \quad \text{with} \quad \begin{cases} P_{g,\infty} = \dfrac{\Gamma_{og}}{\Gamma_g} \\ \Gamma_g = 2\Gamma_{go} + \Gamma_{og}. \end{cases}} \tag{10.3}$$

Fitting the $P_g(t)$ and $P_o(t)$ curves obtained when pre-selecting $|g\rangle$ yields : $P_g(0) = 0.93$, $\Gamma_{go} = 13.4$ ms$^{-1}$ and $\Gamma_{og} = 50$ ms$^{-1}$. The steady state populations are $P_{g,\infty} = \frac{\Gamma_{og}}{2\Gamma_{go}+\Gamma_{og}} = 0.65$ and $P_{o,\infty} = 1 - P_{g,\infty} = 0.35$. The solid lines shown in Figure 10.4(a) correspond to the theory from Eq. (10.3) applied with the rates obtained from this fit of the data with $|g\rangle$ pre-selection and for different initial populations : $P_g(0) = 0.93$, 0.65 and 0.275. The effective relaxation rate for $|g\rangle$ is given by $\Gamma_g = 2\Gamma_{go} + \Gamma_{og} = 76.8$ ms$^{-1}$, which corresponds to a time scale $T_{\text{parity}} = 1/\Gamma_g = 13$ µs. Note that this lifetime for the odd state is about a factor ×10 smaller than what was found in experiments with atomic contacts [88]. Surprisingly, the parity switching time measured by Hays *et al.* on similar nanowire weak links was also found to be much bigger, around $T_{\text{parity}} \approx 160$ µs. Finally, note that the hierarchy $\Gamma_{og} > \Gamma_{go}$ was also found in atomic contacts weak links.

## 10.2 Driven dynamics & coherence

### 10.2.1 Evidencing the excited state

Let us now investigate the effect of a drive tone at frequency $f_1$. To do so, we use the same readout sequence as in Figure 10.3 but prepend before it a driving pulse at frequency $f_1$. This allows to perform a two-tone spectroscopy of the weak link at the sweet spot gate voltage $V_g = 0.695$ V, which is presented in Figure 10.5(a). The measured spectrum shows a parabolic-shaped line with a minimum $f_A(\delta = \pi) = 9.28$ GHz, typical of a pair transition (PT) to the lowest-lying ABS manifold, as well as a set of four single-quasiparticle transitions (SQPT), shown in green, with vanishing intensity away from $\delta \sim \pi$.

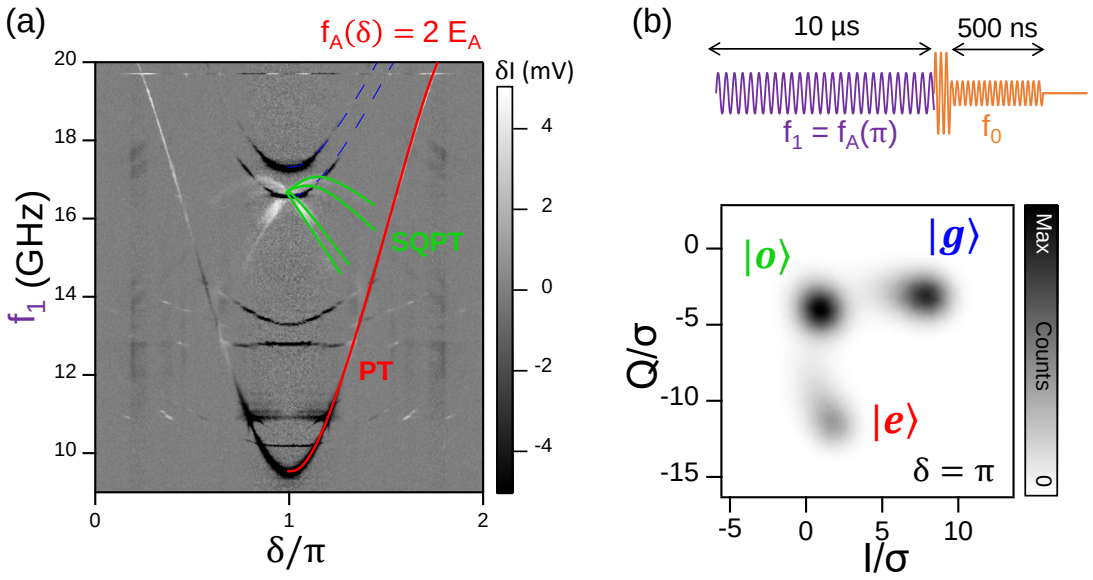


**Figure 10.5:** (a) Two-tone spectroscopy performed at $V_g = 0.695$ V showing a pair transition (red), labelled PT, and a set of single-particle transitions (green), denoted SQPT. The dashed blue lines correspond to half the frequency of the PT with offsets 11.8 and 12.5 GHz. The $I$ quadrature obtained after numerical demodulation at $\omega_{\rm IF}/2\pi = 50$ MHz is plotted as a function of the superconducting phase-difference $\delta$ across the weak link and the frequency $f_1$ of the driving tone. Each data point is obtained by averaging the $I$ outcome of 1000 demodulated pulses consisting of a 220 ns fast-load pre-pulse followed by a 500 ns readout square pulse at $f_0 = 6.6075$ GHz. This readout sequence was preceded by a 10 µs square saturating drive pulse at the frequency $f_1$. (b) Histogram showing the outcome of 10 million measurement pulses taken at $\delta = \pi$ at the sweet spot in gate with a driving tone (violet pulse) at the frequency of the pair transition (PT) $f_1 = f_A(\delta = \pi) = 9.28$ GHz. The pulse sequence shown in orange consists of a high amplitude fast-load pre-pulse of 220 ns duration followed by a 500 ns square pulse for readout. Compared to Figure 10.3(c), a third cloud is now visible in the histogram, positioned symmetrically to $|g\rangle$ with respect to the $|o\rangle$ cloud. Because it appears only when driving at $f_A$, this cloud is associated to the excited state, labeled $|e\rangle$.

When driving at the frequency of the pair transition $f_1 = f_A(\delta = \pi) = 9.28$ GHz, we observe a new cloud appearing in the histogram of the $IQ$ values at $\delta = \pi$ (see Figure 10.5(b)). Because it only appears when driving at this frequency, we attribute it to the lowest excited state of even parity, denoted $|e\rangle$, which is obtained by creating two electron-like excitations in the lowest ABS manifold. This interpretation is supported by the fact that the clouds corresponding to $|g\rangle$ and $|e\rangle$ are located almost symmetrically with respect to that corresponding to $|o\rangle$. Indeed, as demonstrated in Section H.1 for the case of zero-length junctions (and easily generalizable to the finite-length case), the resonator shifts in $|g\rangle$, $|e\rangle$ and $|o\rangle$ verify the following half-sum rule : $(\delta f_r^{|g\rangle} + \delta f_r^{|e\rangle})/2 = \delta f_r^{|o\rangle}$. This is a quite general result, true even when contributions from the continuum are included, but as a key point of Refs [64, 50], it holds only for non-interacting many-body states, which may explain why a perfect symmetry about the odd state cloud is not observed here.

[64]: Kurilovich et al. (2021), 'Microwave response of an Andreev bound state'
[50]: Fatemi et al. (2021), 'Microwave susceptibility observation of interacting many-body Andreev states'

### 10.2.2 Coherent manipulation of the $|g\rangle \rightarrow |e\rangle$ transition

To confirm the clouds identification, we perform a Rabi flopping experiment at the frequency of the pair transition $|g\rangle \rightarrow |e\rangle$ at $\delta = \pi$, as identified from Figure 10.5(a). To do so, we vary the duration $t_d$ of a square driving pulse of frequency $f_1 = f_A(\delta = \pi) = 9.28$ GHz preceding the readout pulse sequence. For each value of the drive duration, we fit with a mixture of three gaussians the associated histogram of the $I, Q$ outcomes obtained by demodulating 50000 readout pulses. The

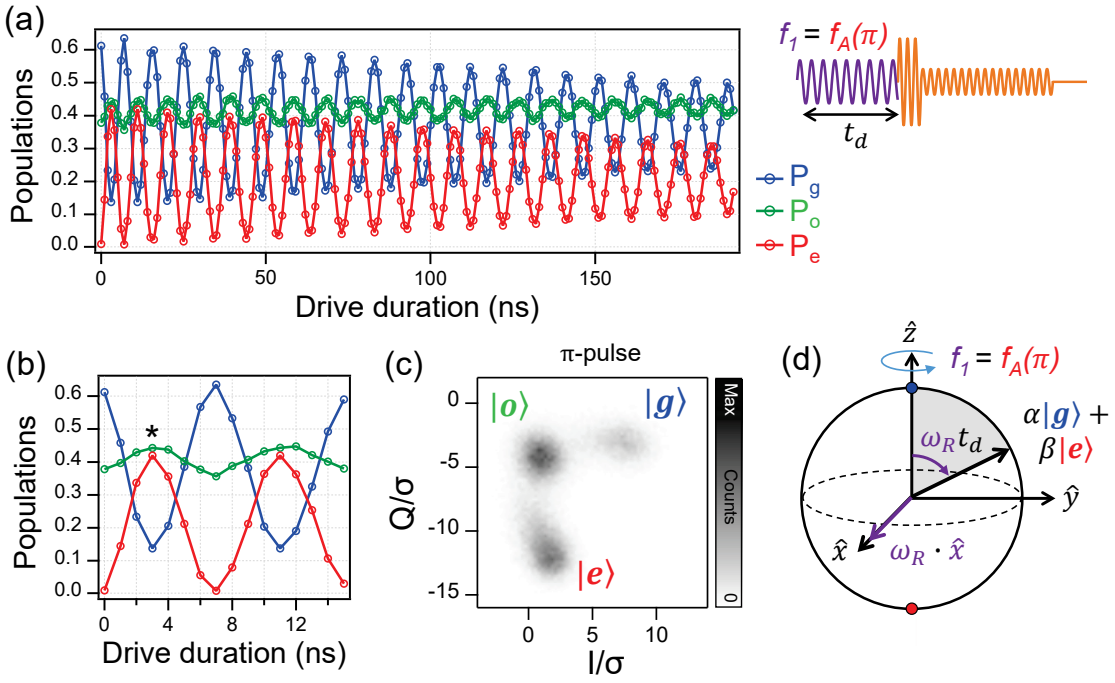


**Figure 10.6:** Coherent manipulation of an Andreev Pair Qubit. (a) Rabi flopping of the $|g\rangle$,$|e\rangle$ populations as a function of the drive pulse duration $t_d$. The drive frequency is set to $f_1 = 9.28$ GHz, which corresponds to the frequency of the pair transition at $\delta = \pi$ depicted in Figure 10.5(a). (b) Enlargement on the first 14 ns of the data from panel (a). An asterisk indicates the drive duration corresponding to a $\pi$ pulse. For each value of the drive duration, the populations of the three states are extracted by fitting with a mixture of three gaussians the histograms of the $I, Q$ outcomes obtained by demodulating 50000 readout pulses. Such an histogram is shown in panel (c), corresponding to the situation where a $\pi$ pulse drive was sent. It illustrates the transfer of population from $|g\rangle$ to $|e\rangle$ due to the coherent drive. (d) Bloch sphere representation of the Andreev Pair Qubit state, describing the effect of the coherent drive as a rotation $R_\theta^{\hat{x}}$ at the Rabi frequency $\omega_R$ of the state vector around the $\hat{x}$ axis. Starting from the north pole, associated to $|g\rangle$, a pulse of duration $t_d$ drives the qubit to a coherent superposition $\alpha|g\rangle + \beta|e\rangle$.

normalized height of the three gaussians gives access to the associated state population, which we can then monitor as a function of the drive pulse duration. This is illustrated in Figure 10.6(a), which shows coherent oscillations of the populations with $t_d$, with a clear oscillatory transfer between $P_g$ and $P_e$. This evolution is described qualitatively using a Bloch sphere representation of the $|g\rangle \rightarrow |e\rangle$ qubit state (see Figure 10.6(d)), where the north (resp. south) pole corresponds to $|g\rangle$ (resp. $|e\rangle$). The effect of a resonant drive is then seen as a rotation $R_\theta^{\hat{x}}$ of the state vector around the $\hat{x}$ axis at the Rabi frequency $\omega_R$ proportional to the drive amplitude, with a polar angle $\theta = \Omega_R t_d$, itself proportional to the drive pulse duration. Starting from the north pole, associated to $|g\rangle$, a pulse of duration $t_d$ then drives the qubit to a coherent superposition $\alpha|g\rangle + \beta|e\rangle$, with $\alpha = \cos(\theta/2)$ and $\beta = \sin(\theta/2)$. Subsequent readout will therefore find the system with a probability $|\alpha|^2 \propto \cos^2(\Omega_R t_d/2)$ in $|g\rangle$ and a probability $1 - |\alpha|^2$ in $|e\rangle$. In addition to this simple picture, we also observe a small oscillation in the odd state population $P_o$ in phase with the oscillation in $P_e$. At first sight, this is surprising since the drive tone being used is resonant with the transition between two even-parity states, and we do not expect microwaves to couple states of different parity. This oscillation is understood here as a consequence of relaxation before measurement: there is a finite delay between the driving pulse and the readout one, and the duration of the readout pulse is also finite. In this time interval part of the $|e\rangle$ population relaxes to $|o\rangle$ or $|g\rangle$ leading to an oscillation of $P_o$ in phase with that of $P_e$. Note that

similar measurements on atomic contacts did not show such an effect [21], indicating that the rate $\Gamma_{eo}$ is significantly larger here. The measurement of $\Gamma$'s is described the next section.

[21]: Janvier (2016), 'Coherent manipulation of Andreev Bound States in an atomic contact', p. 92

The damping of the oscillations is associated both to the relaxation rate of $|e\rangle$ and to the dephasing rate at the Rabi frequency [111]. In order to measure these rates independently, other pulse sequences are used. First, using the measured Rabi oscillations, we define a $\theta = \pi$ driving pulse which sets the qubit into its maximally excited state. From Figure 10.6(b), we see that $|e\rangle$ reaches a maximum for a drive duration $t_\pi = 3$ ns, highlighted by a black asterisk in the figure. The associated histogram is shown in Figure 10.6(c), where the population transfer from the $|g\rangle$ cloud to the $|e\rangle$ one is observed. Once again, this transfer appears uncomplete because of transitions during the measurement.

[111]: Ithier et al. (2005), 'Decoherence in a superconducting quantum bit circuit'

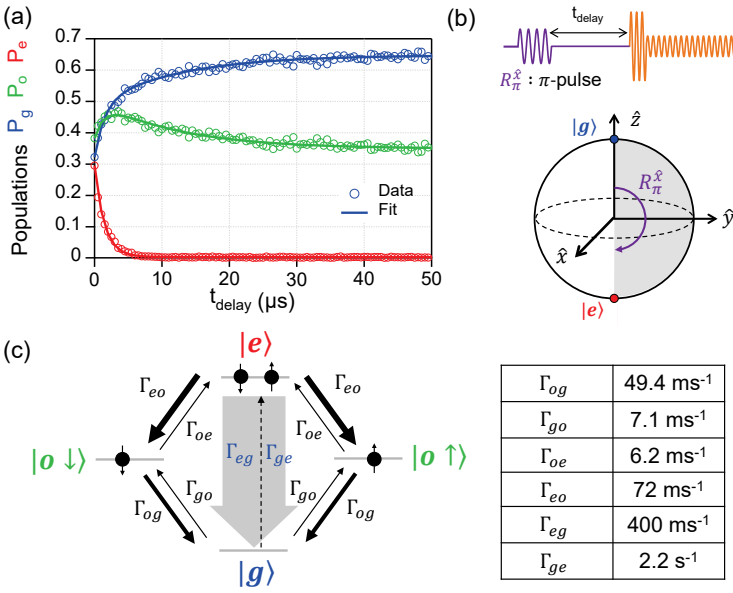


| | |
|---|---|
| $\Gamma_{og}$ | 49.4 ms$^{-1}$ |
| $\Gamma_{go}$ | 7.1 ms$^{-1}$ |
| $\Gamma_{oe}$ | 6.2 ms$^{-1}$ |
| $\Gamma_{eo}$ | 72 ms$^{-1}$ |
| $\Gamma_{eg}$ | 400 ms$^{-1}$ |
| $\Gamma_{ge}$ | 2.2 s$^{-1}$ |

**Figure 10.7:** Relaxation dynamics. (a) Evolution of the ground, odd and excited states populations $P_g$, $P_o$, $P_e$ as a function of the time delay $t_{\text{delay}}$ after a $\pi$-pulse. $P_e$ decays exponentially to zero over a typical time scale of 1.5 μs. (b) Schematics of the pulse sequence, consisting of a square drive pulse (violet) of duration $t_\pi = 3$ ns to prepare the system in its maximally excited state, followed by the usual readout sequence (orange) which is delayed with respect to the drive pulse end by a time $t_{\text{delay}}$. In a Bloch sphere representation, the $\pi$-pulse by definition corresponds to a rotation $R_\pi^{\hat{x}}$ of the state vector, which is brought to the south pole associated to the excited state $|e\rangle$. (c) Three-state model of the system with six different rates. The associated master equation is solved and the best fit of the dynamics is displayed as solid lines in panel (a) on top of the experimental data. The extracted rates are summarized in the given table and represented on the state diagram with arrows' thickness proportional to the relative rates. The $\Gamma_{ge}$ rate which is several orders of magnitude lower than the others is depicted with a dashed arrow.

### 10.2.3 Lifetime of the excited state

To access the lifetime of the excited state, we drive the pair qubit into its maximally excited state by use of a $\pi$-pulse, and measure its state with the same readout sequence as before, but after a delay $t_{\text{delay}}$. The relaxation dynamics of the three states' populations is shown in Figure 10.7(a). As the delay is increased, the population $P_e$ of the excited state decreases because it relaxes back to the ground state. $P_e$ is observed to decay exponentially over a time scale $T_1 \sim 1.8$ μs.The relaxation of the ground state population $P_g$ to its steady-state value $P_{g,\infty} = 0.65$ is

found to be well captured by a double exponential increase with time scales $\tau_{g,1}, \tau_{g,2} = 1.8, 15.7$ µs. As for the odd state, its population $P_o$ shows a non-trivial evolution characterized by a fast initial increase, a bump at $t_{\text{delay}} \sim 3$ $\mu$s, and finally a long-time decrease to its steady-state value $P_{o,\infty} = 0.35$ over a $\sim 14$ µs. This relaxation dynamics can be well accounted for by the following three-state master equation, with six rates and two initial populations $P_g(0)$ and $P_e(0)$:

$$\begin{cases} P'_e(t) = \Gamma_{ge} P_g(t) - (\Gamma_{eg} + 2\Gamma_{eo}) P_e(t) + \Gamma_{oe} P_o(t) \\ P'_g(t) = -(\Gamma_{ge} + 2\Gamma_{go}) P_g(t) + \Gamma_{eg} P_e(t) + \Gamma_{og} P_o(t). \end{cases} \tag{10.4}$$

The six rates are defined in the state diagram in Figure 10.7(c). Using the normalization condition $P_g + P_e + P_o = 1$, we can rewrite this system in function of $P_g$ and $P_e$ only:

$$\begin{cases} P'_e(t) = (\Gamma_{ge} - \Gamma_{oe}) P_g(t) - (\Gamma_{eg} + 2\Gamma_{eo} + \Gamma_{oe}) P_e(t) + \Gamma_{oe} \\ P'_g(t) = -(\Gamma_{ge} + 2\Gamma_{go} + \Gamma_{og}) P_g(t) + (\Gamma_{eg} - \Gamma_{og}) P_e(t) + \Gamma_{og}. \end{cases} \tag{10.5}$$

It assumes an analytical solution, but the expressions for $P_g(t)$ and $P_e(t)$ are long and cumbersome and are therefore not given here *in extenso*. The solution of the master equation Eq. (10.5) is used to fit the data of Figure 10.7(a) with the six rates as free parameters and the initial populations fixed by the data. This model is found to fit well the data (see solid lines in Figure 10.7(a)) and the extracted rates are summarized in the table of Figure 10.7(c). From Eq. (10.5), we identify the typical relaxation rate of the excited state $\Gamma_1 = \Gamma_{eg} + 2\Gamma_{eo} + \Gamma_{oe} = 550$ ms$^{-1}$, from which we deduce the typical lifetime of $|e\rangle$, $T_1 = 1/\Gamma_1 = 1.8$ µs (= $\tau_{g,1}$). The other relevant rate, associated to the long-time regain of $P_g$ after the $\pi$ pulse is identified to $\Gamma_g = \Gamma_{ge} + 2\Gamma_{go} + \Gamma_{og}$, which corresponds to $\tau_{g,2} = 1/\Gamma_g = 15.7$ µs.

The dominant rate is found to be $\Gamma_{eg} = 400$ ms$^{-1}$. We can also deduce the rates $\Gamma_{\text{in}}$, $\Gamma_{\text{out}}$ for getting a single quasiparticle in or out : $\Gamma_{\text{in}} = 2\Gamma_{go} = 14.2$ ms$^{-1}$ and $\Gamma_{\text{out}} = \Gamma_{og} = 49.4$ ms$^{-1}$. Remarkably, the rate $\Gamma_{\text{in2}}$ (resp. $\Gamma_{\text{out2}}$) for getting in (resp. out) a *second* quasiparticle is found to be different than $\Gamma_{\text{in}}$ ($\Gamma_{\text{out}}$) for the first one : $\Gamma_{\text{in2}} = \Gamma_{oe} = 6.2$ ms$^{-1}$ and $\Gamma_{\text{out2}} = 2\Gamma_{eo} = 144$ ms$^{-1}$. This asymmetry $\Gamma_{eo} \neq \Gamma_{og}$ (resp. $\Gamma_{go} \neq \Gamma_{oe}$) for removing (resp. adding) a quasiparticle might be interpreted as a consequence of a Coulomb interaction effect beyond mean-field, which was the subject of Chapter 8.

As illustrated in Figure 10.8(a), the initial excited state population can be slightly increased by preparing the system in $|g\rangle$ by state pre-selection, before applying the $\pi$-pulse. Although pre-selection is demonstrated to work well and an initial population $P_g = 0.93$ is achieved, only ~half of this population is at best found in $|e\rangle$ after the measurement sequence: with a $\pi$-pulse one obtains an initial population $P_e(0) = 0.43$ instead of 0.3 without pre-selection. Using the rates extracted from the dataset without pre-selection, we capture well the population evolutions of all data sets by merely changing the populations at $t_{\text{delay}} = 0$ (see Figure 10.8(c)).

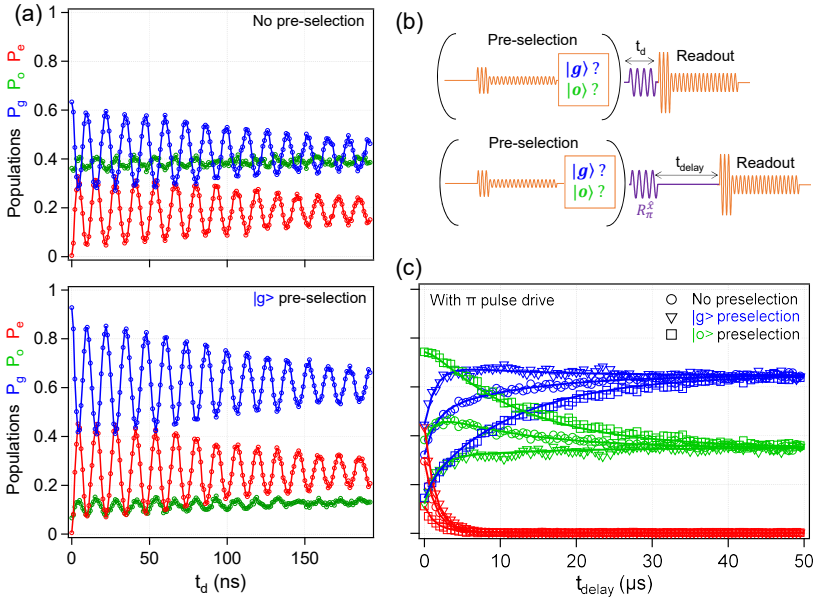


**Figure 10.8:** (a) Rabi oscillations at the frequency of the pair transition for $\delta = \pi$, at the sweet spot gate voltage $V_g = 0.695$ V. The evolution of the populations $P_g$, $P_o$ and $P_e$ is plotted as a function of the drive pulse duration $t_d$ with (bottom) or without (top) pre-selection of $|g\rangle$ before manipulation. (b) Schematics of the pulse sequences used for Rabi measurements (a) and relaxation measurements (c), with state pre-selection. (c) Evolution of the state populations $P_g$, $P_o$ and $P_e$ as a function of the delay after a $\pi$-pulse for three different cases: no state pre-selection (circle), with $|g\rangle$ (triangle) or $|o\rangle$ (square) pre-selection. The duration of the $\pi$-pulse is determined from (a). Solid lines are predictions from the master equation model using the rates extracted from the fit of the data without pre-selection, by just changing the initial populations.

The value of $\Gamma_1$ that is found here is about four times larger than what was measured in experiments with atomic contacts [21] [2] . Indeed, both the direct rate $\Gamma_{eg}$ and the relaxation channel through the odd state is observed to be four times faster than for atomic contacts. Relaxation through the odd states occurs at a rate $\Gamma_{1,\text{odd}} = \frac{\Gamma_{eo}\Gamma_{og}}{\Gamma_{eo}+\Gamma_{og}} = 30\ \text{ms}^{-1}$, which is about ×4 larger than for atomic contacts, although the rates ratio for the two relaxation channels $\frac{\Gamma 1,\text{even}}{\Gamma 1,\text{odd}} \approx 13$ is similar. This fast relaxation from $|e\rangle$ to $|o\rangle$ limits the maximal $P_e$ accessible with a $\pi$-pulse, so that even with $|g\rangle$ pre-selection, the maximum $P_e$ accessible does not exceed $\sim 0.4$. As another remarkable difference with atomic contacts, we observe that reciprocal processes for poisoning and de-poisoning events do not have similar rates here: $\Gamma_{go} \neq \Gamma_{go}$ and $\Gamma_{eo} \neq \Gamma_{oe}$. The de-poisoning processes that remove quasiparticles are about ×10 faster than the poisoning processes. The comparison here is done for a given working point in gate and flux. To complete the analysis, one should perform in the future similar measurements for the rates as a function of the frequency of the pair transition to allow for a fair comparison between nanowire- and atomic contact weak links.

[21]: Janvier (2016), 'Coherent manipulation of Andreev Bound States in an atomic contact', p. 146

2: To perform a fair comparison one have to consider the rates obtained for an atomic contact with a similar Purcell relaxation rate.

### 10.2.4 Coherence

To conclude the characterization of this nanowire-based Andreev pair qubit, we now present the measurements performed to quantify its coherence properties at $\delta = \pi$. The latter is known to be limited by two effects: pure relaxation at a rate $\Gamma_1$ which we just characterized, and pure dephasing at a rate $\Gamma_\Phi$, which originates from fluctuations of the qubit

frequency. In particular, since the Andreev energy depends both on $\delta$ and $V_g$, noise in flux and gate voltage can directly affect the coherence of an Andreev Pair Qubit. To minimize these two possible sources of dephasing, one generally tries to work in so-called "sweet spots", where the qubit frequency dispersion with the external parameters (here $\Phi$ and $V_g$) exhibits a local extremum. This way, qubit operation remains insensitive at first order to these possible noise sources. Therefore, for the best performance we characterized our pair qubit at $\delta = \pi$ and at $V_g = 0.695$ V where the pair transition frequency exhibits a minimum both in flux and gate voltage.

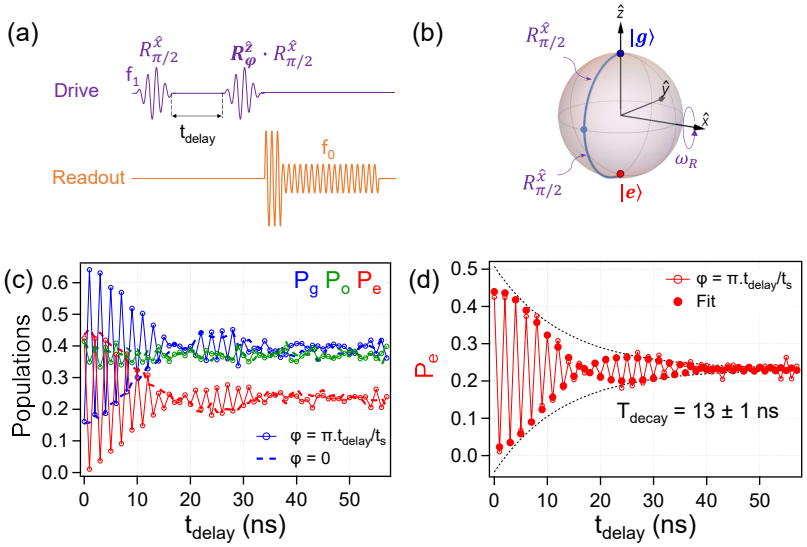


**Figure 10.9:** Ramsey experiment and two-tone spectroscopy of an Andreev Pair Qubit, suggesting the presence of a bi-stable charge fluctuator (BF). (a) Ramsey sequence, consisting in two $\pi/2$ rotations $R^{\hat{x}}_{\pi/2}$ separated by a time delay $t_{\text{delay}}$. A $t_{\text{delay}}$-dependent phase $\varphi$ can be added to the second $\pi/2$-pulse to introduce oscillations in the Ramsey pattern and allow for a more accurate fit. Contrary to the previous data, the drive pulses were this time designed with a gaussian envelope with FWHM=16 ns. (b) Corresponding Qubit trajectory on the Bloch sphere for $\varphi = 0$. (c) Measured evolution of the populations $P_g$, $P_e$ and $P_o$ as a function of the time delay $t_{\text{delay}}$ between the two $\pi/2$-pulses of a Ramsey sequence. Oscillations in the populations are obtained by setting alternatively $\varphi$ to 0 and $\pi$. Data without the $\varphi$ rotations are shown with dashed lines. (d) Fit of the $P_e$ evolution with Eq. (10.6) showing an exponential damping of the oscillations with $t_{\text{delay}}$ over a typical decay time $T_{\text{decay}} = 13 \pm 1$ ns, as well as a beating with a half-periodicity in $t_{\text{delay}}$ of about 24 ns, corresponding to a $\sim 20$ MHz detuning.

### Ramsey experiment

To characterize the dephasing time $T_\Phi = 1/\Gamma_\Phi$ of our qubit, we perform a Ramsey sequence, with consists in applying two driving $\pi/2$-pulses separated by a delay $t_{\text{delay}}$ and measuring the qubit state right afterwards. The first pulse ideally drives the qubit to an equal superposition $(|g\rangle + |e\rangle)/\sqrt{2}$ ; in the Bloch sphere representation, this amounts to bringing the state vector from the north pole to the equator, as shown in Figure 10.11(a). If $t_{\text{delay}}$ is short and no dephasing occurs between the two pulses, the second one then drives the qubit to $|e\rangle$, associated to the south pole of the Bloch sphere. If dephasing occurs during the delay, then the state vector will diffuse on the equator, *i.e.* the state will change from $(|g\rangle + |e\rangle)/\sqrt{2}$ to $(|g\rangle + e^{i\Psi}|e\rangle)/\sqrt{2}$. After the second $\pi/2$-pulse, the qubit will therefore be in $\{x, y, z\} = \{\sin(\Psi), 0, -\cos(\Psi)\}$, corresponding to the state $\sin(\Psi/2)|g\rangle + \cos(\Psi/2)|e\rangle$. The second $\pi/2$-pulse will then

bring the qubit to $|e\rangle$ with an oscillating probability $\cos^2(\Psi/2) = (1 + \cos(\Psi))/2$. If the phase is randomly distributed, then the qubit will be in a random mixture of $|g\rangle$ and $|e\rangle$. For a white dephasing noise, one expects an exponential damping of the $P_e$ oscillations with $t_{\text{delay}}$ over a time scale $T_2^*$, which is related to the pure dephasing time $T_\Phi$ by $(T_2^*)^{-1} = (2T_1)^{-1} + T_\Phi^{-1}$ [111].

[111]: Ithier et al. (2005), 'Decoherence in a superconducting quantum bit circuit'

To allow for an accurate fit of this decay, we introduce oscillations by adding a $t_{\text{delay}}$-dependent phase $\varphi(t_{\text{delay}})$ to the second $\pi/2$-pulse. This corresponds to turning the direction of the second pulse in the $xy$ plane. Figure 10.9(a) shows the result of such a Ramsey experiment performed in sweet spot conditions ($V_g = 0.695$ V, $\delta = \pi$) for both $\varphi = 0$ and $\varphi = \pi \times t_{\text{delay}}/t_s$ with a sampling time $t_s = 1$ ns. For $t_{\text{delay}} = 2n$ with $n \in \mathbb{N}$, $\varphi = 0$ and the driving sequence performs an equivalent $\pi$-pulse ; indeed a maximum $P_e = 0.64$ is observed at $t_{\text{delay}} = 0$. For $t_{\text{delay}} = (2n+1)t_s$, $\varphi = \pi$ and the second $\pi/2$-pulse is then expected to bring the qubit back in $|g\rangle$: indeed, Figure 10.9(a) shows a maximum in $P_g$ and a minimum in $P_e$ at $t_{\text{delay}} = t_s = 1$ ns. This trend extends further with $P_e$ and $P_g$ oscillating between local maxima and minima at each $t_s$ increment of $t_{\text{delay}}$. Besides the expected exponential decay of the coherent signal, one also observes a strong beating pattern with a half-periodicity in $t_{\text{delay}}$ of about 24 ns, corresponding to a $\sim 20$ MHz detuning. This evolution can be phenomenologically captured with the following functional form:

$$P_g(t) = \Big(P_g(0) - P_{g,\infty}\Big)\cos\Big[\varphi(t_{\text{delay}})\Big]\cos\Big[2\pi\Delta t_{\text{delay}} + \phi\Big]e^{-\frac{t_{\text{delay}}}{T_{\text{decay}}}} + P_{g,\infty}. \tag{10.6}$$

Fitting $P_e$ with this expression, we obtain $T_{\text{decay}} = 13 \pm 1$ ns for the exponential decay of the Ramsey oscillations and a beating frequency $\Delta = 20.6 \pm 0.8$ MHz, as shown in Figure 10.9(b).

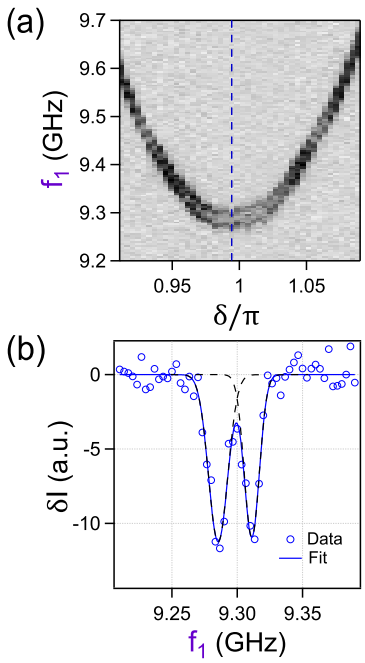


**Figure 10.10:** (a) Two-tone spectroscopy of the pair qubit frequency around $\delta = \pi$ with a finer frequency resolution than in Figure 10.5, evidencing a split-peak structure of the qubit transition line. (b) Linecut of (a) at $\delta = \pi$ showing a clear 20 MHz splitting of the qubit frequency around $f_A \approx 9.30$ GHz. A gaussian fit of the two peaks is overlaid in solid blue line. Individual contributions to the lineshape are shown in dashed black lines.

### Evidence of a charge bi-stable fluctuator

Further insight on the origin of this beating can be gained from the two-tone spectroscopy of the transition line with increased frequency resolution compared to Figure 10.5, see Figure 10.10. It shows a split-peak structure of the pair transition line close to $\delta = \pi$. The linecut at $\delta = \pi$ shown in Figure 10.10(b) evidences a $\sim 20$ MHz splitting of the transition line. This splitting, which is a signature of a discrete environment, seems to be associated to a fluctuation of the weak link transmission, as the splitting is maximal at $\delta = \pi$ and apparently vanishes away from $\pi$. It could originate from the presence of a charged impurity at the surface of the weak link behaving as a bistable fluctuator (BF). Such an impurity can couple to the qubit and if the rate of its incoherent switching is slow enough, it can result in two discrete frequency values for the qubit, as observed in the Ramsey pattern.

Effects due to individual BFs have been observed both in spectroscopy and in time-resolved measurements and their impact on the coherence of solid state qubit was modelled by Falci *et al.* [112]. They showed that even if the BF is not resonant with the qubit, it can strongly affect it. Indeed, provided that its switching rate is slower than the induced splitting $\Delta$ of the qubit frequency, it then makes the working point of the qubit

[112]: Falci et al. (2005), 'Initial Decoherence in Solid State Qubits',

bi-stable and amplifies defocusing from high frequency noise during $t_{\text{delay}}$. Even if the qubit is initially well prepared by the first $\pi/2$-pulse, during $t_{\text{delay}}$ the BF may switch it to a different working point, which will result in damped beats in the coherent oscillations and a split-peak qubit lineshape in spectroscopy, exactly as observed in Figure 10.9. Although in our case the origin and nature of this BF is unclear, it would not be surprising that the quality of the weak link surface had degraded since these measurements were taken during the 17th cool-down of the sample.

Now because of this beating in the Ramsey oscillations, the decay time extracted with the phenomenological equation (10.6) should not be interpreted as the dephasing time $T_2^*$. To better evidence the effect of this beating, we perform a Ramsey experiment at various values of the driving frequency $f_1$, see Figure 10.11. When $f_1$ differs from the qubit frequency by an amount $\Delta/2\pi$, the Rabi frequency changes from $\omega_R$ to $\Omega_R = \sqrt{\omega_R^2 + \Delta^2}$, and the rotation axis in the Bloch sphere changes from $\hat{x}$ to $\hat{x}'$, which is directed along the unitary vector $\{\frac{\omega_R}{\Omega_R}, 0, \frac{\Delta}{\Omega_R}\}$.

Denoting by $\theta$ the angle between $\hat{x}$ and $\hat{x}'$, we illustrate graphically in Figure 10.11(a) the effect of such a detuning $\Delta \neq 0$ on the trajectory of the qubit state vector in the Bloch sphere induced by a Ramsey sequence. In absence of drive, $\omega_R = 0$ and the rotation vector $\Omega_R \cdot \hat{x}'$ reduces to $\Delta \cdot \hat{z}$, *i.e.* during $t_{\text{delay}}$ when the drive is off the state vector rotates around $\hat{z}$, moving on the Bloch sphere equator at the detuning frequency $\Delta$. With the same analysis as above for the effect of a dephasing $\Psi$ during $t_{\text{delay}}$, we deduce that a finite detuning results in an oscillation of $P_e$ and $P_g$ at an angular frequency $\Delta$, which evolve with $t_{\text{delay}}$ with the same decaying envelope as at zero detuning.

Figure 10.11(b) shows the result of such a measurement at $\delta = \pi$ with the population of the ground state $P_g$ oscillating with $t_{\text{delay}}$ as the drive frequency $f_1$ gets detuned from $f_A \approx 9.286$ GHz. These experimental data are compared to calculations taking into account (panel (c)) or not (panel (d)) the presence of a BF. Those calculations were obtained from a phenomenological model describing the expected geometrical trajectories in the Bloch sphere for a Ramsey sequence. The rotation matrix around $\hat{x}'$ by an angle $\theta$ is given by:

$$R[\omega_R, \Delta, \theta] = \begin{pmatrix} \frac{\omega_R^2}{\omega_R^2+\Delta^2}(1-c)+c & -\frac{\Delta}{\sqrt{\omega_R^2+\Delta^2}}s & \omega_R\frac{\Delta}{\omega_R^2+\Delta^2}(1-c) \\ \frac{\Delta}{\sqrt{\omega_R^2+\Delta^2}}s & c & \frac{-\omega_R}{\sqrt{\omega_R^2+\Delta^2}}s \\ \omega_R\frac{\Delta}{\omega_R^2+\Delta^2}(1-c) & \frac{\omega_R}{\sqrt{\omega_R^2+\Delta^2}}s & \frac{\Delta^2}{\omega_R^2+\Delta^2}(1-c)+c \end{pmatrix}, \tag{10.7}$$

where we abbreviated $c = \cos(\theta)$ and $s = \sin(\theta)$. Assuming that the $\pi/2$-pulse duration $t_{\pi/2}$ is tuned at a frequency $f_{1,0}$ corresponding to a detuning $\Delta_0$, *i.e.* $\frac{\pi}{2} = \Omega_R(\Delta_0)t_{\pi/2}$, the rotation angle $\theta_\Delta$ due to a pulse at another detuning $\Delta$ is then $\theta_\Delta = \frac{\Omega_R(\Delta)}{\Omega_R(\Delta_0)}\frac{\pi}{2}$.

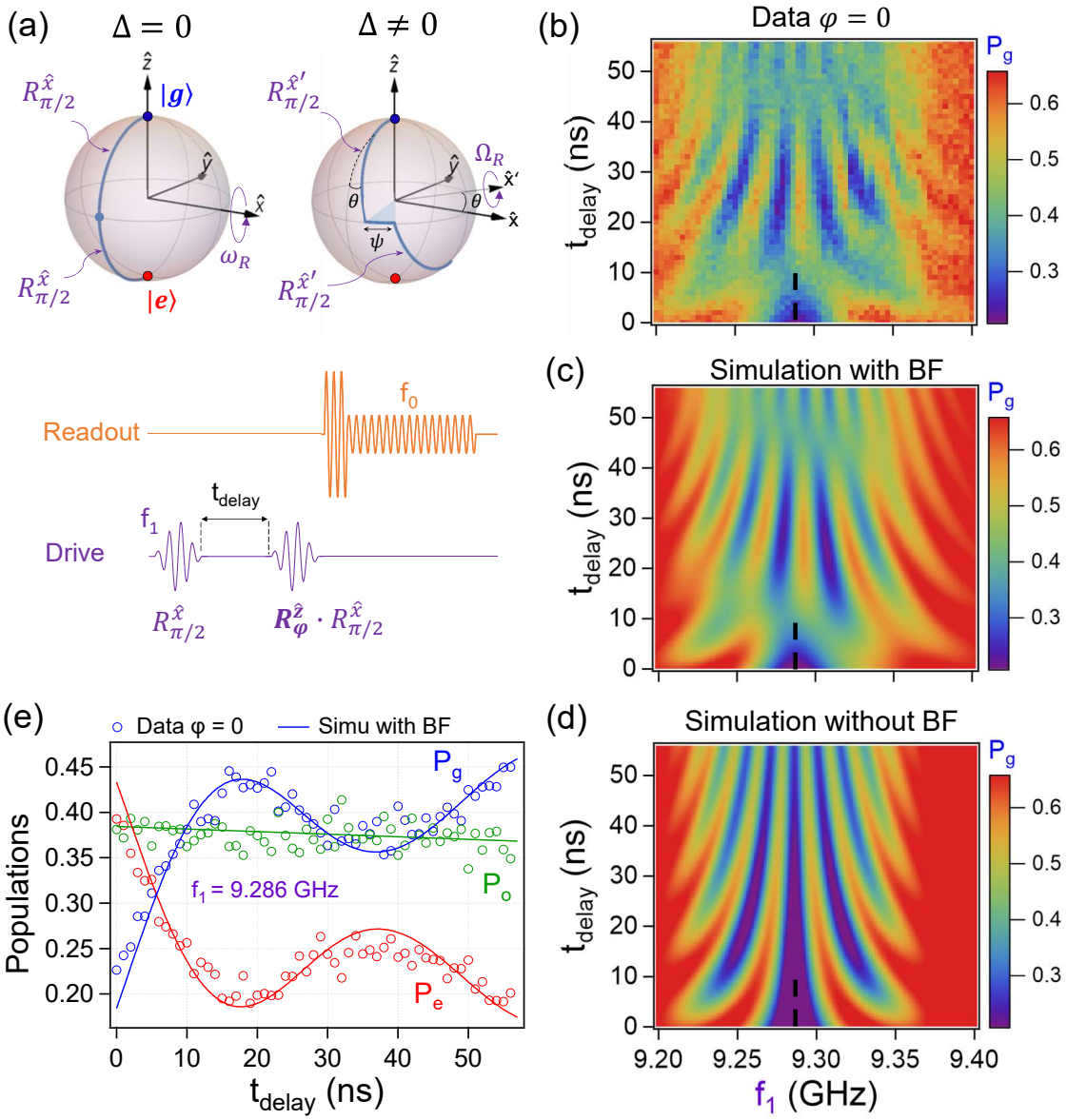


**Figure 10.11:** Effect of a bi-stable charge fluctuator (BF) on a Ramsey measurement of an Andreev Pair Qubit. (a) Qubit trajectory on the Bloch sphere associated to a Ramsey sequence, consisting in two $\pi/2$ rotations $R^{\hat{x}}_{\pi/2}$ separated by a time delay $t_{\text{delay}}$. When the drive frequency $f_1$ has a finite detuning $\Delta/2\pi = f_1 - f_a$ to the qubit frequency $f_a$, the qubit rotates at a generalized Rabi frequency $\Omega_R = \sqrt{\omega_R^2 + \Delta^2}$ and around a modified axis, denoted $\hat{x}'$, which is tilted by an angle $\theta = \tan(\Delta/\omega_R)$ with respect to $\hat{x}$. After the first $\pi/2$ rotation, the qubit follows a free evolution during a time $t_{\text{delay}}$, corresponding to a rotation at the angular frequency $\Delta$ around the $\hat{z}$ axis that dephases the qubit by an angle $\Psi = \Delta \cdot t_{\text{delay}}$. (b) Experimental data for $\varphi = 0$ showing the oscillations of the ground state population $P_g$ with the drive frequency $f_1$ and the time $t_{\text{delay}}$ between the two $\pi/2$-pulses of the Ramsey sequence. The $\pi/2$-rotations were performed using 16 ns gaussian pulses, the amplitude of which was obtained by a prior calibration from a power Rabi measurement at the frequency $f_{1,0} = 9.286$ GHz. Panel (d) shows a calculation of the Ramsey pattern for $\omega_R/2\pi = 25.6$ MHz and $T_2^* = 50$ ns assuming a single transition frequency $f_a = 9.286$ GHz. This calculations reproduces qualitatively the measured pattern but does not capture the damped beating visible in the data. To improve the comparison, we assume that the transition line is split in two frequencies $f_a$ and $f_b$ due to the switching of the BF. Panel (c) shows the expected Ramsey pattern deduced from Eq. (10.10) for an equal weight superposition ($\alpha = 0.5$) of the responses at the two frequencies. Best comparison is obtained for $f_a = 9.28$ GHz, $f_b = 9.3065$ GHz, which are about $\sim 20$ MHz apart, as was evidenced by two-tone spectroscopy of the transition line in Figure 10.9(c,d). (e) Linecut at $f_1 = 9.286$ GHz comparing data from (b) and the calculation with BF from (c).

Starting from $\{x, y, z\} = \{0, 0, 1\}$ associated to $|g\rangle$, the point on the Bloch sphere reached after the first $\pi/2$ pulse has the following coordinates:

$$R[\omega_R, \Delta, \theta_\Delta] \cdot \begin{pmatrix} 0 \\ 0 \\ 1 \end{pmatrix} = \left\{ \frac{2\Delta\omega_R}{\Omega_R(\Delta)^2} \sin^2\left(\frac{\theta_\Delta}{2}\right),\ -\frac{\omega_R}{\Omega_R(\Delta)} \sin(\theta_\Delta),\ 1 - \frac{2\omega_R^2}{\Omega_R(\Delta)^2} \cos^2\left(\frac{\theta_\Delta}{2}\right) \right\}. \tag{10.8}$$

During $t_{\text{delay}}$, the qubit vector then experiences a free evolution, corresponding to a rotation around $\hat{z}$ at the angular frequency $\Delta$, given by $R[0, \Delta, \Delta \cdot t_{\text{delay}}]$. Finally, the second $\pi/2$-pulse amounts to applying a second time the rotation matrix $R[\omega_R, \Delta, \theta_\Delta]$. The asymptotic state can be easily found: if $t_{\text{delay}} \gg 2\pi/\Delta$, then the state vector has diffused all along the circle of constant latitude reached after the first $\pi/2$-pulse ; the mean z-coordinate $z_\infty$ after the second $\pi/2$-pulse is then given by :

$$\begin{aligned} z_\infty &= \frac{1}{2\pi} \int_0^{2\pi} \mathrm{d}\delta\ R[\omega_R, \Delta, \theta_\Delta] \cdot R[0, \Delta, \delta] \cdot R[\omega_R, \Delta, \theta_\Delta] \cdot \begin{pmatrix} 0 \\ 0 \\ 1 \end{pmatrix} \\ &= \frac{1}{\Omega_R^4} \left( \Delta^2 + \omega_R^2 \cos(\theta_\Delta) \right)^2. \end{aligned} \tag{10.9}$$

The probability to have reached the excited state is deduced from $P_e = (1 - z_R)/2$, with $z_R$ the z-coordinate of the point on the Bloch sphere reached at the end of the sequence. After some algebra, one finds the following expressing for $P_e$:

$$\begin{aligned} P_e(t_{\text{delay}}) = P_{e,\infty} + \sin^2\left(\frac{\theta_\Delta}{2}\right) \frac{\omega_R^2}{\Omega_R^4} \Big[ \left( \omega_R^2 + (2\Delta^2 + \omega_R^2) \cos(\theta_\Delta) \right) \cos(\Delta t_{\text{delay}}) \\ - 2\Delta\Omega_R \sin(\theta_\Delta) \sin(\Delta t_{\text{delay}}) \Big], \end{aligned} \tag{10.10}$$

with $P_{e,\infty} = (1 - z_\infty)/2$ and $z_\infty$ given by Eq. (10.9). For $\Delta = 0$, this expression reduces to $P_e = (1 - \cos(2\theta_0))/2 = \sin^2(\theta_0) = 1$, as expected. Finally we introduce phenomenologically the exponential damping of the oscillations with

$$P_e^{\text{fit}}(\Delta, \Delta_0) = P_{e,\infty} + \Big[ P_e(t_{\text{delay}}) - P_{e,\infty} \Big] e^{-t_{\text{delay}}/T_2^*}. \tag{10.11}$$

In Figure 10.11(d) we plot the expected evolution of $P_g^{\text{fit}} = 1 - P_e^{\text{fit}} - P_o$ for a transition frequency at $f_a = 9.286$ GHz ($\Delta_0/2\pi = f_{1,0} - f_a = 0$), $\omega_R/2\pi = 25.6$ MHz and $T_2^* = 50$ ns. The odd state population $P_o$ shows only a very weak linear dependence with $t_{\text{delay}}$ and was first fit to a straight line. The result shares some resemblance with the data but we miss the observed beating pattern in the Ramsey oscillations. Considering that due to the BF there exists two transition frequencies $f_a$ and $f_b$ with relative weight $\alpha$, we compare the data with $\alpha \cdot P_e^{\text{fit}}(\Delta_a, \Delta_{0,a}) + (1-\alpha) \cdot P_e^{\text{fit}}(\Delta_b, \Delta_{0,b})$, where $\Delta_i/2\pi = f_1 - f_i$ and $\Delta_{0,i}/2\pi = f_{1,0} - f_i$ with $i \in \{a, b\}$. This second calculation now captures rather well the measured Ramsey pattern. The best agreement with the data from Figure 10.11(b) is obtained for $\omega_R/2\pi = 25.6$ MHz with the two qubit frequency values $f_a = 9.28$ GHz and $f_b = 9.3065$ GHz, which is consistent with the $\sim 20$ MHz peak splitting that was observed in Figure 10.9(d). $f_{1,0} = 9.286$ GHz is the frequency at which the $\pi/2$-pulses were tuned for this measurement.

We find an exponential decay time of the order $T_2^* = 50$ ns, a value almost $\times 4$ bigger than the $T_{\text{decay}} = 13$ ns that we had with the phenomenological expression Eq. (10.6). A linecut at $f_1 = f_{1,0} = 9.286$ GHz in Figure 10.11(e) shows that the measured populations from panel (b) are globally well captured by the calculation with BF from panel (c).

The effect of the BF can also be seen in a Rabi flopping measurement where the drive frequency $f_1$ is varied. In Figure 10.12(a), we illustrate the effect of such a detuning on the trajectory on the Bloch sphere. A drive pulse of duration $t_d$ rotates the qubit state vector by an angle $\Omega_R \cdot t_d$ around $\hat{x}'$ with $\Omega_R = \sqrt{\omega_R^2 + \Delta^2}$. As $\Delta$ is increased, the circle described on the Bloch sphere gets smaller and closer to the North pole, associated to $|g\rangle$. The $\{x, y, z\}$-point on the sphere reached after $t_d$ is given by:

$$R[\omega_R, \Delta, \Omega_R \cdot t_d] \cdot \begin{pmatrix} 0 \\ 0 \\ 1 \end{pmatrix} = \left\{ \frac{\Delta \omega_R}{\Omega_R^2} \Big( 1 - \cos(\Omega_R t) \Big),\ -\frac{\omega_R}{\Omega_R} \sin(\Omega_R t),\ \frac{\Delta^2 + \omega_R^2 \cos(\Omega_R t)}{\Omega_R^2} \right\}, \tag{10.12}$$

with the rotation matrix defined in Eq. (10.7). From this, we deduce the evolution of the ground state population:

$$P_g(t_d) = \frac{1 + z(t_d)}{2} = \frac{1}{2} + \frac{\Delta^2 + \omega_R^2 \cos(\Omega_R t)}{2\Omega_R^2}. \tag{10.13}$$

As for the Ramsey sequence calculation, this expression does not take into account the presence of the odd state. As a first approximation, on can consider its population constant and simply rescale $P_g$ accordingly. Also, we further introduce a phenomenological exponential decay over a time $T_{\text{decay}}^{\text{Rabi}}$:

$$P_g^{\text{fit}}(\omega_R, \Delta_a, t_d) = P_{g,\infty} + \Big[ P_g(t_d) - P_{g,\infty} \Big] e^{-t_d / T_{\text{decay}}^{\text{Rabi}}}. \tag{10.14}$$

In Figure 10.12(b) we present this detuned Rabi measurement in a 200 MHz window around the pair transition frequency and we compare it with theory assuming again two possible frequencies for the transitions. In Figure 10.12(c), we plot $\alpha \cdot P_g^{\text{fit}}(\omega_R, \Delta_a, t_d) + (1 - \alpha) \cdot P_g^{\text{fit}}(\omega_R, \Delta_b, t_d)$ with $P_g^{\text{fit}}$ from Eq. (10.14). The calculation was performed using the same values for the two qubit frequencies deduced from the detuned Ramsey measurement calculation in Figure 10.11(c), *i.e.* $f_a = 9.28$ GHz and $f_b = 9.3065$ GHz. The best agreement with the data was found with a relative weight $\alpha = 0.65$ between the two qubit frequencies, a Rabi frequency $\omega_R/2\pi = 85$ MHz and an exponential decay time $T_{\text{decay}}^{\text{Rabi}} = 170$ ns. Importantly, note that the frequency axis range differs for the data (b) and the calculation (c) by about a factor $\times 1.5$. For some yet unexplained reason, the oscillations frequency was observed to increase faster with the detuning than Eq. (10.13) predicts. A linecut at $f_1 = 9.286$ GHz is shown in Figure 10.11(d) to compare data and calculation. It shows in particular that the oscillation period in the measured data slightly increases with $t_d$, which is again an effect of the beating between the oscillation patterns centered in $f_a$ and $f_b$. Capturing quantitatively these fine effects would require a more elaborate model taking into account the presence of perhaps more fluctuators, which is out of the scope of the present work.

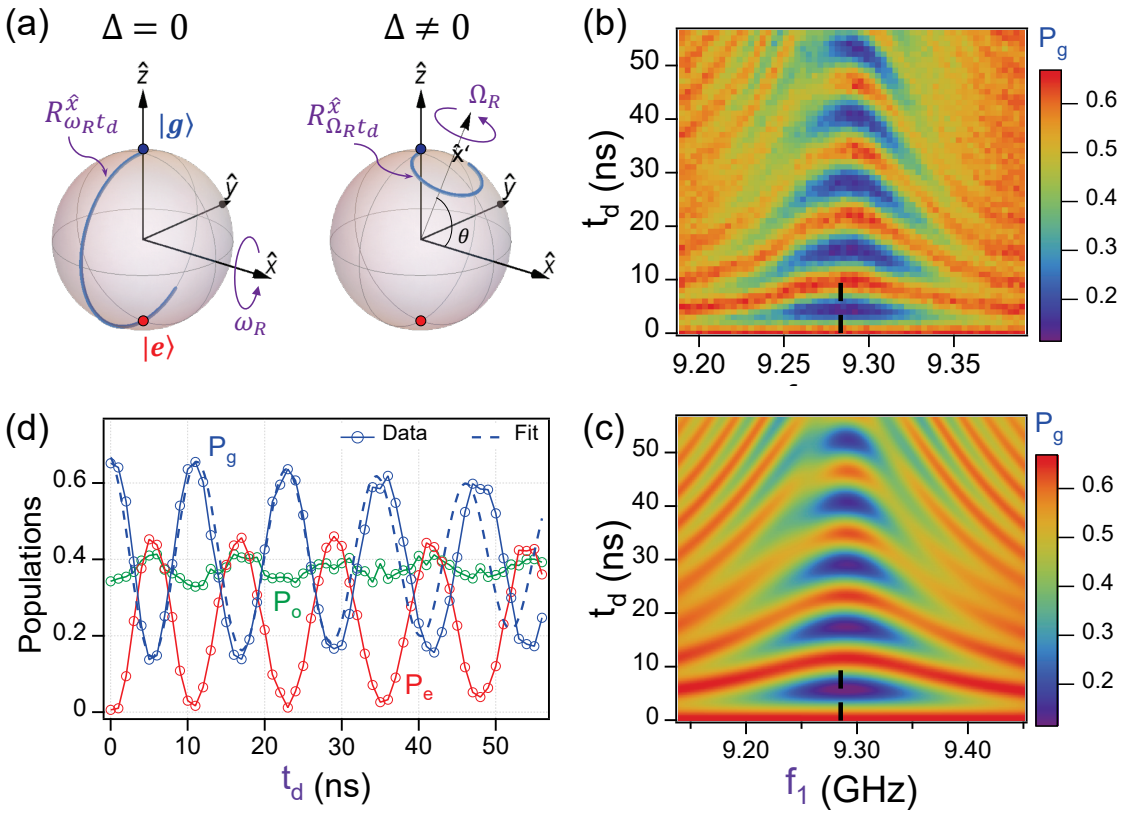


**Figure 10.12:** Effect of detuning on the Rabi oscillations of an Andreev Pair Qubit. (a) A resonant driving pulse ($\Delta = 0$) of duration $t_d$ rotates the qubit around the $\hat{x}$-axis of the Bloch sphere by an angle $\omega_R \cdot t_d$, with $\omega_R$, the Rabi frequency which is proportional to the drive amplitude. As a finite detuning $\Delta \neq 0$ is introduced, the rotation axis $\hat{x} \rightarrow \hat{x}'$ gets tilted by an angle $\theta = \tan \Delta/\omega_R$ and the Rabi frequency is modified to $\Omega_R = \sqrt{\omega_R^2 + \Delta^2}$, which has the effect to lower the amplitude of the $P_e$ oscillations with $t_d$ as the circle described on the Bloch sphere gets smaller and closer to the north pole, associated to $|g\rangle$. (b) Measured Rabi oscillations of the ground state population $P_g$ as a function of drive duration $t_d$ and frequency $f_1$ on a $\sim$ 200 MHz range around the pair qubit transition frequency. (c) Theory from Eqs. (10.13,10.14) assuming the presence of a bi-stable fluctuator, which has the effect to split the qubit transition frequencies in two possible values $f_a$ and $f_b$. Same values were used for $f_a$ and $f_b$ as in Figure 10.11. Best fit was obtained here with $\alpha = 0.65$, $\omega_R/2\pi = 85$ MHz and an exponential decay time for the oscillations of $T_{\text{decay}}^{\text{Rabi}} = 170$ ns. Note that the scale in the $f_1$ axis is different compared to (b). (d) Linecut at $f_1 = 9.286$ GHz highlighted by a dashed black line in (b,c). Data is shown in solid lines and open disks and theory for $P_g$ from (c) is overlaid in dashed blue line. For completeness we also show the extracted values of $P_e$ and $P_o$. A small oscillation is observed in the $P_o$ population, which likely arises from the fast relaxation from $|e\rangle$ to $|o\rangle$ that may happen in the $\sim$ 200 ns time lapse between the end of the drive pulse and the readout, due to the measurement pre-pulse used to fast-load the resonator cavity before readout.

### Hahn echo experiment

To further characterize dephasing noise, we performed a Hahn echo pulse sequence. It consists in a Ramsey sequence in the middle of which an extra $\pi$-pulse has been added, as illustrated in Figure 10.13(a). This has the effect to filter out the noise at frequencies lower than $1/t_{\text{delay}}$ [111, 113], including the low frequency charge noise arising from the incoherent switching of the charge BF. Additional oscillations are obtained by rotating the second $\pi/2$ pulse by $\varphi = \frac{\pi}{32}\frac{t_{\text{delay}}}{1\text{ ns}}$. The beating in the population oscillations is no longer visible and their decay time is observed to be about a factor $\times 10$ longer than for a Ramsey sequence, see Figure 10.13(b). Fitting the oscillations with an exponentially damped cosine, a characteristic decay time $T_{2E} = 404$ ns is obtained, which although smaller is comparable in magnitude to the value measured for an atomic-contact-based pair qubit [21].

[111]: Ithier et al. (2005), 'Decoherence in a superconducting quantum bit circuit'
[113]: Bylander et al. (2011), 'Noise spectroscopy through dynamical decoupling with a superconducting flux qubit'

[21]: Janvier (2016), 'Coherent manipulation of Andreev Bound States in an atomic contact', p.98-99

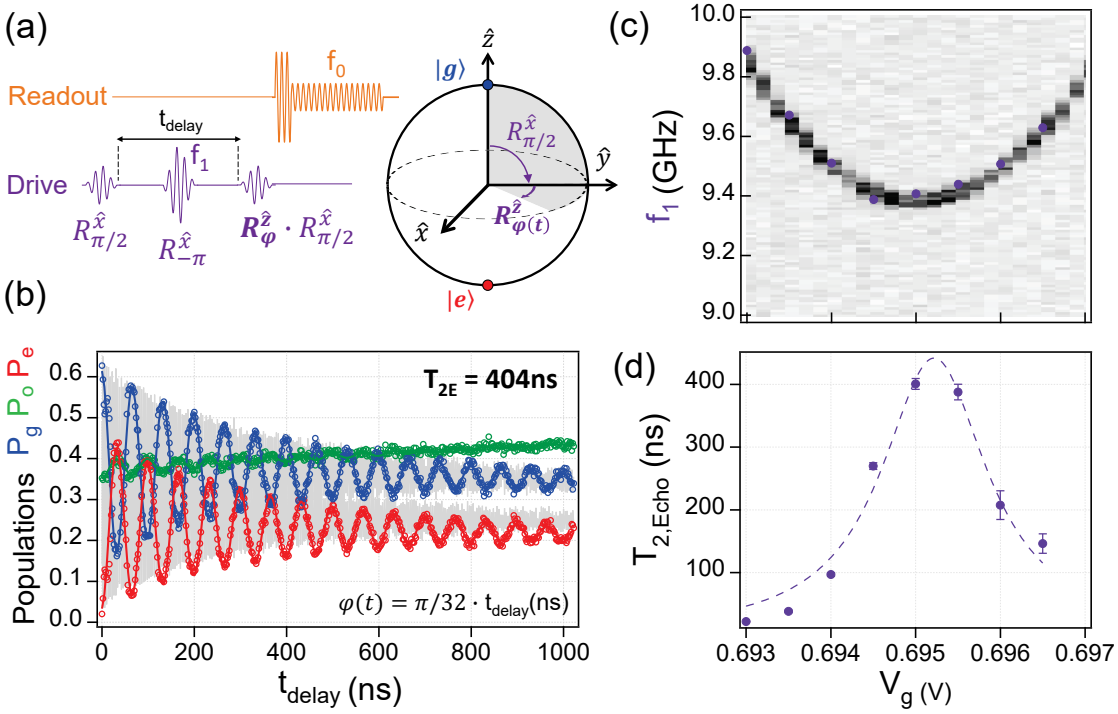


**Figure 10.13:** Coherence of a nanowire-based Andreev Pair Qubit. (a) Hahn echo sequence consisting for the drive (violet) in two $\pi/2$-pulses at frequency $f_1$ separated by a time delay $t_{\text{delay}}$. An extra $\pi$-pulse is added in the middle to filter-out the noise with frequency lower than $1/t_{\text{delay}}$. The second $\pi/2$-pulse may be dephased by an amount $\varphi(t)$ with respect to the first one. Once it has finished, the readout sequence (orange) at frequency $f_0$ is played on the resonator. The effect of a $\pi/2$-pulse is illustrated on the Bloch sphere. (b) Populations $P_g$, $P_o$ and $P_e$ as a function of $t_{\text{delay}}$ measured at $\delta = \pi$ at the gate sweet spot $V_g = 0.695$ V. To allow for a more accurate fit of the decay, we make the populations oscillate with $t_{\text{delay}}$ with a 64 ns periodicity by dephasing the second $\pi/2$-pulse by an amount $\varphi(t) = 2\pi/64 \cdot t(\text{ns})$. The $\pi-$ and $\pi/2$-rotations were performed using 16-ns-long gaussian pulses, the amplitude of which was obtained by a prior calibration from a power Rabi measurement. The $\pi$-pulse was set with a negative amplitude, so as to avoid any saturation of the microwave components at times $t_{\text{delay}} < 16$ ns when the pulses overlap. Therefore, when all three pulses fully overlap, the drive is equivalent to a 0-pulse and we measure the system in $|g\rangle$. Experimental data are shown in circles and a fit with an exponentially decaying sine function is overlaid. In background is shown in light grey the extracted populations for an other Echo measurement with this time $\varphi(t) = \pi/5 \cdot t(\text{ns})$; its fit gives a characteristic decay time for the oscillations of $T_{2E} = 404$ ns. (c) Two-tone spectroscopy evidencing the dispersion with gate voltage $V_g$ of the pair transition frequency $f_A(V_g)$ around the sweet spot at 0.695 V. (d) Evolution of the measured characteristic echo time $T_{2E}$ with $V_g$, showing a maximum of 404 ns at the sweet spot location. Away from $V_g = 0.695$ V, first-order electrostatic noise contributes to dephasing, causing $T_{2E}$ to quickly drop. This can then be modeled using the relation for exponential coherence decay $1/T_{2E} = \Gamma_c + 2\pi(\partial f/\partial V_g)^2 V_{\text{rms}}^2/1\text{Hz}$. Best fit is shown in dashed purple line and yields $V_{\text{rms}} = 3.6 \pm 0.3$ nV and $\Gamma_c = 2.3 \pm 0.1$ $\mu\text{s}^{-1}$.

To quantify the effect of electrostatic noise, we repeated the same measurement away from the gate voltage sweet spot, as shown in Figure 10.13(c,d). We observe a drastic reduction of $T_{2E}$ as one moves away from $V_g = 0.695$ V, which corresponds to the minimum of the parabolic dispersion of the pair qubit frequency with gate voltage. Away from this sweet spot, first-order electrostatic noise contributes to dephasing, causing $T_{2E}$ to drop. Such behaviour can be modeled using the relation for exponential coherence decay $1/T_{2E} = \Gamma_c + 2\pi\left(\frac{\partial f}{\partial V_g}\right)^2 \frac{V_{\text{rms}}^2}{1\text{Hz}}$ [114].

From the parabolic-like dispersion of the transition frequency with $V_g$ evidenced in Figure 10.13(c), we estimate $\partial f/\partial V_g = (-0.15 + 0.216 \times V_g)$ GHz/μV where $V_g$ is given in Volts. Best fit of the $T_{2E}$ dependence with $V_g$ is shown in dashed line in Figure 10.13(d); it yields an effective root-mean-square voltage noise $V_{\text{rms}} = 3.6 \pm 0.3$ nV and a $V_g$-independent dephasing rate $\Gamma_c = 2.3 \pm 0.1$ $\mu\text{s}^{-1}$. At the sweet spot, we estimate $\frac{\partial^2 f}{\partial V_g^2} = 0.22$ kHz/μV², which makes negligible any coupling to second-order noise, so that at the sweet spot, $T_{2E}$ is given by $\Gamma_c$.

[114]: Martinis et al. (2003), 'Decoherence of a superconducting qubit due to bias noise',

To summarize this section, we have demonstrated the realization of an Andreev Pair Qubit based on a InAs nanowire weak link. Characterization of its relaxation and dephasing times show slightly smaller although comparable performances in magnitude as the ones reported for a similar qubit implemented using an atomic contact junction. As a main difference, we have observed that nanowire weak links may be significantly more sensitive to their electrostatic environment. Because of their finite-length, their performances as a charge qubit may be affected by the switching of local charge impurities located nearby which, even if non-resonant with the qubit, can drastically reduce its coherence properties. The fact that a single impurity on a white noise background causes a substantial suppression of the coherent signal raises the problem of reliability of such an Andreev pair qubit as a charge-based device.

# Towards an Andreev *spin* qubit 11

In this chapter we now tackle the time-domain manipulation of single-particle transitions (SQPT). Those involve many-body states with odd parity differing by the pseudospin of one quasiparticle. Manipulating SQPTs therefore amounts to manipulating the pseudospin of a single quasiparticle in the weak link. The lowest-lying SQPTs in our microwave spectra are understood as transitions from the first to the second ABS manifolds, *i.e.* processes of the type $|1\sigma\rangle \rightarrow |2\sigma'\rangle$. Unfortunately, with the present design of our experiment, we could not resolve in the $IQ$ plane the two spin states $|1\uparrow\rangle$ and $|1\downarrow\rangle$, differing by the pseudospin of the quasiparticle trapped in the lowest ABS level, nor could we resolve $|2\uparrow\rangle$ and $|2\downarrow\rangle$. In Section 10.2 of the previous chapter, we demonstrated the discrimination of three clouds in the $IQ$ plane, which we interpreted as the many-body ground state $|g\rangle$, the excited state $|e\rangle = |1\uparrow 1\downarrow\rangle$ and an *odd* state, which at least enclosed contributions from $|1\uparrow\rangle$, $|1\downarrow\rangle$. Therefore, we were not able to track the spin states population, although we could demonstrate manipulation of SQPTs by looking at the mean $I$ and $Q$ value of the demodulated readout pulses.



## 11.1 Manipulation of a single quasiparticle

In Figure 11.1(a) we present a two-tone spectrum measured with sample S2 showing a bundle of four SQPT lines (green) along with four pair transitions (blue). This spectrum shows an unusual situation characterized by a rather flat pair transition dispersing only over $< 2$ GHz and by all the lowest transition lines lying below the resonator frequency, $f_r \approx 6.606$ GHz. The resulting small detuning between the SQPT lines and the resonator came along with a strong dispersive shift which, as we are now going to report, allowed to perform coherent manipulation of the SQPTs.

### 11.1.1 Driving a single quasiparticle

The effect of driving the four SQPT transitions with square pulses is investigated in Figure 11.2 at two illustrative values of the phase, close to $\delta = 0$ and $\delta = \pi$, shown respectively as orange and cyan lines in Figure 11.1(a). By varying the duration $t_d$ of the driving pulse, we induced Rabi flopping of the quasiparticle population between the two lowest ABS doublets, evidenced as coherent oscillations in the average $Q$ level of the demodulated readout pulses. These oscillations appear whenever the frequency $f_1$ of the driving pulse is set close to resonance with one of the four SQPT transitions. As the driving frequency $f_1$ gets detuned, the Rabi frequency $\Omega_R$ increases, which results in a typical 'chevron' pattern centered around each of the four transitions, as already described in Figure 10.12 for the manipulation of a pair transition. Note

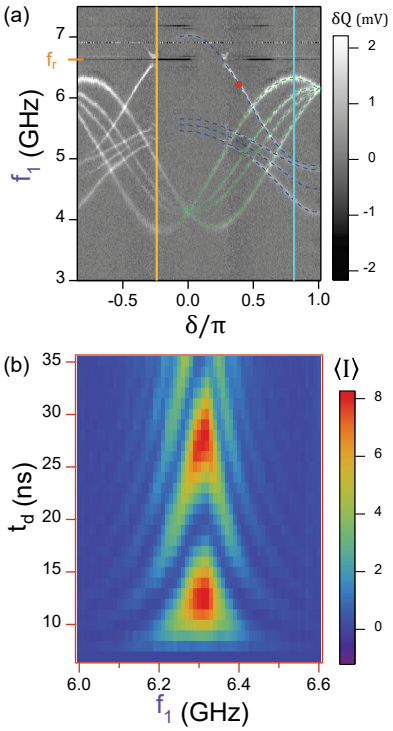


**Figure 11.1:** (a) Two-tone spectroscopy performed at $V_g = 1.07$ V (different cooldown than in Figure 10.5) showing a bundle of four single-quasiparticle transitions (SQPT) highlighted in green lines and a group of four pair transitions highlighted in blue (likely to be mixed pair transitions). The resonator frequency, $f_r \approx 6.606$ GHz, is indicated in orange on the left axis. The vertical lines highlight two $\delta$ values of interest, $\delta = -0.24\pi$ (orange) and $\delta = 0.81\pi$ (cyan) at which further characterization was performed (see Figure 11.2). (b) Average level of the $I$ quadrature after a driving pulse of duration $t_d$ and frequency $f_1$, evidencing the effect of driving at a pair transition frequency, highlighted by the red dot in (a).

that in contrast to coherent manipulation of quasiparticle pairs that has been demonstrated in the previous chapter, these measurements now demonstrate the coherent manipulation of a *single* quasiparticle excitation of a superconductor. Recently, such a manipulation was independently demonstrated by Hays *et al.* in Refs [41, 42], who went a step further by demonstrating single-shot readout of the quasiparticle's spin trapped in an Andreev doublet. In Section 11.2, we will discuss possible reasons why in our case the fine structure of the many-body states could not be evidenced in our histogrammed time-resolved measurements.

[41]: Hays et al. (2020), 'Continuous monitoring of a trapped superconducting spin'
[42]: Hays et al. (2021), 'Coherent manipulation of an Andreev spin qubit'

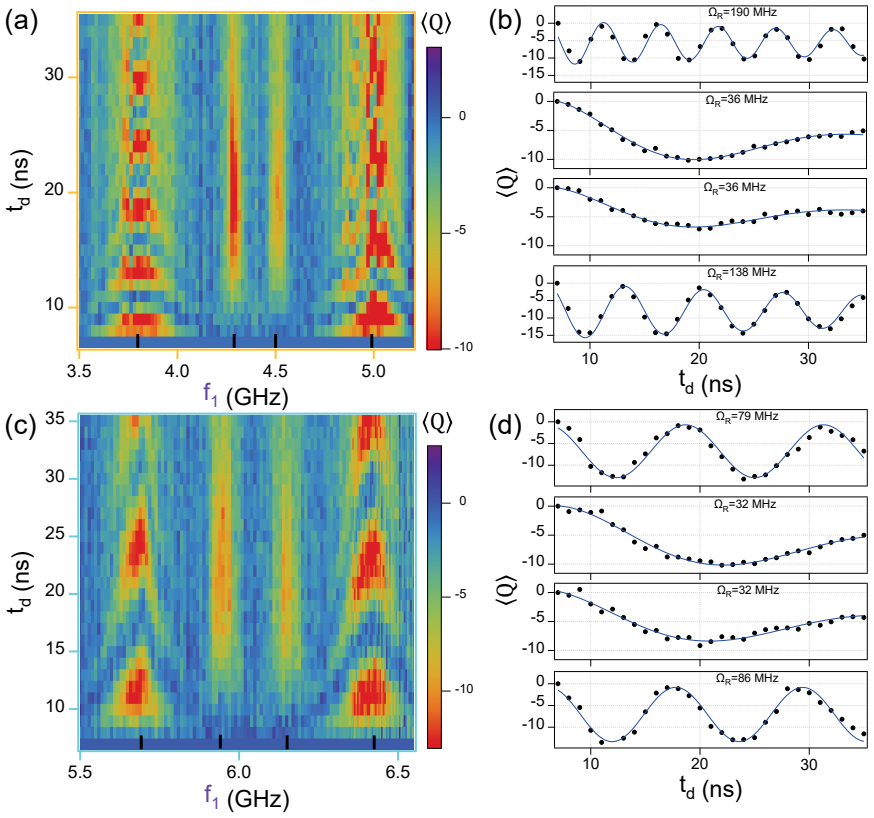


**Figure 11.2:** Driving single-quasiparticle transitions. Rabi oscillations as a function of the drive duration $t_d$ and frequency $f_1$ on a $1-1.5$ GHz window around the four visible SQPT transitions for the two phase values highlighted in orange and cyan in Figure 11.1(a): $\delta = -0.24\pi$ (panel (a)) and $\delta = 0.81\pi$ (panel (c)). Each data point is obtained by averaging the $Q$ outcome of $\sim 500000$ demodulated pulses consisting of a 172 ns fast-load pre-pulse followed by a 500 ns readout square pulse at $f_0 = 6.6071$ GHz. The readout sequence is preceded by a square driving pulse of duration $t_d$ incremented by multiples of 1 ns. (b,d) Rabi flopping of each of the four SQPT. The data points shown in black dots correspond to cuts at the frequencies indicated by black ticks in panels (a,c): $f_1 = 3.798$, 4.289, 4.500 and 4.990 GHz for panel (a) and $f_1 = 5.692$, 5.941, 6.151 and 6.425 GHz for panel (c). Best fits with an exponentially decaying sine function are shown in blue lines on top of the data with the associated value of the Rabi frequency $\Omega_R$ extracted from the fits.

### Spin-flipping *vs.* spin-conserving transitions

In Figure 11.2(b,c), we observe that the two outer lines, corresponding to pseudo-spin conserving transitions, show similar Rabi frequencies. Likewise, fitting the Rabi oscillations of the two inner lines, associated to pseudo-spin flipping transitions, gives identical Rabi frequencies. Remarkably, close to $\delta = 0$ (phase bias shown in orange), the Rabi frequency associated to the pair of pseudo-spin conserving transitions is about a factor $4-5$ larger than the one for pseudo-spin-flipping

transitions. Close to $\delta = \pi$ (phase bias shown in cyan), the same ordering is observed but with only a factor $\sim 3$ between the pseudospin-conserving and flipping transitions. As the amplitude of the driving pulse was set constant over the whole measurement, this variation in Rabi frequencies suggests a quantitative difference in the matrix elements associated to both families of transitions. This is in qualitative agreement with the discussion from Section 6.4.2 where we showed that in the general case, for an almost symmetric drive field in the transverse direction of the nanowire, spin-flipping transitions are strongly suppressed and hence harder to drive compared to spin-conserving ones.

Coherent oscillations could also be measured when driving at the frequency of the other four transition lines visible in the spectrum, which are likely associated to pair transitions as their phase dispersion exhibit a global minimum at $\delta = \pi$. In Figure 11.1(b), we show a Rabi measurement performed in a situation where such a transition line was well separated spectrally from the four SQPTs and close enough to the resonator frequency $f_r$ to allow for a strong dispersive shift and a good coupling to the readout resonator. We observe a typical "chevron" pattern, evidencing the increase of the Rabi frequency $\Omega_R$ when the drive is detuned from the transition frequency, as was discussed in detail in Section 10.2.4.

### 11.1.2 Relaxation dynamics

We then investigated the relaxation dynamics of a quasiparticle of either pseudospin trapped in the second ABS manifold. For each of the four SQPT transitions, we measure the relaxation dynamics after a $\pi$-pulse, as illustrated in Figure 11.3. Compared to the spectrum from Figure 11.1(a), lines had drifted after a few days: The new spectrum is shown in Figure 11.3(a), which differs slightly from Figure 11.1(a), mainly by the position of the SQPT lines, which dropped in frequency by about $\sim 0.5$ GHz.

In Figure 11.3(b), we show a detuned Rabi measurement, varying its frequency $f_1$ in the $5-6$ GHz range associated to the four SQPT lines. As observed in Figure 11.2(a,c), the driven dynamics of the two pseudospin-flipping transitions is again much slower here than for the two pseudospin-conserving transitions. Note that for this new situation, the detuned Rabi measurement now shows an extra chevron pattern associated to an additional transition line close to the top SQPT transition. After close inspection, this line already appeared very faintly in the previous two-tone spectrum of Figure 11.1(a) but was lying above the top SQPT and therefore did not show in Figure 11.2(a,c). As the spectrum drifted, this unidentified line moved in the frequency range of interest and now mixes with the chevron patterns associated to the four SQPTs (see Figure 11.3(b)).

To measure the relaxation dynamics, we first performed a Rabi measurement at the frequency of each of the four SQPTs to determine the duration $t_d$ to set in order to achieve a $\pi$-pulse. This value is highlighted with an asterisk in Figure 11.3(c) for each of the four SQPTs. We then measure for each transition frequency the average $I$ level as a function of the time delay $t_{\text{delay}}$ after such a $\pi$-pulse. As shown in Figure 11.3(d), we can fit this spontaneous evolution with a decaying exponential to extract the inter-doublet relaxation time $\tau_{2\sigma,1\sigma'}$ associated to each SQPT

transition $|1\sigma'\rangle \rightarrow |2\sigma\rangle$, with $\sigma, \sigma' \in \{\uparrow, \downarrow\}$. All four relaxation times are of the order $2-3$ $\mu$s, which is about the same timescale found by Hays *et al.* in Ref. [41]. However, it is puzzling that the relaxation times do not only depend on the state initially populated, but also from the state from which the transition was performed: $\tau_{2\uparrow,1\downarrow} \neq \tau_{2\uparrow,1\uparrow}$, $\tau_{2\downarrow,1\downarrow} \neq \tau_{2\downarrow,1\uparrow}$. This could be due to the fact that the transition lines are closely packed, and that when driving one transition, neighbouring ones are also affected, so that the initial states are not exactly the same in each measurement.

[41]: Hays et al. (2020), 'Continuous monitoring of a trapped superconducting spin'

These spontaneous relaxation times must be interpreted with care since they encompass decay to both $|1\uparrow\rangle$ and $|1\downarrow\rangle$. Still, Hays *et al.* observed that the inter-doublet decay was essentially spin-conserving. We can therefore suspect that the measured $|2\uparrow\rangle \rightarrow |1\downarrow\rangle$ decay mainly reflects the fast $|2\uparrow\rangle \rightarrow |1\uparrow\rangle$ relaxation and that the spin depolarization associated to $|1\uparrow\rangle \rightarrow |1\downarrow\rangle$ and happening on a longer timescale $\tau_s$ may in our case not result in a measurable change of the average $I$ level, given that those spin states could not be resolved in our $IQ$ histograms. Supplemental data on the coherent manipulation of the measured lines are provided in Figure 11.4, where we extract the Rabi frequency of the main transition lines at three different values of $\delta$ close to $\pi$. Although a clear difference in $\Omega_R$ can be evidenced between SQPTs that are either spin-flipping or spin-conserving, no systematic trend is visible for the other transition lines, which resemble PTs. The analysis however is made more complicated by the fact that in this region of $\delta$ the PTs are closely packed with the SQPTs, resulting in highly interfering chevron patterns in the detuned Rabi measurements of Figure 11.4(b,c).

### 11.1.3 Coherence

Finally, we evaluate the coherence time associated with coherent superpositions of the type $|1\sigma\rangle + |2\sigma'\rangle$ by applying a Hahn echo sequence at each SQPT frequency. The results are reported in column (e) of Figure 11.3. The relaxation dynamics of superpositions $\alpha|1\sigma\rangle + \beta|2\sigma\rangle$ with the same spin texture are well fitted by an exponential decay that gives a characteristic time $T_{2,\mathrm{Echo}} \sim 150$ ns. The relaxation time associated to superpositions $\alpha|1\sigma\rangle + \beta|2\overline{\sigma}\rangle$ with opposite spin is faster and at the limit of our resolution. Indeed, in this experiment the Hahn echo sequence is composed by a $\pi-$pulse that lasted 12 ns and $\pi/2-$pulse 10 ns and hence $t_{\mathrm{delay}}$ started at 32 ns. The values we report here are similar to those obtained by our colleagues at Yale in a nanowire weak link similar to ours [42]: they found out a $\mathrm{T}_{2,\mathrm{Echo}}$ associated with $\alpha|1\sigma\rangle + \beta|2\sigma\rangle$ superpositions around $\sim 100$ ns and for $\alpha|1\sigma\rangle + \beta|1\overline{\sigma}\rangle$, $\mathrm{T}_{2,\mathrm{Echo}} \sim 50$ ns. Note that the coherence timescale observed in our system is comparable to the one observed in spin-orbit qubits implemented either in InAs nanowires [115] or InSb nanowires [116] quantum dots.

[42]: Hays et al. (2021), 'Coherent manipulation of an Andreev spin qubit'

[115]: Nadj-Perge et al. (2010), 'Spin-orbit qubit in a semiconductor nanowire'

[116]: Berg et al. (2013), 'Fast Spin-Orbit Qubit in an Indium Antimonide Nanowire'

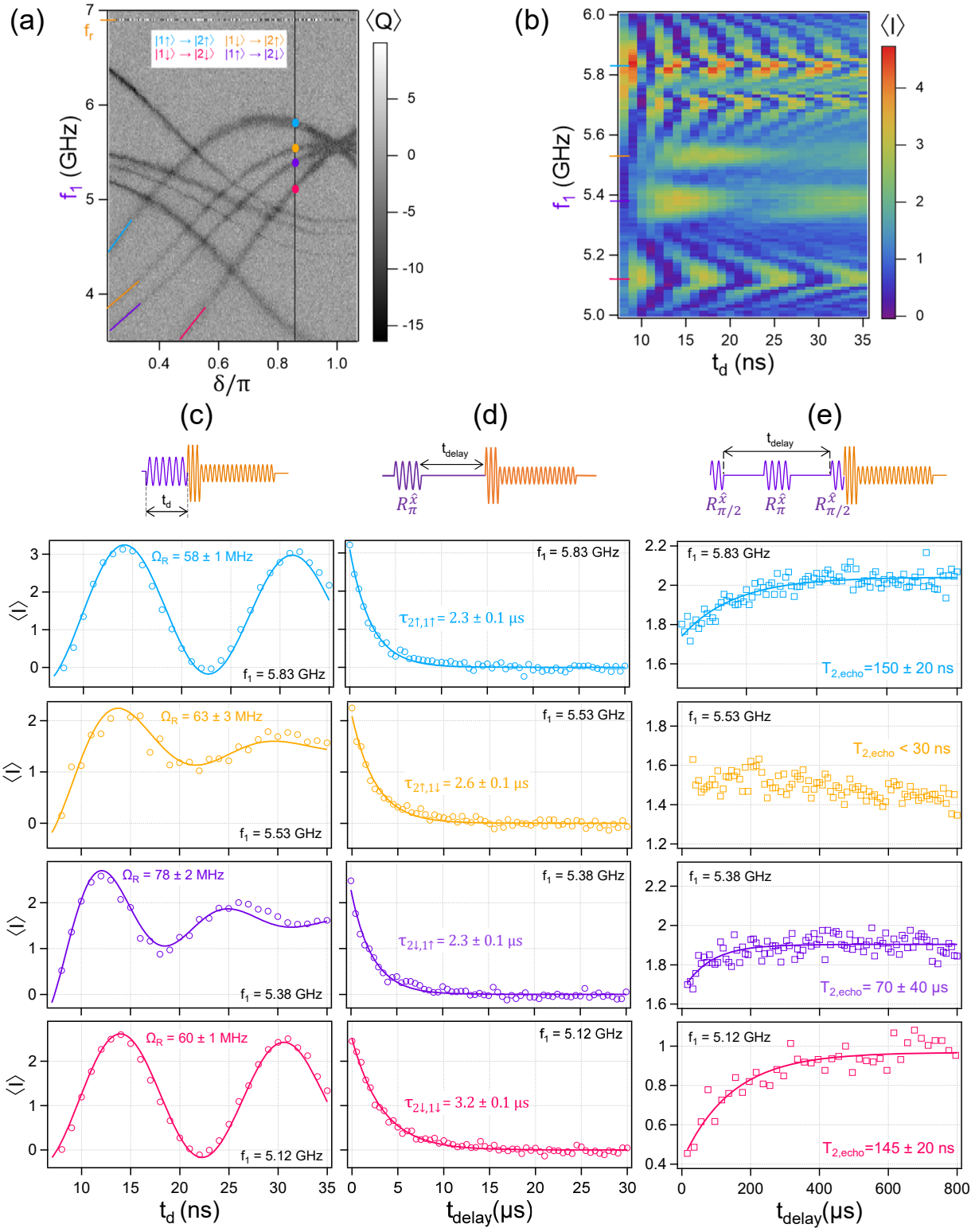


**Figure 11.3:** Relaxation and coherence dynamics of a single quasiparticle. (a) Two-tone spectrum evidencing the phase dispersion near $\delta = \pi$ of the four SQPT transitions $|1\sigma\rangle \rightarrow |2\sigma'\rangle$ between the lowest and second lowest ABS manifolds, encoded in cyan, orange, violet and magenta lines. The transition lines have drifted by about −0.5 GHz compared to Figure 11.1(a). (b) Average $I$ level of the demodulated readout pulse as a function of the duration $t_d$ of a square driving pulse, evidencing Rabi oscillations whenever the driving frequency $f_1$ becomes close to resonance with one of the four SQPTs, which central frequency is marked with colored ticks on the frequency axis $f_1 = 5.83$ (cyan), 5.53 (orange), 5.38 (violet) and 5.12 GHz (magenta). Measurements were performed at $\delta = 0.85\pi$, indicated by a black line in panel (a). Column (c) Effect of a resonant drive for each of the four SQPTs at $\delta = 0.85\pi$ as a function of the drive duration $t_d$. Compared to panel (b), the oscillations show a smaller Rabi frequency, because we set a lower power for the drive so as to better define a $\pi$-pulse for each SQPT. For each curve, the best fit with an exponentially decaying sine function is shown in solid lines and the extracted Rabi frequency $\Omega_R$ is displayed on the graph. Column (d) Average $I$ level as a function of the time $t_{\text{delay}}$ after a $\pi$-pulse, the duration of which being indicated with an asterisk on the x-axis of the corresponding graphs in (c) for each of the four SQPTs. The relaxation is well fit with an exponential decay (solid lines), from which we extract the associated spontaneous relaxation times $\tau_{1\sigma',2\sigma}$ for each of the four processes $|2\sigma\rangle \rightarrow |1\sigma'\rangle$. Column (e) Average $I$ level as a function of the time $t_{\text{delay}}$ after a Hahn echo sequence for each of the four SQPTs. The exponential fit allows to obtain an estimation of $T_{2,\text{echo}}$.

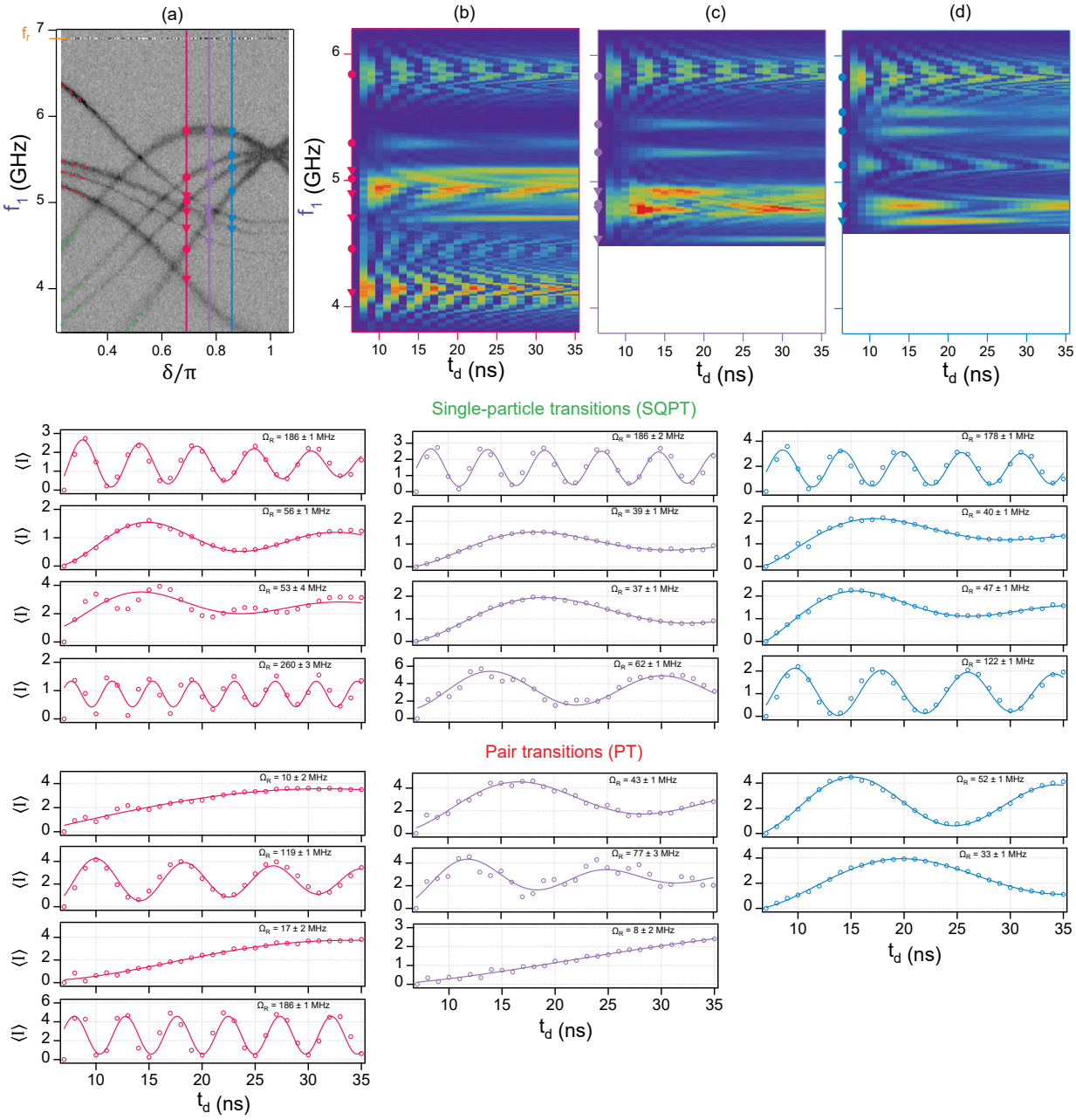


**Figure 11.4:** Coherent manipulation of SQPTs and PTs at different phase values. (a) Two-tone spectrum evidencing the phase dispersion near $\delta = \pi$ of the four SQPT transitions $|1\sigma\rangle \rightarrow |2\sigma'\rangle$. Same as in Figure 11.3(a) but we now highlight at three phase values $\delta = 0.69\pi$ (magenta), $0.77\pi$ (violet) and $0.85\pi$ (blue) the frequencies of the four SQPT transitions (disks) and of some of the pair transitions (triangles) at which further characterization is performed. (b,c,d) Detuned Rabi measurement performed at each of the three phase values highlighted in (a). For each case, we show the Rabi oscillations measured when driving at the central frequency of each SQPT lines (denoted with disks on the frequency axis) and of some PT lines (denoted with triangles). Best fit with an exponentially decaying sine function is shown in solid lines for each curve, with the associated value of the extracted Rabi frequency $\Omega_R$. The two spin-flipping SQPTs systematically show a smaller $\Omega_R$ by a factor $\sim 3-5$ compared to the two spin-conversing SQPTs.

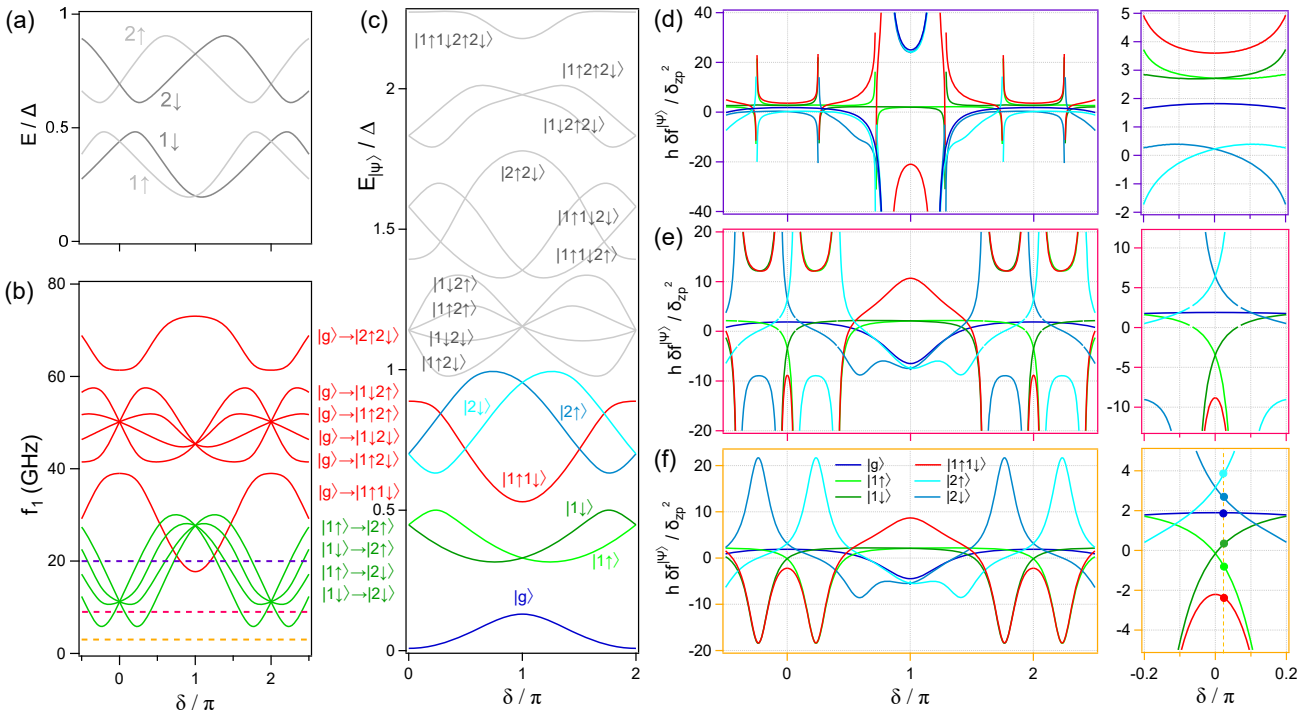


**Figure 11.5:** Resonator shift associated to the lowest-lying many-body states of a nanowire weak link, as estimated from a tight-binding calculation. (a) Typical energy spectrum of spin-split ABS levels as a function of phase $\delta$ (parameters similar to Figure 4.8, but changed slightly so as to have only 2 ABS manifolds). (b) Energy of all possible transitions between the two ABS manifolds, labelled 1 and 2. Pair transitions (PT) of the type $|g\rangle \rightarrow |n\sigma m\sigma'\rangle$ with $n, m \in \{1,2\}$ and $\sigma, \sigma' \in \{\uparrow,\downarrow\}$ are shown in red and single-quasiparticle transitions (SQPT) $|1\sigma\rangle \rightarrow |2\sigma'\rangle$ are shown in green. (c) Energy $E_{|\Phi\rangle}$ of all many-body states $|\Phi\rangle$ involving the two ABS doublets, and neglecting interactions (see Chapter 8). The ground state $|g\rangle$ corresponds to all negative energy levels being filled, *i.e.* $E_{|g\rangle} = (1/2)\Sigma_{i<0,\sigma}E_{i\sigma}$, where 3040 states were included in the sum to ensure convergence. The ground state energy at $\delta = 0$ is taken as the reference of the energy ladder. (d-f) Resonator shift $\hbar\delta f_r^{|\Phi\rangle}$ associated to each of the six lowest lying many-body states $|\Phi\rangle \in \{|g\rangle, |1\uparrow\rangle, |1\downarrow\rangle, |2\uparrow\rangle, |2\downarrow\rangle, |1\uparrow 1\downarrow\rangle\}$ shown in color in (c), for three illustrative values of the resonator frequency $f_r$ = 3, 9 and 20 GHz, highlighted in dashed lines in (b). While the continuum is taken into account to estimate $E_{|g\rangle}$, its contribution to the shift through virtual transitions was neglected. Enlargement of (d-f) are provided close to $\delta = 0$, showing that the separation of all six lowest lying many-body states is only possible in a restricted phase range.

## 11.2 Spin states could not be resolved

Although coherent manipulation of the pseudospin of a single quasiparticle could be demonstrated, extended characterization of the spin dynamics was not achievable, because the readout did not allow to discriminate $|1\uparrow\rangle$ and $|1\downarrow\rangle$. Sample S2 was measured in many different conditions of gate voltage and phase, none of which allowed to evidence clearly more than 3 clouds in the histogram of $I$ and $Q$ outcomes, which we attributed to $|g\rangle$, $|e\rangle = |1\uparrow 1\downarrow\rangle$ and an odd mixed state $|o\rangle$ probably encompassing $|1\uparrow\rangle$, $|1\downarrow\rangle$ and perhaps other many-body states. Given that single-quasiparticle transitions could be routinely observed between these different spin states, it seems rather puzzling at first sight that our time-resolved data did not reveal these sub-states as well. However, let us remember that the signal in two-tone spectroscopy only requires that the resonator shift changes between the spin states ($\delta f_r^{|2\sigma\rangle} \neq \delta f_r^{|1\sigma'\rangle}$), while discriminating $|1\uparrow\rangle$,$|1\downarrow\rangle$, $|2\uparrow\rangle$ and $|2\downarrow\rangle$ requires that the clouds in the $IQ$ plane corresponding to the associated shifts be all distinct, which is a much stricter condition.

In Figure 4.8, we had shown the evolution with $\delta$ of the resonator shift associated to usual transitions for two illustrative cases, where the lowest SQPTs were crossing or not the resonator line. Figure 4.8(e) showed in particular that all SQPTs $|1\sigma\rangle \rightarrow |2\sigma'\rangle$ were contributing to a finite resonator shift for almost any value of the phase $\delta$, with maxima where the phase curvature difference between the two manifolds 1 and 2 is highest. This explains why in the general case, all four SQPTs may be seen in two-tone spectra over the full range of phase. In contrast, as we now show, all four substates $|1\uparrow\rangle$,$|1\downarrow\rangle$, $|2\uparrow\rangle$ and $|2\downarrow\rangle$ actually contribute to four well-distinct resonator shifts only in a small region of phase close to $\delta = 0$.

We illustrate this effect on a situation with only two ABS manifolds in the gap (Figure 11.5(a)), which is the minimal scenario to account for both PTs and SQPTs. The associated transition spectrum is given in Figure 11.5(b), with SQPTs shown in green lines and PTs in red. In Figure 11.5(c), we plot the energy $E_{|\Phi\rangle}$ of all possible many-body states arising from creating excitations in the two ABS manifolds, and focus on the six lowest ones, corresponding to $|\Phi\rangle \in \{|g\rangle, |1\uparrow\rangle, |1\downarrow\rangle, |2\uparrow\rangle, |2\downarrow\rangle, |1\uparrow 1\downarrow\rangle\}$. Their associated resonator shifts $\delta f_r^{|\Phi\rangle}$ are depicted in Figure 11.5(d) for three illustrative values of the resonator frequency, $f_r = 3,\ 9$ and $20$ GHz, shown in dashed lines in panel (b). Panel (d) corresponds to a situation deep in the dispersive regime where both the PT and the SQPTs are crossing the resonator line. Panel (f) illustrates on the other hand the adiabatic regime where all transitions are detuned from $f_r$. Finally, panel (e) shows an intermediate situation, where only the SQPT cross the resonator close to $\delta = 0$. The shifts were computed from Eqs. (4.33,4.34,4.36), which require knowledge of the matrix elements of the current operator coupling the different states. They were estimated from a tight-binding calculation with 60 sites for the normal region and 350 sites in each superconducting lead*. From Figure 11.5(c), we observe that the energy of $|1\uparrow\rangle$ and $|1\downarrow\rangle$, shown respectively in light and deep green lines, have about opposite slopes with $\delta$ around $\delta = \pi$, *i.e.* they carry opposite supercurrents. More crucially, we further observe that their phase curvature near $\delta = \pi$ is almost zero, meaning that they essentially do *not* shift the resonator in the adiabatic regime, while $|g\rangle$ and $|e\rangle = |1\uparrow 1\downarrow\rangle$ well contribute to finite and (almost) opposite resonator shifts by their respective phase curvatures (see Figure 11.5(f)). Close to $\delta = \pi$, we therefore do not expect to be able to separate well $|1\uparrow\rangle$ and $|1\downarrow\rangle$. However, in a small region around $\delta \in [-0.1\pi, +0.1\pi]$, the shifts associated to all six many-body states may actually show distinct values, allowing for their separation in the $IQ$ plane, as illustrated in Figure 11.5(d-f). When moving away from $\delta = 0$, the shifts for $|1\uparrow\rangle$ and $|1\downarrow\rangle$ start coinciding with the shifts from $|g\rangle$ and $|e\rangle$. As for the higher states $|2\uparrow\rangle$ and $|2\downarrow\rangle$, they contribute to almost the same resonator shift as $|g\rangle$ when $\delta$ is close to $\pi$.

* Taking that many sites for the two leads allows to describe properly the continuum, which actually carries some phase dependence too given the finite-size of the weak link. Computing the resonator shifts requires estimating first the energy $E_{|g\rangle}$ of the many-body ground state, by summing the contributions from all negative-energy states. The phase-dependence of this quantity is observed to converge slowly with the number of states in the sum. In practice, we need to include states until $\sim 2\Delta$ to estimate properly $E_{|g\rangle}$. The energies are obtained by numerical diagonalization of the system Hamiltonian, with dimension $(700 + 60) \times 2$ chains $\times\, 2$ (spin) $\times\, 2$ (electron/hole) $= 6080$. Given this matrix size, such diagonalization is computationally expensive ; it was performed on a cluster by A. Reynoso from Balseiro Institute in Bariloche.

From this analysis, we expect to observe only three clouds in the $IQ$ histograms when operating near $\delta = \pi$: the middle one, which we denoted $|o\rangle$, is expected to correspond to $|1\downarrow\rangle$ and $|1\uparrow\rangle$ and the other two clouds on either side should correspond to $|g\rangle$ and $|e\rangle$. This illustrative analysis supports the state identification which we performed in Figure 10.6 and throughout all the time-domain data presented in Chapter 9. It also shows that $|2\uparrow\rangle$ and $|2\downarrow\rangle$ may collapse on the $|g\rangle$ cloud near $\delta = \pi$. In this case, driving SQPT transitions would not light up a new cloud in the $IQ$ histogram, but only change the internal distributions of the 3 clouds. Since most of the $IQ$ histograms we measured were taken close to $\delta = \pi$, this could explain our difficulties in evidencing $|1\downarrow\rangle$ and $|1\uparrow\rangle$. On the other hand, we carried out extensively single-tone spectroscopies of the resonator on the full $0 - 2\pi$ phase range, none of which showing clearly distinct values of $f_r$ that could be associated to a splitting of $|1\downarrow\rangle$ and $|1\uparrow\rangle$ close to $\delta = 0$. Note however that for such measurements, the discrete dips in $|S_{21}(f)|$ associated to the resonator frequencies in each states are further weighted by the average state populations, which smooths out the pattern, making the state discrimination possibly harder.

As a final remark, the ordering of the shifts predicted by this analysis for the six lowest-lying many-body states and illustrated in Figure 4.8(f) is consistent with the one reported by Hays *et al.* in Ref. [41]. In this work, single-shot readout of the spin states was demonstrated in a small phase range close to $\delta = 0$. The SQPT lines were about 6 GHz higher than the resonator frequency, which corresponds qualitatively to the case depicted in Figure 4.8(f), for which the shift is expected to be dominated by the ABS curvature. The measured phase dependence near $\delta = 0$ of $|g\rangle$, $|1\uparrow\rangle$ and $|1\downarrow\rangle$ in Ref. [41] also coincides qualitatively with the picture given in panel (f). One could wonder how this picture would change in presence of Coulomb interactions in the weak link. As a first step, we showed on an illustrative case in Figure 8.9(b) how the energies of the lowest-lying many-body states would evolve for increasing values of the interaction strength, although it was calculated for different parameters and the effect of the continuum was not included at the time. Further work is needed to evaluate properly the impact of interactions on the state-dependent resonator shift.

[41]: Hays et al. (2020), 'Continuous monitoring of a trapped superconducting spin'

Stepping back a little, this analysis illustrates the general difficulty in implementing an Andreev Spin Qubit at zero magnetic field, given that it requires fine-tuning the gate voltage $V_g$ (to find a situation in which a set of SQPTs comes close enough to the resonator to allow a good coupling), and then fine-tuning of the phase $\delta$ to isolate a working point in the restricted phase range near $\delta = 0$ where $|1\downarrow\rangle$ and $|1\uparrow\rangle$ show distinct resonator shifts.

# Experimental techniques

# Samples fabrication 12



Although six samples were fabricated and cooled down at low temperature during my thesis, I only report data taken on two of them, which are named for simplicity S1 and S2. In the others, the coupling between the weak link and the resonator was either too weak or too large, or no flux modulation was observed, indicating the failure of either the etching or the recontacting of the nanowires. Samples S1 and S2 correspond to two generations of CPW resonators. The main difference concerns the coupling scheme between the resonator and the nanowire weak link: In sample S1 it was achieved through a mutual inductance (section 5.2.1) whereas in sample S2 the coupling was galvanic (section 5.2.2).

**Overview of the fabrication of the samples:**

- **Sample S1:** Fabrication of the Nb resonator. Au alignment marks. Deposition of nanowires. Etching of Al to define the weak link in the nanowire. Au side-gate. Al loop connected to the nanowire and coupled to the resonator.
- **Sample S2:** Fabrication of the NbTiN resonator. Alumina patches. Au alignement marks and local back-gates. Deposition of a nanowire above the gate. Etching of Al to define the weak link in the nanowire. Deposition of Al patches to contact the ends of the nanowire.

The chip design comprises mm-$\mu$m-size features as well as small patterns down to $\approx$ 100 nm. Therefore fabrication involves both optical and electron-beam lithography. The process flow starts on a whole 2-inch wafer with the steps concerning the fabrication of the resonators. The wafer is then diced into chips (3×10 mm) that are individually processed to incorporate the nanowires and perform the remaining steps. In the following we describe the process flows that have been used.

## 12.1 Resonator fabrication

The starting point in both samples is a 2-inch monocrystalline (100) intrinsic ($\rho > 4$ $k\Omega$.cm) Silicon wafer covered with 500 nm of thermally grown $SiO_2$. In sample S1, a 150-nm-thick Nb film was deposited by RF sputtering whereas for sample S2 the superconducting material used was NbTiN film (80 nm thick) also deposited by RF sputtering but in another machine. We observed that NbTiN gives higher internal quality factor resonators but they provide a non-negligible kinetic inductance ($\approx$ 0.6 pH/sq) that must be taken into account when designing the resonators. The recipe to transfer to the wafer the patterns of the optical masks depicted in Figure 12.1 and Figure 12.2 is the following (all baking steps are done on hot plates; optical lithography exposures are performed with Süss MicroTec MJB4 mask aligner):

- **Superconducting deposition:**

  Sample S1: Nb deposition by RF magnetron sputtering: 150 nm (rate 2 nm/s)

  Sample S2: NbTiN deposition by RF magnetron sputtering: 80 nm (rate 0.8 nm/s, sample temperature 600°C)

- **Resonator patterning**

  (a) Photoresist deposition: 1-$\mu$m-thick Shipley S1813 (spinning 4000 rpm, baking at 110°C, 1 min)

  (b) Optical lithography: UV exposure through the mask shown in Figure 12.1 or Figure 12.2, in hard contact (dose: 200 mJ/cm$^2$).

  (c) Development: dissolution of exposed resist in Microposit MF-319 developer for 1 min, subsequently rinsed in DI water and blown dry with nitrogen.

  (d) Etching: Reactive ion etching of unprotected superconducting material using a gas mixture of $CF_4$ (20 sccm) and $Ar$ (10 sccm) at a pressure of 50 $\mu$bar. The etching process, which lasts between 3 and 5 minutes, is monitored by optical interferometry on a control sample placed nearby.

  (e) Resist removal: in a warm bath (70°C) of Microposit 1165 remover (N-methyl-2-pyrrolidone) for $\sim$ 10 min, subsequently rinsed in DI water and blow dry with nitrogen.

  (f) Cleaning: $O_2$ plasma (5 sccm) at 100 W and a pressure of 50 $\mu$bar during 2 min.

- **Gate dielectric (Alumina) patch (only for S2)** In S2, the gate goes over the ground plane of the resonator. Insulation is provided by an Alumina layer, deposited at the position of the small pink rectangle shown in Figure 12.2(c).

  (a) Photoresist deposition: 1.7 $-$ $\mu$m-thick of Microposit LOL-2000 spun at 4000 rpm and baked at 150°C for 1 min. 5 $\mu$m Shipley S1805 spun at 4000 rpm and baked at 110°C for 1 min.

  (b) Optical lithography: UV exposure through the mask shown in Figure 12.2, in vacuum contact (dose: 150 mJ/cm$^2$). (c) Development: dissolution of exposed resist in MF319 developer for 1 min, subsequently rinsed in DI water and blow dry under nitrogen.

  (d) Cleaning: $O_2$ plasma (5 sccm) at 100 W and a pressure of 50 $\mu$bar during 2 min.

  (e) Alumina layer: e-beam evaporation of 65-nm-thick film at a rate of 0.1 nm/s, and at an angle of 40 using planetary rotation of the wafer holder.

  (f) Lift-off: the resist stack covered with alumina is finally removed with a warm (80°C) bath of 1165 remover for $\sim$ 10 min, subsequently rinsed in DI water and blow dry under nitrogen.

  (g) Cleaning: $O_2$ plasma (5 sccm) at 100 W and a pressure of 50 $\mu$bar during 2 min.

- **Coating for dicing & individual chip processing**

  E-beam resist bilayer deposition: ~400-nm-thick copolymer MMA (8.5) MAA EL10 spun at 4000 rpm, baked at 150C for 3 min. $\sim$ 270$-$nm-thick PMMA (950K) ethyl-lactate spun at 4000 rpm, baked at 150C for 3 min. UV3 coating to protect the bilayer from debris produced when dicing the wafer: spun at 2000 rpm and baked at 120C for 2 min.

After dicing the processed wafer, each chip is ready for the next steps. Some of them were directly used, without any further processing, for preliminary experiments devoted to characterize the resonators. In next sections we explain in detail the integration of nanowire weak links into individual resonators.

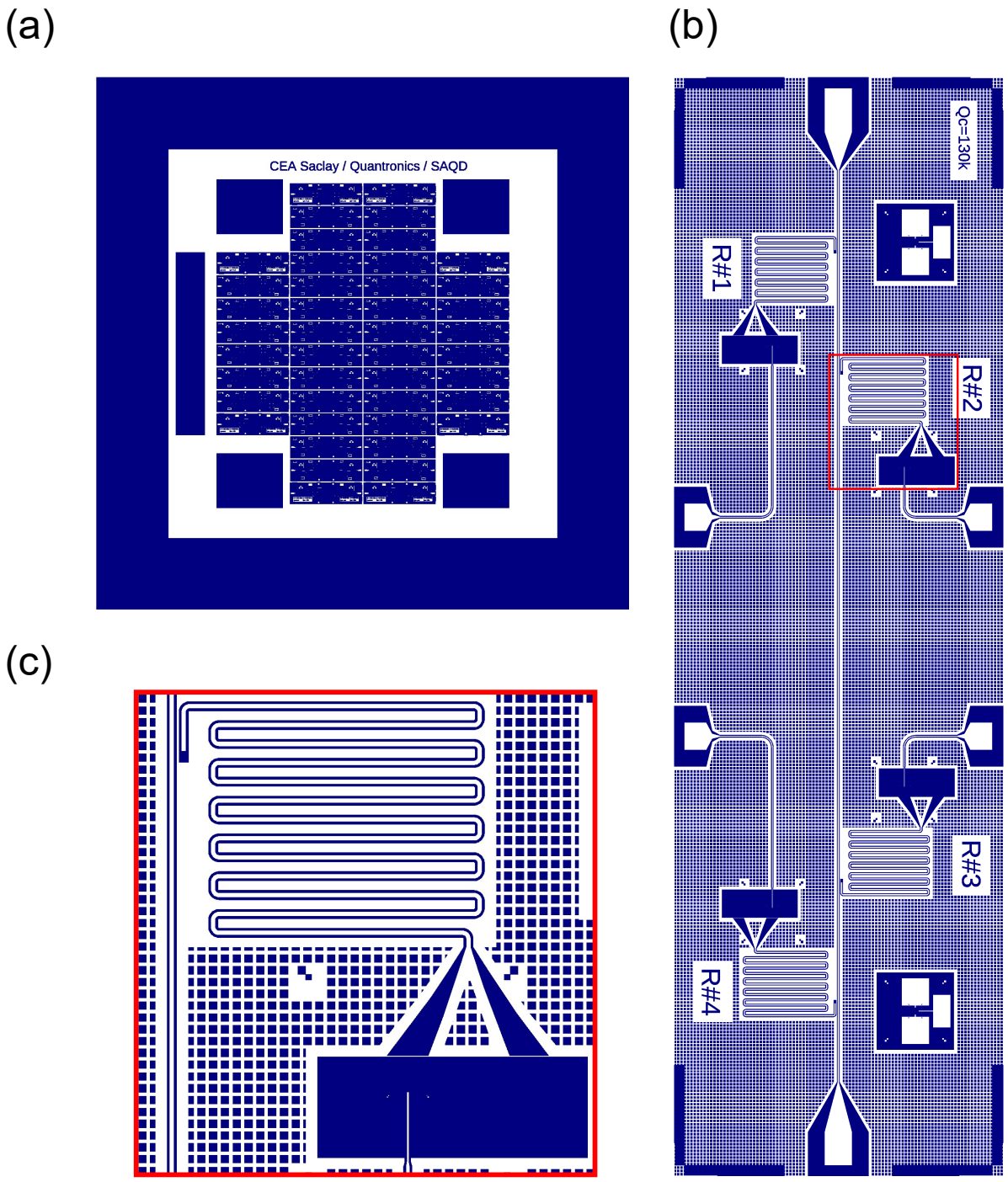


**Figure 12.1:** Optical lithography mask S1 (resonators). (a) The mask includes 44 individual chips of $3 \times 10$ mm$^2$ with different coupling quality factors, number of resonators and gates. (b) Individual chip view corresponding to the one we used in experiments. The chip includes 4 resonators with slightly different resonance frequencies. (c) Close view of resonator R#2, highlighted in red in (b) .

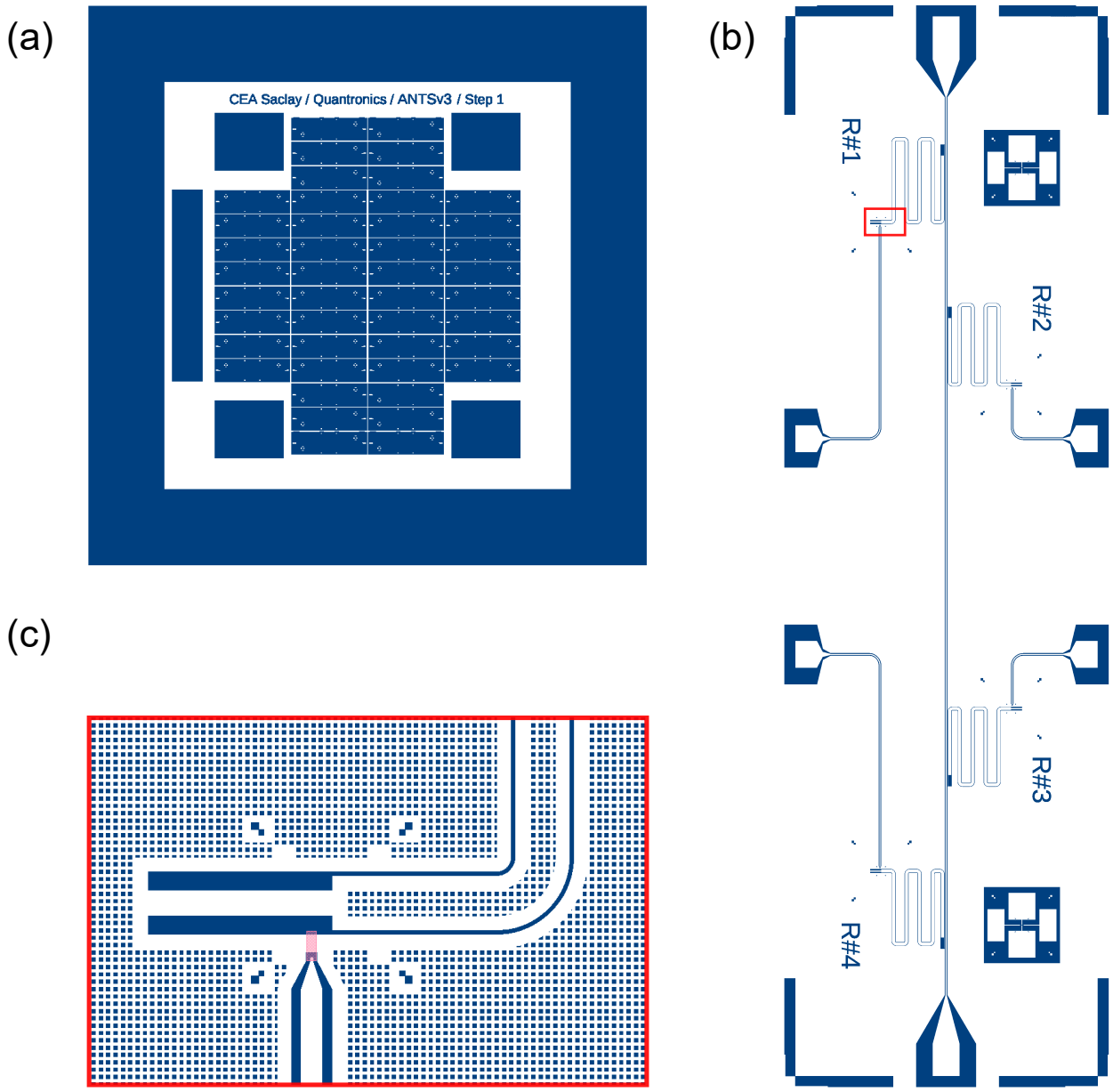


**Figure 12.2:** Optical lithography mask S2 (resonators). (a) The mask includes 44 individual chips of $3 \times 10$ mm$^2$ with different coupling quality factors, number of resonators and gates. (b) Individual chip view (for the sake of clarity the lattice of 2×2 $\mu$m squares is not represented) corresponding to the one we used in experiments. The chip includes 4 resonators with slightly different resonance bare frequencies. Highlighted in red, the ending region of resonator R#1 where the coupling with the nanowire will take place. (c) Close view of this region. The nanowire will be deposited with a micromanipulator across the bottom narrow gap region of the CPW, to the right of the pink rectangle, which corresponds to the optical mask layer for the alumina patches

## 12.2 Nanowire weak link fabrication

### 12.2.1 InAs-Al core-full shell nanowires

The nanowires used in this thesis work were synthesized by Peter Krogstrup (Copenhagen university). The batch name is QDEV439. It contains ~10-$\mu$m-long nanowires with an InAs core diameter of about 140 nm, featuring a hexagonal cross section and covered by an epitaxial Al shell about ~ 25 nm-thick. They were grown in the wurtzite phase along the [0001] crystalline direction on a (111)B InAs substrate by the Au-catalysed vapour–liquid–solid method. An aluminum evaporation was subsequently performed to cover each of the six facets, following the recipe of Ref. [37].

[37]: Krogstrup et al. (2015), 'Epitaxy of semiconductor-superconductor nano-wires'

### 12.2.2 Nanowire deposition

High precision alignment marks were defined by means of e-beam lithography in the region where nanowires are subsequently deposited. In sample S1, nanowires were picked up and dropped on the sample using as a tip a Nylon fiber extracted from a cleanroom's wipe and glued to the end of a 250-$\mu$m-diameter needle. The fiber diameter, ~ 9 $\mu$m, was about 50 times larger than the diameter of the nanowires. With this home-made tip, a bunch of nanowires was deposited with a placement precision of the order of 50-100 $\mu$m.

For sample S2, we had set up a micro-manipulation station (see Figure 12.5) and the nanowires were deposited one by one. The station consists in a Eppendorf 3-axis micro-manipulator (TransferMan® 4r) that controls the position of a home-made tip holder, to which a 100-nm-radius tungsten STM tip (72X Tungsten Wire 3 mil from American Probe & Technologies Inc.) is attached. The micro-manipulator is associated with a digital microscope (Keyence®) that allows to monitor the transfer process: a single nanowire is catched with the STM tip from the small piece of wafer with nanowires, then deposited on the desired region of our sample with a precision of the order of a few $\mu$meters. With some practice, a nanowire can be displaced on the surface of the sample to better adjust its final position. Figure 12.3 shows optical images after deposition of nanowires on sample S1 and S2.

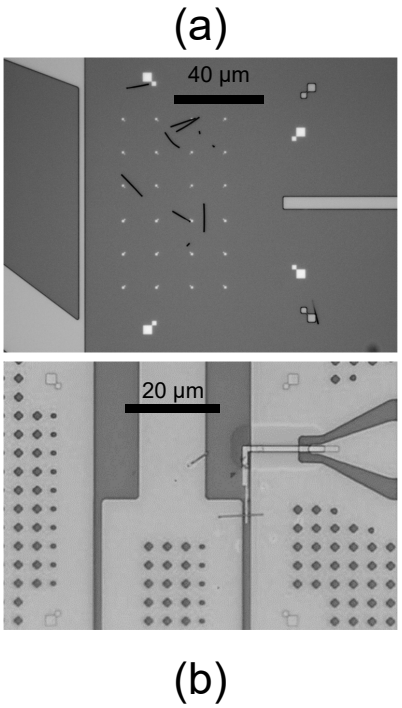


**Figure 12.3:** (a) Optical image of sample S1 after NW deposition using a home-made tip under a binocular microscope (b) Optical image of sample S2 after NW deposition using our micromanipulation station.

### 12.2.3 Weak link definition process

After NW deposition, samples are covered with a layer of PMMA (950K) A6 e-beam resist. After opening small windows over the nanowires, the aluminum shell is wet-etched to create the weak links. In order to center the position of the windows, images of the NWs are incorporated into the e-beam software and positioned using the alignment marks (Figure 12.4 (a) and (b)). After e-beam lithography and development, and prior to wet etching of the aluminum shell, the exposed sample surface is cleaned under a mild $O_2$ plasma to eliminate organic residues. The wet etch process consists in dipping the sample for 15 sec in Al etchant (Transene-D) at a temperature of 50°C, and immediately rinse it in DI water for 30 sec. The PMMA is then removed using hot acetone. The wet

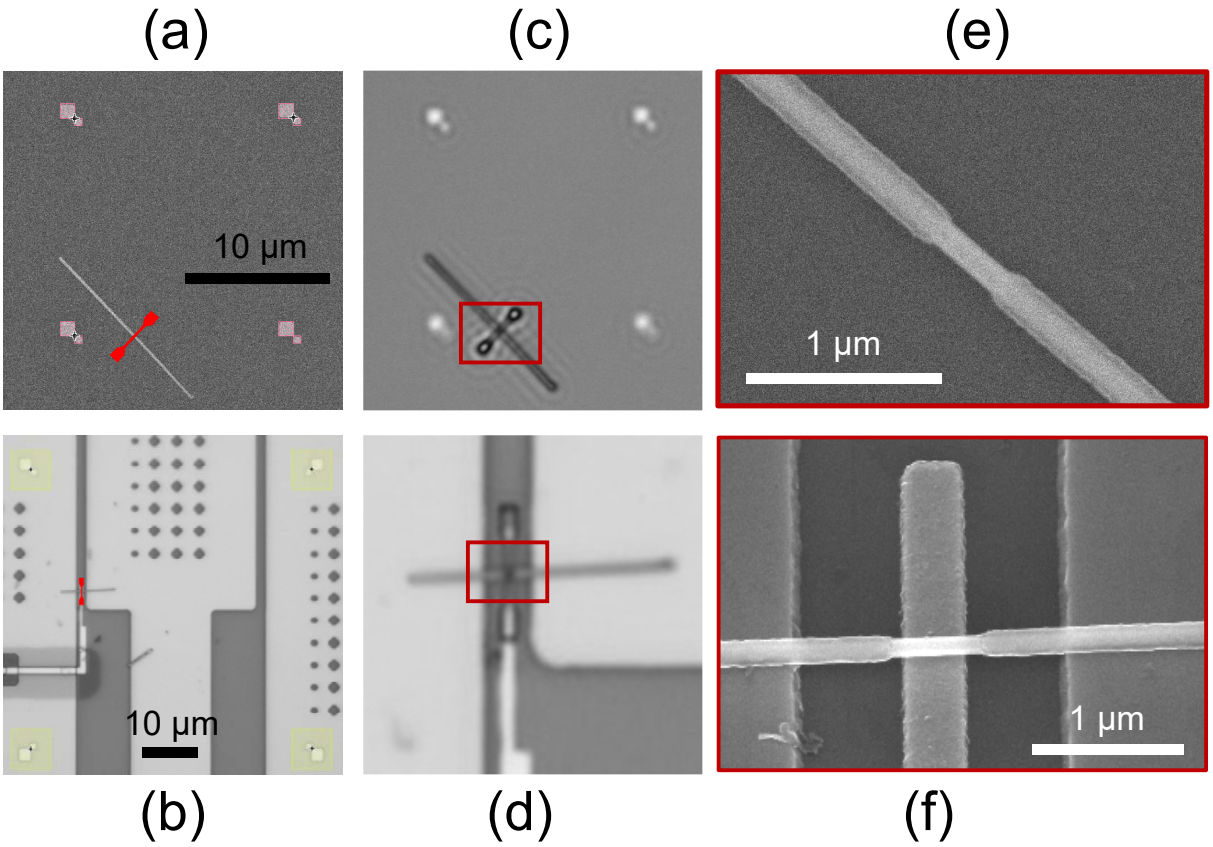


**Figure 12.4:** Weak link definition process.Top (bottom) row corresponds to sample S1 (S2). (a) and (b) Images of deposited NW are incorporated into the writing e-beam software and centered with the help of the alignment marks in order to define the etching windows (red) on top of the NWs. (c) and (d) Close view , for samples S1 and S2 respectively, of the etching window opened over the NW. The image is blurred since the optical microscope is at its resolution limit.(e) and (f) SEM image of the weak link region after wet etching.

etching process proved to be not 100% reproducible because it relies on surface chemistry, which is highly dependent on the surface state of the nanowires and/or the substrate, *i.e.* on the presence of eventual residues or contaminants for example. Nanowires processed together on the same chip and having therefore all witnessed the same chemical treatment, could be etched quite differently, with variabilities in the size of the weak link on the order of 50%. For this reason, this step is realized first: in case of failure, the nanowire can be replaced by another one. Figure 12.4 (e) and (f) shows the SEM images of S1 and S2, respectively, after the etching process. The semiconducting region appears clean and the facets of the NW are apparent.

### 12.2.4 Nanowire gates

In sample S1, side gates were fabricated after obtaining the weak links. In order to position them as close as possible to the weak link, high resolution SEM images were incorporated into the e-beam lithography software as in the previous step and gates were custom-defined for each nanowire. The process is the following:

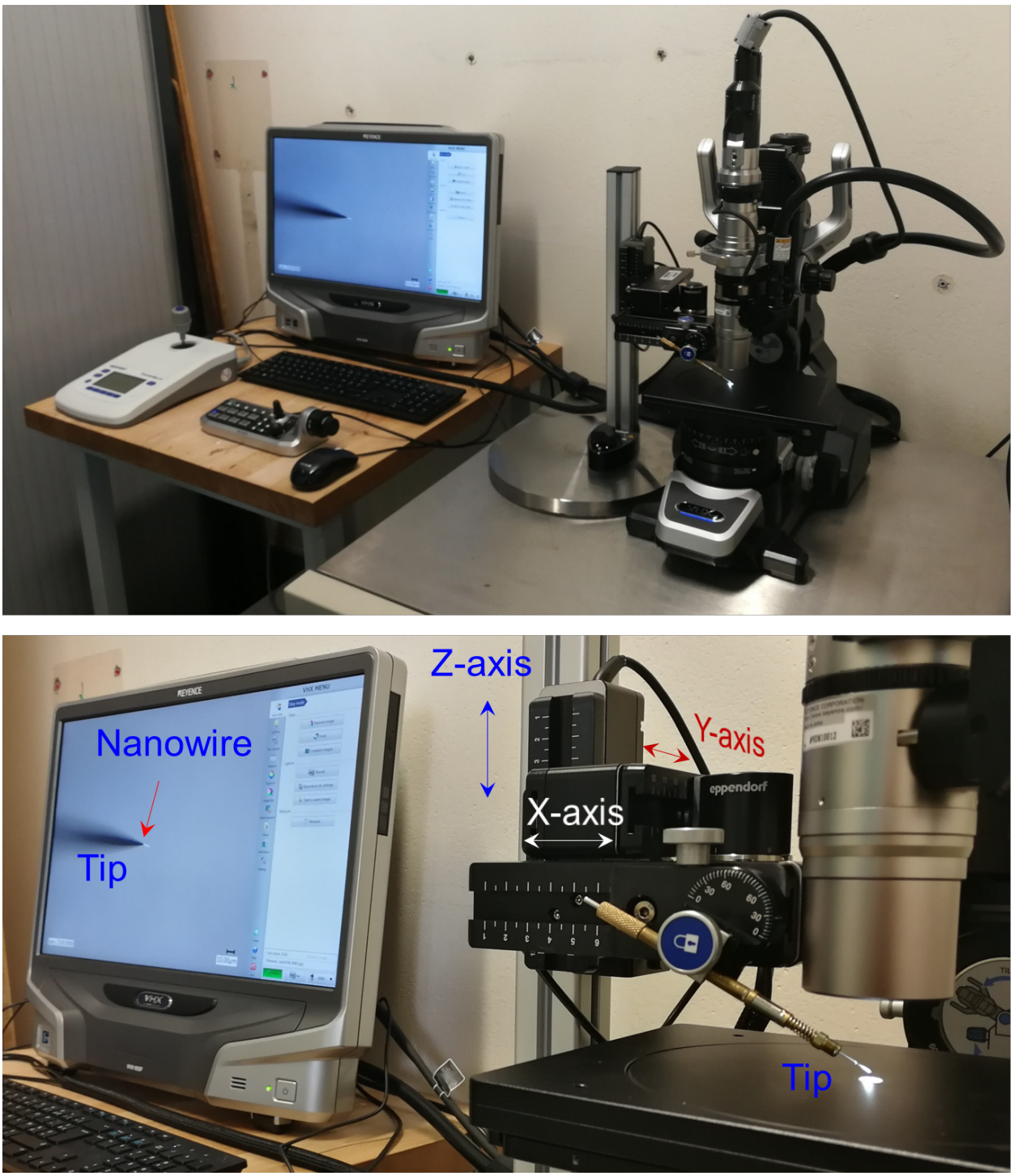


**Figure 12.5:** View of the micromanipulation station for nanowire deposition. The station consists in a Eppendorf 3-axis micro-manipulator (TransferMan® 4r) that controls the position of a home-made tip holder. The control pad with the joystick (upper image on the left-hand side) allows to move the tip on the X-Y plane whereas the swivel (top part of the joystick) controls the Z -axis. A 100-nm-radius tungsten STM tip is attached to a home-made holder. The micro-manipulator is associated with a digital microscope (Keyence) that allows to monitor the transfer process: a single nanowire is catched with the STM tip from the small piece of wafer with nanowires, then deposited on the desired region of our sample with a precision of the order of a few $\mu$meters.

- Coating: bilayer of MMA(8.5)MMA EL10 / PMMA(950K)A6 (~ 400 / 300 nm thick respectively) baked @ 150°C
- E-beam lithography at 30keV
- Ti/Au deposition: after mild Ar milling, 3 nm thick layer of Ti, followed by 50 nm of Au is deposited at a rate of 0.1nm/sec and 0.5 nm/sec respectively.
- Lift-off: in hot acetone (60°C) during 15 min. Rinsed in IPA under mild US. Blow dry under nitrogen.

Limited gate stability was observed on sample S1: two-tone spectra showed slow drifts and from time to time sudden jumps. Furthermore, gate sweeps displayed hysteresis. We attributed this behaviour to the presence of deep charge traps in the nearby silicon dioxide dielectric substrate determining the electrostatic environment of the semiconductor weak link. Having in mind this hypothesis, we decided to fabricate gates differently by placing them underneath the weak link. In sample S2, gates were fabricated at the same time as the alignment marks. Since the nanowires were deposited on top of the NbTiN film, and across the CPW resonator gap, the weak links were suspended typically ~100 nm above the gates. This way there is no dielectric between the weak link and the metallic gate, which furthermore screens the charges in the substrate. With this gate configuration, spectra were much more stable, and hysteresis in gate sweeps almost negligible.

### 12.2.5 Nanowire contacts

The last fabrication step consists in contacting the nanowires' aluminum shell to the loop that allows phase biasing the weak link. The process flow is as follows:

- Coating: bilayer of MMA(8.5)MMA EL10 / PMMA(950K) EL baked at 150°C
- E-beam lithography at 30keV
- Alumina dry etch: in order to get superconducting contacts, the oxide layer on top of the nanowires' Al shell must be removed prior to Al evaporation. This is done by means of Ar-milling (sequences of 10 sec of etching / 40 sec of waiting time to avoid overheating and hence damaging the PMMA mask).
- Al deposition: after Ar milling, 130-nm-thick Al layer is deposited at a rate of 1nm/sec.
- Lift-off: in hot acetone (60°C) during 15 min. Rinsed in IPA under mild US. Blow dry under nitrogen.

Figure 12.6 and Figure 12.7 show details of the region where the CPW resonator and the nanowire weak link are coupled, in samples S1 and S2, respectively.

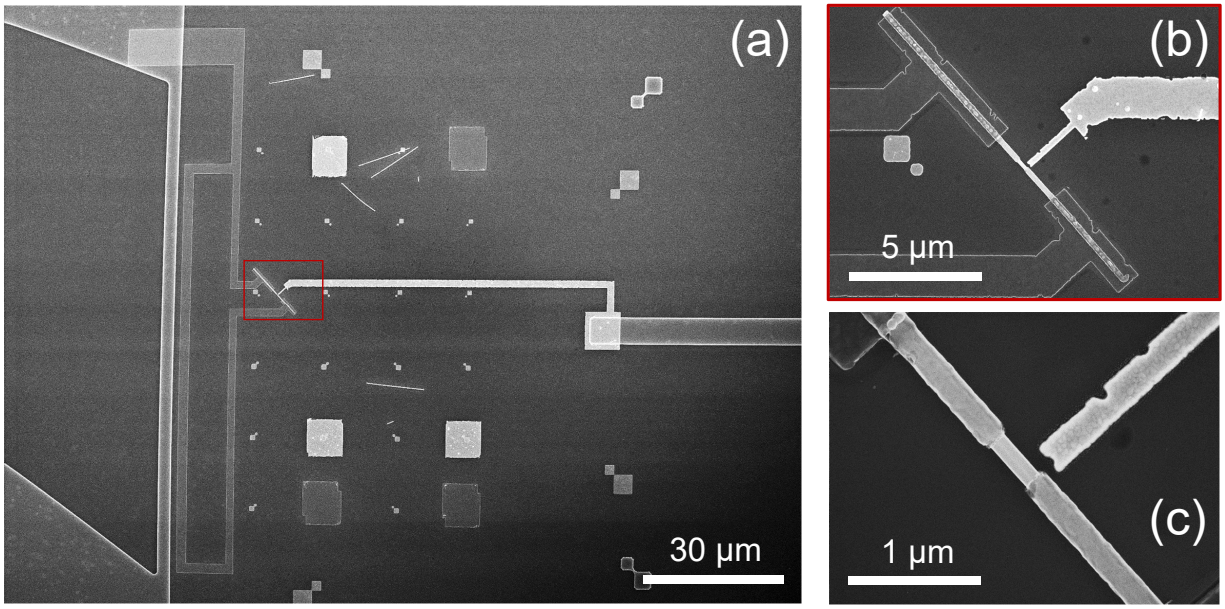


**Figure 12.6:** SEM images of Sample S1. (a) zoom on the shorted-end of the CPW resonator (on the left) coupled to Al loop containing the NW (inside red box). Note that the Al loop is connected to the ground plane (upper left corner) to provide a reference for the dc voltage applied on the gate (thin horizontal bright electrode). (b) close view of the InAs-Al core-shell nanowire. (c) Zoom on the weak link. The Al shell was removed over 370 nm to form the weak link. A close-by side electrode is used to gate the semiconducting exposed region and drive microwave transitions between ABS.

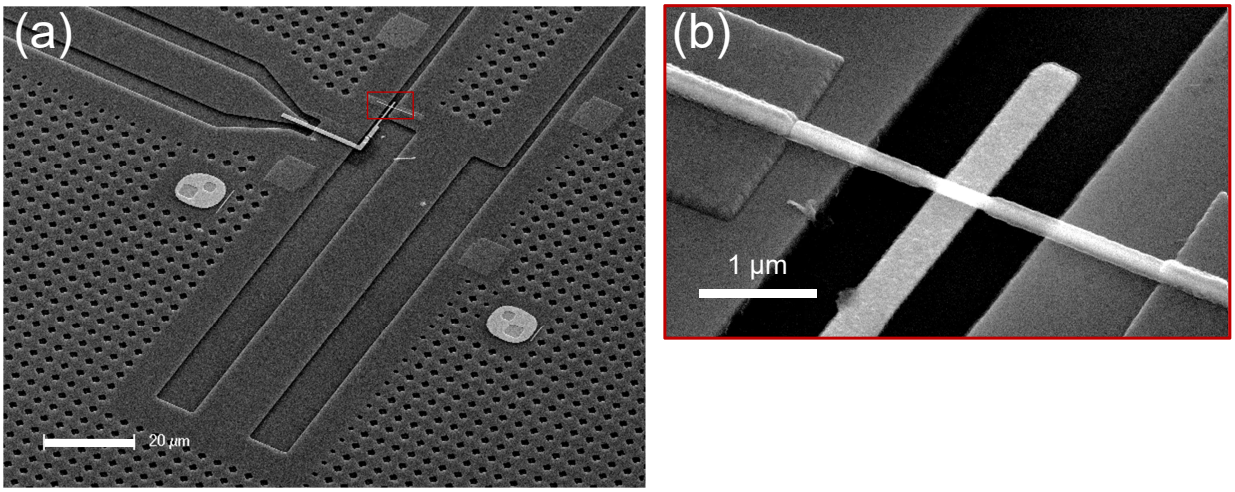


**Figure 12.7:** SEM images of Sample S2 (tilted). (a) Zoom on the shorted-end of the CPW resonator.The nanowire (inside red box) connects the central conductor of the CPW and the ground plane, thus forming a superconducting loop that allows to control the phase difference across the nanowire weak link. (b) close view of red box in (a) The Al shell was removed over 600 nm to form the weak link. A local back gate electrode underneath the semiconductor exposed region is used to control the dc properties of the weak link and drive microwave transitions between ABS.

# Low temperature measurements 13

During this thesis, the experiments were performed in two different dry dilution refrigerators. Most of the spectroscopy experiments (chapters 6 and 8) were carried out in a Cryoconcept fridge (base temperature 30 mK), whereas the time-domain data (Chapter 9) were taken in a BlueFors LD-250 refrigerator (base temperature 10 mK) installed in 2020. Views of the two room temperature control desks and of the dilution refrigerators are given in Figure 13.1 and Figure 13.2



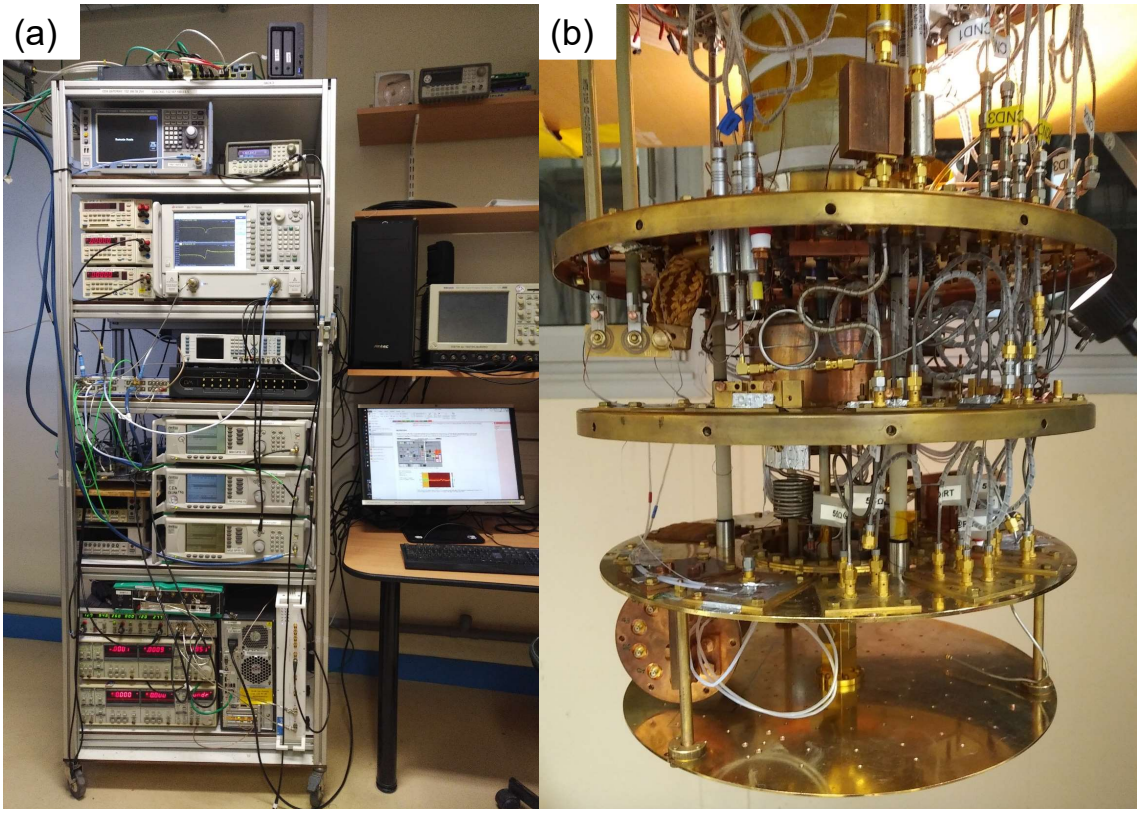


**Figure 13.1:** (a) View of the control desk of the experiment with Cryoconcept refrigerator, shown in (b), with the sample box at the bottom left.

.

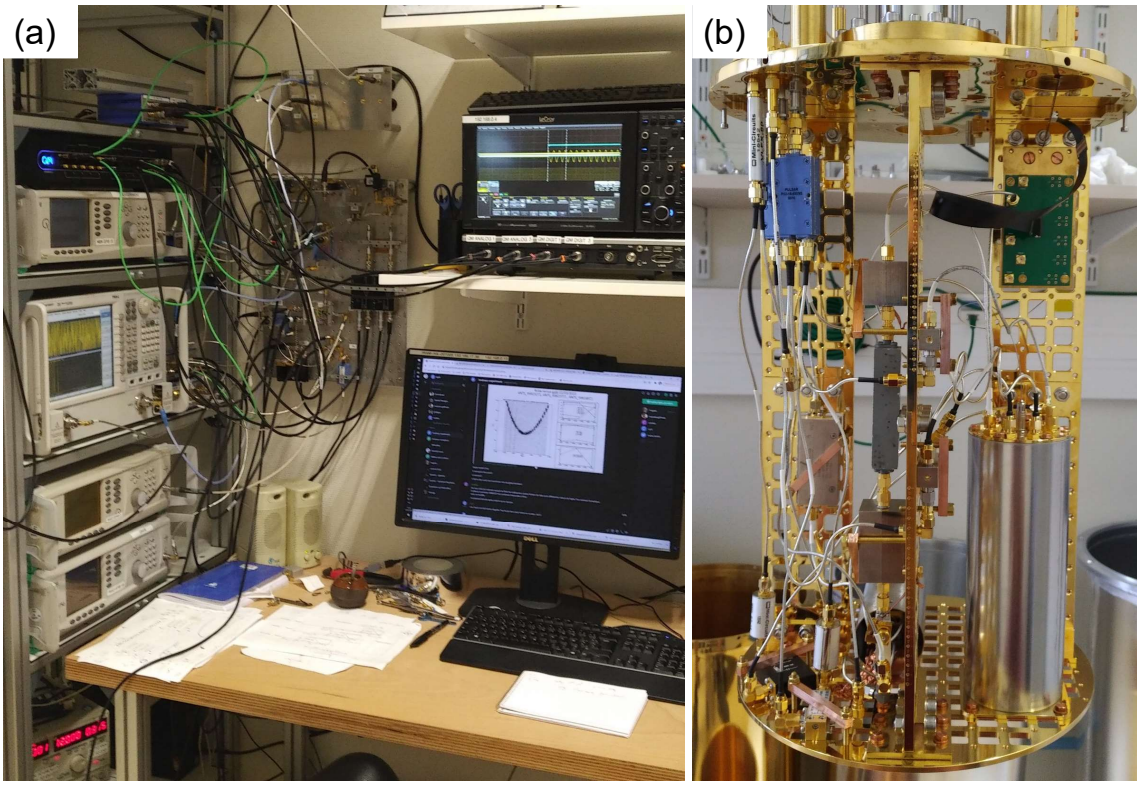


**Figure 13.2:** (a) View of the control desk of the experiment with BlueFors refrigerator, shown in (b), with the sample box on the right hand side.

## 13.1 Sample holder

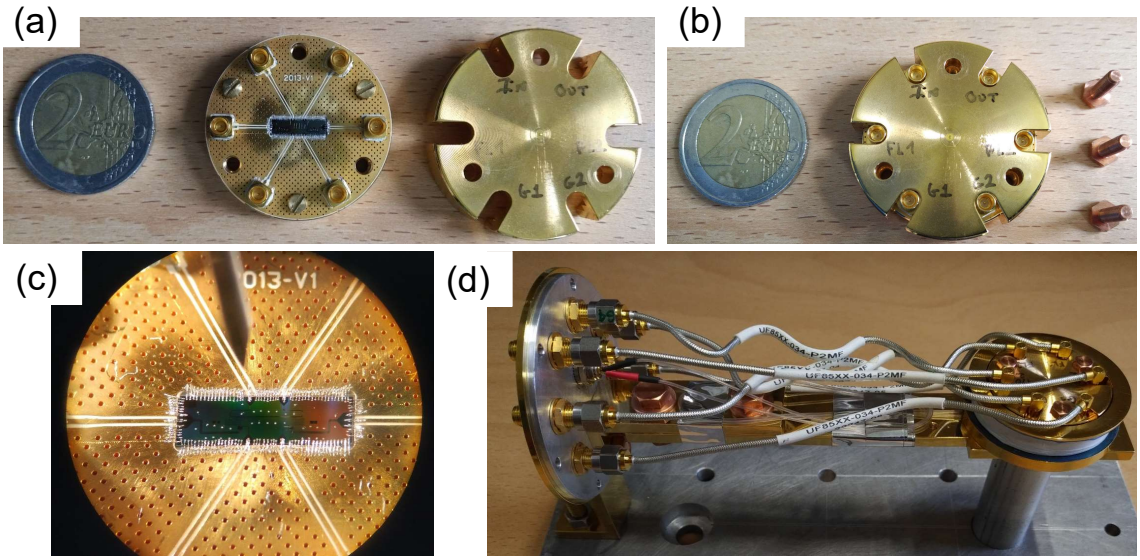


**Figure 13.3:** (a,b) Views of the sample holder, open and closed. A two-Euros coin gives the scale. (c) Sample wire-bonded to PCB. (d) Closed sample holder mounted inside a flat superconducting coil (white Teflon tape covers its windings). The ensemble is enclosed in a double cryoperm/aluminum cylindrical shield, seen in Figure 13.2(b).

The silicon chips are glued on a printed circuit board (PCB), using a droplet of UV3 resist. As shown in Figure 13.3, wire bonding allows the connection to the PCB, including many connections to the ground plane all around the sample. The PCB, which has six SMP connectors soldered

onto it, is mounted in a cylindrical gold plated copper box. The box is placed coaxially inside a flat superconducting coil on a copper holder thermally anchored to the refrigerator mixing chamber. The ensemble is enclosed in two cylindrical shields, the inner one made of aluminum, the outer one of Cryoperm.

## 13.2 Wiring inside the dilution refrigerator

### 13.2.1 Cryoconcept® fridge

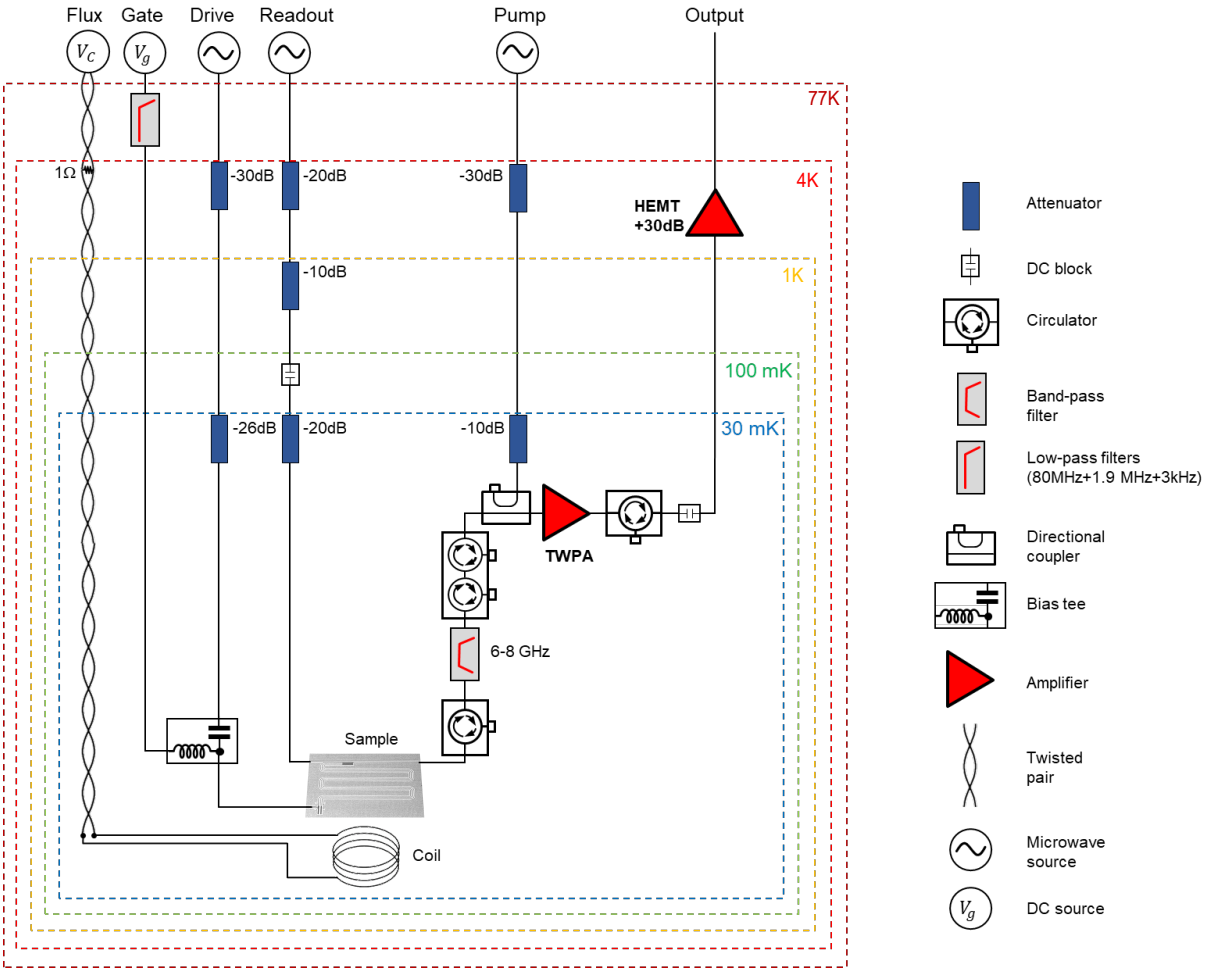


**Figure 13.4:** Schematics of the wiring of the experiments presented in chapters 6 and 8

.

The wiring of the Cryoconcept fridge is schematically represented in Figure 13.4. The signals sent to the sample are attenuated by a succession of XMA attenuators. The measurement signal is amplified first at base temperature by a TWPA (developed at Lincoln Laboratories and provided to us by Will Oliver), followed by a HEMT (Low Noise Factory 4 – 16 GHz, +40 dB) at the 4K stage. The coaxial line between the two amplifiers is superconducting (NbTiN), in order to have as little attenuation as possible but low heat conduction. The circulators between the sample and the HEMT are from Quinstar 8 – 12 GHz (simple and double), and a Pamtech broadband insulator. The 6 – 8 GHz bandpass filter is from Microtech. The DC gate port is a coaxial line, equipped with Mini-Circuit VLFX-80+

and SLP-2.5 low-pass filters. A bias tee (Anritsu K250), placed at base temperature, allows to combine DC and AC voltages on the gate. A small superconducting coil placed next to the sample, biased using a twisted pair and filtered by the combination of its inductance and a 1 Ω resistor, is used to phase-bias the weak link . Additionally, a two-axis home-made magnet (not shown in the figure) is used to probe the magnetic-field dependence of the weak link spectrum. The two Helmholtz coils are biased through HTc superconducting wires, and filtered with the parallel combination of their inductance and 9 Ω resistors placed at the 77 K stage.

### 13.2.2 Bluefors® fridge

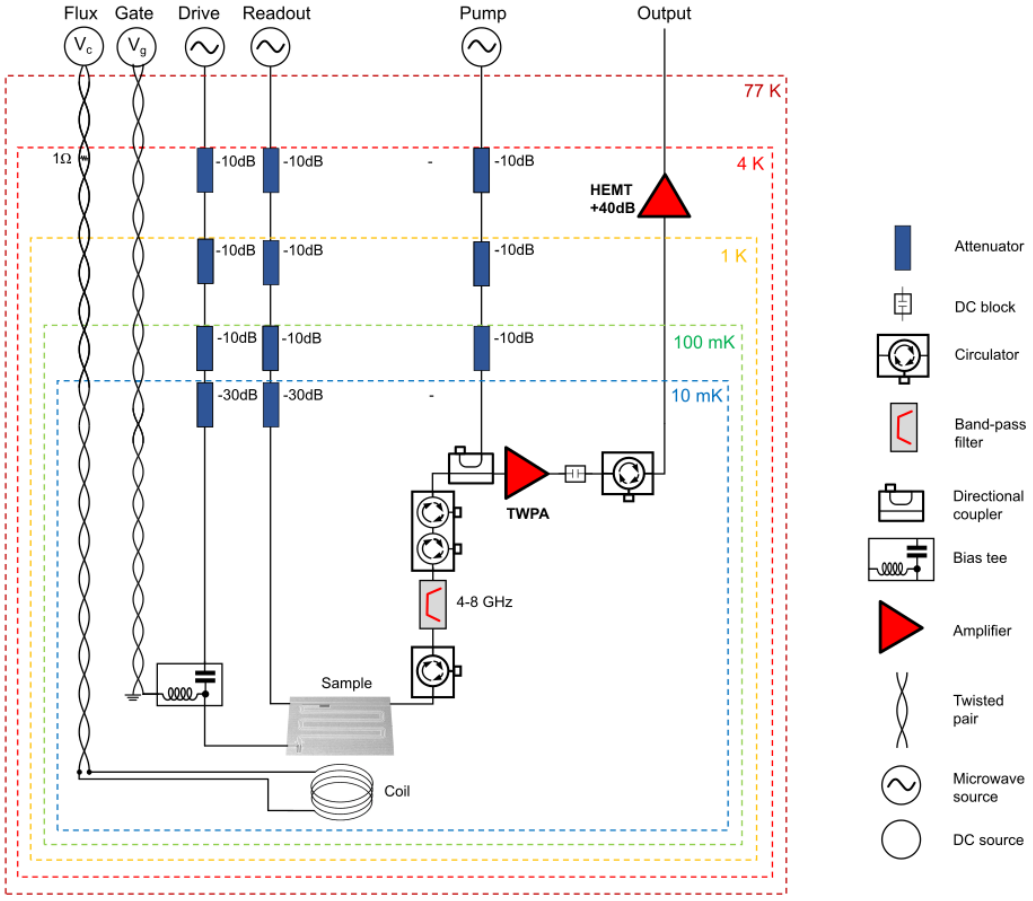


**Figure 13.5:** Schematics of the wiring of the experiments presented in chapter 9

The wiring of the BlueFors fridge was very similar, see Figure 13.5, except for minor changes like the position of the attenuators. The main difference concerns the DC gate bias, which is done through a twisted pair fabricated on long flexible PCBs by our colleague Çağlar Girit at Collège de France, and includes a low-pass RC filter at base temperature. The coil on the sample holder (see Figure 13.3) was wired from a 100 $\mu$m-diameter NbTiN wire, 800 turns on 10 layers. To avoid short-circuits to ground, the metallic mandrel (gold plated copper) was covered with blue-tape on the sides and Kapton tape at the bottom.

# Microwave measurements 14

## 14.1 Microwave wiring

For the first spectroscopy measurements performed in the Cryoconcept fridge we used a rather simple room-temperature microwave setup, shown in Figure 14.1. Simple mixers are used to pulse the measurement tone (frequency $f_0$.) In some experiments, we had two measurement lines allowing to measure resonators around 3 GHz and 9 GHz (blue and red lines). The corresponding signals were mixed with IQ mixers, filtered, amplified, then sent to two lock-ins (in the figure, SR830). The drive signal at frequency $f_1$ is chopped with an arbitrary waveform generator (Agilent AWG 33250) delivering a square signal at a frequency given as a reference to the the lock-ins.

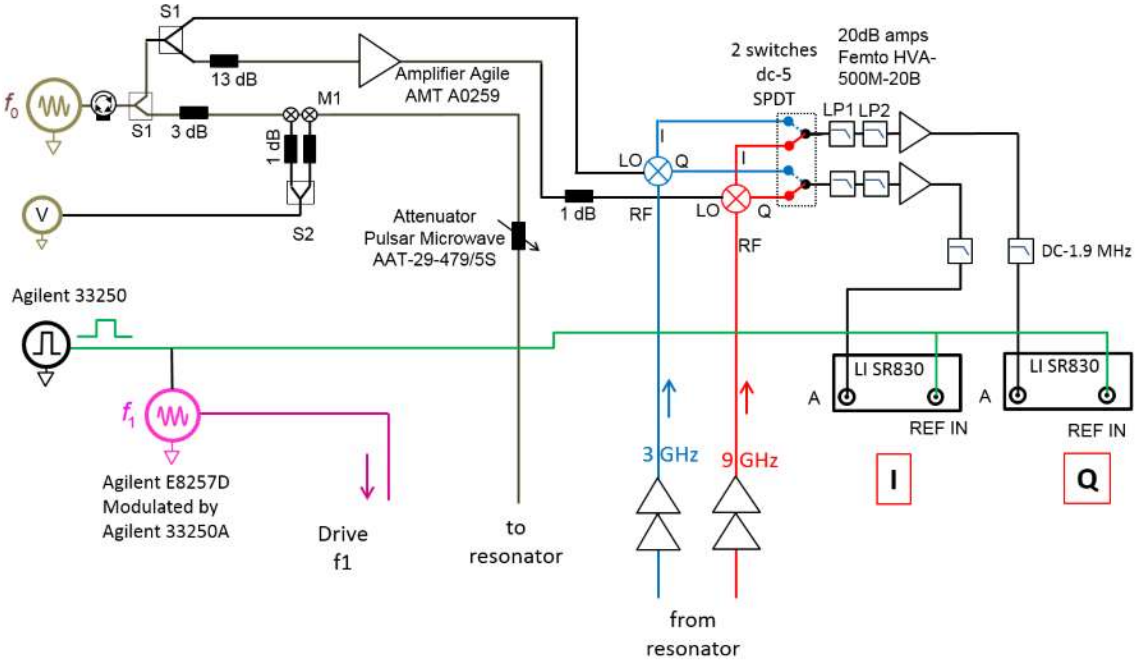


**Figure 14.1:** Schematics of the room temperature microwave wiring of the experiment in the lab with Cryoconcept fridge.

.

In the subsequent experiments, the setup was enriched and modified so that all the different types of measurements and the different controls could be performed without disconnecting anything. The present (January 2022) state of the corresponding wiring of the experiment is shown in Figure 14.2. Several computer-controlled mechanical switches (Mini-circuit RC-4SPDT-A18), shown as blue rectangles, allow to route the signals. The green rectangles are microwaves sources (Anritsu MG3292 or MG3294), a vector network analyser (Keysight PNA-L), a signal analyser (Rohde and Schwarz FSV), an oscilloscope (Lecroy Waverunner 601). The Quantum Machine OPX appears split in 3 grey rectangles in the diagram: analog outputs (left), digital markers (bottom right) and analog inputs

(top right). The connections to the ports of the experiment at the top of the dilution refrigerator are symbolized with the purple disks Drive (drive tone, connects to "Drive" in Figure 13.5), Resonator (connects to "Readout" in Figure 13.5), Meas (connects to "Output" in Figure 13.5).

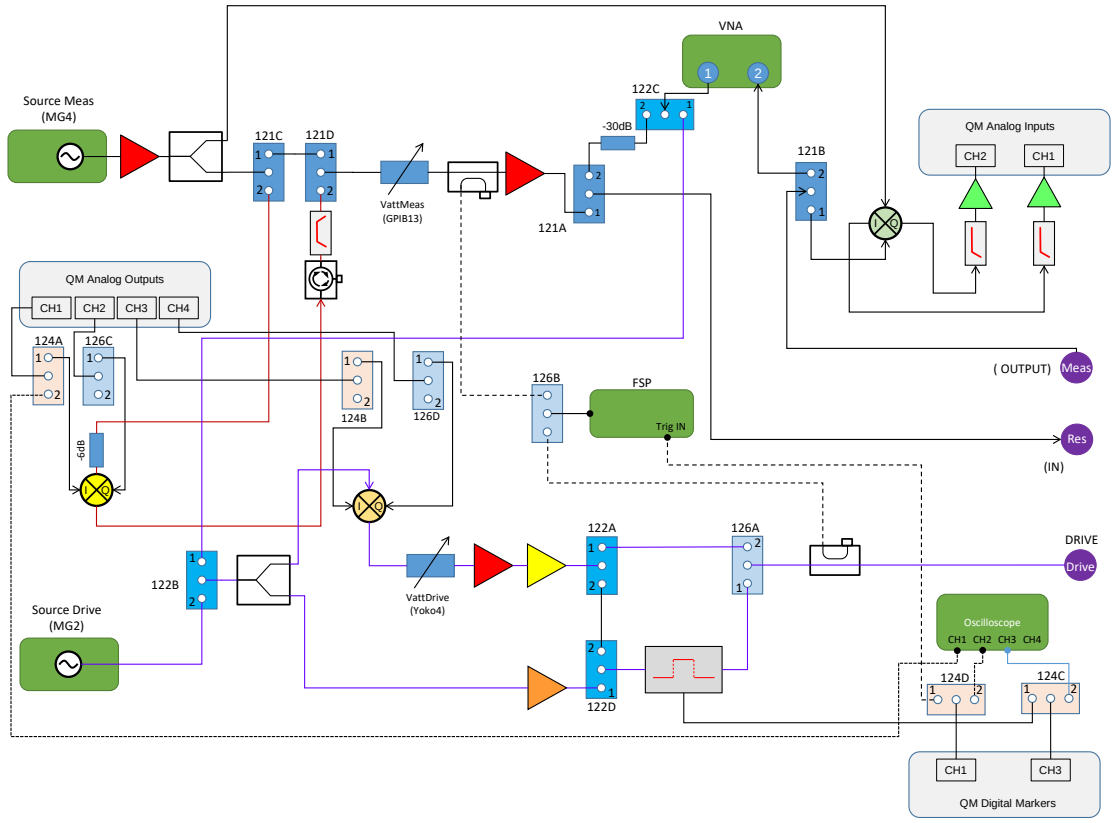


**Figure 14.2:** Schematics of the room temperature microwave setup. The identification of the different elements is provided by Figure 14.3.

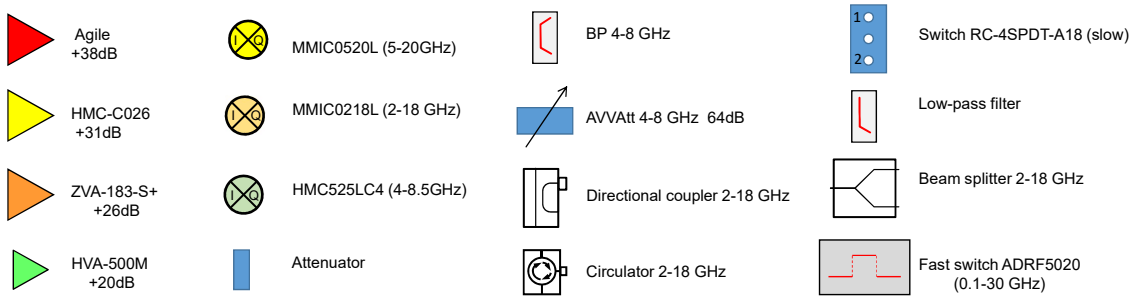


**Figure 14.3:** Caption for Figure 14.2.

The actual setup is shown in Figure 14.4.

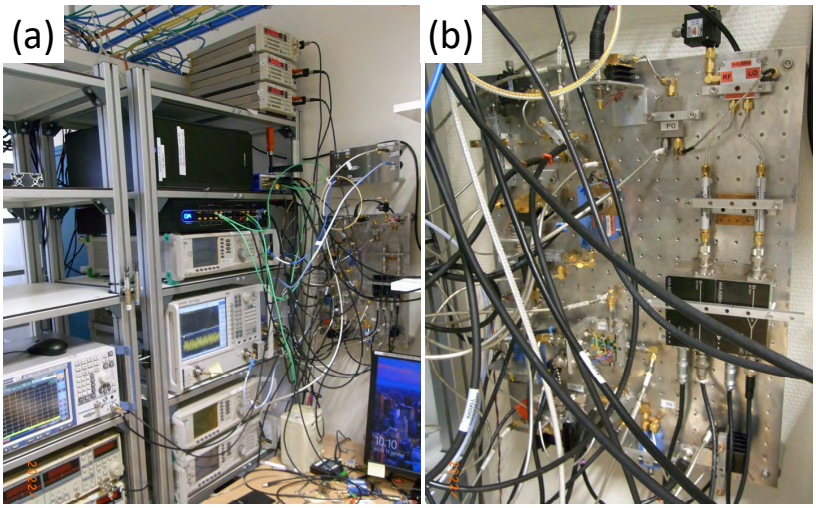


**Figure 14.4:** Room temperature microwave setup as of January 2022: (a) General view; (b) close view on the mixers' board.

.

In Figure 14.5, we show the parts of the circuit used in spectroscopy experiments performed with the Quantum Machine.

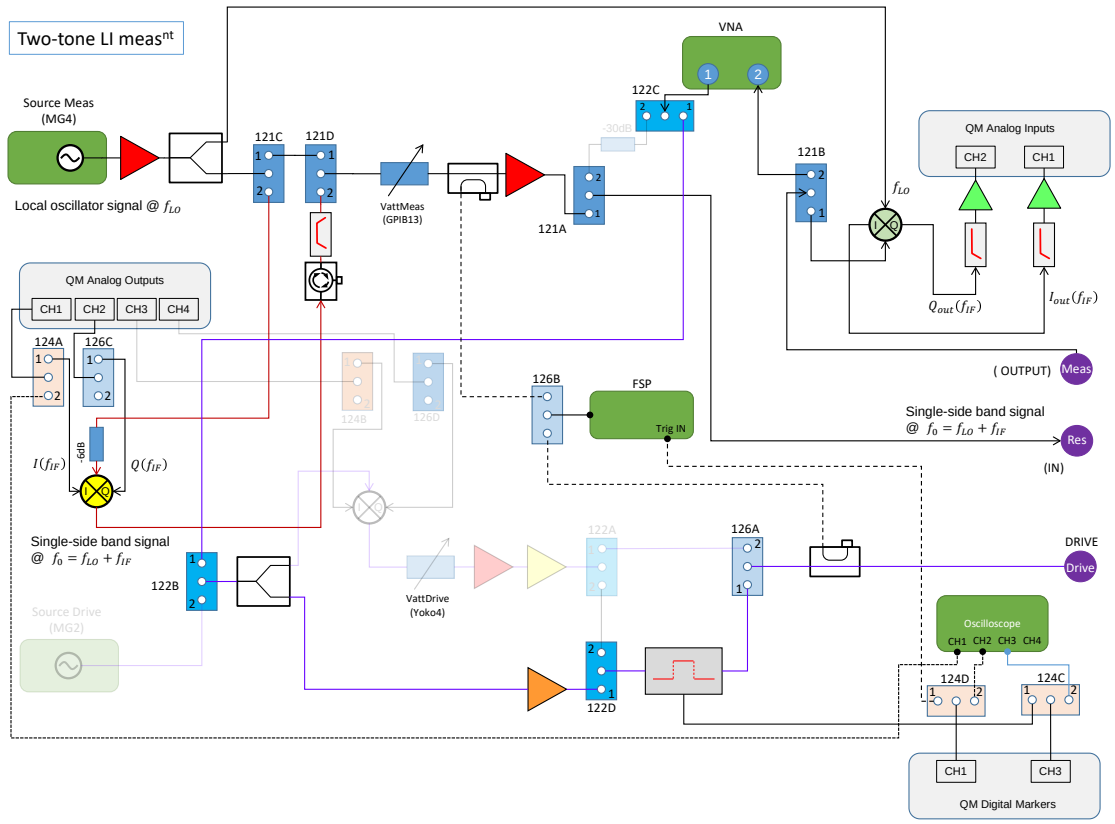


**Figure 14.5:** Microwave circuit for spectroscopy experiments. The drive tone generated by the VNA in CW mode (on the top of the figure) is chopped by the rapid switch (on the bottom), commanded by a digital output of the QM (bottom right).

.

## 14.2 Spectroscopy

For measurements of the spectrum, the drive and measurement tones were applied simultaneously. Two differential methods were used to measure the effect of the drive tone.

- In the first one, illustrates with Figure 14.1, the drive tone was chopped using a 3 kHz square voltage signal gating the microwave source itself. The same signal was used to synchronize lock-in amplifiers (two Stanford Research LI830, or the two ports of a Zürich Instruments UHFLI 600 MHz), which give the amplitude of the corresponding modulation in $I$ and $Q$. The time constant of the lock-ins was set to $10 - 50$ ms. One practical advantage of the Zürich Instruments Lock-in over the Stanford Research ones is that it could be addressed through a network port, much more rapid than the GPIB interface, which makes a difference when the points of a spectrum are transferred one by one to the computer.
- The second method uses the Quantum Machine: one output of the QM drives a switch (Analog Devices ADRF5020) on the drive signal. The signal is a series of 33 $\mu$s-long pulses with of 10 times high/low value. Each pulse is demodulated with alternative signs, so that one directly obtains the difference of $\langle I \rangle$ and $\langle Q \rangle$ with drive on and off.

## 14.3 Time-domain measurements

### 14.3.1 Generation of pulses

Microwave pulses were obtained by single side-band mixing low-frequency pulses generated with a waveform generator and microwave tones from a microwave source. The principles of single side band mixing is described in Section I.1. The waveform generator was a Quantum machine® OPX, which also allowed acquisition of the measurements and demodulation. The pulse envelope was defined with $\omega_{\text{IF}}/2\pi \approx 50$ MHz. The microwave sources were either Anritsu MG3692 (up to 20 GHz), Anritsu MG3694 (up to 40 GHz), or a Keysight PNA-L network analyser used in CW mode (up to 20 GHz). IQ mixers are from Marki MMIQ-0218L (for drive tone) and MMIQ-0520 (for measurement tone).

### 14.3.2 Demodulation

Demodulation of the $I$ and $Q$ component of each measurement pulse was performed using a QUA program (QUA is the Python-based programming language used to address the Quantum Machine). The principles of demodulation are exposed in Section I.2. A large number of measurements (typically a few thousands) are acquired, then treated using two method. In the first one, one only takes the average values of $I$ and $Q$. In the second one, the histograms of the measured values are analyzed as a mixture of $n_c$ gaussian components, depending on the number of clouds that are observed (typically 3). Using the Python class `sklearn.mixture.GaussianMixture` from the Scikit-learn

library for machine learning [117], each measurement is ascribed to one cloud, and one obtains the populations of the $n_c$ clouds.

## 14.4 State pre-selection

Most of the pulse sequences that we have used for measurements of Rabi oscillations, measurements of lifetime and coherence times are standard. Less standard is the state pre-selection method used in the experiments described in Sections 10.1.2 and 10.2.3. The way we do it is by repeating measurement pulses and demodulating the results till a given state is obtained with a high level of confidence. This is done at reduced amplitude of the pulse measurement (by a factor 3), otherwise one has to wait too long for the cavity to empty before the actual manipulation that follows can be performed. Figure 14.6 illustrates the pre-selection procedure. In (b), we show histogrammed value of the measurements with low amplitude and normal pulses. The clouds corresponding to states $|g\rangle$ and $|o\rangle$ partly overlap with the small amplitude pulses. Dashed lines indicate the threshold values of $I$ used to decide that a given state has been measured, with sufficient accuracy. The subsequent manipulation follows after a dead time of a few $\mu$s to ensure that the number of photons in the cavity has sufficiently decreased.

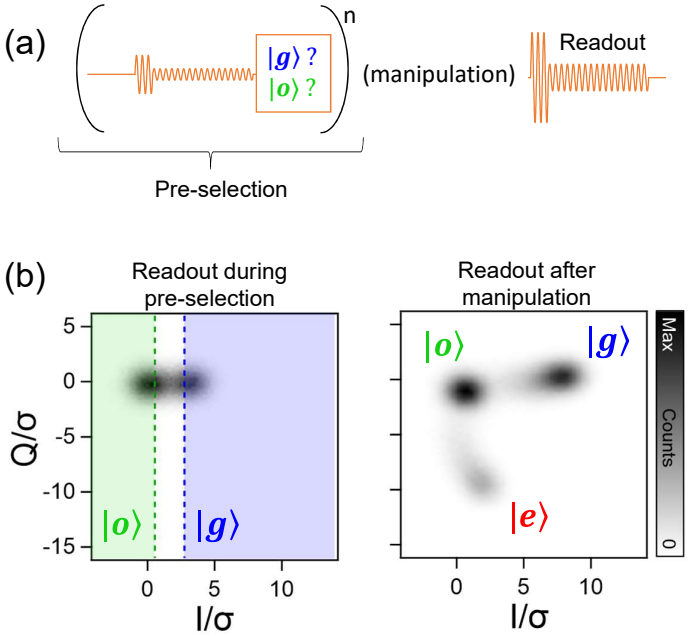


**Figure 14.6:** (a) Pulse: low power measurement pulses are repeated till the required state is measured. (b) Comparison of the histogrammed output of low amplitude measurements, like during the preselection, and standard measurements.

# Data acquisition 15

## 15.1 QuantroLab

Data acquisition is based on the integrated development environment (IDE) QuantroLab, which has been developed in the Quantronics group since 2012 by Andreas Dewes, Vivien Schmitt, Daniel Flanigan and Denis Vion. We benefited not only from the IDE itself, under constant development, but also from the instrument drivers and front panels written by others in the group.

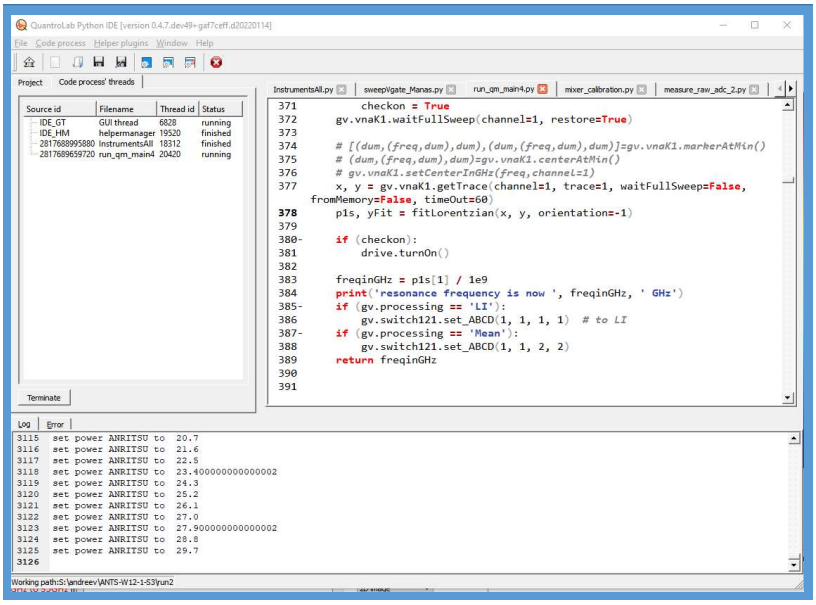


**Figure 15.1:** IDE main window, with a Python program opened.

.

QuantroLab allows controlling the experiment with Python programs (see Figure 15.1) and benefit from three "helpers" (see Figure 15.2):

- The instrument manager, in which all connected instruments appear, and can be addressed using commands and front panels.
- The data manager, which allows real-time plotting of data (2D or 3D plots).
- The loop manager, which allows to control running loops during a measurement: loop direction, step, start and end values can be changed in real time; a loop can be paused and restarted, set to auto-reverse or auto-restart.

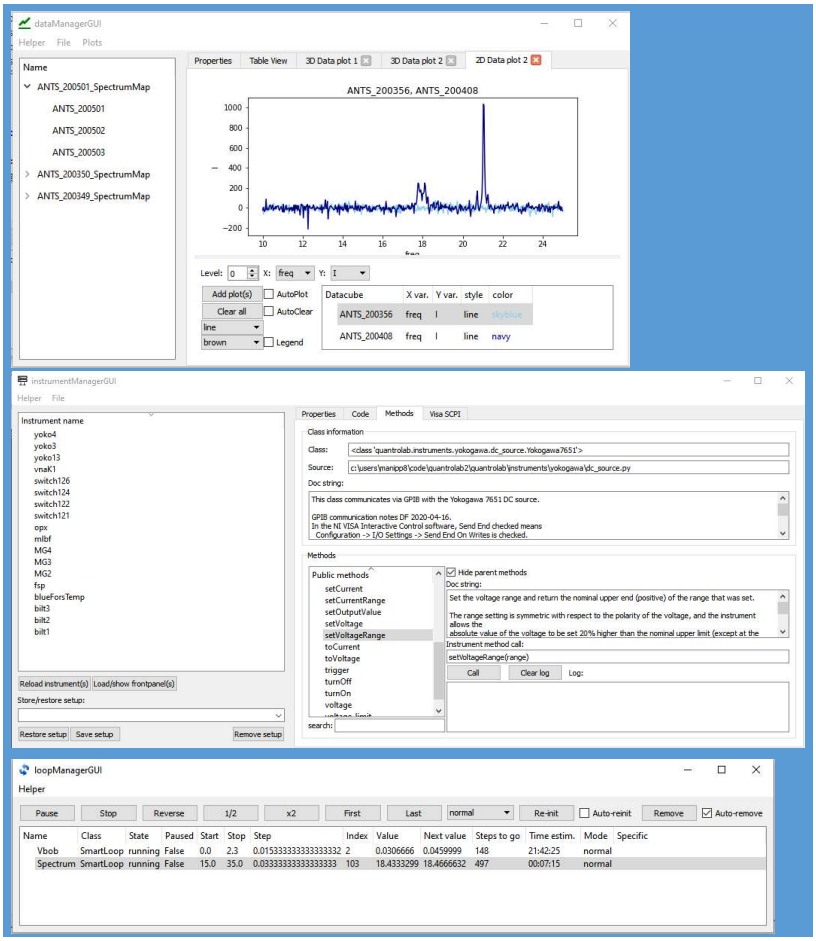


**Figure 15.2:** IDE Helpers: from top to bottom, the Data manager, the Instruments manager and the Loops manager.

.

## 15.2 Command files

In the experiments of this thesis, several types of measurements are performed repetitively, and each type of measurement requires specific tunings. We used an interface written with Igor Pro software (Wavemetrics®) that allows setting up graphical interfaces and programming, as shown in Figure 15.3. In this interface, one chooses the type of measurement by selecting the corresponding tab, which contains all the parameters previously used for this specific measurement. As soon a one tab is selected or one parameter is modified, a text command file is saved on the computer, and a text recapitulating all the settings is copied to the clipboard, ready to copy to the lab book. We use essentially a single Python program IDE, which performs measurements according to the information read in the command file. Hence, after defining the measurement in the Igor interface, one just has to launch this Python program.

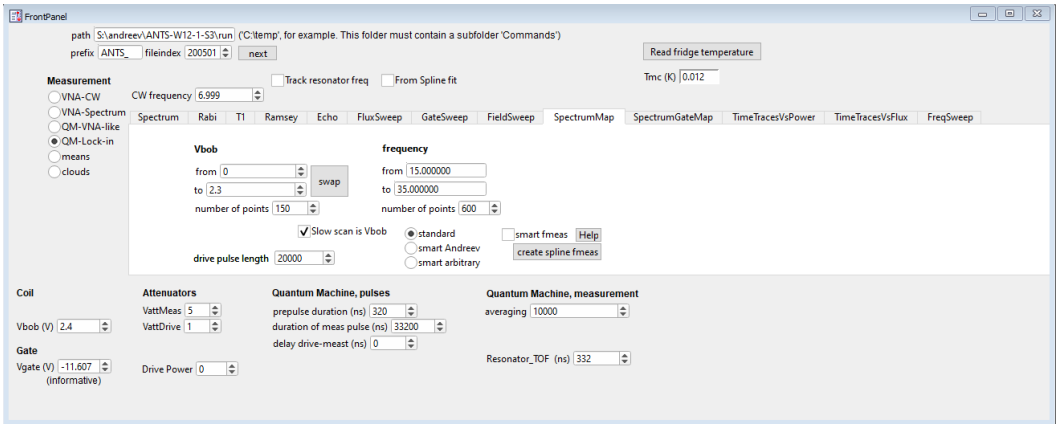


**Figure 15.3:** Igor interface used to write command files.

We developed some convenient tools, like the measurement of spectra in a non-rectangular region in the phase, frequency plane $(\delta, f_1)$. After loading in Igor a spectrum, one draws a spline to define a specific path $f_1(\delta)$. In the front panel, one loads this path and define a measurement region as a frequency interval of a given amplitude around this path. When reading the command file, the Python program sweeps the corresponding snake-shaped window.

# Conclusions 16



## 16.1 Summary of the results

**Spin.** One key result of this thesis work is the experimental observation of the *fine structure* of the Andreev states in InAs nanowire weak links, as an effect of the Rashba spin-orbit interaction. It is revealed by the existence of distinct spectroscopic lines, which we interpret as atomic-like transitions of a quasiparticle between two spin-split ABS doublets. A minimal two-band model accounting for the spin-orbit interaction in the nanowire is shown to explain these generic features and their evolution with magnetic field, and confirms the role of spin in the underlying processes. Compared to experiments performed with atomic contacts, where only transitions involving pairs of quasiparticles were possible, this new family of transitions offers a route, alternative to quantum dots, to manipulate a single fermionic spin and implement an *Andreev spin qubit*.

In collaboration with the group of A. Levy Yeyati, we developed a general framework to describe the coupling of a resonator to a multilevel system of ABS, which can be applied to model both single-tone and two-tone spectroscopies. Although a quantitative modelling of the spectrum of finite-length weak links is in general out of reach as it requires knowledge of the energy of all subgap states and of the continuum, this theory allows to capture in some limits several observed features in the experiment, such as the effect on the resonator shift of the levels' curvature and the crossing of virtual transitions with the resonator frequency.

In addition, we reported data with clear evidence of direct intra-manifold spin-flip transitions of a single quasiparticle in the absence of any Zeeman field. These transitions, which were initially predicted to be strongly suppressed when no magnetic field is applied, are shown to be possible when the transverse symmetry of the weak link is broken, which can be achieved by means of a gate type of driving.

**Charge.** ABSs are generally perceived as chargeless states that only carry supercurrent. Nevertheless, charging effects may be at play when the weak link transmission is imperfect. The measured spectra suggest that ABS in different channels of a nanowire junction are weakly interacting, pointing at the relevance of Coulomb interactions in the electrodynamics of finite-length weak links. To evidence this effect, we identified recurring transition lines in the microwave spectra, which we interpret as mixed pair transitions involving pairs of quasiparticles in different ABS doublets. Using different models, we show that such mixed transitions are highly sensitive to electron-electron interactions, which lead

to a modification of their spectral signatures characterized by a generic splitting of their degeneracies at $\delta = 0$ and $\pi$. In some cases, this splitting is reminiscent of the singlet/triplet physics of two interacting spins 1/2. Altogether, our measurements show that an interacting multi-channel theory is in general needed and that a minimal model to describe nanowire spectra should include both spin-orbit coupling and the junction's finite length. The relevance of the ABS charge was independently established by Fatemi *et al.*, who evidenced by single-tone spectroscopy a violation of particle-hole symmetry of the even states [50], as another signature of Coulomb interactions.

[50]: Fatemi et al. (2021), 'Microwave susceptibility observation of interacting many-body Andreev states'

Although the present work focused mainly on spectroscopy, we also report results on time-domain experiments, in particular preliminary ones on the manipulation of an Andreev spin. We demonstrate the coherent driving of a single quasiparticle between two different ABS doublets, although the populations of the associated spin superpositions could not be extracted. From tight-binding calculations of the resonator shift expected for the lowest-lying many-body states, we show that single-shot readout of a quasiparticle spin may actually be achievable only in a restricted range of superconducting phase difference around $\delta = 0$, which constrains the operation of the weak link as a spin qubit and may explain our difficulties in discriminating the spin states, as most of our time-resolved measurements focused on the region around $\delta = \pi$.

## 16.2 Future challenges & perspectives

We envision two future perspectives. First, in the continuity of the present work, to realize the spectroscopy of ABS in an InAs nanowire-based junction under high axial magnetic field. Second, to apply the spectroscopy techniques that we developed to the investigation of multi-terminal nanowire-based junctions.

### 16.2.1 Spectroscopy under high B field

One interesting path to be explored in the future, is the evolution of the Andreev spectrum of InAs-nanowire weak links under high axial magnetic field. Indeed, recent tunneling spectroscopy experiments in full-shell nanowires claim that this hybrid system could be driven into a topological phase by a flux-induced winding of the phase around the superconducting shell [45]. To reach it, one quantum of applied flux should thread the nanowire section, corresponding to a phase twist of $2\pi$ in the shell. For nanowires with $d = 150$ nm diameter like the ones used in this thesis, this would require to apply a longitudinal field of about $\phi_0/(\pi d^2/4) \approx 120$ mT, much lower than the stringent 1 T parallel field which was suggested in previous proposals [43, 44]. Although tunneling experimental results must be taken with care after the editorial expression of concern published in July 2021, a new experiment using a different spectroscopic technique (namely, photon absorption spectroscopy), could bring additional input about this rich system and possibly elucidate the controversy. In Appendix J, I present the progress made towards this experiment.

[45]: Vaitiekėnas et al. (2020), 'Flux-induced topological superconductivity in full-shell nanowires'

[43]: Lutchyn et al. (2010), 'Majorana Fermions and a Topological Phase Transition in Semiconductor-Superconductor Heterostructures'
[44]: Oreg et al. (2010), 'Helical Liquids and Majorana Bound States in Quantum Wires'

### 16.2.2 Microwave spectroscopy of multi-terminal nanowire junctions

A new class of junctions is now becoming accessible to experiments: **multi-terminal junctions**, which are weak links between more than two superconducting electrodes. Remarkably, several recent theoretical works predict that such junctions can show topologically non-trivial effects even if the leads are made from conventional superconductors and no exotic materials are used to make the weak link [118, 46, 48].

[118]: Heck et al. (2014), 'Single fermion manipulation via superconducting phase differences in multiterminal Josephson junctions'
[46]: Yokoyama and Nazarov (2015), 'Singularities in the Andreev spectrum of a multiterminal Josephson junction'
[48]: Xie et al. (2017), 'Topological Andreev bands in three-terminal Josephson junctions'

In such a multi-terminal junction, the energy of the ABS, always inside the superconducting gap, depends on the superconducting phase of each superconducting electrode. Topological effects are predicted to arise for certain values of the superconducting phase differences between the terminals, when the gap in the excitation spectrum fully closes, *i.e.* when the energy of the lowest ABS becomes exactly zero, even in presence of disorder. Due to the $2\pi$-periodicity of the superconducting phases, there exists a formal analogy between the band structure of a periodic solid, in which states' energy depends on the components $\{k_x, k_y, k_z\}$ of the electron wave vector, and the spectrum of Andreev states [46, 47]. Consequently, the ABS spectrum of a junction with $N$ terminals simulates a $(N-1)$- dimensional solid, with the $(N-1)$ phase differences playing the role of the components of the wave vector. In this analogy, the vanishing of the energy of ABS corresponds to the physics of a **Weyl semimetal**, the 3-dimensional analog of a Dirac material.

[46]: Yokoyama and Nazarov (2015), 'Singularities in the Andreev spectrum of a multiterminal Josephson junction'
[47]: Riwar et al. (2016), 'Multi-terminal Josephson junctions as topological matter'

Recent advances in material science now allow fabrication of complex networks of crystalline semiconducting nanowires with epitaxial interfaces with superconductors (see Figure 16.1(a)). Using a technique based on growing intersecting nanowires in etched trenches, Gazibegovic *et al.* have demonstrated the realization of multi-junction and multi-terminal nanostructures [119], which are now available for experimentalists to test these predictions of topological effects.

[119]: Gazibegovic et al. (2017), 'Epitaxy of advanced nanowire quantum devices'

So far, existing experiments on multi-terminal junctions focused mainly on transport properties, and the results are poorly understood [120, 121, 122, 123]. The reason is that when finite voltages are applied, phase differences vary. The occupation of ABS becomes time-dependent, and Landau-Zener tunneling, relaxation processes, emission of photons and phonons to the environment are at the origin of very complex, uncontrolled processes. Probing the junctions at equilibrium requires circuit-QED techniques, of which we have demonstrated here the optimization for the spectroscopy of nanowire junctions. Possible designs to couple a multi-terminal junction to a microwave resonator are shown in Figure 16.1.

[120]: Plissard et al. (2013), 'Formation and electronic properties of InSb nanocrosses'
[121]: Pfeffer et al. (2014), 'Subgap structure in the conductance of a three-terminal Josephson junction'
[122]: Pankratova et al. (2020), 'The multi-terminal Josephson effect'
[123]: Draelos et al. (2019), 'Supercurrent Flow in Multiterminal Graphene Josephson Junctions'

Interestingly, the localized Weyl semimetal idea was recently generalized to an even simpler case, the one of a Josephson tunnel junction array [124, 125]. It could be argued that the physics of such system would be very similar to the multi-terminal one (exchange of Cooper pairs between islands and reservoirs influenced by offset potentials and phases), so that ultimately the key interesting facet of implementing it with actual ABSs would be to access to odd-fermion-number states and their unique physics (i.e. with spin-orbit as in Ref. [118]).

[124]: Fatemi et al. (2021), 'Weyl Josephson circuits'
[125]: Peyruchat et al. (2021), 'Transconductance quantization in a topological Josephson tunnel junction circuit'

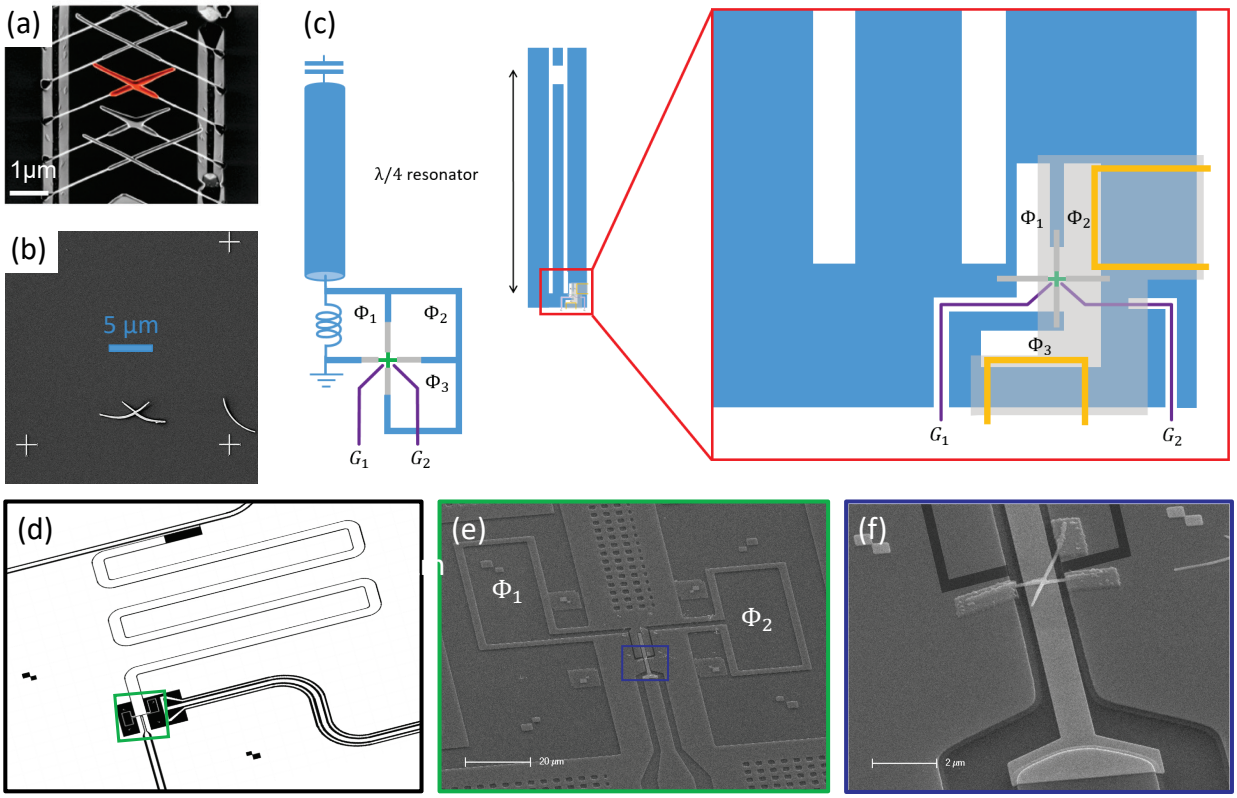


**Figure 16.1:** Towards the microwave spectroscopy of multi-terminal Josephson junctions based on crossed nanowires. (a) Epitaxy of InSb nanocrosses, obtained from the growth in etched trenches of (almost) intersecting InP nanowires which serve as stems for InSb nanowire growth (adapted from Ref. [119]). Radial overgrowth is then performed to merge the two wires into a nanocross (red). (b) InAsSb nanocross obtained from a collaboration with T. S. Jespersen and P. Krogstrup at the Niels Bohr Institute (Copenhagen) and grown with a similar approach as in (a). (c) Schematic setup to couple a 4-terminal nanowire junction to a superconducting microwave resonator. The junction (weak link in green, superconducting electrodes in grey) is placed in proximity to the shorted end of a quarter-wave resonator, shown in blue. Electrostatic gates (magenta) allow tuning the properties of the weak link. The fluxes $\phi_{1,2,3}$ through 3 superconducting loops are tuned with DC currents in local flux lines (yellow) and a global magnetic field. Light grey area is an insulating layer between the gates and the superconducting ground plane. (d) Device for a preliminary 3-terminal spectroscopy using a CPW implementation for the resonator and two loops for the phase bias of the junction, which are shown in the green inset (e). A local flux line is used to bias one of the loops with a flux $\phi_1$, while the other is sensitive mainly to an external magnetic flux $\phi_2$ and lies by design in the symmetry axis of the flux line to avoid cross-talk. (f) Electron micrograph showing an InAsSb nanocross like the one in (b) hanging above a local gate. Three legs of the nanocross are contacted to define the two loops (unfinished sample: the picture was manually edited to separate the contact pads and illustrate the desired geometry).

# Appendices

# Superconductors viewed as information mirrors

# A

Some recent works offering a modern way of looking at Andreev reflection from the perspective of quantum information theory. The starting point is the following : when a normal metal becomes superconducting, electrons pair up to form a macroscopic coherent state, the BCS state, which is independent of the initial quantum state of the electrons that formed the condensate, giving the wrong impression that all the information encoded in the microscopic degrees of freedom of the electrons has been erased. One can wonder what happens to the information falling into the superconductor after the formation of the condensate ?

In Ref. [126], Manikandan *et al.* show that Andreev reflection of a pure spin state can be thought about as a deterministic quantum information transfer described by a unitary scattering matrix, in which the spin state of the incoming electron — possibly in a superposition state of spin $\uparrow$ and spin $\downarrow$ — is mapped exactly onto the outgoing hole. Since the superconducting ground state consists of paired electrons in singlet states, while the incoming electron is permitted to enter the superconductor, its spin information is actually reflected.

[126]: Manikandan and Jordan (2017), 'Andreev reflections and the quantum physics of black holes'

Due to the proximity effect from the superconductor, entangled pairs of quasiparticles may be created at the interface as resonances between the electronic states of the metal and of the superconductor. They correspond to low-lying excitations of the Fermi sea where an electron with $k < k_F$ is promoted to a higher energy level with $k' > k_F$, thus leaving behind a vacancy (hole) in the Fermi sea. An incoming electron undergoing Andreev reflection can be seen to interact with such an electron-hole pair, by binding with the electron-like quasiparticle to form a Cooper pair in the condensate, while the remaining hole-like excitation is reflected backwards. In such a process, the spin information is deterministically transferred from the incoming electron to the outgoing hole, with both the initial shared entangled pair (the electron-hole pair) and the final entangled pair (the Cooper pair) always spin singlets, thus leaving the whole transformation unitary.

In this picture, a superconductor can eventually be viewed as a special kind of *mirror*[1] , transmitting particles while fully reflecting their spin information. By sandwiching a normal metal between two such mirrors, a geometry commonly known as a *Josephson weak link*, one can then expect to *confine* spin information[2] . If this junction is designed in such a way that the naturally occurring spin degeneracy is lifted, one could expect it to serve as a platform to implement a novel kind of spin quantum dot, that could be operated as a qubit.

1: Sharing some similarity with *phase-conjugation* mirrors in optics, where light is reflected straight back the way it came from, no matter the angle of incidence on the mirror.

2: In a real system, with finite transmission, Andreev reflection no longer happens with probability one, meaning that electrons may also undergo a normal specular reflection at the interface.

To push further the analogy between superconductors and information mirrors, Puspus *et al.* analyzed the spin entanglement of the BCS ground state and showed in Ref. [127] that its information content, measured by the *entanglement* entropy between the two spin sectors, scales like the number of electrons in a shell $2\Delta$ about $\mu$, *i.e.* like the Fermi surface area. This "area" law for the entanglement entropy is closely related to Andreev reflection happening at the normal metal-superconductor

[127]: Puspus et al. (2014), 'Entanglement spectrum and number fluctuations in the spin-partitioned BCS ground state'

interface, which provides an interesting new perspective of looking at it: pairs that contribute the largest to the entropy are precisely those pairs that enter and leave the condensate during Andreev reflections. The information contained in the BCS state therefore corresponds to a physical process, Andreev reflections, which can be thought about as the microscopic origin of a superconductor's entropy. They provide a mechanism to understand how proximity effect operates at the microscopic level and how metal electrons near a superconductor are converted to Cooper pairs, thereby extending the superconducting correlations into the metal.

# Effect of symmetries in spin 1/2 systems

# B

## B.1 Kramers degeneracy

Time-reversal symmetry (TRS) is the symmetry of physical laws under the transformation $T : t \mapsto -t$. In quantum mechanics, the time-reversal operation is represented by an *anti-unitary* operator $T = \mathscr{U}K$ where $K$ denotes complex conjugation and $U$ is an unitary transformation $\mathscr{U}^\dagger = \mathscr{U}^{-1}$. As a consequence of this anti-unitarity, one may have either $T^2 = 1$ or $-1$. [1] The sign value depends on the total spin of the system being an integer (+) or half-integer (−).

If TRS is a symmetry of the system, $[H, T] = 0$, then for every eigenstate $|\psi\rangle$ the time-reversed state $T|\psi\rangle$ is also an eigenstate with the same energy. Though it may be identical to the original state, this cannot be for a half-integer spin system, since TRS reverses all angular momenta and reversing a half-integer spin cannot yield the same state. One can show[2] that if $T^2 = -1$, then the states $|\psi\rangle$ and $|T\psi\rangle$ are actually orthogonal: a general result called **Kramers theorem**. This implies that every energy level of a time-reversal symmetric system is at least doubly degenerate if it has half-integer spin. This applies in particular to Andreev states, which are fermionic spin 1/2 states by nature.

1: Proof
$T^2 = \mathscr{U}K\mathscr{U}K = UU^* = \mathscr{U}(\mathscr{U}^T)^{-1} = \Phi$, where $\Phi$ is a diagonal matrix of phases. Then $\mathscr{U} = \Phi\mathscr{U}^T$ and $\mathscr{U}^T = \mathscr{U}\Phi$, so that $\mathscr{U} = \Phi\mathscr{U}\Phi$, meaning that the coefficients in $\Phi$ are $\pm 1$, which implies $T^2 = \pm 1$.

2: We assume $[T, H] = 0$ and $T^2 = -1$.
Consider $H|\psi\rangle = E|\psi\rangle$, then $TH|\psi\rangle = HT|\psi\rangle = H|T|\psi\rangle = ET|\psi\rangle$ *i.e.* $|T|\psi\rangle$ is also an eigenstate with energy E.
Now suppose that $T$ is a linear operator : $|T\psi\rangle = c|\psi\rangle$ with $c \in \mathbb{C}$. Then $T^2|\psi\rangle = -|\psi\rangle = Tc|\psi\rangle = c^*T|\psi\rangle = |c|^2|\psi\rangle$ implying $|c|^2 = -1$, which cannot be.
Therefore $|T\psi\rangle \perp |\psi\rangle$ and $\deg(E) \geq 2$.

## B.2 Consequence for the band structures of solids

Electrons in solids are well described by means of *Bloch functions*, which take the form of plane waves modulated by a periodic function : $\psi_{n\boldsymbol{k}\sigma}(\boldsymbol{r}) = e^{i\boldsymbol{k}\cdot\boldsymbol{r}}u_{n\boldsymbol{k}\sigma}(\boldsymbol{r})$, with $n$ the band number, $\boldsymbol{k}$ the electron wavevector and $\sigma \in \{+1, -1\}$ labels the spin index associated to spin ↑ and spin ↓ electrons. If a Bloch state $\psi_{n\boldsymbol{k}\uparrow}$ has energy $\epsilon_{n\boldsymbol{k}\uparrow}$, then its time-reversed state $T\psi_{n\boldsymbol{k}\uparrow} = -\psi_{n-\boldsymbol{k}\downarrow}$ has energy $\epsilon_{n-\boldsymbol{k}\downarrow}$, which implies $\epsilon_{n\boldsymbol{k}\sigma} = \epsilon_{n-\boldsymbol{k}-\sigma}$ because of TRS (Kramers degeneracy apply, because electron is a spin 1/2).

In addition, for a solid with space inversion symmetry, one can show that $\epsilon_{n\boldsymbol{k}\sigma} = \epsilon_{n-\boldsymbol{k}\sigma}$. Then for a solid with *both* symmetries, we expect a global two-fold degeneracy at each $\boldsymbol{k}$-point, $\epsilon_{n\boldsymbol{k}\sigma} = \epsilon_{n-\boldsymbol{k}-\sigma} = \epsilon_{n\boldsymbol{k}-\sigma}$. However, if there is TRS but no space inversion symmetry, then the two-fold degeneracy at a $\boldsymbol{k}$-point is no longer guaranteed, except at special $\boldsymbol{k}$-points that differ from $-\boldsymbol{k}$ by only a reciprocal lattice vector $\boldsymbol{G}$, *i.e.* $\boldsymbol{k} = -\boldsymbol{k} + \boldsymbol{G}$, which are commonly known as *Time-reversal invariant momenta* (TRIM). In addition, a band crossing at a TRIM is protected, *i.e.* it is robust to any perturbation that preserves TRS [128]. This general result has profound consequences on the spectrum of half-integer spin systems : bands come in pairs and the degeneracy is split in $\vec{k}$-space between $\vec{k}$ and $-\vec{k}$, except at the TRIMS, as illustrated in Figure B.1(a).

[128]: Bernevig and Hugues (2013), *Topological Insulators and Topological Superconductors*, p. 37

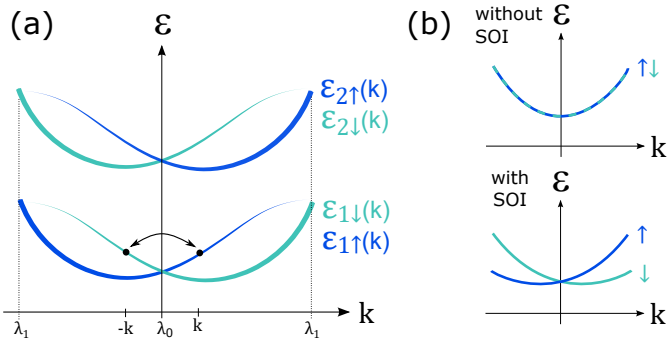


**Figure B.1:** (a) Kramers degeneracy: due to TRS, bands come in pairs and the degeneracy is split in $\vec{k}$-space between $\vec{k}$ and $-\vec{k}$, except at special points $\lambda_0$, $\lambda_1$ called *time-reversed invariant momenta* (TRIM), where $\vec{k} \equiv -\vec{k}$ mod$\vec{G} \in$ reciprocal lattice. (b) Effect of SOI on the energy levels of a system with TRS but no space-inversion symmetry.

In the absence of spin-orbit interaction (SOI), $\epsilon_{n-\boldsymbol{k}-\sigma} = \epsilon_{n-\boldsymbol{k}\sigma}$. This means that for a crystal *without* space-inversion symmetry, it is still common to have $\epsilon_{n\boldsymbol{k}} = \epsilon_{n-\boldsymbol{k}}$, because TRS further ensures that $\epsilon_{n\boldsymbol{k}\sigma} = \epsilon_{n-\boldsymbol{k}-\sigma}$. This imposes a symmetric energy spectrum with global two-fold spin degeneracy, as shown in Figure B.1(b). Except at TRIMs, SOI is expected to break this degeneracy, but the spectrum still looks symmetric because of the Kramers degeneracy, as illustrated in Figure B.1(b).

**Time-reversal invariant momenta (TRIM)**

$$\begin{cases} \epsilon_\sigma(\vec{k}) = \epsilon_{-\sigma}(-\vec{k}) \\ \vec{k} \equiv -\vec{k} \ \mathrm{mod}\vec{G} \end{cases} \quad \Rightarrow \quad \epsilon_\sigma(\vec{k}) = \epsilon_{-\sigma}(\vec{k}) \quad \text{at a TRIM}$$

Now for the specific case of Andreev states, their energy depends on the superconducting phase $\delta$ across the weak link. Since this phase is $2\pi$-periodic and originates from the application of a magnetic flux, we have the following two symmetries for the system Hamiltonian: $H(\delta + 2\pi) = H(\delta)$ and $TH(\delta)T^{-1} = H(-\delta)$. Consequently, the Andreev spectrum over $\delta$ must be mirror-symmetric around $\delta = 0, \pi$. This is indeed verified in Figure 2.4 and Figure 2.5. Each Andreev level is split in doublets of $\uparrow, \downarrow$ states which must cross in energy at the two time-reversal invariant phases $\delta = 0, \pi$.

# Tight-binding description of weak links

# C

The normal region of the weak link can be described by means of the following tight-binding Hamiltonian, which can be viewed as a discretized version of the continuum model presented in Appendix E. It assumes two chains (labelled $\tau = 1, 2$) of discrete longitudinal sites (indexed by $i$) on which electrons can hop :

$$\begin{aligned} H_0 = &\sum_{i,\tau,\sigma} (\epsilon_{i,\tau} - \mu) c^\dagger_{i,\tau,\sigma} c_{i,\tau,\sigma} + t_x c^\dagger_{i,\tau,\sigma} c_{i+1,\tau,\sigma} \\ &+ \sum_{i,\tau,\sigma} t_y c^\dagger_{i,\tau,\sigma} c_{i,\tau+1,\sigma} + \sigma \alpha_x c^\dagger_{i,\tau,\sigma} c_{i+1,\tau,\bar{\sigma}} \\ &+ i\alpha_y c^\dagger_{i,\tau,\sigma} c_{i,\tau+1,\bar{\sigma}} + \text{h.c.}\ , \end{aligned} \tag{C.1}$$

where $c^\dagger_{i,\tau,\sigma}$ creates an electron with pseudospin $\sigma$ on the longitudinal site $i$ belonging to the transverse chain $\tau$ ; $\epsilon_{i,\tau}$ denotes the onsite potential, $\mu$ the chemical potential, and $t_{x,y}$, $\alpha_{x,y}$ are spin-conserving and spin-flip hopping amplitudes in the longitudinal and transverse direction respectively.

This allows to describe the minimal two transverse bands scenario. Diagonalizing Eq. (C.1) in the $(c_{i,1,\uparrow}, c_{i,1,\downarrow}, c_{i,2,\uparrow}, c_{i,2,\downarrow})$ basis yields the following expression for the energy dispersion of the bands :

$$\begin{aligned} E_{n\sigma} = &\frac{\epsilon_1 + \epsilon_2}{2} - \mu + 2t_x \cos(k \cdot a) \\ &+ (-1)^n \left[ \left( \frac{\epsilon_1 - \epsilon_2}{2} \right)^2 + \alpha_y^2 + t_y^2 + 4\alpha_x^2 \sin(k \cdot a)^2 \right. \\ &\left. + 4s(3 - 2n)\alpha_x \sin(k \cdot a) \sqrt{\left( \frac{\epsilon_1 - \epsilon_2}{2} \right)^2 + t_y^2} \right]^{1/2}, \end{aligned} \tag{C.2}$$

where $n \in \{1, 2\}$ labels the band number and $s \in \{-1, +1\}$ denotes the pseudospin index $\sigma = \downarrow (\uparrow)$.

We start from the situation with no spin-orbit interaction ($\alpha_x = \alpha_y = 0$, left column in Figure C.1). In the first Brillouin zone, $k \in \left[ -\frac{\pi}{a}, +\frac{\pi}{a} \right]$ with $a$ the size of the unit cell, the two bands are well described by two energy shifted cosine arches (see Figure C.1(a), left):

$$E_n \sim -2|t_x| \cos(k \cdot a) \overset{a \to 0}{\approx} -2|t_x| \left( 1 - \frac{(k \cdot a)^2}{2} \right) = \frac{\hbar^2 k^2}{2m^*} + \text{cst}, \tag{C.3}$$

from which we recover the usual energy parabolas in the continuum limit $a \to 0$. As the two cosine bands are energy-shifted copies, they have the same Fermi velocity $v_{n\sigma}$ evolution with $k$ (see Figure C.1(b), left). At a given energy value fixed by the chemical potential $\mu$, there exists a Fermi velocity difference between both $n = 1, 2$ bands (see Figure C.1(c), left), but we are seeking a situation where this difference exists between the two pseudospin subbands within a given band $n$. As longitudinal spin-orbit interaction is added ($\alpha_x \neq 0$, middle column), the two transverse bands split into two $k$-shifted copies associated to both pseudospin $\sigma \in \{\uparrow, \downarrow\}$.

This $k$-shift is given by :

$$k_\alpha = \pm\frac{1}{a}\arccos\left[\frac{1}{\sqrt{1+\left(\frac{\alpha_x}{t_x}\right)^2}}\right] \quad \text{with} \quad \begin{cases} t_x = \dfrac{\hbar^2}{2m^*a^2} \\ \alpha_x = \dfrac{\alpha}{2a}. \end{cases} \tag{C.4}$$

Using that $(1+x^2)^{-1/2} \overset{x\to 0}{\approx} 1 - x^2/2$ and $\arccos(1-x^2/2) \overset{x\to 0}{\approx} x$, we recover the expected continuum limit : $k_\alpha \overset{a\to 0}{\approx} m^*\alpha/\hbar^2$. As shown in Figure C.1(c) (middle), the Fermi velocities still remain identical for both pseudospin $\sigma$ at a given energy ; this is because the associated subbands are copies from each other merely shifted by $k_\alpha$.

Now, when introducing transverse spin-orbit interaction ($\alpha_y \neq 0$), mixing between the two transverse bands occurs. Comparing Figure C.1(d) for $\alpha_y = 0$ (middle) and $\alpha_y \neq 0$ (right), one observes that subband hybridization due to transverse spin-orbit interaction gives rise to a finite Fermi velocity difference between the two spin textures of the lowest band, which peaks close to the hybridization points $k_1$ and $k_2$ (indicated by black arrows). The expression for these momenta is obtained by searching the $k$-values that cancel the term under the square root in Eq. (C.2) :

$$\begin{cases} k_1 = -\dfrac{1}{a}\arcsin\dfrac{\sqrt{4t_y^2+(\epsilon_1-\epsilon_2)^2}}{4\alpha_x} \\ k_2 = -\dfrac{\pi}{a} - k_1. \end{cases} \tag{C.5}$$

Although a Fermi velocity difference does also exist close to the bottom of the second band, it does not show a clear peak as for the lowest $n = 1$ band. Beware that this is an artefact due to the truncation to two lowest bands : if a third transverse band $n = 3$ had been taken into account, such a feature would have also been present for the $n = 2$ band. But if the chemical potential lies close to the bottom of the lowest band, such a minimal 2-band model is enough to grasp the physics.

When reasoning in terms of ABS, the quantity that intervenes in the equations is not the Fermi velocity $v_{n\sigma}$, but the adimensional ratio $\lambda_{n\sigma} = \frac{L}{\xi_{n\sigma}}$ between the weak link length $L$ and the energy-dependent superconducting coherence length $\xi_{n\sigma} = \hbar v_{n\sigma}/\Delta$ with $\Delta$ the superconducting gap. This ratio directly determines the number of ABS in the $[-\Delta, \Delta]$ energy range around $\mu$. More precisely, the number of ABS in the gap is given by $1 + \lfloor 2\lambda/\pi \rfloor$ or $2 + \lfloor 2\lambda/\pi \rfloor$, depending on $\delta$ and $\tau$. Lifting the spin degeneracy of the ABS requires having different $\lambda_{n\sigma}$ for the two pseudospin $\sigma = \uparrow, \downarrow$. Therefore, the quantity $\delta\lambda_n = \lambda_{n\downarrow} - \lambda_{n,\uparrow}$ determines the spin splitting of the Andreev states.

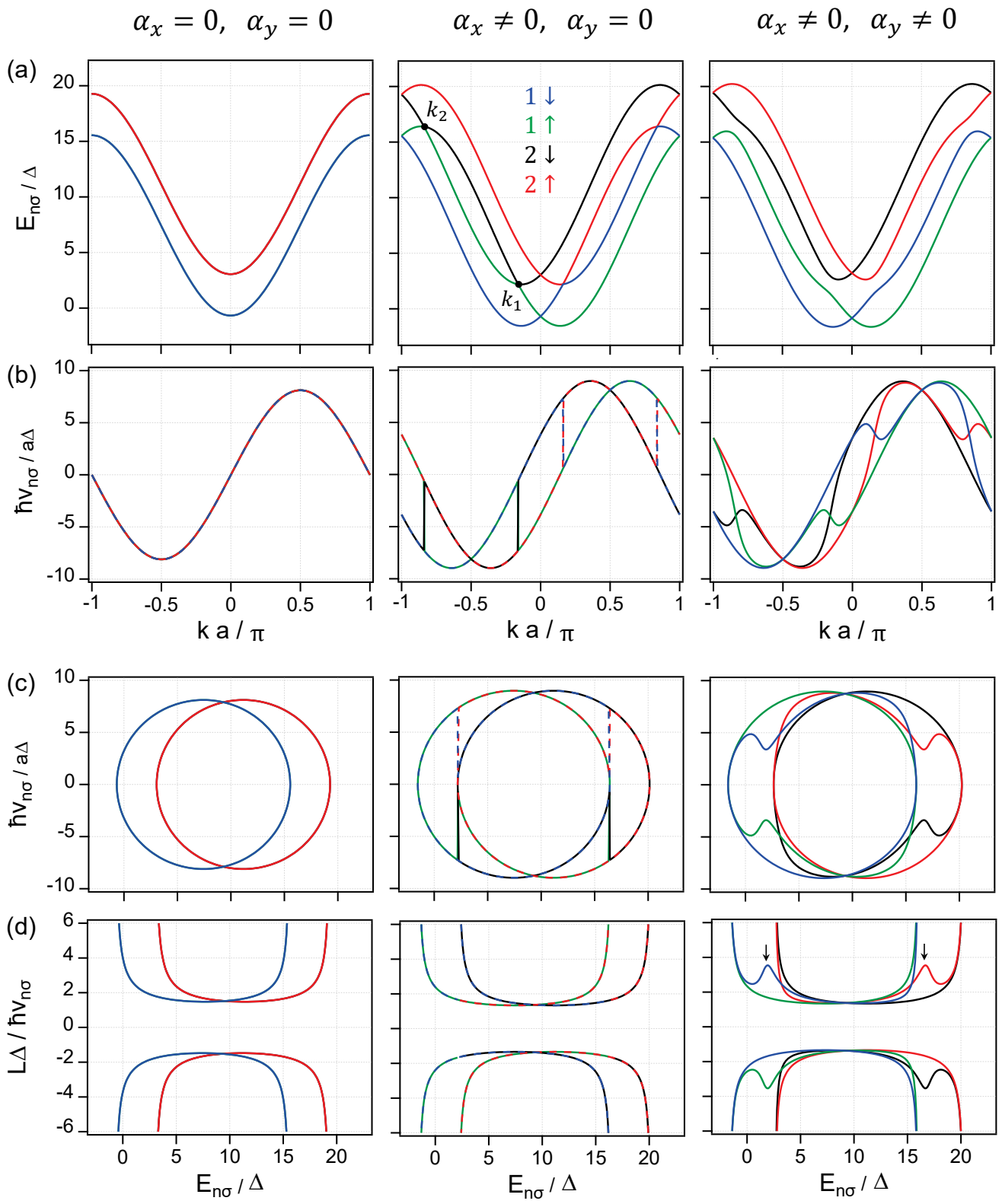


**Figure C.1:** (a) Energy dispersion $E_{n\sigma}/\Delta$ of two transverse bands $n \in \{1, 2\}$ as a function of the electron quasi-momentum k for three different cases (from left to right) : without any spin-orbit interaction ($\alpha_x = \alpha_y = 0$), with 1D-spin-orbit ($\alpha_x \neq 0, \alpha_y = 0$) and with 2D-spin orbit ($\alpha_x \neq 0, \alpha_y \neq 0$). The curves were computed from Eq. (C.2) for the following parameters : $t_0 = \hbar^2/2m^* = 1656.51399$ meV.nm$^2$ ($m^* = 0.023m_e$), $\Delta = 0.2$ meV, $a = L/N = 12$ nm, $L = 500$ nm, $W = 100$ nm, $(\epsilon_1, \epsilon_2) = (1.15, 0.8) \cdot 2t_0/a^2$, $\mu = 0.595$ meV, $\alpha = a \cdot \alpha_x = W \cdot \alpha_y = 16$ meV.nm, $t_x = -0.85 \cdot t_0/a^2$, $t_y = -1.0 \cdot t_0/W^2$. (b) Fermi velocity $v_{n\sigma} = (1/\hbar)\partial_k E_{n\sigma}$ of each subband $n\sigma$ as a function of the electron quasi-momentum $k$ (normalization by the unit cell size $a$). Addition of spin-orbit ($\alpha \neq 0$) has the effect to make the velocities pseudospin-dependent. (c) Same curves as in (b) but plotted as a function of the subband energies $E_{n\sigma}$. To highlight the degeneracies, some of the curves were plotted in dashed lines to show the ones below. (d) Ratio of the weak link length $L$ over the energy-dependent superconducting coherence length $\xi_{n\sigma} = \hbar v_{n\sigma}/\Delta$ associated to each subband $n\sigma$ as a function of their energy $E_{n\sigma}/\Delta$. Transverse spin-orbit ($\alpha_y \neq 0$) gives rise to a finite Fermi velocity difference for the two spin textures associated to a given band $n$. This quantity peaks close to the hybridization points $k_1$ and $k_2$, highlighted by black arrows in the lowest rightmost plot.

# On the origin of spin-orbit interaction in InAs nanowires

# D

For wurtzite WZ nanowires, the $\hat{x}$ and $\hat{y}$ directions are geometrically distinct from $\hat{z}$, yielding different effective masses in the longitudinal and transverse directions. Close to the Γ point, the lowest conduction bands can be approximated with the following quadratic Hamiltonian :

$$H_0 = \frac{\hbar^2}{2}\left[\frac{1}{m^*_\perp}(k_x^2 + k_y^2) + \frac{1}{m^*_\parallel}k_z^2\right]. \tag{D.1}$$

In the following we choose a coordinate system having the $\hat{z}$-axis along the [0001] crystalline direction of the WZ structure. The spin-orbit Hamiltonian of the conduction electrons in bulk WZ semiconductors can be derived from $k \cdot p$ perturbation theory, with the following functional form [129, 63] :

$$H_{SO} = [\alpha\vec{\Omega}^R(\vec{k}) + \gamma\vec{\Omega}^D(\vec{k})]\cdot\vec{\sigma} \quad \text{with} \begin{cases} \vec{\Omega}^R(\vec{k}) = (k_y, -k_x, 0), \\ \vec{\Omega}^D(\vec{k}) = (bk_z^2 - k_x^2 - k_y^2)(k_y, -k_x, 0). \end{cases} \tag{D.2}$$

It shows terms both linear and cubic in momentum, originating from the bulk inversion asymmetry of WZ structures. Quantizing this spin-orbit field $\vec{\Omega}_{[0001]}(\vec{k}) = \alpha\vec{\Omega}^R(\vec{k}) + \gamma\vec{\Omega}^D(\vec{k})$ along the confining $\hat{x}$ and $\hat{y}$ directions does not yield a term linear in $k_z$, since each term contains odd powers of transverse momentum, which integrate to zero. Therefore, intrinsic bulk effects are expected to vanish for [0001] WZ nanowires !

On the other hand, if we consider a WZ nanowire grown along the $[01\bar{1}0]$, the spin orbit field reads

$$\vec{\Omega}_{[01\bar{1}0]}(\vec{k}) = [\alpha + \gamma(bk_x^2 - k_y^2 - k_z^2)](0, -k_z, k_y), \tag{D.3}$$

where the coordinate system was rotated so that the nanowire axis now points along $z$=$[01\bar{1}0]$. By quantizing this spin-orbit field in the transverse directions $\hat{x}$ and $\hat{y}$, we obtain this time :

$$\vec{\Omega}_{[01\bar{1}0]}(\vec{k}) = k_z\,(0, -\alpha - \gamma(\kappa^2 - k_z^2), 0), \tag{D.4}$$

with $\kappa^2 = \langle m|b\hat{k}_x^2 + \hat{k}_y^2|m\rangle$, the expectation value of the transverse kinetic term in the transverse mode $m$. For this other crystalline direction, we observe that a term linear to $k_z$ is this time always present and is expected to give the dominant contribution to spin-orbit splitting.

From this analysis, it would appear at first sight that [0001] WZ nanowires, like the ones used in this thesis, would be surprisingly the worst candidates for spin-orbit applications and that ZB nanowires or WZ ones grown along other directions like $[01\bar{1}0]$ would be much better suited. This analysis, however, holds only in the single-mode limit. We know on the other hand that the InAs nanowires measured experimentally host several transverse conduction modes [39]. For such multimode nanowires, the above *intramode* result remains valid, however we expect to have an

[129]: Fu and Wu (2008), 'Spin-orbit coupling in bulk ZnO and GaN'
[63]: Campos et al. (2018), 'Spin-orbit coupling effects in zinc-blende InSb and wurtzite InAs nanowires'

[39]: Goffman et al. (2017), 'Conduction channels of an InAs-Al nanowire Josephson weak link'

additional *intermode* contribution to intrinsic SOI, which can be non-zero between transverse modes of different parity. The measured spin-orbit coupling for conventional WZ nanowires grown in the [0001] direction would thus result from bulk contributions of intermode intrinsic SOI and extrinsic contributions due to the structural inversion asymmetry of the confinement.

Comparing experimentally the SOI in InAs WZ nanowires grown in the conventional [0001] and in the perpendicular [01$\bar{1}$0] direction has been challenging due to the inherent difficulty of obtaining wire growth along directions different from the preferred [0001]. An experimental study carried out by Jespersen *et al.* [130] showed recently that surprisingly, the spin-orbit strengths extracted from low-temperature magneto-resistance measurements show actually comparable values in both cases ! Thus, the intraband intrinsic contribution does not add substantially to the effective SOI of InAs WZ nanowires, as would have been naïvely expected. This would finally point rather towards extrinsic structural asymmetry as the main source of the measured SOI. Indeed in Ref. [36], Scherübl *et al.* demonstrate that the SOI strength can be strongly increased, up to a factor 2, using the electric field from an external nearby gate, with Rashba SOI strength in the $\alpha \approx 20 - 40$ meV.nm range.

[130]: Jespersen et al. (2018), 'Crystal orientation dependence of the spin-orbit coupling in InAs nanowires'

[36]: Scherübl et al. (2016), 'Electrical tuning of Rashba spin-orbit interaction in multigated InAs nanowires'

Due to the large surface-to-volume ratio of these nanowires, surface effects play an important role in their transport properties. In particular, for low band-gap semiconductors like InAs or InSb, the Fermi level at the surface is known to be pinned inside the conduction band, which results in the formation of a tubular conducting channel around the nanowire surface, known as an *accumulation layer* [131, 132]. Electrons in this conduction channel would therefore be strongly sensitive to the electric field from the interface with vacuum and the one generated externally by electrostatic gates. This goes in favour of the structural inversion asymmetry as the main source of the observed linear Rashba SOI in InAs WZ nanowires. Quantitative estimations of this effect for geometries relevant to recent experiments on InAs nanowires were performed in Ref. [133] and showed good comparison with the Rashba strength dependence on gate voltage extracted from magneto-resistance measurements.

[131]: Degtyarev et al. (2017), 'Features of electron gas in InAs nanowires imposed by interplay between nanowire geometry, doping and surface states'

[132]: Bringer and Schäpers (2011), 'Spin precession and modulation in ballistic cylindrical nanowires due to the Rashba effect'

[133]: Escribano et al. (2020), 'Improved effective equation for the Rashba spin-orbit coupling in semiconductor nanowires'

# Scattering model for ABS in Rashba nanowires

# E

The aim of this Appendix is to present the scattering model used to derive the ABS energies in a multichannel Rashba nanowire, in particular the single-barrier model which we used to fit the experimental data from Chapter 6. This theory was developped by our theoretician colleague Sunghun Park. The derivation was given in Ref. [32] assuming an ideal junction with no backscattering. Some results for the case with finite transparency were printed in the supplementary of Ref. [51], but the full derivation was never completely detailed. Hence I felt the need to reproduce it here, to make justice to this theoretical model which was used throughout this thesis to describe our experimental results.

[32]: Park and Levy Yeyati (2017), 'Andreev spin qubits in multichannel Rashba nanowires'

[51]: Tosi et al. (2019), 'Spin-Orbit Splitting of Andreev States Revealed by Microwave Spectroscopy'

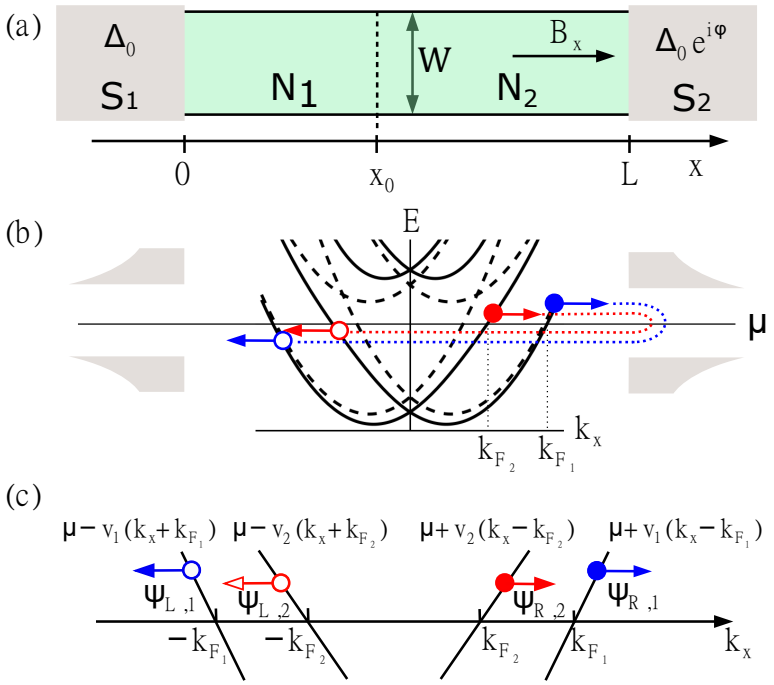


**Figure E.1:** (a) Sketch of a quasi 1D Rashba nanowire proximity coupled on both sides to $s$-wave superconductors, thus forming a Josephson weak link with length $L$ and width $W$. We assume the presence in the nanowire of a point-like barrier at $x = x_0$ resulting in some finite backscattering. A possible external magnetic field $B_x$ is applied along the nanowire axis $\hat{x}$. (b) Energy dispersion of the lowest two transverse bands in the nanowire at zero magnetic field. The case of no SOI mixing $\eta = 0$ is drawn in dashed line and the $\eta \neq 0$ appears in solid lines. Two right-moving electrons (blue and red disks) with different Fermi velocities due to the finite $\eta$ are reflected as holes (blue and red circles) through Andreev reflections at $x = L$. (c) Linearization of the bands around the chemical potential $\mu$.

## E.1 System description & model Hamiltonian

We consider a multichannel nanowire Josephson weak link with Rashba spin-orbit coupling as discussed in [32]. Electrons in a quasi-one dimensional nanowire are free to move in the $\hat{x}$ direction and are confined in

the $\hat{y}$ and $\hat{z}$ directions by a harmonic potential. This is actually a good approximation for nanowires grown in a wurtzite phase along the [0001] crystal direction, like the InAs nanowires used in this thesis. Indeed, in such nanowires, the $\hat{y}$ and $\hat{z}$ directions are known to be geometrically distinct from the $\hat{x}$, yielding different effective masses $m^*_\perp$ and $m^*_\parallel$ for the conduction band electrons in the transverse and longitudinal directions.

We consider the situation described in Figure E.1. Two superconducting electrodes separated by a distance $L$ in the $\hat{x}$ direction are proximity coupled to the nanowire forming a Josephson junction. The Bogoliubov-de Gennes (BdG) Hamiltonian for this cylindrical Josephson junction is

$$H^{3D}_{BdG} = \frac{1}{2}\int d^3r\ \Phi^\dagger(r)[(\mathscr{H}_0 - \mu)\tau_z + \mathscr{H}_R\tau_z + \mathscr{H}_Z + \mathscr{H}_S]\Phi(r), \quad \text{(E.1)}$$

where the field operator $\Phi(r)$ is the four-component Nambu spinor $\Phi = (\Phi_\uparrow, \Phi_\downarrow, \Phi^\dagger_\downarrow, -\Phi^\dagger_\uparrow)^T$ and $\mu$ is the chemical potential. $\mathscr{H}_0$ describes the quasi-one dimensional nanowire, which is well approximated close to the $\Gamma$ point by the following quadratic Hamiltonian* :

$$\mathscr{H}_0 = \frac{p_x^2}{2m^*_\parallel} + \frac{p_y^2 + p_z^2}{2m^*_\perp} + U_b(x) + U_c(y,z), \quad \text{(E.2)}$$

where $U_b(x) = U_0\delta(x - x_0)$ represents a potential barrier at $x = x_0$ with $0 < x_0 < L$ used to model back-scattering in the normal region, and $U_c(y,z) = m^*_\perp\omega_0^2(y^2 + z^2)/2$ is the harmonic confinement potential with $\omega_0$, the associated angular frequency. We define an effective diameter for the nanowire by $W = 2\sqrt{\hbar/(m^*_\perp\omega_0)}$. The Rashba spin-orbit interaction $\mathscr{H}_R$ and the Zeeman interaction $\mathscr{H}_Z$ are given by :

$$\mathscr{H}_R = -\alpha p_x\sigma_y + \alpha p_y\sigma_x, \quad \text{(E.3)}$$

$$\mathscr{H}_Z = \frac{g\mu_B}{2}B_x\sigma_x, \quad \text{(E.4)}$$

where $\alpha$ is the strength of the spin-orbit coupling and $B_x$ is an external magnetic field applied along the $\hat{x}$ direction, $g \approx 2$ is the Landé factor of the electron and $\mu_B$ the Bohr magneton. The validity of such linear spin-orbit field for InAs nanowires is discussed in Appendix D. The Pauli matrices $\sigma_{x,y,z}$ and $\tau_{x,y,z}$ act in the spin and Nambu spaces respectively. $\mathscr{H}_S$ is the induced $s$-wave pairing potential due to the proximity effect with the two superconducting electrodes,

$$\mathscr{H}_S = \Delta(x)(\cos\delta(x)\tau_x - \sin\delta(x)\tau_y), \quad \text{(E.5)}$$

where the induced gap $\Delta(x)$ and the superconducting phase $\delta(x)$ are given by $\Delta(x)e^{i\delta(x)} = \Delta_0$ at $x < 0$, $\Delta_0 e^{i\delta} = \Delta_0$ at $x > L$, and zero elsewhere. Here, $\delta$ is the superconducting phase difference. We assume that the Zeeman field is weak so that we can treat $\mathscr{H}_Z$ as a perturbation.

[134]: Faria Junior et al. (2016), 'Realistic multiband k.p approach from ab initio and spin-orbit coupling effects of InAs and InP in wurtzite phase'
[135]: Luo et al. (2016), 'k.p theory of free-standing narrow band gap semiconductor nanowires'

* The bandstructure of InAs nanowires with hexagonal cross-section was computed in Refs. [134, 135] using a realistic multiband $k \cdot p$ approach from *ab initio*, showing that the conduction bands overall possess good parabolic dispersions.

### E.1.1 Mapping of the BdG Hamiltonian to a 1D model Hamiltonian

We project the total Hamiltonian in Eq. (E.1) onto the subspace spanned by the lowest two relevant transverse subbands to obtain a one-dimensional Hamiltonian. By solving $(p_y^2 + p_z^2)/(2m_\perp^*) + U_c(y,z)$ in Eq. (E.2), we find the subband eigenvalues and eigenstates,

$$E_n^\perp = \hbar\omega_0(n+1) = \frac{4\hbar^2}{m_\perp^* W^2}(n+1), \tag{E.6}$$

$$\phi_{0s}^\perp(y,z) = \frac{2}{\sqrt{\pi}W} e^{-2(y^2+z^2)/W^2}\chi_s, \tag{E.7}$$

$$\phi_{1s}^\perp(y,z) = \frac{4\sqrt{2}y}{\sqrt{\pi}W} e^{-2(y^2+z^2)/W^2}\chi_s, \tag{E.8}$$

where $n = 0, 1$, and $\phi_{0s}^\perp(y,z)$ is the eigenstate with $E_0^\perp$ and $\phi_{1s}^\perp(y,z)$ the one with $E_1^\perp$. $\chi_{s=\uparrow,\downarrow} = (1/\sqrt{2})[1, i(-i)]^T$ are the eigenstates of $\sigma_y$. The one-dimensional Hamiltonian projected to this basis is given by

$$H_{\mathrm{BdG}}^{\mathrm{1D}} = \frac{1}{2}\int dx\ \Phi'^\dagger(x)[(\mathscr{H}_0' - \mu)\tau_z + \mathscr{H}_R'\tau_z + \mathscr{H}_Z' + \mathscr{H}_S]\Phi'(x), \tag{E.9}$$

where $\Phi'(x)$ is the eight-component operator $\Phi' = (\Phi_{0\uparrow}, \Phi_{0\downarrow}, \Phi_{1\uparrow}, \Phi_{1\downarrow}, \Phi_{0\downarrow}^\dagger, -\Phi_{0\uparrow}^\dagger, \Phi_{1\downarrow}^\dagger, -\Phi_{1\uparrow}^\dagger)^T$ with the subscript $ns$ referring to the transverse quantum number $n = 0, 1$ and the spin $s = \uparrow, \downarrow$, and

$$\mathscr{H}_0' = \frac{p_x^2}{2m_\parallel^*} + E_+^\perp + E_-^\perp\Sigma_z + U_b(x), \tag{E.10}$$

$$\mathscr{H}_R' = -\alpha p_x\tilde{\sigma}_z + \eta\tilde{\sigma}_y\Sigma_y, \tag{E.11}$$

$$\mathscr{H}_Z' = \frac{g\mu_B}{2}B_x\tilde{\sigma}_y, \tag{E.12}$$

where $E_\pm^\perp = (E_0^\perp \pm E_1^\perp)/2$. $\tilde{\sigma}_{x,y,z}$ are the Pauli spin matrices written in the basis $\{\chi_\uparrow, \chi_\downarrow\}$, and $\Sigma_{x,y,z}$ are the Pauli matrices acting on the space associated to the transverse degree of freedom. The coefficient $\mu$ in Eq.(E.11) describes the coupling between the different transverse subbands with opposite spins through the spin-orbit coupling, and is given by

$$\begin{aligned}\eta &= \int dydz\ \phi_{0\downarrow}^{\perp\dagger}(y,z)\mathscr{H}_R\phi_{1\uparrow}^\perp(y,z)\\ &= -\int dydz\ \phi_{0\uparrow}^{\perp\dagger}(y,z)\mathscr{H}_R\phi_{1\downarrow}^\perp(y,z)\\ &= \frac{\sqrt{2}\alpha\hbar}{W}.\end{aligned} \tag{E.13}$$

We solve first $\mathscr{H}_0' + \mathscr{H}_R'$ in the absence of a potential barrier $U_b(x)$. We focus on the single-channel energy regime. The dispersion relation is then given by

$$E(k_x) = \frac{\hbar^2 k_x^2}{2m_\parallel^*} + E_+^\perp - \sqrt{(E_-^\perp \mp \alpha\hbar k_x)^2 + \eta^2}, \tag{E.14}$$

where the − sign is for $\Phi_{0\uparrow}$ and $\Phi_{1\downarrow}$ and the + sign for $\Phi_{0\downarrow}$ and $\Phi_{1\uparrow}$. The Fermi velocities $v_{j=1,2}$ of the co-propagating electrons with momenta $k_x = k_{F1}$ and $k_{F2}$ respectively, in the different spin subbands at $E(k_x) = \mu$ are

$$\begin{aligned} v_1 &= \frac{\hbar k_{F1}}{m^*_{\parallel}} + \alpha \cos\theta_1, \\ v_2 &= \frac{\hbar k_{F2}}{m^*_{\parallel}} - \alpha \cos\theta_2, \end{aligned} \tag{E.15}$$

where the $\theta_1, \theta_2 \in [\pi/2, \pi]$ angles are given by

$$\begin{aligned} \theta_1 &= \frac{E^{\perp}_{-} - \alpha\hbar k_{F1}}{\sqrt{(E^{\perp}_{-} - \alpha\hbar k_{F1})^2 + \eta^2}}, \\ \theta_2 &= \frac{E^{\perp}_{-} + \alpha\hbar k_{F2}}{\sqrt{(E^{\perp}_{-} + \alpha\hbar k_{F2})^2 + \eta^2}}. \end{aligned} \tag{E.16}$$

The eigenstates $\psi_{R,j=1,2}$ ($\psi_{L,j=1,2}$) involving right (left) moving electrons with the velocity $v_j$ can be expresses as

$$\begin{aligned} \psi_{R,1} &= -\mathscr{T}\psi_{L,1} = e^{ik_{F1}x}\left(\sin\frac{\theta_1}{2}, 0, 0, -\cos\frac{\theta_1}{2}\right)^T, \\ \psi_{R,2} &= \mathscr{T}\psi_{L,2} = e^{ik_{F2}x}\left(0, \sin\frac{\theta_2}{2}, \cos\frac{\theta_2}{2}, 0\right)^T, \end{aligned} \tag{E.17}$$

where $\mathscr{T} = -i\tilde{\sigma}_y\Sigma_0 K$ is the time-reversal operator with the complex conjugation operator $K$.

### E.1.2 Linearization of the one-dimensional model Hamiltonian

We now linearize the dispersion relation around the chemical potential $\mu$ and assume that the four-component spinor parts of the eigenstates in Eq. (E.17) remain the same within the subgap energy range $\mu - \Delta_0 < E < \mu + \Delta_0$. We write the electron field operator in terms of the left and right propagating fields,

$$\begin{pmatrix} \Phi_{0\uparrow}(x) \\ \Phi_{0\downarrow}(x) \\ \Phi_{1\uparrow}(x) \\ \Phi_{1\uparrow}(x) \end{pmatrix} = R_1(x)\begin{pmatrix} \sin\theta_1/2 \\ 0 \\ 0 \\ -\cos\theta_1/2 \end{pmatrix} + L_2(x)\begin{pmatrix} \sin\theta_2/2 \\ 0 \\ 0 \\ -\cos\theta_2/2 \end{pmatrix} + R_2(x)\begin{pmatrix} 0 \\ \sin\theta_2/2 \\ \cos\theta_2/2 \\ 0 \end{pmatrix} + L_1(x)\begin{pmatrix} 0 \\ \sin\theta_1/2 \\ \cos\theta_1/2 \\ 0 \end{pmatrix}. \tag{E.18}$$

Then, the linearized model which is valid around the Fermi level can be expresses as

$$H^L_{\mathrm{BdG}} = \frac{1}{2}\int dx \tilde{\Phi}^{\dagger}(x)\begin{pmatrix} \tilde{\mathscr{H}}_{\mathrm{kin}} + \tilde{\mathscr{H}}_b + \tilde{\mathscr{H}}_Z & \Delta(x)e^{i\delta(x)} \\ \Delta(x)e^{-i\delta(x)} & -\tilde{\mathscr{H}}_{\mathrm{kin}} - \tilde{\mathscr{H}}_b + \tilde{\mathscr{H}}_Z \end{pmatrix}\tilde{\Phi}(x) \tag{E.19}$$

where $\tilde{\Phi}(x)$ is the eight-component field operator in the left and right propagating field basis $\tilde{\Phi}(x) = (R_1(x), L_2(x), R_2(x), L_1(x), R_1^{\dagger}(x), L_2^{\dagger}(x), R_2^{\dagger}(x), L_1^{\dagger}(x))$.

The kinetic term $\tilde{\mathscr{H}}_{\text{kin}}$ and the potential barrier $\tilde{\mathscr{H}}_b$ in this model are

$$\tilde{\mathscr{H}}_{\text{kin}} = \begin{pmatrix} -i\hbar v_1\partial_x - \hbar v_1 k_{F1} & 0 & 0 & 0 \\ 0 & i\hbar v_2\partial_x - \hbar v_2 k_{F2} & 0 & 0 \\ 0 & 0 & -i\hbar v_2\partial_x - \hbar v_2 k_{F2} & 0 \\ 0 & 0 & 0 & i\hbar v_1\partial_x - \hbar v_1 k_{F1} \end{pmatrix}, \tag{E.20}$$

$$\tilde{\mathscr{H}}_b = U_0\delta(x-x_0)\begin{pmatrix} 1 & \cos[(\theta_1-\theta_2)/2] & 0 & 0 \\ \cos[(\theta_1-\theta_2)/2] & 1 & 0 & 0 \\ 0 & 0 & 1 & \cos[(\theta_1-\theta_2)/2] \\ 0 & 0 & \cos[(\theta_1-\theta_2)/2] & 1 \end{pmatrix}. \tag{E.21}$$

The Zeeman term has the following form

$$\tilde{\mathscr{H}}_Z = i\frac{g\mu_B}{2}B_x\begin{pmatrix} 0 & 0 & -\cos[(\theta_1-\theta_2)/2] & 1 \\ 0 & 0 & 1 & -\cos[(\theta_1-\theta_2)/2] \\ \cos[(\theta_1-\theta_2)/2] & -1 & 0 & 0 \\ -1 & \cos[(\theta_1-\theta_2)/2] & 0 & 0 \end{pmatrix}. \tag{E.22}$$

At zero Zeeman field, the BdG equation is

$$\begin{pmatrix} \tilde{\mathscr{H}}_{\text{kin}} + \tilde{\mathscr{H}}_b & \Delta(x)e^{i\delta(x)} \\ \Delta(x)e^{-i\delta(x)} & -\tilde{\mathscr{H}}_{\text{kin}} - \tilde{\mathscr{H}}_b \end{pmatrix}\Psi(x) = \epsilon\Psi(x), \tag{E.23}$$

where $\Psi(x) = (\psi^e_{R1}(x), \psi^e_{L2}(x), \psi^e_{R2}(x), \psi^e_{L1}(x), \psi^h_{R1}(x), \psi^h_{L2}(x), \psi^h_{R2}(x), \psi^h_{L1}(x))$.

This equation can be split into the two following ones

$$\left[\begin{pmatrix} -i\hbar v_1\partial_x - \hbar v_1 k_{F1} & 0 & 0 & 0 \\ 0 & i\hbar v_2\partial_x - \hbar v_2 k_{F2} & 0 & 0 \\ 0 & 0 & i\hbar v_1\partial_x + \hbar v_1 k_{F1} & 0 \\ 0 & 0 & 0 & -i\hbar v_2\partial_x + \hbar v_2 k_{F2} \end{pmatrix}\right.$$
$$+U_0\delta(x-x_0)\begin{pmatrix} 1 & \cos[(\theta_1-\theta_2)/2] & 0 & 0 \\ \cos[(\theta_1-\theta_2)/2] & 1 & 0 & 0 \\ 0 & 0 & -1 & -\cos[(\theta_1-\theta_2)/2] \\ 0 & 0 & -\cos[(\theta_1-\theta_2)/2] & -1 \end{pmatrix}$$
$$\left.+\Delta(x)\begin{pmatrix} 0 & 0 & e^{i\delta(x)} & 0 \\ 0 & 0 & 0 & e^{i\delta(x)} \\ e^{-i\delta(x)} & 0 & 0 & 0 \\ 0 & e^{-i\delta(x)} & 0 & 0 \end{pmatrix}\right]\begin{pmatrix} \psi^e_{R1}(x) \\ \psi^e_{L2}(x) \\ \psi^h_{R1}(x) \\ \psi^h_{L2}(x) \end{pmatrix} = \epsilon\begin{pmatrix} \psi^e_{R1}(x) \\ \psi^e_{L2}(x) \\ \psi^h_{R1}(x) \\ \psi^h_{L2}(x) \end{pmatrix}, \tag{E.24}$$

and

$$\left[\begin{pmatrix} -i\hbar v_2\partial_x - \hbar v_2 k_{F2} & 0 & 0 & 0 \\ 0 & i\hbar v_1\partial_x - \hbar v_1 k_{F1} & 0 & 0 \\ 0 & 0 & i\hbar v_2\partial_x + \hbar v_2 k_{F2} & 0 \\ 0 & 0 & 0 & -i\hbar v_1\partial_x + \hbar v_1 k_{F1} \end{pmatrix}\right.$$
$$+U_0\delta(x-x_0)\begin{pmatrix} 1 & \cos[(\theta_1-\theta_2)/2] & 0 & 0 \\ \cos[(\theta_1-\theta_2)/2] & 1 & 0 & 0 \\ 0 & 0 & -1 & -\cos[(\theta_1-\theta_2)/2] \\ 0 & 0 & -\cos[(\theta_1-\theta_2)/2] & -1 \end{pmatrix}$$
$$\left.+\Delta(x)\begin{pmatrix} 0 & 0 & e^{i\delta(x)} & 0 \\ 0 & 0 & 0 & e^{i\delta(x)} \\ e^{-i\delta(x)} & 0 & 0 & 0 \\ 0 & e^{-i\delta(x)} & 0 & 0 \end{pmatrix}\right]\begin{pmatrix} \psi^e_{R2}(x) \\ \psi^e_{L1}(x) \\ \psi^h_{R2}(x) \\ \psi^h_{L1}(x) \end{pmatrix} = \epsilon\begin{pmatrix} \psi^e_{R2}(x) \\ \psi^e_{L1}(x) \\ \psi^h_{R2}(x) \\ \psi^h_{L1}(x) \end{pmatrix}. \tag{E.25}$$

## E.2 Subgap ABS for zero magnetic field

The Andreev levels for $|\epsilon| < \Delta_0$ are determined by matching the wave functions of Eqs. (E.24) and (E.25) at $x = 0$ and $x = L$, and from the boundary condition across the delta function potential at $x = x_0$ used in [136, 137]. We assume perfect Andreev reflections at the two interfaces $x = 0, L$. It is enough to consider Eq. (E.24) because a solution of Eq (E.25) is obtained by exchanging the $1, 2$ indices in $v_1, k_{F1}, v_2, k_{F2}$. Let us write the wavefunction associated to each of the four pieces of the system. In the left superconducting region $x < 0$, we have

[136]: Peng et al. (2016), 'Signatures of topological Josephson junctions'
[137]: Heck et al. (2017), 'Zeeman and spin-orbit effects in the Andreev spectra of nanowire junctions'

$$\Psi_{S1}(x) = a_1 e^{ik_{F1}x+q_1x}\begin{pmatrix}\beta\\0\\1\\0\end{pmatrix} + b_1 e^{-ik_{F2}x+q_2x}\begin{pmatrix}0\\1\\0\\\beta\end{pmatrix}, \tag{E.26}$$

where $q_{j=1,2} = (\Delta_0/(\hbar v_j))\sqrt{1-(\epsilon/\Delta_0)^2}$ and $\beta = \epsilon/\Delta_0 - i\sqrt{1-(\epsilon/\Delta_0)^2}$. $a_1$ and $b_1$ are the coefficients. In the normal region at $0 < x < x_0$, we write

$$\Psi_{N1}(x) = a_2 e^{ik_{e1}x}\begin{pmatrix}1\\0\\0\\0\end{pmatrix} + b_2 e^{ik_{h1}x}\begin{pmatrix}0\\0\\1\\0\end{pmatrix} + c_2 e^{-ik_{e2}x}\begin{pmatrix}0\\1\\0\\0\end{pmatrix} + d_2 e^{-ik_{h2}x}\begin{pmatrix}0\\0\\0\\1\end{pmatrix}. \tag{E.27}$$

where we have defined

$$\begin{cases} k_{ej} = k_{Fj} + \tilde{k}_j \\ k_{hj} = k_{Fj} - \tilde{k}_j \end{cases} \quad \text{with } \tilde{k}_j = \frac{\epsilon}{\hbar v_j}. \tag{E.28}$$

Similarly, we can write the wave function at $x_0 < x < L$ as

$$\Psi_{N2}(x) = a_3 e^{ik_{e1}x}\begin{pmatrix}1\\0\\0\\0\end{pmatrix} + b_3 e^{ik_{h1}x}\begin{pmatrix}0\\0\\1\\0\end{pmatrix} + c_3 e^{-ik_{e2}x}\begin{pmatrix}0\\1\\0\\0\end{pmatrix} + d_3 e^{-ik_{h2}x}\begin{pmatrix}0\\0\\0\\1\end{pmatrix}. \tag{E.29}$$

Finally, in the right superconducting region $x > L$, the wave function is given by :

$$\Psi_{S2}(x) = a_4 e^{ik_{F1}x - q_1 x} \begin{pmatrix} 1 \\ 0 \\ \beta e^{-i\delta} \\ 0 \end{pmatrix} + b_4 e^{-ik_{F2}x - q_2 x} \begin{pmatrix} 0 \\ \beta \\ 0 \\ e^{-i\delta} \end{pmatrix}, \tag{E.30}$$

### E.2.1 Scattering by the potential barrier

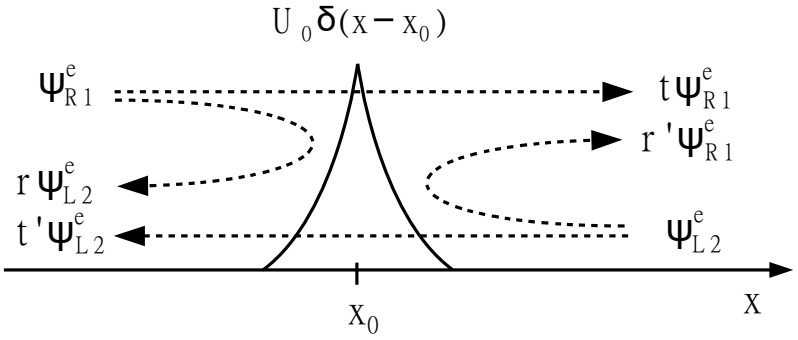


**Figure E.2:** A delta-like barrier is located at position $x = x_0$ to model possible backscattering happening in the nanowire. Electron waves $\psi^e_{R1}(x)$ (right-moving with velocity $v_1$) and $\psi^e_{L2}(x)$ (left-moving with velocity $v_2$) are scattered by the potential barrier with an amplitude probability given respectively by $r$ and $r'$.

The matching condition for the wave functions $\Psi_{N1}(x)$ and $\Psi_{N2}(x)$ at $x = x_0$ can be derived by rearranging Eq. (E.24) with $\Delta(x) = 0$ as

$$-i\hbar\partial_x \begin{pmatrix} \psi^e_{R1}(x) \\ \psi^e_{L2}(x) \\ \psi^h_{R1}(x) \\ \psi^h_{L2}(x) \end{pmatrix} = \Theta(x) \begin{pmatrix} \psi^e_{R1}(x) \\ \psi^e_{L2}(x) \\ \psi^h_{R1}(x) \\ \psi^h_{L2}(x) \end{pmatrix} \tag{E.31}$$

with

$$\Theta(x) = \begin{pmatrix} v_1 & 0 & 0 & \\ 0 & -v_2 & 0 & 0 \\ 0 & 0 & -v_1 & 0 \\ 0 & 0 & 0 & v_2 \end{pmatrix}^{-1}$$

$$\times \left[ -U_0\delta(x-x_0) \begin{pmatrix} 1 & \cos[(\theta_1-\theta_2)/2] & 0 & 0 \\ \cos[(\theta_1-\theta_2)/2] & 1 & 0 & 0 \\ 0 & 0 & -1 & -\cos[(\theta_1-\theta_2)/2] \\ 0 & 0 & -\cos[(\theta_1-\theta_2)/2] & -1 \end{pmatrix} \right.$$

$$\left. - \begin{pmatrix} -\hbar v_1 k_{F1} & 0 & 0 & 0 \\ 0 & -\hbar v_2 k_{F2} & 0 & 0 \\ 0 & 0 & \hbar v_1 k_{F1} & 0 \\ 0 & 0 & 0 & \hbar v_2 k_{F2} \end{pmatrix} + \epsilon \right] \tag{E.32}$$

We can obtain the solution as

$$\begin{pmatrix} \psi^e_{R1}(x_f) \\ \psi^e_{L2}(x_f) \\ \psi^h_{R1}(x_f) \\ \psi^h_{L2}(x_f) \end{pmatrix} = U(x_f, x_i) \begin{pmatrix} \psi^e_{R1}(x_i) \\ \psi^e_{L2}(x_i) \\ \psi^h_{R1}(x_i) \\ \psi^h_{L2}(x_i) \end{pmatrix}, \tag{E.33}$$

with

$$U(x_f, x_i) = \exp\left\{ \frac{i}{\hbar} \int_{x_i}^{x_f} dx\ \Theta(x) \right\} \tag{E.34}$$

Specifically, we can compute

$$\begin{aligned} U(x_0 + 0^+, x_0 - 0^+) &= \exp\left[ -\frac{i}{\hbar} U_0 \begin{pmatrix} v_1 & 0 & 0 & \\ 0 & -v_2 & 0 & 0 \\ 0 & 0 & -v_1 & 0 \\ 0 & 0 & 0 & v_2 \end{pmatrix}^{-1} \begin{pmatrix} 1 & \cos\frac{\theta_1-\theta_2}{2} & 0 & 0 \\ \cos\frac{\theta_1-\theta_2}{2} & 1 & 0 & 0 \\ 0 & 0 & -1 & -\cos\frac{\theta_1-\theta_2}{2} \\ 0 & 0 & -\cos\frac{\theta_1-\theta_2}{2} & -1 \end{pmatrix} \right] \\ &= e^{iA_0} \begin{pmatrix} \mathbf{A} & 0 \\ 0 & \mathbf{A} \end{pmatrix}, \end{aligned} \tag{E.35}$$

with

$$\mathbf{A} = \begin{pmatrix} \cos d - i u_s \frac{\sin d}{d} & -i u_2 \frac{\sin d}{d} \cos\left(\frac{\theta_1-\theta_2}{2}\right) \\ i u_1 \frac{\sin d}{d} \cos\left(\frac{\theta_1-\theta_2}{2}\right) & \cos d + i u_s \frac{\sin d}{d} \end{pmatrix} \quad \text{with } A_0 = u_a \tag{E.36}$$

where we defined

$$d = \frac{1}{2}\sqrt{u_1^2 + u_2^2 - 2u_1 u_2 \cos(\theta_1 - \theta_2)} \tag{E.37}$$

and introduced the following notations : $u_s = (u_1 + u_2)/2$, $u_a = (u_1 - u_2)/2$ with $u_j = v_j/v_0$ and $v_0 = \hbar v_1 v_2 / U_0$.

From Eqs. (E.27), (E.29) and (E.35), we can write the boundary conditions at $x = x_0$ for the electronic and hole components respectively :

$$\begin{pmatrix} a_3 e^{ik_{e1}x_0} \\ c_3 e^{-ik_{e2}x_0} \end{pmatrix} = e^{iA_0} \mathbf{A} \begin{pmatrix} a_2 e^{ik_{e1}x_0} \\ c_2 e^{-ik_{e2}x_0} \end{pmatrix} \tag{E.38}$$

$$\begin{pmatrix} b_3 e^{ik_{h1}x_0} \\ d_3 e^{-ik_{h2}x_0} \end{pmatrix} = e^{iA_0} \mathbf{A} \begin{pmatrix} b_2 e^{ik_{h1}x_0} \\ d_2 e^{-ik_{h2}x_0} \end{pmatrix} \tag{E.39}$$

The matrix $M = e^{iA_0}\mathbf{A}$, which is actually the *transfer matrix* associated to the delta function barrier, can be written in terms of reflection and transmission coefficients. We introduce

$$M = \frac{1}{t'} \begin{pmatrix} tt' - rr - & \sqrt{\frac{v_j}{v_i}} r' e^{i\varphi} \\ -\sqrt{\frac{v_i}{v_j}} r e^{-i\varphi} & 1 \end{pmatrix} \tag{E.40}$$

so that

$$\Psi(x_0 + 0^+) = \begin{pmatrix} M_{12} & 0 & 0 & 0 \\ 0 & M_{21} & 0 & 0 \\ 0 & 0 & M_{12} & 0 \\ 0 & 0 & 0 & M_{21} \end{pmatrix} \Psi(x_0 - 0^+) \tag{E.41}$$

with $\varphi = (k_{e1} + k_{e2})x_0$. The reflection $r, r'$ and transmission $t, t'$ coefficients are determined by

$$te^{-iu_a} = t'e^{iu_a} = \left(\cos d + iu_s \frac{\sin d}{d}\right)^{-1}, \tag{E.42}$$

$$re^{-i\varphi} = r'e^{i\varphi} = -ie^{i\varphi}\sqrt{u_1 u_2}\frac{\sin d}{d}\cos\frac{\theta_1 - \theta_2}{2}\sqrt{tt'}. \tag{E.43}$$

### E.2.2 Boundary matching at $x = 0, L$

The matching of the wave functions in Eqs. (E.26,E.27) at $x = 0$ yields

$$\begin{pmatrix} a_1\beta \\ b_1 \\ a_1 \\ b_1\beta \end{pmatrix} = \begin{pmatrix} a_2\beta \\ c_2 \\ b_2 \\ d_2\beta \end{pmatrix}. \tag{E.44}$$

Similarly, matching at $x = L$ gives

$$\begin{pmatrix} a_3 e^{ik_{e1}L} \\ c_3 e^{-ik_{e2}L} \\ b_3 e^{ik_{h1}L} \\ d_3 e^{ik_{h2}L} \end{pmatrix} = \begin{pmatrix} a_4 e^{ik_{F1}L - q_1 L} \\ b_4 e^{-ik_{F2}L - q_2 L}\beta \\ a_4 e^{ik_{F1}L - q_1 L - i\delta}\beta \\ b_4 e^{-ik_{F2}L - q_2 L - i\delta} \end{pmatrix}. \tag{E.45}$$

### E.2.3 Andreev energy spectrum

Using Eqs. (E.38,E.40,E.44,E.45), we find the equation

$$\mathrm{Det}\left[1 - \begin{pmatrix} \beta e^{-ik_{h1}a} & 0 \\ 0 & \beta^{-1}e^{ik_{h2}a} \end{pmatrix} M_{21}^{-1} \begin{pmatrix} \beta e^{i(k_{e1}-k_{h1})(L-a)-i\delta} & 0 \\ 0 & \beta^{-1}e^{i(k_{e2}-k_{h2})(L-a)-i\delta} \end{pmatrix} M_{21} \begin{pmatrix} e^{ik_{e1}a} & 0 \\ 0 & e^{-ik_{e2}a} \end{pmatrix}\right] = 0, \tag{E.46}$$

resulting in the following transcendental equation for the ABS energies, corresponding to the wave functions $\psi^e_{R1}(x), \psi^e_{L2}(x), \psi^h_{R1}(x), \psi^h_{L2}(x)$ :

$$\mathrm{Re}\left[Te^{i(\tilde{k}_1 - \tilde{k}_2)L - i\delta} + Re^{i(\tilde{k}_1 + \tilde{k}_2)(L-2x_0)} - \beta^2 e^{i(\tilde{k}_1 + \tilde{k}_2)L}\right] = 0 \tag{E.47}$$

where $\tilde{k}_j = \epsilon/(\hbar v_j)$ and $\beta = \epsilon/\Delta_0 - i\sqrt{1 - (\epsilon/\Delta_0)^2}$. We defined the global transmission and reflection probabilities as $T = |t|^2 = 1 - R = 1 - |r|^2$, which are independent of the energy $\epsilon$. For the wavefunctions $\psi^e_{R2}(x), \psi^e_{L1}(x), \psi^h_{R2}(x), \psi^h_{L1}(x)$, the associated transcendental equation is obtained from Eq. (E.47) by exchanging the $1, 2$ indices in $\tilde{k}_j$.

Introducing the reduced energy $\tilde{\epsilon} = \epsilon/\Delta_0$, the ratios $\lambda_j = L\tilde{k}_j/\tilde{\epsilon} = L/\xi_j$ with $\xi_j = \hbar v_j/\Delta_0$ the superconducting coherence lengths associated to both modes $j = 1, 2$, and the reduced barrier position $x_r = 2x_0/L - 1 \in [-1, 1]$, we can expand Eq. (E.47) to finally get :

$$\boxed{\begin{aligned} T\cos\left[(\lambda_1 - \lambda_2)\tilde{\epsilon} \mp \delta\right] \; + \; (1-T)\cos\left[(\lambda_1 + \lambda_2)\tilde{\epsilon}x_r\right] = \\ \cos\left[2\arccos(\tilde{\epsilon}) - (\lambda_1 + \lambda_2)\tilde{\epsilon}\right] \end{aligned}} \tag{E.48}$$

### E.2.4 Double-barrier model

A more physical way to incorporate back-scattering in the model is to consider that the two potential barriers are located at the left ($x = 0$) and right ($x = L$) interfaces with the superconductors. Using a similar derivation, one would obtain this time the following transcendental equation for the ABS energies :

$$\begin{aligned}
&\sin(\overline{\epsilon}_1 - \arccos\tilde{\epsilon})\sin(\overline{\epsilon}_2 - \arccos\tilde{\epsilon}) \\
&\quad = (2 - T_L - T_R)\sin(\overline{\epsilon}_1)\sin(\overline{\epsilon}_2) \\
&\quad - (1 - T_L)(1 - T_R)\sin(\overline{\epsilon}_1 + \arccos\tilde{\epsilon})\sin(\overline{\epsilon}_2 + \arccos\tilde{\epsilon}) \\
&\quad - 2\sqrt{(1 - T_L)(1 - T_R)}\cos(\varphi_{\text{tot}})(1 - \tilde{\epsilon}^2),
\end{aligned} \tag{E.49}$$

where $\overline{\epsilon}_j = \tilde{\epsilon}\lambda_j + (-1)^j s\delta/2$, $T_{L/R}$ are the transmission probabilities at the left and right interfaces and $\varphi_{\text{tot}} = (k_{F1} + k_{F2})L - (\theta_L + \theta_R)$ is the total accumulated phase with $\theta_{L/R}$ the scattering phases acquires at the $\nu = L/R$ interfaces :

$$\theta_\nu = \arg\Big(\cos d_\nu + i\frac{\sin d_\nu}{d_\nu}\frac{v_s}{v_\nu}\Big), \tag{E.50}$$

where $d_\nu$ and $v_\nu$ are defined as $d$ in Eq. (E.37), replacing $U_0$ by $U_\nu$. Although this model seems more physical than the single-barrier model that we derived in detail, it predicts similar shapes for the spin-split ABSs and offers a similar fitting quality of the experimental data from Chapter 6. The transcendental equation for the ABS energy shows a more cumbersome expression, but the number of fitting parameters is the same as before : two transmissions instead of one transmission and the position barrier.

## E.3 Subgap ABS for a finite magnetic field

We incorporate the Zeeman effect as a first order perturbation. Below, we use the wave functions $\Psi_u(x, \delta)$ and $\Psi_d(x, \delta)$ written in the original basis used in Eq. (E.19) :

$$\Psi_u = (\psi^e_{R1}, \psi^e_{L2}, 0, 0, \psi^h_{R1}, \psi^h_{L2}, 0, 0)^T \tag{E.51}$$

$$\Psi_d = (0, 0, \psi^e_{R2}, \psi^e_{L1}, 0, 0, \psi^h_{R2}, \psi^h_{L1})^T \tag{E.52}$$

We project $\mathscr{H}_Z$ in Eq. (E.22) onto the subspace spanned by $\Psi_u$ and $\Psi_d$, leading to a $2 \times 2$ matrix,

$$H_P = \begin{pmatrix} \epsilon_u(\delta) & \mathbb{B}_x \\ \mathbb{B}_x^* & \epsilon_d(\delta) \end{pmatrix}. \tag{E.53}$$

The diagonal terms are Andreev level energies at zero Zeeman field,

$$\epsilon_{u/d} = \int_{-\infty}^{+\infty} dx\ \Psi^\dagger_{u/d}(x, \delta) \begin{pmatrix} \tilde{\mathscr{H}}_{\text{kin}} + \tilde{\mathscr{H}}_b & \Delta(x)e^{i\delta(x)} \\ \Delta(x)e^{-i\delta(x)} & -\tilde{\mathscr{H}}_{\text{kin}} - \tilde{\mathscr{H}}_b \end{pmatrix} \Psi_{u/d}(x, \delta), \tag{E.54}$$

As for the off-diagonal terms, they are given by

$$\begin{aligned}\mathbb{B}_x &= \int_{-\infty}^{+\infty} dx\ \Psi_u^\dagger(x,\delta)\begin{pmatrix}\tilde{\mathscr{H}_Z} & 0\\ 0 & \tilde{\mathscr{H}_Z}\end{pmatrix}\Psi_d^\dagger(x,\delta)\\ &= i\frac{g\mu_B B_x}{2}\int_{-\infty}^{+\infty} dx\ (\psi_{R1}^{e*}\psi_{L1}^{e}+\psi_{L2}^{e*}\psi_{R2}^{e}+\psi_{R1}^{h*}\psi_{L1}^{h}+\psi_{L2}^{h*}\psi_{R2}^{h}) \quad \text{(E.55)}\\ &\quad -\cos\frac{\theta_1-\theta_2}{2}(\psi_{R1}^{e*}\psi_{R2}^{e}+\psi_{L2}^{e*}\psi_{L1}^{e}+\psi_{R1}^{h*}\psi_{R2}^{h}+\psi_{L2}^{h*}\psi_{L1}^{h}). \quad \text{(E.56)}\end{aligned}$$

ABS energies and states are then obtained by solving the following equation,

$$\begin{pmatrix}\epsilon_u(\delta) & \mathbb{B}_x\\ \mathbb{B}_x^* & \epsilon_d(\delta)\end{pmatrix}\Phi_A = \epsilon_A\Phi_A. \quad \text{(E.57)}$$

from which we deduce

$$\epsilon_{A-} = \epsilon_s - \sqrt{\epsilon_a^2+|\mathbb{B}_x|^2}, \quad \Psi_{A-} = \frac{1}{\sqrt{N_A}}\begin{pmatrix}-\mathbb{B}_x\\ \epsilon_a+\sqrt{\epsilon_a^2+|\mathbb{B}_x|^2}\end{pmatrix} \quad \text{(E.58)}$$

$$\epsilon_{A+} = \epsilon_s + \sqrt{\epsilon_a^2+|\mathbb{B}_x|^2}, \quad \Psi_{A+} = \frac{1}{\sqrt{N_A}}\begin{pmatrix}\epsilon_a+\sqrt{\epsilon_a^2+|\mathbb{B}_x|^2}\\ \mathbb{B}_x^*\end{pmatrix} \quad \text{(E.59)}$$

with the following notations

$$N_A = 2\left(\epsilon_A^2+|\mathbb{B}_x|^2+\epsilon_A\sqrt{\epsilon_a^2+|\mathbb{B}_x|^2}\right) \quad \text{(E.60)}$$

$$\epsilon_s = \frac{\epsilon_u+\epsilon_d}{2}, \quad \epsilon_a = \frac{\epsilon_u-\epsilon_d}{2}. \quad \text{(E.61)}$$

# Dispersive shift : how *quantum* ? F

## F.1 Classical derivation

When a two-level system (TLS) is coupled off-resonantly to an electromagnetic resonator, equivalent to a harmonic oscillator (HO), its transition frequency is shifted in response to the quantum vacuum fluctuations of the electromagnetic field, a phenomenon known as the *Lamb shift* [138]. This dispersive shift, routinely observed in spectroscopy in circuit QED, actually contains a significant contribution from *classical* normal-mode splitting that is not driven by any quantum fluctuations, which raises the following questions: how much of this shift is really quantum in origin ? how much of this shift persists if quantum fluctuations are neglected ?

[138]: Lamb and Retherford (1947), 'Fine Structure of the Hydrogen Atom by a Microwave Method'

In the following section, we derive *classically* the frequency shift acquired by two harmonic oscillators coupled to each other. Remarkably, one recovers the same result for the dispersive shift derived in cQED.

### F.1.1 Coupling schemes

To set these ideas, let us derive the result in the context of electrical circuits and so, do the reasoning in terms of LC resonators. Two couplings schemes are typically considered, either *inductive* or *capacitive* (Figure F.1, Figure F.2). Let us start first with the case of two identical oscillators, which makes the math easier and the results more straightforward to interpret. We will then describe the more general case of two different oscillators *i.e.* of finite detuning.

#### Inductive coupling

Let us define the bare resonance frequency of the uncoupled resonators $\omega_0 = 1/\sqrt{LC}$ and the inductive coupling coefficient $\kappa_i$ as the ratio between the coupling inductance to the oscillator inductance $\kappa_i = \frac{L_m}{L}$. The system can be described by a set of two coupled equations, which can be recast in the following quartic characteristic equation :

$$\begin{cases} j\omega L I_1 - j\dfrac{I_1}{\omega C} + j\omega L_m I_2 = 0 \\ j\omega L I_2 - j\dfrac{I_1}{\omega C} + j\omega L_m I_1 = 0 \end{cases} \Rightarrow \begin{pmatrix} \omega^2 - \omega_0^2 & \omega^2\kappa_i \\ \omega^2\kappa_i & \omega^2 - \omega_0^2 \end{pmatrix} \begin{pmatrix} I_1(\omega) \\ I_2(\omega) \end{pmatrix} = 0$$
$$(\omega^2 - \omega_0^2)^2 - \omega^4\kappa_i^2 = 0.$$

Because it is a polynomial equation of order 4, it has 4 solutions : $\pm\omega_-$ and $\pm\omega_+$ given by $\omega_\pm = \frac{\omega_0}{\sqrt{1\mp\kappa_i}} = \frac{1}{\sqrt{(L\mp L_m)C}}$.

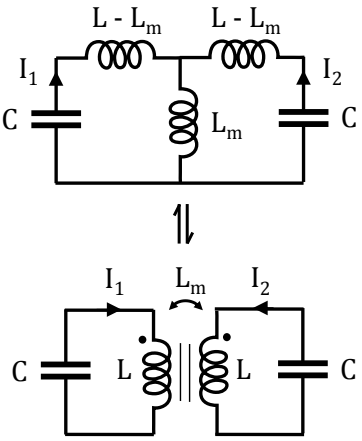


**Figure F.1:** Inductive coupling.

#### Capacitive coupling

Very similarly, one gets for the capacitive case (Figure F.2) the following set of equations :

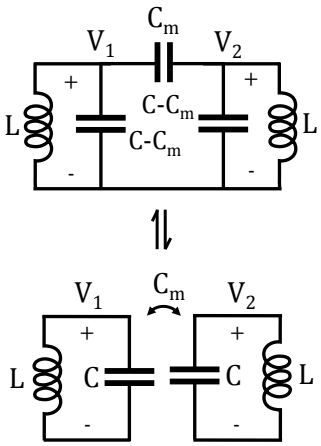


**Figure F.2:** Capacitive coupling.

$$\begin{cases} j\omega CV_1 - j\frac{I_1}{\omega L} - j\omega C_m V_2 = 0 \\ j\omega CV_2 - j\frac{I_1}{\omega L} - j\omega C_m V_1 = 0 \end{cases} \Rightarrow \begin{pmatrix} \omega^2 - \omega_0^2 & \omega^2\kappa_c \\ \omega^2\kappa_c & \omega^2 - \omega_0^2 \end{pmatrix} \begin{pmatrix} I_1(\omega) \\ I_2(\omega) \end{pmatrix} = 0$$
$$(\omega^2 - \omega_0^2)^2 - \omega^4\kappa_c^2 = 0.$$

To get for the characteristic equation the same structure as in the inductive case, one needs to put a minus sign in the definition of the coupling coefficient $\kappa_c = -\frac{C}{C_m}$ with $C_m \geq 0$. Keeping the notation where the $\pm$ sign for the frequencies refers to the ordering of the solutions : $\omega_+ > \omega_-$, one gets $\omega_\pm = \frac{\omega_0}{\sqrt{1\pm\kappa}} = \frac{1}{\sqrt{L(C\mp C_m)}}$.

When the coupling is small enough $\kappa_i, \kappa_c \ll \omega_0$ so that the bare frequencies are only slightly modified, the solutions can be expanded as $\omega_\pm \approx \omega_0(1\pm\kappa/2)$ and $\Delta\omega := \omega_+ - \omega_- = \omega_0\kappa$. This motivates the following general definition for the coupling coefficient : $\kappa := \frac{\omega_+^2 - \omega_-^2}{\omega_+^2 + \omega_-^2} \approx \frac{\Delta\omega}{\omega_0}$.

**Mixed coupling**

In practice the coupling is never fully inductive or capacitive and one generally has to deal with a mixture of both effects (Figure F.3). The coupling coefficient then reflects the competition between inductive and capacitive effects[1] : $\kappa := \frac{\omega_+^2 - \omega_-^2}{\omega_+^2 + \omega_-^2} = \frac{CL_m - LC_m}{LC + L_m C_m} \approx \frac{L}{L_m} - \frac{C}{C_m}$ where we have defined $\omega_\pm = \frac{\omega_0}{\sqrt{1\mp\kappa}}$:

$$\begin{cases} \omega_+ = \dfrac{1}{\sqrt{(L - L_m)(C + C_m)}} \\ \omega_- = \dfrac{1}{\sqrt{(L + L_m)(C - C_m)}}. \end{cases}$$

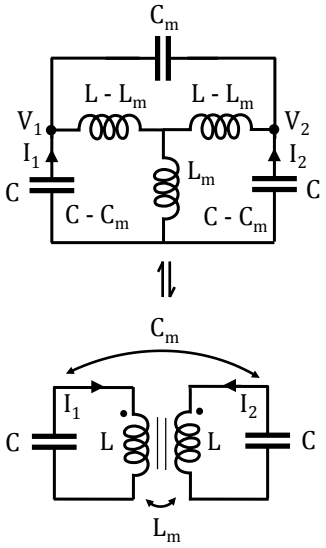


**Figure F.3:** Mixed coupling.

## F.1.2 General case : non-zero detuning

Let us now consider the general case of two distinct oscillators 1 and 2 with bare frequencies $\omega_i = 1/\sqrt{L_i C_i}$ with $i = 1, 2$. The characteristic equation $(\omega^2 - \omega_1^2)(\omega^2 - \omega_2^2) - \omega^4\kappa_1\kappa_2 = 0$ now has the following two positive solutions :

$$\omega_\pm^2 = \frac{1}{2}\frac{1}{1 - \kappa_1\kappa_2}\left(\omega_1^2 + \omega_2^2 \pm \sqrt{(\omega_1^2 + \omega_2^2)^2 + 4\kappa_1\kappa_2\omega_1^2\omega_2^2}\right).$$

Introducing the detuning $\delta$ between the two coupled oscillators and the average frequency $\omega_0$,

$$\begin{cases} \omega_1 = \omega_0 + \delta/2 \\ \omega_2 = \omega_0 - \delta/2 \end{cases} \Rightarrow \begin{cases} \omega_1 - \omega_2 = \delta \ll \omega_0 \\ \omega_1 + \omega_2 = 2\omega_0 \end{cases} \Rightarrow \begin{cases} \omega_1^2 - \omega_2^2 = 2\delta\omega_0 \\ \omega_1\omega_2 = \omega_0^2 - \delta^2/4 \end{cases},$$

which allows to rewrite the two solutions :

1: Interestingly, one sees that by tuning $L_m C = LC_m$ one can cancel the coupling $\kappa = 0$. In structure, it is quite similar to the famous *Heaviside condition* between primary line constants, $LG = RC$, which states the requirement that an electrical transmission line must meet to have no distortion of the transmitted signal. The condition is also an equality between two ratios of *longitudinal* constants over *transverse* constants.

$$\omega_\pm^2 = \frac{\omega_0^2}{1-\kappa_1\kappa_2}\left(1+\frac{\delta^2}{4\omega_0^2} \pm \sqrt{\frac{\delta^2}{\omega^2}+\kappa_1\kappa_2\left(1-\frac{\delta^2}{4\omega_0^2}\right)^2}\right)$$
$$= \frac{\omega_0^2}{1-\kappa_1\kappa_2}\left(1+\frac{\delta^2}{4\omega_0^2} \pm \frac{\delta}{\omega_0}\sqrt{1+\kappa_1\kappa_2\frac{\omega_0^2}{\delta^2}\left(1-\frac{\delta^2}{2\omega_0^2}+\frac{\delta^4}{16\omega_0^4}\right)}\right).$$

**Large detuning $\delta \gg g$ : *dispersive* limit**

Assuming $\kappa_1\kappa_2 \ll (\frac{\delta}{\omega})^2 \ll 1$, one can expand to first order :

$$\omega_\pm^2 \approx \frac{\omega_0^2}{1-\kappa_1\kappa_2}\left(1+\frac{\delta^2}{4\omega_0^2} \pm \frac{\delta}{\omega_0}\left(1-\frac{\kappa_1\kappa_2}{4}+\frac{\kappa_1\kappa_2\omega_0^2}{2\delta^2}\right)\right)$$
$$\omega_\pm \approx \frac{\omega_0}{\sqrt{1-\kappa_1\kappa_2}}\left(1 \pm \frac{\kappa_1\kappa_2\omega_0}{4\delta} \pm \frac{\delta}{2\omega_0}\left(1-\frac{\kappa_1\kappa_2}{4}\right)\right).$$

One obtains the zeroth-order correction to the oscillators frequencies :

$$\omega_\pm = \omega_0\left(1 \pm \frac{\kappa_1\kappa_2\omega_0}{4\delta}\right) + O\left(\frac{\delta}{\omega_0}\right).$$

Introducing the coupling factors $g_i = \frac{\omega_i}{2}\kappa_i$ for $i = 1, 2$, one can rewrite the normal mode splitting of the two oscillators as $\Delta\omega = |\omega_+ - \omega_-| \sim 2\frac{\kappa_1\kappa_2\omega_0^2}{4\delta} \sim 2\frac{g_1 g_2}{\delta}$. [2]

**Normal mode splitting of 2 classical oscillators — *Dispersive* case**

$$\delta\omega_\pm = \pm\frac{g^2}{\delta} \qquad \overbrace{g \ll \underbrace{\delta}_{\text{RWA}} \ll \omega_0}^{\text{disp.}}$$

The first approximation $\kappa_1\kappa_2 \ll (\frac{\delta}{\omega})^2 \ll 1$ amounts to assuming large detuning $\delta \gg \sqrt{g_1 g_2}$, which is generally known as the *dispersive* approximation $\delta \gg g$. Note that one recovers the same expression for the cavity pull as the one obtained from the Jaynes-Cummings hamiltonian in the quantum treatment of two coupled modes.[20]

The second approximation, $\delta \ll \omega_0$, corresponds to the so-called *Rotative Wave Approximation* (RWA), ie. $|\omega_1 - \omega_2| \ll \omega_1 + \omega_2$. With this ordering, $\delta\omega_\pm \ll \delta \ll \omega_0$ and the perturbation approach remains valid : the relative correction to the bare frequencies $\delta\omega_\pm/\omega_0$ stays small.

Going beyond the RWA, one would get the well-known result in the qubit community: $\delta\omega_\pm = \pm g^2\left(\frac{1}{\omega_1-\omega_2}+\frac{1}{\omega_1+\omega_2}\right) = \pm\frac{g^2}{\delta}\left(1+\frac{\delta}{2\omega_0}\right)$ which only assumes the large detuning (=dispersive) approximation $\delta \gg g$ [71, 72]. This limit, in which the qubit and the resonator are far detuned compared to the coupling strength $g$, is generally the one of practical interest, since it allows a nondemolition-type measurement of the qubit by probing the resonator.

2: Since

$$g_1 g_2 = \left(\omega_0+\frac{\delta}{2}\right)\left(\omega_0-\frac{\delta}{2}\right)\frac{\kappa_1\kappa_2}{4}$$
$$= \frac{\kappa_1\kappa_2\omega_0^2}{4}\left(1-\frac{1}{4}\left(\frac{\delta}{\omega_0}\right)^2\right)$$
$$= \frac{\kappa_1\kappa_2\omega_0^2}{4} + O\left(\frac{\delta}{\omega_0}\right).$$

[20]: Blais et al. (2004), 'Cavity quantum electrodynamics for superconducting electrical circuits'

[71]: Zueco et al. (2009), 'Qubit-oscillator dynamics in the dispersive regime'
[72]: Kohler (2018), 'Dispersive readout'

**Small detuning $\delta \ll g$ : *resonant* limit**

Assuming this time the opposite limit $\kappa_1\kappa_2(\frac{\omega}{\delta})^2 \gg 1$:

$$\omega_\pm^2 = \frac{\omega_0^2}{1-\kappa_1\kappa_2}\left(1+\frac{\delta^2}{4\omega_0^2} \pm \frac{\delta}{\omega_0}\sqrt{1+\kappa_1\kappa_2\frac{\omega_0^2}{\delta^2}\left(1-\frac{\delta^2}{2\omega_0^2}+\frac{\delta^4}{16\omega_0^4}\right)}\right)$$
$$\approx \frac{\omega_0^2}{1-\kappa_1\kappa_2}\left(1 \pm \sqrt{\kappa_1\kappa_2}\right),$$

which gives the following mode splitting :

$$|\omega_+ - \omega_-| \approx \omega_0 \frac{\sqrt{1+\kappa}-\sqrt{1-\kappa}}{\sqrt{1-\kappa^2}} = \kappa\omega_0 + O(\kappa^2) = 2g + O(\kappa^2).$$

**Normal mode splitting of 2 classical oscillators — *Resonant* case**

$$\delta\omega_\pm = \pm\tfrac{\omega_0}{2}\kappa = \pm g \qquad \overbrace{\delta \ll g}^{\text{res.}} \underbrace{\ll \omega_0}_{\text{weak coupling}}$$

## F.2 Quantum or not ?

We have just shown that for two coupled harmonic oscillators, the normal-mode splitting predicted by a purely classical description of the modes leads to a dispersive shift analogous to the one in cQED, *i.e.* without taking any quantum fluctuations into account. Actually, a quantum calculation for two HOs would also give the same result: this shift is not influenced by the presence of quantum fluctuations ! By treating the more general case of a weakly anharmonic atom coupled dispersively to a harmonic oscillator, Gely *et al* [139] have shown that two distinct shifts actually occur : one indeed is a purely quantum effect due to vacuum fluctuations, another arises from classical normal-mode splitting. Nevertheless, in the limit of zero anharmonicity, *i.e.* when the TLS is modeled as a purely harmonic oscillator, then the quantum contribution vanishes and the shift is given entirely by classical normal-mode splitting, as described in this appendix.

[139]: Gely et al. (2018), 'Nature of the Lamb shift in weakly anharmonic atoms'

# Admittance/susceptibility formulation of the resonator shift

G

In section 4.1, we showed that the resonator shift is given, up to a prefactor, by the imaginary part of the weak link admittance. This quantity has been computed using linear response theory both for zero-length weak links in the normal and topological regime [140, 136, 141] and also more recently for finite-length weak links in the presence of Coulomb interactions [64] . Let us see that we recover the general result for the resonator shift (Eq. 4.32) using the expressions for the weak link complex admittance given in theses references.

[140]: Kos et al. (2013), 'Frequency-dependent admittance of a short superconducting weak link'
[136]: Peng et al. (2016), 'Signatures of topological Josephson junctions'
[141]: Kurilovich et al. (2021), 'Quantum critical dynamics of a Josephson junction at the topological transition'
[64]: Kurilovich et al. (2021), 'Microwave response of an Andreev bound state'

## G.1 Short superconducting weak link

Kos *et al.* [140] have derived the expression for the admittance of a single-channel point contact of transmission $\tau$ between two superconducting leads in the presence of quasiparticles. The point contact is assumed to host a single Andreev level at energy [142, 143]

$$\boxed{E_A(\delta) = \Delta\sqrt{1 - \tau \sin^2(\delta/2)}.} \tag{G.1}$$

[142]: Beenakker (1991), 'Universal limit of critical-current fluctuations in mesoscopic Josephson junctions'
[143]: Furusaki and Tsukada (1990), 'A unified theory of clean Josephson junctions'

The admittance of the junction is conveniently split in two contributions:

$$Y_{\mathrm{wl}} = \frac{j}{\omega L_J} + \sum_{i=1}^{5} Y_i, \tag{G.2}$$

where the first term describes the $\omega = 0$ admittance of the weak link. It captures the inductive response of the condensate and can be related to the curvature of the Andreev level :

$$L_J^{-1} = -\frac{1}{\varphi_0^2} E_A''(\delta). \tag{G.3}$$

The second term captures the finite frequency admittance originating from quasiparticle transitions. The admittance exhibits a resonant behaviour at frequency $\omega \approx 2E_A$ corresponding to the process where a pair of quasiparticles is created in the Andreev level. The contribution of this process to the weak link admittance is labelled $Y_3(\omega)$ and given by the following expression [140]:

$$\frac{\mathrm{Im}Y_3(\omega)}{G} = \pi \frac{(\Delta^2 - E_A^2)(E_A^2 - \Delta^2\cos^2(\delta/2))}{\hbar\omega E_A^2} \times (p_0 - p_2)\Big(\frac{1}{\hbar\omega - 2E_A} - \frac{1}{\hbar\omega + 2E_A} + \frac{1}{E_A}\Big), \tag{G.4}$$

where $p_0, p_{\uparrow,\downarrow}$ and $p_2$ are the occupation factors *i.e.* the probabilities to have zero, one or two quasiparticles in the Andreev level. To compute the ground state admittance at the resonator frequency $\omega = \omega_0$, let us fix $p_0 = 1, p_2 = 0$.

Introducing the reduced energy $\epsilon_A = E_A/\Delta$, one can rewrite the admittance

$$\omega_0 \mathrm{Im} Y_3(\omega_0) = \frac{\pi G}{\hbar}\Delta^2 \frac{1-\epsilon_A^2}{\epsilon_A^2}(\epsilon_A^2 - \cos^2(\delta/2)) \times \mathscr{R}(\omega, \Delta\epsilon_A), \tag{G.5}$$

where we identified the resonant form factor $\mathscr{R}(\omega, E_A) = \frac{1}{\hbar\omega - 2E_A} - \frac{1}{\hbar\omega + 2E_A} + \frac{1}{E_A}$, and then simplify the middle factor

$$\epsilon_A^2 - \cos^2(\delta/2) = (1-\tau)\sin^2(\delta/2),$$

which appears in the expression for the matrix element of the current operator (given in [52, 40]):

[52]: Park et al. (2020), 'From Adiabatic to Dispersive Readout of Quantum Circuits'
[40]: Bretheau (2013), 'Localized Excitations in Superconducting Atomic Contacts'

$$\begin{aligned}\mathscr{M}^2 = |\langle e|\hat{H}'_{wl}|g\rangle|^2 &= \frac{\Delta^2(1-\tau)}{4}\left(\frac{1}{\epsilon_A} - \epsilon_A\right)^2 \\ &= \frac{\Delta^2}{4}(1-\tau)\underbrace{(1-\epsilon_A^2)}_{\tau\sin^2(\delta/2)}\frac{1-\epsilon_A^2}{\epsilon_A^2}.\end{aligned} \tag{G.6}$$

This allows to express the admittance in terms of the current operator matrix element :

$$\begin{aligned}\omega_0 \mathrm{Im} Y_3(\omega_0) &= \frac{\pi G}{\hbar\tau}\Delta^2\tau(1-\tau)\sin^2(\delta/2)\frac{1-\epsilon_A^2}{\epsilon_A^2}\mathscr{R}(\omega, \Delta\epsilon_A) \\ &= \left(\frac{\mathscr{M}}{\varphi_0}\right)^2 \mathscr{R}(\omega, \Delta\epsilon_A),\end{aligned} \tag{G.7}$$

from which we can deduce the resonator shift, using Eq. (4.19):

$$\begin{aligned}\hbar\delta\omega &= \hbar\frac{\ell^2}{2L}\omega_0^2 \mathrm{Im}\, Y^{\mathrm{wl}}(\omega_0) \\ &= \hbar\frac{\ell^2}{2L}\frac{\omega_0}{\varphi_0^2}\left[-E_A''(\delta) + \mathscr{M}^2\mathscr{R}(\omega, \Delta\epsilon_A)\right].\end{aligned} \tag{G.8}$$

One can identify the prefactor of this expression as $\delta_{\mathrm{zp}}^2 = \frac{\ell^2}{L^2}\frac{\pi\omega_0 L\hbar}{2\pi\varphi_0^2} = \hbar\frac{\ell^2}{2L}\frac{\omega_0}{\varphi_0^2}$, by using $\varphi_0^2 = \frac{\hbar^2}{4e^2} = \frac{R_Q\hbar}{2\pi}$ to rewrite Eq. (4.21) in terms of the participation ratio and the resonator frequency. This finally yields the expression for the resonator shift when the point contact is in its ground state :

$$\boxed{\frac{\hbar\delta\omega}{\delta_{\mathrm{zp}}^2} = -E_A''(\delta) + \mathscr{M}^2\left[\frac{1}{\hbar\omega_0 - 2E_A} - \frac{1}{\hbar\omega_0 + 2E_A} + \frac{1}{E_A}\right].} \tag{G.9}$$

One recovers exactly the result predicted from our general expression given in Eq. (4.32).

## G.2 Finite-length weak link with Coulomb interactions

In a recent paper, Kurilovich *et al.* [64] extended the former theory to a finite-length weak link hosting a single ABS. The main differences compared to a point contact are that

- both the ABS and the continuum states contribute this time to the inductive response of the weak link;
- because of its finite length, the weak link may accommodate electric charge and therefore be sensitive to Coulomb interactions.

The weak link is described as a single-level quantum dot coupled by tunnel junctions to two superconducting leads, which can be viewed as a generalization of the Anderson impurity model. Because of the proximity effect, the dot level turns into an ABS, the energy of which depends both on the phase difference $\delta$ and the gate voltage $V_g$.

The authors show that the weak link can be described at small frequency $\hbar\omega \ll \Delta$ by an effective low-energy Hamiltonian, which smoothly interpolates between the one of a quantum dot weakly coupled to two superconducting leads ($\Gamma \ll \Delta$) and the one of a short junction ($\Gamma \gg \Delta$):

$$E_A(\delta) = \frac{\Delta}{\Delta+\Gamma}\sqrt{\tilde{\epsilon_g}^2 + |\tilde{\gamma}(\delta)|^2}, \tag{G.10}$$

where $\tilde{\epsilon_g} = \left(1+\frac{U}{\Delta}f\right)\epsilon_g, \quad \tilde{\gamma}(\delta) = \left(1+\frac{U}{\Delta}g\right)\gamma(\delta), \quad |\gamma|^2 = \Gamma^2 - 4\Gamma_R\Gamma_L\sin^2(\delta/2)$

with $f(\Gamma/\Delta)$ and $g(\Gamma/\Delta)$, two complicated functions that describe the renormalization of $\epsilon_g$ and $\gamma(\delta)$ by the Coulomb on-site repulsion $U$.

$\Gamma = \Gamma_L + \Gamma_R$ denotes the total tunneling rate to the leads and we write $\delta\Gamma = \Gamma_L - \Gamma_R$ the asymmetry in the left/right tunneling rates. $\epsilon_g$ is the energy of the dot level and is determined by the applied gate $\epsilon_g \approx -eV_g$.

The authors provide an expression for the dynamic part of the current-current response function $\delta\chi_{II}$ of the weak link in its ground state at frequencies $\hbar\omega \ll \Delta$:

$$\delta\chi_{II}(\omega) = -\frac{\varphi_0^{-2}}{E_A}\frac{(\hbar\omega)^2}{4E_A^2-(\hbar\omega)^2}\frac{1}{|\tilde{\gamma}|^2}\left[\tilde{\epsilon_g}^2(\partial_\delta E_A)^2 + \frac{1}{4}\left(\frac{\Delta}{\Delta+\Gamma}\right)^2\left(1+g\frac{U}{\Delta}\right)^4\delta\Gamma^2\left(\Gamma-\frac{|\gamma|^2}{\Delta+\Gamma}\right)^2\right]. \tag{G.11}$$

Let us show that we can recover the expected result for the resonator shift Eq. (4.32) using this expression for the current response of the weak link. First, one can recognize the prefactor in Eq. (G.11) as the resonant form factor $\mathscr{R}(\omega, E_A)$ introduced in the previous section :

$$\frac{1}{\hbar\omega-2E_A} - \frac{1}{\hbar\omega+2E_A} + \frac{1}{E_A} = \frac{\hbar^2\omega^2}{E_A(\hbar^2\omega^2-4E_A^2)}. \tag{G.12}$$

For $\epsilon_g \ll \Gamma$, one can simplify the expression of the Andreev level energy G.10:

$$\boxed{E_A(\delta) \underset{\epsilon_g\ll\Gamma}{\approx} \frac{\Delta}{1+\frac{\Delta}{\Gamma}}\left(1+\frac{U}{\Delta}g\right)\sqrt{1-\tau\sin^2(\delta/2)},} \tag{G.13}$$

which coincides with Eq. (G.1) in the limit of strong tunneling $\Gamma \gg \Delta$

and small interaction $U \ll \Delta$ : the wavefunction spreads from the dot and resides mainly in the leads ; the system is then essentially equivalent to a short junction.

Moreover, the effective transmission $\tau$ of the weak link can be expressed $\tau = 1 - R^2 = 1 - \left(\frac{\delta\Gamma}{\Gamma}\right)^2 = \frac{4\Gamma_L\Gamma_R}{\Gamma^2}$, from which we deduce

$$|\tilde{\gamma}|^2 = \left(1 + \frac{U}{\Delta}g\right)^2 \Gamma^2(1 - \tau\sin^2(\delta/2)) \underset{\epsilon_g \ll \Gamma}{\approx} E_A^2\left(1 + \frac{\Gamma}{\Delta}\right)^2. \tag{G.14}$$

This allows to rewrite the current-current response in a more meaningful way :

$$\begin{aligned}
\delta\chi_{II} &\overset{\epsilon_g \ll \Gamma}{\approx} \frac{1}{\varphi_0^2}\frac{\mathscr{R}(\omega, E_A)}{E_A^2\left(1+\frac{\Gamma}{\Delta}\right)^2}\frac{1}{4}\left(\frac{\Delta}{\Delta+\Gamma}\right)^2\left(1+g\frac{U}{\Delta}\right)^4\Gamma^2(1-\tau)\left[\Gamma - \frac{1}{\Delta+\Gamma}\frac{\left(1+\frac{\Gamma}{\Delta}\right)^2 E_A^2}{\left(1+\frac{U}{\Delta}g\right)^2}\right]^2 \\
&= \frac{1-\tau}{4\varphi_0^2}\frac{\mathscr{R}(\omega, E_A)}{E_A^2}\left(\frac{\Gamma}{\Delta+\Gamma}\right)^4\left(1+g\frac{U}{\Delta}\right)^4\left[\Delta^2 - \frac{\Delta+\Gamma}{\Gamma}\frac{E_A^2}{\left(1+\frac{U}{\Delta}g\right)^2}\right]^2 \\
&= \frac{1-\tau}{4\varphi_0^2}\frac{\mathscr{R}(\omega, E_A)}{E_A^2}\left[\Delta^2\frac{\left(1+\frac{U}{\Delta}g\right)^2}{\left(1+\frac{\Delta}{\Gamma}\right)^2} - \frac{\Gamma}{\Delta+\Gamma}E_A^2\right]^2 = \frac{\mathscr{R}(\omega, E_A)}{\varphi_0^2}\mathscr{M}_*^2,
\end{aligned} \tag{G.15}$$

where we have defined the modified matrix element

$$\mathscr{M}_* = \frac{\sqrt{1-\tau}}{2}\frac{1}{E_A}\left[\Delta_*^2 - \frac{\Gamma}{\Delta+\Gamma}E_A^2\right], \tag{G.16}$$

and modified gap

$$\Delta_* = \Delta\frac{1+\frac{U}{\Delta}g}{1+\frac{\Delta}{\Gamma}} = \begin{cases} \Delta + o\left(\frac{\Delta}{\Gamma}\right) & \Gamma \gg \Delta \\ \Gamma + \frac{\Gamma}{\Delta}\left(\frac{U}{\pi} - \Gamma\right) + o\left(\frac{\Gamma}{\Delta}\right) & \Gamma \ll \Delta. \end{cases} \tag{G.17}$$

When the tunneling between the dot and the leads is strong *i.e.* $\Gamma \gg \Delta$, the ABS wavefunction spreads into the leads and the effect of interactions is diluted : $\Delta_* \approx \Delta$ and the $U$ correction appears only in second order in $\Delta/\Gamma$. On the other hand, when the tunneling is weak, the ABS stays mainly localized on the dot, the effect of interactions is stronger and $\Delta_* \approx \Gamma$ at leading order.

Note that $\mathscr{M}_*$ has the same functional form and reduces to the matrix element of the current operator for a short junction, Eq. (G.6) in the limit $\Gamma \gg \Delta \gg U$:

$$\mathscr{M} = |\langle e|\hat{H}'_{wl}|g\rangle| = \frac{\Delta\sqrt{1-\tau}}{2}\left(\frac{\Delta}{E_A} - \frac{E_A}{\Delta}\right) = \frac{\sqrt{1-\tau}}{2}\frac{1}{E_A}(\Delta^2 - E_A^2).$$

Although the expression for the normalization function $g(\Gamma/\Delta)$ is cumbersome (see Eq. (B15) in [64]), it assumes simple asymptotic expressions

in the limits $\Gamma \gg \Delta$ and $\Gamma \ll \Delta$:

$$g(x) = \begin{cases} \frac{1}{\pi x^2}(2 - \ln 2x) + o(x^2) & \Gamma \gg \Delta \\ \frac{1}{\pi} - x & \Gamma \ll \Delta \end{cases},$$

from which we deduce a final expression for the matrix element in the limit $\epsilon_g, \Delta \ll \Gamma$:

$$\mathscr{M}_* \approx \frac{\sqrt{1-\tau}}{2} \frac{1}{E_A} \left[ \frac{\Delta^2}{\left(1 + \frac{\Delta}{\Gamma}\right)^2} \left(1 + \frac{1}{\pi} \frac{U}{\Delta} \left(\frac{\Delta}{\Gamma}\right)^2 (2 - \ln \frac{2\Gamma}{\Delta})\right)^2 - \frac{\Gamma}{\Delta + \Gamma} E_A^2 \right]. \tag{G.18}$$

At first order in $\Delta/\Gamma$, the Coulomb interaction $U$ no longer plays any role and one (almost) recovers the result for the short junction:

$$\mathscr{M}_* = \frac{\Delta\sqrt{1-\tau}}{2} \left[ \frac{\Delta}{E_A} - \frac{E_A}{\Delta} \left(1 - \frac{\Delta}{\Gamma}\right) \right] + o\left(\frac{\Delta}{\Gamma}\right) \underset{\Gamma \gg \Delta}{\approx} \mathscr{M}. \tag{G.19}$$

Finally, using Eq. (4.18), we obtain the following expression for the resonator shift when the dot weak link is in its ground state:

$$\begin{aligned} \hbar\omega &= \frac{\hbar \ell^2}{2L} \omega_0 \chi_{II} \\ &= \delta_{\mathrm{zp}}^2 \varphi_0^2 \left( \partial_\phi^2 E_g(\phi) + \delta\chi_{II}(\omega_0) \right) \\ &= \delta_{\mathrm{zp}}^2 \left( E_g''(\delta) + \mathscr{R}(\omega_0, E_A) \mathscr{M}_*^2 \right), \end{aligned} \tag{G.20}$$

with

$$E_g(\delta) = E_{\mathrm{cont}} - E_A(\delta) + \begin{cases} U\left(\frac{\Delta}{2\Gamma}\right)^2 & \Gamma \gg \Delta \\ \frac{U}{4} & \Gamma \ll \Delta \end{cases}$$

$$\boxed{\frac{\hbar\delta\omega}{\delta_{\mathrm{zp}}^2} = E_g''(\delta) + \mathscr{M}_*{}^2 \left[ \frac{1}{\hbar\omega_0 - 2E_A} - \frac{1}{\hbar\omega_0 + 2E_A} + \frac{1}{E_A} \right].} \tag{G.21}$$

Once again, one recovers exactly the result predicted from our general expression, Eq. (4.32).

# Resonator shift in zero-length weak links

# H

## H.1 Calculation of the resonator shift

The case of zero-length weak links is the simplest, as the BdG equation can be solved analytically. For a single conduction channel of transmission $\tau$, there is only one pair of Andreev states within the gap (see Figure 4.7(a)), with energies $E_{\pm1,\sigma} = \pm E_A(\delta) = \pm\Delta\sqrt{1-\tau\sin^2(\delta/2)}$ [7, 8, 9], which are coupled through the matrix element of the current operator $\hat{H}'_{wl}$ [144, 16], given by:

$$\mathscr{M} = \mathscr{M}_{-1\sigma,1\sigma} = \frac{\Delta\sqrt{1-\tau}}{2}\left(\frac{\Delta}{E_A} - \frac{E_A}{\Delta}\right). \tag{H.1}$$

From these two subgap levels, labeled ±1, there are only 3 possible many-body states for the weak link, depicted in Figure 4.7(a): the ground state $|g\rangle$ where the negative level $-1$ is occupied as well as all negative states from the continuum ; the odd parity state $|o\rangle$ obtained by creation of one quasiparticle of either spin in the upper level +1, $|o\rangle = |1\sigma\rangle = \gamma^\dagger_{1\sigma}|g\rangle$ ; and the doubly-excited state with even parity $|e\rangle = |1\uparrow 1\downarrow\rangle = \gamma^\dagger_{1\uparrow}\gamma^\dagger_{1\downarrow}|g\rangle$. The space spanned by the two states of even parity, $|g\rangle$ and $|e\rangle$, allows to implement an *Andreev pair qubit*, the frequency of which being given by $f_A = 2E_A/h$.

Let us now compute the resonator frequency shift when the weak link is in each of these 3 many-body states. The results are illustrated in Figure H.1 for the case of a resonator at $f_r = 0.2\Delta/h$ in two emblematic limits: the *adiabatic* regime, where the Andreev pair qubit frequency $f_A$ is taken far from $f_r$ ($\tau = 0.8$), and the *dispersive* regime, where $f_A$ crosses the resonator frequency $f_r$ ($\tau = 0.999$) therefore allowing for exchange of virtual photons.

For each many-body state of the weak link, the associated resonator frequency shift (dashed red line in Figure H.1) results from the sum of four contributions. The first one corresponds to the contribution of the curvature $E''_{|\Psi\rangle}$ of the many-body state $|\Psi\rangle$ (green lines in Figure H.1). The second one (blue lines) is associated with virtual transitions between the Andreev levels -1 and +1, coupled by the matrix element $\mathscr{M}_{-1\sigma,1\sigma}$ and reads:

$$\mathscr{V}_{-1\sigma,1\sigma} = \frac{\mathscr{M}^2}{h}\left(\frac{2}{f_A} - \frac{1}{f_A - f_r} - \frac{1}{f_A + f_r}\right), \tag{H.2}$$

The third type of contribution (orange lines), is associated with virtual transitions between an Andreev level and states in the continuum $\mathscr{C}^-$ at energies $E < -\Delta$ or $\mathscr{C}^+$ at energies $E > \Delta$. Using the expressions for the matrix elements of $\hat{H}'_{wl}$ given in Refs. [145, 144], and introducing a broadening of $10^{-3}\Delta$, one finds that the associated shift grows positive from $\delta = 0$, presents a maximum, and exhibits a negative dip when $\Delta - E_A = hf_r$. This is characteristic of a threshold behavior associated with the continuum, also discussed in Ref. [140].

[7]: Beenakker and Houten (1991), 'Josephson current through a superconducting quantum point contact shorter than the coherence length'
[8]: Furusaki and Tsukada (1991), 'Dc Josephson effect and Andreev reflection'
[9]: Bagwell (1992), 'Suppression of the Josephson current through a narrow, mesoscopic, semiconductor channel by a single impurity'
[144]: Zazunov et al. (2014), 'Quasiparticle trapping, Andreev level population dynamics, and charge imbalance in superconducting weak links'
[16]: Janvier et al. (2015), 'Coherent manipulation of Andreev states in superconducting atomic contacts'

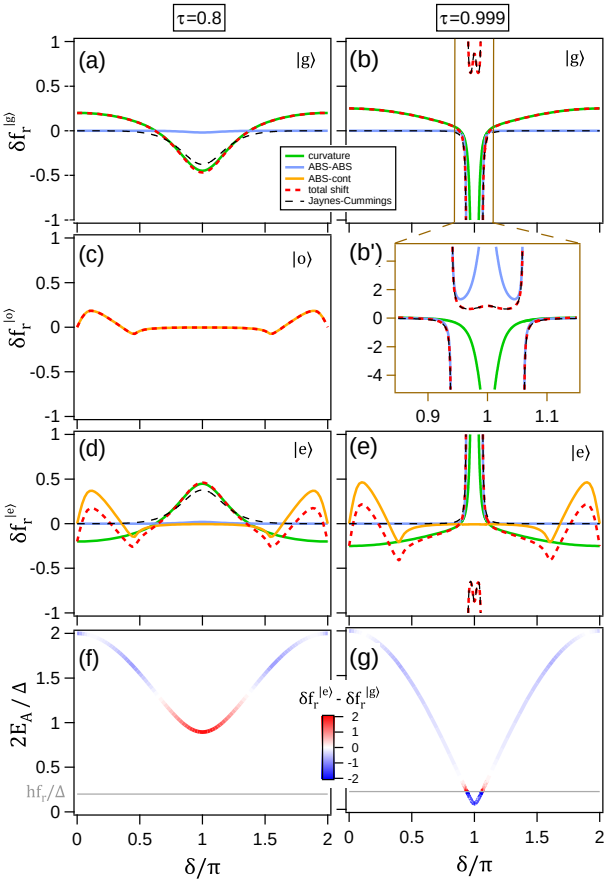


**Figure H.1:** Zero-length one-channel junction. (a-e) Resonator frequency shifts (in units of $\delta_{zp}^2\Delta/h$) for two values of the channel transmission $\tau$, and (f,g) transition energy $2E_A$ with color-coded frequency change when driving the system from $|g\rangle$ to $|e\rangle$, all as a function of the phase $\delta$. The bare resonator frequency, shown as a black line in (f,g), was taken at $f_r = 0.2\Delta/h$. In the left panels, $\tau = 0.8$, and the transition frequency is always larger than $hf_r$; in the right ones, $\tau = 0.999$, and $2E_A$ crosses $hf_r$. Total frequency shifts $\delta f_r^{|g\rangle,|o\rangle,|e\rangle}$ in state $|g\rangle$ (a,b,b'), $|o\rangle$ (c) and $|e\rangle$ (d,e) are shown with dashed red lines. They are decomposed into three contributions: states' curvature $E''_{|g\rangle,|o\rangle,|e\rangle}$ (green lines), virtual transitions among Andreev levels (blue lines) and virtual transitions from Andreev levels to continuum levels (orange lines). The resonator shift $\delta f_r^{\mathrm{JC}}$ obtained from the Jaynes-Cummings approximation is shown in black dashed lines.

The last contribution, which results from virtual transitions from states in $\mathscr{C}^-$ to states in $\mathscr{C}^+$, is negligible.

### Shift in $|g\rangle$

In the ground state, the level $-1$ and all levels in the negative continuum $\mathscr{C}^-$ are doubly occupied, so that the factor $1/2$ in Eq. 4.35 cancels out with a factor 2 for the spin, and

$$\frac{h\delta f_r^{|g\rangle}}{\delta_{\mathrm{zp}}^2} = E''_{|g\rangle} + \sum_{\substack{i<0\\ j>0}} \mathscr{V}_{i,j}, \tag{H.3}$$

where we dropped the spin indices since $\hat{H}'_{wl}$ conserves the spin for zero-length junctions. In the zero-length limit, the energy of the states in the continuum does not depend on phase [73], and $E''_{|g\rangle} = -E''_A$. The second term reads

$$\sum_{\substack{i<0\\ j>0}} \mathscr{V}_{i,j} = \mathscr{V}_{-1,1} + \sum_{i\in\mathscr{C}^-} \mathscr{V}_{i,1} + \sum_{j\in\mathscr{C}^+} \mathscr{V}_{-1,j} + \sum_{\substack{i\in\mathscr{C}^-\\ j\in\mathscr{C}^+}} \mathscr{V}_{i,j}. \tag{H.4}$$

[73]: Levchenko et al. (2006), 'Singular length dependence of critical current in superconductor/normal-metal/superconductor bridges'

Since $\mathscr{V}_{i,j} = -\mathscr{V}_{j,i}$ and $\mathscr{V}_{i,j} = -\mathscr{V}_{-i,-j}$, one obtains, neglecting virtual transitions from $\mathscr{C}^-$ to $\mathscr{C}^+$ (last term in Eq. (H.4)),

$$\boxed{\frac{h\delta f_r^{|g\rangle}}{\delta_{\rm zp}^2} \approx -E_A'' + \mathscr{V}_{-1,1} + 2\sum_{j\in\mathscr{C}^+} \mathscr{V}_{-1,j}.} \tag{H.5}$$

The computation of the shift in $|g\rangle$ can be summarized graphically as follows:

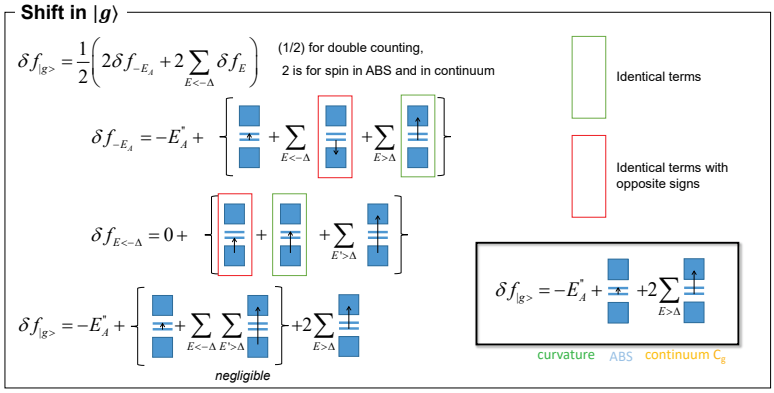


In practice, because of the large energy $E_{-1,j} > E_A + \Delta$ for a transition to $\mathscr{C}^+$, the last term in Eq. H.5 can always be neglected and one is left with

$$\frac{h\delta f_r^{|g\rangle}}{\delta_{\rm zp}^2} \approx -E_A'' + \frac{\mathscr{M}^2}{h}\left(\frac{2}{f_A} - \frac{1}{f_A - f_r} - \frac{1}{f_A + f_r}\right). \tag{H.6}$$

When $f_A \gg f_r$, the three terms from $\mathscr{V}_{-1,1}$ compensate and the frequency shift is entirely due to $E_A''$, as shown in Figure H.1(a) and far from $\delta = \pi$ in Figure H.1(b). When $|f_r - f_A| \ll \Delta$ there is a compensation between $-E_A''$ and $\mathscr{M}^2\frac{2}{hf_A}$ (green and blue lines in Figure H.1(b,b')), *i.e.* the contribution due to $\hat{H}_{wl}''$ vanishes [52], and the frequency shift is essentially the one that can be derived from the Jaynes-Cummings Hamiltonian [146, 71]

$$\delta f_r^{|g\rangle,\rm JC} = -\left(\frac{g(\delta)}{2\pi}\right)^2\left(\frac{1}{f_A - f_r} + \frac{1}{f_A + f_r}\right), \tag{H.7}$$

with $g(\delta) = \mathscr{M}\delta_{\rm zp}/\hbar$. At the scale of Figure H.1(b'), $\delta f_r^{|g\rangle,\rm JC}$ (shown in black dotted line) and the exact $\delta f_r^{|g\rangle}$ coincide within the linewidth. The rotating-wave approximation (RWA), which consists in neglecting the second term:

$$\delta f_r^{|g\rangle,\rm RWA} = -\frac{\left(g(\delta)/2\pi\right)^2}{f_A - f_r}, \tag{H.8}$$

overestimates the little bump of $\delta f_r^{|g\rangle}$ at $\delta = \pi$ by a factor $\sim 2$. Altogether, if when $f_A > f_r$ $f_r^{|g\rangle,\rm JC}$ remains a rather good approximation for the total shift (see black dashed line in Figure H.1(a)), but it fails to capture the smooth inductive contribution to the shift away from $\delta = \pi$ arising from the states' curvature.

[52]: Park et al. (2020), 'From Adiabatic to Dispersive Readout of Quantum Circuits'

[146]: Johansson et al. (2006), 'Readout methods and devices for Josephson-junction-based solid-state qubits'

[71]: Zueco et al. (2009), 'Qubit-oscillator dynamics in the dispersive regime'

**Shift in $|o\rangle$**

The odd parity state $|o\rangle = \gamma_{1\sigma}^{\dagger}|g\rangle$ has energy $E_g + E_A = 0$. The shift of the resonator in this case is

$$\delta f_r^{|o\rangle} = \delta f_r^{|g\rangle} + \delta f_r^{(1)}. \tag{H.9}$$

Using

$$\frac{h\delta f_r^{(1)}}{\delta_{\mathrm{zp}}^2} = E_A'' + \mathscr{V}_{1,-1} + \sum_{j\in\mathscr{C}^-} \mathscr{V}_{1,j} + \sum_{j\in\mathscr{C}^+} \mathscr{V}_{1,j}, \tag{H.10}$$

and $\mathscr{V}_{1,j} = -\mathscr{V}_{-1,j}$, one obtains

$$\boxed{h\delta f_r^{|o\rangle} \approx \sum_{j\in\mathscr{C}^+} \left(\mathscr{V}_{-1,j} + \mathscr{V}_{1,j}\right).} \tag{H.11}$$

Although the odd state does not disperse with $\delta$ ($E'_{|o\rangle} = 0$), one obtains a finite shift associated to transitions from Andreev states to continuum states, which becomes sizable when $E_A$ approaches $\Delta$ (see Figure H.1(c)).

The computation of the shift in $|o\rangle$ can be summarized graphically as follows:

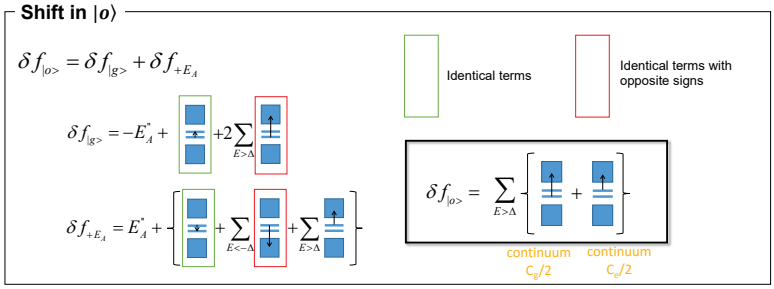


**Shift in $|e\rangle$**

The excited state $|e\rangle = \gamma_{1\uparrow}^{\dagger}\gamma_{1\downarrow}^{\dagger}|g\rangle$ has energy $E_g + 2E_{1\sigma} = E_A$. The shift in this state (shown in Figure H.1(d,e)) is

$$\delta f_r^{|e\rangle} = \delta f_r^{|g\rangle} + 2\delta f_r^{(1)}, \tag{H.12}$$

and one gets

$$\boxed{\frac{h\delta f_r^{|e\rangle}}{\delta_{\mathrm{zp}}^2} \approx E_A'' - \mathscr{V}_{-1,1} + 2\sum_{j\in\mathscr{C}^+} \mathscr{V}_{1,j}.} \tag{H.13}$$

When $E_A \ll \Delta$ the continuum contributions can be neglected and $\delta f_r^{|e\rangle} \approx -\delta f_r^{|g\rangle}$. This is no longer the case when $E_A$ approaches $\Delta$, a situation in which both $2\sum_{j\in\mathscr{C}^+} \mathscr{V}_{1,j}$ and $E_A''$ contribute to the shift, as shown in Figure H.1(d,e).

The computation of the shift in $|e\rangle$ can be summarized graphically as follows:

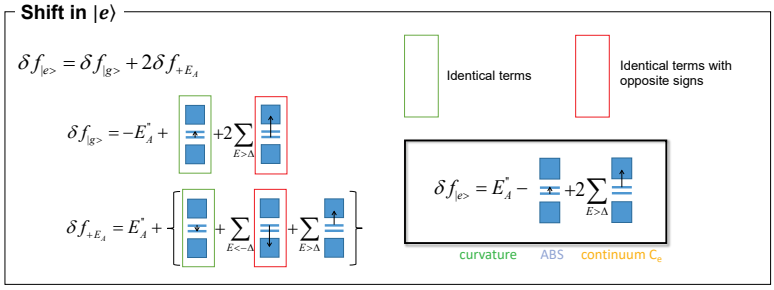


Finally, note that the shifts predicted by Eq. (H.5, H.11, H.13) verify the following half-sum rule, $(\delta f_r^{|g\rangle} + \delta f_r^{|e\rangle})/2 = \delta f_r^{|o\rangle}$, as expected for non-interacting many-body states [64, 50].

[64]: Kurilovich et al. (2021), 'Microwave response of an Andreev bound state'
[50]: Fatemi et al. (2021), 'Microwave susceptibility observation of interacting many-body Andreev states'

**Shift for a $|g\rangle \to |e\rangle$ transition**

Now that we have expressed the resonator frequency shift associated to the three possible many-body states of a zero-length weak link, we can estimate the frequency shift when the system is externally driven with microwaves, in particular when it is driven from $|g\rangle$ to $|e\rangle$, which is what we probe in our two-tone spectroscopy measurements. The frequency shift that governs the measured signal is given by $\Delta f_r = \delta p_{|e\rangle}\left(\delta f_r^{|e\rangle} - \delta f_r^{|g\rangle}\right)$, with $\delta p_{|e\rangle}$ the population change in the excited state due to the microwave excitation.

In Figure H.1(f,g), the quantity $\delta f_r^{|e\rangle} - \delta f_r^{|g\rangle}$ is encoded in the color of the line showing the phase dependence of the pair transition energy $2E_A(\delta)$. For $\tau = 0.8$, it is dominated by the curvature term $2E_A''$, except when $E_A$ approaches $\Delta$ and virtual transitions to the continuum enter in $\delta f_r^{|e\rangle}$. For $\tau = 0.999$, close to $\delta = \pi$, the terms associated to virtual transitions between ABS causes a change of sign of $\Delta f_r$ when $2E_A$ crosses $hf_r$, as expressed by the dispersive approximation (Eq. (H.7)).

## H.2 Revisiting experiments on atomic contacts

The zero-length limit for the weak link was tackled in a previous experiment [16], dealing with atomic contacts between two superconducting aluminium electrodes hosting a small number of transport channels. The microwave spectroscopy of such system was performed near phase $\delta \approx \pi$ and allowed to reveal the phase dependence of the pair transition frequency associated to the $|g\rangle \to |e\rangle$ process.

In Ref. [16], the superconducting loop containing the atomic contact was coupled to a microwave resonator at $f_r = 10.1$ GHz measured in reflection (see Figure H.2). Atomic contacts with various channel transmissions were formed and probed with the same sample. Two types of measurements were performed, which we are now going to compare with the resonator shift theory that we just developed. The first type of measurement consists in a *single-tone continuous-wave* (CW) spectroscopy of the resonator. It gives direct access to the resonator shift for the different many-body occupations of the weak link. The second

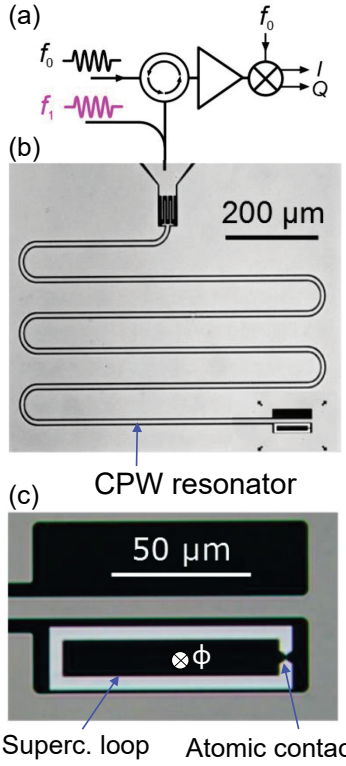


**Figure H.2:** Setup of the atomic contact experiment. (a) The measurement (frequency $f_0$) and drive (frequency $f_1$) signals are routed to a microwave CPW resonator. After amplification, the reflected signal at $f_0$ is homodyne detected by an IQ mixer and its two quadratures (I and Q) are digitized. (b) Optical micrograph of the quarter-wave CPW resonator, inductively coupled at its shorted end to an aluminium loop containing the constriction where the atomic contact is formed. (c) Detailed view of the loop.

type of measurement is a *two-tone spectroscopy* of the resonator, for which an additional microwave tone is used to drive transitions between ABS. In this case, as will be explained below, the resonator frequency is only indirectly monitored, since the detection scheme relies on a homodyne detection at a fixed measurement frequency. Although this time the recorded signals are the two quadratures of the measurement field reflected by the resonator, not its frequency, it is still possible by means of some calibrations to retrieve the associated resonator shift and compare it with theory. This is possible for example when the resonator shift is small enough so that the two quadratures can be linearized around the resonator frequency (see Section 6.5).

**Single-tone CW resonator spectroscopy**

Let us first discuss single-tone continuous-wave (CW) spectroscopy data taken on seven different atomic contacts, as shown in Figure H.3. To acquire these data, the microwave response of the resonator is probed with a vectorial network analyzer (VNA) as a function of flux $\varphi = 2\pi\Phi/\Phi_0$, with no drive applied on the weak link. Over a small flux range around $\varphi = \pi$, the amplitude of the reflection coefficient $|S_{11}|$ displays up to three distinct local minima (in dark) as a function of frequency, as shown in Figure H.3(a-g). The positions $f_{1,3}$ of these minima were extracted by fitting $|S_{11}|(f)$ with the linear combination $\sum_{i=1}^{3} p_i |S_{11}^0|(f, f_i)$ of resonance lines $|S_{11}^0|(f, f_i)$ corresponding to a single resonance centered at $f_i$. The extracted $f_i$ are shown with symbols in Figure H.3((a'-g'). These data can essentially be understood by considering the contribution of just one dominant channel of transmission $\tau_1$ such that the corresponding Andreev frequency $f_{A1}$ comes very close to the resonator frequency $f_r$ (a,b) or crosses it (c-g). The data are ordered with increasing $\tau_1$ from (a) to (g). The three resonances are attributed to partial occupancy of ground $|g\rangle$, odd $|o\rangle$ and excited $|e\rangle$ states for the corresponding channel. As shown in Eqs. (H.5,H.13), and since, according to the analysis of Section H.1, contributions of the continuum can safely be neglected for phases close to $\pi$, the frequency shifts associated with ground and excited state are opposite (Figure H.3(a,b)), and the frequency shift associated with the odd state is close to zero (Figure H.3(a,e)). Note that in order to explain a small residual global shift, it is necessary to consider the contribution of one or two additional channels with smaller transmissions, as explained below.

The resonator frequency shift is obtained from Eqs. (H.5, H.11, H.13), adding the contributions of all channels. The bare resonator frequency $f_r$ was determined from measurements of the resonator with open contacts. The phase $\delta$ across the contact actually differs slightly from $\varphi = 2\pi\Phi/\Phi_0$ due to the phase drop across the loop inductance. Indeed, when a weak link is placed inside a superconducting loop with geometric inductance $\ell$ threaded by a magnetic flux $\Phi$, the screening current due to the weak link leads to a phase drop across the loop inductance. This leads to the following relation between the reduced flux $\varphi = 2\pi\Phi/\Phi_0$ and the phase $\delta$ across the weak link:

$$\delta = \varphi - \beta i_{|\Psi\rangle}(\delta), \tag{H.14}$$

with the screening parameter $\beta = \ell\Delta/\varphi_0^2$, $\varphi_0 = \Phi_0/2\pi$, and $i_{|\Psi\rangle} =$

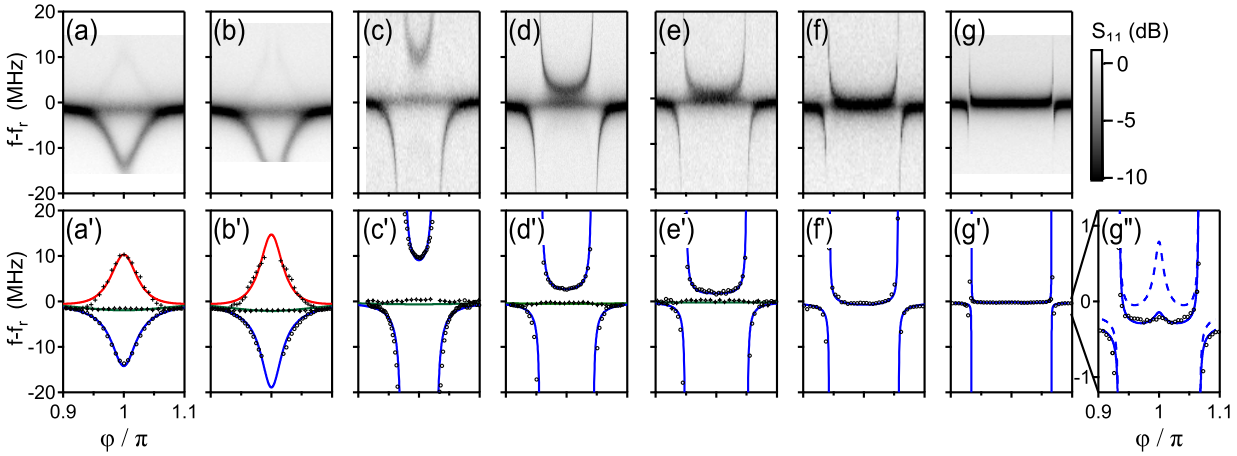


**Figure H.3:** Fit of single-tone continuous-wave spectroscopy data taken with a vector network analyzer (VNA) on a series of atomic contacts obtained from the same sample (described in Ref. [16]), with resonator at $f_r = 10.1$ GHz . (a-g) Raw data, with reflection coefficient of the resonator $S_{11}$ coded with gray scale. By fitting $S_{11}(f)$ at each flux with the sum of shifted resonance curves, up to three values of the frequency shift could be extracted ((a'-g') and (g"), symbols). They are associated with the shifts in states $|g\rangle$, $|o\rangle$ and $|e\rangle$ of the channel with the largest transmission. Solid line are fits with complete theory, using $\delta_{\rm zp} = 0.0042$ and $\Delta/h = 44.3$ GHz. Blue: $\delta f_{r,|g\rangle}$, green: $\delta f_{r,|o\rangle}$ (with respect to 1st channel), red in (a',b'): $\delta f_{r,|e\rangle}$. Fit parameters are given in Table H.1. In (g"), the dashed line corresponds to $\delta f_r^{|g\rangle}$ in the rotating wave approximation (Eq. H.8).

$\varphi_0 I_{|\Psi\rangle}/\Delta = (1/\Delta)\partial E_{|\Psi\rangle}/\partial\delta$ the reduced current associated to the weak link in state $|\Psi\rangle$. For a single-channel zero-length weak link, one expects the following currents: $i_{|g\rangle} = -\partial\sqrt{1-\tau\sin^2(\delta/2)}/\partial\delta$, $i_{|e\rangle} = -i_{|g\rangle}$ and $i_{|o\rangle} = 0$. In practice, due to its small geometric inductance, the phase drop along the loop is negligible compared to the phase drop $\delta$ across the weak link. However, when the weak link hosts highly transmitted channels, as was the case here with atomic contacts, the supercurrent carried by the weak link can become large enough so that $\delta$ no longer varies linearly with the applied flux $\Phi$ and the correction due to the loop inductance comes into play*. From the estimated loop inductance $\ell \approx 0.1$ nH [21], we obtain the screening parameter $\beta = 0.03$ used to fit the data.

In a first step, the value of $\delta_{zp} = 0.0042$, common to all contacts, was determined by fitting Figure H.3(d), taken on a contact for which a fit of the two-tone spectroscopy yielded $\tau_1 = 0.992$ [16]. This value agrees well with the nominal value expected from the mutual coupling design (see Section 5.2.1). This two-tone spectrum will be later presented in Section 21 (see Figure H.4). For the other contacts, the fitting parameters are the transmissions $\tau_i$ of two or three channels. All parameters are given below in Table H.1.

The transmission $\tau_1$ of the most-transmitted channel is the essential fit parameter, as it determines the overall shape of the spectra. In the last column of Table H.1, we indicate the minimal value of the Andreev frequency associated to this transmission $f_{A1}^{\rm min} = f_{A1}(\pi) = 2\Delta\sqrt{1-\tau_1}$. When $f_{A1}^{\rm min} < f_r$ (c–g), one observes an avoided crossing.

* For finite length weak links, this effect is expected to manifest to a lesser extent, since the current carried by the ground state is to be smaller by at least a factor $1/(1+L/\xi)$ [32], where $L$ is the length of the weak link and $\xi$, the superconducting coherence length. Indeed, we did not need to invoke any finite loop inductance effect to model the data measured on the nanowire weak link experiment, as we will see in Section 6.5.

| contact | run | $f_r$ (GHz) | $\tau_1$ | $\tau_2$ | $\tau_3$ | $f_{A1}^{\min}$ (GHz) |
|---|---|---|---|---|---|---|
| (a) | I | 10.1345 | 0.9850 | 0.9428 | 0.9428 | 10.85 |
| (b) | I | 10.1345 | 0.9856 | 0.9468 | 0.9468 | 10.63 |
| (c) | III | 10.1091 | 0.9890 | 0.9 | - | 9.29 |
| (d) | I | 10.1345 | 0.9922 | 0.8783 | - | 7.82 |
| (e) | III | 10.1091 | 0.9945 | 0.6561 | - | 6.57 |
| (f) | II | 10.1364 | 0.9967 | 0.9692 | - | 5.09 |
| (g) | I | 10.1345 | 0.9996 | 0.8497 | - | 1.77 |

**Table H.1:** The data of Figure H.3 were taken during different cooldowns (runs) of the same sample, labelled I, II and III. In runs I and III, the bare resonator frequency $f_r$ was measured when the contact was open, whereas for run II it was a fit parameter.

A second channel with transmission $\tau_2$, and for Figure H.3(a',b') a third one with transmission $\tau_3$ taken equal to $\tau_2$, are taken into account. In the small phase interval considered here, the effect of these other channels is simply a constant overall shift of the order of a MHz.

The predictions for $\delta f_r$ assuming the most-transmitted channel to be in $|g\rangle$, $|o\rangle$ or $|e\rangle$ are shown with blue, green and red lines in Figure H.3. The $\delta-$ and $\tau-$ dependence of the coupling constant $g$ is an essential ingredient to obtain a consistent fit of all the data at once. The difference between the full theory and the JC contribution is very small at the scale of Figure H.3. In Figure H.3(a–c), since $|f_{A1}(\pi) - f_r| \ll f_{A1}(\pi) + f_r$, the counter-rotating term $\propto 1/(f_{A1} + f_r)$ can also be neglected, and the RWA is sufficient. When $\tau_1$ is closer to 1 (Figure H.3(d–g)), $f_{A1}$ becomes significantly smaller than $f_r$ near $\delta = \pi$ and the counter-rotating term must be taken into account, as illustrated in Figure H.3(g") where the RWA prediction shown with a dashed line departs clearly from the data. Overall, this series of single-tone CW spectroscopies show that the measured resonator shift associated to the many-body occupancies of the atomic contact weak link can be well described by our theory for zero-length junctions. Let us now extend it to model the two-tone spectroscopy measurements that were performed on the same system.

### Two-tone spectroscopy

To further illustrate the agreement with our theory for the resonator shift, let us now focus on the two-tone spectrum measured for the atomic contact of Figure H.3(d) [16] that is shown in Figure H.4. A single pair transition is observed in the measurement window, corresponding to a channel with transmission $\tau \approx 0.992$. To acquire this data a strong microwave pulse is used to drive the $\{|g\rangle, |e\rangle\}$ two-level system, during a time exceeding its relaxation and dephasing times, immediately followed by a microwave tone probing the resonator. The two quadratures of the signal reflected by the resonator are measured by homodyne detection, as depicted in Figure H.2. In Figure H.4, the color scale represents the change of amplitude $\delta A$ of one of these quadratures, relatively to its value in the absence of excitation. It depends on the steady state occupancy of the states after the excitation pulse and on the frequency shift of the resonator in each state. For this data taken on a very high-transmission contact and around $\delta = \pi$, the resonator frequency shifts are dominated by the dispersive shifts, with negligible effects from the states in the continuum, and therefore the rotation wave approximation (Eq. (H.8)) applies: $\delta f_r^{|g\rangle} \simeq -\delta f_r^{|e\rangle} \simeq -\left(g(\delta)/2\pi\right)^2/(f_A - f_r)$ with $g(\delta) \simeq g(\pi)E_A(\pi)/E_A(\delta)$ (from Eq. (H.1), when $E_A \ll \Delta$).

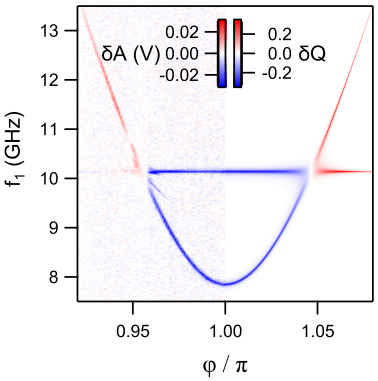


**Figure H.4:** Two-tone spectrum measured on the same atomic contact as for Figure H.3d. Left: experimental data. Colorscale corresponds to the change of amplitude of a quadrature of the reflected signal. Right: calculated spectrum, where the color encodes the change in $S_{11}$, scaled in order to fit at best the data.

As mentioned earlier, in our two-tone spectra, the measured quantity is not the resonator frequency shift. Therefore, to make contact with our theory, one needs first to relate the amplitude of the signal reflected by the resonator to the frequency shift of the latter. When the resonator frequency is $f_r + \delta f_r$, the complex reflection coefficient of a measurement tone at frequency $f_r + \delta f_m$ is known to be given by [16]

[16]: Janvier et al. (2015), 'Coherent manipulation of Andreev states in superconducting atomic contacts', p. 38

$$S_{11}(\delta f_r) = 1 - \frac{1}{1 + Q_{\text{ext}}/Q_{\text{int}}} \left(1 + \mathrm{e}^{i\theta}\right), \tag{H.15}$$

with

$$\theta = -2 \arctan\left(2Q_t(\delta f_r - \delta f_m)/f_r\right), \tag{H.16}$$

where one recognizes the equation of a circle of radius $1/(1+Q_{\text{ext}}/Q_{\text{int}})$ in the complex plane. In this expression, $Q_{\text{int}}$, $Q_{\text{ext}}$ and $Q_t$ are the internal, external and total quality factors of the resonator. When driving the system, if it is in an even state (probability $1 - p_o$), the occupancies of the ground and excited states change by $\delta p_g$ and $\delta p_e = -\delta p_g$, resulting in a change of $S_{11}$ by $\delta S_{11} = \delta p_g (S_{11}(\delta f_r^{|g\rangle}) - S_{11}(\delta f_r^{|e\rangle}))$. Putting everything together, one gets, for $\delta f_m = 0$,

$$\delta S_{11} = \delta p_g \frac{8i}{1 + \frac{Q_{\text{ext}}}{Q_{\text{int}}}} \frac{u}{1 + 4u^2} = i\delta Q, \tag{H.17}$$

with $u = Q_t \delta f_r^{|g\rangle}/f_r$. We have now almost all the pieces to compare the two-tone spectrum with the theory for the resonator shift, except the expression for the population transfer $\delta p_g$, due to the driving tone. To compute $\delta p_g$, one can use the steady-state solution of the Bloch equations [93] adapted for the presence of the odd state:

[93]: Palacios-Laloy (2010), 'Superconducting qubit in a resonator', p. 111

$$\delta p_g = \frac{p_e^0 - \frac{1-p_o}{2}}{1 + \frac{1+(T_2\delta\omega)^2}{T_1 T_2 \omega_R^2}}, \tag{H.18}$$

with $T_1$ and $T_2$ the life time and coherence time, $\delta\omega = 2\pi(f_1 - f_A)$ the detuning between the drive frequency $f_1$ and the Andreev pair qubit frequency $f_A$, and $\omega_R$ the Rabi frequency. For simplicity, we assume here that $T_1$ and $T_2$ are constant: $T_1 = 4$ $\mu$s and $T_2 = 38$ ns (values measured at $\delta = \pi$). Since the excitation acts on the phase across the contact, the Rabi frequency depends on $\delta$: $\omega_R \propto \mathscr{M}^2$ (see Eq. H.1). The drive tone being sent through the resonator, its amplitude is filtered: $\omega_R \propto (1 + Q_t^2(f_1/f_r - f_r/f_1)^2)^{-1/2}$. In the fitting of the data, $\omega_R$ is set to $2\pi \times 4.2$ MHz at $\delta = \pi$ in order to reproduce the measured line width. Using $Q_t = 2200$, $Q_{\text{int}} = 4800$, $f_r = 10.13$ GHz, and $g(\pi)/2\pi = 72$ MHz, one obtains the fit shown on the right hand side of Figure H.4, with the color scale of $\delta Q$ adapted to match the data. Not only does the change in the $Q$ quadrature reproduce the changes $\delta A$ in the measured quadrature on the resonance line $f_A(\delta)$, but one also predicts a signal at $f_1 = f_r$, which has its origin in the very large Rabi frequency when the drive signal is not filtered by the resonator. At this precise frequency, the strong detuning $\delta\omega$ is compensated by the large $\omega_R$ in Eq. (H.18), and $\delta p_g$ is non-zero even if the drive is far from the resonant frequency $f_A$. This feature is clearly visible in the data, although not as strong as in the calculation for $f_A > f_r$ perhaps due to an effect of the resonator non-linearity not included in the model.

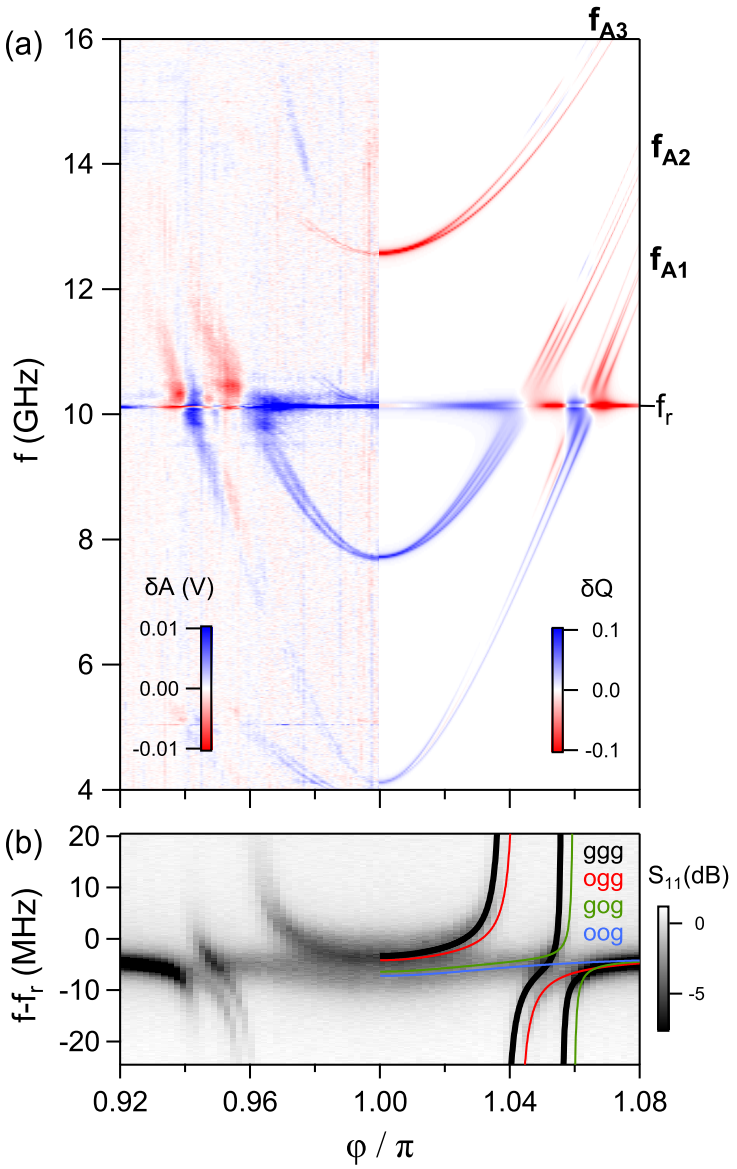


**Figure H.5:** Two-tone spectrum of an atomic contact with several highly transmitted channels. On the right half of the figure, calculated spectrum with identification of three Andreev transitions with frequencies $f_{A1,2,3}$. Lines color corresponds to the calculated change in $Q$ quadrature of $S_{11}$. (b) Grayscale encodes the reflection coefficient amplitude $|S_{11}|$. Lines on the right-hand side are theoretical resonator shifts depending on the states occupancy: black (ggg): all channels in ground state; Red: first channel in odd state (ogg); Green: 2nd channel in odd state (gog); Blue: first and second channel in odd state (oog). A global shift of −3.4 MHz was applied to the theory curves, which can be attributed to the effect of several low-transmitting channels that are not visible in the two-tone spectrum.

One can play a similar game and fit an even more complex spectrum from an atomic contact with more than one highly transmitted channel. In Figure H.5, we show the two-tone spectroscopy and the single-tone CW data of such a contact, obtained with the same sample and showing a double avoided crossing. In the two-tone spectroscopy (Figure H.5(a)), one observes three Andreev pair transitions (labeled $f_{A1}$, $f_{A2}$ and $f_{A3}$) corresponding to channels with transmissions $\tau_1$ =0.998, $\tau_2$ =0.992 and $\tau_3$ =0.980, with minimum transition frequencies (at $\delta = \pi$) of 4.1, 7.7, and 12.6 GHz. Out of the three, two transition lines $f_{A1}$ and $f_{A2}$ cross the resonator at 10.1 GHz.

The experimental data (left half of Figure H.5(a)) show split transition lines at $\delta \neq \pi$. This splitting comes from the fact that the phase across the contact can take several values at a given applied magnetic flux $\Phi$, depending on the occupancies of the ABS associated to each channel. Indeed, due to the finite loop inductance and the relevance of the superconducting phase, the channels are not strictly independent. As already mentioned in Section H.2 on single-tone spectroscopy, the phase $\delta$ across the contact, which is shared by all the channels, is in general not proportional to the reduced flux $\varphi$ and depends on the loop current, due to the finite loop inductance. In the presence of several channels which can be either in the ground or the odd state (we neglect the occupancy of the excited states), this current can actually take several values, depending on the occupancies of the Andreev dots associated to each channel. If the current in one channel is modified (because the Andreev dot changes state), the phase across the contact changes for all dots, leading to an effective coupling between the channels. This effect was already discussed qualitatively in [21], but here we provide an additional quantitative modeling of this splitting.

[21]: Janvier (2016), 'Coherent manipulation of Andreev Bound States in an atomic contact', p.165 (Appendix C)

To calculate the spectrum from theory, we use Eq. (H.15) (with $\delta f_m = -0.4$ MHz) for each state $|\Psi\rangle$, and compute the weighted average $S_{11} = \sum_{|\Psi\rangle} p_{|\Psi\rangle} S_{11}(|\Psi\rangle)$ using the probabilities $p_{|\Psi\rangle}$ for each state. The probabilities to find each channel in the odd state were taken constant, $p_{o1} = 0.55$, $p_{o2} = 0.5$, $p_{o3} = 0.4$, determined by fitting the phase dependence of $S_{11}(\phi)$ at an excitation frequency where no transition is observed ($f_1 = 16$ GHz). In presence of the excitation pulse, the change in each $p_{|\Psi\rangle}$ was obtained from Eq. (H.17). For simplicity, we assumed $T_1 = 4\ \mu$s and $T_2 = 38$ ns at each phase and for each state. Depending on the state of the other channels, a transition from $|g\rangle$ to $|e\rangle$ in one channel leads to different changes in $S_{11}$, as illustrated in Figure H.6. The resulting calculated spectrum is shown in the right half of Figure H.5(a), in which we represent the changes $\delta Q$ in the $Q$ quadrature. Fainter lines in the data are multi-photon transitions (at $f_{Ai}/n$), or transitions involving two channels ($f_{A1} + f_{A2}$ and $(f_{A2} + f_{A3})/2$), not included in the theoretical plot. They appear because the spectroscopy was performed at a particularly strong drive power. Despite the crude simplifications in the analysis, the changes $\delta A$ in the amplitude of the reflected signal in Figure H.5(a) are well reproduced by the calculated changes in the $Q$ quadrature of $S_{11}$. Similar agreement is found on the other quadrature.

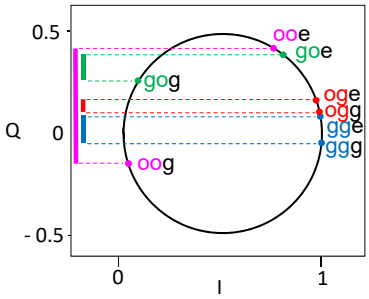


**Figure H.6:** Representation in the $IQ$ plane of $S_{11}$ at $\varphi = 1.04\pi$, for the states involved in transitions on the third channel (see dashed line in Figure H.5(a)). Depending on the state of the two first channels, the change of $Q$ takes very different values, the largest change corresponding to $|oog\rangle \rightarrow |ooe\rangle$ (in magenta). In Figure H.5(a), $\delta Q$ for the four transitions is further scaled by the probability of each initial state, *e.g.* $p_{o1}p_{o2}(1 - p_{o3})$ for $|oog\rangle \rightarrow |ooe\rangle$. Among the four transition lines, only this one is clearly visible in Figure H.5(a).

In Figure H.5(b) we show the single-tone spectroscopy of the resonator. The resonator frequency shift calculated under the assumption that the three channels are in the ground state is shown as a black solid line. Features associated with configurations in which one (red and green lines) or both (blue line) of the two most-transmitted channels are in the odd state are also observed. Horizontal shifts of the red and green lines with respect to the black ones result from the phase drop across the loop inductance, different in each configuration. The analysis of the data of Figure H.5 illustrates how, in a multi-channel weak link, the frequency shift associated with a transition in one channel can depend strongly on the occupancy of the Andreev states in the others, therefore adding further complexity in the modeling of a two-tone spectrum.

# Principles of pulse generation & demodulation

# I

## I.1 Single sideband mixing

To obtain the microwave pulses at the frequency of interest, we use a single sideband mixing technique based on IQ mixers. In this method, a continuous microwave at frequency $\omega_{\mathrm{LO}}$ is applied to the *local oscillator* (LO) port of the mixer, and AC-modulated signals at an intermediate frequency $\omega_{\mathrm{IF}}$ in the $0-100$ MHz range are applied on both the I and Q ports to translate the frequency to the targeted value and define the pulse envelope. The output microwave pulse is then picked on the RF port of the IQ mixer, resulting from the combining of the I and Q signals mixed with a respectively in-phase and in-quadrature LO tone. A functional diagram of the mixer is depicted in Figure I.1.

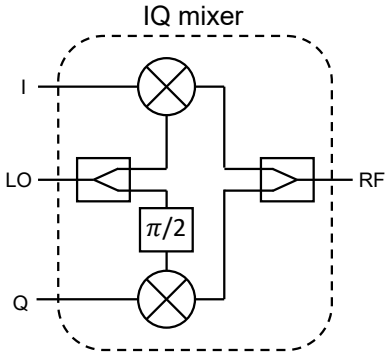


**Figure I.1:** Functional diagram of an IQ mixer.

Ideally, to generate a microwave pulse $S_{\mathrm{in}}(t)$ at the frequency $\omega_{\mathrm{RF}} = \omega_{\mathrm{LO}} + \omega_{\mathrm{IF}}$ with a slowly-varying envelope $A_{\mathrm{in}}(t)$ and phase $\varphi_{\mathrm{in}}$, one would use a LO carrier $LO(t) = A_L \cos(\omega_{\mathrm{LO}} t)$ in addition to I and Q signals at the intermediate frequency $\omega_{\mathrm{IF}}$ with the same envelope $A_{\mathrm{in}}(t)$ and phase $\varphi_{\mathrm{in}}$, but at a $\pi/2$ phase difference from each other. The resulting RF signal at the mixer output would then take the following form :

$$\begin{aligned} S_{\mathrm{in}}(t) &= LO(t)\cdot I(t) + LO(t+\frac{\pi}{2\omega_{\mathrm{LO}}})\cdot Q(t) \\ &= A_L A_{\mathrm{in}}(t)\Big[\cos(\omega_{\mathrm{LO}}t)\cos(\omega_{\mathrm{IF}}t+\varphi_{\mathrm{in}}) - \sin(\omega_{\mathrm{LO}}t)\sin(\omega_{\mathrm{IF}}t+\varphi_{\mathrm{in}})\Big] \\ &\propto A_{\mathrm{in}}(t)\cos(\omega_{\mathrm{RF}}t+\varphi_{\mathrm{in}}), \end{aligned} \tag{I.1}$$

which corresponds up to a prefactor to the targeted waveform for the RF pulse. However in practice, as any microwave components, IQ mixers do suffer from some imperfections. In addition to their operation bandwidth, generally limited to a few GHz, and their RF saturation power around a few dBm, they are characterized by a finite amplitude and phase imbalance between the I and Q branches. This means that contrary to the ideal case of Eq. (I.1), the IQ mixing rather takes the form $LO(t)\cdot I(t) + (1+\alpha)LO(t+\frac{\pi}{2\omega_{\mathrm{LO}}}+\beta)\cdot Q(t)$, where $\alpha$ is typically $1-2$ dB and the phase imbalance $\beta$ is at best a few degrees. These imperfections result in the following mixing :

$$\begin{aligned} S_{\mathrm{in}}(t) &\propto \cos(\omega_{\mathrm{LO}}t)\cos(\omega_{\mathrm{IF}}t+\varphi_{\mathrm{in}}) + (1+\alpha)\cos(\omega_{\mathrm{LO}}t+\frac{\pi}{2}+\beta)\sin(\omega_{\mathrm{IF}}t+\varphi_{\mathrm{in}}) \\ &= \frac{1}{2}\Big[\cos\Big((\omega_{\mathrm{LO}}-\omega_{\mathrm{IF}})t-\varphi_{\mathrm{in}}\Big) + \cos\Big((\omega_{\mathrm{LO}}+\omega_{\mathrm{IF}})t+\varphi_{\mathrm{in}}\Big) \\ &\qquad + (1+\alpha)\sin\Big((\omega_{\mathrm{LO}}+\omega_{\mathrm{IF}})t+\varphi_{\mathrm{in}}+\frac{\pi}{2}+\beta\Big) \\ &\qquad - (1+\alpha)\sin\Big((\omega_{\mathrm{LO}}-\omega_{\mathrm{IF}})t-\varphi_{\mathrm{in}}+\frac{\pi}{2}+\beta\Big)\Big]. \end{aligned} \tag{I.2}$$

Defining $\omega_+ = \omega_{\mathrm{RF}} \equiv \omega_{\mathrm{LO}} + \omega_{\mathrm{IF}}$ and $\omega_- \equiv \omega_{\mathrm{LO}} - \omega_{\mathrm{IF}}$ for the frequencies

of the upper and lower sidebands, we get :

$$\begin{aligned} S_{\text{in}}(t) \propto \frac{1}{2}\Big[&\cos(\omega_- t - \varphi_{\text{in}}) + \cos((\omega_+ t + \varphi_{\text{in}}) \\ &+ (1+\alpha)\Big[\cos(\omega_+ t + \varphi_{\text{in}})\cos(\beta) - \sin(\omega_+ t + \varphi_{\text{in}})\sin(\beta)\Big] \\ &- (1+\alpha)\Big[\cos(\omega_- t - \varphi_{\text{in}})\cos(\beta) + \sin(\omega_- t - \varphi_{\text{in}})\sin(\beta)\Big] \end{aligned} \tag{I.3}$$

$$\begin{aligned} &\underset{\beta \ll 1}{\approx} \left(1 + \frac{\alpha}{2}\right)\cos(\omega_+ t + \varphi_{\text{in}}) - \frac{\alpha}{2}\cos(\omega_- t - \varphi_{\text{in}}) \\ &\quad - \frac{\beta}{2}(1+\alpha)\Big[\sin(\omega_+ t + \varphi_{\text{in}}) + \sin(\omega_- t - \varphi_{\text{in}})\Big]. \end{aligned} \tag{I.4}$$

This shows that for small but finite imbalance $\alpha, \beta \ll 1$, in addition to the desired RF signal, the IQ mixing gives also rise to a spurious signal at the lower sideband frequency $\omega_-$. These mixer imperfections are known to decrease with increasing LO power, therefore the initial LO tone generated by a microwave source is generally first amplified to typically $15 - 20$ dBm before entering the mixer. Even under these conditions, the amplitude and phase imbalances remain significant and corrections are needed to suppress or at least minimize the lower sideband signal. To do so, we compensate by applying I and Q signals with slightly different amplitudes and phases obtained from a preliminary calibration, involving a spectrum analyzer to minimize the power at the unwanted sideband.

## I.2 Demodulation

Now, after routing $S_{\text{in}}(t)$ to the sample, we want to detect the outgoing signal $S_{\text{out}}(t) = \mathscr{F}^{-1}\{\mathscr{F}\{S_{\text{in}}(t)\} \cdot S_{21}(\omega)\} \equiv A_{\text{out}}(t)\cos(\omega_{\text{RF}} t + \varphi_{\text{out}})$ and extract its amplitude and phase, which encode information on the weak link state. This process of extracting the waveform information $\{A_{\text{out}}, \varphi_{\text{out}}\}$ of a modulated signal is called "demodulation". As we will show, it can be thought about as a projection from the waveform space onto a 2D plane with coordinates I and Q.

For $S_{\text{in}}(t)$ given by a square unit-step or a fast-load pulse, the analytical expression for the outgoing signal was derived in the previous section using complex amplitude notations (see Eqs. (9.5, 9.13)). To relate to this complex notation, we can express the real input signal $S_{\text{in}}(t)$ in terms of its I and Q components :

$$\begin{aligned} S_{\text{in}}(t) &= A_{\text{in}}(t)\cos(\omega_{\text{RF}} t + \varphi_{\text{in}}) \\ &= A_{\text{in}}(t)\Big[\cos(\omega_{\text{RF}} t)\cos(\varphi_{\text{in}}) - \sin(\omega_{\text{RF}} t)\sin(\varphi_{\text{in}})\Big] \\ &= I_{\text{in}}(t)\cos(\omega_{\text{RF}} t) + Q_{\text{in}}(t)\sin(\omega_{\text{RF}} t) \end{aligned} \tag{I.5}$$

$$\text{with} \begin{cases} I_{\text{in}}(t) = A_{\text{in}}(t)\cos(\varphi_{\text{in}}) \\ Q_{\text{in}}(t) = -A_{\text{in}}(t)\sin(\varphi_{\text{in}}) \end{cases},$$

which shows that any signal can be described by a point in a 2D plane, determined by its amplitude $A_{\text{in}}(t)$ and phase $\varphi_{\text{in}}$ (see Figure I.2). With this, we can rewrite the input signal in terms of real and imaginary parts of a complex amplitude input, for which we know the associated output

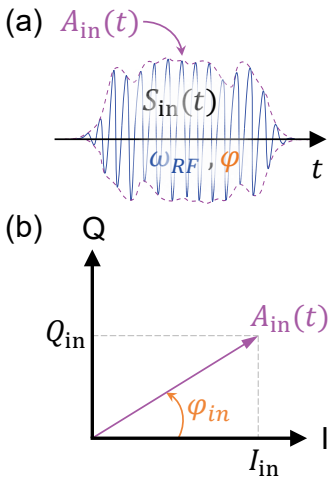


**Figure I.2:** (a) A microwave pulse is described as a slowly varying waveform $A_{\text{in}}(t)$ on a fast-oscillating carrier at the frequency $\omega_{\text{RF}}$ and phase $\varphi_{\text{in}}$. (b) Any such signal can be decomposed into its in-phase (I) and quadrature (Q) components in a frame rotating at frequency $\omega$. $\varphi_{\text{in}}$ is counted clockwise to keep with the minus sign convention in Q.

from Eqs. (9.8, 9.15):

$$S_{\text{in}}(t) = \text{Re}\left[I_{\text{in}}(t)e^{j\omega_{\text{RF}}t}\right] + \text{Im}\left[Q_{\text{in}}(t)e^{j\omega_{\text{RF}}t}\right]. \tag{I.6}$$

By linearity of the response, the real output signal $S_{\text{out}}(t)$ is then obtained by simply adding up the two responses for the real and imaginary parts.

Once the input signal at frequency $\omega_{\text{RF}}$ has crossed the sample transmission line, a *heterodyne detection* is performed (see Figure I.3) by down-converting the output signal $S_{\text{out}}(t) = A_{\text{out}}(t)\cos(\omega_{\text{RF}}t + \varphi_{\text{out}})$ using another IQ mixer with the same LO tone that was used for the single-sideband generation (this ensures that a well-defined phase relation between input and output signals is maintained). The output signal picked on the I port is then given by :

$$\begin{aligned} I_{\text{out}}(t) &\propto A_{\text{out}}(t)\cos(\omega_{\text{LO}}t)\cos(\omega_{\text{RF}}t + \varphi_{\text{out}}) \\ &= \frac{A_{\text{out}}(t)}{2}\left[\cos(\omega_{\text{IF}}t + \varphi_{\text{out}}) + \cancel{\cos\left((2\omega_{\text{LO}} + \omega_{\text{IF}})t + \varphi_{\text{out}}\right)}\right] \\ &\approx \frac{A_{\text{out}}(t)}{2}\cos(\omega_{\text{IF}}t + \varphi_{\text{out}}), \end{aligned} \tag{I.7}$$

where the second term oscillating at $2\omega_{\text{LO}} + \omega_{\text{IF}}$ is discarded by low-pass filtering above $2\omega_{\text{IF}}$. Similarly, the output signal on the Q port is :

$$\begin{aligned} Q_{\text{out}}(t) &\propto -A_{\text{out}}(t)\sin(\omega_{\text{LO}}t)\cos(\omega_{\text{RF}}t + \varphi_{\text{out}}) \\ &= -\frac{A_{\text{out}}(t)}{2}\left[\cancel{\sin\left((2\omega_{\text{LO}} + \omega_{\text{IF}})t + \varphi_{\text{out}}\right)} - \sin((\omega_{\text{IF}})t + \varphi_{\text{out}})\right] \\ &\approx \frac{A_{\text{out}}(t)}{2}\sin(\omega_{\text{IF}}t + \varphi_{\text{out}}). \end{aligned} \tag{I.8}$$

These two signals $\{I_{\text{out}}(t), Q_{\text{out}}(t)\}$ are subsequently digitized with a sampling period $\delta t$ in a chosen time window during which their amplitude $A_{\text{out}}$ remains constant:

$$\begin{cases} I_{\text{out}}[k] = \dfrac{A_{\text{out}}}{2}\cos[\omega_{\text{IF}}k\delta t + \varphi_{\text{out}}] \\ Q_{\text{out}}[k] = \dfrac{A_{\text{out}}}{2}\sin[\omega_{\text{IF}}k\delta t + \varphi_{\text{out}}]. \end{cases} \tag{I.9}$$

Applying the same procedure as for the input signal $S_{\text{in}}(t)$ in Eq. (I.5), one can rewrite the two output signals in terms of their I and Q components with respect to $\omega_{\text{IF}}$ :

$$\begin{cases} I_{\text{out}}[k] \propto \underbrace{\left[\dfrac{A_{\text{out}}}{2}\cos(\varphi_{\text{out}})\right]}_{I_1}\cos[\omega_{\text{IF}}k\delta t] + \underbrace{\left[-\dfrac{A_{\text{out}}}{2}\sin(\varphi_{\text{out}})\right]}_{Q_1}\sin[\omega_{\text{IF}}k\delta t] \\ Q_{\text{out}}[k] \propto \underbrace{\left[\dfrac{A_{\text{out}}}{2}\sin(\varphi_{\text{out}})\right]}_{I_2}\cos[\omega_{\text{IF}}k\delta t] + \underbrace{\left[\dfrac{A_{\text{out}}}{2}\cos(\varphi_{\text{out}})\right]}_{Q_2}\sin[\omega_{\text{IF}}k\delta t]. \end{cases}$$

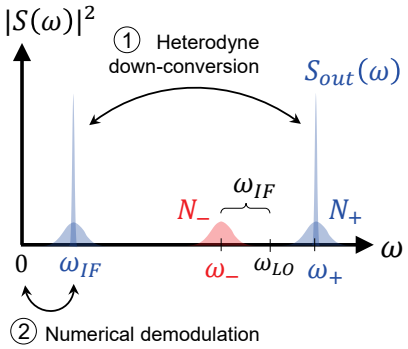


**Figure I.3:** Frequency representation of the demodulation and heterodyne detection processes. The output signal $S_{\text{out}}(t) = A_{\text{out}}\cos(\omega_{\text{RF}}t + \varphi_{\text{out}})$ at frequency $\omega_{\text{RF}} = \omega_+$ is mixed with a strong LO tone. After low-pass filtering, the resulting I and Q outputs, oscillating at the intermediate frequency $\omega_{\text{IF}}$ are digitized and then demodulated numerically to recover the slowly-varying amplitude $A_{\text{out}}$

In practice, these I and Q components are obtained by numerical demodulation of $\{I_{\text{out}}[k], Q_{\text{out}}[k]\}$ at the intermediate frequency $\omega_{\text{IF}}$ :

$$\begin{bmatrix} I_{\text{out,cos}} \\ Q_{\text{out,cos}} \end{bmatrix} \equiv \frac{2}{N} \sum_{k=0}^{N} \begin{bmatrix} I_{\text{out}}[k] \\ Q_{\text{out}}[k] \end{bmatrix} \cos\left[k\omega_{\text{IF}}\delta t\right] \approx \frac{A_{\text{out}}}{2} \begin{bmatrix} \cos\left(\varphi_{\text{out}}\right) \\ \sin\left(\varphi_{\text{out}}\right) \end{bmatrix} = \begin{bmatrix} I_1 \\ I_2 \end{bmatrix}, \tag{I.10}$$

where the second equality is obtained assuming that the sample size corresponds to an integer number of periods: $N\delta t \times \frac{\omega_{\text{IF}}}{2\pi} \in \mathbb{N}$. If this is not verified, a residual error scaling as $\propto 1/N$ will be present. Similarly,

$$\begin{bmatrix} I_{\text{out,sin}} \\ Q_{\text{out,sin}} \end{bmatrix} \equiv \frac{2}{N} \sum_{k=0}^{N} \begin{bmatrix} I_{\text{out}}[k] \\ Q_{\text{out}}[k] \end{bmatrix} \sin\left[k\omega_{\text{IF}}\delta t\right] \approx \frac{A_{\text{out}}}{2} \begin{bmatrix} -\sin\left(\varphi_{\text{out}}\right) \\ \cos\left(\varphi_{\text{out}}\right) \end{bmatrix} = \begin{bmatrix} Q_1 \\ Q_2 \end{bmatrix}. \tag{I.11}$$

From this decomposition, we see that by computing the following combinations, one can extract the amplitude $A_{\text{out}}$ of the outgoing signal :

$$\begin{cases} I_{\text{demod}} & \equiv +I_1 + Q_2 = A_{\text{out}} \cos\left(\varphi_{\text{out}}\right) \\ Q_{\text{demod}} & \equiv -Q_1 + I_2 = A_{\text{out}} \sin\left(\varphi_{\text{out}}\right), \end{cases} \tag{I.12}$$

from which we easily recover the output amplitude and phase :

$$\begin{cases} A_{\text{out}} = \sqrt{I_{\text{demod}}^2 + Q_{\text{demod}}^2} \\ \varphi_{\text{out}} = \arctan\left(Q_{\text{demod}}/I_{\text{demod}}\right). \end{cases} \tag{I.13}$$

In practice, $I_{\text{demod}}$ and $Q_{\text{demod}}$ are obtained by computing numerically the real and imaginary part of the following complex amplitude :

$$\begin{aligned} A_{\text{demod}} &= \frac{2}{N} \sum_{k=0}^{N} \Big( I_{\text{out}}[k] + jQ_{\text{out}}[k] \Big) e^{-jk\omega_{\text{IF}}\delta t} \\ &= \frac{2}{N} \sum_{k=0}^{N} \Big( I_{\text{out}}[k] + jQ_{\text{out}}[k] \Big) \Big( \cos\left(k\omega_{\text{IF}}\delta t\right) - j\sin\left(k\omega_{\text{IF}}\delta t\right) \Big) \\ &= \frac{2}{N} \sum_{k=0}^{N} \Big( \underbrace{I_{\text{out}}[k]\cos\left(k\omega_{\text{IF}}\delta t\right)}_{\to I_1} + \underbrace{Q_{\text{out}}[k]\sin\left(k\omega_{\text{IF}}\delta t\right)}_{\to Q_2} \Big) \\ &\quad + j\Big( \underbrace{Q_{\text{out}}[k]\cos\left(k\omega_{\text{IF}}\delta t\right)}_{\to I_2} - \underbrace{I_{\text{out}}[k]\sin\left(k\omega_{\text{IF}}\delta t\right)}_{\to Q_1} \Big), \end{aligned} \tag{I.14}$$

from which we finally deduce :

$$\begin{cases} I_{\text{demod}} = \text{Re}[A_{\text{demod}}] \\ Q_{\text{demod}} = \text{Im}[A_{\text{demod}}]. \end{cases} \tag{I.15}$$

Importantly, the advantage of computing the four demodulation products $I_1$ , $Q_1$ , $I_2$ and $Q_2$ instead of just performing $I_{\text{demod}} = 2I_1$ and $Q_{\text{demod}} = 2I_2$ is that the particular combinations given in Eq. (I.12) happen to cancel out any spurious signal possibly transmitted at the lower sideband frequency $\omega_-$, resulting from the imperfection of the IQ mixers. Indeed, redoing the same derivation above for a signal $N_-(t) = N_- \cos\left(\omega_- t + \varphi_-\right)$, we would find the following expressions for the two signals at the mixer

output :

$$\begin{cases} I_{\omega_-}(t) \propto \underbrace{\left[+\frac{N_-}{2}\cos(\varphi_-)\right]}_{I_{1,-}}\cos(\omega_{\mathrm{IF}}t) + \underbrace{\left[+\frac{N_-}{2}\sin(\varphi_-)\right]}_{Q_{1,-}}\sin(\omega_{\mathrm{IF}}t) \\ Q_{\omega_-}(t) \propto \underbrace{\left[+\frac{N_-}{2}\sin(\varphi_-)\right]}_{I_{2,-}}\cos(\omega_{\mathrm{IF}}t) + \underbrace{\left[-\frac{N_-}{2}\cos(\varphi_-)\right]}_{Q_{2,-}}\sin(\omega_{\mathrm{IF}}t), \end{cases}$$

and then :

$$\begin{cases} I_{\mathrm{demod},-} & \equiv +I_{1,-} + Q_{2,-} = 0 \\ Q_{\mathrm{demod},-} & \equiv -Q_{1,-} + I_{2,-} = 0. \end{cases} \tag{I.16}$$

Note that the above derivation was performed assuming ideal IQ mixers. The finite imbalance of real components will naturally prevent from reaching perfect cancellation of the lower sideband. Still, it is good practice to perform the numerical demodulation this way.

# Towards measurements of ABS at high magnetic fields

J

*In this Appendix, I present the progress made towards the ABS spectroscopy under high axial magnetic field.*

During my thesis work, the highest field we applied was a few tens of mT, which was enough to get a measurable Zeeman shift of the Andreev levels and confirm the spin nature of the measured transitions [51]. We did not explore the behavior at higher fields mainly due to three reasons. First, we observed that the internal quality factor of sCPW resonators degrades at moderate fields much smaller than the critical field of the resonators' material ($H_{c2} \sim 6$ T in NbTiN). It is well known that NbTiN is a type-II superconductor and that even a small magnetic field ($H_{c1} \sim 1\mu$T) results in the creation of Abrikosov vortices. When exposed to microwave fields, vortices oscillate causing dissipation. In order to mitigate this problem and keep internal quality factor high, next generation of resonators has to minimize the number of vortices (for example by using a CPS topology instead of CPW and eliminating the contribution of large superconducting ground planes) and to limit their dynamics (by introducing pinning centers for vortices into the regions where microwave currents take place). The last point is discussed in Ref. [147]. In this work, Kroll *et al.* reported high-Q resonators under parallel field up to 6 T by introducing lithographically defined defects to pin vortices.

Second, the connection between the thin (~25 nm) Al-shell of nanowires and the NbTiN of the resonator is made of ~130 nm thick Al. This thickness cannot be reduced to ensure a reliable connection and hence the Al will become normal above ~10 mT even for parallel fields. In order to circumvent this problem Al patches must be replaced by a superconducting layer supporting high magnetic fields like for example NbTiN. This requires to develop a new nanofabrication step combining Ar etching to eliminate the Alumina layer on top of the nanowires with sputtering NbTiN deposition through a PMMA mask.

Third, any small misalignment in the field would contribute to a perpendicular flux through the chip and therefore, once the first two issues has been solved, perturb the phase bias of the weak link. In such conditions, probing the Andreev spectrum by microwave spectroscopy would become challenging, as the superconducting phase difference $\delta$ would need to be continuously readjusted each time the field would be swept. To avoid such a complication, a straightforward improvement would be to switch to a *gradiometric* design [148, 149], where the nanowire would be embedded in two adjacent symmetric superconducting loops instead of one (see Figure J.1). Any external uniform field would contribute to equal fluxes through each of the two symmetric loops and therefore generate equal currents that are canceled out at the junction, thus rendering the device insensitive to first order to any misalignment in the parallel Zeeman field (Figure J.1a). More generally, even when no Zeeman field is to be applied, implementing such a gradiometric scheme would also have the advantage to help reducing the sensitivity to the ambient magnetic-field

[51]: Tosi et al. (2019), 'Spin-Orbit Splitting of Andreev States Revealed by Microwave Spectroscopy'

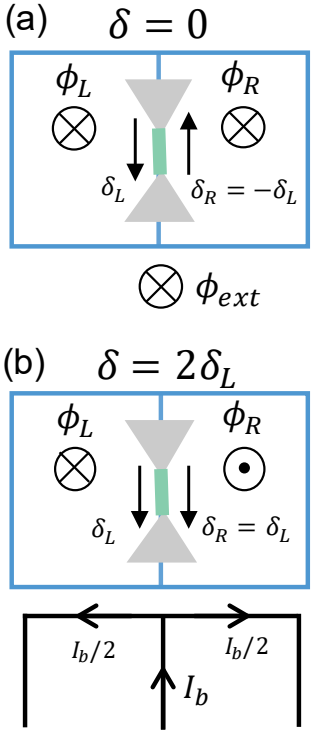


**Figure J.1:** Gradiometric scheme for magnetic field noise insensitive devices. (a) If an external flux $\phi_{\text{ext}}$ is applied, the two loops pick up the same flux so that not net superconducting phase difference arises across the weak link $\delta = 0$. (b) The superconducting phase difference $\delta$ across the nanowire can be generated using a current bias $I_b$ in a nearby flux line. Because the left/right loops are symmetric, the current bias generates opposite fluxes in both loops, so that the partial phase drop at the weak link due to each loop, $\delta_L$ and $\delta_R$, add up constructively.

[147]: Kroll et al. (2019), 'Magnetic-Field-Resilient Superconducting Coplanar-Waveguide Resonators for Hybrid Circuit Quantum Electrodynamics Experiments'

[148]: Pita-Vidal et al. (2020), 'Gate-Tunable Field-Compatible Fluxonium'

[149]: Wesdorp et al. (2021), 'Dynamical polarization of the fermion parity in a nanowire Josephson junction'

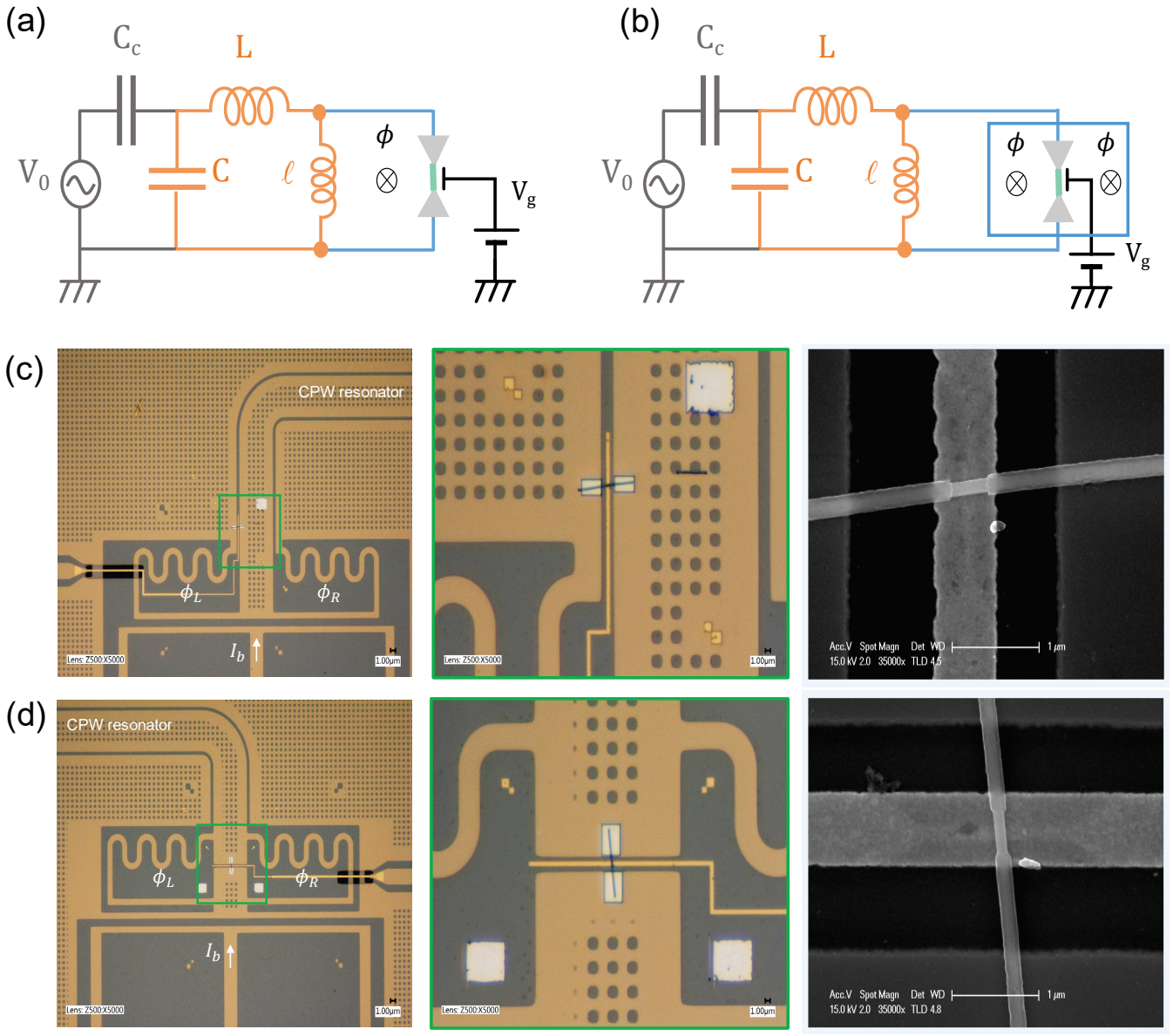


**Figure J.2:** Comparison between the standard (a) and gradiometric (b) design of sCPW resonators. (c) Sample with the standard design where the NW shunts the gap of the CPW resonator on one side, therefore closing the left loop. Note that the inductive wire shorting the CPW has been designed with a wiggly shape to increase its length and crank up the NW/resonator coupling. (d) Sample with gradiometric loops. The NW is deposited on the central condutor of the CPW between the two symmetric loops. A current bias $I_b$ is applied in a nearby flux line that generates opposite fluxes in both loops, as described in Figure J.1 and giving rise to a superconducting phase difference across the weak link. SEM pictures of the nanowire deposited on each device are shown on the right.

noise and therefore likely improve the coherence properties of the device. Note however that in this gradiometric configuration the nanowire cannot be phase biased using the homogeneous magnetic flux $\phi_{\text{ext}}$ of an external coil. One solution is to resort to a local current line to put flux in the nearby loop (Figure J.1b). Although the gradiometric loops are designed to be symmetric, the unavoidable imprecision in the manual deposition of the nanowire would lead to a small imbalance between the effective area of the two gradiometer loops. Therefore, a compensating coil would still be required.

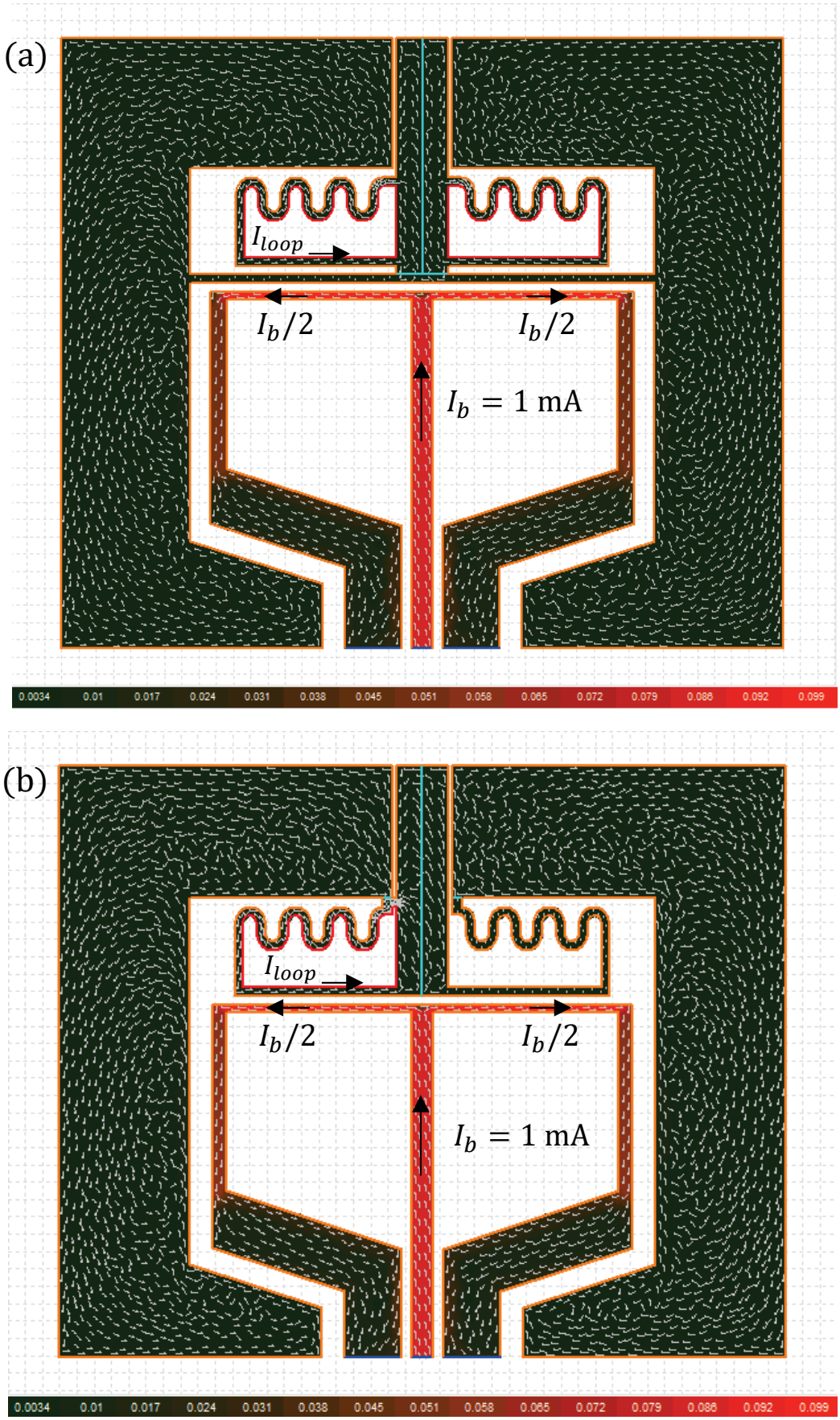


**Figure J.3:** Current distribution in the gradiometric (a) and standard (b) designs when a DC current bias of $I_b = 1$ mA is applied to the flux fline (the differences between the two designs are more visible in Figure J.5, note that in (b) the right loop is not closed). Data was simulated using the 3D-MLSI software for inductance extraction. The direction of the current flow is shown with white arrows and the magnitude of the current density is encoded in colorscale in mA/µm.

To design the current bias line, we need to estimate its mutual coupling $M$ to the weak link loop in order to compute the current bias $I_b$ needed to put one flux quantum in it. Indeed, an arbitrarily high DC current cannot be driven through the flux line, as it could dissipate in the residual resistance of the bias tee and warm up the mixing chamber of the fridge (see Section 13.2 for a schematic of the fridge wiring). The bias tee that we had at hand was measured to have about 1Ω resistance at liquid nitrogen temperature*. Assuming a cooling power of 17 µW at 20 mK, this means we should not drive a current higher than $\sqrt{17\mu W/1\Omega} \approx 4$ mA. With a safety margin of a factor 10, this means that the mutual coupling should be high enough so that a current of $I_b^{\max} = 400\ \mu$A could generate a flux quantum $\phi_0$ in the superconducting loop, *i.e.* we should have $M > \phi_0/I_b^{\max} \approx 5$ pH.

To guide the design of the flux line, we used the simulation tool "3D-MLSI" for extraction of inductances of multilayer superconductor circuits [150]. This software allows for 2D magneto-static simulations by solving numerically the Maxwell-London equations on a triangulated mesh using the finite element method. As well as extracting self and mutual inductances for the defined 2D conductors, it also allows to simulate and visualize the currents flowing in the superconducting films and the 3D magnetic field distribution around them. We used it to simulate two geometries, corresponding to the standard design with an improved coupling and the gradiometric design. The two devices fabricated with these geometries are presented in Figure J.2 and the results of the magneto-static simulations are shown in Figure J.3. They allow to visualize the current distribution in the superconducting film arising from a typical current bias of $I_b = 1$ mA in the flux line. In Figure J.4, we show for each geometry the dependence of the mutual inductance $M$ on the distance $d$ separating the current line to the superconducting loops. Using the nominal loop length $L = 93\ \mu$m and assuming an effective loop width $w_{\text{eff}} = 8.9\ \mu$m, it can be well fitted by the simple analytical formula estimating the mutual coupling between a rectangular loop and a straight wire assuming infinitely thin wires [21] :

$$M = \frac{\mu_0}{2\pi} L \ln\left(\frac{d+w}{d}\right), \tag{J.1}$$

where $w$ is the width of the rectangular loop and $L$ its length. Results for the geometries of the two fabricated devices are plotted in Figure J.3 and a zoom-in around the loop is shown in Figure J.5. The simulation of the standard design — with a $d = 5\ \mu$m gap between the weak link loop and the flux line — gives a mutual inductance $M = 15.6$ pH and a loop inductance $L_{\text{loop}} = 195$ pH (Figure J.5b). The inductance of the flux line is estimated to $L_{\text{fl}} = 857$ pH. From this, we can compute the associated coupling coefficient $k = M/\sqrt{L_{\text{loop}} L_{\text{fl}}} = 38\%$. For the gradiometric design, the presence of a 5 µm wide ground strip between the flux line and the loop (necessary to short the resonator's end to ground) makes the minimal achievable loop-flux line separation necessarily larger. The mutual coupling between both is therefore expected to be weaker ; the simulation yields about a factor 2 difference, we get $M = 7.8$ pH for the gradiometric design and $L_{\text{loop}} = 193$ pH (Figure J.5a). In this case, the

[150]: Khapaev (2004), *3D-MLSI: Extraction of Inductances of Multilayer Superconductor Circuits*

[21]: Janvier (2016), 'Coherent manipulation of Andreev Bound States in an atomic contact', pp.61-62

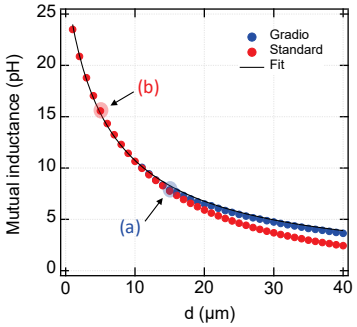


**Figure J.4:** Mutual inductance $M$ as a function of the distance $d$ between the current line and the superconducting loop, simulated using 3D-MLSI for the two geometries described in Figure J.2. The simulated data is fitted with the theory for the coupling between a straight wire and a rectangular loop (Eq. (J.1)). The values of the mutual inductance corresponding to the geometries (a) and (b) of Figure J.5 are highlighted by arrows.

* We later found a better bias tee, SHF's BT45 B (20kHz-45GHz), with about 5 Ω at room temperature but only $R \approx 0.4\ \Omega$ at 77 K.

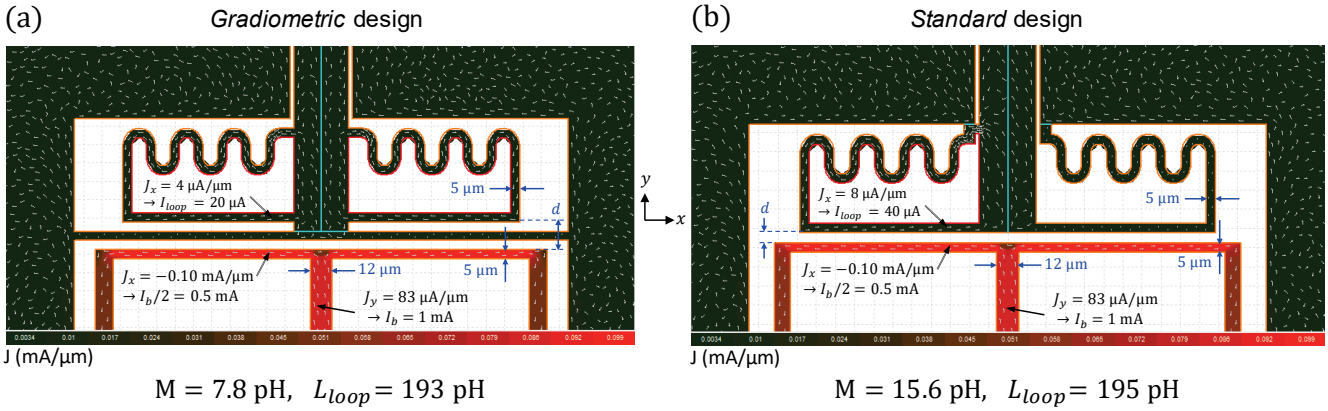


**Figure J.5:** Extraction of the loop inductance $L_{\text{loop}}$ and the mutual inductance $M$ with the flux line for the gradiometric (a) and standard (b) designs. The current density when a DC bias of $I_b = 1$ mA is applied to the flux fline is shown in colorscale. The ratio of the current $I_{\text{loop}}$ induced in the loop to the bias current $I_b/2$ in the left part of the flux line is estimated to $0.02/0.5 = 4\%$ for the gradiometric design and to $0.04/0.5 = 8\%$ for the standard design, which has no ground strip between the loop and the flux line.

coupling coefficient is estimated to $k = M/\sqrt{L_{\text{loop}} L_{\text{fl}}} = 19\%$. For both designs, the mutual is higher than the 5 pH value that we had targeted, therefore it should allow to phase bias properly the nanowire while remaining in a safe mode of operation for the fridge and the device.

When first measuring the devices depicted in Figure J.2, the flux modulation of the resonances was showing a hysteretic and jumpy behaviour. The effect was present both when applying an external flux using the small coil or a DC current in the flux line. We later understood that this was due to a spurious DC loop involving the ground plane around the resonator and a bonding wire that we had put above the flux line to connect the ground planes. This extra loop was therefore screening the external field until the critical current of this loop was reached, at which point it would let some flux enter the loop (which would manifest as a sudden jump in the resonance frequency) and decrease the flux focusing, and so on. Once this bonding wire was removed, the flux bias worked properly.

For the gradiometric resonator, a regular modulation of the resonance frequency was measured, with a period of 0.49 mA. This coincides well with the expected value from simulation, using the $M_{\text{th}} = 7.8$ pH computed by 3D-MLSI : the current should be $\phi_0/M_{\text{th}} = 0.26$ mA, hence 0.52 mA to drive in the flux line (factor 2 because the flux line is left/right symmetric and current is split in two). From the measured value of the period, we therefore estimate the mutual coupling to be $M_{\text{ext}} = 2\phi_0/0.49\text{mA} = 8.4$ pH.

For the standard resonator, without any gradiometric loops, the resonance frequency was also modulating regularly with the applied external flux. For the sample with a galvanic coupling to the nanowire, the weak link loop had a nominal surface of 1000 µm² and the coil period for the resonance modulation was about 0.10 mA. For this new sample with an increased loop surface of 2600 µm², we therefore expected a coil period smaller by a factor 2.6, *i.e.* about 0.039 mA. The voltage that we had to apply on the coil to sweep one period was about 0.021 mA, which is a factor two away from the expected value. Note that there is likely to be some flux focusing around the sample due to the bonding wires, the sample box, etc.

and so an exact agreement with the nominal value was not to be expected. Interestingly, we still measured a modulation of the resonance frequency of the gradiometric resonator when an external flux was applied with the coil, but the coil period was this time measured to be around 0.89 mA, *i.e.* about a factor 40 bigger than for the standard resonator, therefore proving the efficiency of the gradiometric design. Unfortunately this sample had other issues for the spectroscopy applications and we did not measure it further.

# Gallery of two-tone nanowire spectra

K

In the following we present a collection of various two-tone microwave spectra acquired over different cooldowns of the sample S2 for many different values of the gate voltage. The grayscale represents the magnitude of the in-phase (I) and quadrature (Q) components of the demodulated measurement field. Since some transition lines sometimes appear with a better contrast one one quadrature rather than the other, we present both for the sake of completeness. The I quadrature corresponds to the top plot when the spectra are in portrait format or to the left plot when they are in landscape format. The associated single-tone spectroscopy of the resonator is shown below with the same phase axis.

To guide the reading of the spectra, the main transition lines were highlighted in color : the lowest pair transition (red), the lowest set(s) of single-quasiparticle transitions (green) and the four mixed pair transitions (blue), whenever they were visible. Additional lines at higher frequencies, showing phase dispersions reminiscent of pair transitions, may have also been highlighted in blue in some spectra, like in Figures K.22 and K.24. In some of them, intra-manifold spin-flipping transitions are visible at frequencies $f_1 < 5$ GHz (see Figures K.4, K.8, K.9, K.13, K.14 and K.22-K.24). To confirm their identification, their frequency expected from the observed set of single-quasiparticle transitions was plotted in green dotted lines. The dashed lines appearing in some spectra correspond to replicas at $\pm f_r$ of some of the transition lines. In some cases, the full phase dispersion of the mixed pair transitions in solid blue lines could be recovered from their visible replicas at lower frequencies (dashed blue), see Figures K.9, K.10, K.13 and K.26.

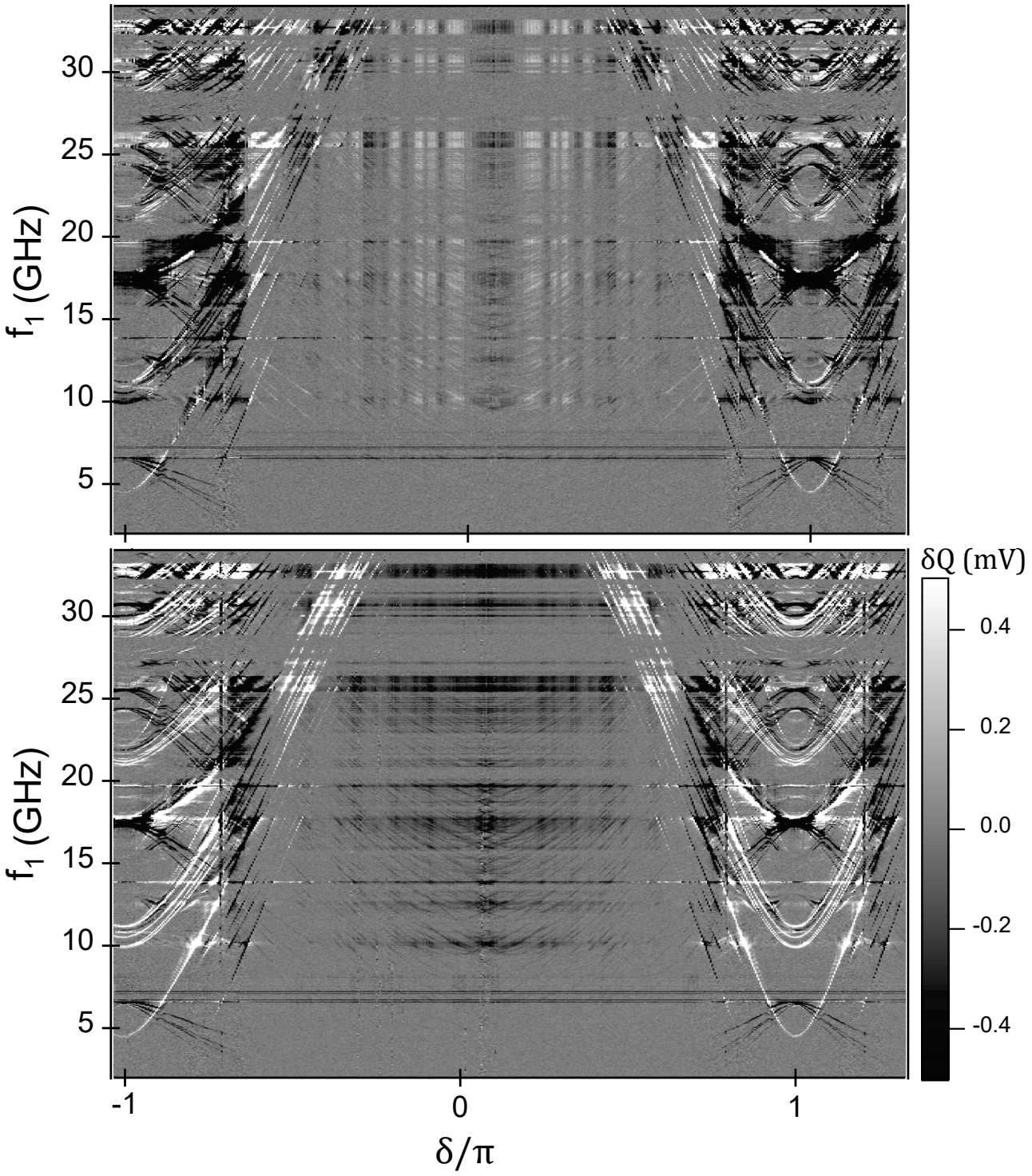


**Figure K.1**

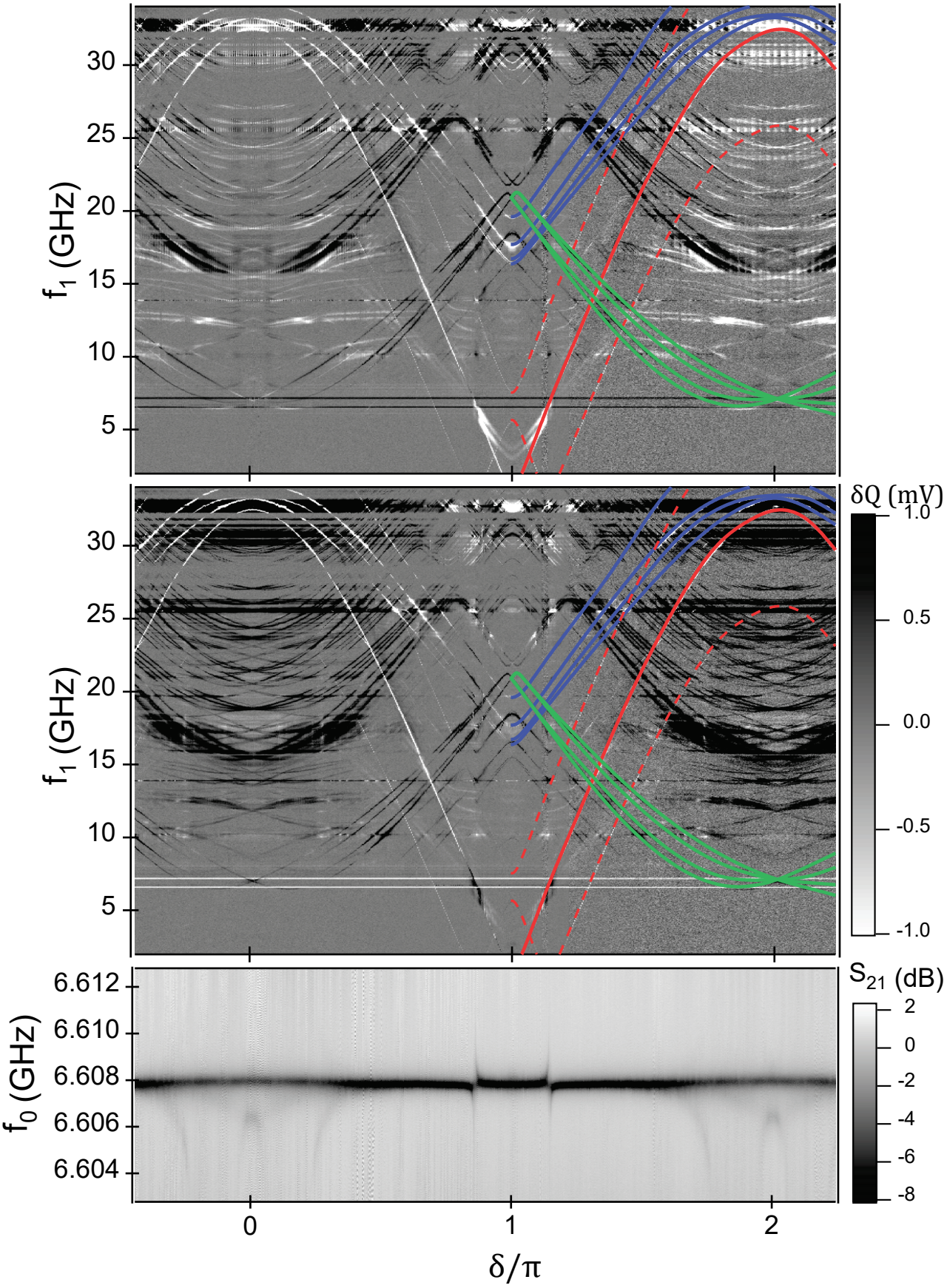
30
25
20
15
10
5
f1 (GHz)
δQ (mV)
1.0
0.5
0.0
-0.5
-1.0
6.612
6.610
6.608
6.606
6.604
f0 (GHz)
S21 (dB)
2
0
-2
-4
-6
-8
0
1
2
δ/π

Figure K.2

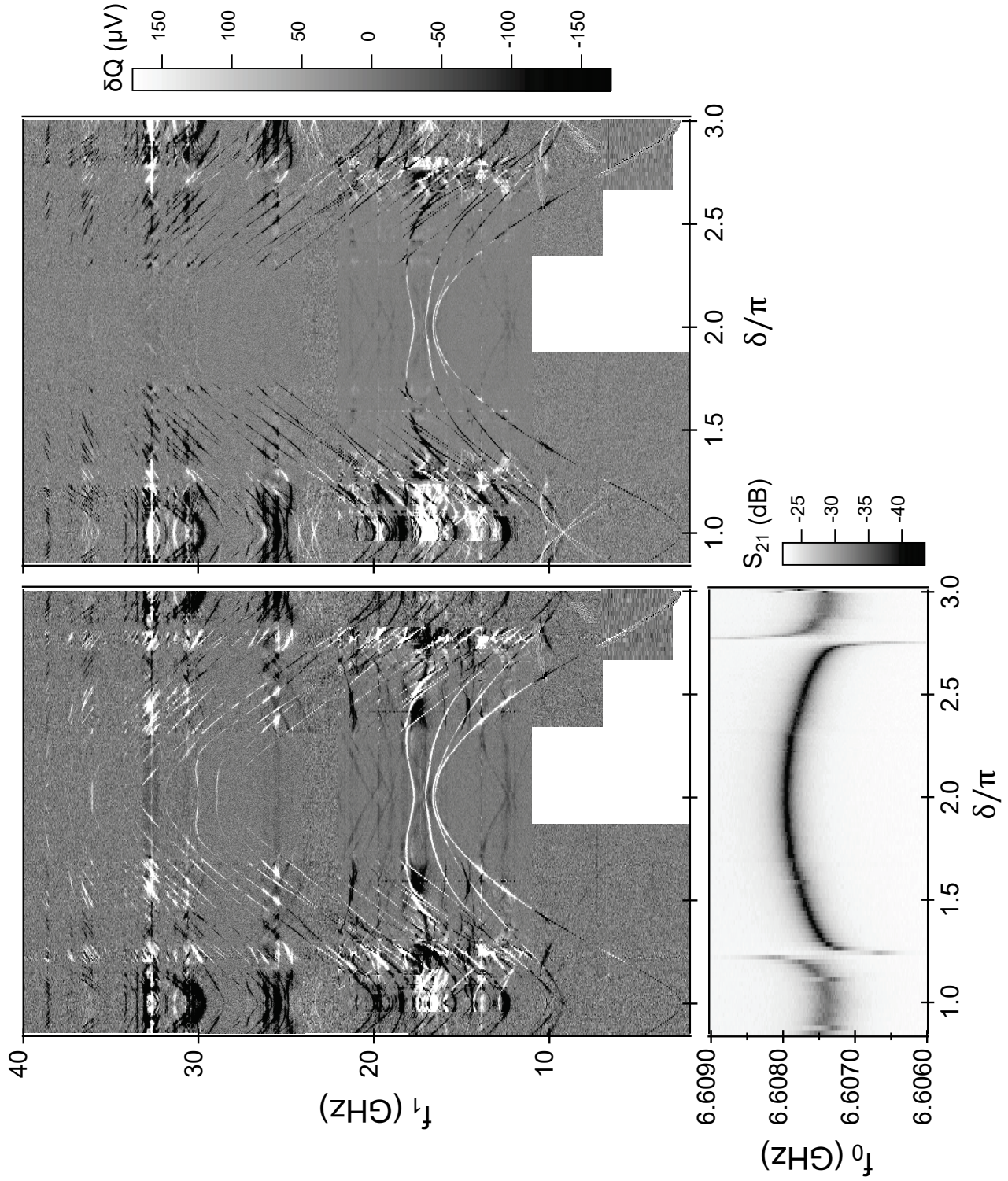
δQ (μV)
150
100
50
0
-50
-100
-150
f₁ (GHz)
40
30
20
10
1.0
1.5
2.0
2.5
3.0
δ/π
S21 (dB)
-25
-30
-35
-40
f₀ (GHz)
6.6090
6.6080
6.6070
6.6060

**Figure K.3**

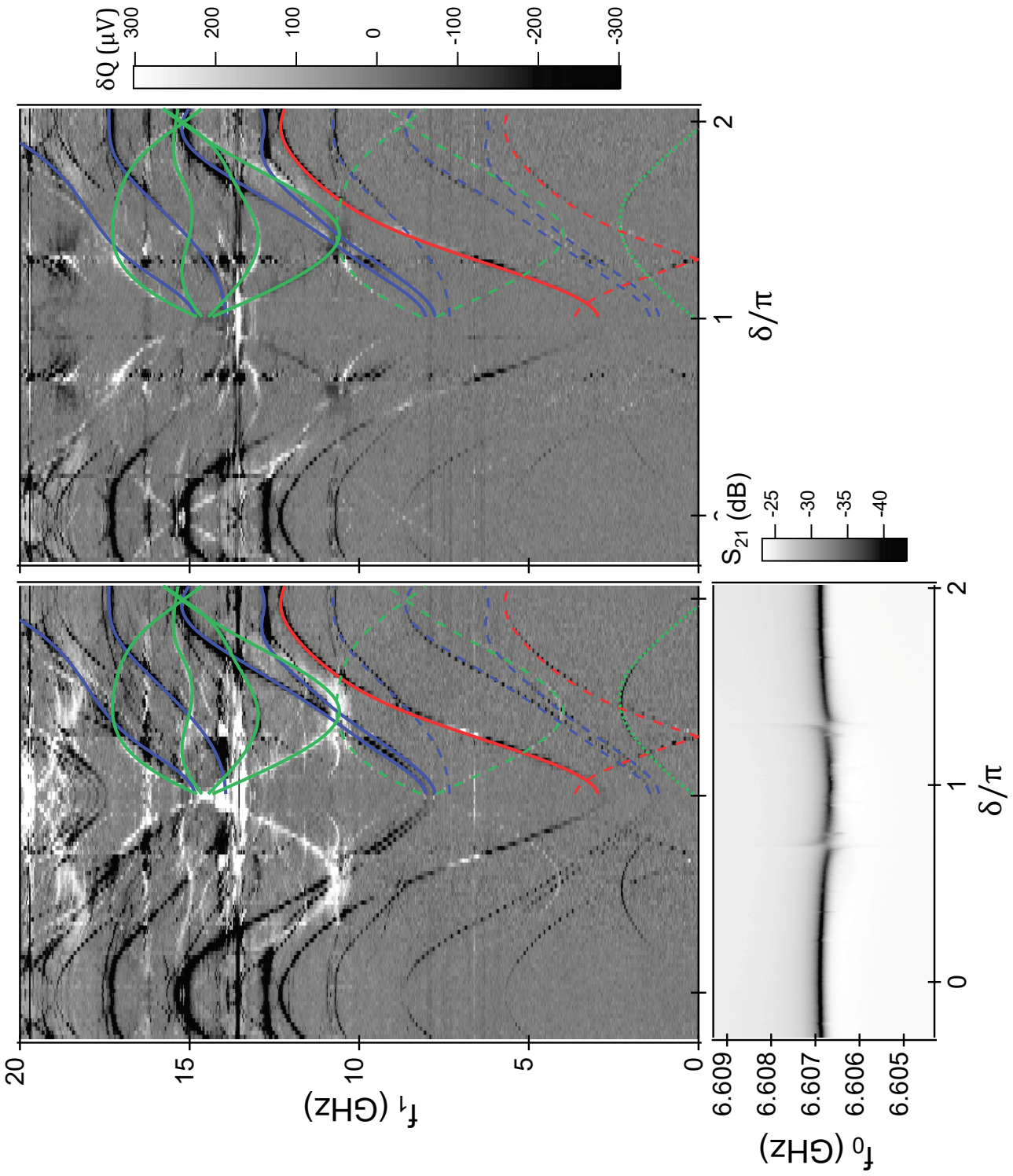
δQ (μV)
300
200
100
0
-100
-200
-300
20
15
10
5
0
f₁ (GHz)
2
1
δ/π
Ŝ21 (dB)
-25
-30
-35
-40
6.609
6.608
6.607
6.606
6.605
f₀ (GHz)
0
1
2
δ/π

**Figure K.4**

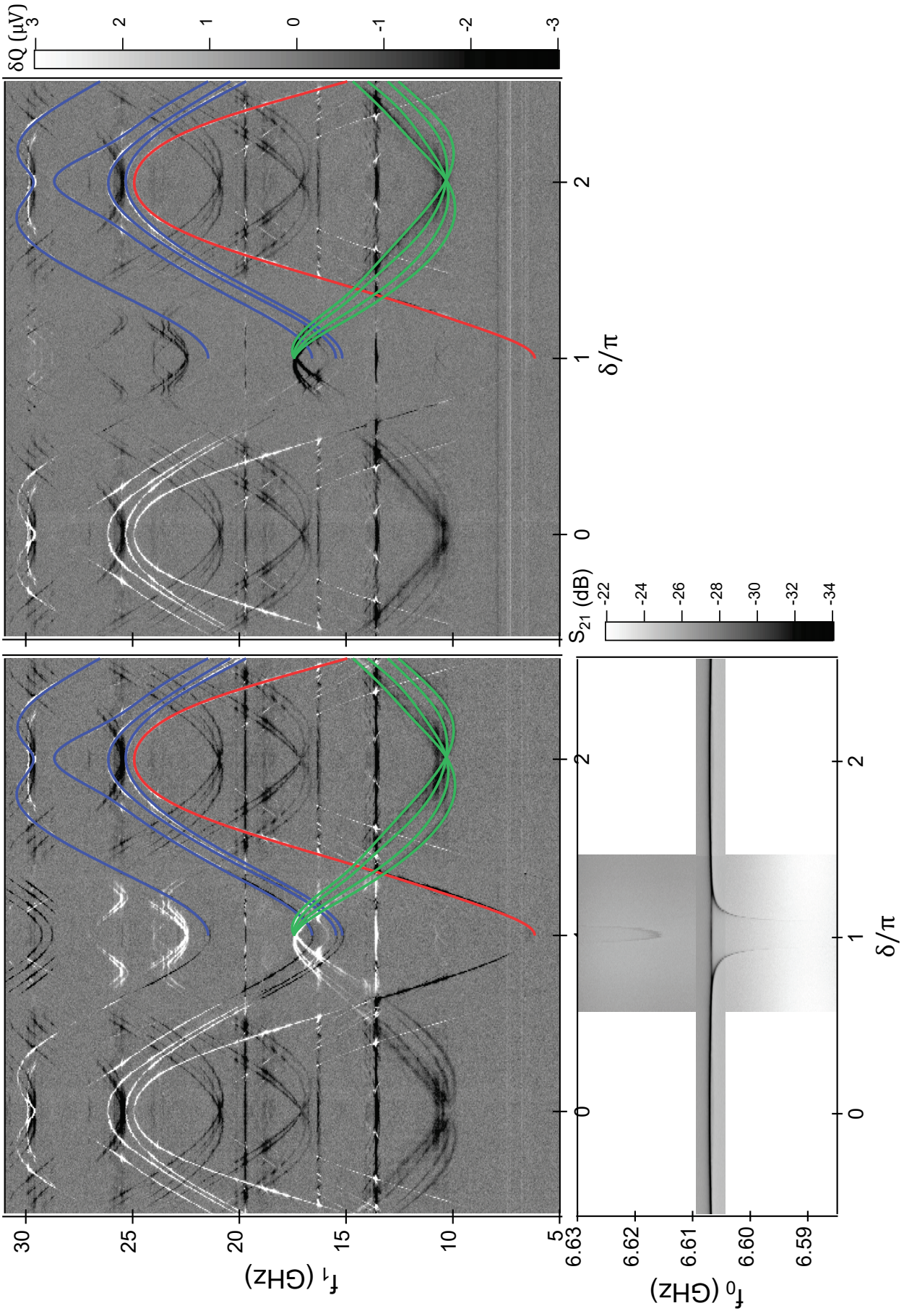
δQ (μV)
3
2
1
0
-1
-2
-3
f₁ (GHz)
30
25
20
15
10
5
δ/π
0
1
2
S21 (dB)
-22
-24
-26
-28
-30
-32
-34
f₀ (GHz)
6.63
6.62
6.61
6.60
6.59

**Figure K.5**

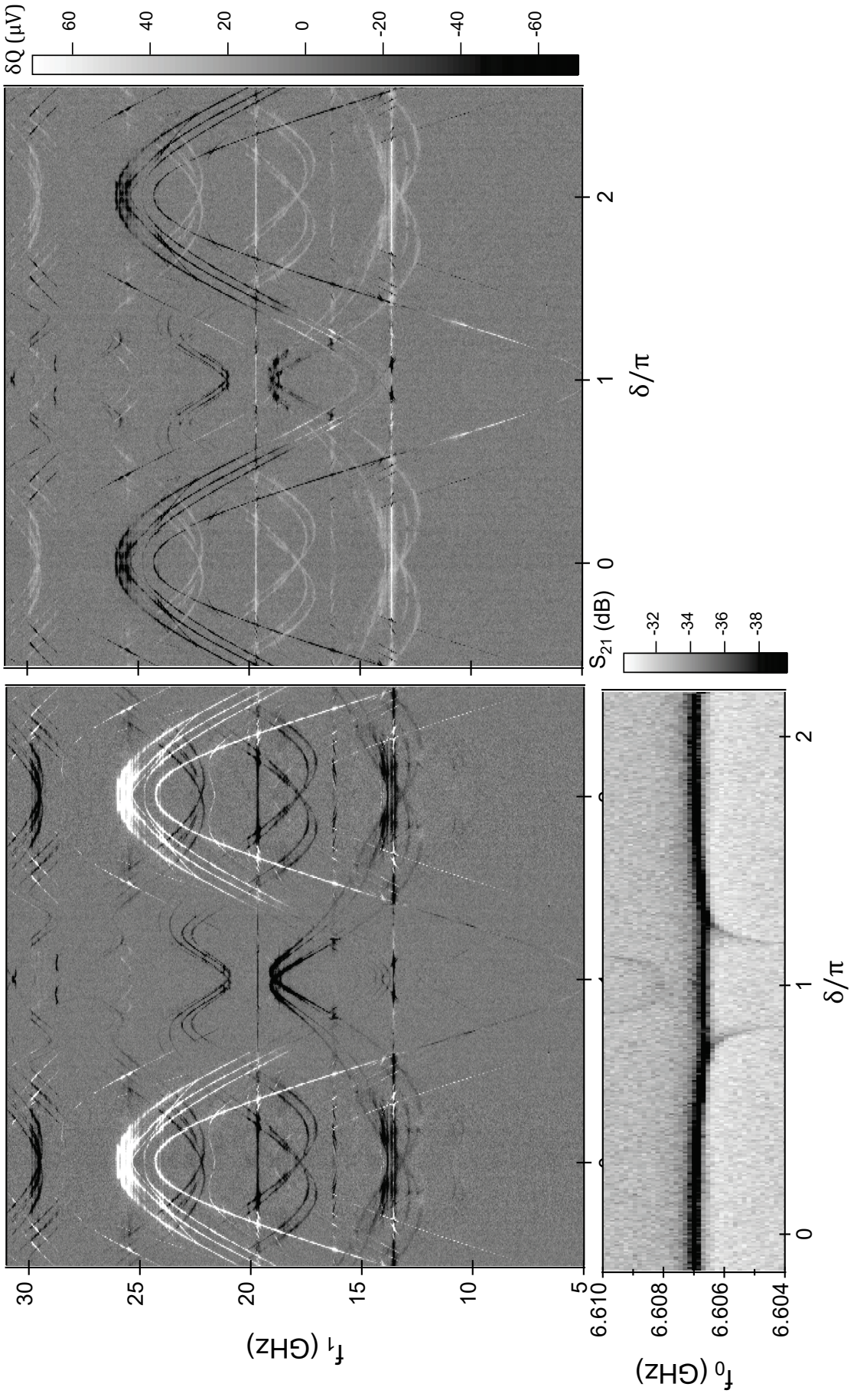


**Figure K.6**

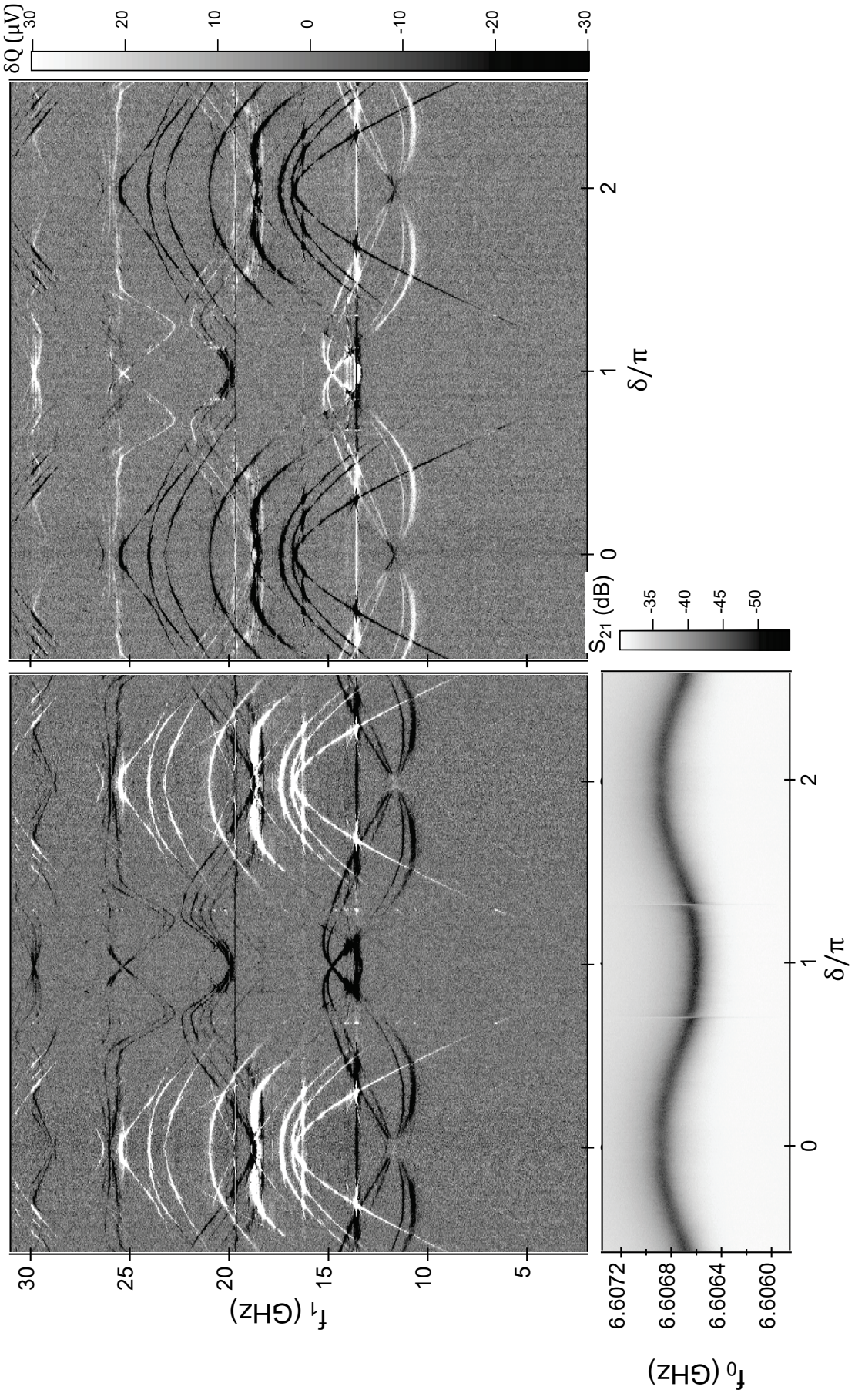
δQ (μV)
30
20
10
0
-10
-20
-30
f₁ (GHz)
30
25
20
15
10
5
0
1
2
δ/π
S21 (dB)
-35
-40
-45
-50
f₀ (GHz)
6.6072
6.6068
6.6064
6.6060
0
1
2
δ/π

**Figure K.7**

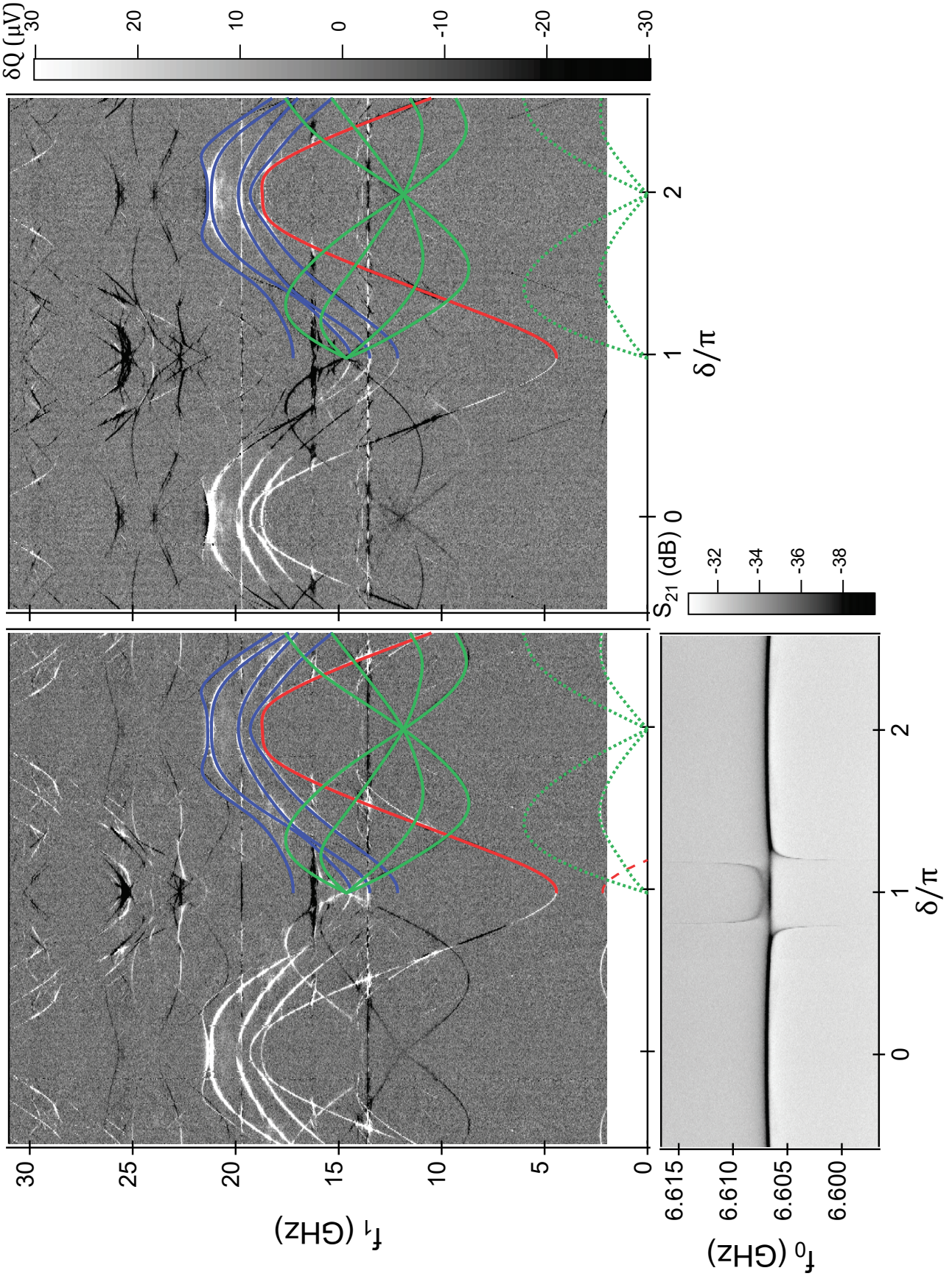
δQ (μV)
30
20
10
0
-10
-20
-30
f₁ (GHz)
30
25
20
15
10
5
0
δ/π
0
1
2
S21 (dB)
-32
-34
-36
-38
f₀ (GHz)
6.615
6.610
6.605
6.600
δ/π
0
1
2

**Figure K.8**

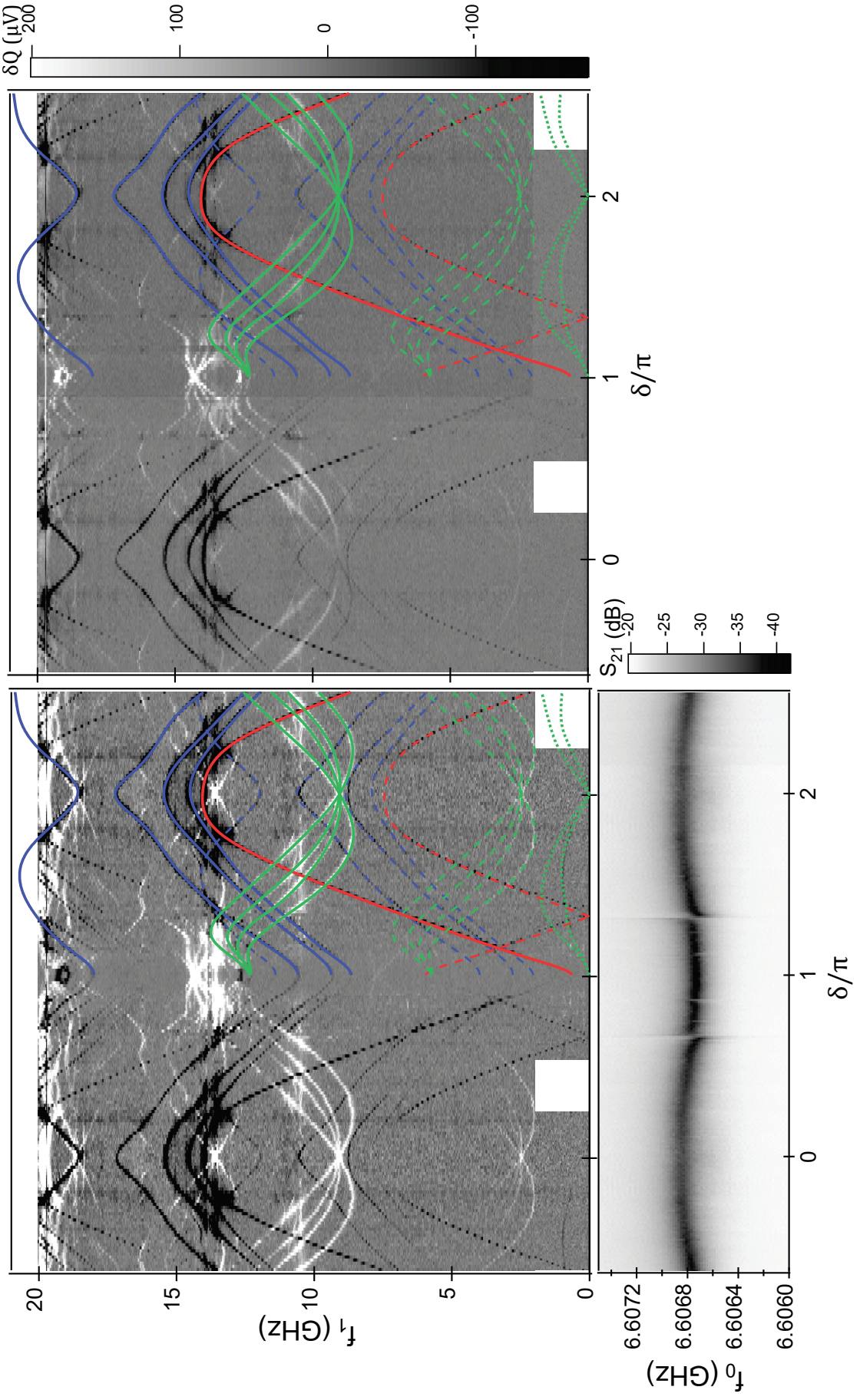
δQ (μV)
200
100
0
-100
f₁ (GHz)
20
15
10
5
0
δ/π
0
1
2
S21 (dB)
-20
-25
-30
-35
-40
f₀ (GHz)
6.6072
6.6068
6.6064
6.6060
δ/π
0
1
2

**Figure K.9**

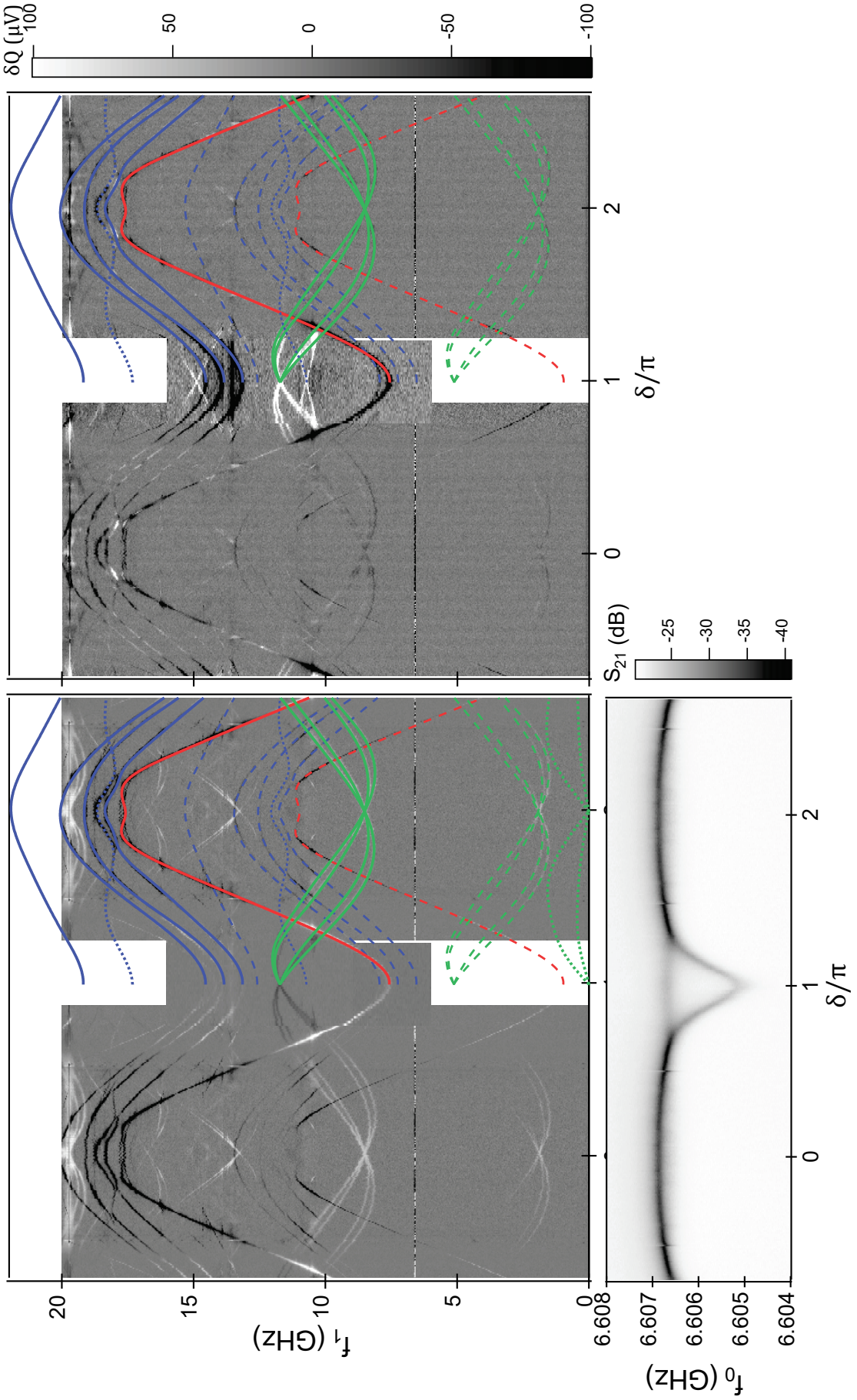
δQ (μV)
100
50
0
-50
-100
f₁ (GHz)
20
15
10
5
0
δ/π
0
1
2
S21 (dB)
-25
-30
-35
-40
f₀ (GHz)
6.608
6.607
6.606
6.605
6.604

**Figure K.10**

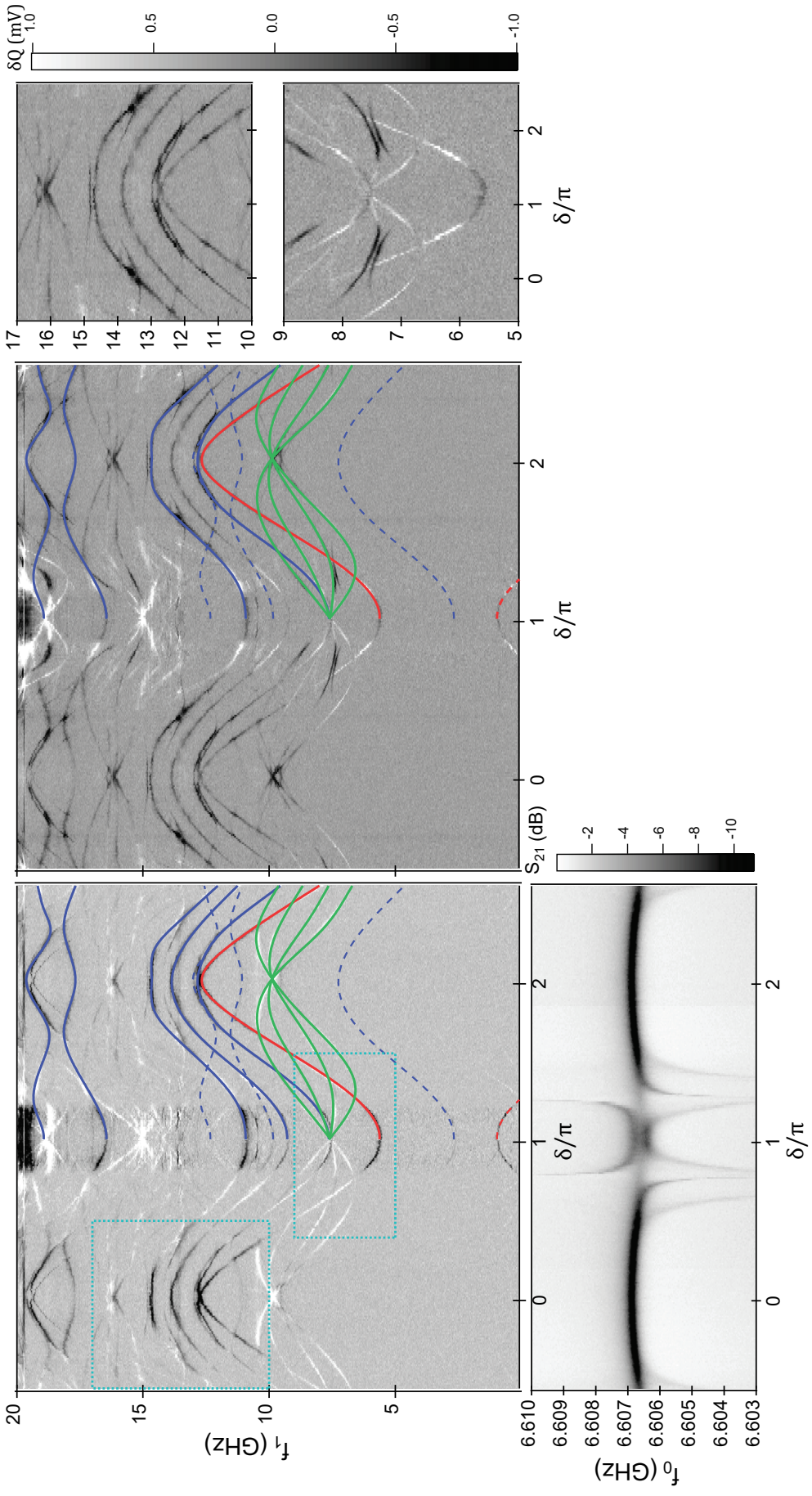


**Figure K.11**

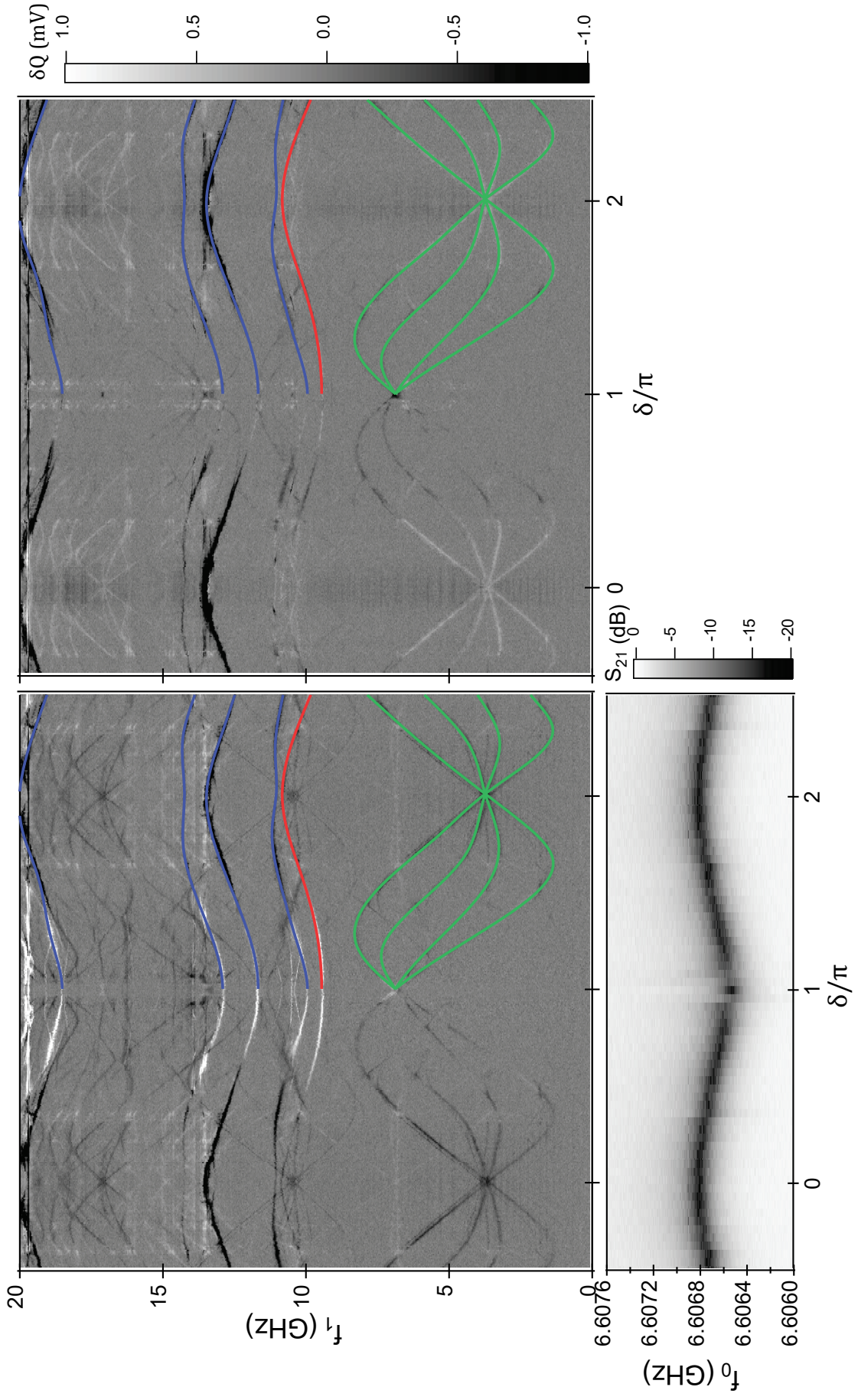
δQ (mV)
1.0
0.5
0.0
-0.5
-1.0
f₁ (GHz)
20
15
10
5
0
δ/π
0
1
2
S21 (dB)
0
-5
-10
-15
-20
f₀ (GHz)
6.6076
6.6072
6.6068
6.6064
6.6060
δ/π
0
1
2

**Figure K.12**

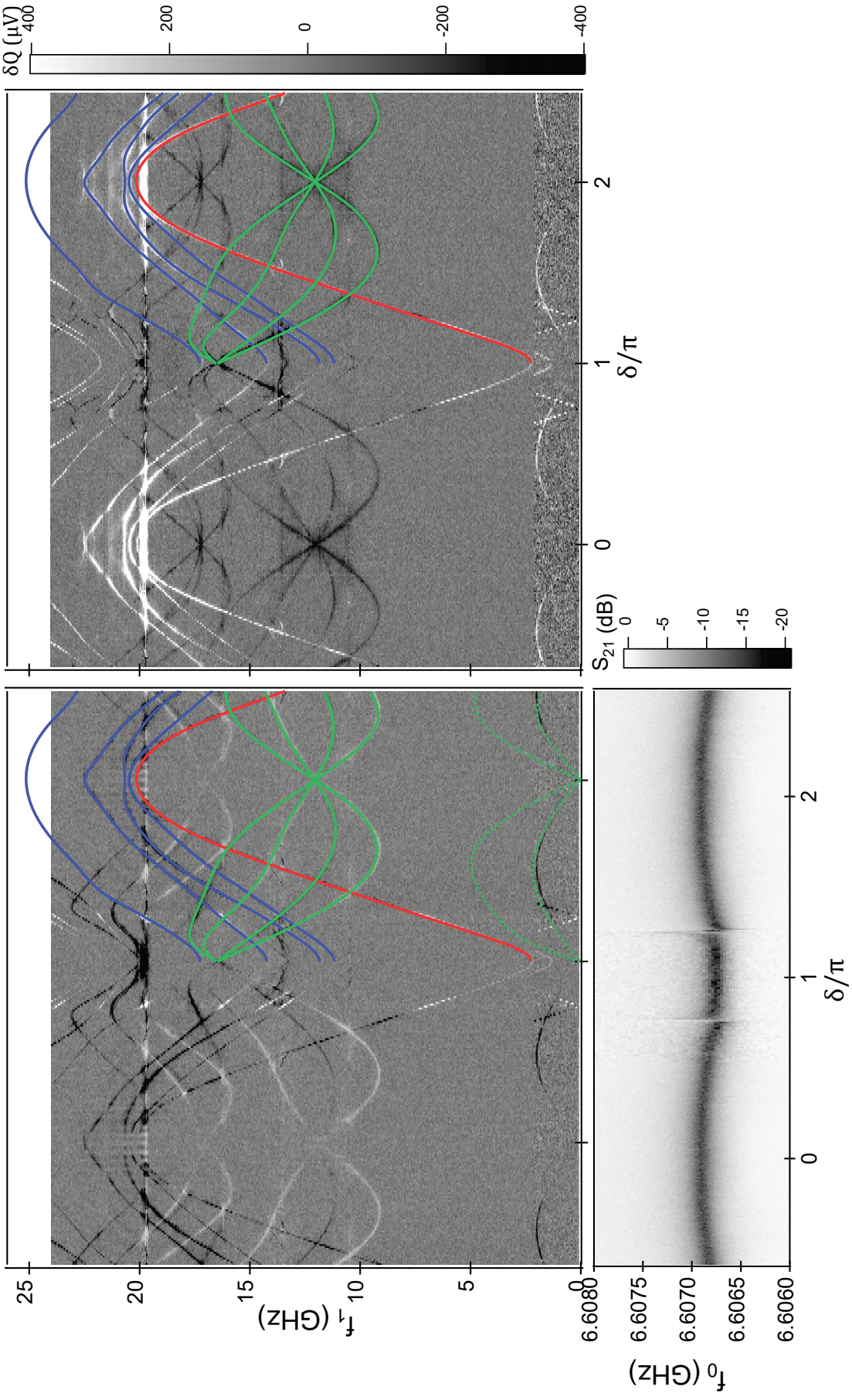
δQ (μV)
400
200
0
-200
-400
f₁ (GHz)
25
20
15
10
5
0
δ/π
0
1
2
S₂₁ (dB)
0
-5
-10
-15
-20
f₀ (GHz)
6.6080
6.6075
6.6070
6.6065
6.6060
δ/π
0
1
2

**Figure K.13**

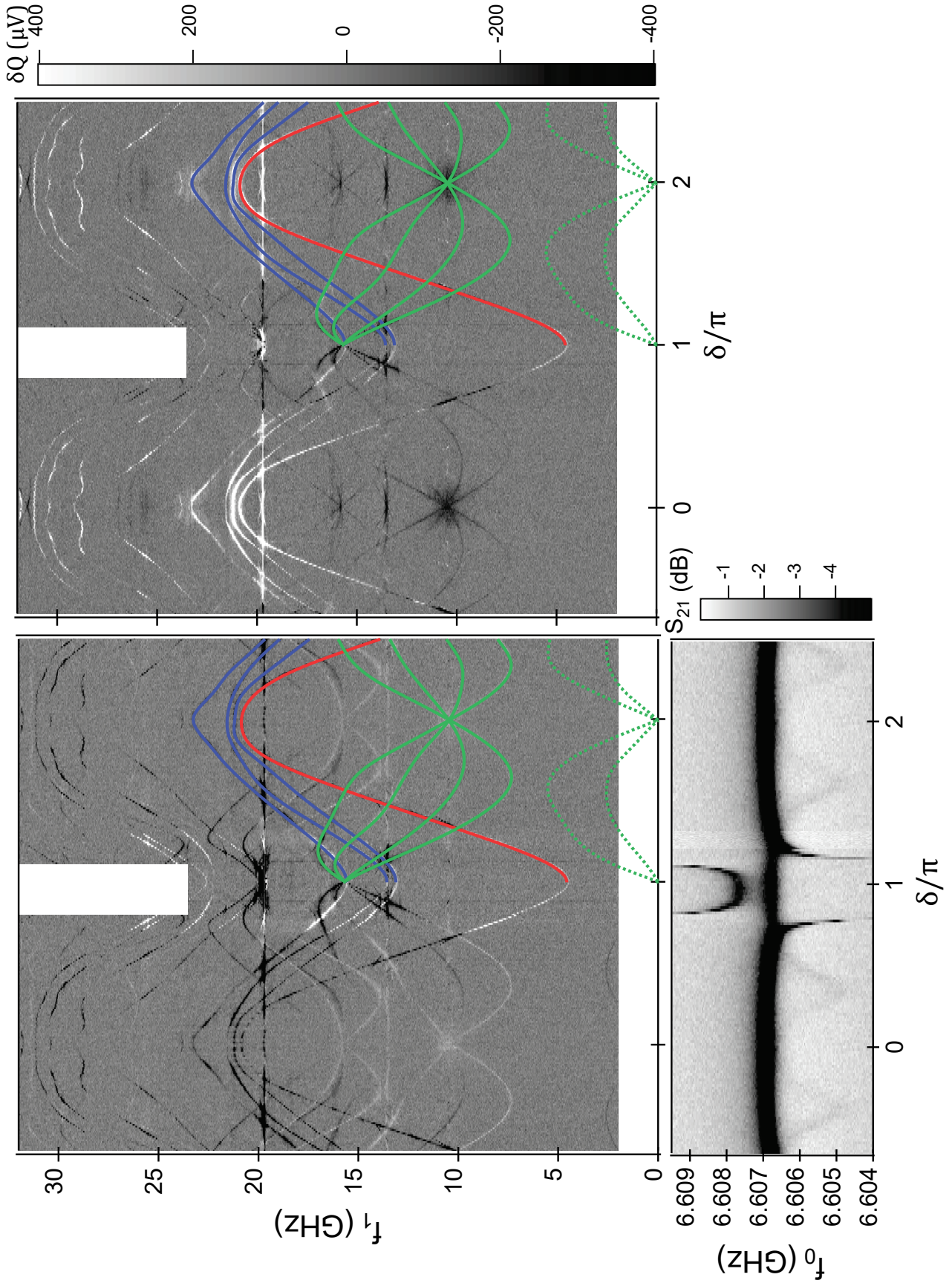


**Figure K.14**

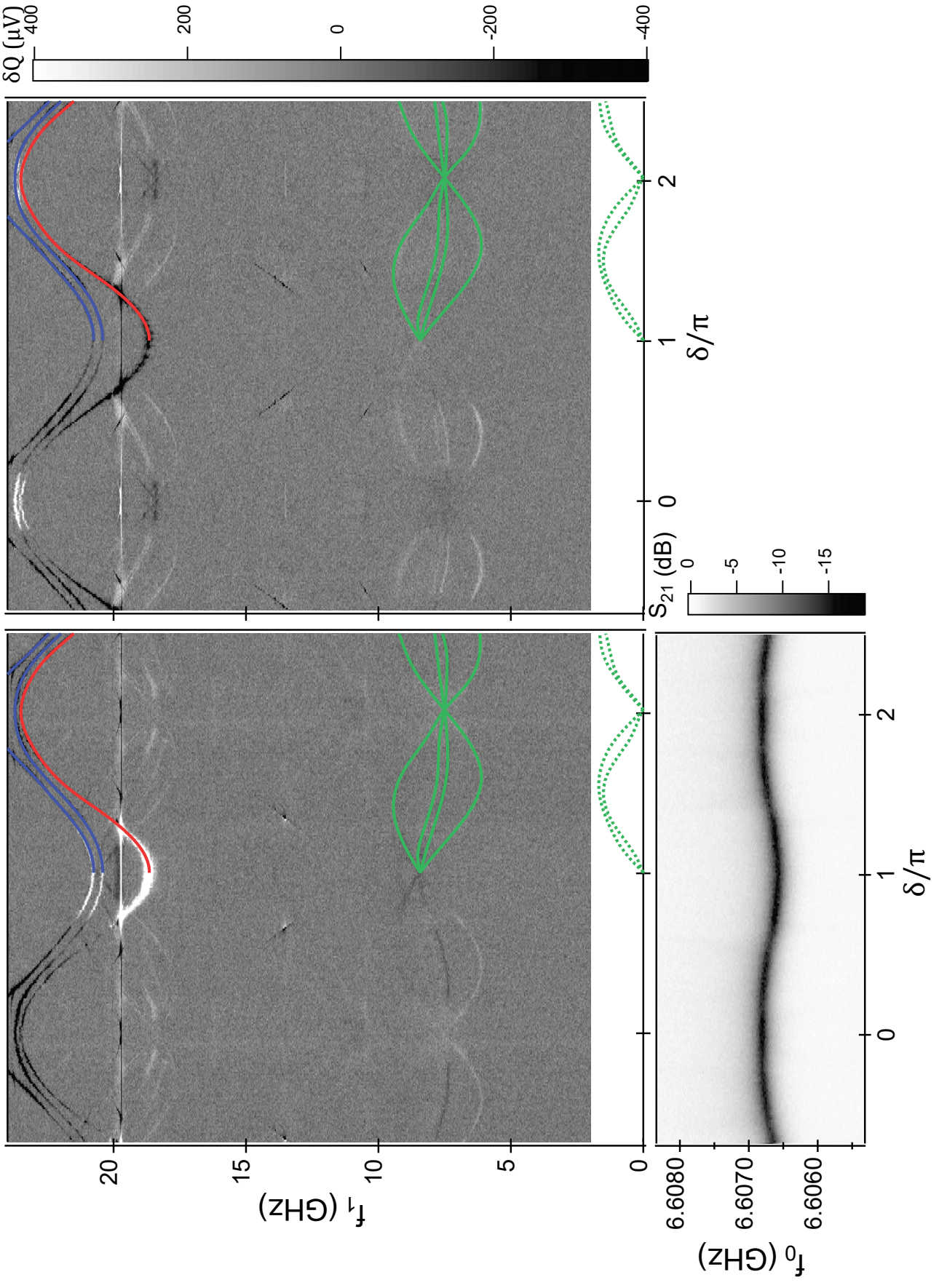
δQ (μV)
400
200
0
-200
-400
f₁ (GHz)
20
15
10
5
0
δ/π
0
1
2
S21 (dB)
0
-5
-10
-15
f₀ (GHz)
6.6080
6.6070
6.6060
δ/π
0
1
2

**Figure K.15**

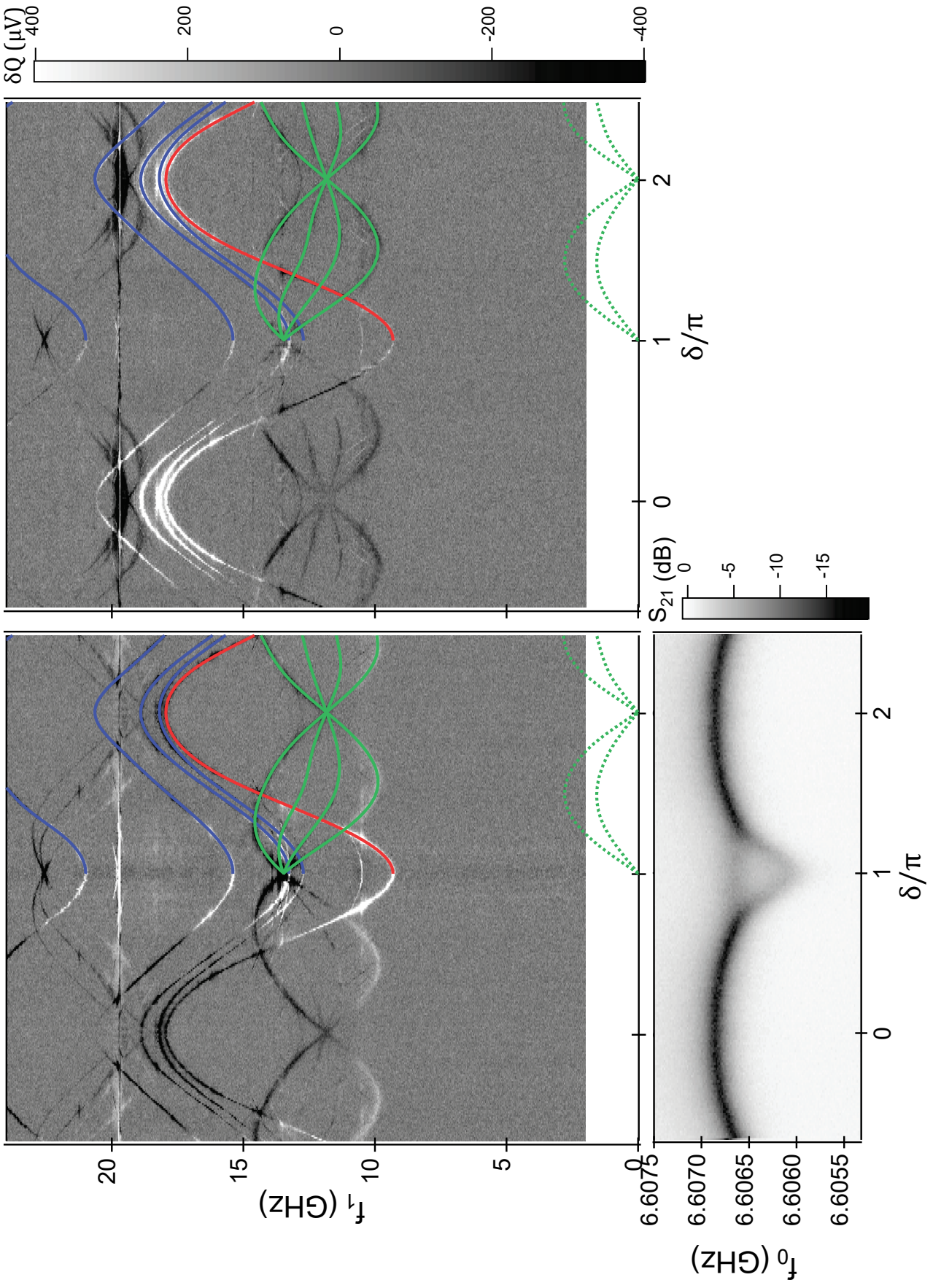
δQ (μV)
400
200
0
-200
-400
S21 (dB)
0
-5
-10
-15
δ/π
f1 (GHz)
f0 (GHz)
6.6075
6.6070
6.6065
6.6060
6.6055

**Figure K.16**

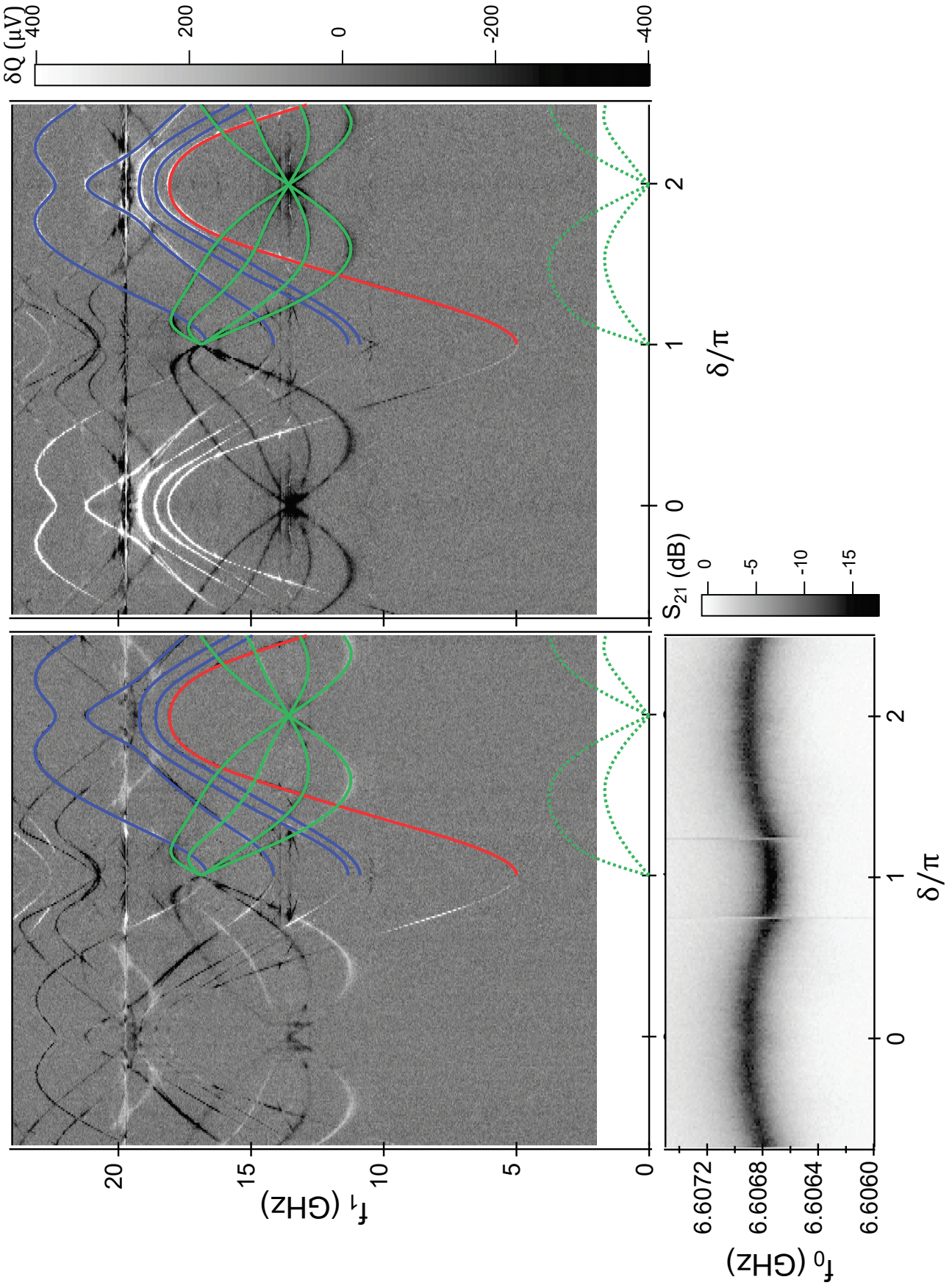
δQ (μV)
400
200
0
-200
-400
f₁ (GHz)
20
15
10
5
0
δ/π
0
1
2
S21 (dB)
0
-5
-10
-15
f₀ (GHz)
6.6072
6.6068
6.6064
6.6060
δ/π
0
1
2

**Figure K.17**

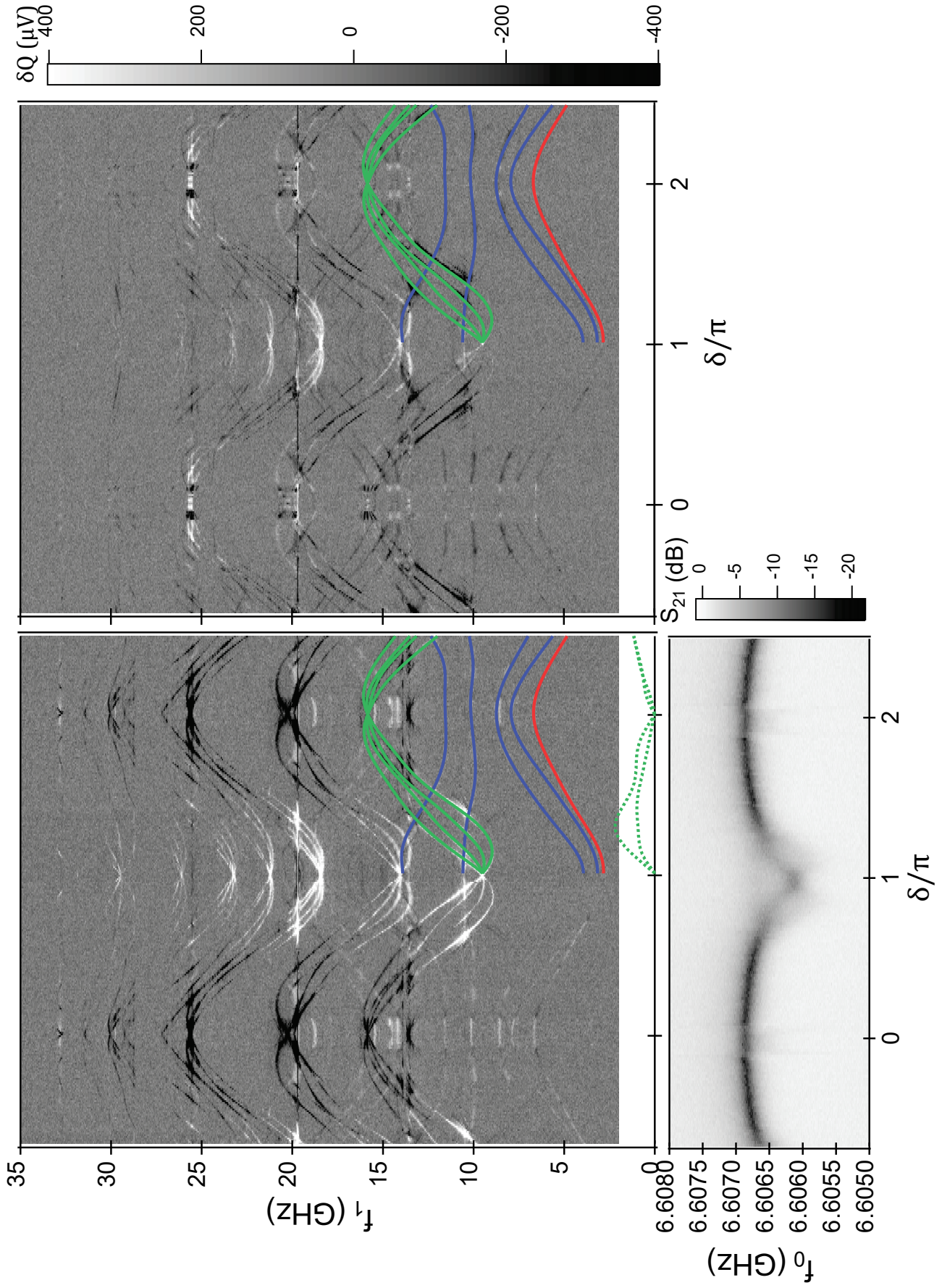


**Figure K.18**

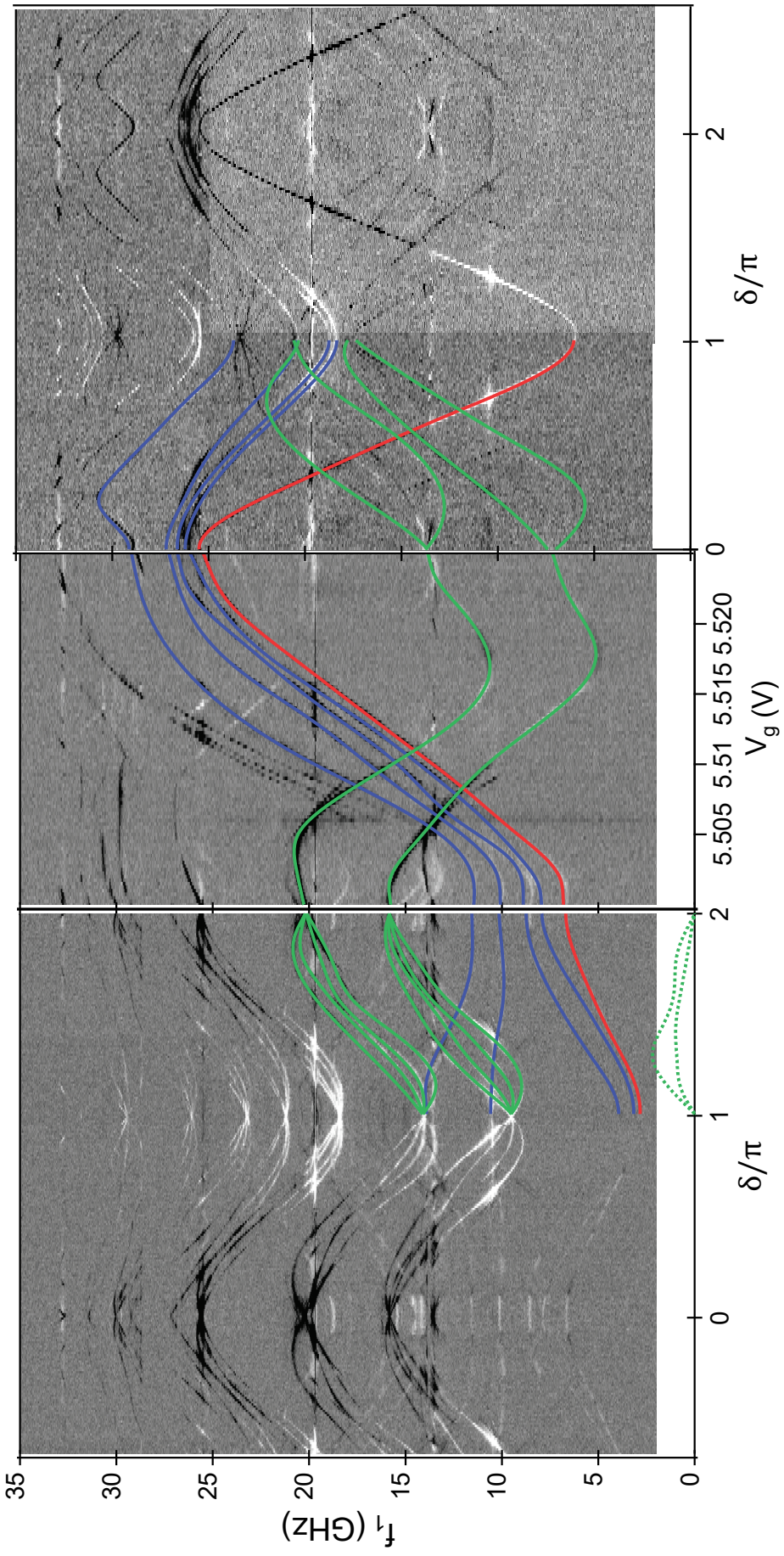


**Figure K.19**

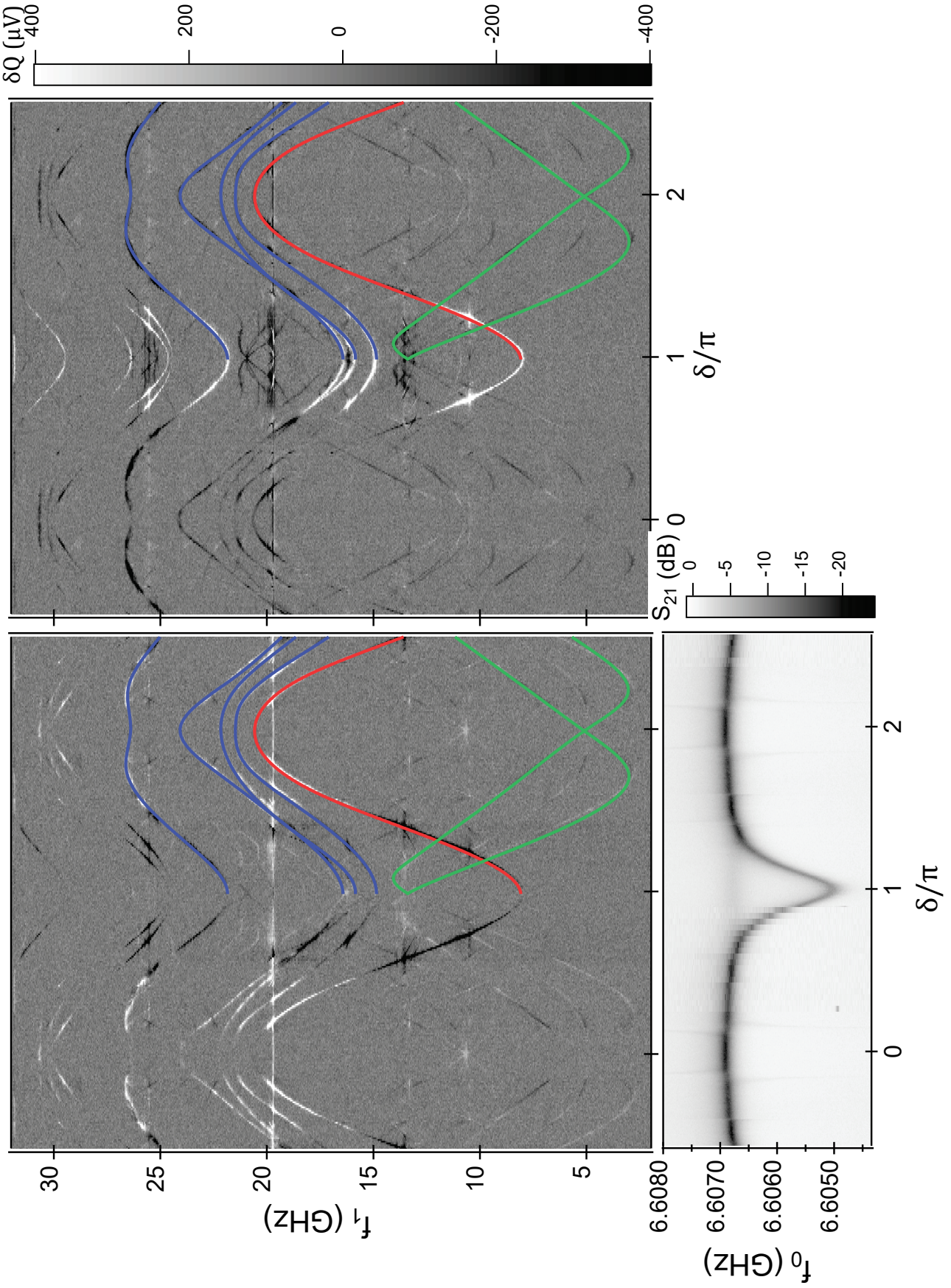
δQ (μV)
400
200
0
-200
-400
30
25
20
15
10
5
f₁ (GHz)
δ/π
0
1
2
S₂₁ (dB)
0
-5
-10
-15
-20
6.6080
6.6070
6.6060
6.6050
f₀ (GHz)
δ/π
0
1
2

**Figure K.20**

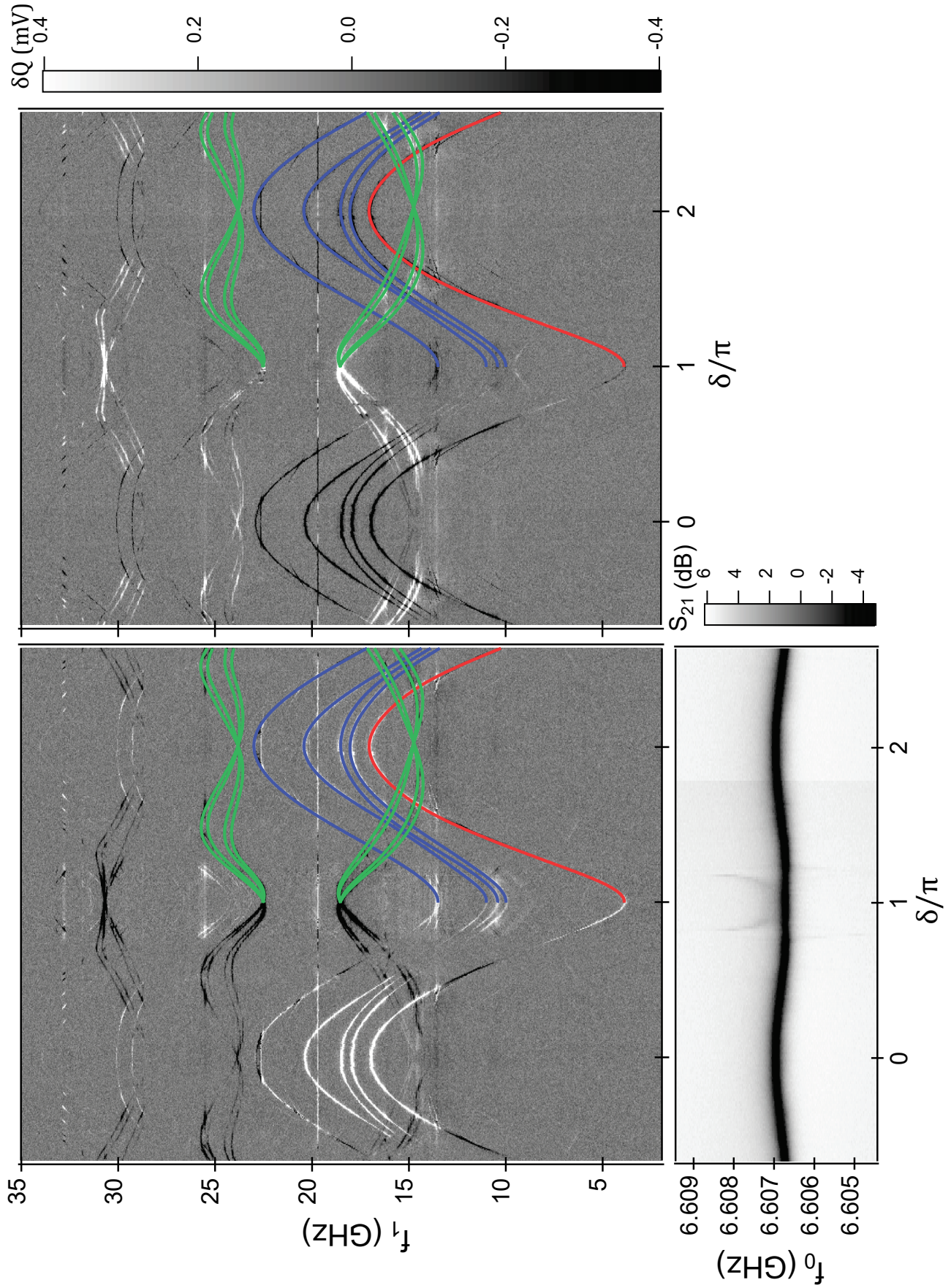
δQ (mV)
0.4
0.2
0.0
-0.2
-0.4
S21 (dB)
6
4
2
0
-2
-4
f1 (GHz)
35
30
25
20
15
10
5
f0 (GHz)
6.609
6.608
6.607
6.606
6.605
0
1
2
δ/π

**Figure K.21**

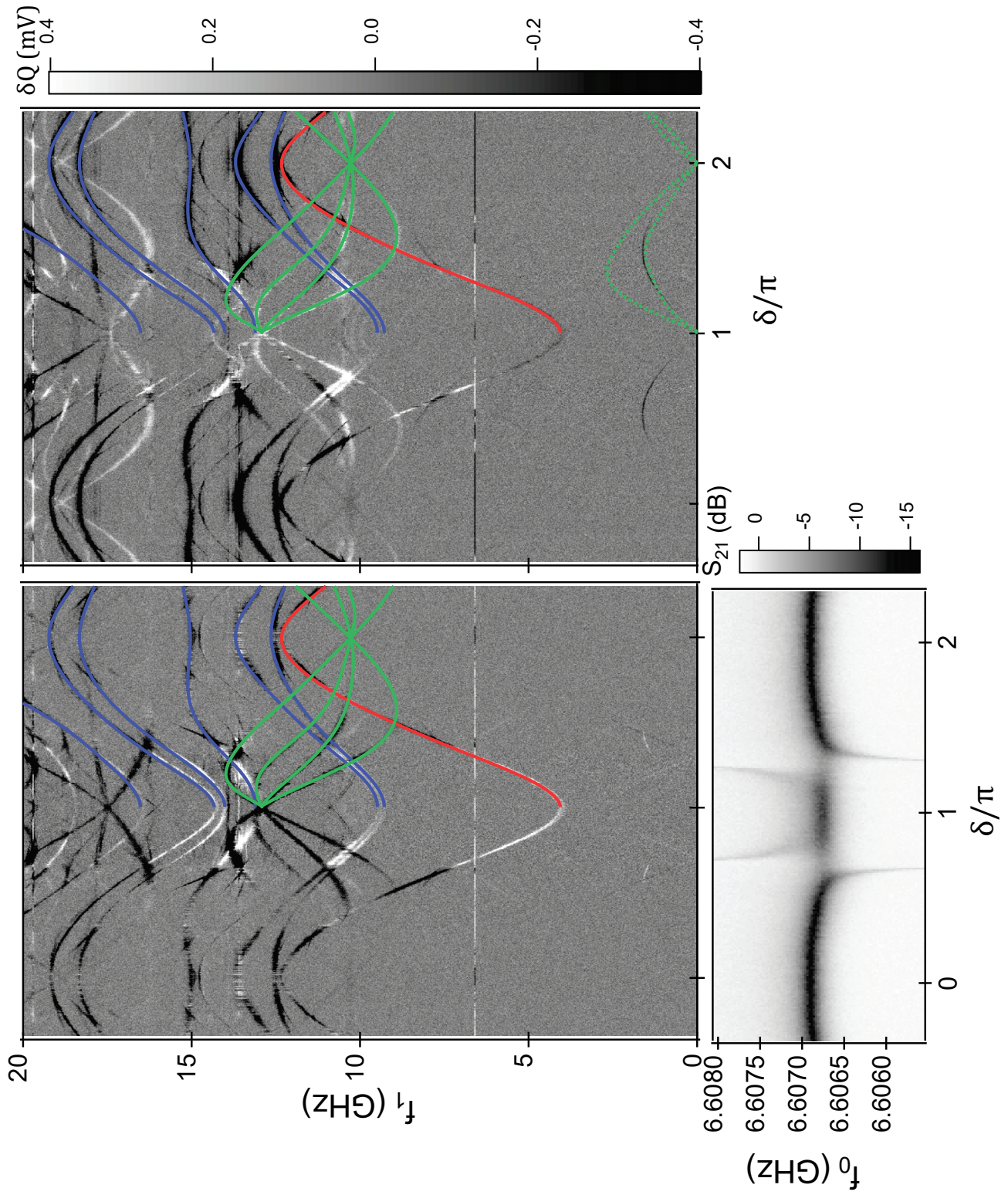
δQ (mV)
0.4
0.2
0.0
-0.2
-0.4
f₁ (GHz)
20
15
10
5
0
δ/π
2
1
S21 (dB)
0
-5
-10
-15
f₀ (GHz)
6.6080
6.6075
6.6070
6.6065
6.6060
δ/π
0
1
2

**Figure K.22**

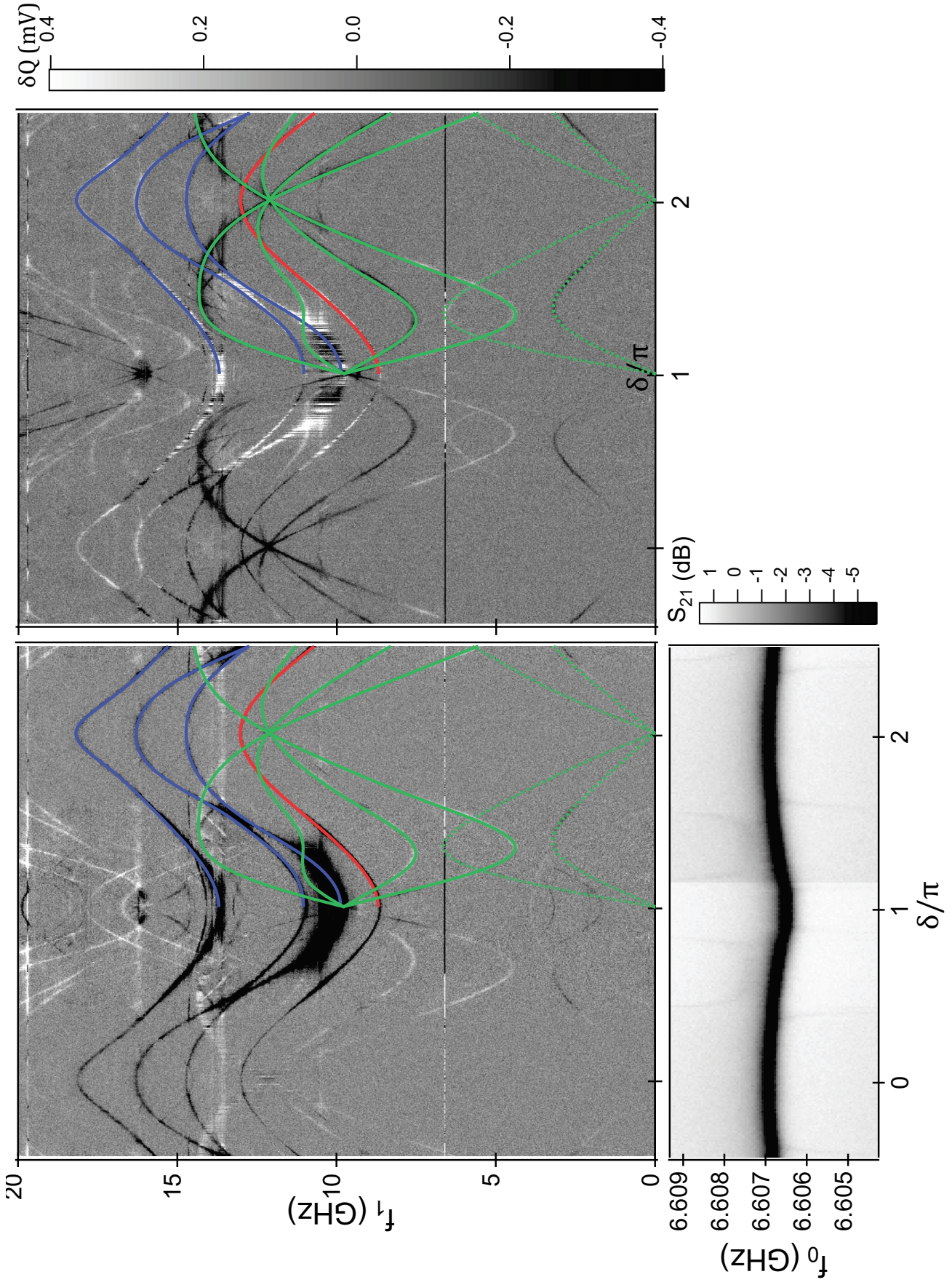
δQ (mV)
0.4
0.2
0.0
-0.2
-0.4
f₁ (GHz)
20
15
10
5
0
δ₁/π
1
2
S21 (dB)
1
0
-1
-2
-3
-4
-5
f₀ (GHz)
6.609
6.608
6.607
6.606
6.605
0
1
2
δ/π

**Figure K.23**

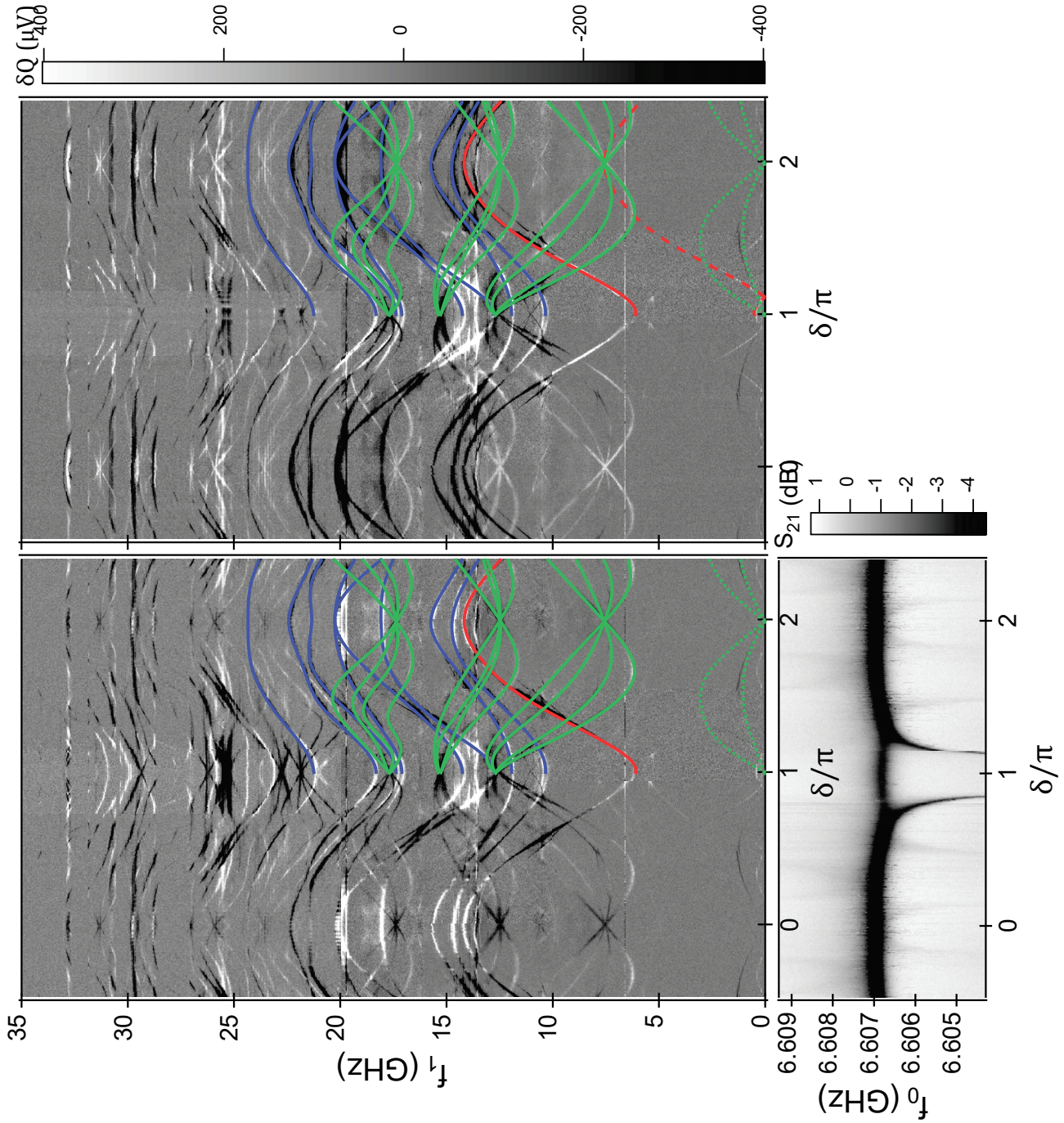
δQ (μV)
400
200
0
-200
-400
f₁ (GHz)
35
30
25
20
15
10
5
0
δ/π
0
1
2
S21 (dB)
1
0
-1
-2
-3
-4
f₀ (GHz)
6.609
6.608
6.607
6.606
6.605
δ/π
0
1
2

**Figure K.24**

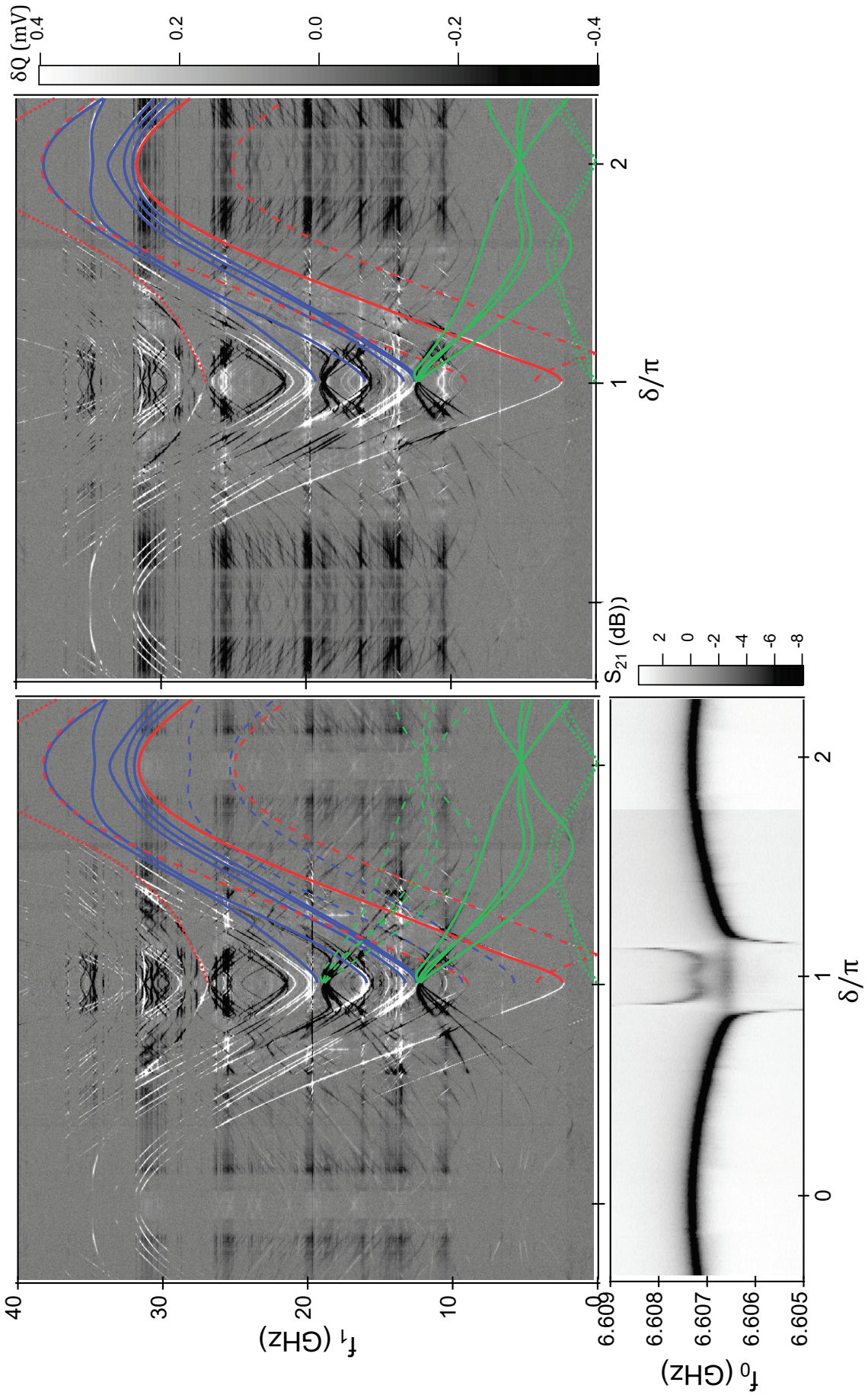
δQ (mV)
0.4
0.2
0.0
-0.2
-0.4
S21 (dB)
2
0
-2
-4
-6
-8
f1 (GHz)
40
30
20
10
0
δ/π
0
1
2
f0 (GHz)
6.609
6.608
6.607
6.606
6.605

**Figure K.25**

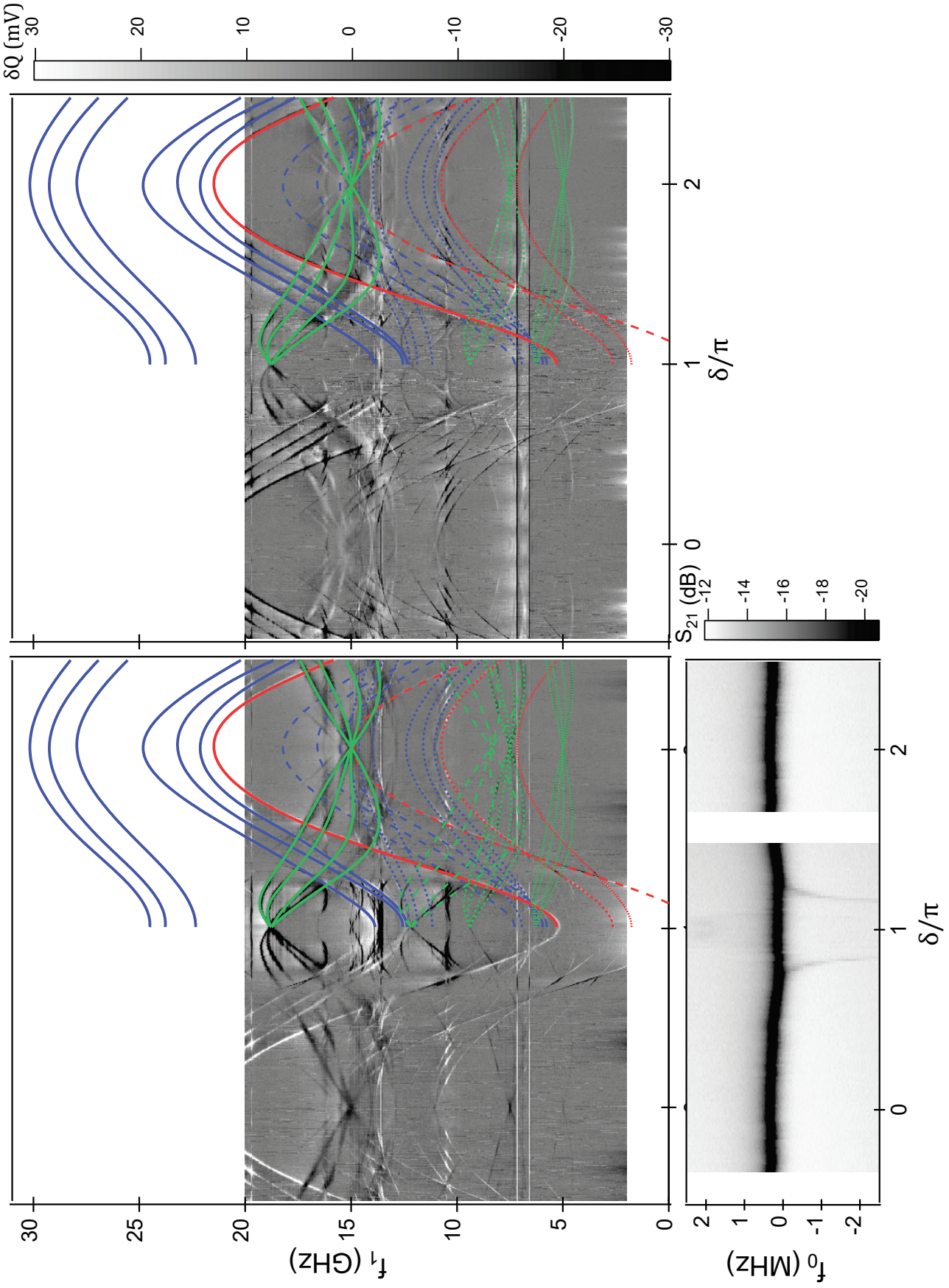
δQ (mV)
30
20
10
0
-10
-20
-30
f₁ (GHz)
30
25
20
15
10
5
0
δ/π
0
1
2
S21 (dB)
-12
-14
-16
-18
-20
f₀ (MHz)
2
1
0
-1
-2
δ/π
0
1
2

**Figure K.26**

# Bibliography


[1] J. M. Martinis, M. H. Devoret, and J. Clarke, Energy-Level Quantization in the Zero-Voltage State of a Current-Biased Josephson Junction. *Phys. Rev. Lett.* **55**, 1543–1546 (1985) (cited on page xix).

[2] M. H. Devoret and R. J. Schoelkopf, Superconducting Circuits for Quantum Information: An Outlook. *Science* (2013) (cited on pages xix, 1).

[3] P. Krantz, M. Kjaergaard, F. Yan, T. P. Orlando, S. Gustavsson, and W. D. Oliver, A quantum engineer's guide to superconducting qubits. *Appl. Phys. Rev.* **6**, 021318 (2019) (cited on pages xix, 1).

[4] A. A. Golubov, M. Y. Kupriyanov, and E. Il'ichev, The current-phase relation in Josephson junctions. *Rev. Mod. Phys.* **76**, 411–469 (2004) (cited on pages xix, 1).

[5] A. F. Andreev, Electron spectrum of the intermediate state of superconductors. *Sov. Phys. JETP* **22**, 455–458 (1966) (cited on pages xix, 1, 25).

[6] I. O. Kulik, Macroscopic quantization and proximity effect in s-n-s junctions. *Sov. Phys. JETP* **30**, 944 (1970) (cited on pages xix, 1, 19, 25).

[7] C. W. J. Beenakker and H. van Houten, Josephson current through a superconducting quantum point contact shorter than the coherence length. *Phys. Rev. Lett.* **66**, 3056–3059 (1991) (cited on pages xix, 1, 19, 213).

[8] A. Furusaki and M. Tsukada, Dc Josephson effect and Andreev reflection. *Solid State Commun.* **78**, 299–302 (1991) (cited on pages xix, 1, 19, 213).

[9] P. F. Bagwell, Suppression of the Josephson current through a narrow, mesoscopic, semiconductor channel by a single impurity. *Phys. Rev. B* **46**, 12573–12586 (1992) (cited on pages xix, 1, 19, 21, 213).

[10] A. F. Andreev, The thermal conductivity of the intermediate state in superconductors. *Sov. Phys. JETP* **19**, 1228–1231 (1964) (cited on pages xix, 16).

[11] P. G. de Gennes and D. Saint-James, Elementary excitations in the vicinity of a normal metal-superconducting metal contact. *Phys. Lett.* **4**, 151–152 (1963) (cited on pages xix, 16).

[12] D. Saint-James, Excitations élémentaires au voisinage de la surface de séparation d'un métal normal et d'un métal supraconducteur. *J. Phys. (Paris)* **25**, 899–905 (1964) (cited on pages xix, 16).

[13] J.-D. Pillet, C. H. L. Quay, P. Morfin, C. Bena, A. Levy Yeyati, and P. Joyez, Andreev bound states in supercurrent-carrying carbon nanotubes revealed. *Nat. Phys.* **6**, 965–969 (2010) (cited on pages xix, 1–2).

[14] L. Bretheau, Ç. Ö. Girit, H. Pothier, D. Esteve, and C. Urbina, Exciting Andreev pairs in a superconducting atomic contact. *Nature* **499**, 312–315 (2013) (cited on pages xix, 1).

[15] L. Bretheau, Ç. Ö. Girit, C. Urbina, D. Esteve, and H. Pothier, Supercurrent Spectroscopy of Andreev States. *Phys. Rev. X* **3**, 041034 (2013) (cited on pages xix, 1–2).

[16] C. Janvier, L. Tosi, L. Bretheau, Ç. Ö. Girit, M. Stern, P. Bertet, P. Joyez, D. Vion, D. Esteve, M. F. Goffman, H. Pothier, and C. Urbina, Coherent manipulation of Andreev states in superconducting atomic contacts. *Science* **349**, 1199–1202 (2015) (cited on pages xix, 1–2, 64, 80, 88, 92, 213, 217, 219–221).

[17] D. J. van Woerkom, A. Proutski, B. van Heck, D. Bouman, J. I. Väyrynen, L. I. Glazman, P. Krogstrup, J. Nygård, L. P. Kouwenhoven, and A. Geresdi, Microwave spectroscopy of spinful Andreev bound states in ballistic semiconductor Josephson junctions. *Nat. Phys.* **13**, 876–881 (2017) (cited on pages xix, 1).

[18] E. Lee, X. Jiang, M. Houzet, R. Aguado, C. Lieber, and S. Franceschi, Spin-resolved Andreev levels and parity crossings in hybrid superconductor-semiconductor nanostructures. *Nat. Nanotech.* **9** (2013) (cited on pages xix, 1–2).

[19] M. Hays, G. de Lange, K. Serniak, D. van Woerkom, D. Bouman, P. Krogstrup, J. Nygård, A. Geresdi, and M. Devoret, Direct Microwave Measurement of Andreev-Bound-State Dynamics in a Semiconductor-Nanowire Josephson Junction. *Phys. Rev. Lett.* **121**, 047001 (2018) (cited on pages xix, xxii, 1, 3, 51, 80, 88, 131).

[20] A. Blais, R.-S. Huang, A. Wallraff, S. M. Girvin, and R. J. Schoelkopf, Cavity quantum electrodynamics for superconducting electrical circuits: An architecture for quantum computation. *Phys. Rev. A* **69**, 062320 (2004) (cited on pages xx, 2, 206).

[21] C. Janvier, Coherent manipulation of Andreev Bound States in an atomic contact. PhD thesis (Université Paris-Saclay, 2016) (cited on pages xx, xxii, 4, 54–56, 62, 64, 96, 122, 136, 138, 145, 219, 223, 232).

[22] J. Michelsen, V. S. Shumeiko, and G. Wendin, Manipulation with Andreev states in spin active mesoscopic Josephson junctions. *Phys. Rev. B* **77**, 184506 (2008) (cited on pages xxi, 3).

[23] S. De Franceschi, L. Kouwenhoven, C. Schönenberger, and W. Wernsdorfer, Hybrid superconductor-quantum dot devices. *Nat. Nanotech.* **5**, 703–711 (2010) (cited on pages xxi, 3).

[24] J. Linder and J. W. A. Robinson, Superconducting spintronics. *Nat. Phys.* **11**, 307–315 (2015) (cited on pages xxi, 3).

[25] E. Prada, R. Aguado, and P. San-Jose, Measuring Majorana nonlocality and spin structure with a quantum dot. *Phys. Rev. B* **96**, 085418 (2017) (cited on pages xxi, 3).

[26] A. Zazunov, R. Egger, M. Alvarado, and A. Levy Yeyati, Josephson effect in multiterminal topological junctions. *Phys. Rev. B* **96**, 024516 (2017) (cited on pages xxi, 3).

[27] M.-T. Deng, S. Vaitiekėnas, E. Prada, P. San-Jose, J. Nygård, P. Krogstrup, R. Aguado, and C. M. Marcus, Nonlocality of Majorana modes in hybrid nanowires. *Phys. Rev. B* **98**, 085125 (2018) (cited on pages xxi, 3).

[28] S. Hart, H. Ren, M. Kosowsky, G. Ben-Shach, P. Leubner, C. Brüne, H. Buhmann, L. W. Molenkamp, B. I. Halperin, and A. Yacoby, Controlled finite momentum pairing and spatially varying order parameter in proximitized HgTe quantum wells. *Nat. Phys.* **13**, 87–93 (2017) (cited on pages xxi, 3).

[29] N. M. Chtchelkatchev and Y. V. Nazarov, Andreev Quantum Dots for Spin Manipulation. *Phys. Rev. Lett.* **90**, 226806 (2003) (cited on pages xxi, 4, 21).

[30] C. Padurariu and Y. V. Nazarov, Theoretical proposal for superconducting spin qubits. *Phys. Rev. B* **81**, 144519 (2010) (cited on pages xxi, 4, 21).

[31] A. A. Reynoso, G. Usaj, C. A. Balseiro, D. Feinberg, and M. Avignon, Spin-orbit-induced chirality of Andreev states in Josephson junctions. *Phys. Rev. B* **86**, 214519 (2012) (cited on pages xxi, 4).

[32] S. Park and A. Levy Yeyati, Andreev spin qubits in multichannel Rashba nanowires. *Phys. Rev. B* **96**, 125416 (2017) (cited on pages xxi, 4, 26–27, 46, 49, 55, 67, 82, 87, 89–90, 93, 126, 193, 219).

[33] B. Béri, J. H. Bardarson, and C. W. J. Beenakker, Splitting of Andreev levels in a Josephson junction by spin-orbit coupling. *Phys. Rev. B* **77**, 045311 (2008) (cited on pages xxi, 4, 21).

[34] J. Cayao, E. Prada, P. San-Jose, and R. Aguado, SNS junctions in nanowires with spin-orbit coupling: Role of confinement and helicity on the subgap spectrum. *Phys. Rev. B* **91**, 024514 (2015) (cited on pages xxi, 4).

[35] P. Roulleau, T. Choi, S. Riedi, T. Heinzel, I. Shorubalko, T. Ihn, and K. Ensslin, Suppression of weak antilocalization in InAs nanowires. *Phys. Rev. B* **81**, 155449 (2010) (cited on pages xxi, 5).

[36] Z. Scherübl, G. Fülöp, M. H. Madsen, J. Nygård, and S. Csonka, Electrical tuning of Rashba spin-orbit interaction in multigated InAs nanowires. *Phys. Rev. B* **94**, 035444 (2016) (cited on pages xxi, 5, 29, 82, 192).

[37] P. Krogstrup, N. L. B. Ziino, W. Chang, S. M. Albrecht, M. H. Madsen, E. Johnson, J. Nygård, C. M. Marcus, and T. S. Jespersen, Epitaxy of semiconductor-superconductor nano-wires. *Nature Mater.* **14**, 400–406 (2015) (cited on pages xxii, 3, 29, 162).

[38] W. Chang, S. M. Albrecht, T. S. Jespersen, F. Kuemmeth, P. Krogstrup, J. Nygård, and C. M. Marcus, Hard gap in epitaxial semiconductor-superconductor nanowires. *Nature Nanotech.* **10**, 232–236 (2015) (cited on pages xxii, 2, 29).

[39] M. F. Goffman, C. Urbina, H. Pothier, J. Nygård, C. M. Marcus, and P. Krogstrup, Conduction channels of an InAs-Al nanowire Josephson weak link. *New J. Phys.* **19**, 092002 (2017) (cited on pages xxii, 2, 191).

[40] L. Bretheau, Localized Excitations in Superconducting Atomic Contacts: Probing the Andreev doublet. PhD thesis (Ecole Polytechnique X, 2013) (cited on pages xxii, 4, 14, 63, 209).

[41] M. Hays, V. Fatemi, K. Serniak, D. Bouman, S. Diamond, G. de Lange, P. Krogstrup, J. Nygård, A. Geresdi, and M. H. Devoret, Continuous monitoring of a trapped superconducting spin. *Nature Phys.* **16**, 1103–1107 (2020) (cited on pages xxii, 3, 6–7, 51, 67, 88–89, 149, 151, 156).

[42] M. Hays, V. Fatemi, D. Bouman, J. Cerrillo, S. Diamond, K. Serniak, T. Connolly, P. Krogstrup, J. Nygård, A. Levy Yeyati, A. Geresdi, and M. H. Devoret, Coherent manipulation of an Andreev spin qubit. *Science* **373**, 430–433 (2021) (cited on pages xxii, 3, 6–7, 51, 67–68, 87, 95, 149, 151).

[43] R. M. Lutchyn, J. D. Sau, and S. Das Sarma, Majorana Fermions and a Topological Phase Transition in Semiconductor-Superconductor Heterostructures. *Phys. Rev. Lett.* **105**, 077001 (2010) (cited on pages xxiii, 180).

[44] Y. Oreg, G. Refael, and F. von Oppen, Helical Liquids and Majorana Bound States in Quantum Wires. *Phys. Rev. Lett.* **105**, 177002 (2010) (cited on pages xxiii, 180).

[45] S. Vaitiekėnas, G. W. Winkler, B. van Heck, T. Karzig, M.-T. Deng, K. Flensberg, L. I. Glazman, C. Nayak, P. Krogstrup, R. M. Lutchyn, and C. M. Marcus, Flux-induced topological superconductivity in full-shell nanowires. *Science* **367**, 6485 (2020) (cited on pages xxiii, 180).

[46] T. Yokoyama and Y. V. Nazarov, Singularities in the Andreev spectrum of a multiterminal Josephson junction. *Phys. Rev. B* **92**, 155437 (2015) (cited on pages xxiii, 181).

[47] R.-P. Riwar, M. Houzet, J. S. Meyer, and Y. V. Nazarov, Multi-terminal Josephson junctions as topological matter. *Nat. Comm.* **7**, 11167 (2016) (cited on pages xxiii, 181).

[48] H.-Y. Xie, M. G. Vavilov, and A. Levchenko, Topological Andreev bands in three-terminal Josephson junctions. *Phys. Rev. B* **96**, 161406 (2017) (cited on pages xxiii, 181).

[49] S. Vaitiekėnas, M.-T. Deng, J. Nygård, P. Krogstrup, and C. Marcus, Effective $g$ Factor of Subgap States in Hybrid Nanowires. *Phys. Rev. Lett.* **121**, 037703 (2018) (cited on pages 3, 86).

[50] V. Fatemi, P. D. Kurilovich, M. Hays, D. Bouman, T. Connolly, S. Diamond, N. E. Frattini, V. D. Kurilovich, P. Krogstrup, J. Nygård, A. Geresdi, L. I. Glazman, and M. H. Devoret, Microwave susceptibility observation of interacting many-body Andreev states. *arXiv:2112.05624 [cond-mat]* (2021) (cited on pages 3, 48, 51, 97, 109, 134, 180, 217).

[51] L. Tosi, C. Metzger, M. Goffman, C. Urbina, H. Pothier, S. Park, A. Levy Yeyati, J. Nygård, and P. Krogstrup, Spin-Orbit Splitting of Andreev States Revealed by Microwave Spectroscopy. *Phys. Rev. X* **9**, 011010 (2019) (cited on pages 11, 27, 49, 54, 78, 88, 92, 193, 229).

[52] S. Park, C. Metzger, L. Tosi, M. Goffman, C. Urbina, H. Pothier, and A. Levy Yeyati, From Adiabatic to Dispersive Readout of Quantum Circuits. *Phys. Rev. Lett.* **125**, 077701 (2020) (cited on pages 11, 33, 43, 209, 215).

[53] C. Metzger, S. Park, L. Tosi, C. Janvier, A. A. Reynoso, M. F. Goffman, C. Urbina, A. Levy Yeyati, and H. Pothier, Circuit-QED with phase-biased Josephson weak links. *Phys. Rev. Res.* **3**, 013036 (2021) (cited on pages 11, 33, 68, 78, 91).

[54] F. J. M. Cañadas, C. Metzger, S. Park, L. Tosi, P. Krogstrup, J. Nygård, M. F. Goffman, C. Urbina, H. Pothier, and A. Levy Yeyati, Signatures of interactions in the Andreev spectrum of nanowire Josephson junctions. *arXiv:2112.05625 [cond-mat]* (2021) (cited on pages 11, 107).

[55] V. V. Schmidt, V. V. Schmidt, P. Müller, and A. V. Ustinov, The Physics of Superconductors: Introduction to Fundamentals and Applications. (Springer Science & Business Media, 1997) (cited on page 14).

[56] E. Prada, P. San-Jose, M. W. A. de Moor, A. Geresdi, E. J. H. Lee, J. Klinovaja, D. Loss, J. Nygård, R. Aguado, and L. P. Kouwenhoven, From Andreev to Majorana bound states in hybrid superconductor-semiconductor nanowires. *Nature Rev. Phys.* **2**, 575–594 (2020) (cited on pages 19, 104).

[57] E. V. Bezuglyi, A. S. Rozhavsky, I. D. Vagner, and P. Wyder, Combined effect of Zeeman splitting and spin-orbit interaction on the Josephson current in a superconductor–two-dimensional electron gas–superconductor structure. *Phys. Rev. B* **66**, 052508 (2002) (cited on page 22).

[58] I. V. Krive, S. I. Kulinich, R. I. Shekhter, and M. Jonson, Charge and spin effects in mesoscopic Josephson junctions (Review). *Low Temp. Phys.* **30**, 554–567 (2004) (cited on page 22).

[59] O. V. Dimitrova and M. V. Feigel'man, Two-dimensional S-N-S junction with Rashba spin-orbit coupling. *JETP* **102**, 652–660 (2006) (cited on page 22).

[60] L. Dell'Anna, A. Zazunov, R. Egger, and T. Martin, Josephson current through a quantum dot with spin-orbit coupling. *Phys. Rev. B* **75**, 085305 (2007) (cited on page 22).

[61] G. Dresselhaus, Spin-Orbit Coupling Effects in Zinc Blende Structures. *Phys. Review* **100**, 580–586 (1955) (cited on page 23).

[62] Y. A. Bychkov and E. I. Rashba, Oscillatory effects and the magnetic susceptibility of carriers in inversion layers. *J. Phys. C Solid State Phys.* **17**, 6039–6045 (1984) (cited on page 25).

[63] T. Campos, P. E. Faria Junior, M. Gmitra, G. M. Sipahi, and J. Fabian, Spin-orbit coupling effects in zinc-blende InSb and wurtzite InAs nanowires: Realistic calculations with multiband $k \cdot p$ method. *Phys. Rev. B* **97**, 245402 (2018) (cited on pages 29, 191).

[64] P. D. Kurilovich, V. D. Kurilovich, V. Fatemi, M. H. Devoret, and L. I. Glazman, Microwave response of an Andreev bound state. *arXiv:2106.00028 [cond-mat]* (2021) (cited on pages 33, 36–37, 40, 47, 97, 109, 134, 208, 210–211, 217).

[65] D. M.Pozar, Microwave Engineering, 4rd Ed. John Wiley & Sons, Inc. (2011) (cited on pages 33, 51).

[66] M. Trif, O. Dmytruk, H. Bouchiat, R. Aguado, and P. Simon, Dynamic current susceptibility as a probe of Majorana bound states in nanowire-based Josephson junctions. *Phys. Rev. B* **97**, 041415 (2018) (cited on page 37).

[67] N. Trivedi and D. A. Browne, Mesoscopic ring in a magnetic field: Reactive and dissipative response. *Phys. Rev. B* **38**, 9581–9593 (1988) (cited on page 37).

[68] B. Dassonneville, Dynamics of Andeev states in a normal metal-superconductor ring : supercurrent fluctuations and spectroscopy of the minigap. PhD thesis (Paris XI, 2014) (cited on page 37).

[69] M. Hays, Realizing an Andreev Spin Qubit - Exploring Sub-gap Structure in Josephson Nanowires Using Circuit QED. PhD thesis (Yale University, 2020) (cited on pages 38, 72).

[70] U. Vool and M. Devoret, Introduction to quantum electromagnetic circuits. *Int. J. Circuit Theory Appl.* **45**, 897–934 (2017) (cited on page 42).

[71] D. Zueco, G. M. Reuther, S. Kohler, and P. Hänggi, Qubit-oscillator dynamics in the dispersive regime: Analytical theory beyond the rotating-wave approximation. *Phys. Rev. A* **80**, 033846 (2009) (cited on pages 45, 206, 215).

[72] S. Kohler, Dispersive readout: Universal theory beyond the rotating-wave approximation. *Phys. Rev. A* **98**, 023849 (2018) (cited on pages 45, 206).

[73] A. Levchenko, A. Kamenev, and L. Glazman, Singular length dependence of critical current in superconductor/normal-metal/superconductor bridges. *Phys. Rev. B* **74**, 212509 (2006) (cited on pages 47, 214).

[74] Y.-H. Baek, L. H. Truong, S.-W. Park, S.-J. Lee, Y.-S. Chae, E.-H. Rhee, H.-C. Park, and J.-K. Rhee, 94-GHz Log-Periodic Antenna on GaAs Substrate Using Air-Bridge Structure. *IEEE Antennas Wirel. Propag. Lett.* **8**, 909–911 (2009) (cited on page 53).

[75] J. P. Dehollain, J. J. Pla, E. Siew, K. Y. Tan, A. S. Dzurak, and A. Morello, Nanoscale broadband transmission lines for spin qubit control. *Nanotechnology* **24**, 015202 (2012) (cited on page 53).

[76] A. Vasylchenko, L. Wang, Z. Ma, W. De Raedt, and G. A. E. Vandenbosch, A very compact CPW-to-CPS balun for UWB antenna feeding. *IEEE 25th Convention of Electrical and Electronics Engineers in Israel* (2008), pp. 446–449 (cited on page 53).

[77] Cadence Design Systems Inc., TX-LINE. (2021) URL: *https://www.awr.com/awr-software/options/tx-line* (cited on pages 57, 62).

[78] K. C. Gupta, R. Garg, and I. J. Bahl, Microstrip Lines and Slotlines. Artech House (1979) (cited on pages 62, 71, 75).

[79] C. Sinclair and S. Nightingale, An equivalent circuit model for the coplanar waveguide step discontinuity. *IEEE MTT-S Microwave Symposium Digest* (1992), 1461–1464 vol.3 (cited on page 64).

[80] M. S. Khalil, M. J. A. Stoutimore, F. C. Wellstood, and K. D. Osborn, An analysis method for asymmetric resonator transmission applied to superconducting devices. *J. Appl. Phys.* **111**, 054510 (2012) (cited on page 65).

[81] C. Deng, M. Otto, and A. Lupascu, An analysis method for transmission measurements of superconducting resonators with applications to quantum-regime dielectric-loss measurements. *J. Appl. Phys.* **114**, 054504 (2013) (cited on pages 65, 125).

[82] I. Besedin and A. P. Menushenkov, Quality factor of a transmission line coupled coplanar waveguide resonator. *EPJ Quantum Technol.* **5**, 1–16 (2018) (cited on page 66).

[83] D. S. Wisbey, A. Martin, A. Reinisch, and J. Gao, New Method for Determining the Quality Factor and Resonance Frequency of Superconducting Micro-Resonators from Sonnet Simulations. *Low Temp. Phys.* **176**, 538–544 (2014) (cited on page 66).

[84] F. Wulschner, J. Goetz, F. R. Koessel, E. Hoffmann, A. Baust, P. Eder, M. Fischer, M. Haeberlein, M. J. Schwarz, M. Pernpeintner, E. Xie, L. Zhong, C. W. Zollitsch, B. Peropadre, J.-J. Garcia Ripoll, E. Solano, K. G. Fedorov, E. P. Menzel, F. Deppe, A. Marx, and R. Gross, Tunable coupling of transmission-line microwave resonators mediated by an rf SQUID. *EPJ Quantum Technol.* **3**, 1–10 (2016) (cited on page 67).

[85] C. Bockstiegel, Y. Wang, M. R. Vissers, L. F. Wei, S. Chaudhuri, J. Hubmayr, and J. Gao, A tunable coupler for superconducting microwave resonators using a nonlinear kinetic inductance transmission line. *Appl. Phys. Lett.* **108**, 222604 (2016) (cited on page 67).

[86] Sonnet Software Inc., Using even and odd mode parameters. (2020) URL: *https://www.sonnetsoftware.com/support/help-17/Sonnet_Suites/Sonnet%20Suites%20Documentation.html?UsingEvenandOddModeParameters1.html* (cited on page 72).

[87] C. R. Paul, Inductance: Loop and Partial. John Wiley & Sons (2011) (cited on page 75).

[88] M. Zgirski, L. Bretheau, Q. Le Masne, H. Pothier, D. Esteve, and C. Urbina, Evidence for Long-Lived Quasiparticles Trapped in Superconducting Point Contacts. *Phys. Rev. Lett.* **106**, 257003 (2011) (cited on pages 80, 131, 133).

[89] C. Fasth, A. Fuhrer, L. Samuelson, V. N. Golovach, and D. Loss, Direct Measurement of the Spin-Orbit Interaction in a Two-Electron InAs Nanowire Quantum Dot. *Phys. Rev. Lett.* **98**, 266801 (2007) (cited on page 82).

[90] M. T. Björk, A. Fuhrer, A. E. Hansen, M. W. Larsson, L. E. Fröberg, and L. Samuelson, Tunable effective $g$ factor in InAs nanowire quantum dots. *Phys. Rev. B* **72**, 201307 (2005) (cited on page 86).

[91] R. S. Deacon, Y. Kanai, S. Takahashi, A. Oiwa, K. Yoshida, K. Shibata, K. Hirakawa, Y. Tokura, and S. Tarucha, Electrically tuned $g$ tensor in an InAs self-assembled quantum dot. *Phys. Rev. B* **84**, 041302 (2011) (cited on page 86).

[92] S. d'Hollosy, G. Fábián, A. Baumgartner, J. Nygård, and C. Schönenberger, G-factor anisotropy in nanowire-based InAs quantum dots. *AIP Conf. Proc.* **1566**, 359–360 (2013) (cited on page 86).

[93] A. Palacios-Laloy, Superconducting qubit in a resonator : test of the Legget-Garg inequality and single-shot readout. PhD thesis (Université Pierre et Marie Curie - Paris VI, 2010) (cited on pages 91, 221).

[94] J. Cerrillo, M. Hays, V. Fatemi, and A. Levy Yeyati, Spin coherent manipulation in Josephson weak links. *Phys. Rev. Research* **3**, L022012 (2021) (cited on page 95).

[95] M. Cheng and R. M. Lutchyn, Josephson current through a superconductor/semiconductor-nanowire/superconductor junction: Effects of strong spin-orbit coupling and Zeeman splitting. *Phys. Rev. B* **86**, 134522 (2012) (cited on page 104).

[96] A. Manolescu, D. C. Marinescu, and T. D. Stanescu, Coulomb interaction effects on the Majorana states in quantum wires. *J. Phys.: Condens. Matter* **26**, 172203 (2014) (cited on page 108).

[97] I. L. Kurland, I. L. Aleiner, and B. L. Altshuler, Mesoscopic magnetization fluctuations for metallic grains close to the Stoner instability. *Phys. Rev. B* **62**, 14886–14897 (2000) (cited on page 108).

[98] C. Padurariu and Y. V. Nazarov, Spin blockade qubit in a superconducting junction. *Europhys. Lett.* **100**, 57006 (2012) (cited on pages 108, 110, 116).

[99] E. Vecino, A. Martin-Rodero, and A. Levy Yeyati, Josephson current through a correlated quantum level: Andreev states and $\pi$ junction behavior. *Phys. Rev. B* **68**, 035105 (2003) (cited on page 110).

[100] T. Meng, S. Florens, and P. Simon, Self-consistent description of Andreev bound states in Josephson quantum dot devices. *Phys. Rev. B* **79**, 224521 (2009) (cited on page 110).

[101] M. Alvarado, A. Iks, A. Zazunov, R. Egger, and A. Levy Yeyati, Boundary Green's function approach for spinful single-channel and multichannel Majorana nanowires. *Phys. Rev. B* **101**, 094511 (2020) (cited on page 110).

[102] F. S. Bergeret, A. Levy Yeyati, and A. Martin-Rodero, Josephson effect through a quantum dot array. *Phys. Rev. B* **76**, 174510 (2007) (cited on page 112).

[103] J. Feist, Quantumalgebra.jl - quantum operator algebra in julia. (2021) URL: *https://github.com/jfeist/QuantumAlgebra.jl* (cited on page 114).

[104] A. Megrant, C. Neill, R. Barends, B. Chiaro, Y. Chen, L. Feigl, J. Kelly, E. Lucero, M. Mariantoni, P. J. J. O'Malley, D. Sank, A. Vainsencher, J. Wenner, T. C. White, Y. Yin, J. Zhao, C. J. Palmstrøm, J. M. Martinis, and A. N. Cleland, Planar superconducting resonators with internal quality factors above one million. *Appl. Phys. Lett.* **100**, 113510 (2012) (cited on page 122).

[105] J. Heinsoo, C. K. Andersen, A. Remm, S. Krinner, T. Walter, Y. Salathé, S. Gasparinetti, J.-C. Besse, A. Potočnik, A. Wallraff, and C. Eichler, Rapid High-fidelity Multiplexed Readout of Superconducting Qubits. *Phys. Rev. Appl.* **10**, 034040 (2018) (cited on page 122).

[106] A. Bienfait, Magnetic resonance with quantum microwaves. PhD thesis (Université Paris-Saclay, 2016) (cited on page 122).

[107] D. McClure, H. Paik, L. Bishop, M. Steffen, J. M. Chow, and J. M. Gambetta, Rapid Driven Reset of a Qubit Readout Resonator. *Phys. Rev. Appl.* **5**, 011001 (2016) (cited on page 126).

[108] C. A. Ryan, B. R. Johnson, J. M. Gambetta, J. M. Chow, M. P. da Silva, O. E. Dial, and T. A. Ohki, Tomography via correlation of noisy measurement records. *Phys. Rev. A* **91**, 022118 (2015) (cited on page 129).

[109] E. Magesan, J. M. Gambetta, A. Córcoles, and J. M. Chow, Machine Learning for Discriminating Quantum Measurement Trajectories and Improving Readout. *Phys. Rev. Lett.* **114**, 200501 (2015) (cited on page 129).

[110] C. C. Bultink, B. Tarasinski, N. Haandbæk, S. Poletto, N. Haider, D. J. Michalak, A. Bruno, and L. DiCarlo, General method for extracting the quantum efficiency of dispersive qubit readout in circuit QED. *Appl. Phys. Lett.* **112**, 092601 (2018) (cited on page 129).

[111] G. Ithier, E. Collin, P. Joyez, P. J. Meeson, D. Vion, D. Esteve, F. Chiarello, A. Shnirman, Y. Makhlin, J. Schriefl, and G. Schön, Decoherence in a superconducting quantum bit circuit. *Phys. Rev. B* **72**, 134519 (2005) (cited on pages 136, 140, 145).

[112] G. Falci, A. D'Arrigo, A. Mastellone, and E. Paladino, Initial Decoherence in Solid State Qubits. *Phys. Rev. Lett.* **94**, 167002 (2005) (cited on page 140).

[113] J. Bylander, S. Gustavsson, F. Yan, F. Yoshihara, K. Harrabi, G. Fitch, D. G. Cory, Y. Nakamura, J.-S. Tsai, and W. D. Oliver, Noise spectroscopy through dynamical decoupling with a superconducting flux qubit. *Nature Phys.* **7**, 565–570 (2011) (cited on page 145).

[114] J. M. Martinis, S. Nam, J. Aumentado, K. M. Lang, and C. Urbina, Decoherence of a superconducting qubit due to bias noise. *Phys. Rev. B* **67**, 094510 (2003) (cited on page 146).

[115] S. Nadj-Perge, S. M. Frolov, E. P. a. M. Bakkers, and L. P. Kouwenhoven, Spin-orbit qubit in a semiconductor nanowire. *Nature* **468**, 1084–1087 (2010) (cited on page 151).

[116] J. W. G. van den Berg, S. Nadj-Perge, V. S. Pribiag, S. R. Plissard, E. P. A. M. Bakkers, S. M. Frolov, and L. P. Kouwenhoven, Fast Spin-Orbit Qubit in an Indium Antimonide Nanowire. *Phys. Rev. Lett.* **110**, 066806 (2013) (cited on page 151).

[117] Scikit-learn developers, Sklearn.mixture.gaussianmixture. (2021) URL: *https://scikit-learn.org/stable/modules/generated/sklearn.mixture.GaussianMixture.html* (cited on page 175).

[118] B. van Heck, S. Mi, and A. R. Akhmerov, Single fermion manipulation via superconducting phase differences in multiterminal Josephson junctions. *Phys. Rev. B* **90**, 155450 (2014) (cited on page 181).

[119] S. Gazibegovic, D. Car, H. Zhang, S. C. Balk, J. A. Logan, M. W. A. de Moor, M. C. Cassidy, R. Schmits, D. Xu, G. Wang, P. Krogstrup, R. L. M. Op het Veld, K. Zuo, Y. Vos, J. Shen, D. Bouman, B. Shojaei, D. Pennachio, J. S. Lee, P. J. van Veldhoven, S. Koelling, M. A. Verheijen, L. P. Kouwenhoven, C. J. Palmstrøm, and E. P. A. M. Bakkers, Epitaxy of advanced nanowire quantum devices. *Nature* **548**, 434–438 (2017) (cited on pages 181–182).

[120] S. R. Plissard, I. van Weperen, D. Car, M. A. Verheijen, G. W. G. Immink, J. Kammhuber, L. J. Cornelissen, D. B. Szombati, A. Geresdi, S. M. Frolov, L. P. Kouwenhoven, and E. P. A. M. Bakkers, Formation and electronic properties of InSb nanocrosses. *Nature Nanotech.* **8**, 859–864 (2013) (cited on page 181).

[121] A. H. Pfeffer, J. E. Duvauchelle, H. Courtois, R. Mélin, D. Feinberg, and F. Lefloch, Subgap structure in the conductance of a three-terminal Josephson junction. *Phys. Rev. B* **90**, 075401 (2014) (cited on page 181).

[122] N. Pankratova, H. Lee, R. Kuzmin, M. Vavilov, K. Wickramasinghe, W. Mayer, J. Yuan, J. Shabani, and V. E. Manucharyan, The multi-terminal Josephson effect. *Phys. Rev. X* **10**, 031051 (2020) (cited on page 181).

[123] A. W. Draelos, M.-T. Wei, A. Seredinski, H. Li, Y. Mehta, K. Watanabe, T. Taniguchi, I. V. Borzenets, F. Amet, and G. Finkelstein, Supercurrent Flow in Multiterminal Graphene Josephson Junctions. *Nano Lett.* **19**, 1039–1043 (2019) (cited on page 181).

[124] V. Fatemi, A. R. Akhmerov, and L. Bretheau, Weyl Josephson circuits. *Phys. Rev. Res.* **3**, 013288 (2021) (cited on page 181).

[125] L. Peyruchat, J. Griesmar, J.-D. Pillet, and Ç. Ö. Girit, Transconductance quantization in a topological Josephson tunnel junction circuit. *Phys. Rev. Res.* **3**, 013289 (2021) (cited on page 181).

[126] S. K. Manikandan and A. N. Jordan, Andreev reflections and the quantum physics of black holes. *Phys. Rev. D* **96**, 124011 (2017) (cited on page 184).

[127] X. M. Puspus, K. H. Villegas, and F. N. C. Paraan, Entanglement spectrum and number fluctuations in the spin-partitioned BCS ground state. *Phys. Rev. B* **90**, 155123 (2014) (cited on page 184).

[128] B. A. Bernevig and T. L. Hugues, Topological Insulators and Topological Superconductors. Princeton University Press (2013) (cited on page 186).

[129] J. Y. Fu and M. W. Wu, Spin-orbit coupling in bulk ZnO and GaN. *J. Appl. Phys.* **104**, 093712 (2008) (cited on page 191).

[130] T. S. Jespersen, P. Krogstrup, A. M. Lunde, R. Tanta, T. Kanne, E. Johnson, and J. Nygård, Crystal orientation dependence of the spin-orbit coupling in InAs nanowires. *Phys. Rev. B* **97**, 041303 (2018) (cited on page 192).

[131] V. E. Degtyarev, S. V. Khazanova, and N. V. Demarina, Features of electron gas in InAs nanowires imposed by interplay between nanowire geometry, doping and surface states. *Sci. Rep.* **7**, 3411 (2017) (cited on page 192).

[132] A. Bringer and T. Schäpers, Spin precession and modulation in ballistic cylindrical nanowires due to the Rashba effect. *Phys. Rev. B* **83**, 115305 (2011) (cited on page 192).

[133] S. D. Escribano, A. Levy Yeyati, and E. Prada, Improved effective equation for the Rashba spin-orbit coupling in semiconductor nanowires. *Phys. Rev. Res.* **2**, 033264 (2020) (cited on page 192).

[134] P. E. Faria Junior, T. Campos, C. M. O. Bastos, M. Gmitra, J. Fabian, and G. M. Sipahi, Realistic multiband k.p approach from ab initio and spin-orbit coupling effects of InAs and InP in wurtzite phase. *Phys. Rev. B* **93**, 235204 (2016) (cited on page 194).

[135] N. Luo, G. Liao, and H. Q. Xu, K.p theory of freestanding narrow band gap semiconductor nanowires. *AIP Adv.* **6**, 125109 (2016) (cited on page 194).

[136] Y. Peng, F. Pientka, E. Berg, Y. Oreg, and F. von Oppen, Signatures of topological Josephson junctions. *Phys. Rev. B* **94**, 085409 (2016) (cited on pages 198, 208).

[137] B. van Heck, J. I. Väyrynen, and L. I. Glazman, Zeeman and spin-orbit effects in the Andreev spectra of nanowire junctions. *Phys. Rev. B* **96**, 075404 (2017) (cited on page 198).

[138] W. E. Lamb and R. C. Retherford, Fine Structure of the Hydrogen Atom by a Microwave Method. *Phys. Review* **72**, 241–243 (1947) (cited on page 204).

[139] M. F. Gely, G. A. Steele, and D. Bothner, Nature of the Lamb shift in weakly anharmonic atoms: From normal-mode splitting to quantum fluctuations. *Phys. Rev. A* **98**, 053808 (2018) (cited on page 207).

[140] F. Kos, S. E. Nigg, and L. I. Glazman, Frequency-dependent admittance of a short superconducting weak link. *Phys. Rev. B* **87**, 174521 (2013) (cited on pages 208, 213).

[141] V. D. Kurilovich, C. Murthy, P. D. Kurilovich, B. van Heck, L. I. Glazman, and C. Nayak, Quantum critical dynamics of a Josephson junction at the topological transition. *Phys. Rev. B* **104**, 014509 (2021) (cited on page 208).

[142] C. W. J. Beenakker, Universal limit of critical-current fluctuations in mesoscopic Josephson junctions. *Phys. Rev. Lett.* **67**, 3836–3839 (1991) (cited on page 208).

[143] A. Furusaki and M. Tsukada, A unified theory of clean Josephson junctions. *Phys. B: Condens. Matter*, LT-19 **165-166**, 967–968 (1990) (cited on page 208).

[144] A. Zazunov, A. Brunetti, A. Levy Yeyati, and R. Egger, Quasiparticle trapping, Andreev level population dynamics, and charge imbalance in superconducting weak links. *Phys. Rev. B* **90**, 104508 (2014) (cited on page 213).

[145] D. G. Olivares, A. Levy Yeyati, L. Bretheau, Ç. Ö. Girit, H. Pothier, and C. Urbina, Dynamics of quasiparticle trapping in Andreev levels. *Phys. Rev. B* **89**, 104504 (2014) (cited on page 213).

[146] G. Johansson, L. Tornberg, V. S. Shumeiko, and G. Wendin, Readout methods and devices for Josephson-junction-based solid-state qubits. *arXiv:0602585 [cond-mat]* (2006) (cited on page 215).

[147] J. Kroll, F. Borsoi, K. van der Enden, W. Uilhoorn, D. de Jong, M. Quintero-Pérez, D. van Woerkom, A. Bruno, S. Plissard, D. Car, E. Bakkers, M. Cassidy, and L. Kouwenhoven, Magnetic-Field-Resilient Superconducting Coplanar-Waveguide Resonators for Hybrid Circuit Quantum Electrodynamics Experiments. *Phys. Rev. Applied* **11**, 064053 (2019) (cited on page 229).

[148] M. Pita-Vidal, A. Bargerbos, C.-K. Yang, D. Woerkom, W. Pfaff, N. Haider, P. Krogstrup, L. Kouwenhoven, G. Lange, and A. Kou, Gate-Tunable Field-Compatible Fluxonium. *Phys. Rev. Applied* **14**, 064038 (2020) (cited on page 229).

[149] J. J. Wesdorp, L. Grünhaupt, A. Vaartjes, M. Pita-Vidal, A. Bargerbos, L. J. Splitthoff, P. Krogstrup, B. van Heck, and G. de Lange, Dynamical polarization of the fermion parity in a nanowire Josephson junction. *arXiv:2112.01936 [cond-mat, physics:quant-ph]* (2021) (cited on page 229).

[150] M. M. Khapaev, 3D-MLSI: extraction of inductances of multilayer superconductor circuits. (2004) URL: *http://vmbak.cs.msu.ru/sotr/vmhap/3dmlsi/3dmlsi.htm* (cited on page 232).

# List of symbols

**Acronyms**

| | |
|---|---|
| AR | Andreev reflection. |
| VNA | Vector Network Analyzer. |
| SNR | Signal over noise ratio. |
| WL | Weak link. |
| NW | Nanowire. |
| AC | Atomic contact. |
| PT | Pair transition. |
| SQPT | Single-quasiparticle transition. |
| SEM | Scanning electron microscope. |
| BdG | Bogoliubov-de Gennes. |
| cQED | Circuit quantum electrodynamics. |
| ABS | Andreev Bound States. |
| APQ | Andreev Pair Qubit. |
| ASQ | Andreev Spin Qubit. |
| BF | Bistable fluctuator. |
| TRS | Time-reversal symmetry. |
| SOI | Spin-orbit interaction. |
| WZ | Wurtzite structure. |
| ZB | Zinc-blende structure. |
| TB | Tight binding. |
| TRIM | Time-reversal invariant momenta. |
| PCB | Printed circuit board. |
| CPW | Coplanar waveguide. |
| CPS | Coplanar stripline. |
| sCPW | Shunted coplanar waveguide. |
| TWPA | Traveling wave parametric amplifier. |
| HEMT | High electron mobility transistor. |
| TL | Transmission line. |

**Physical constants**

| | |
|---|---|
| $c$ | Speed of light in vacuum $c \approx 2.99792 \times 10^{8}$ m/s. |
| $e$ | Electron charge $e \approx 1.60217 \times 10^{-19}$ C. |
| $\hbar$ | Reduced Planck's constant $h/2\pi \approx 1.05457 \times 10^{-34}$ m²kg/s. |
| $\varphi_0$ | Reduced magnetic flux quantum $\hbar/(2e) \approx 3.29106 \times 10^{-16}$ Wb. |

université PARIS-SACLAY

ÉCOLE DOCTORALE
Physique en Île-de-France (PIF)

**Titre :** Effets de spin et de charge dans les états liés d'Andreev
**Mots clés :** Matière condensée, Transport Quantique, Circuits supraconducteurs, Cryogénie, Micro-ondes

**Résumé :** Nous présentons les résultats d'expériences sondant les propriétés des états d'Andreev dans des liens faibles supraconducteurs à base de nanofils d'Arséniure d'Indium (InAs). Les états d'Andreev sont des états fermioniques localisés qui apparaissent à la jonction (ou lien faible) entre deux électrodes supraconductrices. Ils sont au coeur de la description microscopique de l'effet Josephson. Les nanofils d'InAs permettent d'obtenir des liens faibles de longueur finie, caractérisés par un couplage spin-orbite et des propriétés de conduction ajustables électrostatiquement.

Par la technique d'électrodynamique quantique en circuit (cQED), qui consiste à coupler le lien faible à un résonateur micro-onde de fort facteur de qualité, les états d'Andreev peuvent être isolés efficacement du bruit extérieur, et la lecture de la fréquence du résonateur donne accès à leur occupation microscopique. Nous modélisons ce couplage pour atteindre une sensibilité optimale et comprendre en détail la réponse du résonateur couplé au lien faible.

Nous avons mesuré les spectres des états d'Andreev, et leur dépendance en différence de phase supraconductrice. Ces spectres mettent en évidence deux effets. Le premier est la levée de la dégénérescence de spin des états du fait du couplage spin-orbite. Cela se traduit par des lignes spectroscopiques caractérisant le changement de l'état de spin d'une quasi-particule unique dans le lien faible. Le second est l'influence des interactions coulombiennes entre quasi-particules, réminiscentes de la séparation entre états singulet et triplet de deux spins 1/2 en interaction. La modélisation théorique des liens faibles de longueur finie permet de rendre compte de ces effets.

Nous caractérisons également les états d'Andreev par des mesures temporelles. Des bits quantiques sont obtenus soit en utilisant l'état fondamental et un état où une paire de quasi-particules est excitée ; soit deux états avec une quasi-particule dans des états d'Andreev différents. Nous avons mesuré les temps de vie et de cohérence de ces deux types de « qubits d'Andreev ».

**Title :** Spin and charge effects in Andreev Bound States
**Keywords :** Condensed matter, Quantum transport, Superconducting circuits, Cryogenics, Microwaves

**Abstract :** We probe experimentally the properties of Andreev states in superconducting weak links based on Indium Arsenide (InAs) nanowires. Andreev states are localized fermionic states that appear at the junction (or weak link) between two superconducting electrodes. They are at the core of the microscopic description of the Josephson effect. InAs nanowires implement finite-length weak links characterized by spin-orbit coupling and electrostatically-tunable conduction properties.

By coupling the weak link to a high quality factor microwave resonator, following the circuit quantum electrodynamics (cQED) approach, the Andreev states can be efficiently isolated from external noise, and the resonator frequency readout gives access to their microscopic occupancies. We model this coupling to achieve optimal sensitivity and to understand in detail the response of the resonator coupled to the weak link.

We have performed the microwave spectroscopy of Andreev states, and measured their dependence on the superconducting phase difference. The spectra reveal two effects. The first one is the lifting of the states' spin degeneracy due to spin-orbit coupling. This results in spectroscopic lines characterizing the change of the spin state of a single quasiparticle in the weak link. The second one is the influence of Coulomb interactions between quasiparticles, reminiscent of the splitting in singlet and triplet states of two interacting spin-1/2 electrons. Theoretical modeling of finite-length weak links allows to account for these effects.

We also characterize the Andreev states by time-resolved measurements. Quantum bits (qubits) are obtained either using the ground state and a state where a pair of quasiparticles is excited ; or two states with a quasiparticle in different Andreev states. We have measured the lifetimes and coherence times of these two types of "Andreev qubits".